Traçage des sédiments dans les séries syn-orogéniques du bassin d'Aquitaine

Stéphane Mustafa Al Reda

Thèse de doctorat

NNT : 2020UPASS100

université PARIS-SACLAY

Traçage des sédiments dans les séries syn-orogéniques du Bassin d'Aquitaine

Thèse de doctorat de l'université Paris-Saclay

École doctorale n° 579, sciences mécaniques et énergétiques, matériaux et géosciences (SMEMAG)
Spécialité de doctorat : Terre solide : géodynamique des enveloppes supérieures, paléobiosphère
Unité de recherche : Université Paris-Saclay, CNRS, GEOPS, 91405, Orsay, France.
Référent : Faculté des sciences d'Orsay

Thèse présentée et soutenue à Orsay, le 30 juin 2020, par

Stéphane Mustafa AL REDA

Composition du Jury

Philippe SARDA Professeur, Université Paris-Sud	Président
Andrew CARTER Professeur, University of London	Rapporteur & Examinateur
Frédéric MOUTHEREAU Professeur, Université Toulouse 3	Rapporteur & Examinateur
Raphaël PIK Directeur de recherche, Université de Lorraine	Examinateur
Frédéric CHRISTOPHOUL Maître de conférence, Université Toulouse 3	Examinateur
Jocelyn BARBARAND Professeur, Université Paris-Sud	Directeur de thèse
Cécile GAUTHERON Professeure, Université Paris-Sud	Co-directrice de thèse
Eric LASSEUR Ingénieur, BRGM	Invité
Charlotte FILLON Ingénieure, TOTAL	Invitée

This thesis is funded in the framework of the source-to-sink project by BRGM and TOTAL

Résumé étendu

La zone de dépôt continentale d'un système source to sink constitue une archive sédimentaire importante pour la compréhension de la formation de la chaîne et son étude est primordiale pour une meilleure compréhension de son développement. Cette étude se focalise sur le versant nord des Pyrénées, le bassin d'Aquitaine, dont les sédiments syn-orogéniques datant de l'Éocène sont préservés et affleurent dans sa partie orientale, les Corbières. Ces sédiments, en majorité conglomératiques connus sous le nom de « Série de Palassou » traduisent une phase d'érosion majeure des reliefs, accompagnant la continentalisation des bassins au cours de l'Yprésien et la période de raccourcissement principale de l'orogenèse pyrénéenne. La série de Palassou a été classifiés en trois unités tectono-stratigraphiques suivant la nature des clastes. Les unités 1 et 3 (Yprésien supérieur – Lutétien et Priabonien respectivement) semblent contenir du matériel méso-cénozoïque, l'unité 2 (Lutétien moyen/supérieur - Bartonien) présente une forte dominance de roches paléozoïques. L'objectif de cette thèse est de reconstruire le remplissage du bassin d'avant-pays nord-pyrénéen au cours de l'Éocène afin de mieux comprendre le comportement de la zone de dépôt continentale. Les approches qui ont été utilisés dans le cadre de cette thèse sont la sédimentologie, la thermochronologie basse température et le traçage des sources. Le couplage de ces 3 approches a permis de mieux contraindre l'enregistrement thermique dans les dépôts de l'Éocène et identifier l'origine et la dynamique des dépôts.

Les deux premières unités de la série de Palassou ont fait l'objet d'études sédimentologiques dans ce travail de thèse. Trois logs stratigraphiques ont été étudiés dans le synclinal de Talairan représentant le remplissage de l'unité 1, ainsi que deux autres plus à l'ouest représentant la transition de l'unité 1 à l'unité 2. Les environnements de dépôts caractérisés dans l'unité 1 montrent une progradation marquée par des avancées de faciès conglomératiques qui, sur une verticale, se traduisent par des dépôts chenalisés de plus en plus grossiers et amalgamés. Ils sont suivis par une retrogradation vers des faciès de plaine alluviale voire même des niveaux lacustres. Les dépôts étudiés dans le synclinal de Talairan correspondent à trois séquences de remplissage sédimentaires piégés dans le synclinal. Ce n'est qu'à partir de la quatrième séquence, montrant la transition de l'unité 1 à l'unité 2, que les sédiments sont étendus au-delà du synclinal de Talairan. Cet élargissement de la zone de dépôt est contemporain avec un changement de la nature des clastes lors du passage de l'unité 1 à l'unité 2 et traduit un élargissement de l'aire drainée dans la source. Une reconstruction paléogéographique issue principalement de ces résultats a permis de suivre l'évolution du maximum de progradation pour les unités 1 et 2 entre l'Yprésien moyen et le Lutétien moyen.

Des clastes de granite issus de l'unité 2, ainsi que quelques échantillons de granite de la Zone Nord Pyrénéenne et de la Zone Axiale, ont fait l'objet d'étude en thermochronologie basse températures.

Deux méthodes ont été appliqués, la méthode trace de fission sur apatite (AFT) et la méthode (U-Th-Sm)/He sur apatite (AHe). Les âges AFT obtenues sont compris entre 27±2 et 43±4 Ma et sont proches des âges de dépôts. Les âges AHe varient de 13±1 à 76±5 Ma et montrent une grande dispersion des âges. Ceux plus vieux que les âges de dépôt semblent préservés le signal de la source et ceux plus jeune que les âges de dépôts reflètent un événement thermique. Une analyse détaillée des résultats obtenus, ainsi que les résultats de modélisation thermique montrent (1) une exhumation lente de 70 à 55 Ma qui peut être expliquée par un long séjour dans la Zone de Rétention Partielle, (2) un refroidissement Paléocène-Éocène dans la source, (3) un épisode de réchauffement post-dépôt dans le bassin représenté par des âges AHe plus jeunes que l'âge de dépôt et (4) une exhumation finale des dépôts dans le bassin au Miocène. Ces résultats montrent une histoire comparable entre les flancs nord et sud des Pyrénées caractérisée par une forte aggradation des piémonts pendant la phase syn- à tardi-orogénique probablement à l'origine du développement des surface de faible relief à haute altitude dans les Pyrénées, suivie d'une phase d'exhumation Miocène déjà démontrée sur le flanc sud. Ces 2 histoires se déroulent à des moments différents, l'excavation du flanc nord des Pyrénées s'est déroulée entre le début et milieu du Miocène alors que celle du flanc nord s'est déroulée plus tard au cours du Miocène.

Pour la partie traçage des sources, des datations U/Pb sur zircon sont effectuées par LA-ICP-MS sur des clastes de granite de l'unité 2 et sur la matrice des conglomérats des trois unités. Ces analyses sont couplées aux directions de paléocourants mesurés dans les dépôts fluviatiles et aux analyses Raman effectuées sur des clastes de flysch noirs provenant de la transition de l'unité 1 à l'unité 2. Les résultats U/Pb sur zircon montrent une dominance d'âges varisques dans la partie supérieure des dépôts de l'unité 1. Un signal varisque est aussi obtenu pour la matrice de conglomérats de l'unité 2. Les clastes de granite montrent pour la majorité des âges entre 324 et 335 Ma. Quant à l'unité 3, les âges U/Pb montrent un spectre d'âge très variés allant du Varisque au Cadomien. Les analyses Raman sur les flysch noirs montrent des pics de température comprises entre 495 et 587°C, comparable à ceux obtenus dans la Zone Nord Pyrénéenne (ZNP) sur des dépôts de flysch noirs. Des âges U/Pb sur zircon entre 324 et 334 Ma sont obtenus pour certains massifs de la Zone Axiale (ZA) des Pyrénées et pour le bloque Corso-Sarde; cependant, la possibilité d'une source Corso-Sarde est écartée du fait de sa déconnection avec les Corbières à l'Éocène, des directions de paléocourants et du caractère proximal des dépôts. L'interprétation des résultats obtenus montre que les dépôts de l'unité 1 est issue principalement du décapage de la couverture méso-cénozoïque de la ZNP à l'Yprésien supérieur, suivie de l'érosion des massifs Varisques et des dépôts de flysch noirs dans cette zone. Pour l'unité 2, les dépôts s'accompagnent par un changement de la nature des clastes et par un élargissement de la zone de dépôts traduisant des domaines plus larges drainées dans la source. On en déduit une source Pyrénéenne provenant de la ZA pour cette unité. Pour l'unité 3, le spectre large des âges obtenus

suggèrent un bassin versant assez large et un remaniement important l'âge de dépôt de cette unité contemporain avec une phase d'exhumation rapide des Pyrénées montre que la ZA des Pyrénées représente une source des sédiments. En plus, les clastes Méso-Cénozoïques de l'unité 3 suggèrent un remaniement important qui semble provenir probablement du recyclage des sédiments du bassin. L'ensemble de ces résultats a permis de reconstruire le cheminement des sédiments au cours de l'Eocène dans les Corbières et de proposer une reconstruction paléogéographique de ce domaine sur la base de ces résultats.

À la mémoire de mes parents,
je pense fort à vous…

Remerciements:

Ce travail de thèse n'aurait pas pu se faire sans l'aide et le soutien de nombreuses personnes que j'ai eu la chance de rencontrer pendant ces merveilleuses années passées à Orsay. Sachez bien qu'il n'est jamais assez de vous remercier !

Il m'est évident avant tout d'exprimer ma gratitude à Jocelyn Barbarand, mon directeur de thèse. Je vous remercie de m'avoir accompagner dans cette aventure. J'ai pu apprécier, pendant toute cette période, vos compétences scientifiques et vos qualités d'encadrement, qui ont été d'une grande importance pour le bon déroulement de la thèse. Merci pour votre patience, vos conseils et votre soutien dans la réalisation de ce travail. J'ai pu profiter de vos connaissances qui englobent la plupart les questions que je me suis posées. Vous avez toujours été disponible et à l'écoute pour discuter des résultats tout en me forçant à aller plus loin dans l'argumentation de mes interprétations et idées. Tout ceci malgré votre emploi de temps souvent chargé. Un grand merci pour la personne que vous êtes, pour vos qualités humaines. C'était un plaisir d'avoir mener ma thèse sous votre direction !

Je suis très honoré que Messieurs Andry Carter et Frédéric Mouthereau aient accepter de rapporter mon manuscrit de thèse et juger la qualité de mon travail. Je remercie également Raphaël Pik, Frédéric Christophoul, Eric Lasseur et Charlotte Fillon, d'avoir accepté de faire partie de mon jury.

Je tiens à remercier les co-directeurs de ma thèse :

Merci à Cécile Gautheron, avec qui j'ai appris en long et en large la méthode de datation (U-Th-Sm)/He, merci pour ta contribution dans ce travail, depuis l'emploi de la méthode jusqu'à l'interprétation des résultats. Je te remercie pour ton écoute et tes conseils. J'apprécie beaucoup ton savoir et ta passion pour la recherche.

Je remercie Eric Lasseur et Justine Briais pour m'avoir ouvert au monde de la sédimentologie. J'ai appris plein de chose avec vous sur le terrain et j'ai pu profiter de votre expérience dans ce domaine. Merci pour tout !

Merci à Nicolas Loget, pour toutes les discussions intéressantes qu'on a pu avoir et pour sa contribution à la réussite de cette thèse.

Je remercie également les personnes qui ont participé à ce travail en particulier, et à ma formation en général dont :

*Claire Boukari qui m'a épaulé dans la préparation des zircons pour la méthode U/Pb et pour le polissage des plots d'apatite pour la méthode traces de fission
*Frédéric Haurine qui m'a formé sur l'utilisation de l'ICPMS
*Rosella Pinna-Jamme qui m'a initié sur le tri des apatites pour la méthode (U-Th-Sm)/He.
*Serge Miska pour m'avoir formé sur l'utilisation du DRX et pour l'analyse des lames d'argile
*Olivier Dufaure avec qui j'ai appris la préparation des lames d'argile
*Valérie Godard pour la préparation des lames polies de granite
*Julius Nouet et Omar Boudouma pour l'observation des zircons sous miniMEB et MEB.
*Michel Faure pour m'avoir formé sur la l'utilisation de la micro-sonde.

Merci aux chefs et gestionnaires du projet « source to sink » pour l'organisation des écoles thématiques, summer schools et divers réunions. Merci aux chercheurs, post-doctorants et doctorants de ce projet avec qui j'ai pu avoir des échanges intéressants.

Il serait irréaliste de dire qu'une thèse est un long fleuve tranquille : elle est faite de moments de doute, de remises en question et de sentiments de solitude. Mais ce sont eux qui nous donnent la rage de vaincre et l'envie de réussir et au final, aidé de nos amis et notre famille, tous ces moments s'oublient très vite et on n'en retient que le fruit de notre travail : la réussite !

Je retiens la très bonne ambiance qui règne dans les locaux du laboratoire Géosciences Paris Sud. Je commence par Hadrien, la dynamo du bureau. Merci de m'avoir supporter tout ce temps et désolé pour les milliards de fois que je t'ai demandé de baisser le volume de ta musique. J'apprécie beaucoup la personne que tu es, et saches que je regrette ne plus t'avoir comme co-bureau ☹. Je remercie également Margaux, avec qui il est toujours agréable de discuter, merci pour ton écoute, ton encouragement pendant la période de rédaction et ta très bonne humeur. Alexis, le plus sympa de la planète, merci pour tout, pour ta gentillesse, pour ton aide, ta disponibilité et pour le co-voiturage pour rentrer chez moi quand j'habitais à Massy. Merci à Louise, pour les moments qu'on a partagé ensemble (anniversaire, soirées et pauses), pour sa bonne humeur et son dynamisme. Sans oublier Maher, Maxence, Oriane, Caroline, Consuelo, Thomas F., Quentin, Maxim LB, Maxim V., Floriane, Aurélie et Carlos, merci à vous tous pour tous les moments qu'on a partagé ensemble, les pauses de 16h00, le jeu de fléchettes, les sorties au bar/restaurants. Merci à Aurélie pour les pauses café/gâteaux du vendredi. Enfin, un grand merci pour toutes les personnes que j'ai rencontré dans ce labo, personnel permanent et non-permanent. J'en garde un beau souvenir !

Je remercie chaleureusement mes amis libanais d'Orsay. Merci à Elie et Marwa pour leur

humour et bonne humeur. Merci pour les repas, balades sur Paris, voyages et soirées. Merci à M. Tarhini, M. Ayoub et Dima, à ce groupe que j'ai croisé à mon arrivé à Orsay et qui n'ont fait que rajouté de la bonne ambiance et de la joie à nos soirées.

Un grand merci aux personnels du Laboratoire géosciences Le Mans que j'ai rejoint à partir du mois d'octobre 2019 et dans lequel règne une très bonne ambiance. Merci à Salomé qui, grâce à elle, j'ai connu les bienfaits des graines de chia et du kéfir (bio bien sûr !). Merci de nous avoir alerter sur la nécessité de réagir pour sauver la planète (consommer bio et local, éviter le plastique…) et sur les conséquences de l'effet de serre (comme le fait que la saison des brocolis a commencé en février cette année alors que d'habitude elle commence plus tard... c'est très grave !).

Mes remerciements du fond du cœur vont à ma sœur Fatima et mon frère Mohamad qui, sans leur confiance et leur soutien, ce travail n'aurait jamais vu le jour. Un grand merci à mon beau-frère Mohamad, à ma belle-sœur Tala, à mes tontons Michel et Hamed, à mes tatas Liza et Marie-France qui n'ont pas manqué de m'encourager pendant toute cette période. Une pensée pour ma grand-mère Mariam, à qui je dois beaucoup pour avoir financé mes études.

Enfin, il n'est jamais assez de remercier ma source d'inspiration et de force, mes parents ! je pense à vous et je vous aime fort.

Table of Contents

List of figures

List of tables

Chapter 1: Introduction and problematic

Mountain belts are the result of the balance between surface processes, tectonic and climatic forcing (Figure 1.1). Erosion contribute to topography shaping in mountain belts and sediments production. As erosion modifies the distribution of deformation in orogenic belts (Figure 1.1), it is considered a first-order control on orogenesis (Pinter and Brandon, 1997; Sinclair et al., 2005; von Blanckenburg, 2006). Deciphering sedimentary records in foreland basin remains important to understand what governs variations in sediment provenance from the belt through time and reconstruct accurately exhumation patterns in the orogen. To do so, a deep understanding of the integrated sedimentary system is needed. A study of the middle Eocene – Oligocene sediment routing system in the south-central Pyrenees by Allen et al. (2013) allows the understanding of the syn-tectonic evolution of the foreland basin. The study is based on the volumetric ratio of sediment supply and accommodation: small, steep slopes and local sedimentary systems are usually supplied by low sedimentary discharge while large systems with shallow sloping and megafan structures are supplied by high to very high amount of sediments. The same idea considering the ratio of sediment supply and accommodation has been used by Derer et al. (2003) to investigate the depositional history of the Upper Rhine Graben from the late Eocene to the early Oligocene. The objective of this study was to analyse the structural configuration and evolution of the Upper Rhine Graben and their effect on syn-rift sedimentation.

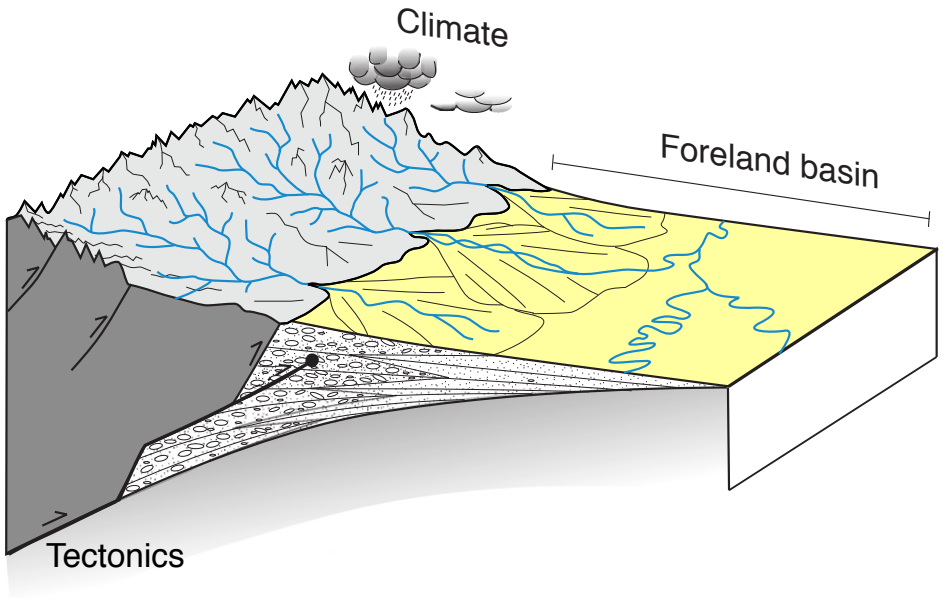

Figure 1.1: Factors controlling orogen development and sediment infilling in foreland basin. (modified from Sinclair and Naylor, 2012).

The relationship between relief emergence and erosion in mountain belts has been investigated in several studies (Montgomery and Brandon, 2002; Hovius and Stark, 2006; Braun et al., 2014; Ducassou et al., 2014). In the Olympic Mountains (USA), the relation between erosion rate and the mean local relief on a high resolution DEM (Digital Elevation Model) reveals that erosion rate

controls tectonic uplift episodes in mountain belt as mentioned by Montgomery and Brandon (2002). When tectonic uplift rates are high, erosion is caused essentially by a high frequency of landslides. However, when tectonic uplift rates are slower, erosion is produced by the generated steep slopes. Such conclusions are central in the understanding of the global sediment flux and the influence of tectonics, climate and erosion in the shaping of the topography of the mountain belt.

A simple way to consider an integrated sedimentary system from source to sink was presented first by Schumm (1977) and described later in detail by Castelltort and Van Den Driessche (2003) and Sadler and Jerolmack (2015). A source to sink system (Figure 1.2) starts in the mountain belt where sediments are produced by erosion, then transported by the drainage network to a transfer zone before being deposited in the sink area, the final destination of sediments. Such system is subdivided, thus, into three zones (Figure 1.2): 1) an erosion and denudation zone taking place in the mountain belt and activated by the forcing parameters climate and tectonics, 2) a transfer zone where sediments are transported by rivers directly to the final sink or stored temporarily and 3) a deposition zone where the final sediment storage occurs. The "transfer zone" is assumed to be the part of the sedimentary system that is neither net-denudational nor net-accumulative (Romans et al., 2016), it is thus considered as a very important indicator of system response to perturbations and a precious archive for reconstructing paleo-sediment routing system. The transfer zone contains dominantly siliciclastic sediments, deposited through sediment transportation from source to sink.

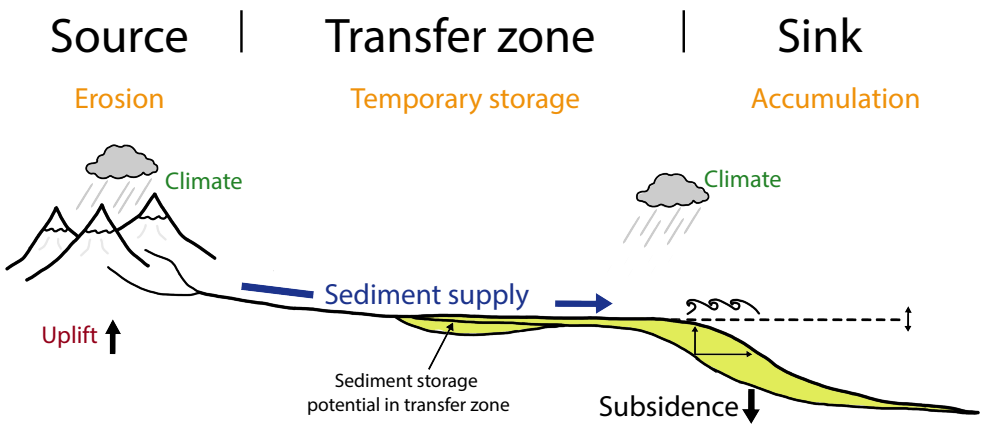

Figure 1.2: Schematic representation of a sediment routing system emphasizing erosion in the source, temporary storage in the transfer zone and accumulation in the sink (modified from Romans et al., 2015).

The source to sink system has been applied to many sedimentary system of which the most representative examples have been applied on the Danube river – Black sea (Central Europe) by Matenco and Andriessen (2013), the Tian Shan – Junggar Basin (northwest China) by Yang et al. (2013) and the Pyrenees – Ripoll basin by Odlum et al. (2019). Changes in the source areas due to past and active tectonics in the Danube River – Black sea controlled the transportation and deposition in the adjacent sinks. Matenco and Andriessen (2013) characterized the Danube River – Black sea

sediment routing system using basin evolution modelling, sediment dynamics in the basin based on stratigraphy and sedimentary studies, sediment input and provenance using thermochronology. Such analysis led to the quantification of different types of connectivity influencing pathways of sedimentary fluxes and the mechanisms of sedimentary distributaries shifting across the basins and their impact on the evolution of geomorphic landforms. The investigation of the Tian Shan ranges – Junggar Basin sediment routing system has been done by Yang et al. (2013) for the Paleozoic - Cenozoic sediments exposed along the basin using U/Pb zircon geochronology and sedimentary studies. Depositional environments have been characterized along the basin and are mainly lacustrine and fluvial. Changes in sediment provenance have been investigated using U/Pb zircon ages and correlated with the major tectonic phases in the belt. Results led to four stages of evolution from the Late Carboniferous to the Neogene characterized by source changing contemporaneous with the major tectonic phases of the orogen (Yang et al., 2013). Sediment provenance evolution from the eastern part of the South Pyrenean foreland basin has been studied by Odlum et al. (2019) using low temperature thermochronology and U/Pb dating methods. Deposited sediments recorded the total evolution of the mountain belt and obtained results in detrital zircon (U-Th-Sm)/He and U/Pb show a middle Eocene change in the source area contemporaneous with the mid-Eocene Climatic Optimum. This may explains a first-order climatic factor that enhanced erosion and increased the exhumation of the belt leading to the change of the source area (Odlum et al., 2019). Tectonic factor is considered in this study to have a second-order control.

The case of the Pyrenean orogen

In this thesis, I have investigated the evolution of the sedimentary records in the Pyrenean foreland basin (Figure 1.3). The Pyrenees is a mountain belt located in the south-west of France and developed due to the collision between the Iberian and European plates from the Late Cretaceous to the Oligocene. The Pyrenean orogen constitutes a doubly vergent orogenic belt subdivided into five distinct structural domains comprising from the north to the south, the Aquitaine Basin, the North Pyrenean Zone, the Axial Zone, the South Pyrenean Zone and the Ebro Basin (Figure 1.3). The geographic area has been selected in the framework of the “Source to Sink” project funded and carried out by TOTAL and the BRGM. The growth of the Pyrenean belt has been demonstrated as essentially due to convergence (Munoz et al. 1986; Vergés et al. 2002; Mouthereau et al. 2014; Ford et al. 2016; Rougier et al. 2016; Ternois et al. 2019) and the influence of climate on the development of the belt could have a first-order influence during the late Eocene as suggested recently by Odlum et al. (2019). Two phases of orogenic growth have been recognized, a first early orogenic phase during the Late Cretaceous, and a second (major) phase between the early Eocene and the Oligocene (Mouthereau et al., 2014; Ford et al., 2016; Vacherat et al., 2016; Ternois et al., 2019). The exhumation of the

Pyrenean orogen has been constrained by plate kinematics in order to estimate the total amount of plate convergence and the distribution of shortening (Choukroune 1989; Roure et al. 1989; Olivet 1996; Beaumont et al. 2000; Rosenbaum et al. 2002; Sibuet et al. 2004; Jammes et al. 2009; Vissers and Meijer 2012; Mouthereau et al. 2014). It was also estimated using low temperature thermochronology to allow a better understanding of the cooling history of Pyrenean massifs (Yelland, 1991; Fitzgerald et al., 1999; Sinclair et al., 2005; Maurel et al., 2008; Gunnell et al., 2009; Vacherat, 2014; Bosch et al., 2016; Vacherat et al., 2016; Ternois et al., 2019). These studies demonstrated a diachronous exhumation of the Pyrenean orogen from the north to the south and from east to west.

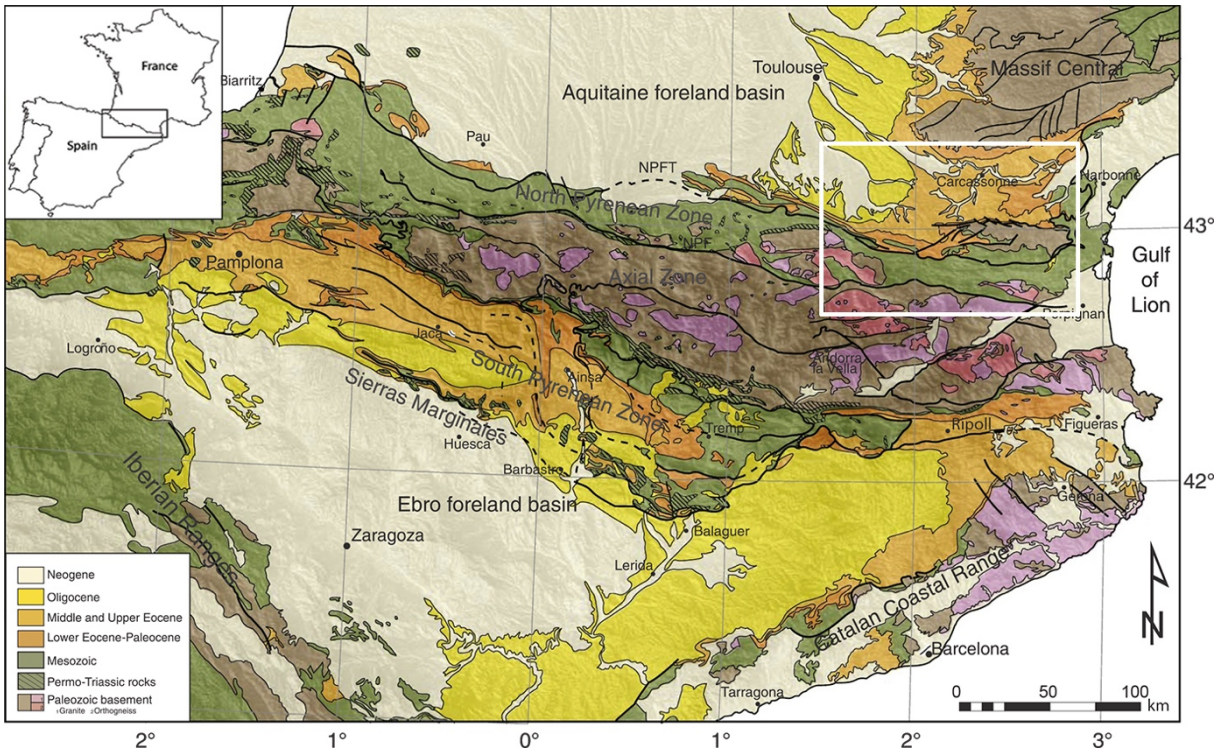

Figure 1.3: Geological map showing the Pyrenean belt and its two foreland basins: the Aquitaine Basin in the north (retro-foreland basin) and the Ebro Basin in the south (pro-foreland basin).White frame represents the studied area (modified from Mouthereau et al., 2014).

The analysis of sediments deposited in the transfer zone of both the retro- (the foreland basin evolving on the upper (European) plate) and pro-foreland (the foreland basin evolving on the subducted (Iberian) plate) basins (Figure 1.3) provides a powerful way to get information about the emergence of the orogen through time. Erosion is activated during the growth of the Pyrenees as a response to tectonic activity, it has recorded the early phases of exhumation of the Pyrenean massifs. Sediments produced by erosion preserve the entire phases of orogenic development. When these sediments are preserved, they could be used to reconstruct the evolution of the sediment routing system. Such study has been accomplished in the eastern (Odlum et al. 2019) and the central part

(Whitchurch et al., 2011) of the southern foreland basin (Figure 1.3) using low temperature thermochronology and U/Pb geochronology dating methods. Obtained data in the basin (pro-foreland) and in the Pyrenean massifs, in addition to climate proxies permit the highlight of the dominant source area and the foreland basin evolution (Odlum et al. 2019). In the central part of the pro-foreland basin, the same methods have been used to understand the evolution of the sediment routing system of this area (Whitchurch et al., 2011). A similar approach is still not available in the north Pyrenean foreland basin.

Previous studies on the syn-orogenic deposits in the north Pyrenean foreland basin show that the sedimentation in the basin recorded a transition phase from marine to continental deposits. The marine deposits contain essentially fine lithologies as marls, fine sandstone and limestone, and fossils like oysters, gastropods and foraminifera, while the fluvial deposits are represented essentially by thick conglomeratic series (Ovtracht and Lenguin, 1977; Plaziat, 1984; Ellenberger et al., 1985; Crochet, 1989; Christophoul et al., 2003). The transition phase occurred during the late Ypresian time. It is characterized by the deposition of a thick late Ypresian-Oligocene conglomeratic series, known as the "Palassou" series cropping out today in the eastern part of the retro-foreland basin (Figure 1.3). The deposition of the Palassou series is contemporaneous with the second phase of the development of the Pyrenees. This part of the basin, infilled with conglomerates is, thus, considered as an evolving transfer zone that is controlled by the development of the Pyrenean belt.

Extensive studies on the age of the Palassou series have been made between 1964 and 1984 and are focused essentially on the determining of the deposition age of this series using biostratigraphy. Fossils like molluscs, birds footprint and mammals have been used to determine the deposition age of the Palassou series (Plaziat 1964, 1970; Tambareau 1976; Plaziat 1981, 1984). As these fossils are the only datable content, the underlying marine Eocene deposits have been also investigated (Tambareau, 1972; Tambareau, 1976; Plaziat, 1984b; Tambareau et al., 1995). Later, a classification of this series into three tectono-sedimentary units based on clast content and petrology has been made by Crochet (1989). The first unit contains clasts derived from the Meso-Cenozoic cover, the second unit clasts are partly derived from Paleozoic plutonic rocks, especially granite, and the third unit content is similar to the first unit, Meso-Cenozoic clasts. Christophoul et al. (2003) discussed the relationship between tectonics and sedimentary infilling in the eastern part of the north Pyrenean foreland basin. However, the link between the evolution of the basin and the exhumation of the Pyrenean orogeny remains poorly investigated. Previous work on the retro-foreland basin was essentially destinated to the understanding of the stratigraphy of the basin and the evolution of sediment infilling. The obtained results have not been linked to the evolution of the topography and exhumation of the Pyrenees. This is why the sediment routing system in the north Pyrenean foreland basin needs to be investigated. The north-eastern part deposits of the basin recorded the entire

exhumation of the Pyrenees and the study of these deposits helps to reconstruct the source to sink system.

Going from the previous work on the Palassou series, the main goal of this thesis is to reconstruct the evolution of the sediment routing system in the north Pyrenean foreland basin. Achieving this goal allows us to understand how the transfer zone of the basin was acting during the Eocene and where the Palassou series are sourced from (Figure 1.3).

We started first sedimentological studies of the Palassou series in order to characterize the geometry of the deposits and their implication in the deformation and the sediment routing system. Second, we aimed to understand the mode of infilling of the basin during the Eocene and the identification of the source area for each unit. This improves our knowledge about the erosion phases in the source area and permits to understand the control of the belt on the organization and evolution of the retro-foreland basin. Third, results obtained in this thesis have been used to reconstruct the paleogeography of the Corbières region (eastern part of the Aquitaine Basin) from the Late Ypresian to the Oligocene. Coupling our results with previous studies in the southern foreland basin have contributed to a global reconstruction of the whole Pyrenean domain during this period.

Organization of the manuscript

The approaches that have been used in this PhD are key to understand the sediment infilling of the Palassou series, to constrain the thermal record in the Eocene deposits and identify the origin and dynamics of the deposits.

The sedimentological studies of Palassou series is focused on the units 1 and 2. They are based on the characterization of the depositional environments among 4 stratigraphic logs and the interpretation of the obtained data in terms of sediment budget for each unit. The obtained results provide information about the geometry of the deposits and their evolution from the Ypresian to the Bartonian. It allows to better understand the implication of the deformation in the belt on the sediment routing system. The mineralogical content of clay analysed using XRD (X-Ray Diffraction) provide information about the erosion phases in the belt.

Low temperature thermochronology is commonly applied in foreland basin studies for quantification of the amount of deposited material in the basin. It is based on the capacity of some minerals like apatite and zircon, to reveal their own cooling history when cooled below a given temperature. Such method improves the understanding of the thermal history of the basin and allows us to estimate the former total thickness of the sedimentary deposits in the Corbières region. Apatite fission track (AFT) and (U-Th-Sm)/He (AHe) on apatite crystals are the methods applied in the low temperature thermochronology part of this thesis. The obtained results give information about the evolution of the transfer zone and the estimation of sediment thickness deposited during the Eocene.

The origin and dynamics of the Palassou series have been investigated using current paleodirections, zircon U/Pb geochronology and Raman Spectroscopy of the Carbonaceous Material (RSCM). U/Pb method has been applied on granite clasts from the units 2 & 3 and conglomerate matrix from the units 1, 2 & 3. RSCM has been applied on black flysch clasts from the unit 1 and the transition unit1-unit2. The combination of these methods allows the determination of the source areas for each unit and their evolution during time. The comparison of the obtained U/Pb ages with other ages in the surrounding reliefs could be helpful in the understanding of the evolution of the drainage system during the Eocene. It allows also the determination of sediment provenances and the reconstruction of the sediment routing system. The application of such method requires, thus, a good control on U/Pb ages in the surrounding reliefs.

Sedimentology, low temperature thermochronology (LTT) and geochronology results produced during this Ph.D improve our knowledge on the evolution of the Palassou series and allows us to better understand the exhumation of the Pyrenees. Obtained results have led to the reconstruction of the sediment routing system in the eastern part of the north foreland basin and provide a global overview of the paleogeography of the Pyrenean domain. This overview is made by associating this work to the sediment routing system results in the south Pyrenean foreland basin.

Chapter 2: Regional context and methodology

Sediment routing in foreland basins requires an integrated knowledge of the sedimentary system and the evolution of possible source areas. This thesis is focused on the study of syn-orogenic sediments deposited in the eastern part of the Pyrenean retro-foreland basin (the Corbières region, France). Postulated surrounding reliefs during the Eocene include the Pyrenees, the French Massif Central and the Corsica-Sardinia block (Lacombe et Jolivet, 2005). The geology of these potential source areas has thus been investigated in detail in the first part of this chapter. The second part presents the state of the art of the used method: apatite fission track (AFT) and (U-Th)/He (AHe) low temperature thermochronology, U/Pb zircon geochronology and the preparation of clay aggregate thin slides for X-Ray Diffraction (XRD) analysis.

The first part (I) of this chapter contains the geological settings of the Pyrenees and the eastern part of the retro-foreland basin in the section (I.1). The geology of the Pyrenees, the French Massif Central (with a focus on the Montagne Noire) and the Corsica-Sardinia block have been reviewed from the Neoproterozoic to the Permian in the section "I.2" with a particular attention to zircon and monazite U/Pb ages obtained in the possible source reliefs. The section "I.3" of the same part focuses on the evolution of the Pyrenean areas from the Triassic to the Miocene time as constrained from kinematic, low temperature thermochronology, geochronology and Raman spectroscopy studies. The main phases of the development of the Pyrenees from the rifting phases to the collision have been investigated in this section. The section "I.4" consists in a reconstruction of the paleogeography of the Pyrenean domain based mainly on Vacherat et al. (2017) results and updated with recent studies on the sediment routing system in the Pyrenean domain.

The second part (II) of this chapter presents recent achievements in low temperature thermochronology, in particular in AFT and AHe as well as zircon U/Pb geochronology, in addition to the analytical conditions used in this thesis.

I. Geological settings and evolution of the Pyrenees, the Montagne Noire and the Corsica-Sardinia block

I.1 Geological setting of the Pyrenees and the eastern part of the Aquitaine Basin

I.1.1 Geological settings of the Pyrenees

The Pyrenean mountain belt is composed of five structures from the north to the south (Figure 2.1). The Aquitaine Basin in the north represents the retro-foreland basin of the belt and contains essentially syn- to post-orogenic deposits. It is separated from the North Pyrenean Zone (NPZ) by the North Pyrenean Frontal thrust (NPFT) (Figure 2.1). The NPZ is characterized by north-vergent reverse faults, exhuming Paleozoic basement rocks including granitic bodies (Agly, Ansignan, Trois Seigneurs, Lacourt, Foix & Ercé), highly deformed Mesozoic deposits, Paleocene and lower Eocene cover rocks (Souquet 1986; Roure et al. 1989; Deramond et al. 1990). The North Pyrenean Zone is separated from the Axial Zone by the North Pyrenean Fault (NPF) (Muñoz, 1992) (Figure 2.1). The Axial Zone consists of Paleozoic rocks affected by LP-HT metamorphism during the Variscan orogeny (Zwart, 1962; Zwart and De Sitter, 1979; Gleizes et al., 1998; Denèle et al., 2014; Olivier et al., 2016), in addition to Cambrian and Ordovician gneiss bodies. The Axial Zone is bounded to the south by the South Pyrenean Zone (SPZ) (Figure 2.1). The latter zone is characterized by south vergent faults translating the Mesozoic and Cenozoic deposits above the Triassic evaporites (Puigdefàbregas et al., 1992; Thomson et al. 2017). The SPZ terminates by the South Pyrenean Frontal Thrust (SPFT) where the Ebro Basin starts. The pro-foreland basin consists of Palaeocene red beds, lower and middle Eocene platform carbonates, and middle Eocene evaporites overlaid by a thick succession of middle and upper Eocene marls (Puigdefabregas et al. 1986; Burbank et al.1992; Vergés et al. 1995a; Ramos et al. 2002; Barrier et al. 2010; Whitchurch et al. 2011).

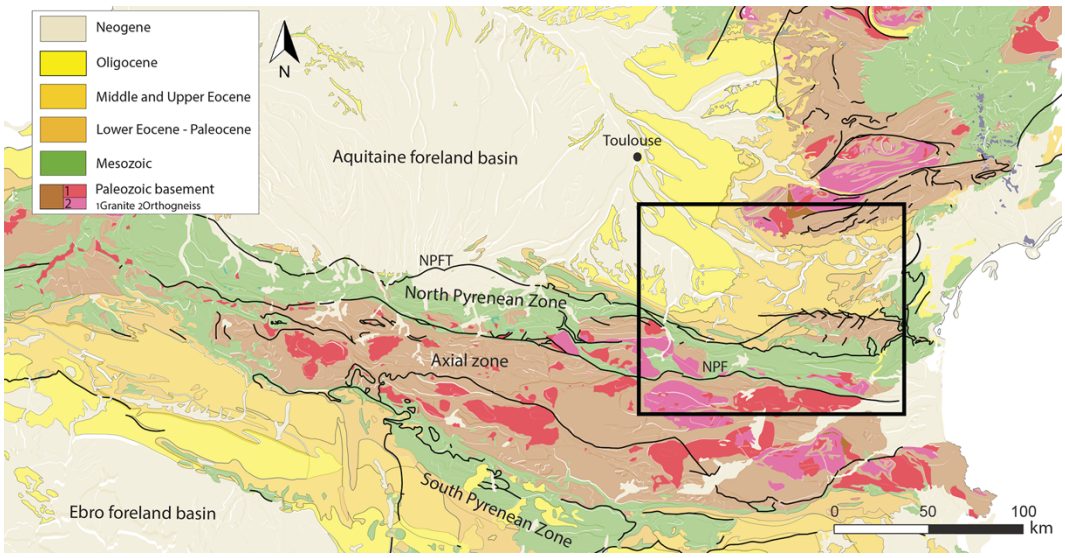

Figure 2.1: Geological map of the Pyrenean domain and the studied area (zoom on the studied area in Figure 2.2). From the north to the south: the Aquitaine Basin, the North Pyrenean Zone (NPZ), the Axial Zone, the South Pyrenean Zone (SPZ) and the Ebro Basin.

I.1.2 The stratigraphy of the Eastern Aquitaine Basin

From the Late Cretaceous, turbidites were deposited contemporaneously with the early orogenic phase of the Pyrenees. This first syn-orogenic phase was followed by the deposition of Palaeocene red beds and Thanetian to Ypresian shelf platform carbonates (Ford et al., 2016). In the eastern part of the Aquitaine Basin, the Corbières region, the last marine deposits preceding the continentalisation of the basin are well dated (Plaziat, 1984). The base of the series contains essentially foraminiferal and bivalve-bearing shelf carbonates (Alveolina limestones, Figure 2.3) (Doncieux 1912; Massieux 1973; Pautal 1985) of early Ilerdian age (Serra-Kiel et al. 1998), followed by blue marls deposits (Figure 2.3) constituted mainly of silty to sandy marls and sandstone (Rey and Bousquet 1981; Plaziat 1984; Pautal 1985; Tambareau et al. 1995) and ending with an Oysters sandstone series (Christophoul et al. 2003). The upper part of the blue marls and Oysters sandstone series (Figure 2.3) form a deltaic environment sourced from the south according to paleo-environmental studies (Rey and Bousquet 1981; Plaziat 1984; Pautal 1985). The evolution from marine to continental sedimentation in the eastern part of the basin, that occurred during the middle Ypresian time, is confirmed by biostratigraphy on molluscs (Doncieux, 1912; Hottinger, 1962; Plaziat, 1970; Plaziat, 1984). The main exhumation phase of the Pyrenees is considered in the basin coeval to the deposition of alluvial and fluvial deposits starting in the late Ypresian, which is known as the Palassou conglomeratic series (Buis and Rey, 1975; Crochet, 1989; Ford et al., 2016) (Figure 2.2) (Figure 2.3). The Palassou series formed three depositional units of late Ypresian to Priabonian age, each one having different clast contents (Crochet 1989) and a thickness around 750 m for the unit 1 east to Limoux (Ovtracht and Lenguin, 1977), ~700 m for the unit 2 near Carcassonne

(Ellenberger et al., 1985) and ~150 m for the unit 3 cropping out near Mirepoix (Cavaillé 1975) (Figure 2.2). Outcrops of these series are well preserved in the Corbières region (Figure 2.2) ; westward, these deposits are buried under the Oligocene to the Pliocene units (Souquet et al. 1975). Deposition of these sequences led to the conversion of the eastern part of the Aquitaine Basin from underfilled to overfilled (Christophoul et al. 2003). The characterization of three tectono-sedimentary units in the Palassou series is based on significant changes in several parameters such as geometry, clasts lithology and texture (Crochet, 1989) (Figure 2.2). The first unit – late Ypresian to Lutetian - is defined by well-consolidated conglomerates with boulders sourced mostly in the Meso-Cenozoic sedimentary cover (Figure 2.2) and cropping out mainly in the Talairan syncline and to the west of the Mouthoumet massif (Figure 2.2). This unit consists of pebble to boulder (mainly carbonates, sandy) conglomerates filling channels and sand bodies, in addition to marls and silt, showing rooted paleosols (Christophoul et al. 2003). The second unit, of late Lutetian-Bartonian age is characterized by a high proportion of clasts derived from plutonic rocks, essentially granitic clasts and is cropping out in the Carcassonne basin (Figure 2.2). The unit is marked by an abrupt change in clasts lithology with a dominance of Variscan material (Crochet, 1989) from the eastern part of Carcassonne basin to Mirepoix. Change in clasts lithology is accompanied by a discordance observed between the units 1 and 2 and a widened catchment area according to Crochet (1989). The third unit deposited during the Priabonian time, is similar to the first unit with carbonate and sandstone clasts derived mainly from the Meso-Cenozoic cover (Figure 2.2). Due to post-deposition evolution, these three units are outcropping from east to west in the Corbières region (Figure 2.2).

Few deposition ages are obtained by biostratigraphy for the Palassou series. A Lutetian age is obtained by Plaziat (1964) for bird footprint ~ 40 Ma and a Priabonian age is estimated for mammals (*Lophiodon Issilense, Lophiodon lautricense*) by Depéret (1910), Hartenberger et al. (1968), Plaziat (1984) and Berger (1990). In addition, the eastern and western parts of the second unit have deposition ages of 41.2-39 and 39-37.8 Ma respectively separated by the late Bartonian age obtained on vertebrate fossils (*Lophiaspis baicheri, Lophiaspis occitanicus, Pachynolophys duvali, Propaleotherium*) by Hartenberger et al. (1968) and Plaziat (1984) (Figure 2.2).

The Oligocene deposits crop out to the west of Mirepoix (Figure 2.2). It consists of thick conglomerate series (~350 m; Cavaillé and Paris, 1976) containing essentially carbonate and sandy pebbles to boulders, intercalated with carbonate layers in the upper part of this series. Biostratigraphic ages on mammals have been obtained by Richard (1946) and Astre (1959) and are attributed to the early and late Stampian (Cavaillé 1975). During the same period occured the opening of the Gulf of Lion that started in the early Oligocene time (Séranne, 1999). The presence of calcareous marine Miocene deposits discordant on the marine Ypresian sediments in the eastern Corbières (Aguilar and Magné 1978; Ellenberger et al. 1985) reflects an erosion phase occurred during the Miocene time. As

the age of the Miocene deposits estimated on bivalves *Crassostrea crassissima* is in the late Burdigalian (or early Langhian ~16 Ma) (Aguilar and Magné 1978), it shows that the erosion phase timing is pre-Langhian. The opening of the Gulf of Lion was correlated to the Têt Valley reactivation that occurred at successive stage starting in the Early Miocene before 16 Ma (Sartégou et al., 2018). The incision is interpreted as possibly caused by an isostatic rebound that compensated for lithospheric thinning from the opening of the Gulf of Lion (Sartégou et al., 2018).

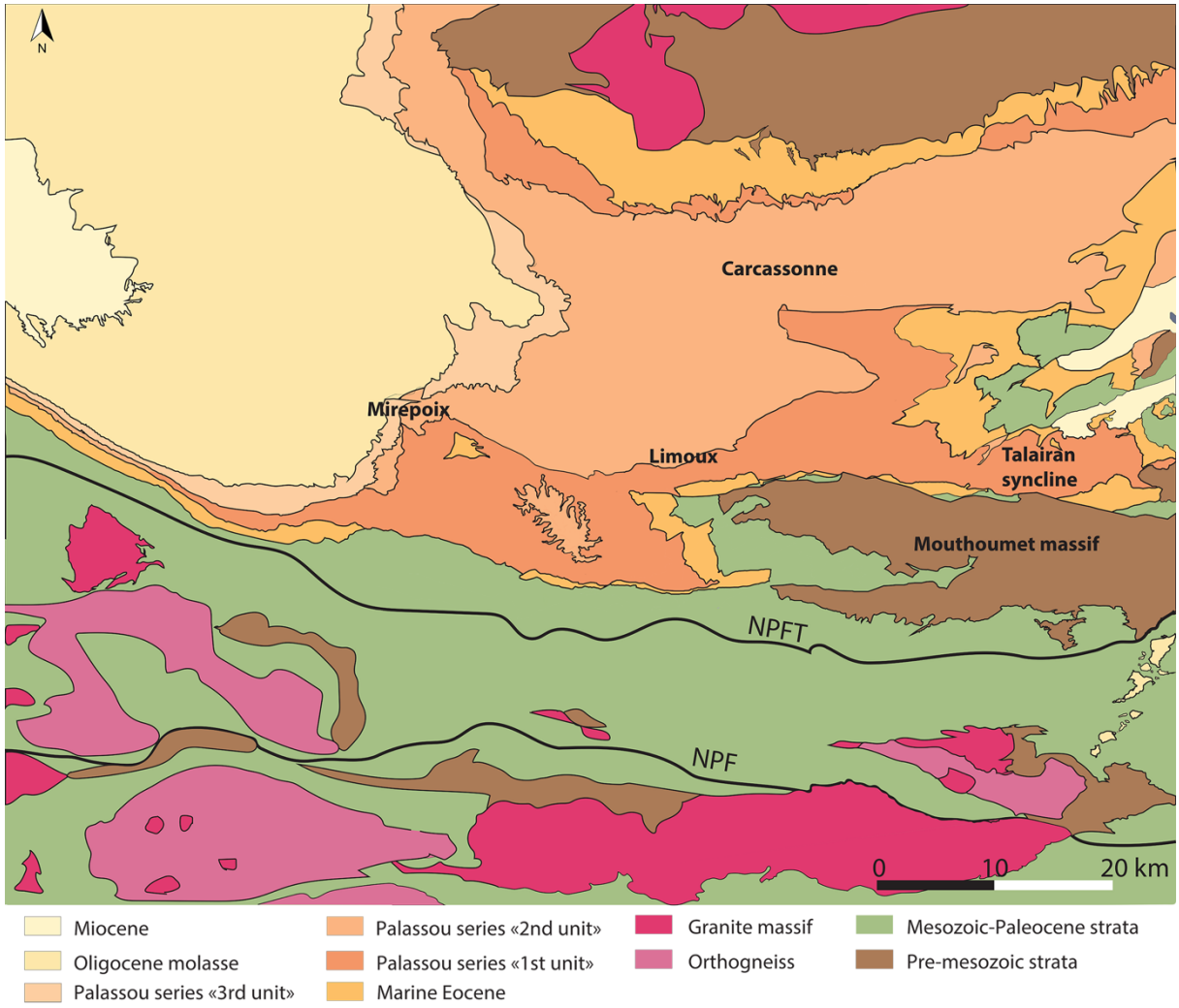

Figure 2.2: Geological map of the Corbières region showing the three tectonostratigraphic units of the Palassou series. NPF: North Pyrenean Fault, NPFT: North Pyrenean Frontal Thrust.

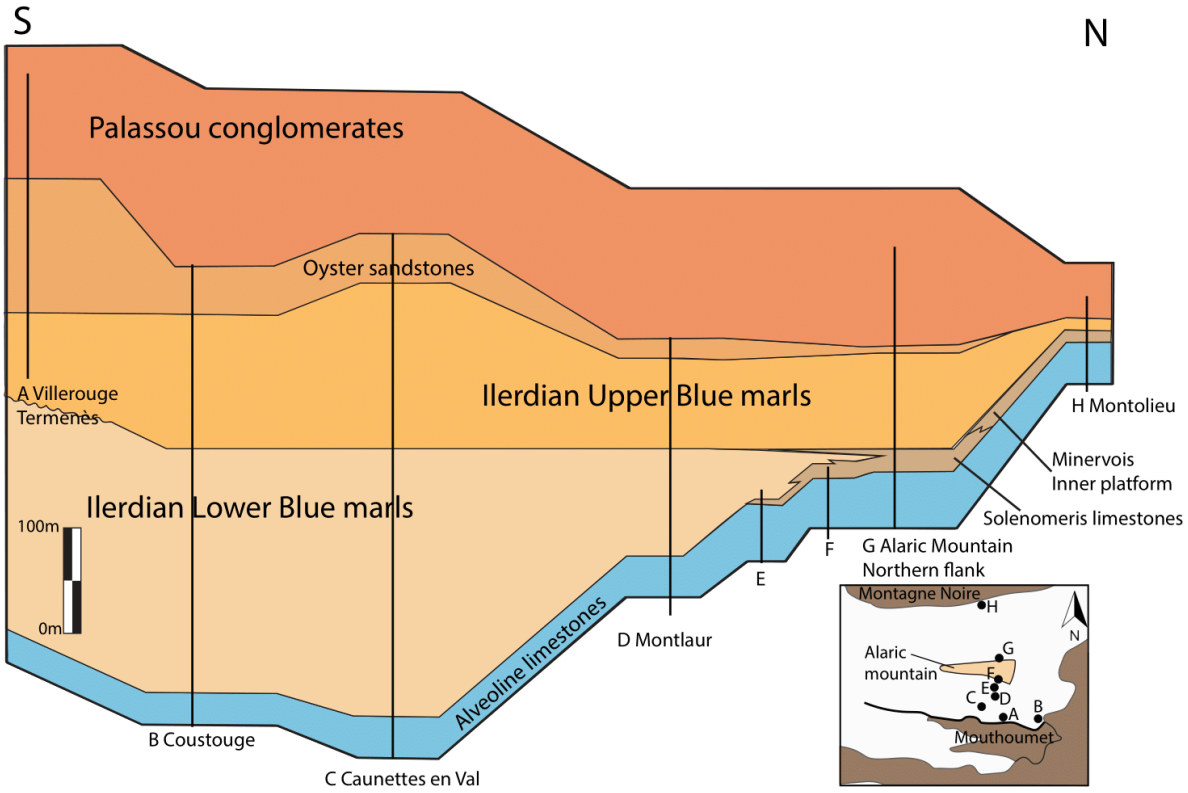

Figure 2.3: Stratigraphic section for the Ypresian and Lutetian times of the eastern part of the Aquitaine Basin modified from Christophoul et al. (2003)

I.2 Evolution of the Pyrenees, the Montagne Noire and the Corsica-Sardinia block from the Neoproterozoic to the Permian

I.2.1 Pre-Variscan evolution of the Pyrenees and the French Massif Central

The Pyrenees and the French Massif Central (FMC) crust portions belong to the Iberian – Catalan – Aquitaine block, known as "Ebroïa" before its Variscan incorporation to the Iberian-Armorican arc (Cocherie et al. 2005). The Ebroïa block is located in Northern Gondwana border during the end of the Neoproterozoic time (between 600 and 542 Ma) (Figure 2.4) and composed by the future Avalonia, Armorica, Ebroïa, etc terranes (Cocherie et al. 2005). This portion of the northern Gondwana border is characterized by an active margin that is identified by a continental arc magmatism and volcano-detrital deposits in the back-arc basin (Neubauer 2002; Von Raumer et al., 2003). The Cadomian orogeny took place essentially between 580 and 540 Ma to the north of the Gondwana (Figure 2.4), and is caused probably by closing of one of these back-arc basins (Cocherie et al., 2005). During the same period, the Pyrenees and the FMC (in particular the Montagne Noire) have accumulated early Cambrian sediments known as "Canaveilles group" onlapping high-grade gneisses as the Canigou, Roc-de-France and Nuria in the eastern Pyrenees and the Somail orthogneiss

in the Montagne Noire (Laumonier et al. 2004; Cocherie et al. 2005; Castiñeiras et al. 2008a; Liesa et al. 2011). During the Cambrian, the western part of the back-arc basin evolved into the Rheic ocean (Von Raumer et al., 2003) (Figure 2.4) and the Ebroïa block remains part of the Gondwana with possible persistence of the active margin to the north (Stampfli and Borel 2002). The oldest metamorphic basement in the Pyrenees and in the nearby Montagne Noire are mainly orthogneiss, micaschists and high-grade paragneisses (Castiñeiras et al., 2008a). Few granitic massifs located in the eastern part of the Pyrenees (Roc-de-France, Canigou, Nuria and Cap-de-Creus) have been advocated as Cadomian "basement" following two main arguments: the first one is the existence of a supposed Lower Cambrian unconformity upon granitic and metamorphic complex, and the second one is U/Pb zircon age for granites from the Canigou massif estimated around 581±10 Ma as for other massifs cited above (Roc-de-France,…).

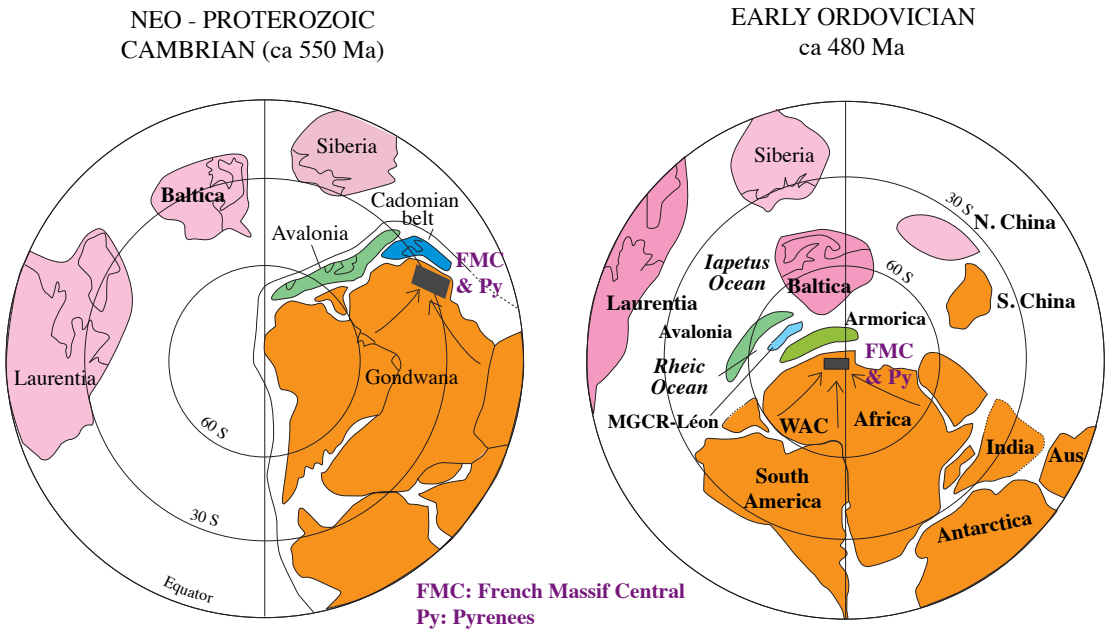

Figure 2.4: Paleogeographic map showing continent evolution between the Neoproterozoic (550 Ma) and the Early Ordovician. The location of the Pyrenees and the Montagne Noire is represented by the black squares. "MGCR" is the Mid-German Crystalline Rise, "FMC" is the French Massif Central and "Py" is for the Pyrenees. Black arrows are the proposed paleocurrent directions according to Lin et al. (2016). Modified from Lin et al. *(2016)*

Studies concluded therefore that large granite and orthogneiss bodies represent a Cadomian basement that is overlain by lower Paleozoic sedimentary cover (Autran and Guitard 1966; Autran and Guitard 1969; Guitard 1970; Vitrac-Michard and Allègre 1975). However, recent geochronological studies suggested an Ordovician age for the granitic bodies (475±10 Ma for Canigou massif, 477±4 Ma for Roc-de-France massif and 457±4 Ma for Nuria massif) and interpreted the granite of Cadomian ages as related to an Ediacaran magmatic event provided by geochronologic data (Cocherie et al. 2005; Casas et al. 2015; Padel et al. 2018). So the debate about the origin and

significance of the Cadomian granitic bodies ended and the Cadomian granitic basement hypothesis is considered as discarded (Liesa et al. 2011). As mentioned by Laumonier et al. (2004), the pre-Variscan (pre-Upper Ordovician) series in the Pyrenees and the Montagne Noire contain Cambrian-Ordovician sedimentary and magmatic rocks and early Ordovician granite bodies (Canigou, Roc-de-France, Nuria and Cap-de-Creus in the Pyrenees, and Mendic 455±2 Ma, Caroux 439±29 Ma/437±8 Ma and Vialais 450±6 Ma in the Montagne Noire) (Gebauer and Grünenfelder, 1976; Roger et al., 2004; Padel, 2016) with no visible Cadomian metamorphic basement.

The evolution of the continental blocks from the Early Ordovician to the Early Carboniferous is proposed by Franke et al. (2017) based on modelling data developed by Torsvik and Cocks (2016) (Figure 2.5). Several studies suggested an intense magmatic activity and sedimentological variations in the southern European formations (French Massif Central including the Montagne Noire, Pyrenees, Armorican Massif, Iberia and the Alps) recorded between the Lower and Middle Ordovician, that reflects the separation of these formations from the north Gondwana margin (Pin and Marini 1993; Stampfli 1996; Neubauer 2002; Stampfli and Borel 2002; von Raumer, et al., 2003).

I.2.2 Variscan evolution of the Pyrenees

The Variscan orogeny resulted from the convergence and collision between two main continents, Laurentia-Baltica and Gondwana (mentioned as NW Africa in Figure 2.5h) causing the closure of two oceanic basins: Rheic and Galicia-Massif Central (Matte, 1991; Mazur et al., 2010) (Figure 2.5). Closure of these two oceans, the Rheic ocean in the north and the Galicia – Massif Central in the south, is characterized respectively by southward and northward subduction (Matte 1991) (Figure 2.5). The Variscan orogeny in the Pyrenees has been extensively studied in order to understand the main events that occurred during the Paleozoic Era (Zwart 1962; Zwart and De Sitter 1979; Druguet and Hutton 1998; Laumonier 2008; Olivier et al. 2008; Denèle et al. 2009; Marignac and Kister 2010; Denèle et al. 2014; Olivier et al. 2016; Hoÿm de Marien et al. 2019). The position of the Pyrenees in the Variscan belt is not as clear as it is for the French Massif Central and Iberian Central Massif. It seems that the Pyrenees were in the southernmost part of the Variscan orogeny and were developed under transpressive conditions (Marignac and Kister, 2010) (Figure 2.6). Modern petrological studies on the central domain (Axial Zone) of the Pyrenees agree on the dominance of a LP-HT (Low Pressure- High Temperature) metamorphism (P< ~4.5 kbar, T> ~550°C) that would be achieved (Hoÿm de Marien et al., 2019). Many studies on Pyrenean granitic and orthogneiss massifs have mentioned that widespread zircon U/Pb ages ranging between 310 and 290 Ma are formed by a calc-alkaline magmatism. This phase is considered coeval with the LP-HT metamorphism strongly represented in the Pyrenees (Denèle et al. 2014; Druguet et al. 2014) (Figure 2.6).

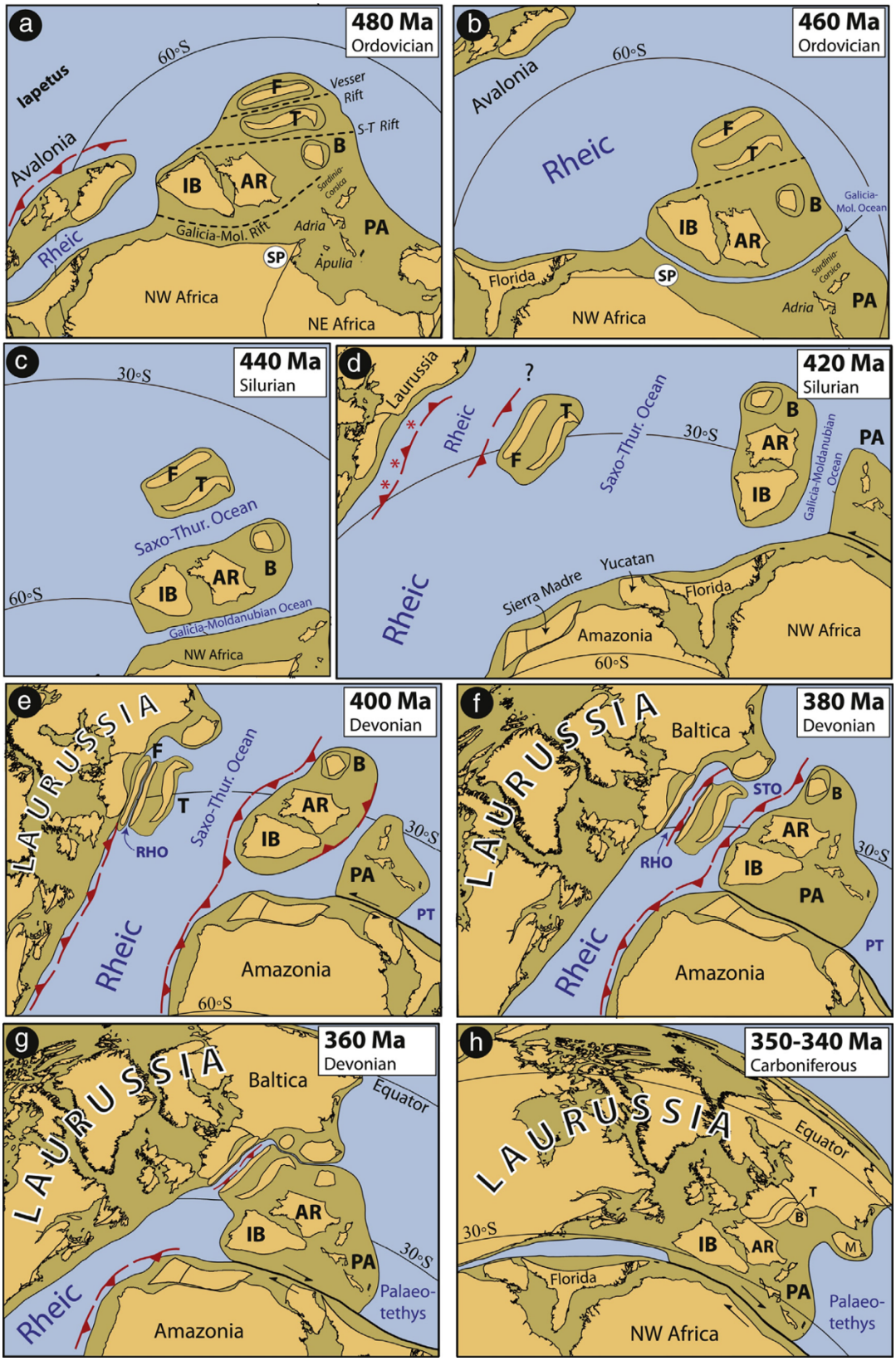

Figure 2.5: Paleogeographic reconstruction of the Variscan orogeny and its surrounding areas from the Early Ordovician to the Early Carboniferous as proposed by Franke et al. (2017). Geographical outlines in light orange are just for guidance and may not be reflect the real shape of the blocks. The position of Corsica-Sardinia block seems to be derivated from a position near the Bohemian Massif (Matte 2001). Plate velocities have been modelled by Torsvik and Cocks (2016) and have been estimated higher during the Paleozoic than during the Mesozoic and the Cenozoic time. PA: Paleo-Adria, AR: Armorica, B: Bohemia, F: Franconia, IB: Iberian Peninsula, RHO: Rheno-Hercynian Ocean, SP: South Pole, S-T: Saxo-Thuringia, STO: Saxo-Thuringian Ocean, T: Thuringia.

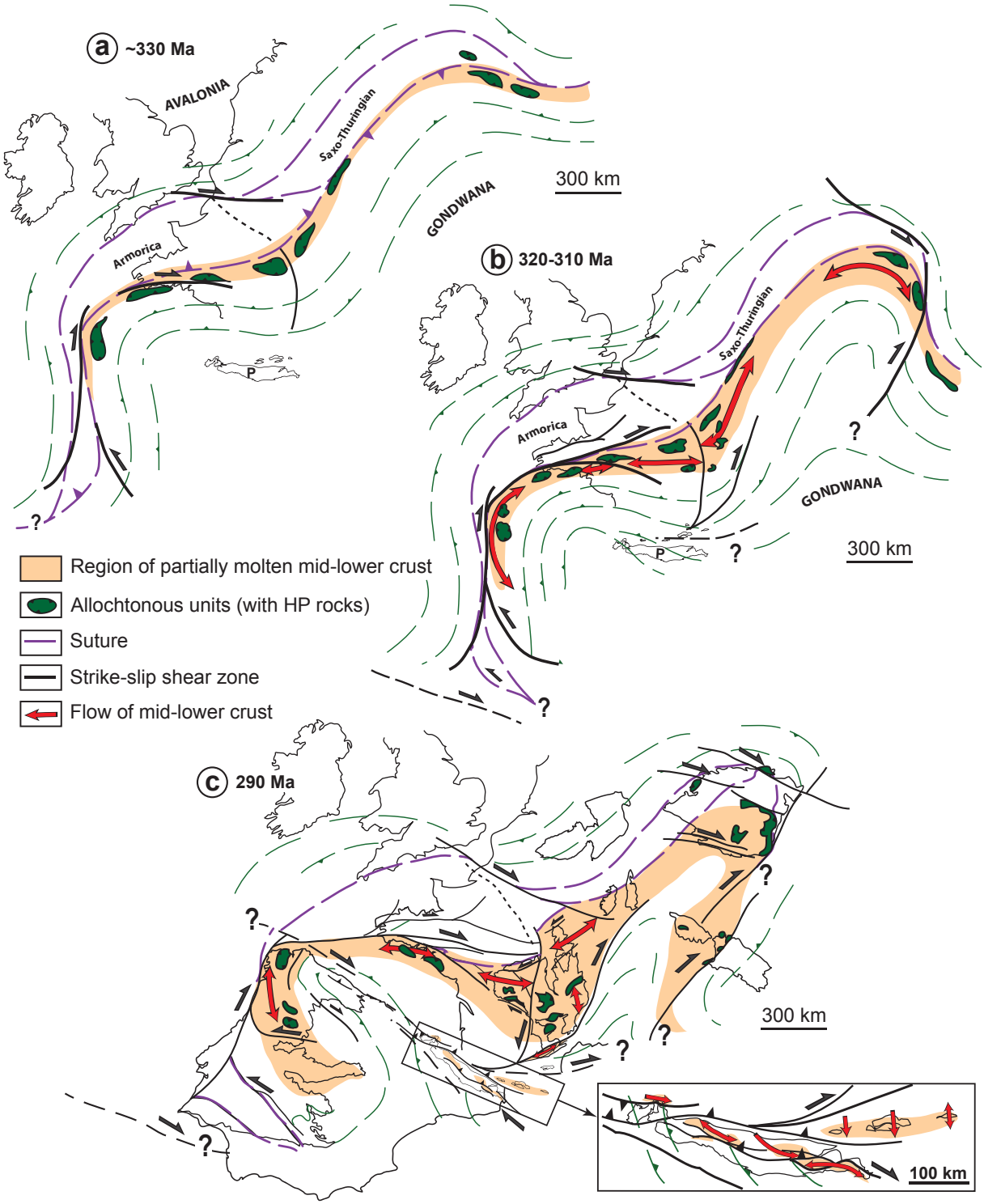

Figure 2.6: The evolution of the Variscan orogeny during the Carboniferous and the Permian, and the involvement of the Pyrenees (P) (a) Around 330 Ma, (b) from 320 to 310 Ma and (c) at 290 Ma (Cochelin et al.*, 2017).*

Zircon grains from leucosomes in the Roc-de-France massif yielded U/Pb ages of 313 ± 13 and 320 ± 13 Ma (Aguilar et al., 2014) and zircons from migmatite in the same massif give U/Pb ages between 307 and 314 Ma (Aguilar et al. 2014; Aguilar et al. 2015).

In addition, Lys-Caillaouas zircon crystals from mafic and granitic magmatic rocks yield crystallization age of ~ 307 Ma in the core of the zircons and it is interpreted as the age of the thermal peak of the LP-HT metamorphism, and the magmatic overgrowths in zircon have an age of ~ 300 Ma interpreted as the emplacement of the pluton (Esteban et al., 2015). Figure 2.7 represents a compilation of U/Pb zircon and monazite ages obtained for igneous Pyrenean and FMC massifs. The timing of the metamorphic events are a matter of debate, recent U/Pb zircon and monazite ages yielded by Mezger and Gerdes (2016) are ranging between 320 and 340 Ma for the orthogneiss Aston-Hospitalet and Bossòst massifs, and are interpreted as coeval to a LP-HT event (Figure 2.7). Most of the authors agree with a widespread LP-HT metamorphism contemporaneous with a magmatic event dated between 310 and 290 Ma (Figure 2.6). Others interpreted the early carboniferous age population as a separate metamorphic event across the Axial Zone of the Pyrenees (Mezger and Régnier, 2016), or argued in favour of an inherited component for the ~ 340 Ma ages (Lopez-Sanchez et al., 2018; Hoÿm de Marien et al. 2019).

The main sediments deposited before, during and after the Variscan orogeny are essentially thick Ediacarian-Ordovician silico-clastic, Silurian to Early carboniferous carbonates, and mid-Carboniferous flyschs. Post-orogenic continental deposition occurred during the Stephanian (c. 304-299 Ma) associated with volcano-clastic deposits.

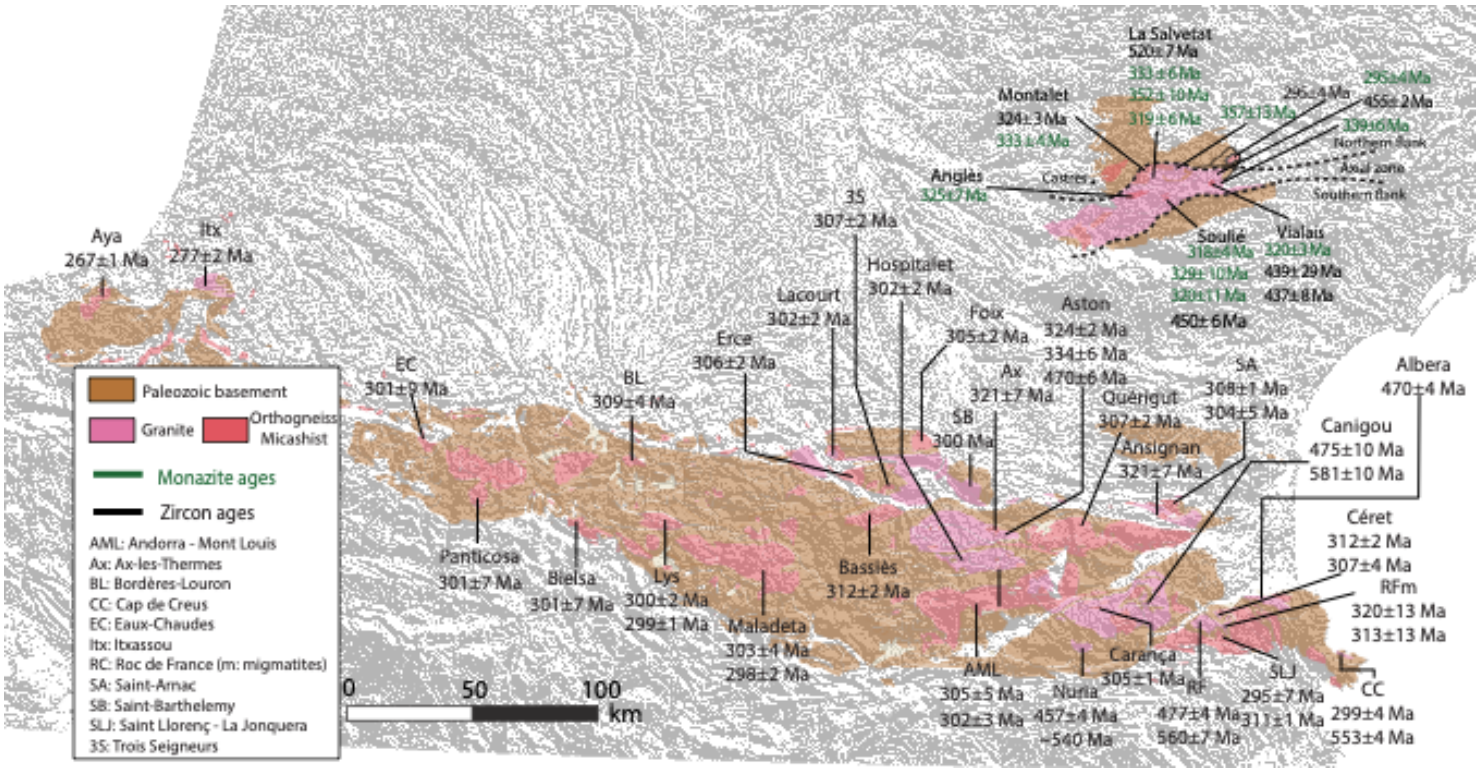

Figure 2.7: Compilation of U/Pb zircon and monazite ages in the Pyrenees and the Montagne Noire (Gebauer and Grünenfelder, 1976; Respaut and Lancelot, 1983; Bruguier et al.*, 2003; Roger* et al.*, 2004; Cocherie* et al.*, 2005; Olivier* et al.*, 2008; Denele* et al.*, 2009; Casas* et al.*, 2010; Faure* et al.*, 2010; Poilvet* et al.*, 2011; Pitra* et al.*, 2012; Aguilar* et al.*, 2014; Faure, Cocherie,* et al.*, 2014; Denèle* et al.*, 2014; Roger* et al.*, 2015; Padel, 2016; Vacherat* et al.*, 2017; Guille* et al.*, 2019).*

I.2.3 Tectonic and metamorphic evolution of the French Massif Central

The French Massif Central experienced several tectonic metamorphic events from the Late Silurian to the Late Carboniferous that are resumed below and in Figure 2.5 (Pin and Peucat 1986; Ledru et al. 1989; Faure et al., 1997; Faure et al. 2005; Faure et al., 2009; Faure et al. 2009; Lin et al. 2016). A Late Silurian to middle Devonian event is characterized by a northward continental subduction of the Gondwana margin beneath the Armorican margin and the formation of high-pressure rocks (Lardeaux et al. 2001; Faure et al. 2009; Faure et al. 2010). It is followed by a late Devonian event characterized by the exhumation of high-pressure rocks (Roig and Faure, 2000; Faure et al., 2008; Faure et al., 2010) and a late Devonian to early Carboniferous event characterized by an intermediate pressure – temperature metamorphism (Roig and Faure 2000; Bellot 2001; Duguet et al. 2007; Melleton et al. 2010). Between 340 and 330 Ma, a middle Carboniferous event took place in the northern part of the FMC. It was responsible for the syn-orogenic extension of the belts and a magmatism accompanied by the deposition of volcanic and sedimentary series (Tufs anthracifères). In the southern part of the FMC, including the Montagne Noire, the middle Carboniferous event is characterized by a S to SW ductile shearing and by the development of rhyolitic to dacitic dykes, microgranite and porphyritic granite of 340-330 U/Pb zircon and monazite ages (Figure 2.7) (Gebauer and Grünenfelder 1976; Arthaud and Matte 1977; Ledru et al. 1989; Faure et al. 2002; Roger et al. 2004; Cocherie et al. 2005; Faure et al. 2005; Cartannaz et al. 2007; Faure et al. 2010; Poilvet et al. 2011; Pitra et al. 2012; Faure et al. 2014; Roger et al. 2015; Padel 2016). From the Serpukhovian to the Baskirian (late Carboniferous), U/Pb ages between 325 to 310 Ma reflect a phase of crustal melting represented by a large amount of granitic intrusions, especially two-mica leucogranite and porphyric monzogranite, widespread in the northwestern and the southeastern part of the FMC (Figure 2.7). The end of Carboniferous is then characterized by the emplacement of cordierite anatectic granite around 300-310 Ma. U/Pb ages from 325 to 300 Ma are also widespread over the Pyrenean massifs as cited in the section I.2.2. During the late Carboniferous – Permian time, sedimentary basins were developed in Europe as a consequence of the late and post-orogenic tectonic relaxation and extensional collapse of the Variscan belt. The upper Carboniferous and Permian basins of the south-west of Europe were infilled mainly by continental, detrital and volcanic deposits as summarized in Cassinis et al. (2000) and Juncal et al. (2019). In all, the FMC is formed of five main tectonic-metamorphic units recognized as follows: a) the late Visean foreland basin, b) the fold-and thrust belt, c) the para-autochthonous unit, d) the Lower Gneiss Unit and 5) the Upper Gneiss Unit (Figure 2.8). The Lower Gneiss Unit was developed during the late Neoproterozoic to the early Paleozoic. It underwent a general medium-pressure metamorphism attributed to the thrusting of the Upper Gneiss Unit which occurred during the Devonian, prior to 350 Ma. The first tectonic event in the Montagne Noire occurred during the

middle Carboniferous. It was confirmed by the large amount of U/Pb zircon and monazite ages between 320 and 340 Ma (Figure 2.7).

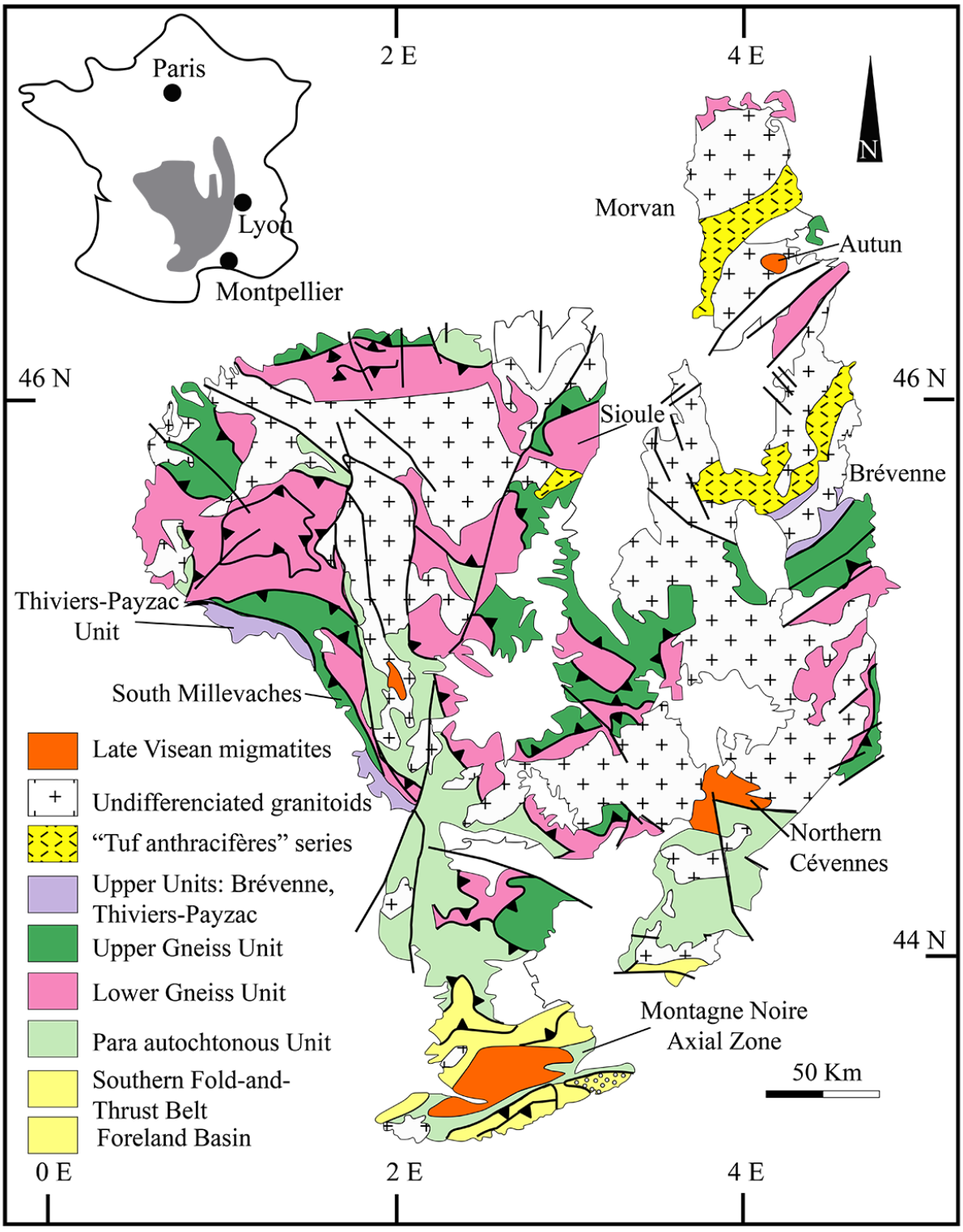

Figure 2.8: Geological map of the French Massif Central modified from Faure et al. (2010).

Geological settings of the Montagne Noire

The Montagne Noire is classically divided into three parts from the south to the north: the Southern Flank, the Axial Zone and the Northern Flank (Figure 2.7). The Southern flank is characterized by sedimentary rocks ranging from the Early Cambrian to Visean, while the Early Cambrian to Silurian rocks are observed in the Northern Flank (Figure 2.7). The Axial Zone consists of a migmatic dome and post-migmatization plutonic rocks. They contain metamorphic rocks mainly gneiss and micaschists (Faure et al., 2010) (Figure 2.7).

I.2.4 Variscan evolution of Corsica-Sardinia block

The Corsica-Sardinia block exposes an almost complete transect of the southern European Variscides. During the Variscan orogeny, three main tectono-metamorphic zones were recognized in the Corsica-Sardinia block. The first zone mentioned as the external zone in Figure 2.9, is a foreland basin located in the south-west of Sardinia and is characterized by folds and thrusts with no metamorphism. The second zone is a nappe zone located in the southeast and the central part of the island and subdivided into external and internal nappes encompassing several stacked tectonic units (Figure 2.9) and the third zone is an inner zone mentioned as the Axial Zone and contains essentially High Grade Metamorphic Core (HGMC) rocks (Figure 2.9).

A tectonic event in the western Mediterranean took place in the Oligocene and the Miocene time launched by the retreat of the Apennine subduction and resulted in the formation of the largest Mediterranean back-arc basin, the Gulf de Lion. This event was characterized by the rotation of the Corsica-Sardina block, which belonged to the Pyrenean orogeny during the pre-Oligocene period, after an Oligocene rifting episode from 32 to 24 Ma (Jolivet et al., 2015).

Sardinia and Corsica represent a segment of the Southern European Variscan belt extended from the Axial Zone in Corsica and northern Sardinia to the External Zone in southwestern Sardinia (Carmignani et al., 1994) (Figure 2.9). The crystalline basement of the Sardinia-Corsica block formed in the early Carboniferous as a result of a collision between the northern Armorica and southern Gondwana continents, which produced intense deformation and high grade metamorphism accompanied by widespread igneous activity (Di Vincenzo et al., 2004). A compilation of U/Pb zircon ages in the Corsica-Sardinia block are presented in Figure 2.9. Based on field relationships, U/Pb zircon ages and petrographic considerations, Rossi et al. (1991) and Ferre and Leake (2001) distinguished three main magmatic sequences in the Corsica-Sardinia block. The first one is an early magmatic sequence (U1) developed in northern Corsica around 340 Ma during N-S shortening (Paquette et al. 2003). U1 melts between 320 and 288 Ma. It results in the production of granodiorites and monzogranites of the U2 sequence which is characterized by a decrease in MgO content and it

forms the largest part of the Corsica-Sardinia block (Ferre and Leake 2001; Paquette et al. 2003; Oggiano et al. 2007). The last sequence U3 was developed around 288 Ma and includes alkaline magmatic phase, post-orogenic plutons and sub-volcanic complexes (Cocherie et al. 2005).

In Corsica, the HGMC rocks crop out in the western part of the island and consist mainly of magmatic rocks. The eastern part of the island consists of Mesozoic ophiolites and sedimentary rocks thrusted to the west during the Cenozoic Alpine orogeny (Rossi et 1991; Faure et al. 2014). U/Pb ages obtained on zircon crystals for magmatic rocks from the western part of the island show mostly Variscan ages ranging between 281 and 345 Ma in addition to few ages obtained in the SE part of Corsica between 407 and 484 Ma and interpreted as derived from the tectonic stacking of the northern Gondwana passive margin, the Paleotethys as proposed by Stampfli et al. (2002) along an active continental margin in the Devonian-Carbonifeorus (Giacomini et al., 2006; Rossi et al., 2009).

The HGMC of Sardinia is considered to be the southern extension of the Variscan metamorphic basement in Corsica (Elter et al., 1990; Ménot and Orsini 1990; Elter et al. 2004; Elter and Pandeli 2005). Geochronological U/Pb ages obtained for magmatic rocks in Sardinia are ranging between 288 and 350 Ma. Middle Ordovician (480-450 Ma) U/Pb zircon and monazite ages (Figure 2.9) for paraderivate rocks from North-East and Southern Sardinia reflects a main magmatic event during this time (Helbing and Tiepolo 2005; Giacomini et al. 2006; Carosi et al. 2012). The Variscan metamorphic phase in Sardinia, is essentially marked in the north-eastern part of the island according to U/Pb zircon ages ranging from 360 to 295 Ma and referred to the magmatic sequences mentioned above (Ferrara et al., 1978; Del Moro et al., 1991; Cortesogno et al., 2004; Di Vincenzo et al., 2004; Palmeri et al., 2004; Helbing and Tiepolo, 2005; Giacomini et al., 2005; Giacomini et al., 2006; Giacomini et al., 2008; Oggiano et al., 2010; Carosi et al., 2012; Casini et al., 2012; Pavanetto et al., 2012; Padovano et al., 2014; Cuccuru et al., 2016; Malusà et al., 2016; Gaggero et al., 2017) (Figure 2.9).

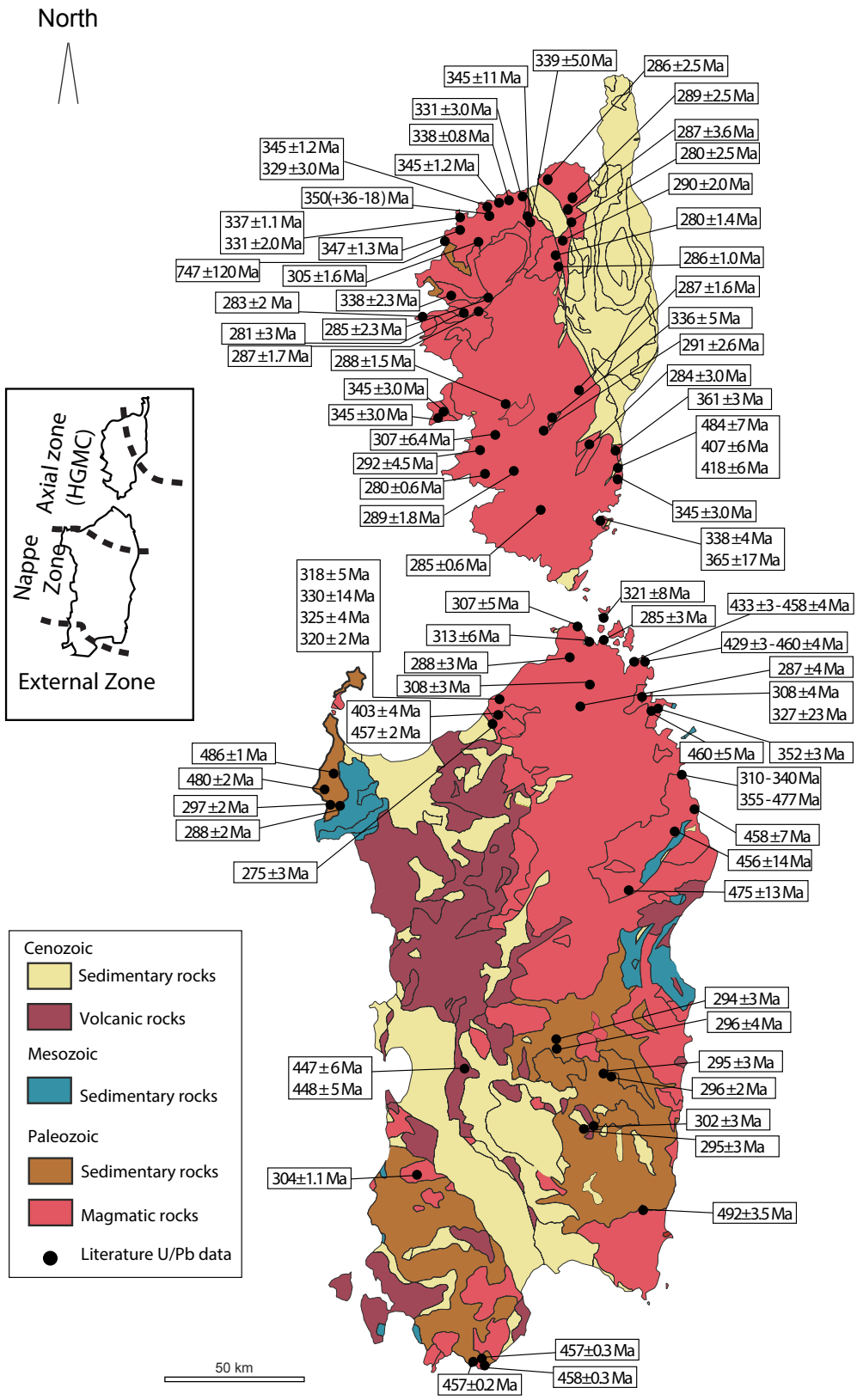

Figure 2.9: Compilation of U/Pb zircon ages for Corsica-Sardinia block. (References: Rossi et al. 1988; Cocherie et al. 1992; Rossi et al. 1995; Paquette et al. 2003; Cortesogno et al. 2004; Palmeri et al. 2004; Cocherie et al. 2005; Helbing and Tiepolo 2005; Giacomini et al. 2005; Oggiano et al. 2007; Renna et al. 2007; Giacomini et al. 2008; Rossi et al. 2009; Giacomo et al. 2010; Carosi et al. 2012; Casini et al. 2012; Faure et al. 2014; Li et al. 2014; Padovano et al. 2014; Edel et al. 2015; Cuccuru et al. 2016; Malusà et al. 2016; Gaggero et al. 2017).

I.3 Evolution of the Pyrenean domain from the Triassic to the Miocene

I.3.1 Mesozoic rifting phases in the Pyrenees

The collapse of the Variscan orogeny during the Triassic was followed in the Late Jurassic by the rifting phase in the Alpine Tethys (Visser, 1992; Vissers and Meijer, 2012a; Vissers and Meijer, 2012b; Ribes et al., 2019) and the opening of the Central Atlantic domain (Schettino and Turco, 2011; Mouthereau et al., 2014; Gómez et al., 2019) due to the break-up of the Pangea. Later, the main rifting phase took place between Iberia and Europe controlling the formation of the most important Pyrenean extensional basins (Puigdefabregas et al., 1986, 1986; Sibuet et al. 2004; Verges and Garcia-Senz, 2001) and Bay of Biscay opening from the late Barremian to the Albian linking the Atlantic ocean with the Tethys. However, the paleogeographic reconstruction of the plate pattern remains a major debate. Kinematic reconstructions of the Iberian plate from the Early Cretaceous to the onset of convergence have led to three proposed models. A transtensional rift model that involves a significant component of dextral strike-slip reactivation and an inversion of the Iberian and European margins during convergence (Figure 2.10A) (Choukroune and Mattauer, 1978; Savostin et al., 1986; Olivet, 1996). The second proposed model consists of a significant subduction beneath the Pyrenees contemporaneous with the opening of the Bay of Biscay during the Albian (Srivastava et al. 1990; Sibuet et al. 2004; Vissers and Meijer 2012a, 2012b) (Figure 2.10B). The third model implies a transcurrent motion of the Iberian plate during the Late Jurassic (~147 Ma) (Schettino and Turco, 2011), arc-normal stretching in the middle-Late Cretaceous, and frontal convergence of Iberia (Jammes et al., 2009) (Figure 2.10C). Current interpretations are highlighting strong partitioning within the Iberian sub plate that partly reconciled these different observations.

As the discrepancies between these three models are large, there is also a debate regarding the maximum basin width, the timing and the amount of movement (Clerc et al. 2016). This main rifting episode (late Barremian to Albian) is accompanied by the deposition of dark-colored flysch sediments referred to as “Flysch Noir” or “Black Flysch” cropping out essentially in the north Pyrenean zone (Debroas and Souquet 1976; Debroas 1978; 1987; Souquet 1985). From the middle Cenomanian to the late Santonian, the basin widened with the rifting and the deposition of Black Flysch onlap the north Pyrenean basins. Authors like Jammes et al. (2010) argued that the period of deposition of Black Flysch is considered as post-rift, however according to Montigny et al. (1986); Debroas (1987) and Debroas (1990) the presence of conglomerates of various ages from the Cenomanian to the late Santonian along the north Pyrenean domain attested to the continuing of the tectonic activity. This main rifting phase is characterized in the North Pyrenean zone by a LP-HT metamorphism which affects the Mesozoic cover between the Albian (110 Ma) and the Santonian (85 Ma) (Albarede and

Michard-Vitrac 1978; Montigny et al. 1986; Golberg 1987; Parseval 1999). Recent studies provided a LP-HT metamorphism map (Figure 2.11) based on more than 100 peak-temperature estimates. These estimates were obtained using Raman Spectroscopy of the Carbonaceous Material (RSCM). The analysis are completed by pressure and temperature estimates based on mineral assemblages, and ^{40}Ar-^{39}Ar ages on amphibole and micas, in addition to U-Pb ages on titanite from metamorphic and magmatic rocks from the north Pyrenean flank (Clerc and Lagabrielle 2014; Clerc et al. 2015; Clerc et al. 2016; Lagabrielle et al. 2016).

Results obtained by Clerc and Lagabrielle (2014), Clerc et al. (2015), Clerc et al. (2016) and Lagabrielle et al. (2016) covered the whole northern flank of the axial zone known as the North Pyrenean Zone (NPZ) (Figure 2.11) and focused on the Mauléon basin, Arguenos-Moncaup, Lherz, Boucheville and the Bas-Agly (Figure 2.11). They have revealed three main domains covering all the NPZ (Clerc et al., 2015) and which are characterized from west to east by 1) a low grade metamorphism with temperatures lower than 350°C in the westernmost part of the NPZ (Mauléon basin) (Figure 2.11), 2) higher temperatures between 300 and 450°C in the central domain (Ballongue, Barousse and Baronnies basins) (Goujou et al., 1988; Clerc et al. 2015), however it exceeds 550°C in Arguenis-Moncaup peridotites, thus reflecting a close location to mantle exposure (Figure 2.11) and 3) the highest grade of metamorphism with temperature over 600°C in the eastern domain including the Aulus, Pays de Sault, Boucheville and Agly basins (Golberg and Leyreloup 1990; Clerc et al. 2015; Clerc et al. 2016; Lagabrielle et al. 2016) (Figure 2.11) (the location of these basins is shown in Figure 2.12).

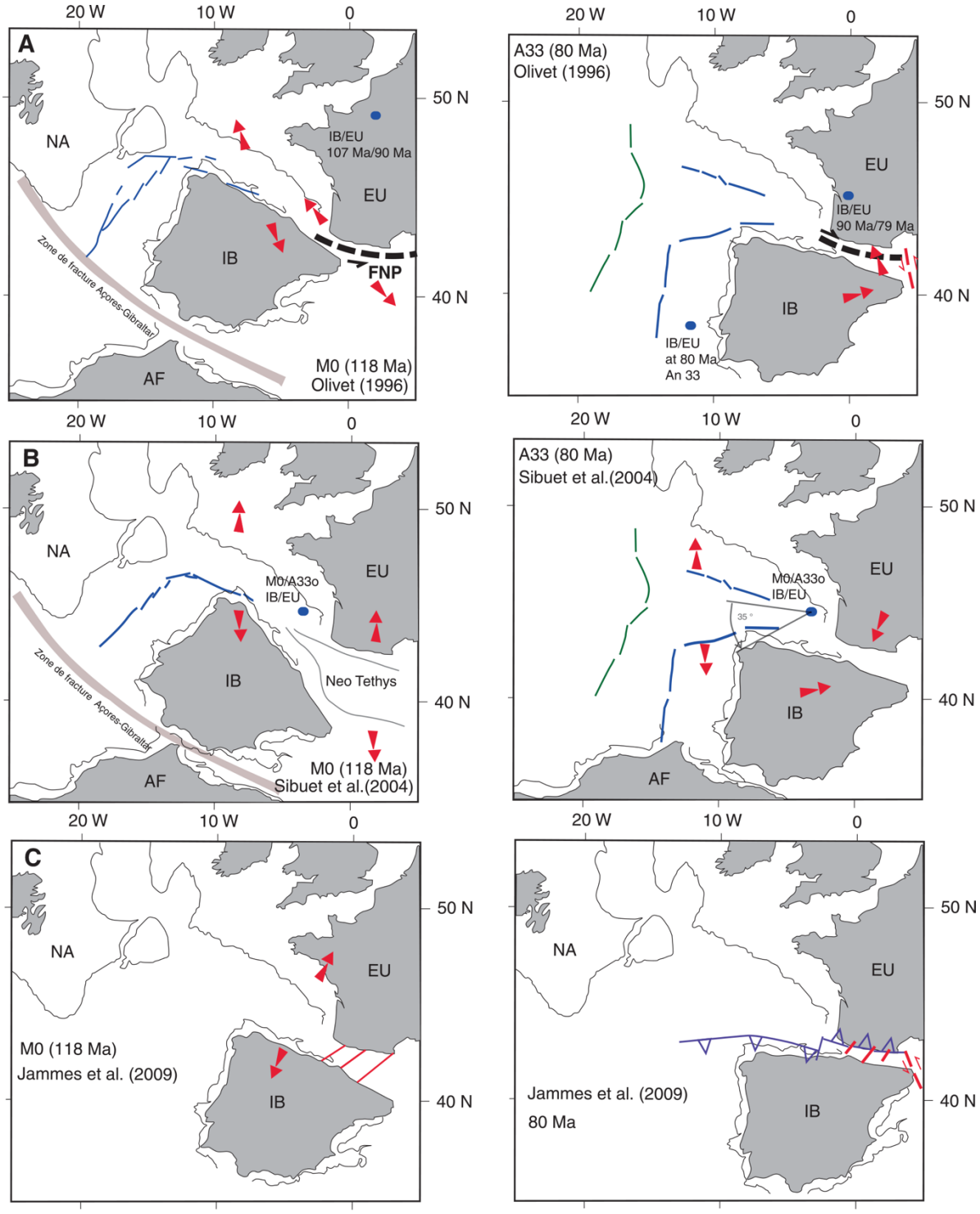

Figure 2.10: The three proposed models of kinematic reconstruction of the Iberian plate from the Early Cretaceous to the onset of convergence (~80 Ma). Modified from Mouthereau et al. *(2014).*

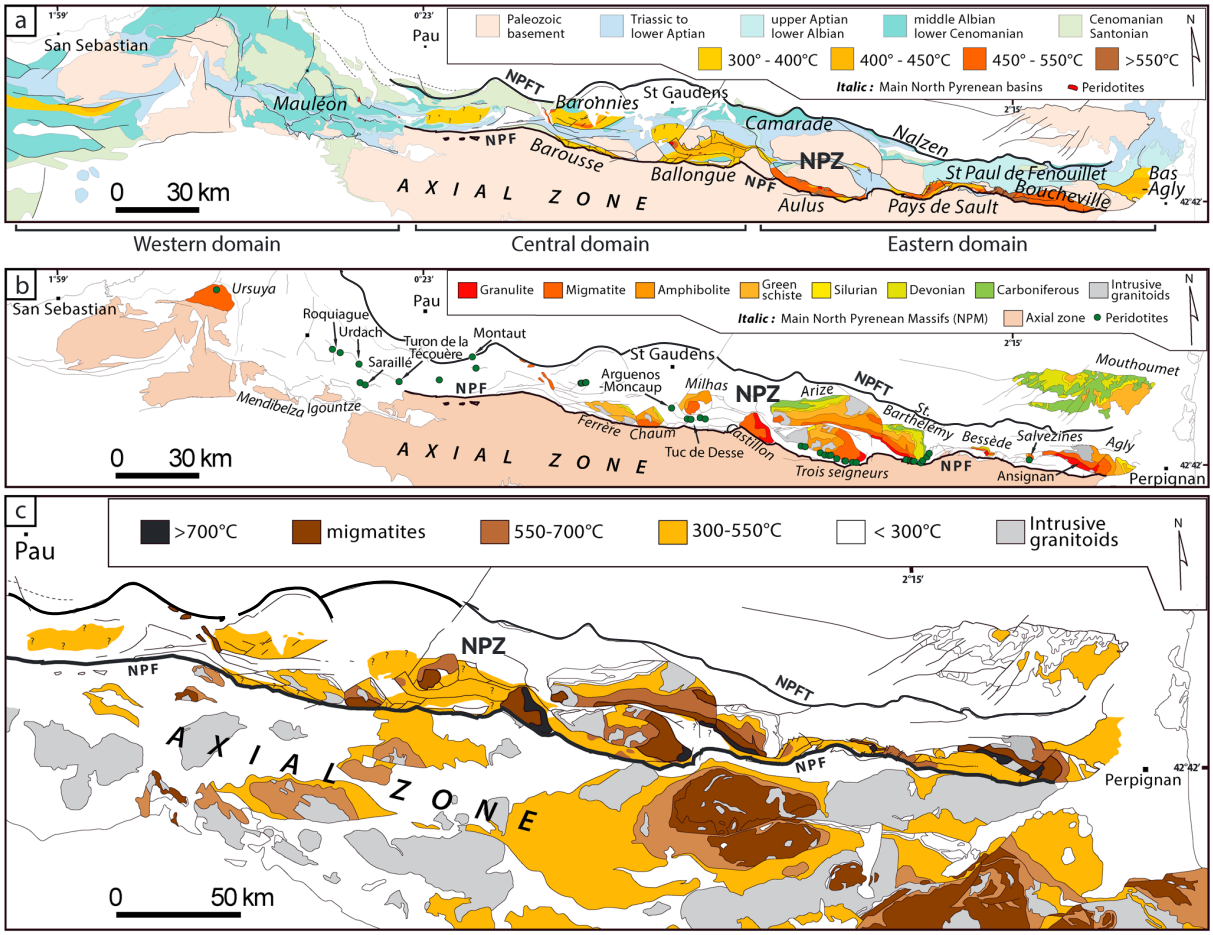

Figure 2.11: Maps of the Pyrenees from Clerc and Lagabrielle (2014) with the compilation of various data obtained from Choukroune and Séguret (1973), Golberg and Leyreloup (1990), BRGM and IGME (1998), Jammes et al. (2009), Clerc and Lagabrielle (2014), Clerc et al. (2015) and from 1/50000 geological maps from the BRGM. A) Isometamorphic map of paleotemperatures compiled from Golberg and Leyreloup (1990), Clerc (2012), Vauchez et al. (2013) b) Location of peridotite bodies in the NPZ c) Isometamorphic map of the Paleozoic basement and the Mesozoic cover for the NPZ and the Axial Zone. NPZ: North Pyrenean Zone, NPFT: North Pyrenean Frontal Thrust, NPF: North Pyrenean Fault.

Moreover, a north-south thermal gradient was observed in the eastern domain with highest temperatures in the southernmost basins like Boucheville and Aulus, and lower temperatures in the northern basin like Saint-Paul-de-Fenouillet and Camarade. Several scenarios have been proposed by Clerc et al. (2015) to explain the thermal increase of temperature towards the east.

A reconstruction of the evolution of magmatism and metamorphism during the main rifting phase is proposed by Clerc et al. (2015) and Lagabrielle et al. (2016). The continental crust was first weakened and thinned during the Aptian – Albian time. It was demonstrated by the occurrence of peridotite bodies underlying the metamorphic pre-rift sediments indicating the attenuation of the rifted continental crust. This led to a crustal boudinage of the continental crust in the NPZ (Figure 2.13-top), then it was altered by hydrothermal circulations as proposed before by Dauteuil and Ricou (1989), Poujol et al. (2010) and Fallourd et al. (2014). From the Cenomanian to the Coniacian, the hyper-thinned domain opened from each side of these boudins, caused the unroofing of the

subcontinental mantle in the eastern part of the NPZ (Figure 2.13-down).

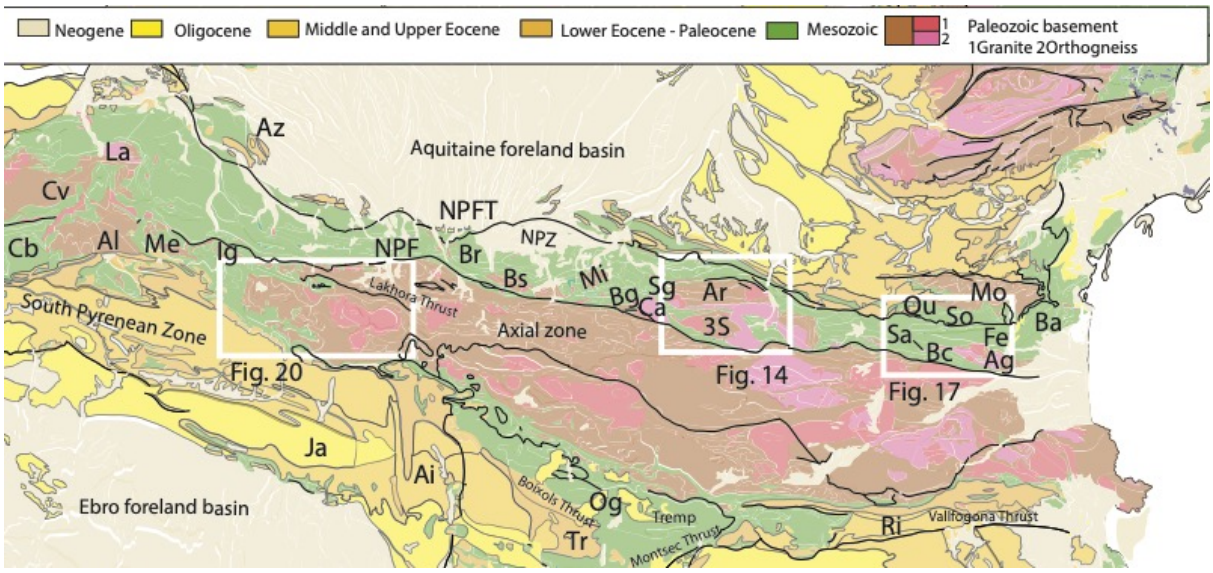

Figure 2.12: Geological map of the Pyrenean domain. 3S: Trois Seigneurs, Ag: Agly Massif, Ai: Ainsa Basin, Al : Aldudes Massif, Ar : Arize Massf, Az : Arzacq Basin, , Ba : Bas-Agly Basin, Bc: Boucheville Basin, Bg : Ballongue Basin, Br : Baronnies Basin, Bs : Barousse Massif, Ca : Castillon Massif, Cb : Cantabrian Basin, Cv : Cinco-Villas Massif, Fe : St-Paul-de-Fenuoillet syncline, Ig : Ignountze Basin, Ja: Jaca Basin, La : Labourd Massif, Me : Mendibelza Massif, Mi : Milhas Massif, Mo : Mouthoumet Massif, Og : Organya Basin, Qu: Quillan Basin, Ri : Ripoll Basin, Sa : Salvezines Massif, Sg : Saint-Girons Basin, So: Sourgraigne-Soulatgé Basin, Tr : Tremp Basin.

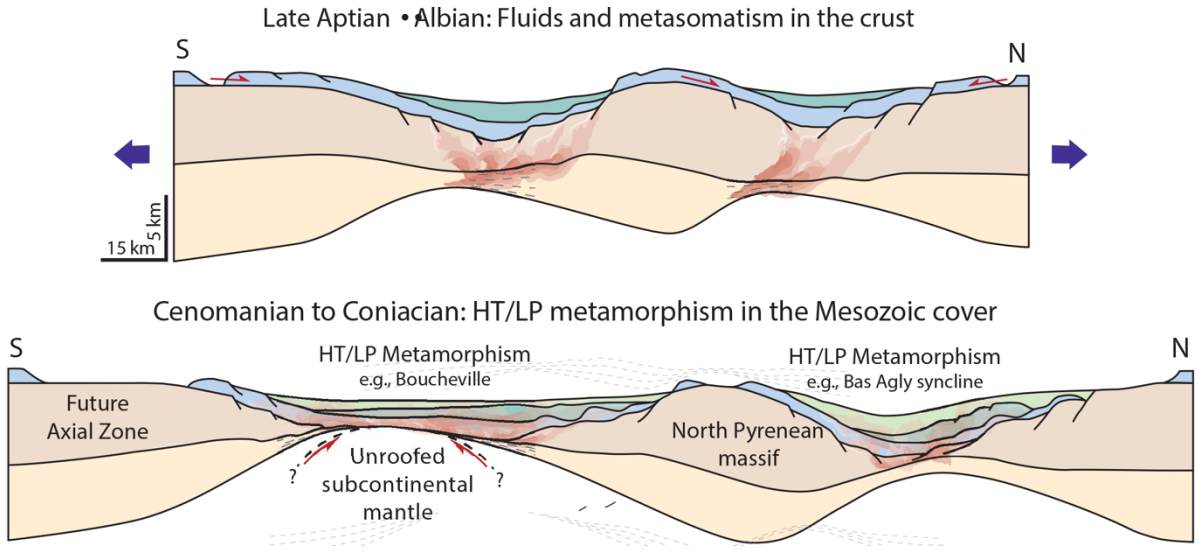

Figure 2.13: Evolution of the Pyrenean Cretaceous magmatism and metamorphism during the main phase of rifting. Top: hydrothermal dominated phase affecting the basement, Down : Phase of HT-LP metamorphism showing the mantle unroofing in the southern part of the east NPZ (Clerc et al.*, 2015).*

I.3.2 Evolution of the Aptian – Santonian rifting phase as constrained by low temperature thermochronology and sedimentology

Throughout the Jurassic and the Early Cretaceous, the European margin recorded slow heating related to the post-rift subsidence. The Aptian-Santonian rifting phase in the Pyrenees has been investigated using low temperature thermochronology by Vacherat (2014), Vacherat et al. 2016, 2017). Inverted low temperature thermochronology data allow distinguishing subsidence and denudation controlled by south dipping normal faults in granitic massifs on the NPZ that reflect rifting from the Albian-Aptian to the late Santonian (Vacherat et al., 2016). In the western Pyrenees, Albian sediments have been studied by Vacherat (2014), the time-temperature paths obtained from inversion of low temperature thermochronology results show a remarkable heating episode around 110 Ma recorded by geothermal gradients and interpreted as high as 80°C/km. Such high geothermal gradient is supposed to result essentially from rift-related mantle exhumation and sediment burial (Vacherat, 2014). Low temperature thermochronology results from Vacherat et al. (2016) on Arize and Trois Seigneurs granitic massifs (Figure 2.14) recorded high temperatures >200°C in agreement with RSCM temperature obtained by Clerc et al. (2015).

For the Trois Seigneurs (3S) massif (Figure 2.15) the inverted thermal models reveal a Permo-Triassic cooling phase (between 300 and 200 Ma) followed by a slow heating episode from 200 to ~130 Ma (southern flank of 3S massif) (Figure 2.15A). This episode of slow heating is interpreted as a post-rift burial (post- late Palezoic – early Mesozoic rifting) caused by sediment deposition (Vacherat et al., 2016). The renewed cooling event in the same massif is documented between 130 and 50 Ma and is recorded differently in the southern and northern flanks of the 3S massif (Figure 2.15, D & A respectively).The cooling in the southern flank of the massif reflects the denudation in the footwall of the south dipping normal faults while the Aulus basin positioned in the hanging wall was subsiding (Figure 2.15, Figure 2.16A&B). The northern flank of the 3S massif did not record cooling which indicated that this part of the massif was located far enough from the main fault (Figure 2.15, Figure 2.16A&B). This part of the massif records subsidence due to the deposition of Cenomanian – Coniacian Black Flysch in the Oust-Massat basin (Figures 2.14, 2.15 and 2.16).

The Arize massif recorded a similar heating history as the 3S massif from 200 Ma (Figure 2.15B) with a cooling episode started at ~110 Ma indicating the occurrence of a denudation phase in the footwall of the south dipping fault located south of the Arize massif (Figure 2.16 A&B). The northern flank of the Arize massif remained hot from ~200 to ~50 Ma (Figure 2.15D) illustrating a post-200 Ma burial phase followed by a tectonically controlled tilting of the massif during the Albo-Cenomanian rifting phase (Albo-Cenomanian sediments in the Camarade basin) (Figure 2.16 A&B). The thermal histories allowed the reconstruction of the tectonic evolution of the area based on time-

temperature paths. It shows that from 130 to 110 Ma occurred a south dipping normal faulting associated to the individualization of tilted blocks.

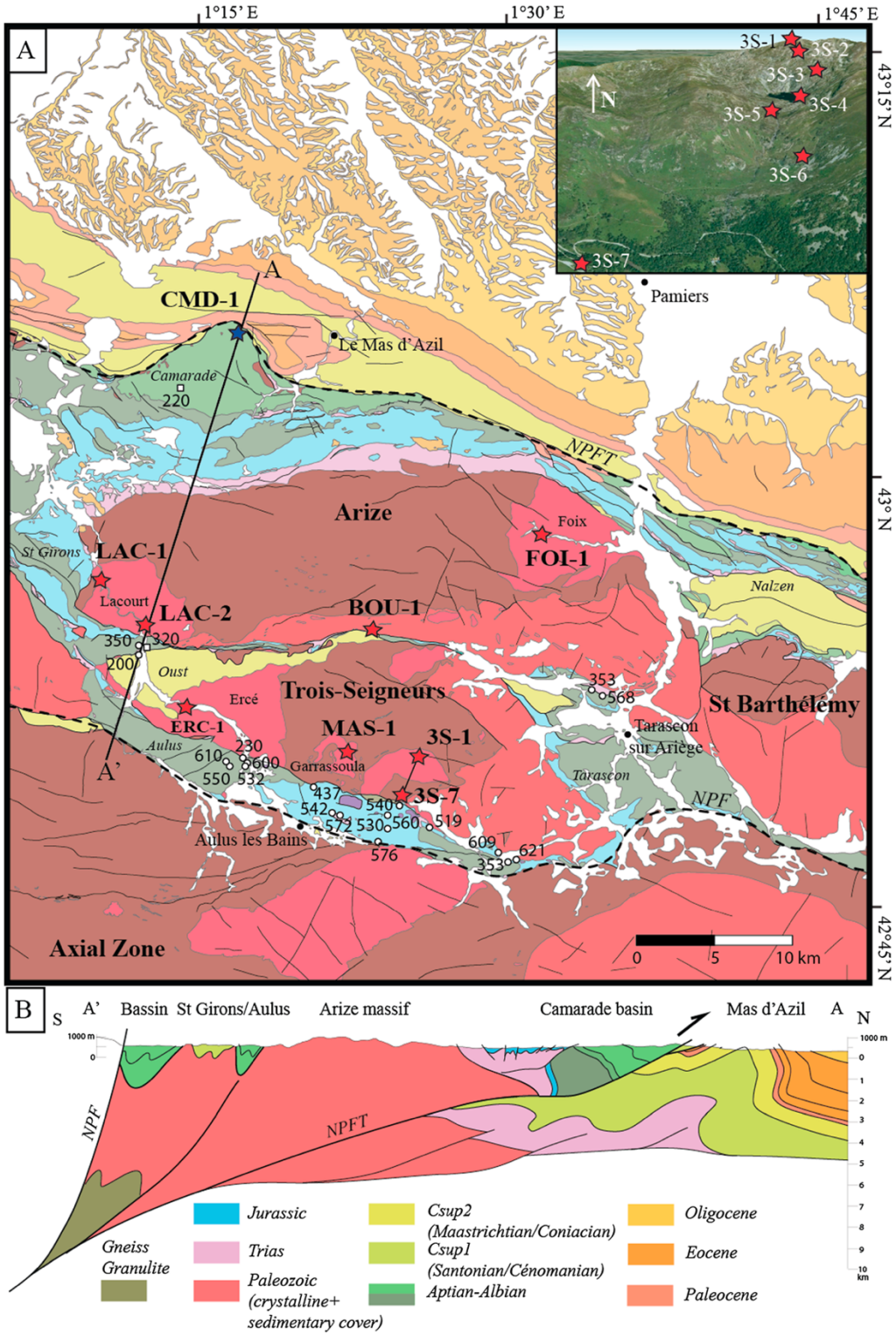

Figure 2.14: Geological map of the central part of the NPZ studied in Vacherat et al. (2016). A) Red and blue stars represent the location of the studied granitic massifs and detrital samples, respectively and white circles represent the location of samples analysed by RSCM from Clerc and Lagabrielle (2014) and their corresponding temperature (°C). The photo in the top to the right shows a 3D view of the Trois Seigneurs (3S) massif and the position of collected samples. B) Cross section of the western Ariège area.

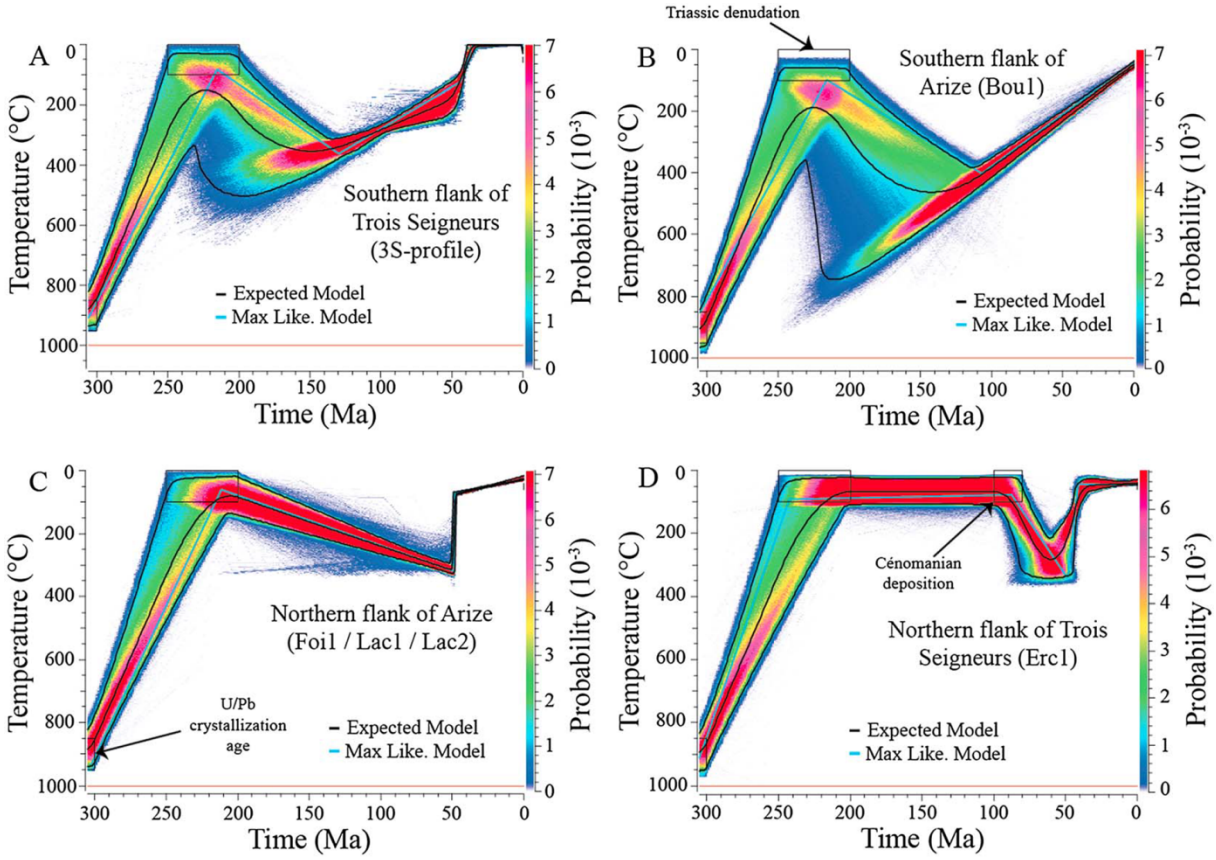

Figure 2.15: Time-temperature paths modelled using QTQt of low temperature thermochronology results obtained for granite samples from 3S and Arize massifs by Vacherat et al.(2016) . Paths (a) and (d) are for the southern and northern flank of the 3S massifs, respectively, and path (b) and (c) are for the southern and northern flanks of the Arize massifs, respectively.

A recent study of Ternois et al. (2019) used low temperature thermochronology combined with geological and geophysical data from literature (most of them have been already mentioned in this chapter) to propose a model for the evolution of the eastern Pyrenean orogen and its retro-foreland basin from the late Santonian to present day. The proposed model is based on the sequential restauration of crustal-scale N-S cross-section through the central Agly Massif (Figure 2.19) by assuming a compressional pure shear. The establishment of the cross-section was based mainly on the results of (Choukroune and Séguret, 1973; Chelalou et al., 2016; Clerc et al., 2016) and modern analogues following Reston (2009), Sutra et al. (2013) and Chenin et al. (2017) and led to a restored hyperextended rift in the eastern Pyrenees in which the Agly-Salvezines block was surrounded by depocenters recording high temperature (113 – 95 Ma) and with mantle exhumation below the Boucheville syncline (Ternois et al., 2019) (Figure 2.17 & Figure 2.19).

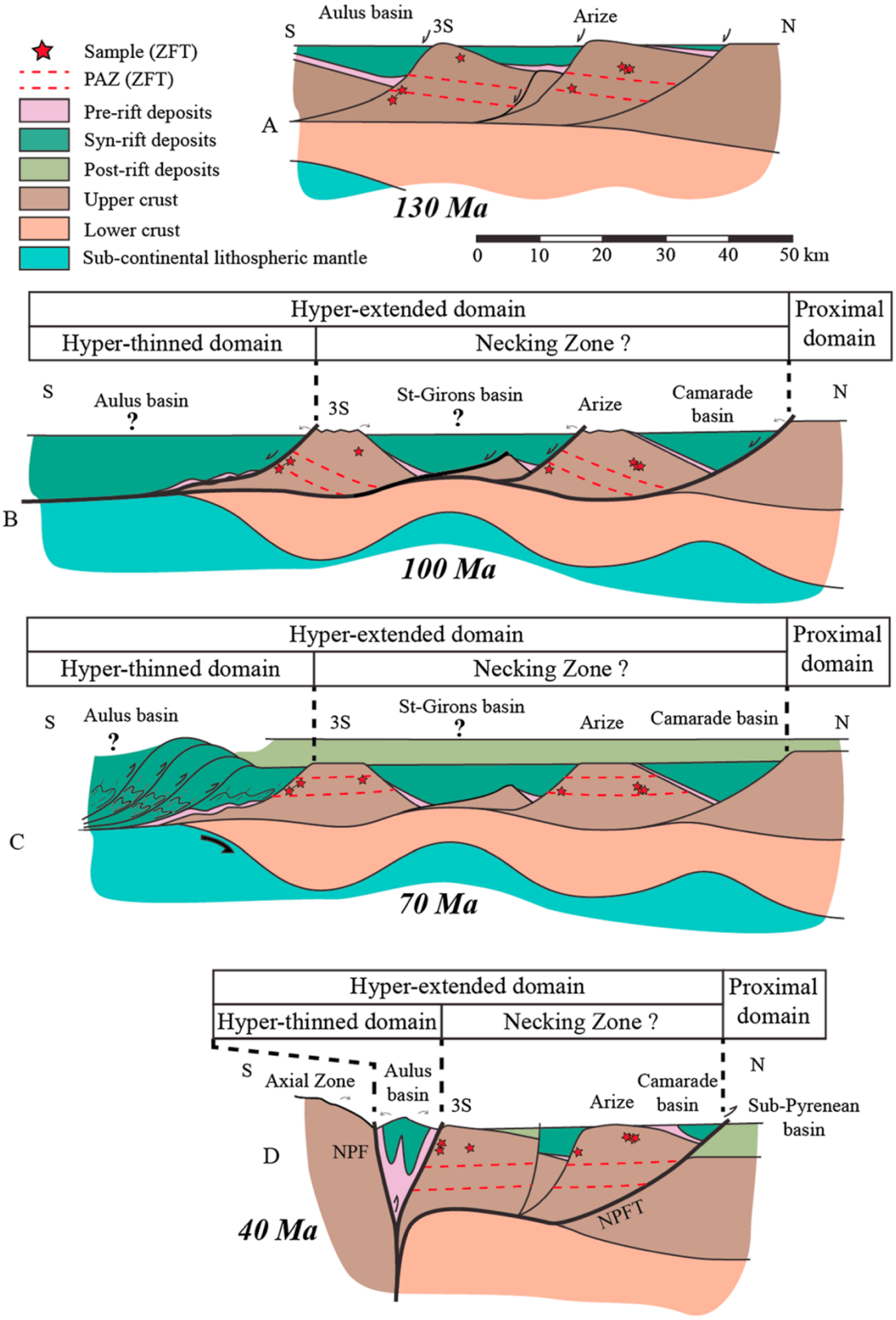

Figure 2.16: Reconstruction of the tectonic evolution of the Ariège area based on thermal modelling results from Vacherat et al. (2016). (a) At 130 Ma, the extension related to the end of the first rifting phase with south dipping normal faults and individualization of tilted block, (b) At 100 Ma, the main phase of rifting is taking place, resulting in extremely thinned domain below the Aulus basin, less thinned northward as for 3S and Arize massifs. The southern flank of both massifs recorded denudation and cooling, whereas the northern flank recorded sediment filling and burial. (c) At 70 Ma, convergence is accommodated in the distal domain (Aulus basin) resulting of a Pyrenean accretional prism. (d) At 40 Ma, full accretion of the remnants of the thinned lithosphere into the orogenic prism.

Low temperature thermochronology results and the deduced thermal events demonstrate that the Agly-Salvezines block was affected by metasomatism (chemical alteration by hydrothermal fluids) from the late Aptian to the middle Cenomanian followed by rapid cooling from 200-250°C by 90 Ma. The Figure 2.19a shows a first order restoration of the Iberian crust between the South Pyrenean Frontal Thrust and the North Pyrenean Fault to an 81 km wide pre-orogenic margin and a narrow distal domain of 33 km wide. The cross-section restauration was inspired from the work of Vergés et al. (1995) and Laumonier et al. (2015). In Figure 2.19b, the proposed cross-section is restored to a 19 km wide proximal domain (Mouthoumet massif), more than 26 km wide NPZ and a 71 km wide Axial Zone and South Pyrenean (Figure 2.19) (Ternois et al., 2019). Keuper evaporites (Figure 2.18) and diapirs act as a decoupling between basement and cover in the eastern part of the retro-wedge (Ternois et al., 2019). In addition, the crust thickening at 84 Ma (Figure 2.19a) is estimated near to 0 km below the Boucheville syncline and around 4 km below the Bas-Agly depocenter. Following Clerc and Lagabrielle (2014), Clerc et al. (2015) and Clerc et al. (2016) the Agly-Salvezines block is thinned to 8 km and buried below at least 2 km of Mesozoic sediments.

A stratigraphic and tectonic study from Rougier et al. (2016) in the central part of the Pyrenees (north to Barousse Massif) (Figure 2.12) suggests that the Lower Cretaceous carbonate platform has been deposited in salt-based extensional depocenters controlled by diapirs. In addition, it is supposed that diapirism was active since the Early Jurassic according to the thickness variations of the Black Dolomites Formation deposited during the Jurassic time, although the main rifting activity is clearly occurring during the Aptian and the Albian (Rougier et al., 2016).

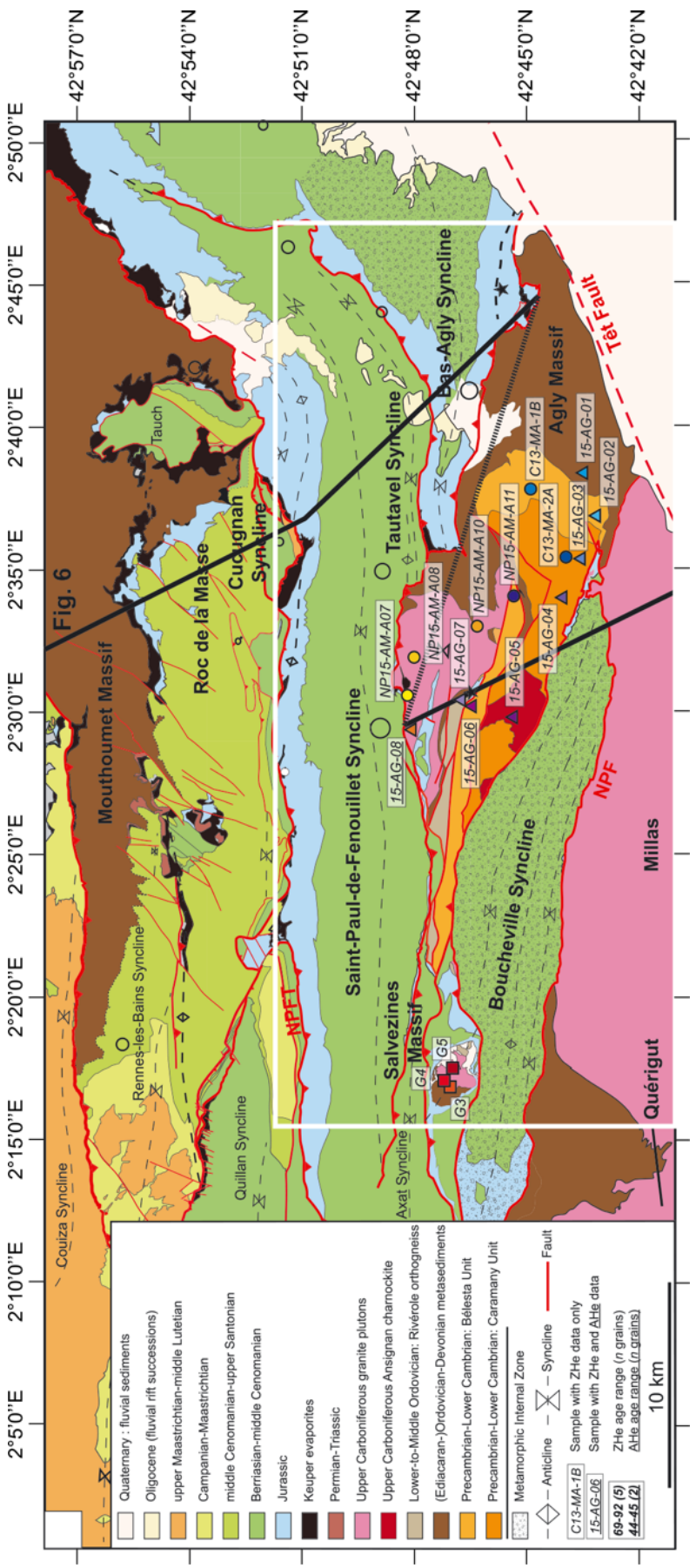

Figure 2.17: Geological map of the eastern part of the North Pyrenean Zone, showing the Agly-Salvezines area and the main structural elements and lithologies. The white square is a zoom of the studied area. Modified from Ternois et al. (2019).

I.3.3 Development of the Pyrenean orogen and infilling of the foreland basins as constrained by plate kinematics, low temperature thermochronology and sedimentology

The onset of convergence in the Pyrenees has been estimated at ~83 Ma and the total amount of Iberia plate convergence is debated depending on different views of crustal shortening process and different amounts of distribution of the shortening. Such studies are mainly based on deep seismic ECORS (Etude Continentale et Océanique par Réflexion et Réfraction Sismique) profile that crossed the Pyrenees. Olivet (1996), Rosenbaum et al. (2002), Sibuet et al. (2004), Vissers and Meijer (2012) estimated about 180 km of total amount of Iberia plate convergence, while Beaumont et al. (2000) estimated a shortening about 165 km and Roure et al. (1989) proposed 100 km of shortening. The main difference in the estimation proposition lies on the vertical distribution of shortening and the type of deformation.

Beaumont et al. (2000) suggested a thin-skin deformation style and a subduction of the whole crust beneath the Axial Zone, while Roure et al. (1989) proposed a thick-skin deformation style with a stacking of the whole Iberian crust above a detachment in the lower crust. Later, Mouthereau et al. (2014) combined existing and new sequentially restored cross sections in the central Pyrenees, European/Iberian plate kinematic reconstructions and low temperature thermochronology and geochronology results in the central Pyrenees to propose a sequential restoration of the central Pyrenees from ~83 Ma to the present. The thicknesses of undeformed crust below both the Aquitaine and the Ebro Basins (~30 and 35 km respectively) are inferred from the ECORS deep seismic profile (Choukroune, 1989; Roure et al., 1989). The temporal evolution of shortening in the Pyrenees and the Iberian Ranges are assumed to represent the total amount of convergence between the Iberian Plate and Europe. The earliest stage of convergence occurred from 83 to 71 Ma. Shortening is assumed to be occurring in a ductile regime due to the originally hot extensional basin in the northern Pyrenees.

The early orogenic convergence phase in the Pyrenees (Campanian – Maastrichtian) (Figure 2.19b) is accompanied by a shortening accommodated across the orogen according to Ternois et al. (2019) and the closing of the mantle domain underlying the Boucheville syncline. By the middle Campanian, the Iberian and European crusts are in contact resulting in an early orogenic edifice of low relief supplying sediments in the early retro- and pro-foreland basins (Ternois et al., 2019). In the sub-Pyrenean area of the central part of the Pyrenees, Rougier et al. (2016) suggest the formation of the narrow flexural Comminges Basin (see Aurignac Region in Figure 2.12) (Figure 2.18) sourced from the east (Bilotte et al. 2005) and comprising marine carbonate and calcareous turbidites deposits recording relatively rapid subsidence. To the north, sediments onlapped onto the Grey Flysch Formation of Coniancian-Santonian age (Figure 2.18) over 5 km across the Aquitaine platform

recording the evolution of a flexural basin. In the NPZ, strata were tilted and salt-related structures tightened. Basement faults began to invert below the Comminges Basin and the diapirs began to squeeze generating anticlines (Rougier et al., 2016).

During the Paleocene time, convergence appeared to stop in the retro-foreland basin according to both kinematic reconstructions (Macchiavelli et al.,2017) and sequential restorations (Grool et al.,2018). In addition, the absence of cooling in low temperature thermochronology results indicate that the massifs remain beneath 2 to 4 km of overburial (Ternois et al., 2019). Sediment deposition in the retro-foreland basin seems to be minimal reflecting the absence of a significant tectonic phase and denudation (Ford et al., 2016). Slow tectonic subsidence occurred in the Comminges Basin in the sub-Pyrenean central domain (Figure 2.18) during the Paleocene until the marine transgression in the early Ypresian (Rougier et al., 2016).

The second orogenic phase started in the early Eocene time during the continent-continent collision (Ternois et al., 2019). Orogen edifice was emerged by the Ypresian time due to the continuing crustal thickening, and led to the onset of subaerial erosion and the exhumation of the Agly-Salvezines block to near surface (Ternois et al., 2019) (Figure 2.19c). The North Pyrenean Frontal Thrust accommodated shortening resulting in the uplift of the Mouthoumet massif according to Christophoul et al. (2003). Shortening was progressively transferred to the Axial Zone and the Pro-wedge with the reactivation of the Asperes Thrust and Cadi-Canigou Thrust accommodating around 13 km shortening (Figure 2.19c) (Ternois et al., 2019).

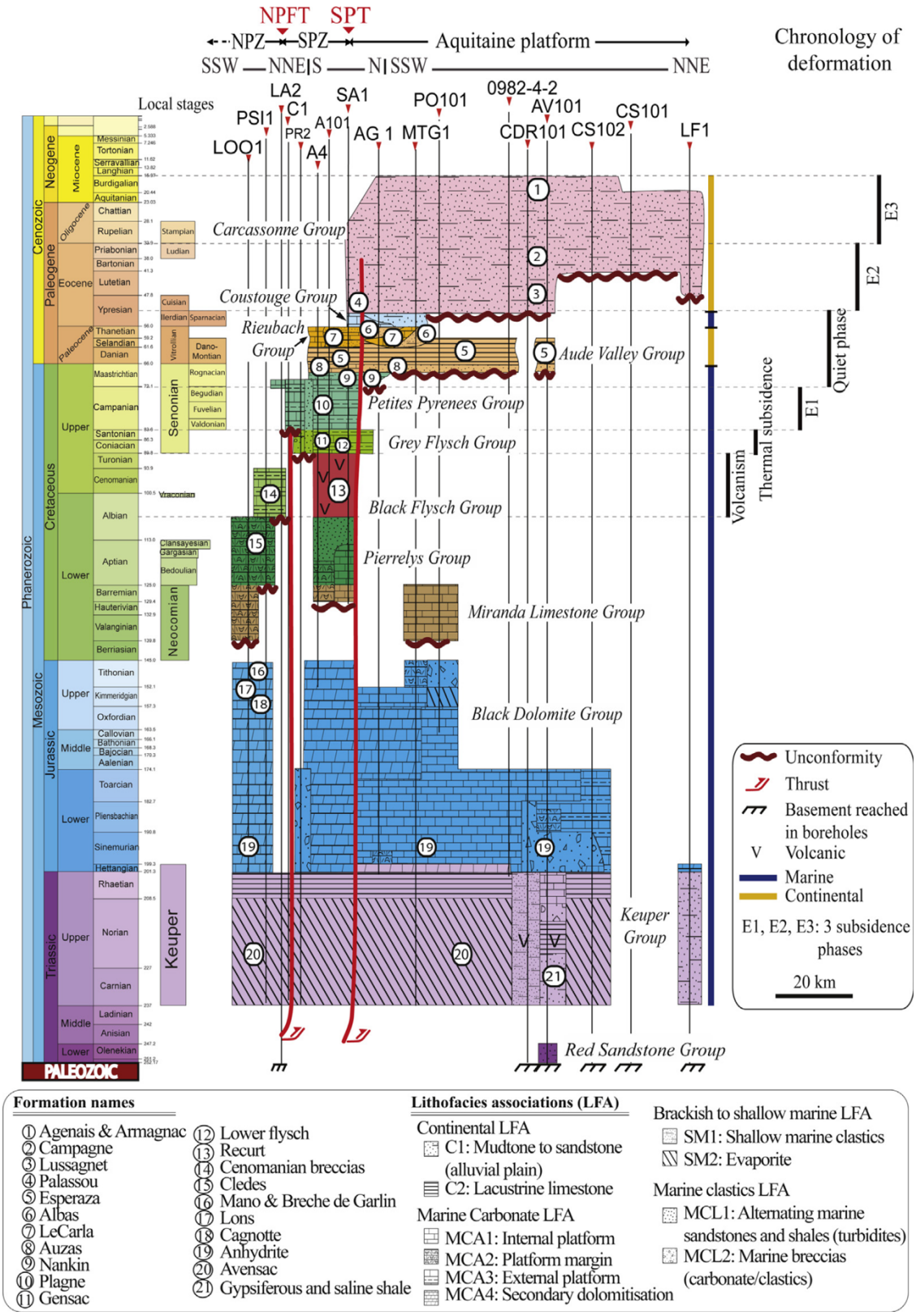

Figure 2.18:Chronostratigraphy from the Early Jurassic to the present day of the central part of the Pyrenean domain from Rougier et al. (2016)

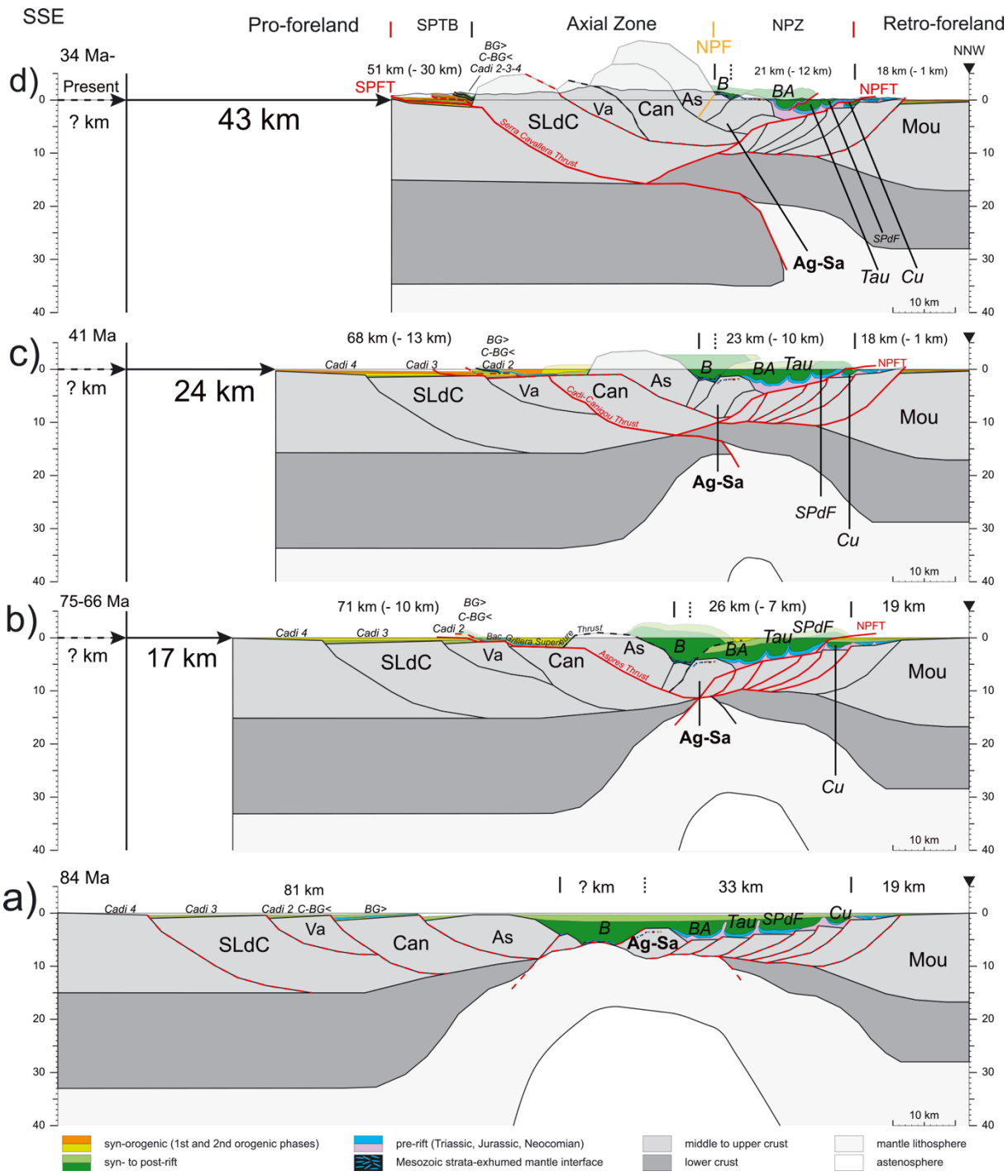

Figure 2.19: Balanced cross-section evolution of the Eastern Pyrenees from Ternois et al. (2019) along a N-S section line located in the eastern part of the NPZ (Figure 2.17). Solid red lines indicate faults that are active, dashed lines indicate faults that were active after the preceding step (those in black being abandoned before those in red). Black lines refer to abandoned faults. The present day Moho is set according to Chevrot et al. (2018) and Diaz et al. (2018). SPFT: South Pyrenean frontal Thrust, NPFT: North Pyrenean Frontal Thrust, NPF: North Pyrenean Faults, SLdC: Saint-Laurent-de-Cerdans, Va: Vallespir, Can: Canigou, As: Aspres, Ag-Sa: Agly-Salvezines, Mou: Mouthoumet, BG>: Bac Grillera Superieure, C-BG<: Coustouge-Bac Grillera Inferieure, B: Boucheville, BA: Bas-Agly, Tau: Tautavel, SPdF: Saint Paul de Fenouillet, Cu: Cucugnan.

The main phase of exhumation in the Pyrenees started from the middle Eocene to the early Oligocene (Yelland, 1991; Fitzgerald et al., 1999; Maurel et al., 2008; Gunnell et al., 2009;

Whitchurch et al., 2011; Rushlow et al., 2013; Mouthereau et al., 2014; Labaume et al., 2016; Vacherat et al., 2016; Bosch et al., 2016; Vacherat et al., 2017; Ternois et al., 2019) as constrained by low temperature thermochronology. ZHe ((U-Th)/He on zircon grains) ages from Ternois et al. (2019) for the Agly-Salvezines block in the eastern part of the NPZ are ranging between 75-70 Ma. They are interpreted as Campanian- Maastrichtian cooling event associated with early orogenic crustal thickening. According to ZHe ages in the central part of the Pyrenees from Mouthereau et al. (2014), a slow cooling is suggested around 75-70 Ma, consistent with previous detrital low temperature thermochronology results in the foreland basin (Beamud et al. 2011; Filleaudeau 2011; Rahl et al. 2011; Whitchurch et al. 2011), which is interpreted as the transition from convergence of the highly extended distal margin to the main episode of orogenic growth. The shortening resulted of the building of the Pyrenean orogen is accompanied by a south migrating exhumation of the Pyrenean basement and the infilling of foreland basins (Mouthereau et al., 2014). According to Grool et al. (2018), the shortening in the retro-wedge was accommodated equally between the early orogenic phase and the main one. Time- temperature paths produced by the inversion of low temperature thermochronology results from Vacherat et al. (2016) in the central part of the Pyrenees, show that the studied massifs (Trois Seigneurs and Arize) were at temperature between 200°C and 300°C when shortening initiated at 83 Ma. From 83 Ma to the main phase of exhumation in the early Eocene (~50 Ma), temperatures were kept relatively high with an estimated geothermal gradient over 80°C/km (Vacherat, 2014; Vacherat et al., 2016) (Figure 2.15). A part of the ductile deformation observed in Aulus and St Girons Mesozoic basins (Figure 2.14) may be originated from this transitional period (Figure 2.16c). Time-temperature paths represented in Figure 2.15 show a cooling at 70-75 Ma for only one path. The observed cooling below 110°C at 75-70 Ma in the southern flank of the Trois Seigneurs and Arize massifs is interpreted as occurring close to the NPZ that might encountered a rapid thermal relaxation during thrusting activity (Mouthereau et al., 2014) (Figure 2.15).

The accommodation of thrusting on relict extensional features led to an inversion dominated thrust stacking in the Axial Zone. Most of the obtained ages in the Axial Zone are ranging between 50 and 33 Ma reflecting the onset of rapid cooling that was previously defined (Yelland, 1991; Fitzgerald et al., 1999; Sinclair et al., 2005; Maurel et al., 2008; Gunnell et al., 2009). Time temperature paths constrained by low temperature thermochronology on apatite crystals show that the Pyrenean massifs exhumed from the north to the south and from east to west. The exhumation of the Agly massif in the NPZ is followed by the exhumation of the north eastern part of the Axial Zone (Quérigut, Mont-Louis, Ax-les-Thermes, Riberot) (Yelland, 1991; Fitzgerald et al., 1999; Maurel et al., 2008; Gunnell et al., 2009; Vacherat et al., 2016) from the middle to the late Eocene times. Later, the southern part of the Pyrenean Axial Zone exhumed progressively from east to west, from the Canigou massif in the east to the Eaux Chaudes massif in the west. Estimated cooling rates are ranging

between 12 to 15°C/Ma in the NPZ and have potentially reached 50°C/Ma between 48 and 45 Ma (Vacherat et al., 2016). Assuming a thermal gradient of 30°C/km, exhumation rates are ranging between 0.5 km/Ma to 1.6 km/My (Vacherat et al., 2016).

In the southern flank of the Axial Zone, thermal modelling of apatite fission-track data obtained for the Canigou massif in the eastern part of the Axial Zone by Maurel et al. (2008), provided an Early Oligocene (~33-28 Ma) cooling history characterized by a fast cooling and exhumation. Fitzgerald et al. (1999) observed a highly asymmetric exhumation pattern in the Maladeta massif during the Oligocene as revealed by AFT results. Exhumation of the massifs from the southern flank of the Axial Zone is faster compared to the one of the northern flank massifs. The Mont-Louis massif, for example, recorded an earlier slow exhumation (middle Eocene, ~40 Ma) according to thermal modelling results (Maurel et al. 2008). Further to the west, in the central part of the Axial Zone, AFT data for the Riberot massif recorded a relatively uniform exhumation all over the massif around 50 Ma. Such different exhumation patterns are interpreted as a change in tectonic style from a dominated thrust stacking to a subsequent internal deformation in the upper crust between the Eocene and the Oligocene (Fitzgerald et al., 1999).

A low temperature thermochronology study of the western Axial Zone of the Pyrenees and the adjacent Chaînons Béarnais (North Pyrenean Zone) by Bosch et al. (2016) has led to a better understanding of tectonic constraints and erosional history of this part of the belt. In the Chaînons Béarnais (between the North Pyrenean Frontal Thrust and Lakora Thrust) (Figure 2.20), ZHe results show ages from 50 to 26 Ma, that are younger than the deposition age. Time – temperature path of these samples shows a heating event followed by a cooling between the middle Eocene and the Oligocene time. Low temperature thermochronology results from the Lakora thrust show a cooling beyond the closure temperature between 36 and 30 Ma interpreted as exhumation (Figure 2.20). Eaux-Chaudes and Balaitous-Panticosa granite massifs in the western part of the Axial Zone (Figure 2.20) provide ZHe and AFT ages having a Late Paleogene to Miocene signal, reflecting a fast cooling between 30 and 20 Ma (Late Oligocene to Aquitanian). Apatite and zircon fission track and (U-Th)/He results show a decrease in cooling ages from the north to the south (Yelland 1991; Fitzgerald et al. 1999; Sinclair et al. 2005; Maurel et al. 2008; Gunnell et al. 2009; Mouthereau et al. 2014; Bosch et al. 2016; Vacherat et al. 2016; 2017; Ternois et al. 2019) and from east to west reflecting a diachronous progression of deformation and exhumation (Figure 2.21).

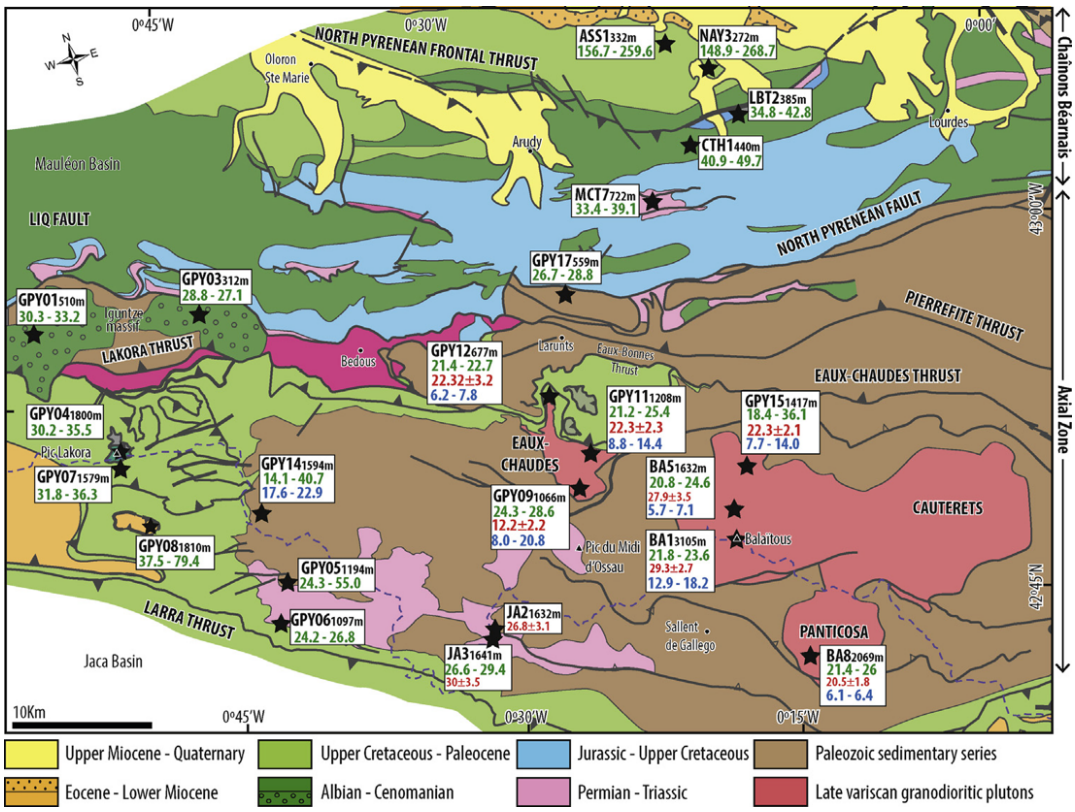

Figure 2.20: Geological map of the western part of the Pyrenean Axial Zone from Bosch et al. (2016) showing the location of the sample and the obtained AHe ages in blue, ZHe ages in green and AFT ages in red. The blue dashed line indicates the drainage divide.

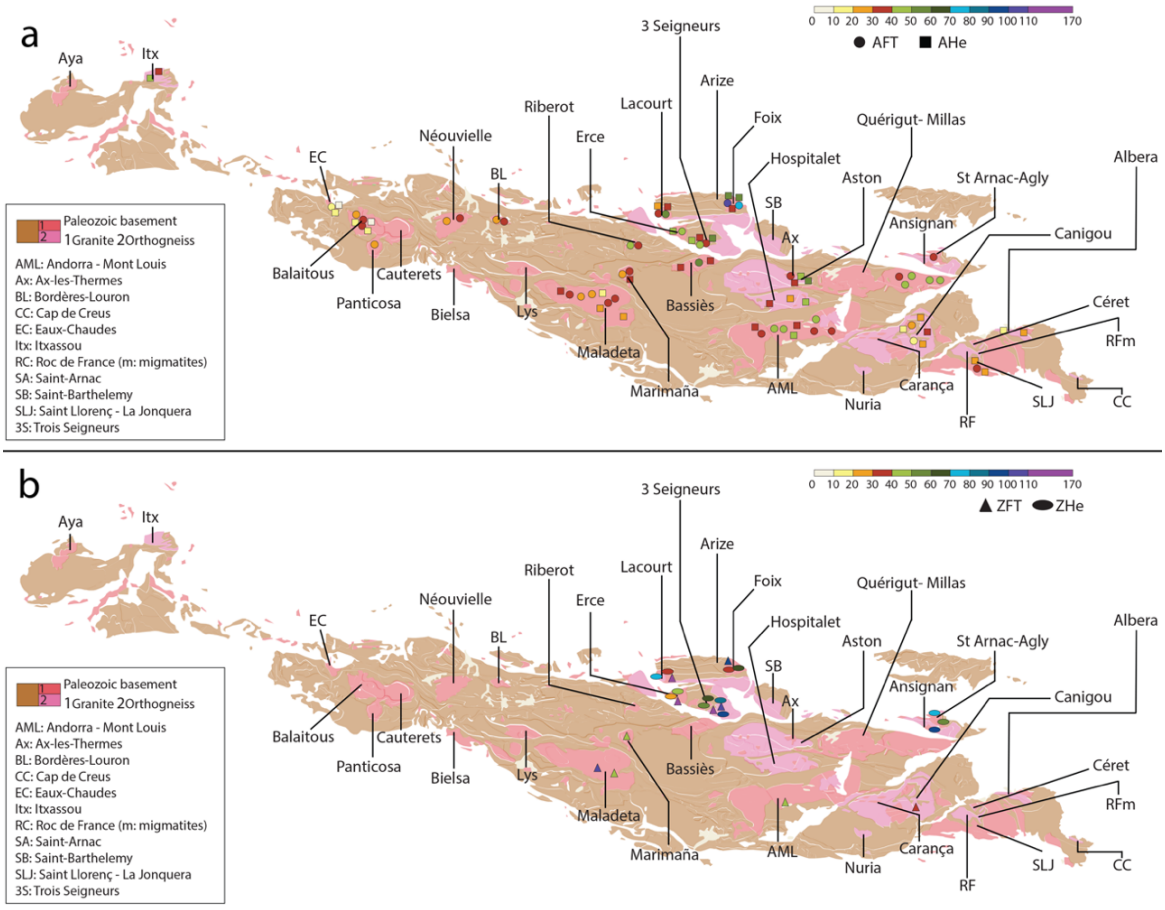

Figure 2.21: Compilations of low temperature thermochronology data obtained in the Axial Zone and the North Pyrenean Zone. a) Compilation of AFT and AHe data b) compilation of ZFT and ZHe data (Yelland, 1991; Fitzgerald et al.*, 1999; Sinclair* et al.*, 2005; Maurel* et al.*, 2008; Gunnell* et al.*, 2009; Mouthereau* et al.*, 2014; Bosch* et al.*, 2016; Vacherat* et al.*, 2016; Vacherat* et al.*, 2017; Ternois* et al.*, 2019).*

The study of the geometry and flexure of the European plate under the north-Pyrenean foreland basin shows that the topographic load of the Pyrenean orogen may be the main source of subsidence in the eastern part of the basin (Angrand et al. 2018). In the central part, the effect of topographic load, buried load, in addition to the post-rift thermal subsidence contribute to the geometry of the basin (Angrand et al. 2018). The geometry of the western part of the basin is mainly controlled by thermal subsidence (Angrand et al. 2018).

I.4 Paleogeographic reconstruction of the Pyrenean domain

A paleogeographic reconstruction is proposed by Vacherat et al. (2017) based on low temperature thermochronology, geochronology and sedimentology results obtained in the Pyrenees, the retro- and pro-foreland basins from the Albian – Santonian rifting phase to the main phase of exhumation of the Pyrenees and the infilling of the basin. In addition to all these results, the restored cross section from Mouthereau et al. (2014), Ford et al. (2016) and Rougier et al. (2016) have been

used too, in order to constrain the dimension of the hyper-extended domain between Iberia and Europe in the NPZ. The paleogeographic reconstruction (Vacherat et al., 2017) lacks information on the syn-orogenic deposits in the retro-foreland basin. This information is very important to reconstruct the sediment routing system from the late Ypresian to the Oligocene time. Such requested data represent the main goal of this thesis. The data have been produced and integrated to the paleogeographic reconstruction of the Pyrenean domain. In order to facilitate the understanding of the paleogeograhic reconstructions below, stratigraphic logs from the South and North Pyrenean foreland basins are represented in Figures 2.22 and 2.23.

I.4.1 The Pyrenean domain during the Albian- Santonian rifting phase

In the reconstruction of Vacherat et al. (2017) for the early Cretaceous rifting event, the necking zone architecture is characterized by a normal thickness while the distal rift architecture is characterized by an extremely-thinned domain floored by the exhumed mantle (Figure 2.24). In the northeastern Pyrenees, the Agly-Salvezines block is considered as emerged and bounded to the north by the wide St-Paul-de-Fenouillet basin as suggested by Clerc and Lagabrielle (2014). In this area, the Boucheville syncline represents a hyper-extended distal domain floored by the continental mantle (Figure 2.24). The Aulus basin, in the central part of the Pyrenean domain, corresponds to an extremely-thinned distal domain, comprising the Trois Seigneurs and Arize massifs considered as a necking zone (Figure 2.16), and to the western part of the Pyrenean domain, the reconstruction proposed by Rougier et al. (2016) shows the emergence of the Pinas Horst during the Cenomanian (Figure 2.24). Farther to the west, the NPFT is prolonged north of the Mauléon basin , close to the Grand Rieu High (Figure 2.24). Vacherat et al. (2017) suggested that the European necking zone in the western part of the Pyrenean domain corresponds to the Grand Rieu High as the Mauléon basin, floored by the subcontinental mantle is present south to this structure (Figure 2.24).

Sediment deposition during the Early Cretaceous in Iberia and Europe started with a carbonate platform (Urgonian facies) (Figure 2.22) and followed, in the SPZ (Organya Basin) by the deposition of 3 km thick hemipelagic marls during the Aptian (Figure 2.12). Subsidence in the SPZ continued with turbidite deposits overlaid by deltaic sandstones of the Turbón Formation during the Cenomanian (Figure 2.22 and 23) (Verges and Garcia-Senz, 2001; Filleaudeau, 2011). These deposits may be part of a larger feeding system located in the west and south, as indicated by the Utrillas Sandstones (Figure 2.22). Although the source of the deposits was debated, they have been interpreted by Rat (1988) as being sourced from the Iberian Meseta and the Cantabrian mountains while Filleaudeau (2011) proposed that it resulted from the erosion of the Ebro block (Figure 2.12).

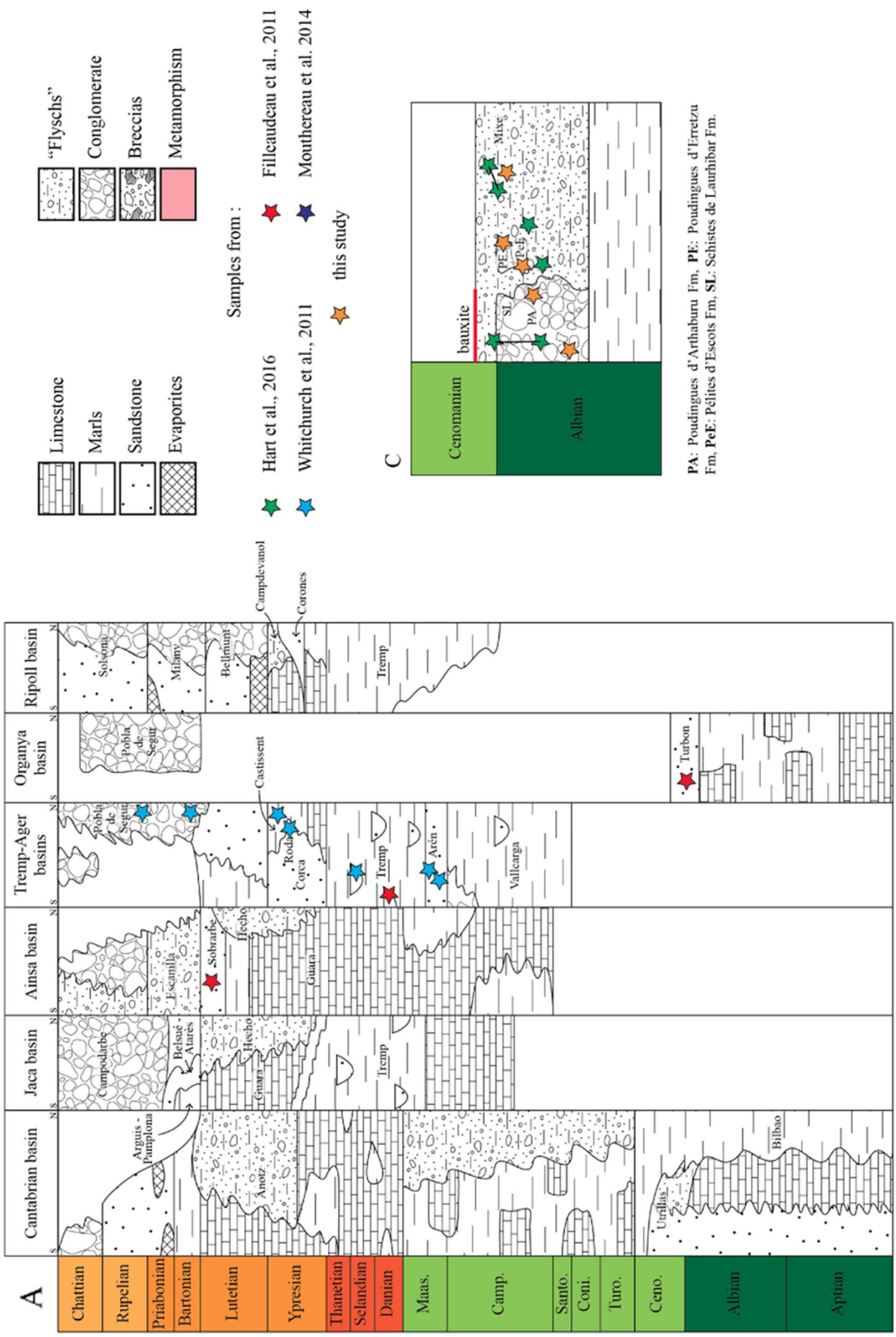

Figure 2.22: Stratigraphic logs from Vacherat et al. (2017) for A) several basins in the South Pyrenean Zone. Stars represent the ages and location of sediments studied in Filleaudeau (2011), Whitchurch et al. *(2011), Mouthereau* et al. *(2014) and Hart* et al. *(2016) C) zoom on the Mauléon Basin Albo-Cenomanian deposits.*

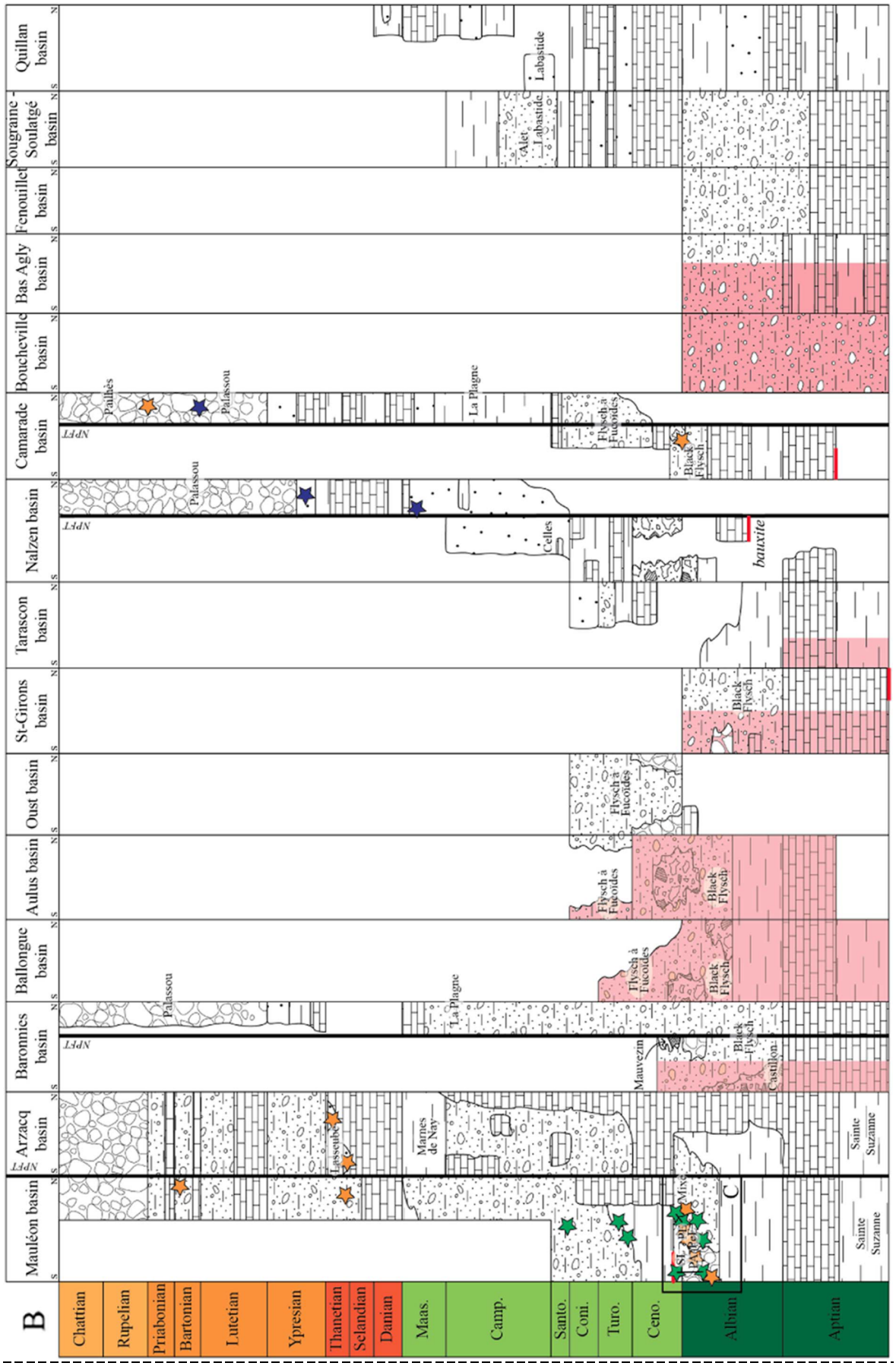

Figure 2.23: Stratigraphic logs from Vacherat et al. (2017) for several basins in the North Pyrenean Zone. Stars represent the ages and location of sediments studies in Filleaudeau (2011), Whitchurch et al. *(2011), Mouthereau* et al. *(2014) and Hart* et al. *(2016)*

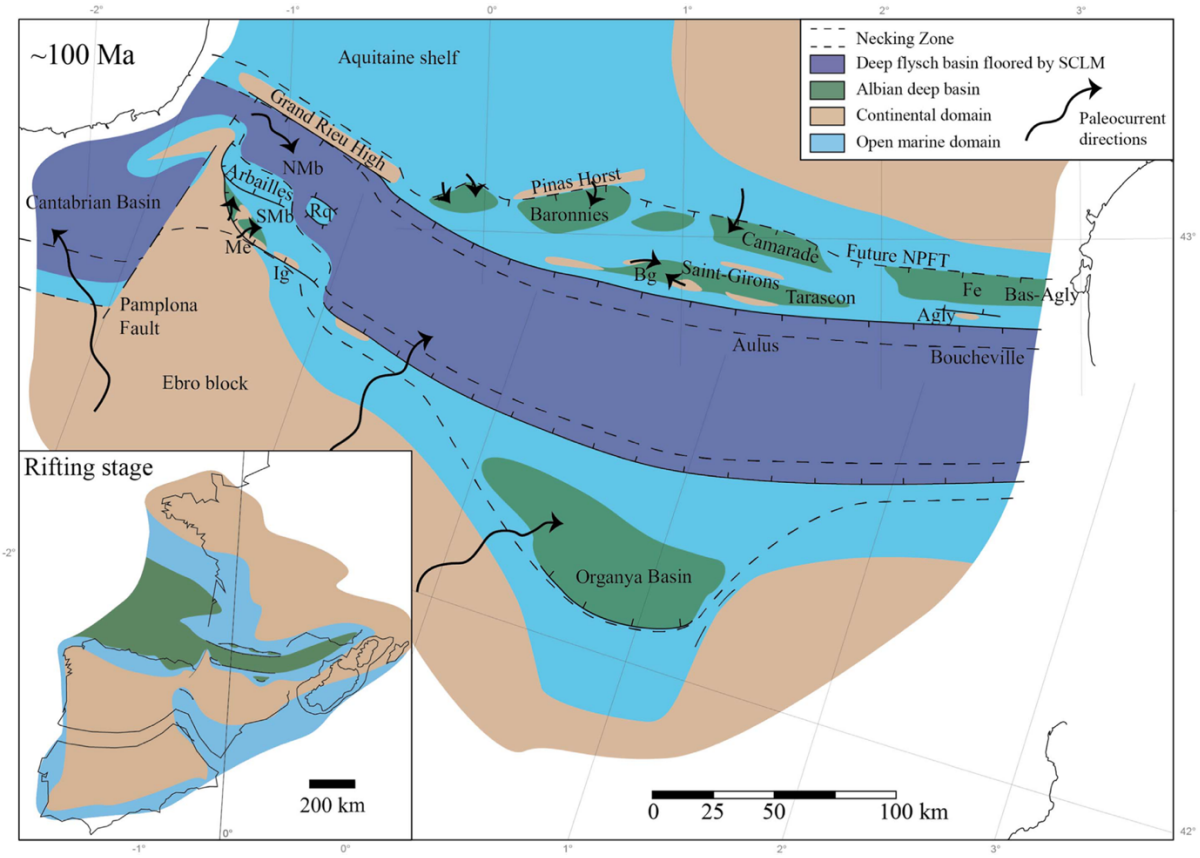

Figure 2.24: Paleogeographic reconstruction of the Pyrenean domain during the Albian - Cenomanian transition. Bg : Ballongue Basin, Fe : Fenouillèdes Basin, Ig : Igountze Basin, Me : Mendibelza Massif, NMb : North-Mauléon Basin, Rq : Roquiague structure, SMb : South-Mauléon Basin. From Vacherat et al. *(2017).*

In the central part of the NPZ and the sub-Pyrenean Zone, Aptian-Albian Black Flyschs were deposited and reached a thickness of 3.5 km. They include sedimentary breccias rich in Paleozoic clasts and Jurassic black dolomites concentrated in the hanging wall of the NPFT (Rougier et al., 2016). Two alkaline magmatic episodes are recognized in the Aurignac region (sub-Pyrenean zone, north of Barousse Massif) (Figure 2.12) from the Late Albian to the Turonian (Rougier et al., 2016),. The first one is a submarine volcanic phase from the Late Albian to the Early Cenomanian and the second one is an intrusive phase from the Late Cenomanian to the Turonian. They are covered by a Cenomanian-Santonian Grey Flysch formation that unconformably overlies the Black Flysch (Monod et al., 2014). In the western part of the NPZ, after the deposition of the Early Cretaceous carbonate platform, subsidence pursued during the Albian and reached a thickness of ~4 km of turbidites. Authors argue that the deposition of such thickness of turbidites is accompanied with the extreme crustal thinning occurring during the Albian (Jammes et al. 2009; Jammes et al. 2010; Clerc 2012; Clerc and Lagabrielle 2014; Tugend et al. 2014; Clerc et al. 2015; Tugend et al. 2015). Paleocurrent directions measured in turbidites indicate an E-directed flow north of the Labourd Massif changing to S-SE in the eastern part of the massif (Boissonnas et al., 1974; Le Pochat et al., 1974; Boltenhagen et al., 1976; Le Pochat et al., 1976; BRGM and IGME, 1998) (Figure 2.12). In the Baronnies Basin,

“Brèches de Castillon” and “Mauzevin” Formations (Figure 2.23) (Figure 2.12) are breccias bearing Paleozoic clasts and have paleocurrent directions to the east then to the south following the orientation of basin-bounding faults (Rougier et al., 2016). In the Camarade Basin, breccia formations show a northern source supposed to be controlled by the activation of the NPFT (Mouthereau et al., 2014; Ford et al., 2016; Vacherat et al., 2016) (Figure 2.12). According to Rougier et al. (2016), the end of the rifting is accompanied by the deposition of Black Flyschs during the early Cenomanian into a large marine domain, up to the northeastern part of the Pyrenees (Vacherat et al., 2017) (Figures 23 and 24).

The main difference between the sediment routing system in the northern and the southern flank of Pyrenees during the Early Cretaceous rifting phase (Figure 2.24) is the existence of an extreme crustal thinning recorded in the NPZ reflecting a narrow and deep basin with N-S and E-W flow directions, whereas in the southern flank, the lack of recorded extension phase produces a feeding system originated from the northern Iberia plate and the Ebro block (Vacherat et al., 2017).

I.4.2 Late Cretaceous reconstruction of the Pyrenean domain

The onset of convergence is estimated around 83 Ma (Mouthereau et al., 2014) as mentioned before. The proposed scenario (Figure 2.25) shows a contact between the two necking zones of the rifted margins and a submarine proto-orogenic prism located in the area of the Aulus Basin. This result is consistent with the results of Ford et al. (2016) and Vacherat et al. (2016) (Figure 2.12) (Figure 2.16). In the northeastern part of the Pyrenees, as low temperature thermochronology results suggest that the Agly-Salvezines block was near to the surface at this time (Ternois et al., 2019), this area was set as emergent domain (Figure 2.25) (Figure 2.12). In the western domain, the inversion of Mauléon Basin during the Late Cretaceous is poorly investigated, however, the Cameros Basin in the south has detected cooling at ~89 Ma (Del Río et al., 2009; Rat et al., 2019) supporting the inversion of the rifted margins in the western Pyrenees (Figure 2.25) (Figure 2.12).

In the eastern part of the South Pyrenean Zone (SPZ), the results of the detrital zircon U/Pb, (U-Th)/He, and detrital rutile U/Pb and geochemistry from Odlum et al. (2019) in south-eastern Pyrenean foreland basin (Figure 2.12) show that during the Late Cretaceous, the foreland basin deposits were sourced from the crustal Early Cretaceous rifting deposits and from distal south-eastern to eastern sources located in the Coastal Catalan Range and potentially from the Corsica-Sardinia block (before Miocene extension).

In the central part of the SPZ, the onset of inversion of the Aptian-Albian Organya Basin (Figure 2.12) on the top of the Boixols Thrust is dated as Campanian and resulted in the rise of the Boixols – Sant Corneli high (Figure 2.12) (Figure 2.25) (Berástegui et al. 1990; Bond and McClay

1995). Such results are supported by low temperature thermochronology, which reflected a synchronous exhumation of the Axial Zone at this time (Filleaudeau 2011; Whitchurch et al. 2011; Filleaudeau et al., 2012). Available constraints on the sedimentary paleoenvironments during the late Campanian – early Maastrichtian (~70 Ma) allow determining the spatial distribution of sedimentary deposits going from deep turbiditic basins, marine to shallow-marine and fluvial deposits.

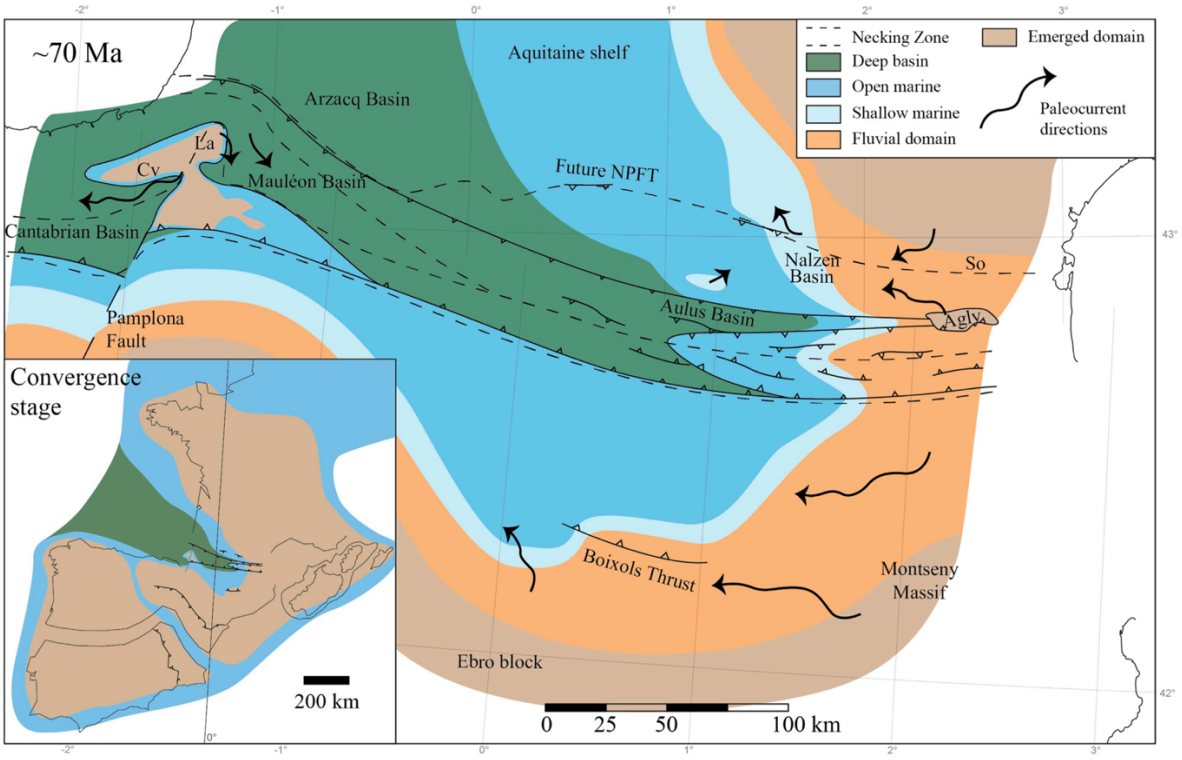

Figure 2.25: Paleogeographic reconstruction of the Pyrenean domain from Vacherat et al. (2017) during the Late Cretaceous. Cv : Cinco-Villas Massif, La : Labourd Massif, So : Sougraigne-Soulatgé Basin

The Tremp Basin in the central part of the SPZ located to the south of the Boixols Thrust (Figure 2.12) was filled by westward prograding Santonian to Campanian deltaic shales with slope carbonates and siliclastic turbidites of the Vallcarga Formation (Ardèvol et al., 2000) (Figure 2.22). They are topped by the shoreface to deltaic sandstones of the Arén Formation deposited from the late Campanian to the Maastrichtian (Figure 2.22). It was followed by fluvial deposits, including meandering depositional environments, lacustrine and paleosoils deposits that took place from the early Maastrichtian to the late Paleocene with the deposition of the Garumian facies of the Tremp Formation (Plaziat 1975; Nijman 1990; Nijman 1998; Ardèvol et al. 2000; Clevis et al. 2004; Pujalte et al. 2009) (Figure 2.22). These sediments are sourced from the east until the late Maastrichtian according to Arbués et al. (1996) and Ardèvol et al. (2000). The low temperature thermochronology work of Whitchurch et al. (2011) suggested an eastern Pyrenees source of these sediments. However, AFT results in the eastern Pyrenees from Yelland (1991) and Herman et al. (2013) show a cooling between 30 and 40 Ma suggesting that they did not reach surface during the Late Cretaceous. Other

proposed sources of these sediments are the Corsica-Sardinia block and the Montseny Massif in the north-eastern part of the Catalan Coastal Ranges containing mainly Variscan and Cadomian plutons emerged at this time (Juez-Larré and Andriessen, 2006) (Figure 2.22). The Ager Basin, located to the south of the Tremp Basin, contains coarser sediments characterized by paleocurrent directions toward the north – northwest reflecting a source in the Ebro Basin (Colombo and Cuevas, 1993; Gómez-Gras et al., 2016).

The Late Cretaceous deposits in the western part of the SPZ are characterized by E-W directed troughs shaping the Cantabrian Basin (Figure 2.12) and filled by marls and calcareous turbidites (Figure 2.22). The occurrence of syn-sedimentary sliding on the southern margin of the Cantabrian Basin, in addition to the E-W paleocurrent directions reflects a tectonic activity of east-west oriented faults and of the NE-SW Pamplona fault (Figure 2.25) (Mathey 1986; Mathey et al. 1999). Sediments are thus sourced from the paleo-high formed Cinco Villas Paleozoic Massif as shown by several Upper Cretaceous strata resting directly on top of the Paleozoic basement and by clasts of Urgonian limestones found in breccias intercalated in the Late Cretaceous (Figure 2.22) (Feuillee et al. 1973; Rat 1988; Mathey et al. 1999).

In the sub-Pyrenean domain and in the NPZ, the Albian turbidite basins are filled until the Maastrichtian by a succession of limestones and marls, e. g. Marnes de Nay formation in Arzacq basin to the west (Figure 2.23). To the east, shallower Santonian sediments of Grès de Celles formation are deposited in the Nalzen basin in the central part of the NPZ and in the eastern part of the NPZ, deltaic sandstones of Turonian ages are deposited in the south of the Mouthoumet Massif (Figure 2.23) (Figure 2.25) in the Sougraigne-Soulatgé and Quillan Basin (Figure 2.12). This sequence is topped by the Campanian deposits of the Grès de Labastide and the continental Grès d'Alet Formations (Figure 2.23).

North of the Arize Massif (central part of the NPZ) and in particular to the north of the NPFT, rare paleocurrent directions are measured in the Campanian to Maastrichtian sandstones that indicate a north-northwest transport direction (Cavaillé and Paris 1976). Low temperature thermochronology and geochronology results in the same zone suggest a source located to the east, probably the Agly-Salvezines block (Vacherat et al., 2017). To the south of the Arize Massif, in the Oust-Massat Basin (Figure 2.12), transgressive calcareous turbidites and breccias of the Flysch à Fucoïdes Formation contains granite pebbles and boulders and shows north-eastern paleocurrent direction (Figure 2.23) (Figure 2.25) (Barrouquère et al., 1976a; Barrouquère et al., 1976b). These deposits are Cenomanian to Coniacian in age and are located directly on top of the northern flank of the Trois Seigneurs Massif (Figure 2.12). To the west, Rougier et al. (2016) suggested that during the early Maastrichtian, the NPFT that marks the contact between the Baronnies Basin and the Pinas Horst to the north was active. The existence of a slight deformation of the marine deposits (Plagne Formation) sealing the fault,

indicating that the Baronnies Basin was thrusted northward over the horst (Figure 2.24). More to the west, Vacherat (2014) showed by low temperature thermochronology that the Labourd Massif (Figure 2.12) cooled during the Late Cretaceous. In the northern part of the Mauléon basin, a series of Cenomanian to Turonian calcareous turbidites shows a south-east paleocurrent direction similar to those measured in the Albian units (Figure 2.23) (Figure 2.12) (Boissonnas et al. 1974; Le Pochat et al. 1974; Boltenhagen et al. 1976; Le Pochat et al. 1976). The calcareous turbidites of the Antzaramendi Formation (Figure 2.23), Coniacian to Santonian age, overlie the eastern flank of the Labourd Massif. Paleocurrent directions measured in this formation (Antzaramendi) show sediment transport towards south-southeast (Boissonnas et al. 1974; Le Pochat et al. 1974).

According to these data, paleocurrent directions in the northern part of the Mauléon Basin remain unchanged during this entire period from the Cenomanian to the Santonian by the presence of the Labourd Massif (Figure 2.25).

I.4.3 Late Paleocene – early Eocene

The onset of rapid syn-orogenic exhumation of the Pyrenees is estimated around ~59 Ma during the Late Paleocene – early Eocene transition (Figure 2.26) constrained by low temperature thermochronology (Ternois et al., 2019). Around 30 km of N-S shortening are suggested by Mouthereau et al. (2014) between 70 and 55 Ma. Low temperature thermochronology, in particular AFT and AHe results from several massifs show cooling ages between 50 and 30 Ma like the Canigou, Andorra-Mont Louis, Ax-les-thermes, Bassiès and Lacourt (see Figure 2.21).

In the central part of the NPZ and in the sub-Pyrenean zone, late Maastrichtian – Selandian deposits are characterized by low-energy fluvial, palustrine and lacustrine sediments (Rougier et al., 2016). During the Thanetian, shallow marine, brackish and fluvial fine-grained sediments are deposited during a series of low-amplitude marine transgressions (Tambareau et al. 1995; Rougier et al. 2016). In the Mauléon basin (Figure 2.12), cooling and exhumation are also occurring around 50 Ma reflecting ongoing closure between Iberia and the European plate (Vacherat, 2014) (Figure 2.26). In the western part of the Axial Zone, in addition to the central and western part of the NPZ, Paleocene deposits are characterized by marine marls and limestones (Lasseube Limestone Formation in the Arzacq Basin) (Figure 2.22) bordered by a large carbonate platform and supplied from the north by the Aquitaine platform and the Massif Central (Figure 2.12), and from the south by an emerged area east of the preserved Pyrenean domain (Plaziat 1984; Biteau et al. 2006) (Figure 2.26). The early Eocene deposits are characterized by a marine transgression in the northern Pyrenees from the Bay of Biscay in the west to the Corbières in the east (Figure 2.12).

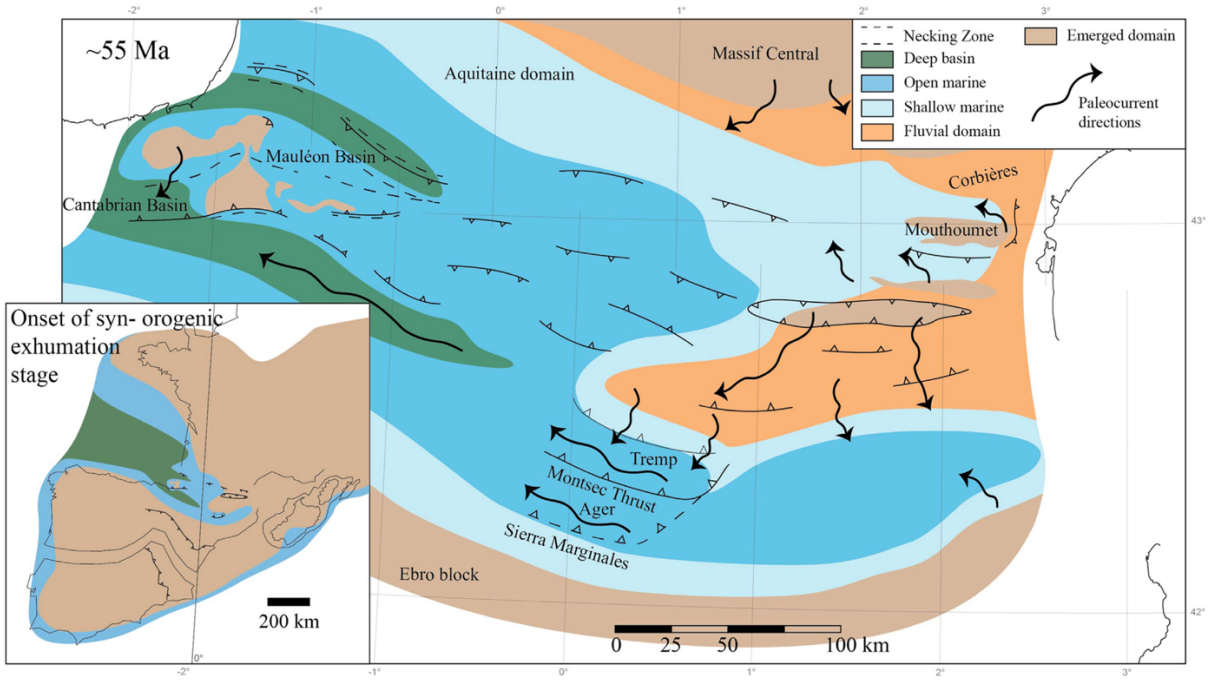

Figure 2.26: Paleogeographic reconstruction of the Pyrenean domain from Vacherat et al. (2017) during the late Paleocene-early Eocene.

From west to east in the southern Pyrenees, the transition from the Late Cretaceous (end of Maastrichtian) to the Paleocene (Danian) in the Cantabrian basin (Figure 2.12) is marked by hemipelagic sedimentation (Rat 1988). This episode is followed by the deposition of a carbonate platform during the Paleocene (Figure 2.22) (Rasser et al. 2005). According to the results of Rosell et al. (2001) and Filleaudeau (2011), from the Danian to the Thanetian, the Tremp basin deposits were sourced from the north (Figure 2.26). From the Ilerdian to the Cuisian ~56-53 Ma, carbonate platform are replaced by siliclastic turbidites in the Cantabrian Basin (Rat 1988), and by southward prograding deltaic system in the central and eastern Pyrenees (Figure 2.22) (Puigdefàbregas and Souquet 1986). These data support sediment supply from the north according to Puigdefabregas et al. (1986) and traduce the emergence of the Pyrenean relief. The individualization of the Tremp piggyback basin took place synchronously with thrusting along the Montsec ramp (Farrell et al.1987; Poblet et al. 1998). The Ager Basin was also individualized as a narrow embayment, due to the onset of the Sierra Marginales Thrust activity (Figure 2.26). The Ager and Tremp basins are filled by N-S detrital sediments that are redistributed by E-W tidal paleocurrents (Mutti et al., 1985; Olariu et al., 2012). The onset of the Pedraforca and the Cadi thrust sheets, in addition to the widening of the thrust belt led to the southward progradation of the fluvio-deltaic Corones Formation (Puigdefabregas et al. 1986; Burbank et al. 1992; Ramos et al. 2002; Serra-Kiel et al. 2003). In the eastern part of the South Pyrenean foreland basin, lower Eocene detrital zircon geo- and thermochronology results from Odlum et al. (2019) reflects a Pyrenean Axial Zone source, that has changed following the change in the catchment system from east-southeast to the north in response to enhanced uplift and erosion in the

Pyrenees.

I.4.4 Middle Eocene – Miocene

Shortening during this phase is estimated to be 30 km between ~55 and 40 Ma along the ECORS profile (Mouthereau *et al.*, 2014). This part of the orogenic development is much more investigated in the southern part of the Pyrenees than its northern part. From the Lutetian (~48 Ma) to the Priabonian (~34 Ma), in the south eastern Pyrenees, prograding deltaic systems are emplaced contemporaneous with the uplifting of the Axial Zone (Puigdefàbregas and Souquet 1986; Puigdefabregas et al. 1986; Ramos et al. 2002; Serra-Kiel et al. 2003) (Figure 2.27) (Figure 2.22). Detrital geo- and thermochronology results from Ripoll basin in Odlum et al. (2019) show Mesozoic sedimentary sources, Paleozoic metasedimentary rocks and Carboniferous – early Permian plutonic rocks recording a progressive tectonic unroofing of the Axial Zone. In the south central Pyrenees, the depositional system is made of alluvial fan sourced from the north (Ardèvol et al., 2000) and connected toward the west to the Lutetian Sobrarbe Delta in the Ainsa basin (Figure 2.27). These deltas are individualized due to the growth of Boltaña anticline and the deformation in the Sierra Marginales (Farrell et al. 1987; Meigs et al. 1996) (Figure 2.22). In the south west Pyrenees, the early to middle Eocene Hecho group turbidites in the Jaca Basin are covered by conglomeratic lobe system derived from the north and deflected to the west along the main basin axis (Figure 2.22) (Figure 2.27) (Caja et al., 2010).

From the late Eocene – early Oligocene (~37 to ~30 Ma), the exhumation of the Axial Zone accelerated (Fitzgerald et al., 1999; Sinclair et al., 2005; Fillon and van der Beek, 2012) leading to the deposition of a prograding fluvio-deltaic sequence from the Priabonian to the early Oligocene in the southeastern Pyrenees (Milany and Solsona deltaic systems) (Figure 2.22) (Figure 2.27) (Puigdefàbregas and Souquet 1986; Puigdefabregas et al. 1986; Serra-Kiel et al. 2003). Sediments are sourced mainly from earlier foreland deposits as the fold-thrust belt continues to propagate toward the foreland (Odlum *et al.*, 2019). In the south central Pyrenees, it leads also to the progressive deposition of the La Pobla de Segur and Sis conglomerates from the north (Organya Basin) to the south (Ager Basin) between 40 and 27 Ma (Duller et al. 2010; Beamud et al. 2011; Whitchurch et al. 2011; Fillon et al. 2013; Michael et al. 2014) (Figure 2.22) (Figure 2.27). During the late Eocene, in the south west Pyrenees, these deposits were recycled toward the west as illustrated by westward progradation of coarse-grained facies in the sandstone Escanilla Formation (Michael et al. 2013; Michael et al. 2014; Michael et al. 2014) (Figure 2.22) and toward the Jaca Basin as it is connected to the Arguis-Pamplona and Belsué-Atarès progradational deltaic deposits (Huyghe et al., 2012) (Figure 2.22) (Figure 2.27). This episode is followed until the early Oligocene by the infilling of the

Jaca Basin with fluvial Campodarbe Formation with east-west paleocurrent directions (Michael et al. 2013; Michael et al. 2014; Michael et al. 2014) (Figure 2.22) (Figure 2.27). Campodarbe fluvial deposits will reach the Ebro Basin between the late Oligocene and the early Miocene (Nichols and Hirst, 1998; Arenas et al., 2001).

The North Pyrenean domain is infilled by fluvial and alluvial depositional environments developed during the Eocene (Figure 2.27). LTT studies in the NPZ and the Axial Zone show that the involvement of most of the Pyrenean Paleozoic basement in the orogenic prism is accelerated during the middle – late Eocene (Yelland, 1991; Morris et al., 1998; Fitzgerald et al., 1999; Sinclair et al., 2005; Jolivet et al., 2007; Gibson et al., 2007; Maurel et al., 2008; Gunnell et al., 2009; Metcalf et al., 2009; Whitchurch et al., 2011; Rushlow et al., 2013; Mouthereau et al., 2014; Bosch et al., 2016; Labaume et al., 2016; Vacherat et al., 2016). Shortening in the North Pyrenean basin lasted until the early Miocene as recorded by the development of the Mas d'Azil, the Lavelanet and the Plantaurel anticlines (Mouthereau et al., 2014). The Gulf of Lion opening took place in the Oligocene and the Miocene time launched by the retreat of the Apennine subduction and correlated to the Têt Valley reactivation in the Pyrenees (Sartégou et al., 2018). The incision is interpreted as possibly caused by an isostatic rebound that compensated for lithospheric thinning from the opening of the Gulf of Lion (Sartégou et al., 2018). This event was characterized by the rotation of the Corsica-Sardina block, which belonged to the Pyrenean orogeny during the pre-Oligocene period (Jolivet et al. 2015).

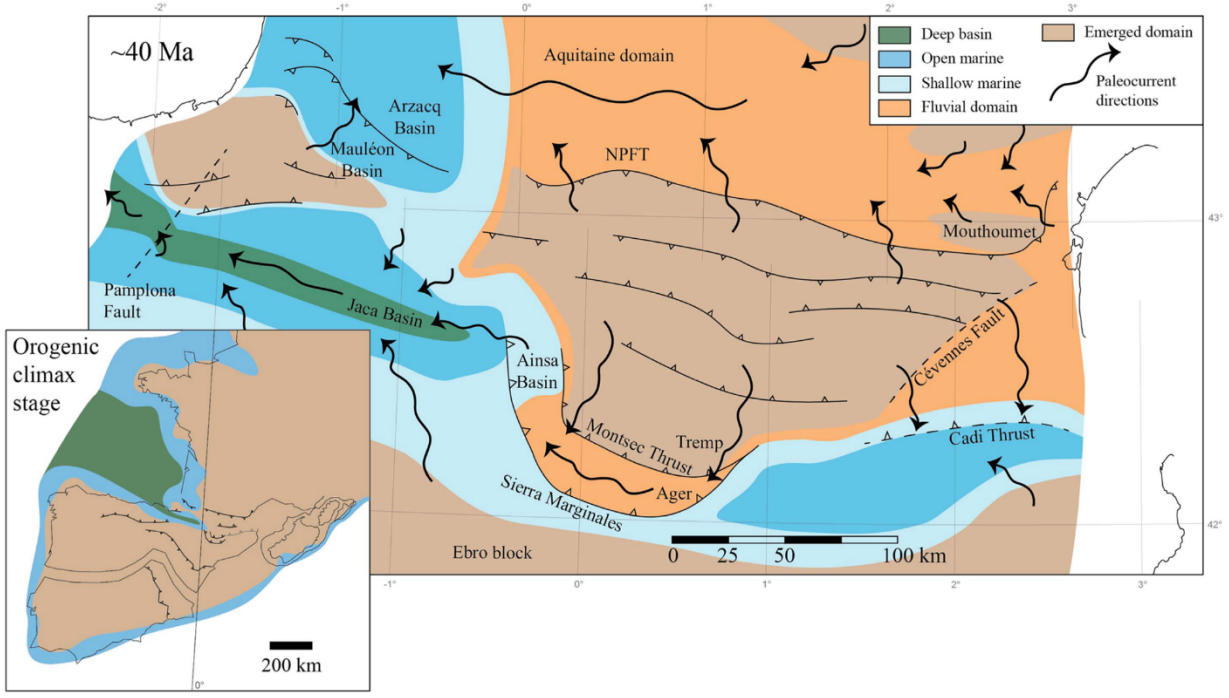

Figure 2.27: Paleogeographic reconstruction of the Pyrenean domain from Vacherat et al. (2017) during the middle Eocene.

II. Thermochronological and geochronological methodologies

II.1 Apatite fission track dating (AFT)

The apatite fission-track (AFT) dating method is used in this study in order to estimate the lag time of sediments to be delivered to the basin. It allows also the characterization of the thermal history of the basin. This method has been widely used for constraining low temperature thermal histories of the upper part of the earth's surface (3 to 5 km) over the past four decades (Donelick et al. 2005). The first general procedure for AFT dating is provided by Wagner (1968). Reviews on the AFT dating techniques have been given by Gallagher et al. (1998), Donelick et al. (2005) and have been summarized in this chapter. So, this chapter is focused on a general overview of the AFT dating technique, in particular the analytical conditions used in this thesis.

II.1.1 Ion track formation

Tracks are damage trails created by swift heavy ion penetrating through solids and forming latent fission tracks. Several models in the literature have described the formation of fission tracks in apatite mineral. Figure 2.28 presents the ion explosion spike model described by Fleischer et al. (1975) based on the spontaneous fission of the radioactive ^{238}U atom and the production of two highly charged heavy particles. The recoil of the charged particles during fission as a result of repulsion causes these charged particles to interact with other atoms in the crystal lattice by ionisation (Figure 2.28). Fission tracks are produced when ionized atoms in the lattice repel each other creating defects in the crystal (Figure 2.28). Defect density is a function of temperature as defects start to be repaired (or annealed) in the range of a given temperature. This range of temperature is called the Partial Annealing Zone (PAZ) during which tracks in crystal start to disappear (Figure 2.29). When temperature is above the PAZ temperature, all defects in the crystal are repaired and tracks completely disappear while once in the PAZ fission tracks will accumulate and only their length will vary according to temperature within the PAZ tracks are accumulated in the crystal (Figure 2.29). The accumulation of these defects allows by following several steps detailed in the methodology part, to constrain the age of the crystal.

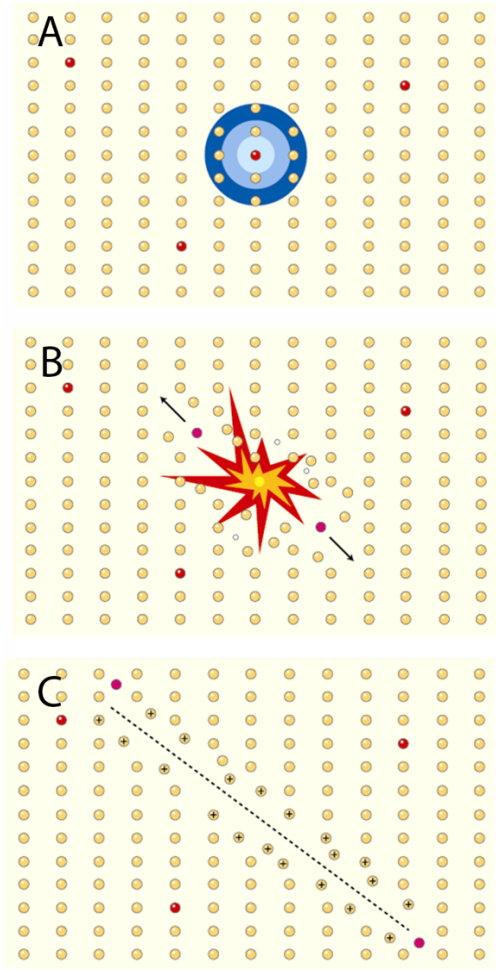

Figure 2.28: Fission track production following the ion spike explosion model from Fleischer et al. (1975). Red circles are ^{238}U atoms in the apatite crystal and white circles correspond to other atoms in the crystal.

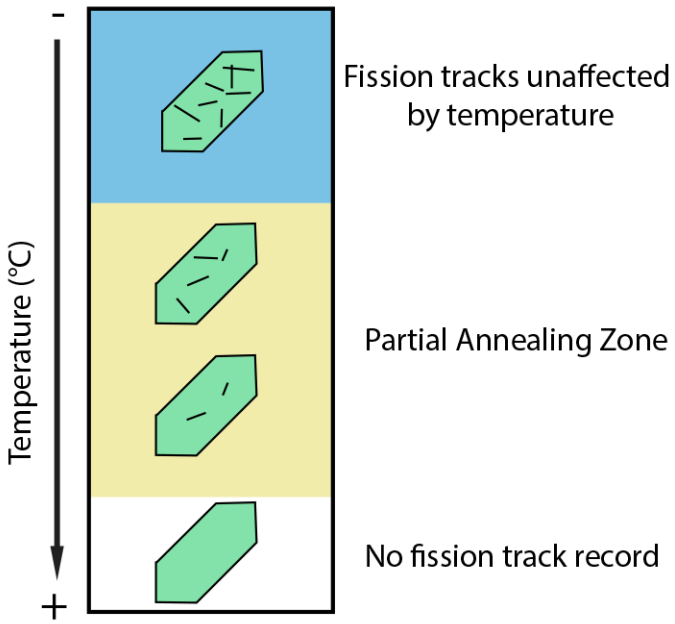

Figure 2.29: Schematic diagram showing the annealing behaviour in apatite fission tracks with temperature

II.1.2 Thermal annealing in apatite crystals

Studies on thermal annealing of apatite crystals argue that above ~120°C, all produced fission tracks among geological timescales are removed (Gleadow and Duddy, 1981; Green et al., 1986) (Figure 2.29). Spontaneous tracks produced over geological time are subject to length shortening as they slowly anneal when temperature exceeds ~60°C (Gleadow and Duddy, 1981) (Figure 2.29). Thus, the temperature range between 60 and 120°C corresponds the Partial Annealing Zone (PAZ). However, several studies such as Green (1988), Gallagher et al. (1998) and Spiegel et al. (2007) recognized that below 60°C the tracks are nearly frozen, which means partially annealed tracks remain short and newly formed tracks essentially keep their initial length (Figure 2.29).

It is clear that annealing is directly related to temperature. However, the crystallographic orientation of crystals has an influence on annealing behaviour. Annealing of tracks perpendicular to the c-axis is faster that tracks parallel to the c-axis (Green et al., 1986). Based on this, tracks in grains parallel to the c-axis are used for track-length measurement.

II.1.3 Track length measurement and distribution

The Apatite Fission Track method has the advantage of recording continuous thermal histories through the measurement of tracks length. The measurement of track length in apatite crystal provides information about the cooling history progression of a sample through the PAZ. Only confined tracks are measured. Such confined tracks are etched fission track that are completely beneath the surface of the crystal and intersected with the surface through another etchable feature that could be a fission track or a defect (Bhandari et al., 1971; Donelick and Miller, 1991). Measurable confined tracks should be approximately within ±10° of the horizontal of the polished surface. Tracks perpendicular to the c-axis of the crystal anneals faster as explained above (Donelick, 1991). At least 100 lengths should be measured for statistically viable data.

II.1.4 Influence of chemistry on the annealing of fission tracks in apatite

However, it was proven that the chemical composition of apatite crystals has an influence on the sensibility of apatite to temperature (Green et al., 1986; Carlson et al., 1999; Barbarand et al., 2003). The most common variety of apatite in the crust is a near end-member fluorapatite. Fluorine (F-) can be, however, substituted by other anions like Cl^- and OH^-. In the case of a substitution with chlorine (Cl^-), apatite is more resistant to annealing according to Gleadow and Duddy (1981), Green et al. (1986), Donelick (1991) and O′Sullivan and Parrish (1995). Such differences in the chemical composition of apatite have influence on the modelled thermal history (Donelick et al. 2005). In

addition, calcium (Ca) could be substituted with Mn, Sr and Rare Earth Element (REE) in apatite, P could be substituted with Si as well. However their role in the annealing behaviour is less well understood and not included in any annealing model (O′Sullivan and Parrish 1995; Gallagher et al. 1998; Barbarand and Pagel 2001; Spiegel et al. 2007). Moreover, D_{par} (mean maximum diameter of fission track etch parallel to the crystallographic c-axis) correlates positively with Cl and OH and negatively with F. Despite that, D_{par} cannot be considered as a proxy for Cl content in apatite as the geometry of D_{par} is not only dependent on the Cl/F ratio, but it includes several chemical elements that are not fully understood yet (Donelick 1993; Barbarand et al., 2003).

II.1.5 Preparation of apatite grains for AFT via the external detector method

As defect width is usually between 3 and 14 nm wide, they can be observed with an optical microscope only after chemical etching (the chemical etching procedure followed in this thesis is described in chapter 4) (Paul and Fitzgerald, 1992). After polishing and chemical etching at 5 M HNO_3 for 20 s at 20 ± 1 °C, the apatite crystal shows confined tracks in the internal part of the apatite and surface tracks in the polished surface of the grain. In this study, we used the external detector method (Reimer et al. 1970; Gleadow and Lovering 1977; Green and Durrani 1978; Gleadow 1981) that consists of placing the polished grain surface of apatite crystals in contact with low U-muscovite sheets. Three glass dosimeters CN-5 as well as two apatite standards (Durango and Fish Canyon Tuf; Hurford, 1990) are joined. Sample were irradiated at the Garching facility (München, Germany) with a nominal fluence of $5x10^{15}$ neutrons/cm^2. After irradiation the mica detectors were etched for 20 min in 40% HF at 20 ± 1 °C. Tracks induced by the fission of the ^{238}U atoms are not recorded in the mica sheets as the binding energy released by thermal neutron bombardment is lower than the critical energy.

After the external detector step, apatite crystals are ready to be counted. However, fission tracks are counted only in a single plane of apatite crystal, the polished surface as shown in Figure 2.30). The total number of **spontaneous** tracks is noted as N_s and the corresponding **spontaneous** track density per cm^2 is noted as ρ_s. The ^{238}U content has to be determined in the same plane where the **spontaneous** fission tracks are counted. The total number of **induced** tracks and the corresponding **induced** track density are proportional to the amount of ^{235}U in the apatite and are noted as N_i and ρ_i respectively. The Zeta calibration factor has been created by Hurford and Green (1983) and is used to correct several parameters which are not well-known as the spontaneous fission decay constant that is uncertain but approximated at $7.5x10^{-17}$ y^{-1} (Roberts et al. 1968; Wagner 1992), and parameters as, irradiation conditions, fission probability, chemical attack efficiency and the individual analyst observation factor. For all these reasons cited above, a correction factor is

accounted to ensure that each AFT age is comparable with other data produced elsewhere.

In this study, tracks are counted and measured at x1000 magnification using a digitized tablet coupled to an optical microscope (Laslett et al., 1984). Fission track ages were calculated using the zeta-calibration method described in Hurford and Green (1982) and have central ages with two-sigma errors. The Chi2 test and age dispersion suggest the presence of only one age population for the samples (Galbraith, 1981; Galbraith and Laslett, 1993). The Dpar represents an independent parameter for the annealing behavior of apatite and is commonly used in annealing models for thermal modelling (such as QTQt or HeFTy (Ketcham, 2005; Gallagher et al. 2012)).

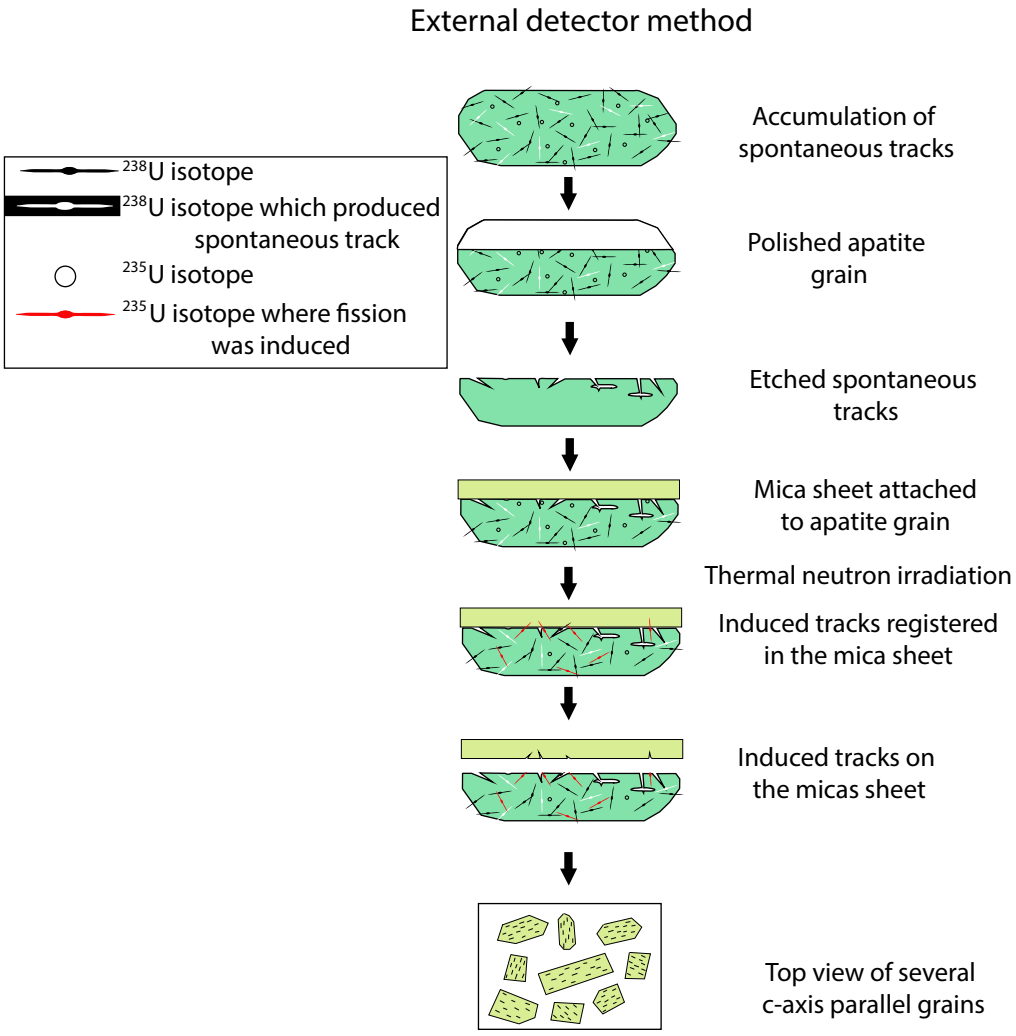

Figure 2.30: Schematic diagram showing the preparation steps of apatite crystals for AFT analysis following the external detector method developed by Hurford and Green (1982) and used in this thesis.

II.2 Apatite (U-Th-Sm)/He (AHe)

The (U-Th-Sm)/He dating technique is a method of low-temperature thermochronology applied to understand the thermal history of the Earth's crust in the upper 2 to 4 km. It is based on the production, ejection and accumulation of ^{4}He atom produced during alpha radioactive decay of ^{235}U, ^{238}U and ^{232}Th chains and ^{147}Sm. The acquisition of (U-Th-Sm)/He age is based on the measurement of the He, U, Th and Sm concentration in the same apatite crystal. Such apparent age is a function of the accumulation of daughter products in the crystal for a certain thermal history (Zeitler et al., 1987; Farley, 2002). He accumulation is a function of temperature, as He can diffuse in crystal depending on temperature, crystal size and diffusion coefficient (Zeitler et al. 1987; Wolf et al. 1996; Farley 2000; Ault et al. 2019). In a given range of temperature, the produced He atoms can diffuse completely or partially out of the crystal, and below a temperature, He diffusion is not significant, and He does not diffuse out of the crystal. The zone of partial diffusion is called the Partial Retention Zone, as a part of He is retained in the crystal (PRZ). Above the temperature of the PRZ, all He produced in the crystal is diffused outside and once temperature is below the PRZ, the retention of He in the crystal is total.

II.2.1 Alpha ejection correction (F_T)

During He production, the alpha particles are ejected with an important kinetic energy and travel a mean stopping distance of ~18 μm in apatite (Farley et al., 1996; Ketcham et al., 2011). The datable apatite crystals have dimensions in the order of hundreds of μm, and thus a significative fraction of alpha particles will be ejected outside of the crystal immediately after being generated. The fraction of ^{4}He retained in the crystal after loss due to this mechanism is termed F_T. The alpha ejection correction (F_T) accounts for the ^{4}He loss by ejection out of the crystal (Figure 2.31). The proportion of alpha particles that are ejected from the crystal depends on i) the stopping distance of each mineral, that is mentioned above for apatite grain and is a function of particle energy, mineral composition and density, ii) the geometry of the grain, including its size and shape and iii) the distribution of parent atoms inside the grain (Farley et al. 1996; Ketcham et al. 2011). For typical crystal radii from 40 to 150 μm, the F_T value ranges from 0.65 to 1 approximately. A 3D modeling software developed by Gautheron et al. (2012) allows calculating the F_T factor for different geometry and crystal dimensions. In the case of fractured crystal during rock crushing or mineral separation, an adjustment needs to be made for the F_T correction factor to account for the broken face (Gautheron et al., 2012; Brown et al., 2013).

The F_T correction has been defined for homogeneous and heterogeneous distribution of parent nuclides (Farley et al. 1996; Hourigan et al. 2005). In the case of this thesis, a homogeneous

distribution of parent nuclides across the crystals is assumed in apatite and the calculation of the F_T ejection factor allows a good determination of AHe corrected age by dividing the raw age by the F_T value (Gautheron et al., 2012; Beucher et al., 2013).

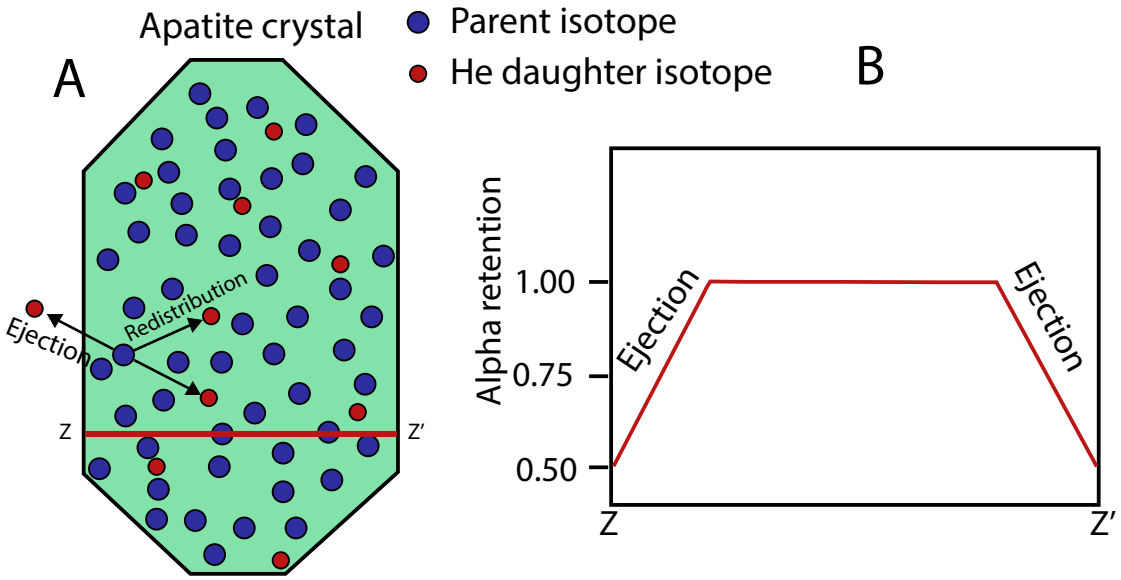

Figure 2.31: A. Schematic diagram of an apatite crystal accumulating and ejecting alpha particles. B. Evolution of the alpha retention from the center of the apatite to the border.

II.2.2 He diffusion and radiation damage in apatite

The first studies of ^{4}He diffusion in apatite assumed a constant diffusion behaviour all over the crystal (Zeitler et al. 1987; Lippolt et al. 1994; Wolf et al., 1996; Farley 2000). Experiments investigating He diffusion in apatite by Zeitler et al. (1987), Wolf et al. (1996) and Farley (2000) have shown that diffusion obeys an Arrhenius relationship suggesting that He diffusion in apatite is thermally activated:

$$\frac{D_{(T)}}{a^2} = \frac{D_0}{a^2} e^{-\frac{E_a}{RT}}$$

Where, $D_{(T)}$ is the diffusivity, D_0 is the diffusivity at infinite temperature, a is the diffusion domain radius (which corresponds to the radius of a sphere having the same surface/volume ratio than the apatite grain), E_a is the activation energy, R is the perfect gas constant and T is the temperature (in Kelvin).

Later, many studies led to a better understanding of the AHe method parameters (e.g. Green and Duddy 2006; Shuster et al., 2006; Flowers et al. 2009; Gautheron et al. 2009; Gerin et al., 2017) and allow defining that the PRZ is crystal dependent and can be ranging from 40 to 120°C. The AHe

ages depend on crystal geometry, grain size (Beucher et al., 2013; Brown et al., 2013), the alpha ejection factor and the R Sphere (see below) (Watson et al. 2010; Ketcham et al. 2011; Gautheron et al. 2012) and the amount of radioactive damages created during U-Th decay (Shuster et al., 2006; Flowers et al. 2009; Gautheron et al. 2009; Gerin et al., 2017). In addition, alpha particles can be implanted by U-Th mineral neighbors influencing He content in the dated crystal (Spiegel et al., 2009). Taking into consideration all these parameters each apatite crystal has its own parameters leading to different (U-Th-Sm)/He ages for the same thermal history and the integration of all those parameters allow to determine the thermal history.

He diffusion in apatite is highly affected by radiation damage in the crystal developed from self-irradiation from natural decay of isotopes of U, Th and Sm, by ionization and electronic excitation and nuclide recoil during alpha decay (Figure 2.32). Such damage is much more intense in zircon and titanite crystals than in apatite crystals due to the higher U and Th amounts (Weber et al. 1986; Ault et al. 2019). Damages anneal with temperature and the amount of damages is a function of U, Th and Sm content in the crystals, time as well as their thermal history. The accumulation of large amounts of radiation damage in the crystal leads to He loss facilitated by the pathway generated due to the connection of radiation damages (Recanati et al., 2017, following the model developed in zircon by Guenthner et al. 2013 and Ketcham et al., 2013). However, as in apatite crystals, the amount of U and Th are lower, the amount of radiation damage is generally not sufficient to allow He loss out of the crystal following connective pathways, but instead radiation damages produce traps that capture helium and prevent it to go out of the crystal (Shuster et al. 2006) (Figure 2.32). To account for radiation damage in apatite, Shuster et al. (2006) developed a model that predicts the amount of damage in the crystal in assuming that the concentration of induced traps is proportional to alpha particles produced. The amount of damage will be function of the eU content (eU=U+0.24xTh), called the effective amount of U and time since damage accumulate without annealing. In crystals having a span of eU and encountering a slow cooling history, the radiation damage effect is significant as there is sufficient time to create He traps and to lead to age dispersion (Flowers et al. 2007; 2009; Flowers 2009; Gautheron et al. 2009; Flowers and Kelley 2011; Murray et al. 2016; Recanati et al., 2017; Weisberg et al. 2018; Ault et al. 2019). With a high amount of U and Th, radiation damage accumulation leads to the increase of the closure temperature in apatite (Shuster and Farley, 2009). Recanati et al. (2017) suggest that below a threshold, He retention increase with alpha doses (alpha dose is the amount of alpha particles produced in apatite since the beginning of accumulation) and above this threshold He retention decreases reflecting damage interconnection.

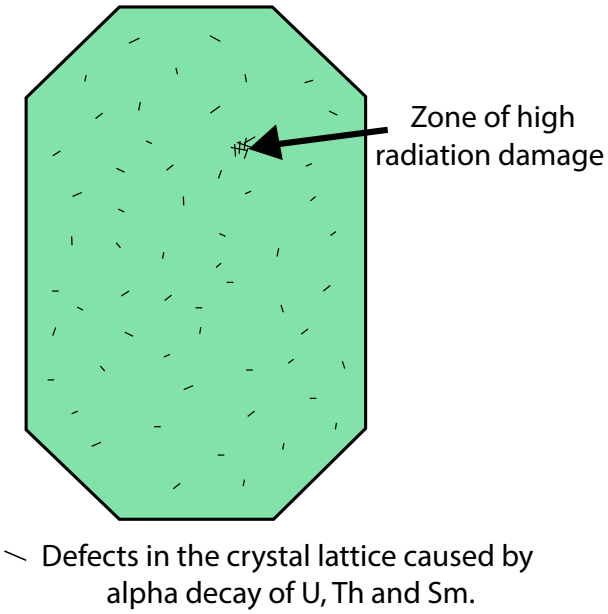

Figure 2.32: Apatite crystal showing defects in the crystal lattice caused by alpha decay of U and a high radiation damage zone.

II.2.3 R Sphere parameter

Additionally, it has been well demonstrated that the diffusion of helium in any geometry can be accurately approximated by modelling diffusion within a sphere which has the same volume to surface ratio as the prismatic grain (Meesters and Dunai 2002; Gautheron and Tassan-Got, 2010; Watson et al., 2010) (Figure 2.33). A simulation of the diffusion process of helium is developed by Gautheron and Tassan-Got (2010) using a Monte Carlo method for complex geometries, as for apatite and zircon. Such parameter is called R Sphere or ESR. The estimation of the R Sphere parameter leads to a correct calculation of He released and therefore He age of the mineral. It is based on the grain size and geometry, the dimensions of analyzed grains being accurately measured including grain length, width and height. Crystal geometry is recorded whether grains are broken or not and no matter how many terminations each grain has. For example, if the grain has the two terminations (two pyramids) it is noted as 2py, for 1 termination it is noted as 1py and for 0 termination it is noted as No py (Figure 2.33). Moreover, when the grain has 1 poorly identified termination, its geometry is noted as 1 broken face or 1bf. If both terminations are poorly identified, the geometry is 2bf.

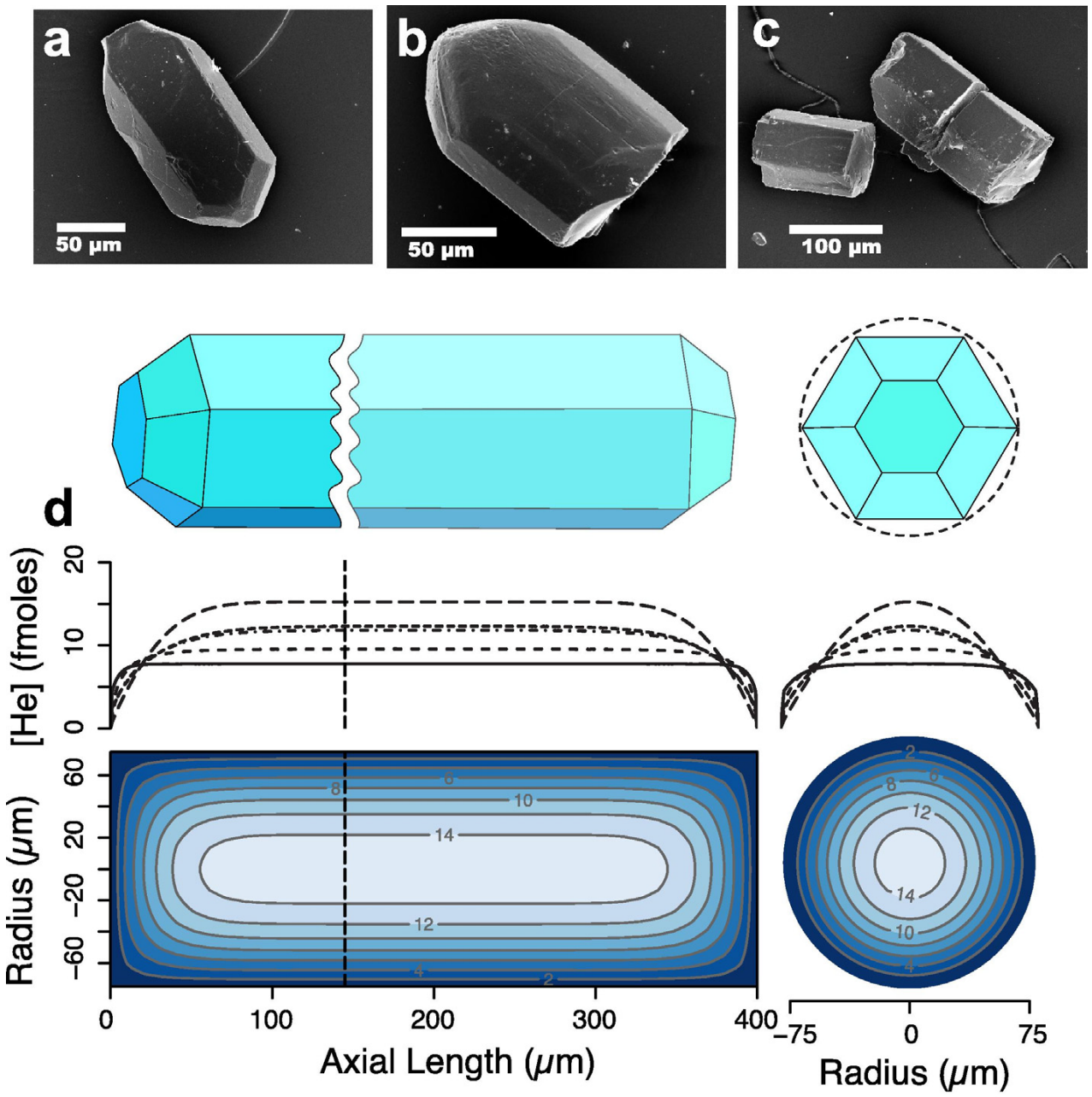

Figure 2.33: a, b & c. Apatite grains observed using scanning electron microscopy and representing different geometries, a) Whole grain with 2 terminations, b) broken crystal with 1 termination and c) broken crystal with no termination. d) Model axial and radial helium diffusion profiles generated for 5 thermal histories from Wolf et al. (1998). Figure from Brown et al. (2013)

II.2.4 Role of damages in He diffusion and ages

It has been shown that F_T factor and R Sphere calculation allows a better estimate of He release from the crystal. Several authors have argued that alpha-recoil damage affects He retentivity of apatite (Green and Duddy 2006; Shuster et al. 2006; Flowers et al. 2007; Flowers et al. 2009; Flowers 2009; Flowers et al. 2009; Gautheron et al. 2009; Shuster and Farley 2009; Flowers and Kelley 2011; Gautheron et al. 2013; Gerin et al. 2017; Recanati et al. 2017; Willett et al. 2017; Weisberg et al.

2018) (Figure 2.33). AHe ages can be more or less dispersed depending on grain size, damage content and thermal history. The interpretation of the obtained AHe ages will only be possible using thermal modelling. The modeling will simulate for each crystal size, the alpha ejection, damage creation and annealing and diffusion for a certain thermal history.

Three He diffusion and damage annealing models exist (Flowers et al. 2009; Gautheron et al. 2009 and Gerin et al. 2017). They use a damage-annealing approach similar to the one developed for apatite fission track (AFT) annealing (Ketcham et al., 2007). The three models have been integrated in the QTQt modelling software (Gallagher et al. 2009; Gallagher, 2012) and only the Flowers et al. (2009) model has been integrated in the HeFTy modelling software (Ketcham, 2005). (U-Th-Sm)/He ages produced in this thesis were modelled using a spherical diffusion domain (based on crystal's equivalent spherical radius), and taking into account eU-dependent radiation damage modulated diffusivity for He, following the model of Gautheron et al. (2009). The use of the Gautheron et al. (2009) model is mainly due to the fact that this model takes into account the creation of defects and their thermal annealing, modifying the He-diffusion kinetics through time.

II.2.5 External sources of age dispersion

The presence of micro-inclusions containing high [U] and [Th] in apatite grains leads to age dispersion as mentioned by Lippolt et al. (1994); House et al. (1997); Farley and Stockli (2002); Fitzgerald et al. (2006); Gautheron et al. (2012) and Brown et al. (2013) (Figure 2.34). Despite that apatite grains are carefully selected and handpicked using a high resolution binocular microscope, it is still possible to have a tiny U-rich inclusion (zircon and monazite for example) that, by alpha-ejection, increases the amount of ^{4}He in the apatite grains and therefore leads to an erroneous age (Figure 2.34). In most cases, the contribution of a micro-inclusion to the age of the apatite is very small, except if the inclusion is very rich in U (>1000 times the apatite U concentration) (Vermeesch et al. 2007; Murray et al., 2014). U and Th concentrations contained in the inclusion will not be measured as the inclusion can not be dissolved by the standard procedure. The measured ^{4}He amount will be higher than the amount coming from the apatite itself due to ^{4}He coming from the inclusion.

He implantation may occur from high U and Th bearing accessory minerals like monazite or zircon being adjacent to the apatite crystal (Figure 2.35) or may arise from high U and Th minerals coating the grain as Fe-Mn oxide (Murray et al., 2011; Murray et al., 2014). The latter case has been studied in details in Murray et al. (2014), where the (U-Th-Sm)/He ages of apatite crystal coated by an U and Th rich source have been measured before and after abrasion of the coating mineral. The effect of implanted ^{4}He from an external source into the apatite grain has been modelled by Gautheron et al., (2012) and investigated experimentally by Spiegel et al. (2009).

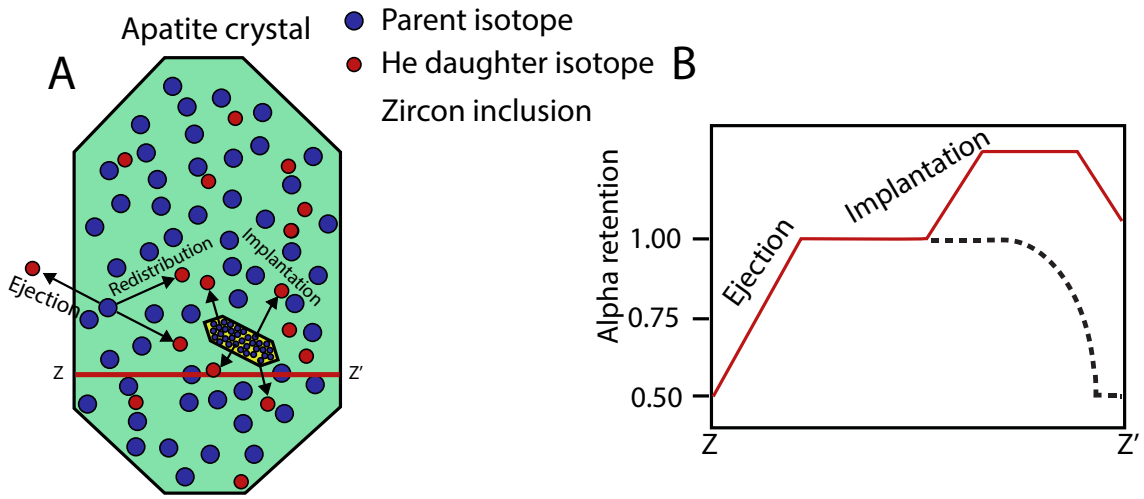

Figure 2.34: Apatite crystal containing a zircon inclusion that implants ^{4}He in the host grain.

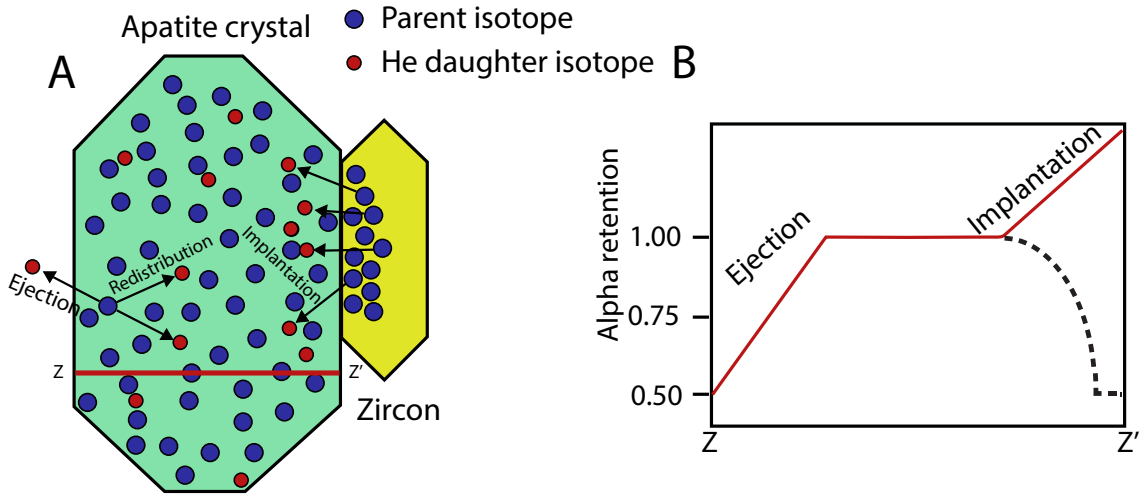

Figure 2.35: Implantation of ^{4}He into apatite crystal coming from an adjacent zircon grain.

Gautheron et al. (2012) demonstrated that an apatite can have around 60% excess He from one neighbour and up to 300% from multiple neighbours. Nonetheless, for an external source containing realistic U and Th concentrations, the excess ^{4}He going into the apatite grain is unlikely to modify significantly AHe ages. Usually, in the case of ^{4}He implantation, authors use grain abrasion to remove the outer 20 µm of the grains (estimated alpha particles ejection distance) which allows a better determination of AHe ages.

The potential effect of grain chemistry on the rate of recoil damage annealing has been studied in Gautheron et al. (2013) and Fox and Shuster (2014). Considering that FT annealing kinetics are related to grain chemistry (Gleadow and Duddy 1981; Green et al. 1986; Donelick 1991; O'Sullivan

and Parrish 1995; Carlson et al. 1999; Barbarand et al. 2003; Donelick et al. 2005; Ketcham et al. 2007) and that the same annealing law (as in AFT) is used in AHe modelling (Flowers et al. 2009; Gautheron et al. 2009), Gautheron et al. (2013) used the model developed in Ketcham et al. (2007) to study the influence of grain chemistry on He diffusion. It has been proposed that the Cl content in apatite can be used to first order to determine the annealing parameter for AHe (Gautheron et al. 2013) and that to understand the AHe ages in terms of temperature sensitivity, the annealing laws need to consider grain chemistry. Recanati et al. (2017) show that dispersed AHe ages can be reproduced when varying the annealing kinetics and alpha recoil damage trapping energy parameters. The age variation can be explained only if the trapping energy evolves from one crystal to another, increasing with the amount of damages. Fox et al. (2019) show that dispersion in detrital AHe ages could be due to crystals coming from different sources, resided at surface temperature at different durations, then encountered a thermal event in the basin after deposition (different pre-depositional conditions lead to different amount of radiation damage measured after a post-deposition heating).

II.2.6 AHe methodology

In order to prevent any natural dispersion problem in apatite, we selected euhedral grains without fractures, with non-visible mineral or fluid inclusion and having a width and thickness >70 µm. The dimensions of apatite crystals were measured under a binocular microscope and equivalent sphere radii (Rs) were calculated to represent the He diffusion domain (Gautheron and Tassan-Got, 2010). Each selected crystal has been enclosed in a platinum aliquot and heated twice using a diode laser at 1050 ± 50 °C during 5 minutes, allowing total He degassing during the first heating step and checking for the presence of He trapped in small inclusions during the second heating step. AHe ages were corrected morphometrically for alpha-ejection (F_T) using Monte Carlo simulation (Ketcham et al., 2011; Gautheron et al., 2012). In a second stage, apatite grains were dissolved in a HNO_3 solution containing a known concentration of ^{42}Ca, ^{235}U, ^{230}Th and ^{149}Sm and analysis was performed using an HR-ICPMS, ThermoScientific Element XR. Durango apatites were also analysed during the same time and provided a mean age of 31.2 ± 1.9 Ma, in agreement with literature data (31.02 ± 0. 22 Ma in McDowell et al., 2005). The one-sigma error on each AHe age should be considered at 9% reflecting errors in the F_T and the analytical error.

II.2.7 Thermal modelling

AFT and AHe obtained ages reflect the mineral integrated thermal history, and are modelled using a simulation program, like QTQt and HeFTy (Ketcham, 2005; Gallagher et al., 2009; Gallagher, 2012). Modelling software determines, using kinetic models, the response of fission track and (U-Th-

Sm)/He systems as a function of time and temperature. It consists of inverting data and determining the most robust time-temperature (T-t) thermal history of the sample with taking into account geological constraints (like deposition ages for example that reflect that the sample is at surface at this time). Two simple examples are represented in Figure 2.36 and 2.37. Modelling in Figure 2.36 shows the cooling and exhumation of a sample toward the surface that started around 82 Ma. Figure 2.37 shows the thermal history of two samples collected at different elevations, the lower sample (A) recorded a total reset followed by exhumation at 20 Ma while sample (B) recorded a complete thermal history as burying is not sufficient to reset ages (Figure 2.37). Thermal histories produced by the software are converted into burial and exhumation histories while assuming a surface temperature based on the estimated geothermal gradient. T-t paths produced with the use of different thermochronometers (AFT and AHe for example) improve the reliability of the thermal history and thus the interpretation of the obtained ages (Winn et al. 2017; Ketcham et al. 2018; Fox et al. 2019).

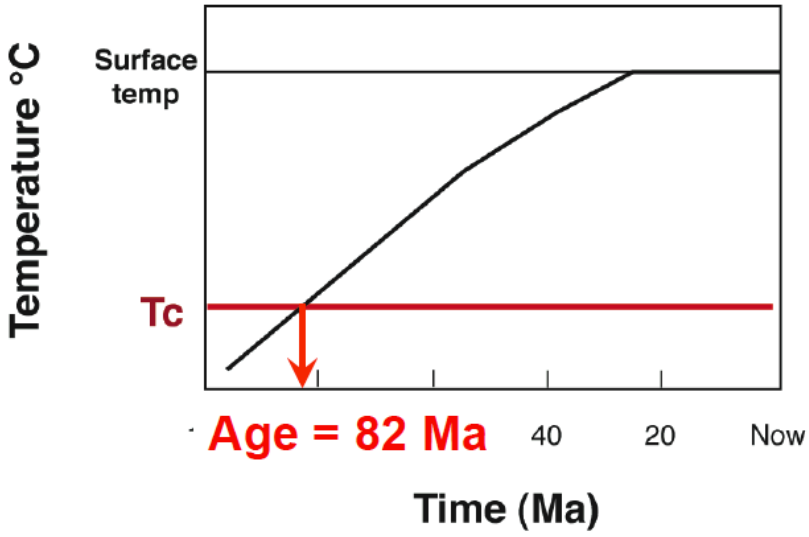

Figure 2.36: Time-temperature path of a sample as suggested by modelling. Tc: closure temperature.

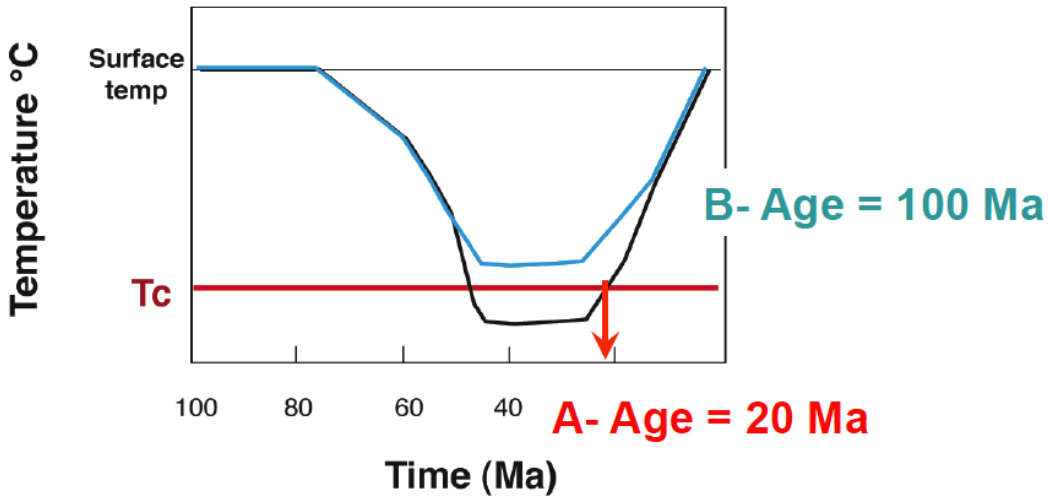

Figure 2.37: Time- temperature path for 2 samples taken from different altitudes. The upper sample is not sufficiently buried and conserved the recorded thermal history, while the lower sample is completely reset. Tc: closure temperature.

Data produced in this thesis have been inverted using the QTQt software (Gallagher et al., 2009; Gallagher, 2012). The inversion procedure consists of fitting as best as possible the AFT and AHe ages in order to determine the most robust time-temperature history and kinetic parameters of low temperature thermochronology systems. It uses a Bayesian transdimensional Markov Chain Monte Carlo (MCMC) algorithm that allows to specify a wide range of thermal history models.

II.3 Zircon U/Pb geochronology

The U-Th-Pb geochronology is based on the radioactive decay of multiple parent isotopes to different stable isotopes of Pb. ^{238}U, ^{235}U and ^{232}Th parent isotopes give ^{206}Pb, ^{207}Pb and ^{208}Pb as stable isotope of Pb respectively, each with different half-lives (Figure 2.38). None of the parent isotope decays directly to Pb, but follows a sequence of alpha and beta decays that creates a series of intermediate daughter isotopes and leads always to the same final stable isotope of Pb (Schoene, 2014).

$$A\text{: } \left(\frac{^{206}Pb}{^{204}Pb}\right) = \left(\frac{^{206}Pb}{^{204}Pb}\right)_0 + \left(\frac{^{238}U}{^{204}Pb}\right)(e^{\lambda_{238}t} - 1)$$

$$B\text{: } \left(\frac{^{207}Pb}{^{204}Pb}\right) = \left(\frac{^{207}Pb}{^{204}Pb}\right)_0 + \left(\frac{^{235}U}{^{204}Pb}\right)(e^{\lambda_{235}t} - 1)$$

$$C\text{: } \left(\frac{^{208}Pb}{^{204}Pb}\right) = \left(\frac{^{208}Pb}{^{204}Pb}\right)_0 + \left(\frac{^{232}Th}{^{204}Pb}\right)(e^{\lambda_{232}t} - 1)$$

Following the isochron technique, a stable isotope of the daughter element is used for normalization, such is the case of ^{204}Pb, the only non-radiogenic isotope of Pb (Figure 2.38). The isotopic ratio of Pb when the system is closed (crystallization of the mineral, closure temperature for zircon crystals 900±50°C (Cherniak and Watson, (2001)) is defined as time 0 in the equations above and t is defined as the time since the system is closed. λ_{238}, λ_{235} and λ_{232} are decay constants of ^{238}U, ^{235}U and ^{232}Th respectively. In some cases, an excess of non-radiogenic Pb could occur naturally and result of a false quantification of the initial Pb (called also common lead and discussed later).

The most used plots for visualization of U-Th-Pb data are the Wetherill Concordia plot and the Tera-Wasserburg diagram. The Wetherill Concordia plot was introduced by Wetherill (1956) (Figure 2.39) and involves the plot of radiogenic ^{206}Pb (noted as ^{206}Pb*) in a ^{206}Pb*/^{238}U ratio versus ^{207}Pb*/^{235}U from the same analysis. The theoritical plot is a non-linear curve (because ^{238}U and ^{235}U have different half-lives) called the Concordia shown in Figure 2.39.

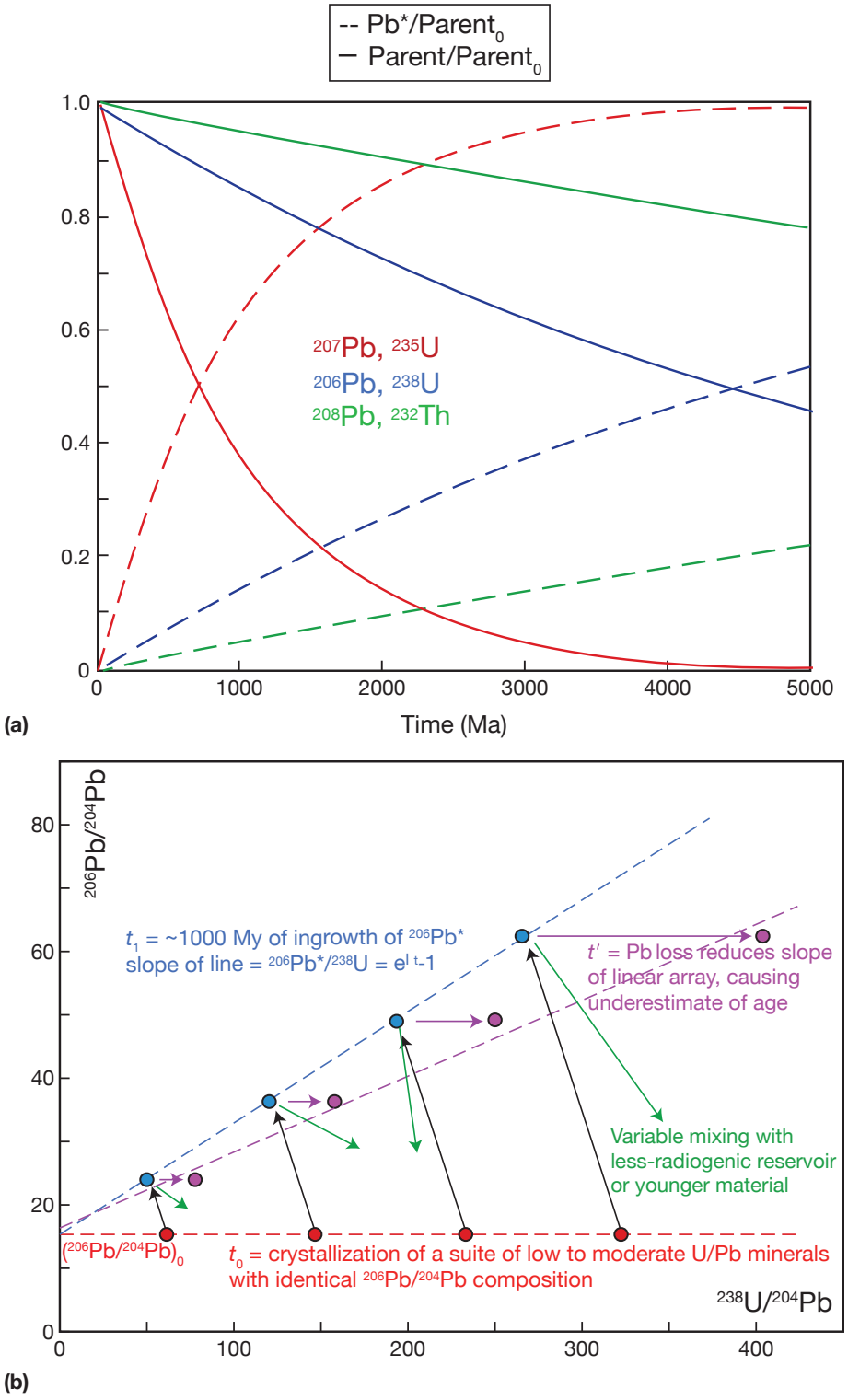

Figure 2.38: a) Diagram representing the different half-lives of ^{238}U, ^{235}U and ^{232}Th by radioactive decay of parent isotopes and production of daughters. b) Evolution of the isochron from t_0 to t_1 representing the usual decrease in parent isotope and increase in daughter product and the changes that occur to the isochron in the case of Pb loss and mixing with a younger material (Schoene, 2014).

When a mineral crystallizes, Pb* accumulation begins in a closed system (t_0 in Figure 2.39). The evolution of $^{206}Pb^*/^{238}U$ and $^{207}Pb^*/^{235}U$ ratios follows the Concordia curve (t_1 in Figure 2.39 ~1700 Ma), except if the mineral experienced a Pb loss for example (explained below), in this case a

Discordia line will appear going through the origin (the upper intercept with the Concordia, reflecting the age at which the Pb loss happened). The lower intersept with the Concordia curve correspond to the real actual age of the mineral (lower intercept) (see t_2 in Figure 2.39, mineral age is approximatively near to 0) (Figure 2.39a). If the system, after the Pb loss, becomes closed again, the produced radiogenic Pb* will follow the Concordia curve (see t_3 in Figure 2.39b) and if the present day is 1200 Ma later, the upper intercept would correspond to the formation age (~2900 Ma in the example of Figure 2.39) and the lower intercept age of the Discordia would correspond to the time of Pb loss event (1200 Ma).

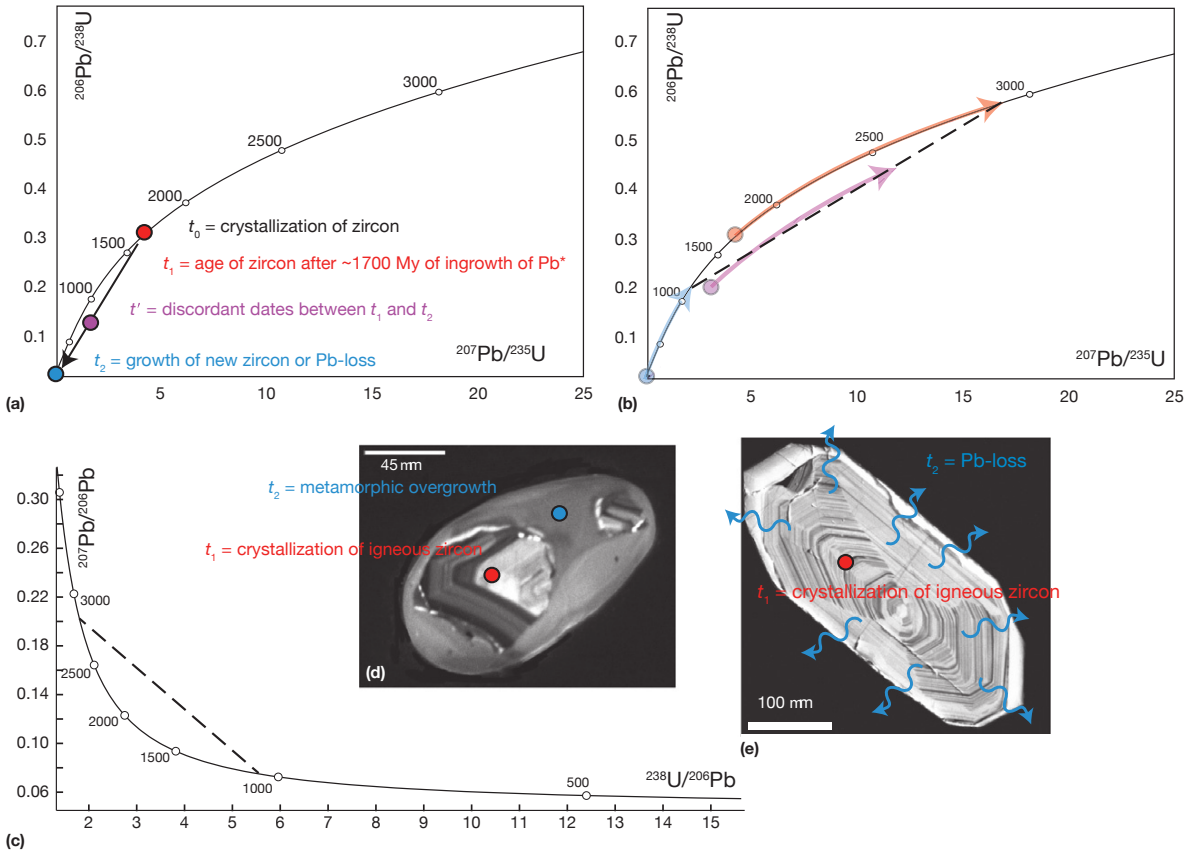

Figure 2.39: Representation of zircon grain growth history in the Wetherill Concordia diagram (a&b) and Tera-Wasserburg diagram. The Wetherill Concordia diagrams illustrate an example of normal ingrowth of daughters' product since crystallization to 1700 Ma followed by a Pb loss or metamorphic overgrowth (d, e) that is represented by a discordia in the diagram (a). The diagram illustrates a new ingrowth of daughter products (b) 1200 My after the Pb loss event. (d) and (e) represents a cathodoluminescence imaging of zircon that experienced Pb loss or metamorphic overgrowth (Schoene, 2014).

The Tera-Wasserburg Concordia diagram consists in placing the $^{238}U/^{206}Pb$ and $^{207}Pb/^{206}Pb$ ratios on the x and y axes, respectively. Concordia and Discordia results are interpreted in the same way as for the Wetherill Concordia plot.

II.3.1 Causes of discordance

Discordance in analysed mineral could be caused by several reasons as 1) mixing of different age domains in the same crystal, 2) Pb loss, 3) intermediate daughter product disequilibrium and 4) initial Pb. It is known that crystals like zircon could contain an old core and one or several generations of younger overgrowth. If such mineral is analysed for U/Pb geochronology, the result can lead to discordant ages. Such overgrowth was initially detected optically in mineral separates (Bickford et al., 1981; Corfu and Ayres, 1984), later by backscatter electron imaging (Wayne and Sinha 1988; Wayne et al., 1992) and finally by cathodoluminescence imaging becoming widely popular (Schenk, 1980; Hanchar and Miller, 1993; Hanchar and Rudnick, 1995). Such analysis is nowadays done ubiquitously before U/Pb dating because it gives a better knowledge about the mineral.

Unlike the mixing and overgrowth problem in minerals that are detected and quantified by backscatter electron and cathodoluminescence imaging, the process of Pb loss has numerous causes that are difficult to quantify. An example of Pb loss event and its interpretation in the context of the U/Pb method is represented in Figure 2.39. Several mechanisms have been identified as contributors to the Pb loss event like crystal plastic deformation (Reddy and Manikyamba, 2006) and low temperature hydrothermal dissolution-reprecipitation (Geisler et al. 2002; Geisler et al. 2003).

Equations of decay systems A, B and C (noted above) illustrate the importance of correcting for common lead in order to obtain an accurate age. In general, in a Wetherill Concordia diagram, the common Pb problem is represented by a line with a slope equal to $(^{206}Pb/^{207}Pb)/(^{238}U/^{235}U)$.

II.3.2 Concordant age, MSWD and associated errors

Several softwares have been developed to plot geochronology results in Wetherill and Tera-Wasserburg Concordia diagrams as Isoplot and IsoplotR by Ludwig (2003) and Vermeesch (2018) respectively. Both softwares are able to calculate, in addition to the ages, the Mean Square of Weighted Deviates called MSWD and the age associated errors. The definition of the MSWD has been discussed in details in Wendt and Carl (1991). It does not correspond to a measure of correlation of the x- and y- axis values. In fact, it is a measure of the ratio of the observed scatter of the points in a diagram (from the best-fit line) to the expected scatter (from the assigned errors and error correlation). If the assigned errors are the only cause of scatter, the MSWD will tend to be near unity and if the MSWD is greater than unity, it means that the observed scatter will exceed the one expected by the analytical uncertainties. In this case, the data are said to be "overdispersed". Moreover, if the MSWD is less than unity, it will indicate that the observed scatter is less than that expected by the analytical uncertainties. In this case, the data are said to be "underdispersed", indicating that the analytical uncertainties were overestimated. In Isoplot and IsoplotR software, three MSWD statistics

are calculated for a sample: the MSWD for concordance (u in Figure 2.40), the MSWD for X-Y equivalence (v in Figure 2.40) and the MSWD for combined equivalence and concordance (w in Figure 2.40). The Concordia age is meaningful only if the data are both equivalent and concordant, so the last MSWD value is the one to take into consideration (Ludwig 2008) (Figure 2.40). In practical use, very high MSWD value must reflect the failure of the assumptions of either data-point equivalence or concordance (Ludwig 1998, 2003; Ludwig 2008).

Errors for the Concordia age are given at 3 levels in Isoplot and IsoplotR. The analytical uncertainty 1σ and 2σ errors calculated by propagating only the assigned data errors, without consideration of the actual scatter of the data points from one another or from the Concordia curve (x in Figure 2.40).

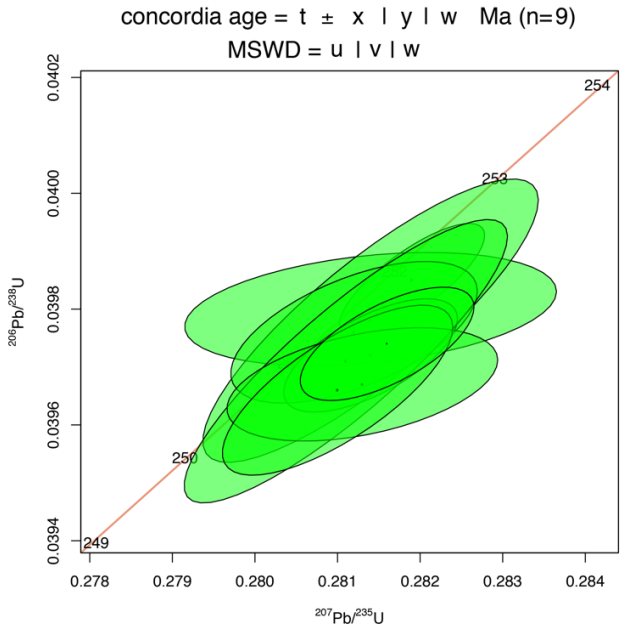

Figure 2.40: Example of a Wetherill Concordia diagram using IsoplotR (Vermeesch, 2018) representing the concordant age, the associated errors and the three MSWD values

The Student's-t factor (y in Figure 2.40) takes into account the fact that the true uncertainty of the data is estimated only for few points. The last calculated error is the yσ√MSWD, y is the studentized factor calculated before and multiplied by 1σ error and the square root of the MSWD. The σ√MSWD error equation takes into account the actual scatter of the data, which must be the result of geological error rather than analytical error. Such equation is calculated automatically in Isoplot (Ludwig, 2008), while in IsoplotR it is directly multiplied by the "y" error.

II.4 Petrography and mineral observation

Petrographic analysis on thin section of granite clasts has been done using an optical microscope LEICA DM750P. Handpicked zircon grains have been observed using a Zeiss SUPRA 55VC Scanning Electron Microscope (SEM) coupled to a Variable Pressure Secondary Electron (VPSE) instrument at the Institut de Sciences de la Terre de Paris (ISTeP). Uranium, thorium and lead isotopes were analysed at GEOPS laboratory using a ThermoScientific Element XR HR-ICP-MS spectrometer coupled with a Photon Machines Teledyne Laser Excimer ArF 193 nm.

II.5 Preparation of clay aggregate thin slides for XRD analysis

Around 75 collected samples have been analysed in order to constrain clay mineral composition among 3 stratigraphic logs in the units 1 and 2 of the Palassou deposits. Collected samples are mostly fine sandstones and silts. The procedure to prepare clay aggregate thin slides starts with crushing the samples in a grinder and reducing to the maximum the size of the grains. Such step allows to refine the size of the grains which is of utmost importance to collect clay grains. Grinded grains are then transferred into a beaker to proceed to the acid attack step, capital for eliminating carbonate and allowing clay mineral suspension. This step consists in dissolving carbonate content in the sample by adding a 6.25% diluted hydrochloric acid solution in the beaker. Once the pH of the solution turns to acidic, it means that the carbonate content in the samples is fully dissolved and no more reaction is occurring with hydrochloric acid to maintain the pH of the solution unchanged. The timing of this step depends on the amount of carbonate in the sample, usually it takes 5 to 10 days to eliminate completely carbonate content in the sample. For clay aggregate analysis, the pH of the solution should be neutral, between 6 and 7, so when the acid attack step is done, the pH of the solution must become neutral by diluting the solution. Dilution constitutes the last step of preparation of clay aggregate and is achieved by adding distilled water to the solution and then by sucking after decantation (Figure 2.41). Repeating this step allows to rise from low pH to neutral pH. At the end, the clay minerals are in suspension and the preparation of the clay aggregate slides is possible. According to Stokes' law, the settling force of the grains after stirring the solution is relative to their weight and size, and for clays, the setting time is estimated at about 1 hour and 35 minutes. So, after stirring the solution containing the grains, a waiting time of 1 hour and 35 minutes is required to extract the clay portion from a depth of 2 cm and spread it on a slide. Samples are then analysed without further processing (so-called normal samples), then in Ethylene Glycol in order to be able to distinguish smectite from chlorite (smectite being a swelling clay).

Figure 2.41: Decantation of the samples during the dilution step, the last step before preparing aggregate clay slides.

II.6 Analytical method of Raman Spectroscopy of Carbonaceous Materials (RSCM)

Raman spectroscopy has been used to characterize the structural evolution of carbonaceous material (CM). During metamorphism, the CM undergoes a transformation from disordered to well-ordered (Wopenka and Pasteris, 1993). Measuring this transformation using Raman spectroscopy allows the determination of a peak temperature attained by metamorphic rocks (Beyssac et al., 2002). Raman analysis in this thesis were performed on polished thin sections using a Renishaw InVia Reflex spectrometer coupled to 3 output laser power of 514.5, 632.8 and 785 nm at the BRGM-Orléans (France). The output laser power reached the surface of the sample through a Leica DM2500 microscope with a x50LW objective. Edge filters eliminated the Rayleigh diffusion and the Raman light was dispersed before being analysed by a Peltier-cooled CCD NIR/UV deep depletion 1024x256 pixels detector.

Chapitre 3: Études sédimentologiques des Poudingues de Palassou

Les deux premières unités des poudingues de Palassou ont fait l'objet d'études sédimentologiques dans ce travail de thèse présentées dans ce chapitre. La première partie comporte une présentation de la stratigraphie des dépôts tertiaires marins (anté-Palassou) et continentaux (la série de Palassou), suivie par les résultats de l'étude sédimentologique menée sur les unités 1 et 2. Une description des principaux environnements de dépôt définis dans 4 coupes (Villerouge/Talairan, la vallée de l'Orbieu, Labastide-en-Val/Clermont-sur-Lauquet et Caunette-en-Val/Pomas) a permis de conclure la première partie avec une interprétation sur la géométrie des sédiments, leur implication dans la déformation et le routage sédimentaire. La deuxième partie de ce chapitre porte sur la présentation des analyses par diffractométrie de rayons X effectuées le long de 2 coupes (Villerouge/Talairan et Labastide-en-Val/Clermont-sur-Lauquet) et sur la transition de l'unité 1 à l'unité 2 dans la coupe de Caunette-en-Val/Pomas. Ces résultats apportent des informations sur les conditions d'altération au cours de l'Yprésien et du Lutétien et discutent de la relation avec les environnements de dépôt.

Contexte structural de la zone d'étude

Les principales structures de la zone des Corbières sont caractérisées par une série d'anticlinaux et de synclinaux migrant vers le nord. Sont cités du sud vers le nord, le massif du Mouthoumet, le synclinal de Talairan, les chaînons de Lagrasse (structure anticlinal), le synclinal de Montlaur et la montagne d'Alaric (Martín-Martín et al. 2001, Christophoul et al., 2003).

L'accident majeur dans cette zone se retrouve au sud, sur la bordure nord du massif du Mouthoumet, et est représenté par le chevauchement sub-horizontal du massif du Mouthoumet sur les séries éocènes. Les différentes structures située entre le synclinal de Talairan et la montagne d'Alaric, ont toutes plus ou moins la même orientation N50E (Martín-Martín et al. 2001), à part la Montagne d'Alaric qui est orienté W-E.

I. Étude sédimentologique de la série de Palassou et son implication sur la caractérisation de la déformation syn-orogénique

I.1 Stratigraphie des dépôts tertiaires antérieurs aux poudingues de Palassou :

La série tertiaire de la zone d'étude débute par des faciès continentaux, lacs et plaines alluviales (Figure 3.1) (Plaziat, 1975 ; Maufrangeas et al. 2020) qui perdurent de la base du Danien au Thanétien avec des lacunes sédimentaires plus ou moins importantes et une brève incursion marine au Sélandien supérieur (Maufrangeas et al., 2020). Le retour à des conditions marines se fait à proximité de la limite Paléocène-Eocène, le PETM (Paleocene-Eocene Thermal Maximum) est exprimé dans des faciès côtiers relativement épais (Maufrangeas et al., 2020). Les dépôts marins qui suivent sont classiquement attribués à l'Ilerdien (Figure 3.1) et montrent des variabilités de faciès importantes entre le nord et le sud. Les données biostratigraphiques et les travaux de sédimentologie (Plaziat 1984; Tambareau et al. 1995) compilées par Martín-Martín et al. (2001), Christophoul et al. (2003) et Carayon (2010) montrent :

- Des dépôts de plate-forme carbonatés relativement isopaques au début de l'Yprésien. (SBZ 5 de Serra-Kiel et al. (1998)).
- Une différenciation relativement marquée entre le nord où les plate-formes carbonatées se développent (Minervois, Alaric) durant les zones SBZ6 à SBZ8, et le sud où des dépôts deltaïques dominent durant tout l'Yprésien inférieur, marqués par plusieurs phases de progradation des dépôts deltaïques.
- Les derniers dépôts marins sont datés de SBZ 9. Ils sont recouverts par les premiers dépôts continentaux attribués aux poudingues de Palassou.

Les variations importantes de faciès et d'épaisseur selon les directions N-S ont été interprétées par Christophoul et al. (2003) (Figure 3.2) et Carayon (2010) comme un enregistrement de l'accélération de la subsidence associé à l'initiation d'un bassin d'avant chaine et la mise en place de chevauchement au front du massif du Mouthoumet, à partir de la zone à SBZ 6 de Serra-Kiel et al. (1998)), soit 55,5 Ma (Gradstein et al., 2012) (Figure 3.3).

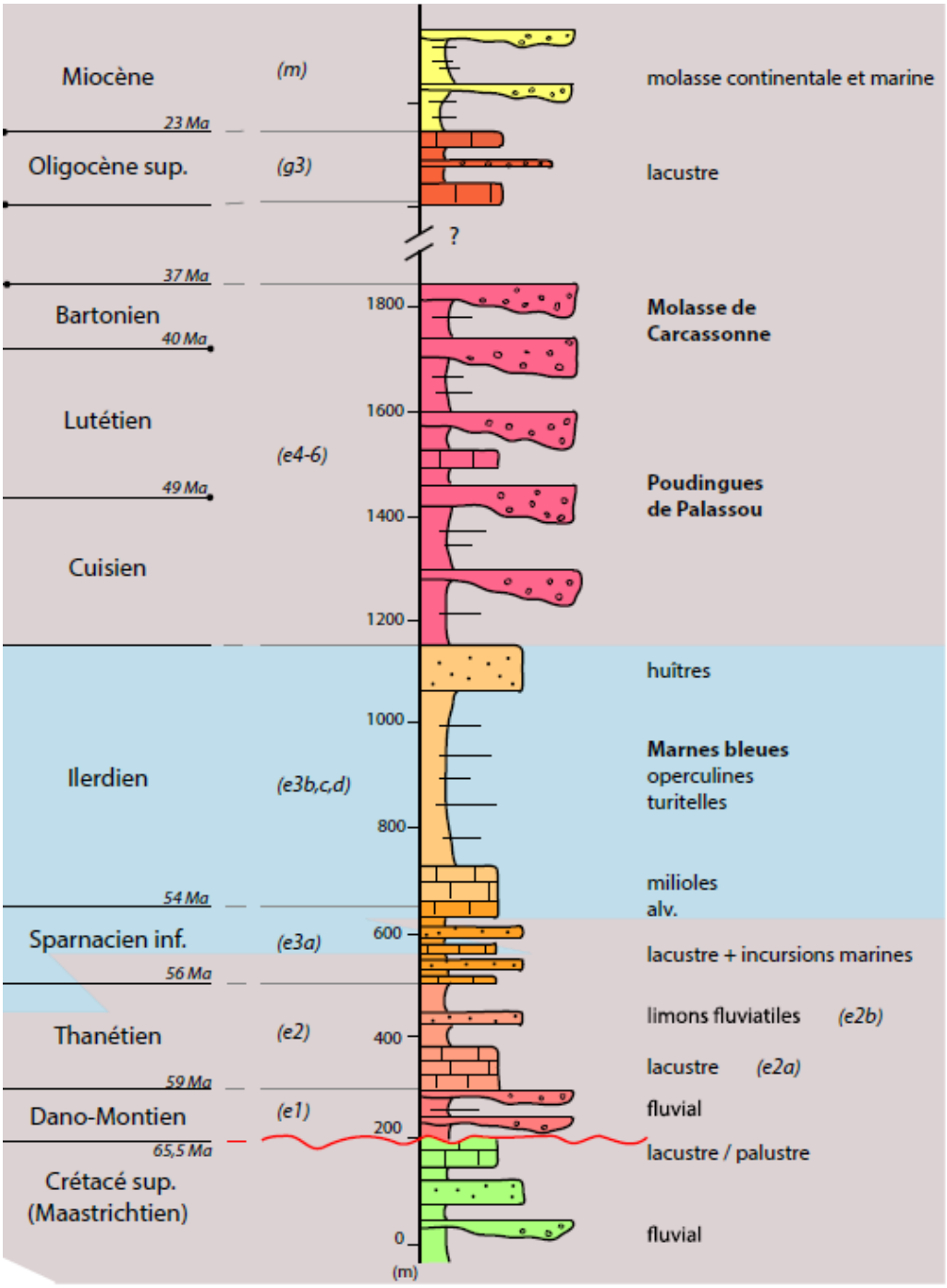

Figure 3.1: Log composite de la feuille de Capendu (Prieur (2019), d'après notice de la feuille Capendu (Ellenberger et al.*, 1985)).*

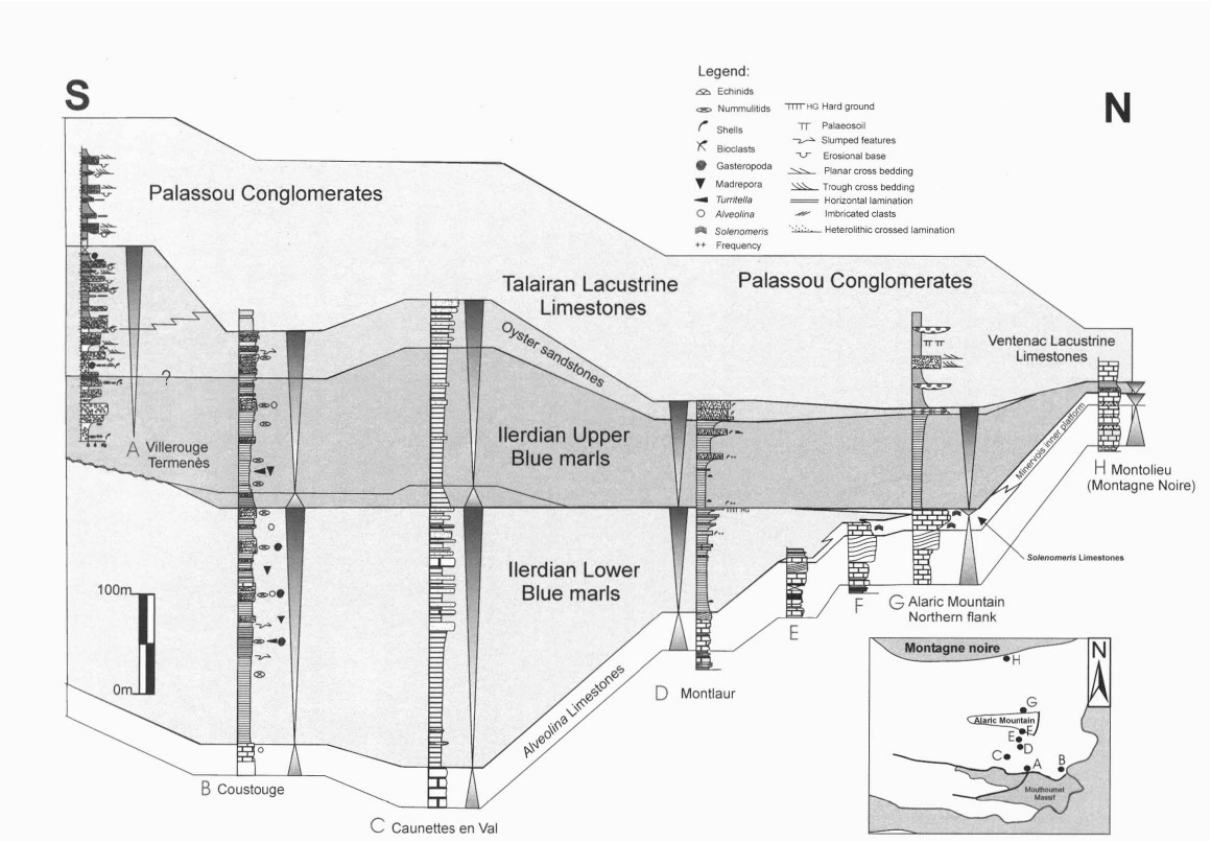

Figure 3.2: Correlation stratigraphique des logs levés dans la série Eocène du bassin. Données de(Massieux, 1973; Rey and Bousquet, 1981; Plaziat, 1984b; Pautal, 1985; Ellenberger et al.*, 1988), Tambareau non publié, Christophoul non publié tirés de Christophoul et al., 2003.*

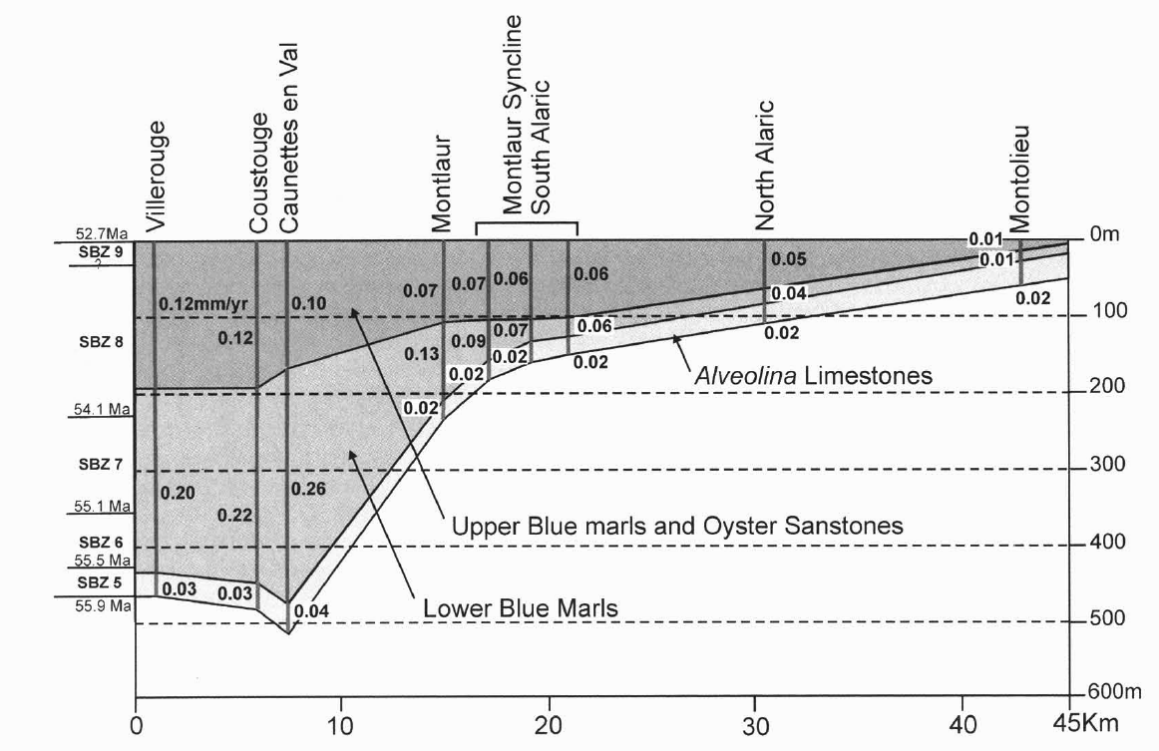

Figure 3.3: Epaisseurs et taux de subsidence (mm/yr) des formation Ilerdiennes calculés par Christophoul et al. (2003) selon la méthode de Einsele (1992). L'axe des « x » représente la distance par rapport au Massif de Mouthoumet.

I.2 Les poudingues de Palassou

I.2.1 Stratigraphie

La stratigraphie de la série de Palassou est basée sur les travaux de Plaziat (1984) et Crochet (1989). Cette série conglomératique syn-orogénique est couramment attribuée au Cuisien s.l, débutant à l'intérieur ou après la biozone SBZ9 (53,5 à 53 Ma).

Crochet (1989) propose une subdivision des poudingues de Palassou en 3 unités tectono-stratigraphiques qui sont l'unité 1 (Yprésien supérieur - Lutétien) caractérisée par la prédominance des galets carbonatés attribués au Méso-Cénozoïque, l'unité 2 (Bartonien) caractérisée par l'apparition et la prédominance de galets de socle et enfin, l'unité 3 (Priabonien) caractérisée par un retour à la prédominance des galets du Méso-Cénozoïque (Figure 3.4). Les différentes unités sont définies à partir de leur contenu en clastes dans la zone d'étude de la thèse comprise entre Limoux et le Mas d'Azil. (Figure 3.4).

Chacune de ces unités est définie par une tendance granocroissante marquée par une abondance de plus en plus importante de niveaux conglomératiques, suivie par des intervalles plus fins, à dominance silteuse, et contenant des volumes plus ou moins importants de calcaires lacustres (Figure 3.4). Les données biostratigraphiques sont relativement rares dans la série de Palassou. La base de cette série est attribuée à l'Yprésien moyen suivant des datations en biostratigraphie sur des nummulites (*Nummulites atacicus, N. globulus*) (Doncieux, 1912; Hottinger, 1962; Plaziat, 1970; Plaziat, 1984b) et des mollusques (Calcaires de Ventenac (*Planorbis pseudorotondatus*) (Ovtracht and Lenguin, 1977). Des gisements de micromammifères (Mirepoix, Crochet, 1989), nord de Douzens (MP12-13) Ellenberger et al.,1988 et Sudre et al.,1992) et des données palynologiques (Bilotte et al., 1988) permettent de dater les dépôts fins intercalés entre les unités 1 et 2 à un intervalle compris entre le Lutétien moyen et le Bartonien basal (Figure 3.4). Les gisements de La Livinière 2, Siran, Pépieux et Casseras permettent d'attribuer un âge Bartonien inférieur à la molasse de Castelnaudary (Sudre et al., 1992) ce qui confirme son équivalence avec les dépôts de la deuxième unité de Palassou définie par Crochet (1989). Une autre dénomination utilisée est la molasse de Carcassonne qui correspond à l'équivalent des unités 1 et 2 dont la limite supérieure est attribuée au Priabonien suivant des datations sur des mamifères (*Lophiodon Issilense, Lophiodon lautricense*) par Depéret (1910), Hartenberger et al. (1968), Plaziat (1984) et Berger (1990), et des vertébrés (*Lophiaspis baicheri, Lophiaspis occitanicus, Pachynolophys duvali, Propaleotherium*) par Hartenberger et al. (1968) et Plaziat (1984).

I.2.2 Sédimentologie des poudingues de Palassou

Les deux premières unités ont été étudiées au cours de ce travail de thèse le long de 4 coupes. Trois coupes ont été levées dans l'unité 1 et la quatrième commence dans l'unité 1 et se termine dans l'unité 2. L'unité 3 n'a pas été caractérisée avec précision car elle affleure mal et est difficile à observer en continu.

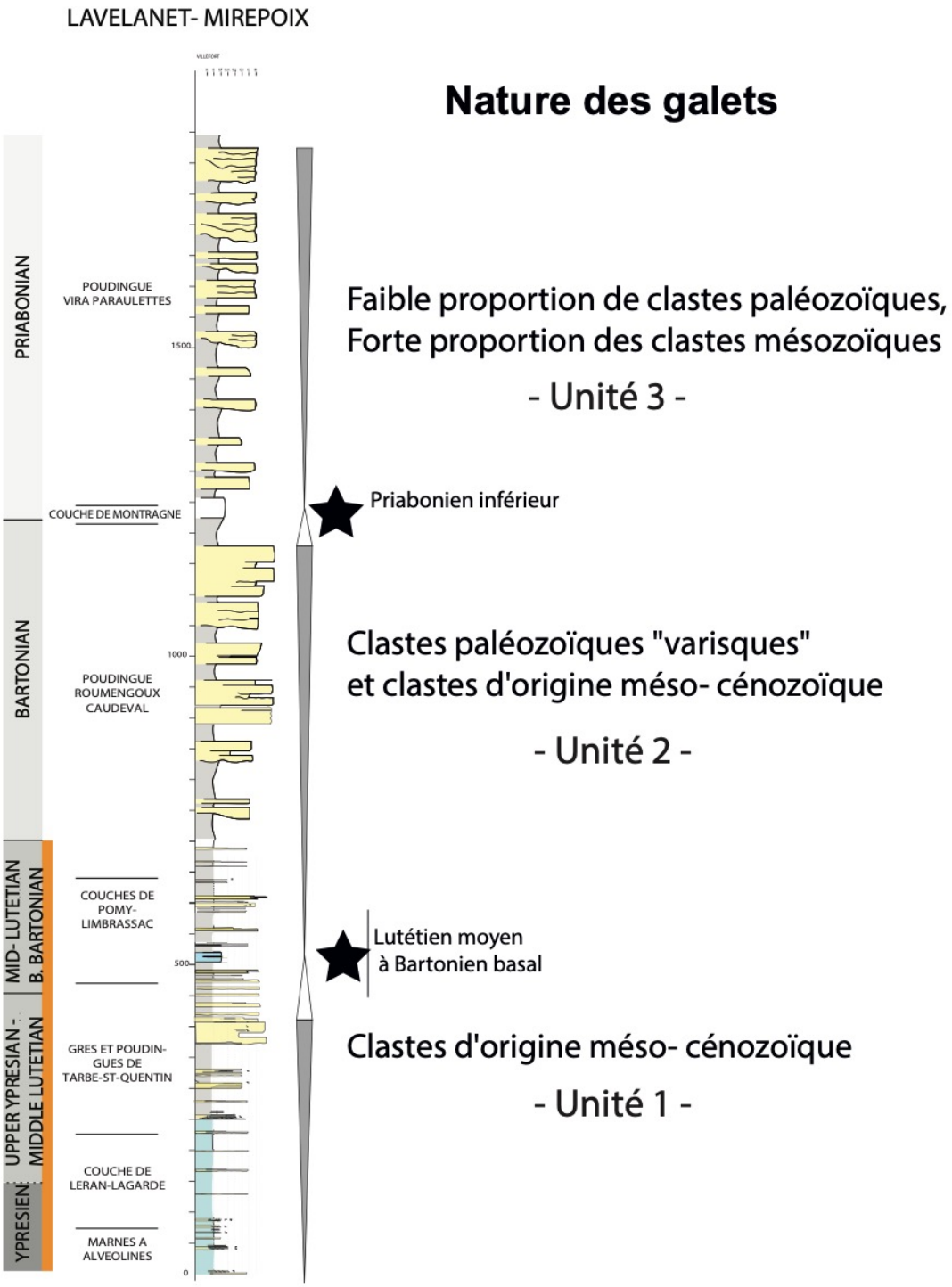

Figure 3.4: Log synthétique de la série de Palassou. Les étoiles correspondent aux limites entre les unités suivant les datations de biostratigraphie.

Plusieurs coupes ont été également levées dans l'unité 1, en particulier lors des stage de M2 de Johann Miguet (Miguet, 2015) et Marine Prieur (2019) (Prieur, 2019).

5 coupes sont présentées ici :

1) la coupe de Villerouge/Talairan, levée au cours de cette thèse (Figure 3.5).

2) la coupe de la vallée de l'Orbieu, levée par Miguet (2015), partiellement complétée lors de cette thèse et finalisée par Prieur (2019) (Figure 3.5).

3) Labastide-en -Val/Clermont-sur-Lauquet, initiée lors de cette thèse et finalisée par Prieur (2019) (Figure 3.5).

4) Caunette-sur-Lauquet/Pomas dont l'étude a été initiée au cours de cette thèse et apporfondie par Prieur (2019) (Figure 3.5). Ces quatre coupes se situent au front du Mouthoumet. Pour compléter cette approche plus à l'ouest

5) la coupe de Chalabre Montjardin réalisée par Miguet (2015) dans la région de Chalabre a été intégrée (Figure 3.5).

Les principaux environnements de dépôts ont été identifiés, pour plus de détails sur les faciès, les corrélations et les géométries des corps sédimentaires, se référer au mémoire de M2 de Marine Prieur (2019) et Prieur et al. (in prep).

Les dépôts conglomératiques sont abondants à proximité des reliefs, il s'agit :

- De dépôts chenalisés dans la plupart des cas et montrant des degrés d'amalgamation plus ou moins importants. Ils correspondent au remplissage de chenaux de haute énergie, de type en tresses ou en méandres, présentant des épaisseurs métriques à plurimétriques.
- De dépôts conglomératiques non organisés présentant une matrice sableuse ou boueuse et ne présentant pas de classement voire un granoclassement inverse. Ils correspondent à des dépôts gravitaires.
- De dépôts conglomératiques à matrice sableuses organisés sous forme de bancs décimétriques granodécroissants empilés à l'intérieur d'intervalles conglométratiques métriques à plurimétriques. Ils correspondent à des dépôts hyperconcentrés de type flash flood.

Les dépôts sableux se présentent :

- Soit intercalés à l'intérieur des dépôts conglomératiques soit à leur sommet ; ils présentent fréquemment des figures de courant de haute énergie telles que des mégarides 3D, ou des lamines planes. Ils correspondent à des dépôts chenalisés moins énergétiques que les conglomérats.

- Soit sous forme de dépôts lenticulaires de sable fins à moyen intercalés à l'intérieur des dépôts fins. Ils correspondent à des dépôts de débordement de type crevasses splay ou à des dépôts lacustres.

Les dépôts fins se présentent sous forme d'argiles et silts, des niveaux carbonatés métriques peuvent être intercalés.

Les niveaux argilo-silteux présentent des couleurs variables de gris vert à rouge, avec des nombreux dépôts marmorisés. Ils montrent fréquemment des évidences de bioturbation ou de pédogenèse (plus fréquemment dans les dépôts rouges ou marmorisés) pouvant aller jusqu'à des paléosols. Ils correspondent à des dépôts de plaine alluviale plus ou moins drainées voire à des dépôts lacustres. Dans de nombreux cas, ces intervalles lacustres se terminent par des intervalles pédogénétisés ce qui montre qu'il s'agit des dépôts lacustres éphémères, hormis dans la partie inférieure de la série dans laquelle des faciès plus profonds sont identifiés (Prieur, 2019).

Les intervalles carbonatés correspondent soit à des dépôts lacustres, soit à des niveaux de paléosols de type calcrêtes.

Trois associations de faciès principales ont été identifiées selon un profil proximal distal.

- Une association constituée d'une dominance de chenaux conglomératiques complexes et amalgamés dont le remplissage peut admettre des passées sableuses grossières, les intercalations de dépôts fins y sont relativement importantes, quelques paléosols peuvent y figurer.
- Une association médiane est constitué de chenaux conglomératiques à sableux peu amalgamés intercalés avec des niveaux de plaine alluviale.
- Une association distale dans laquelle les dépôts fins prédominent, et correspondent à des dépôts de plaine alluviale ou à des dépôts lacustres. Les chenaux intercalés sont d'assez petites tailles et dispersés. Des niveaux sableux peu érosifs correspondant à des dépôts de débordement (crevasses splay) sont fréquents. Des niveaux sableux correspondant à des dépôts gravitaires peuvent également se présenter intercalés dans les dépôts lacustres.

La répartition et les caractéristiques des différentes associations de faciès correspondent à celles d'un système fluviatile distributaire (DFS : Weissmann et al. (2010) et Owen et al. (2015)). Des faciès marins ont été rencontrés à la transition entre les dépôts deltaïques de l'Ilerdien et les premiers dépôts continentaux. Il s'agit essentiellement de dépôts granulaires correspondant à des faciès de type fan delta.

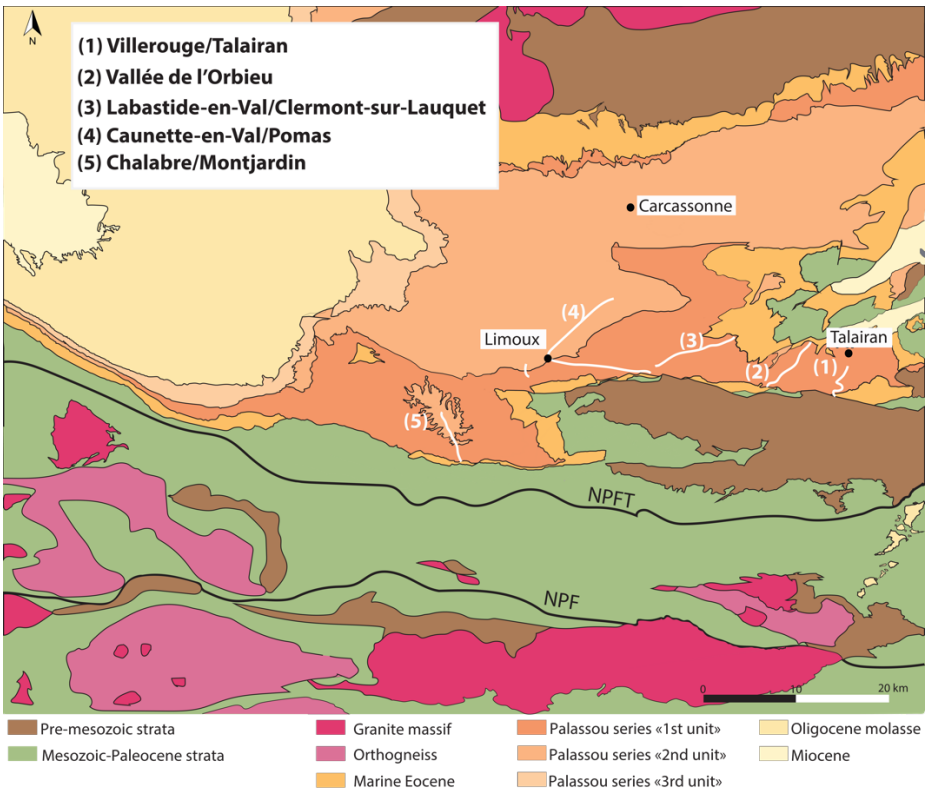

Figure 3.5: Localisation des logs stratigraphiques levés dans les unités 1 et 2 de la série de Palassou.

Les coupes qui ont été levées sont décrites succinctement ci-dessous en reprenant les principales associations d'environnements de dépôt décrits ci-dessus. Les faciès sont quant à eux repositionnés sur les 4 logs et sont décrits dans un tableau (Informations supplémentaires).

La nomenclature et les symboles utilisés sont représentés dans le Tableau 3.1 ci-dessous.

Tableau 3.1: Nomenclature et symboles utilisés dans les logs stratigraphiques des Corbières.

NOMENCLATURE ET SYMBOLES

Structures sédimentaires	Cross bedding	Elèments biogéniques	Figures sédimentaires
Contact Erosif	Obliques 2D	Bivalve	Fantôme racinaire (radicelle)
Forme lenticulaire	Tangentielle (dunes 3D)	Gastéropode	Calcrète
Bioturbation	Lamines planes	Nummulite	**Rides**
intense modérée faible		Plante	Rides de Courant
Limestone			Houle

Coupe de Villerouge-Talairan

La base du log stratigraphique est situé au nord de la ville de Villerouge-Termenès et son sommet au sud de la ville de Talairan (cf log Villerouge-Talairan, Figure 3.6). Il représente les premiers dépôts de la série de Palassou correspondant à la partie inférieure de l'unité 1.

Cette coupe mesure environ 355 mètres d'épaisseur, les pendages mesurés dans cette série évoluent depuis des séries inverse à la base, puis verticales, puis les pendages s'aplanissent progressivement pour finir par des inclinaisons de 10° vers le nord (Figure 3.6). L'évolution de ces pendages montre un dépôt syn tectonique de type wedge. A sa base, il est caractérisé par des séries deltaïques montrant un pendage inverse. En montant dans la série, ces dépôts se chargent progressivement en matériel grossier (gravier et galets) mais contiennent une faune marine. Un environnement de dépôt fluviatile médian se met en place dans les premiers 260 m (Figure 3.6). Il est suivi par des dépôts lacustres, avec intercalation de dépôts deltaïques et de dépôts gravitaires dans lesquels s'enregistrent la fin des dépôts syntectoniques. La coupe s'achève par des environnements de dépôt fluviatiles médians et par une intercalation de calcaires lacustres (Figure 3.6).

Le comblement de cette partie « est » du bassin, située entre les chaînons de Lagrasse au nord et le massif du Mouthoumet au sud, se déroule assez rapidement en fonction des apports depuis la chaîne dont témoignent les environnements de dépôts fluviatiles proximaux ci-après.

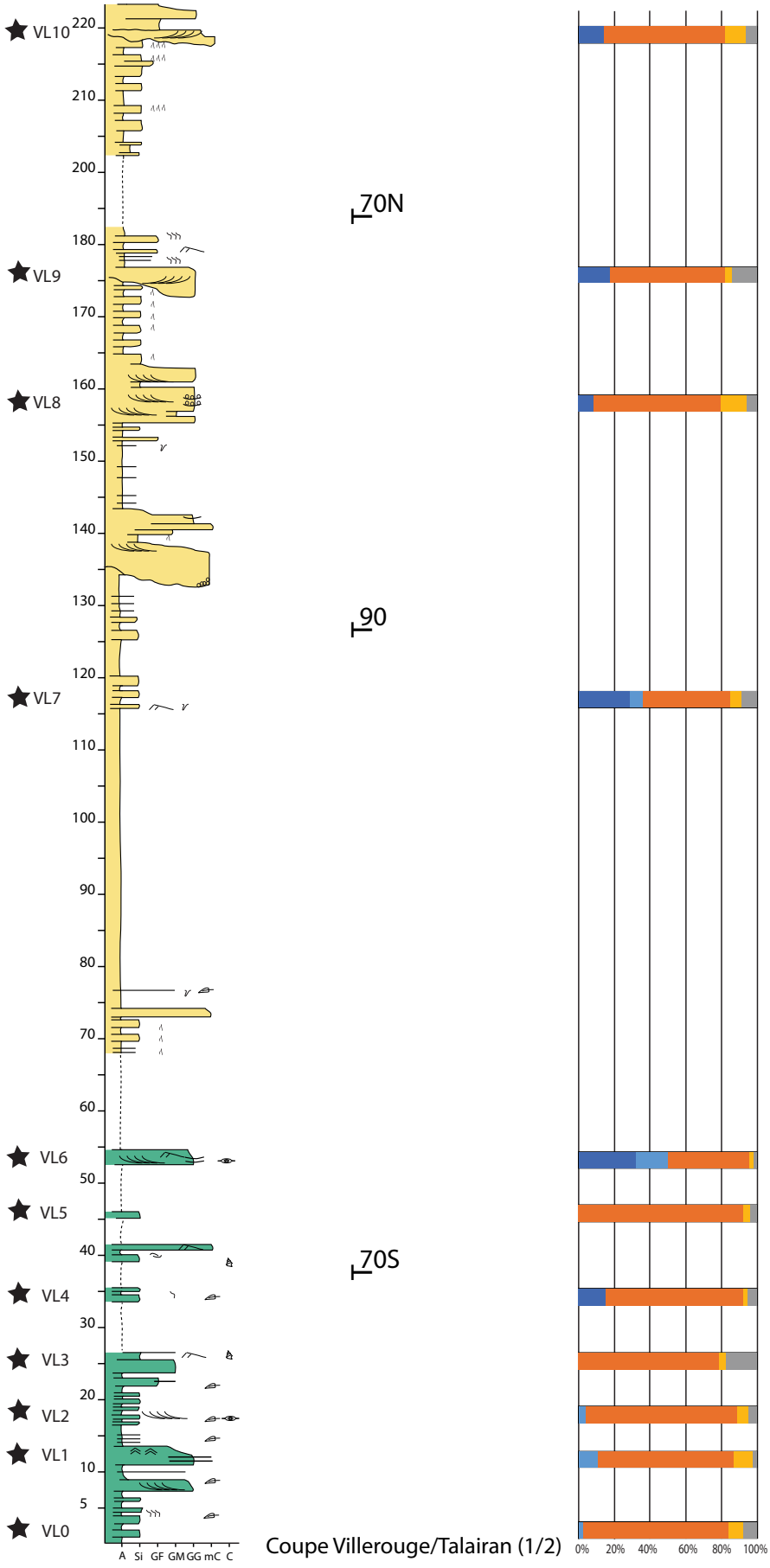

Figure 3.6: Log stratigraphique de Villerouge/Talairan avec les environnements de dépôts caractérisés et les résultats de composition minéralogique en argile (légende sur la page suivante).

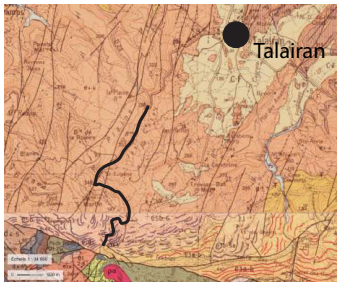

Smectite
Illite
Interstratification
Chlorite
Kaolintie

Villerouge/Talairan

YPRESIAN -LUTETIAN

1/500

Deltaïque
Lacustre
Fluviatile médian

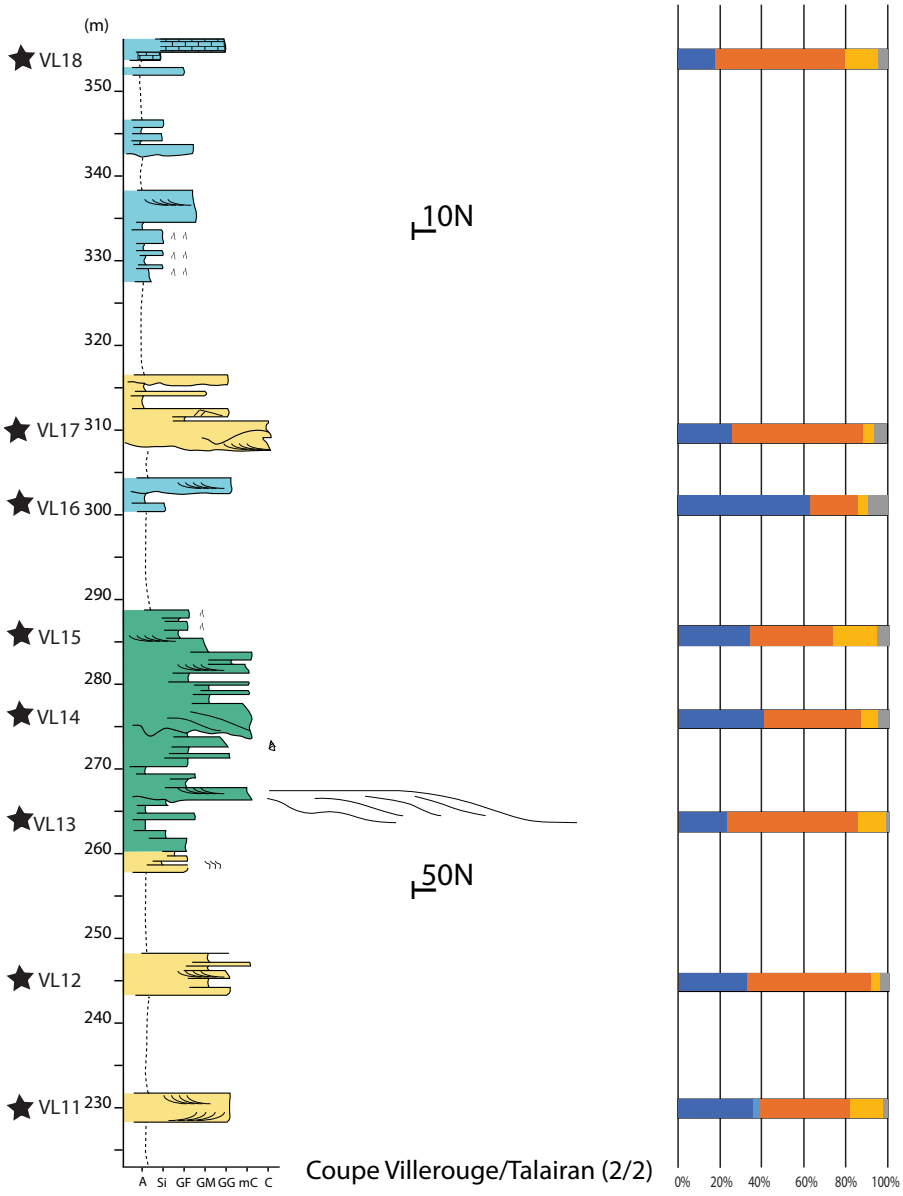

Coupe Villerouge/Talairan (2/2)

Coupe de la vallée de l'Orbieu

Ce log stratigraphique est levé entre le village de Saint-Martin-des-Puits et le village Saint-Pierre-des-Champs tout au long de la rivière l'Orbieu. Trois environnements de dépôt sont caractérisés sur cette coupe, un environnement de dépôt lacustre dans les premiers 50 mètres du log, auquel font suite des dépôts fluviatiles distaux à médians dans lesquels les chenaux sont de plus en plus abondants grossiers et amalgamés ; ils s'achèvent par des dépôts fluviatiles proximaux qui enregistrent l'avancée du système distributaire fluviatile (DFS) (Prieur et al., en cours) (Figure 3.7). L'épaisseur totale de ce log est autour de 700 mètres.

Comparé au log stratigraphique de Villerouge-Talairan, l'environnement de dépôt fluviatile à l'Orbieu est beaucoup plus chargé en bancs de conglomérats à galets et blocs, à bases érosives, et en bancs carbonatés entre ces corps conglomératiques. Les conglomérats montrent fréquemment des dunes métriques, les surfaces d'érosion sont fréquentes montrant des amalgames de chenaux qui peuvent être importants formant des intervalles décamétriques de conglomérats amalgamés. Ces derniers représentent les dépôts les plus proximaux.

Ce log reflète un apport de sédiments plus important, associé à l'accentuation de l'exhumation de la chaîne. La nature des clastes dans les conglomérats des logs de Villerouge-Talairan et de la vallée de l'Orbieu, confirme que la source de ces clastes vient de la couverture du Méso-Cénozoïque, en accord avec les travaux de Crochet (1989).

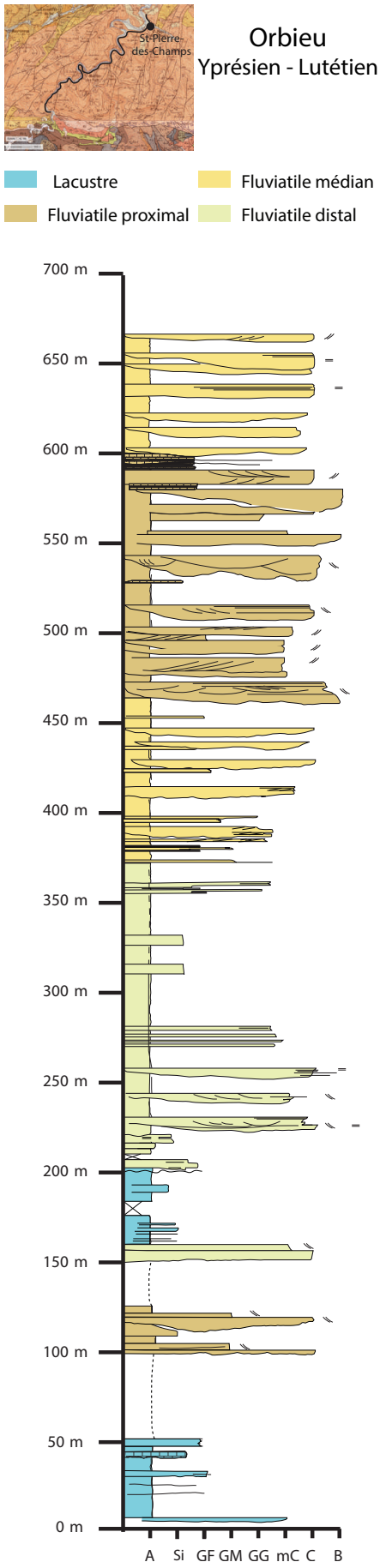

Figure 3.7 : Log stratigraphique de la vallée de l'Orbieu avec les environnements de dépôts caractérisés.

Coupe de Labastide-en-Val/Clermont-sur-Lauquet

Ce log sédimentologique démarre à la base de l'unité 1 du côté du village de Labastide-en-Val dans l'Yprésien et se termine au nord de Clermont-sur-Lauquet dans le Lutétien (Figure 3.8). Il fait environ 510 m d'épaisseur, en incluant les lacunes qui peuvent parfois représenter une quarantaine de mètres. Le début de la coupe est caractérisé par un environnement de dépôt lacustre suivi par une progradation progressive vers un environnement de dépôt fluviatile proximal, formant une barre conglomératique continue, puis une rétrogradation au sommet du log vers un environnement fluviatile médian (Figure 3.8).

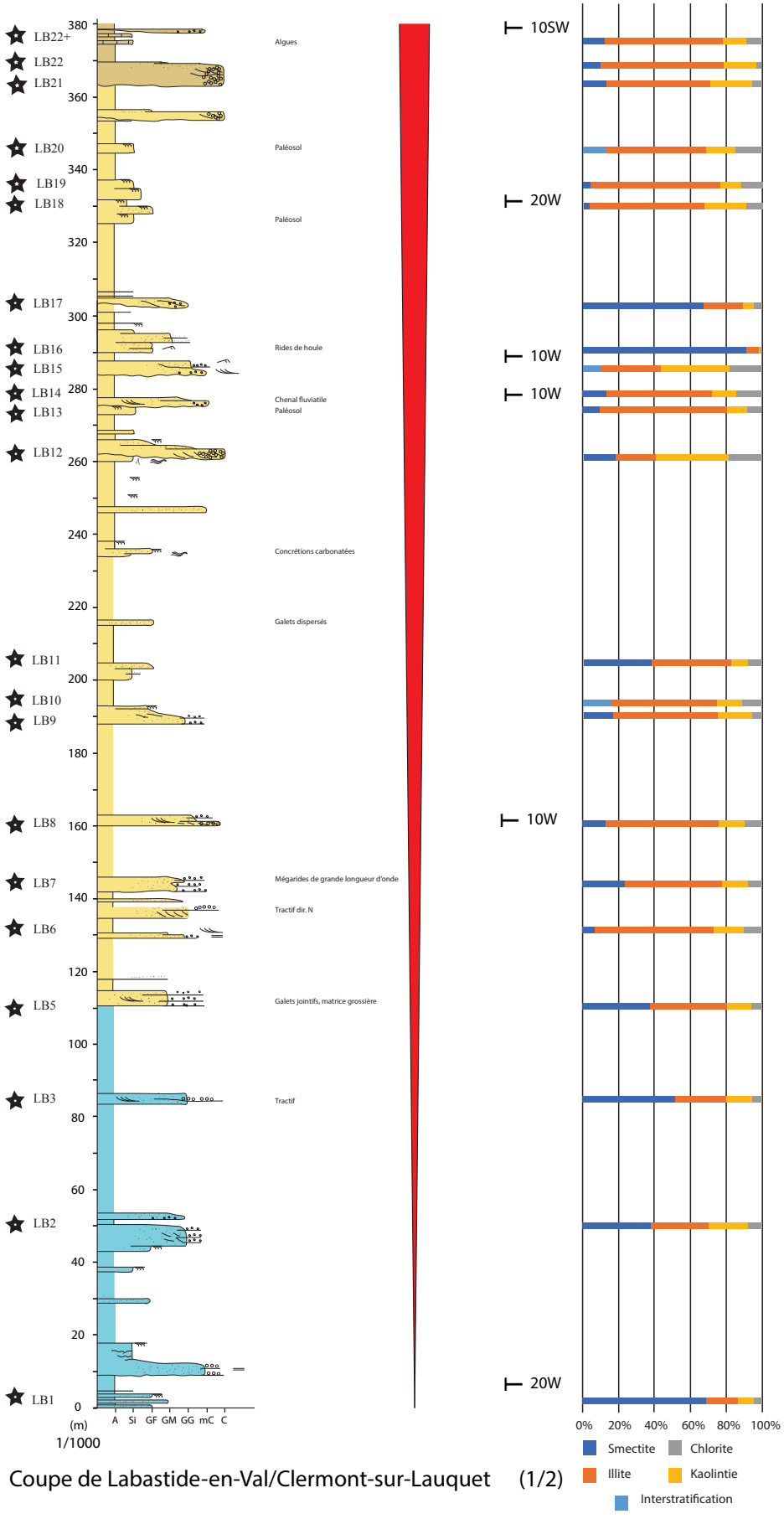

Figure 3.8 : Log stratigraphique de Labastide-en-Val/Clermont-sur-Lauquet avec les environnements de dépôts caractérisés et les résultats de composition minéralogique en argile.

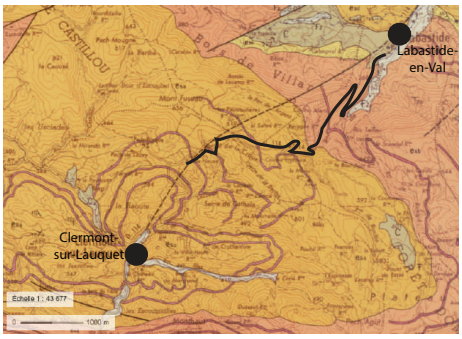

Fluviatile proximal

Fluviatile médian

Lacustre

Résultats DRX

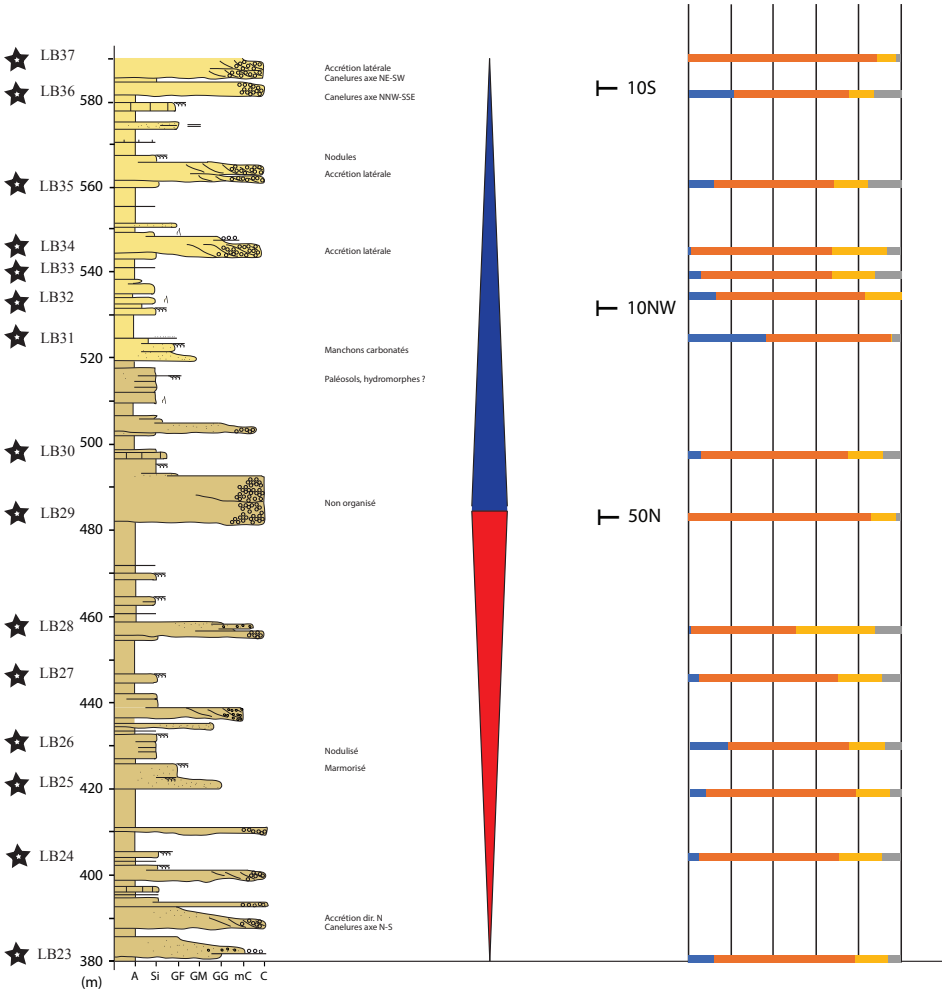

1/1000 Coupe de Labastide-en-Val/Clermont-sur-Lauquet (2/2)

Coupe de Caunette-sur-Lauquetl/Pomas

Cette coupe présente des lacunes difficilement quantifiables liées à d'importantes distances entre des points d'affleurements dispersés.

La base de cette coupe se trouve au nord du massif du Mouthoumet, en particulier, au nord de la ville de Caunette-sur-Lauquet et son sommet se trouve à Pomas (Figure 3.9). Elle représente l'unité 1 et le début de l'unité 2. Le début de la coupe est caractérisé par des dépôts lacustres suivis par des dépôts fluviatiles proximaux. Cette succession montre une progradation du profil de dépôt.

Cette progradation est suivie d'une rétrogradation enregistrée par des dépôts fluviatiles distaux de type méandriforme dispersés dans des dépôts de plaine alluviale, quelques clastes de granite sont visibles dans cet intervalle (Figure 3.9). Ils sont suivis de dépôts de plaine alluviale incluant des niveaux lacustres. Ils forment un intervalle de dépôts fins qui affleure à proximité de Limoux (Magrie) (Figure 3.9). Cet intervalle fin montre une continuité assez importante traçable sur plusieurs kilomètres, visibles sur les cartes au 1/50.000ème de Limoux, Lavelanet et Mirepoix, et a été rapporté à l'intervalle Lutétien moyen à Bartonien basal sur la base de données paléontologiques (Bilotte et al., 1988).

Les dépôts suivants (Bartoniens) représentent une progradation importante marquée par le retour de chenaux massifs souvent amalgamés (DFS médian à proximal) (Figure 3.9). Ils correspondent à l'unité 2 de Palassou décrite par Crochet (1989). Les conglomérats montrent une extension géographique plus importante comparée à celle identifiée à partir des logs précédents (surtout vers Pomas). Les dépôts de Pomas (LMX3 sur la Figure 3.9) montrent des intervalles conglomératiques incluant des dépôts hyperconcentrés faiblement chenalisés alternant avec des dépôts fins. Ils sont interprétés comme la partie distale d'un cône distributaire. Les dépôts conglomératiques du Bartonien montrent une extension géographique plus importante vers le nord. Corrélés grâce à ces variations de taille, par la composition différente des galets, comme démontré précédemment par Crochet (1989) et signalés sur les notices de cartes de Lavelanet et de Limoux, ces dépôts contiennent essentiellement des clastes paléozoïques dont une portion importante de clastes granitiques qui ont fait l'objet d'échantillonnage pour les études géo- et thermo-chronologiques.

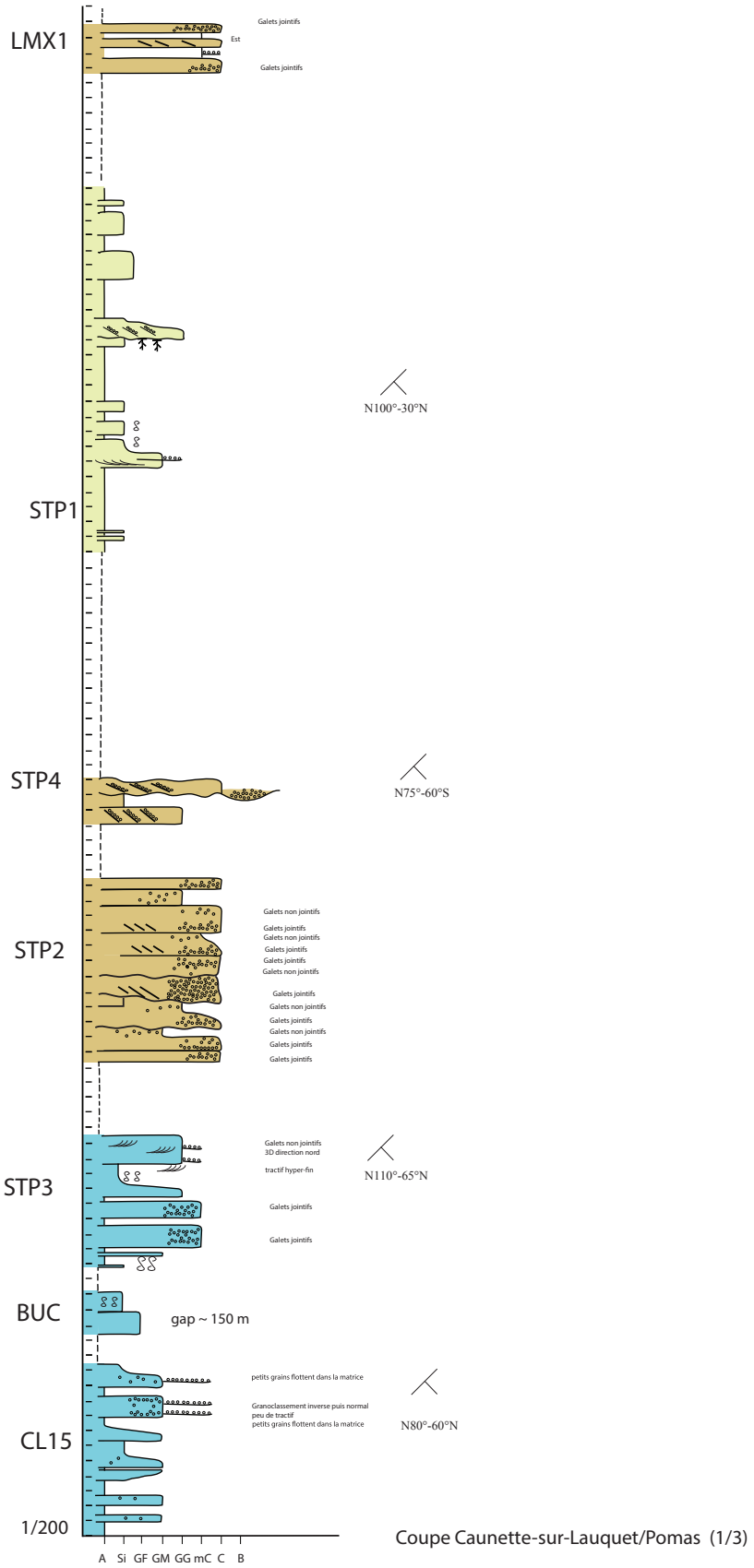

Figure 3.9 : Log stratigraphique de Caunette-sur-Lauquet/Pomas avec les environnements de dépôts caractérisés et les résultats de composition minéralogique en argile.

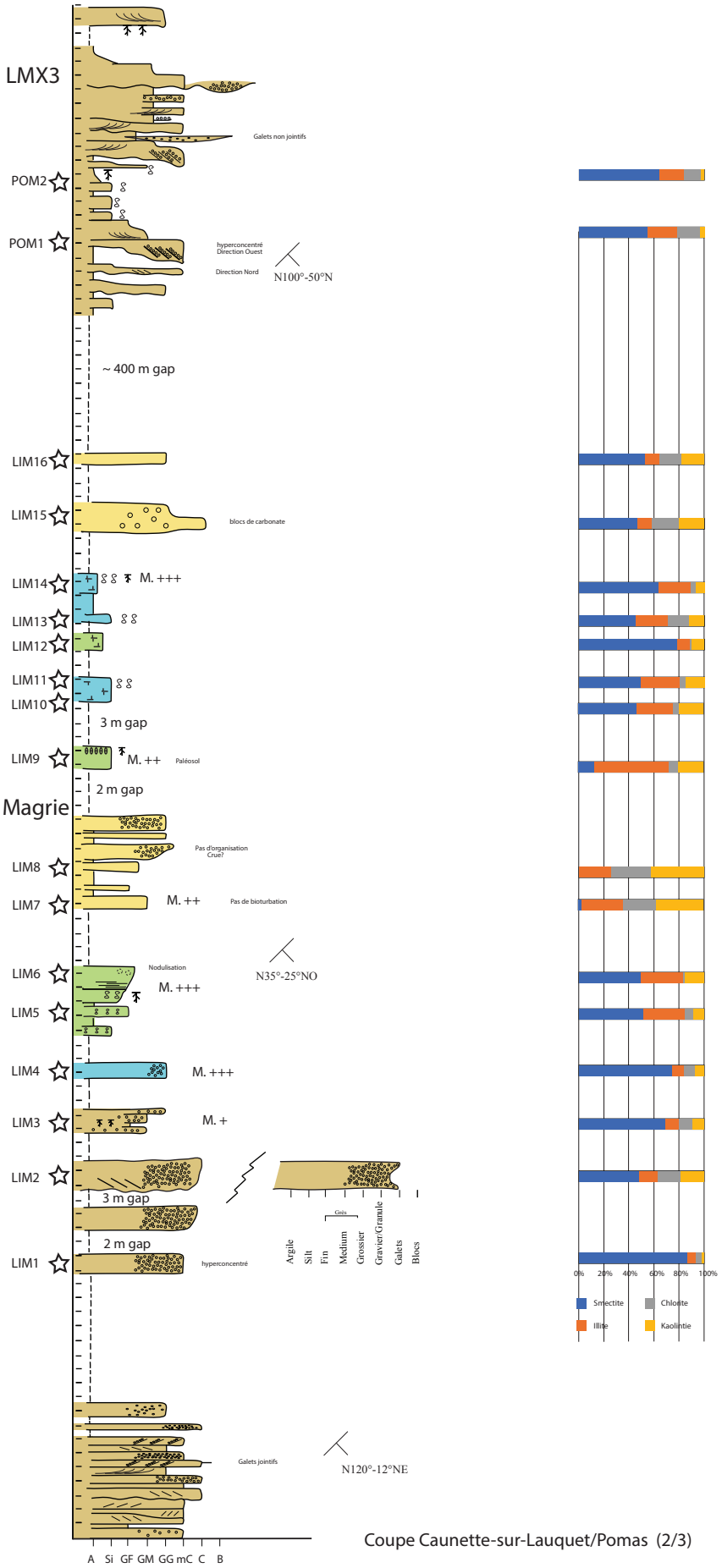

Coupe Caunette-sur-Lauquet/Pomas (2/3)

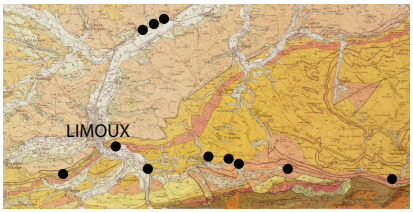

Fluviatile proximal
Fluviatile médian
Fluviatile distal
Plaine alluviale
Lacustre

Log Caunette-sur-Lauquet/ Pomas

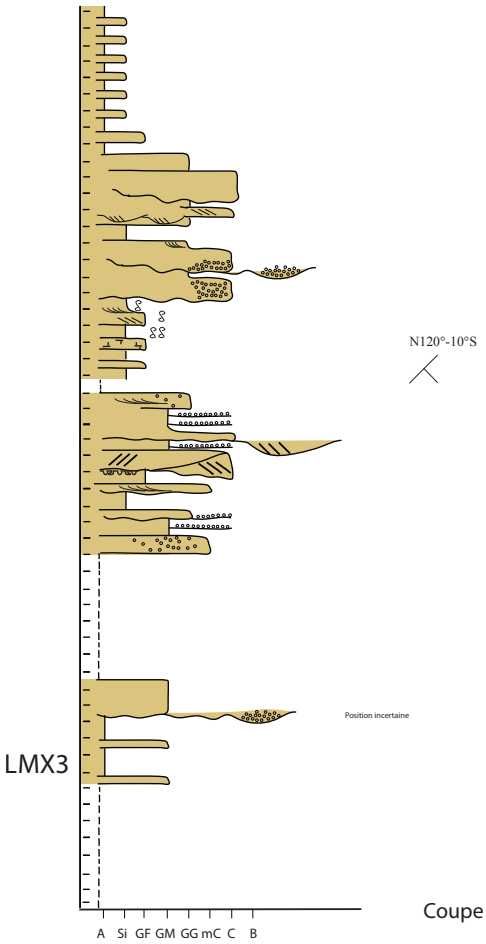

Coupe Caunette-sur-Lauquet/Pomas (3/3)

Coupe de Chalabre- Montjardin

La coupe de Chalabre- Montjardin montre à grande échelle une tendance progradante depuis des dépôts marins riches en dépôts gravitaires suivis par une émersion et une évolution depuis des dépôts fluviatiles médians à proximaux (Figure 3.10). Dans cette première unité, les clastes sont essentiellement constitués de galets méso- cénozoïques. Cette tendance progradante est suivie par une rétrogradation progressive et un retour à des faciès de DFS médian marqué par des intercalations de chenaux conglomératiques à l'intérieur de dépôts de plaine alluviale (Figure 3.10). A l'intérieur de cet intervalle apparaissent dans l'ordre stratigraphique, des galets de flysch noir, puis des clastes paléozoïques et des galets de granite. Crochet (1989) et Crochet dans Bilotte et al. (1988) attribuent cet intervalle à une période Lutétien moyen à Bartonien. Les dépôts supérieurs affleurent très mal dans cette zone, Crochet dans Bilotte et al. (1988) et Crochet (1989), décrivent des dépôts à galets et blocs couramment de 50 cm de diamètre, qu'ils attribuent au Bartonien (unité 2 de Palassou).

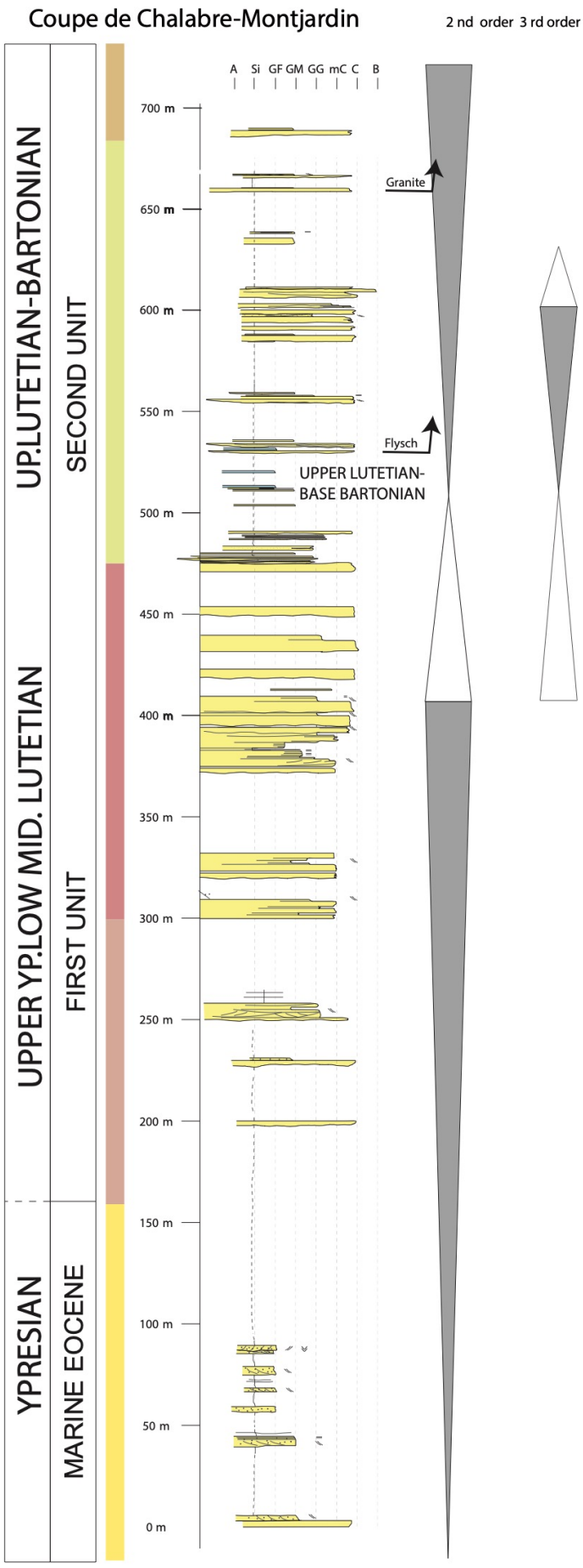

Figure 3.10 : Log stratigraphique de Chalabre/Montjardin

I.3 Géométries sédimentaires, implications sur la déformation et le routage sédimentaire :

Le stage de master 2 de Marine Prieur a permis outre de compléter les levers de coupe et l'interprétation des faciès sédimentaires, de réaliser une cartographie des principaux intervalles de dépôts et des séquences associées. Ces travaux montrent que les différentes coupes présentées ci-dessus correspondent à des séquences différentes du remplissage sédimentaire. Quatre séquences successives sont identifiées dans le remplissage de l'unité 1 (Figure 3.11).

Elles présentent des motifs comparables :

- une progradation marquée par des avancées de faciès conglomératiques qui sur une verticale se traduit par des dépôts chenalisés de plus en plus grossiers et amalgamés.
- une rétrogradation qui se traduit par un moindre amalgame des chenaux avec des faciès de plaine alluviale plus développés voire de niveaux lacustres.

Les dépôts rencontrés à l'est, dans la coupe de Villerouge-Talairan correspondent à la première séquence du remplissage (Figure 3.11). La séquence 2 se développe principalement dans la coupe de l'Orbieu avec la progradation des séries conglomératiques (Figure 3.11). La séquence 3 se développe principalement dans la coupe de Labastide-en-Val où l'essentiel de la sédimentation reste à l'intérieur du synclinal de Talairan comme pour les deux premières séquences. La séquence 4 se développe principalement dans la coupe de Caunette-sur-Lauquet où les travaux réalisés montrent des dépôts conglomératiques qui s'étendent au-delà du synclinal de Talairan et qui correspondent au maximum de progradation de la quatrième séquence (Figure 3.11).

Ces observations montrent :

- le caractère syn-tectonique des dépôts, bien enregistré dans les changements de la coupe de Villerouge qui montre un fonctionnement du chevauchement du Mouthoumet pendant le dépôt.
- le piégeage des trois premières séquences de l'unité Palassou 1 dans le synclinal de Talairan, ceci amène à interpréter le bassin de Talairan comme un bassin en piggy back limité au nord par les chainons de Lagrasse et se remplissant durant les trois premières séquences de l'unité 1,
- la quatrième séquence montre le transport de ce bassin et l'export de sédiments (en particulier grossiers) au-delà du synclinal de Talairan.

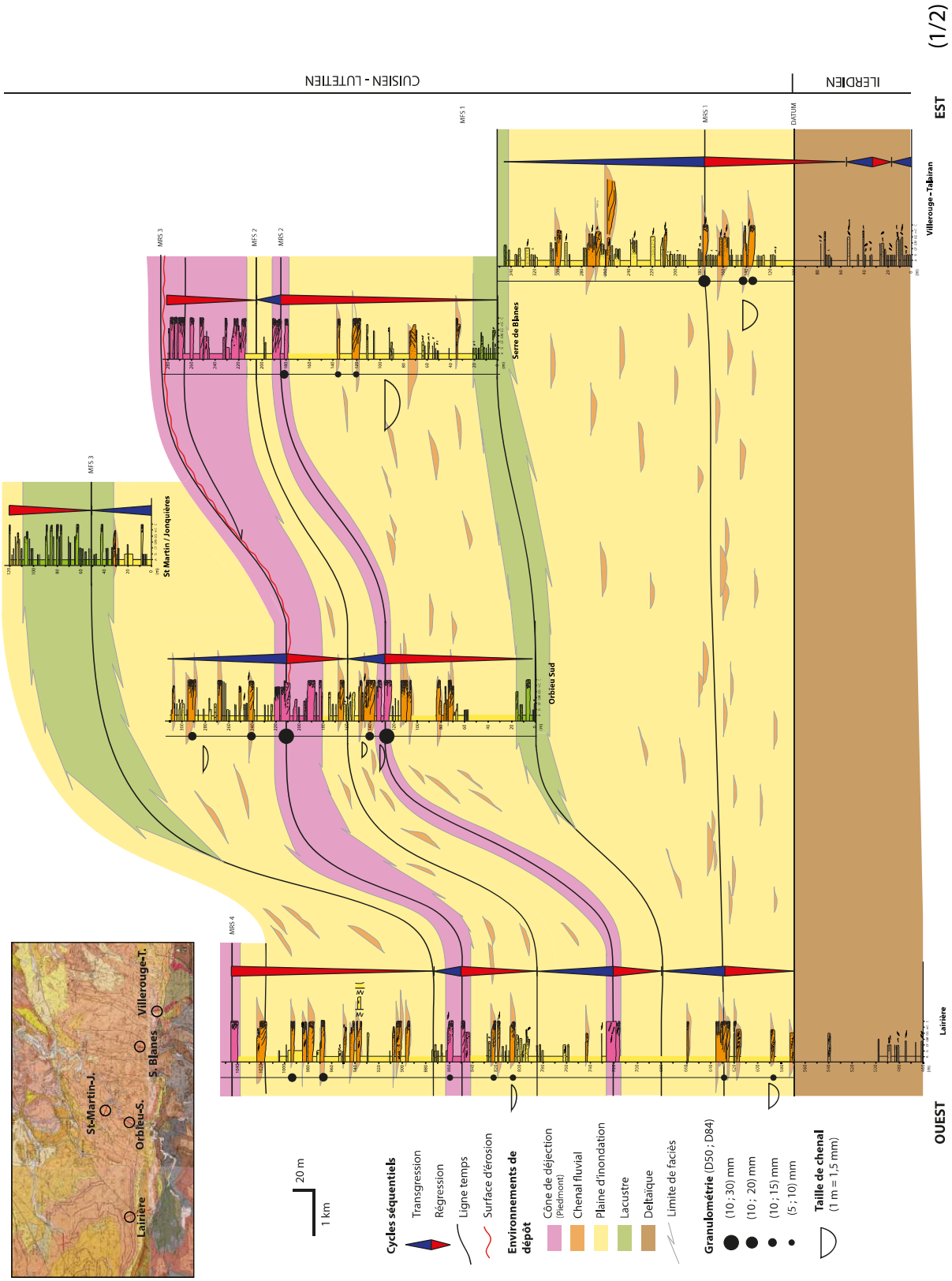

Figure 3.11: Corrélations entre les différentes coupes étudiées dans le synclinal de Talairan. (Prieur, 2019 ; Prieur et al., in prep). Pour le log de Villetriouls (légende ???) l'environnement de dépôt n'est pas clair (plaine alluvial ?)

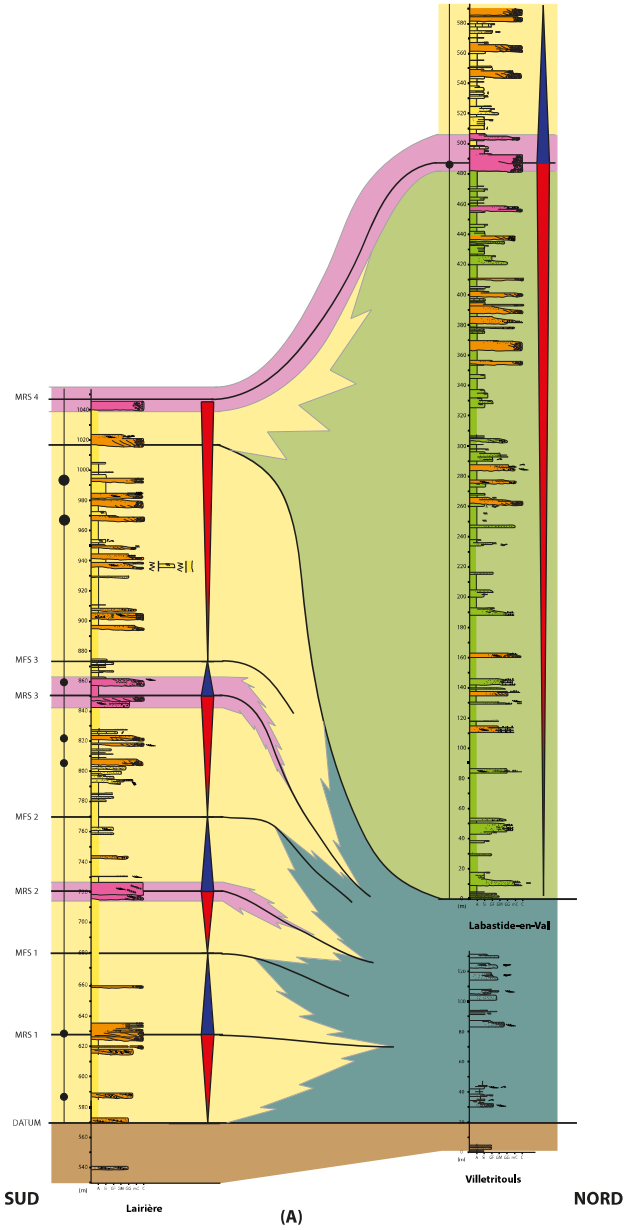

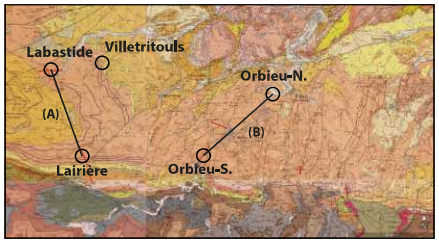

20 m
1 km

Cycles séquentiels

- Transgression
- Régression
- Ligne temps
- Surface d'érosion

Environnements de dépôt

- Cône de déjection (Piedmont)
- Chenal fluvial
- Plaine d'inondation
- Lacustre
- ? ? ?
- Deltaïque
- Limite de faciès

Granulométrie (D50 ; D84)

- (10 ; 30) mm
- (10 ; 20) mm
- (10 ; 15) mm
- (5 ; 10) mm

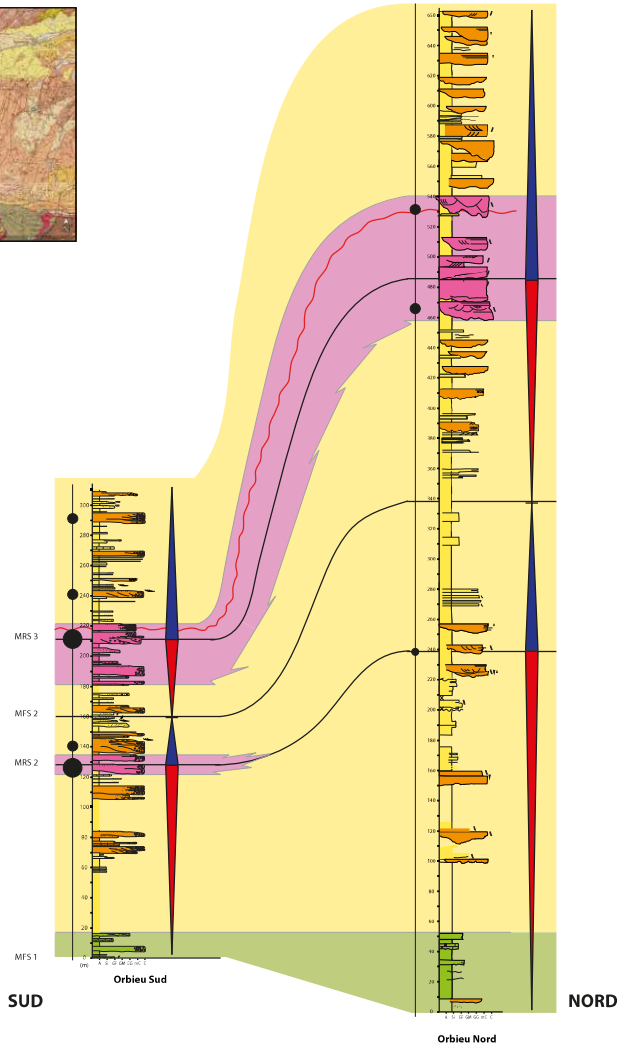

Christophoul et al. (2003) montrent le développement d'un wedge au front de la montagne d'Alaric. Le gisement de Douzens nord, situé dans des dépôts sub plans, a livré un âge Lutétien moyen qui post-date les déformations au front de la Montagne d'Alaric et correspond à l'âge attribué latéralement au sommet de l'unité Palassou 1. Le dépôt de l'unité 1 de Palassou est en conséquent interprété comme un dépôt syn-tectonique accompagnant la propagation en séquences de chevauchements frontaux.

Une reconstruction paléogéographique du maximum de progradation de la quatrième séquence est représentée dans la Figure 3.12 (2nd gravel front) issue des travaux de Prieur (2019). Elle montre l'extension majeure du gravel front de la séquence 4 au Lutétien moyen à supérieur, comparé à celui des séquences 2 et 3 (1st gravel front, Figure 3.12).

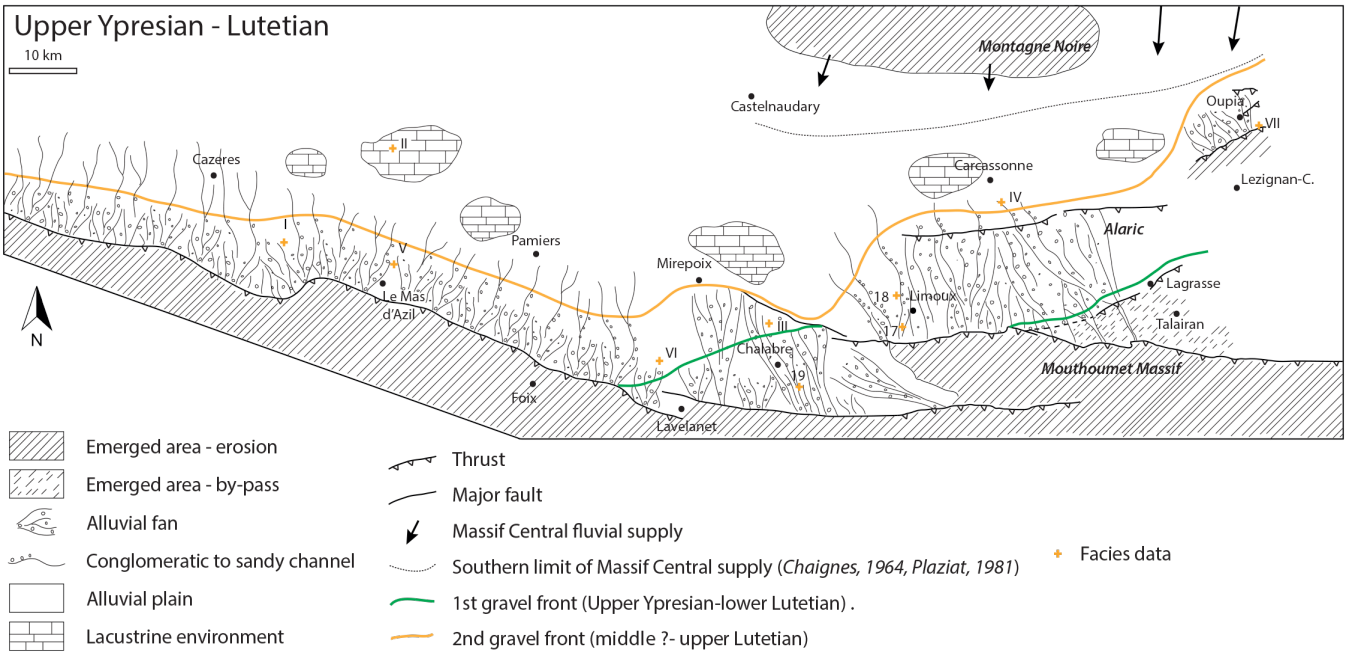

Figure 3.12: Reconstruction paléogéographique du gravel front des séquences 2 et 3 (1st gravel front) et du maximum de progradation de la séquence 4 (2nd gravel front) d'après Prieur et al. (in prep).

II. Analyses par DRX sur des échantillons d'argile de la série de Palassou

Environ 75 échantillons ont été étudiés par diffractométrie de Rayons X pour caractériser le contenu en argile. Ils proviennent des coupes Villerouge/Talairan, Labastide-en-Val/Clermont-sur-Lauquet et Caunette-sur-Lauquet/Pomas (en particulier l'affleurement Magrie). L'objectif était de d'identifier le pic de kaolinite associé au décapage de surfaces pyrénéennes. Ces surfaces pyrénéennes à très faible relief localisées en altitude ont fait l'objet d'études depuis des années (Babault et al., 2005; Bosch et al., 2016; Uzel et al., 2019; Uzel et al., 2020) dans le but de comprendre leur mode de formation. La totalité des échantillons des coupes Villerouge/Talairan et Labastide-en-Val/Clermont-sur-Lauquet permet d'avoir une idée sur la composition minéralogique des argiles dans les dépôts de l'unité 1, tandis que les échantillons de l'affleurement « Magrie » dans la coupe de Caunette-sur-Lauquet/Pomas permettent d'avoir des informations sur les dépôts de la phase de transition de l'unité 1 à l'unité 2. Deux échantillons d'argile ont pu être analysés dans l'affleurement Pomas (unité 2 de Palassou) de cette dernière coupe.

Résultats et discussion

Les résultats de DRX pour les 75 échantillons analysés montrent la présence de smectite, d'illite, de chlorite et de kaolinite dans tous les échantillons en proportions assez variables d'un échantillon à l'autre. Pour le log de Villerouge/Talairan, les interstratifiés sont présents également dans 8 échantillons sur 19 en proportions ne dépassant pas les 15% (cf. le log de Villerouge-Talairan, Figure 3.6). Les minéraux argileux principaux sont globalement l'illite qui peut arriver jusqu'à 80% (échantillon VL0) puis la smectite qui arrive jusqu'à 63% (échantillon VL16). Les pourcentages de kaolinite et de chlorite ne dépassent pas les 20%. En termes d'environnement de dépôt, les dépôts deltaïques montrent un signal illite dominant avec un peu de chlorite, et les dépôts continentaux, un signal illite smectite légèrement plus prononcé dans les dépôts lacustres.

La tendance globale est comparable pour le log de Labastide-en-Val/Clermont-sur-Lauquet sans la présence d'interstratifiés, mais avec toujours la majorité des échantillons ayant un pourcentage élevé d'illite, par exemple le pourcentage d'illite dans l'échantillon LB29 est de 83%. Pour la smectite, 3 échantillons ont un pourcentage remarquable (LB1, LB16 et LB17) pouvant arriver jusqu'à 85% (LB16). Le pourcentage de kaolinite est entre 10 et 40% et celui de chlorite est inférieur à 20% (cf le log de Labastide-en-Val/Clermont-sur-Lauquet, Figure 3.8). En fonction des environnements de dépôt, la proportion de smectite est plus grande dans les dépôts lacustres et

carbonatés.

Pour le log de Caunette-sur-Lauquet/Pomas, les résultats DRX des échantillons de l'affleurement « Magrie » montrent une dominance remarquable de smectite pouvant représenter jusqu'à 85% (échantillon LIM1), puis de l'illite avec un pourcentage entre 5 et 45%, de kaolinite entre 5 et 40% puis de chlorite ne dépassant pas les 16% (cf le log de Caunette-sur-Lauquet/Pomas, Figure 3.9). Les dépôts fluviatiles et de plaine alluviale à la base du log sont accompagnés d'un signal smectite dominant. Plus loin, on retrouve un signal bien différencié riche en kaolinite et en chlorite associé à un environnement de dépôts fluviatile médian assez massif. On remarque ensuite un retour à la smectite dominante avec un environnement de plaine alluviale distale et lacustre. Pour les 2 échantillons de l'affleurement Pomas, les résultats montrent une abondance de smectite (50 à 60%) et un très faible pourcentage de Kaolinite (<10%).

L'abondance de kaolinite dans les pulses terrigènes des environnements de dépôt fluviatiles et celle de la smectite dans les environnements de dépôt lacustres et les plaines alluviales était attendue ; la kaolinite se forme dans des conditions d'altération intenses (en conditions d'hydrolyse intense, la kaolinite s'appauvrit en cations solubles) contrairement à la smectite qui est faiblement drainée (hydrolyse faible, elle conserve ses cations solubles). On remarque que la smectite est souvent plus abondante dans les dépôts lacustres, néanmoins, l'évolution minéralogique en argile ne semble pas varier uniquement en corrélation avec les environnements de dépôts. L'évolution de la teneur en minéraux argileux dépend aussi des conditions d'hydrolyse sur le continent et donc des conditions climatiques.

L'origine détritrique du contenu en minéraux argileux peut également être discutée. Une augmentation de la température due à l'enfouissement pourra entraîner des changements dans la composition minéralogique tout le long d'une coupe. Si le changement de la composition minéralogique des argiles est dû à l'enfouissement, on s'attend à voir une variation verticale continue des pourcentages de minéraux tout au long du log (Kisch, 1979; Chamley et al., 1997). Un tel changement sera dû à la transformation de la smectite en Interstratifiés puis en illite et ceci quand les conditions de diagenèse et l'enfouissement le permettent (<90°C) (McKinley et al. 1999). De même, la kaolinite peut aussi se transformer en illite si les conditions de diagenèse et d'enfouissement le permettent (>70°C) (Bjørlykke and Aagaard, 1992). Cette variation verticale et continue n'est pas observée dans tous les logs stratigraphiques levés et pour lesquels des analyses d'argiles ont été réalisées. Il n'existe donc pas de continuité dans la variation minéralogique des argiles tout au long du log, ce qui semble conforter l'hypothèse de l'origine détritique de l'enregistrement mesuré. De plus, l'absence des interstratifiés dans la composition minéralogique des argiles tout au long des coupes de la vallée de l'Orbieu, Labastide-en-Val/Clermont-sur-Lauquet et Caunette-sur-

Lauquet/Pomas bien que des précurseurs smectitiques existent, soutient également cette hypothèse. La coupe de Villerouge/Talairan montre la présence d'interstratifiés dans très peu d'échantillons repartis de manière aléatoire. Toutes ces raisons nous incitent à écarter la possibilité de changement de composition des argiles liée à la diagenèse. Dans ce cas, la variation de la composition minéralogique des argiles est due aux changements des conditions climatiques et au contrôle des environnements de dépôts.

D'après ces résultats, les minéraux dominants sont donc l'illite et la smectite et pour remonter aux conditions d'altération, il est essentiel de comprendre dans quels contextes se forment ces minéraux. L'illite, par exemple, n'est pas spécifique à un climat ou un environnement de dépôt précis, elle peut se former dans plusieurs contextes et donc n'est pas primordiale dans la détermination des conditions d'altération de la source. Quant à la smectite, elle se forme dans un climat semi-aride et de fortes conditions d'évaporation dans les environnements de dépôt fluviatiles et lacustres (Chamley, 2013). Dans un climat chaud et humide, la smectite est surtout préservée dans les environnements de dépôts marins, lacustres et les plaines d'inondations, dans des endroits où elle ne peut pas être lessivée et ne risque pas de perdre des cations (Chamley, 2013). La kaolinite, se forme essentiellement en climat chaud et humide, plus particulièrement dans les environnements de dépôt fluviatile type rivière en tresse et cône alluvial.

Les résultats obtenus permettent de montrer que la smectite est abondante essentiellement dans les environnements de dépôts lacustres et de plaine alluviales. Ceci montre (i) qu'il existe un contrôle des environnements de dépôt sur la composition minéralogique des argiles, et (ii) que l'abondance de la smectite dans les dépôts lacustres et de plaine alluviale pour le log de Villerouge-Talairan (Yprésien supérieur) confirme que le climat lors du dépôt de ces sédiments était chaud et humide. Pour le log de Labastide-en-Val/Clermont-sur-Lauquet, la smectite est associée à des dépôts fluviatiles et lacustres (plus importante dans les dépôts lacustres) et traduit donc une formation dans un climat assez aride. C'est le cas aussi pour le log de Magrie jusqu'au pic de Kaolinite. Ce pic peut être associé à un pulse terrigène et la grande proportion de kaolinite montre une formation dans un climat chaud et humide.

Ce travail nécessiterait d'être couplé à une étude plus approfondie (isotopes du carbone et de l'oxygène par exemple) pour en tirer plus d'informations sur les conditions d'altération de la source.

Informations supplémentaires

Tableau et planches de faciès

La caractérisation des faciès continentaux fluviatiles est réalisée suivant Miall (1996). Les photos des faciès deltaïques F15 et F22 sont disponibles dans (Prieur, 2019) .

Faciès	Lithologie	Granulométrie		Texture	Grano-classement	Structure	Bioturbation	Fossiles	Processus	Epaisseur des bancs
		component	matrix						écoulement gravitaire : Cohésif/ hyperconcentré ou écoulement de courant	
F1	Conglomérats à blocs	Blocs	Sable grossier	Clastes portés	X	X	X	X	écoulement gravitaire	Métrique à pluri-métrique
F2	Conglomérat à blocs et galets	Blocs à galets	Sable grossier	Clastes portés	X	Obliques 2D	X	X	écoulement de courant tractif	Métrique à pluri-métrique
F3	Conglomérats à galets et gravier	Galets	Sable grossier	Matrice porté	X	Surface érosive	X	X	écoulement gravitaire hyper-concentré Debris flow	Pluri-métrique
F4	Conglomérat à blocs et galets	Blocs à galets	Silt - argile	Matrice porté	Grano-classement faible à nul	Surface faiblement érosive Géométries lenticulaires	X	X	écoulement gravitaire cohésif Debris flow	Métrique à pluri-métrique
F5	Conglomérat à galets	Galets	Sable grossier		Grano-classement faible Mal triés	Lamines planes	X	X	écoulement de courant superficiel	Métrique à pluri-métrique
F6	Conglomérat à galets	Galets	Sable grossier	Matrice portée à claste porté	X	Surface érosive	X	X	écoulement gravitaire hyper-concentré Debris flow	Métrique à pluri-métrique
F7	Conglomérat à galets	Galets	Sable grossier	Clastes portés	X	Surface érosive Obliques 2D	X	X	écoulement de courant tractif	Métrique à pluri-métrique
F8	Conglomérat à gravier	Graviers	Sable grossier	Matrice porté	X	X	X	X	écoulement gravitaire hyper-concentré Debris flow	Métrique à pluri-métrique
F9	Conglomérat à gravier	Graviers	Sable grossier	Clastes portés	X	Oblique 2D	X	X	écoulement de courant	Centimétrique à métrique
F10	Grès moyen à grossier et galet	X	Sable moyen à grossier	Clastes portés	Grano-classement normal à faible	Surface érosive Géométries lenticulaires litage entrecroisé	X	X	écoulement de courant	Centimétrique à métrique
F11	Grès grossier à gravier	X	Sable grossier		Grano-classement faible Mal triés	Surface érosive Géométries lenticulaires Dunes 3D	X	Oncolithes rare	écoulement de courant tractif	Métrique à pluri-métrique
F12	Grès moyen à graviers et galets	X	Sable moyen à grossier		Grano-classement faible Mal triés	Lamines planes	X	X	écoulement de courant superficiel	Métrique à pluri-métrique
F13	Grès grossier à gravier	Graviers	Sable grossier	Clastes portés	X	Grandes dunes 2D	X	X	écoulement de courant tractif	Pluri-métrique
F14	Grès grossier à gravier	Galets	Sable fin à grossier	Matrice portés mal triés	Grano-classement normal à nul	Surface faiblement érosive Clinoformes pluri-métriques	X	Huîtres rare	écoulement gravitaire cohésif Debris flow	Pluri-métrique
F15	Grès moyen à graviers	X	Sable fin à grossier	Clastes portés	Grano-classement normal à nul mal triés	Surface faiblement érosive Dunes 3D	Traces de racines	Nummulites	écoulement de courant tractif	Métrique à pluri-métrique
F16	Grès fin à grossier	X	Sable fin à grossier		Mal triés	Dunes 3D	X	X	écoulement de courant tractif	Métrique
F17	Silt à sable moyen gravier rare	X	Silt à sable moyen		Mal triés présence rare de gravier	X	Bioturbation	X	Décantation suspension	Métrique
F18	Calcaire	X			X	nodules	Traces de racines	X	Pédogenèse; Sol - précipitation chimique (calcrète)	Métrique à pluri-métrique

Tableau de faciès (1/2)

Faciès	Lithologie	Granulométrie		Texture	Grano-classement	Structure	Bioturbation	Fossiles	Processus	Epaisseur des bancs
		component	matrix						écoulement gravitaire : Cohésif/ hyperconcentré ou écoulement de courant	
F19	Calcaire	X			X	marmorisation	X	X	Décantation	Métrique à pluri-métrique
F20	Silt à sable moyen	X	Silt à sable moyen	Matrice porté	Bien triés gravier	Géométrie plane changement progressif de granulométrie	Traces de racines	X	Décantation suspension	Métrique
F21	Alternance d'argile et de silt, grès fin à moyen	X	Silt à sable moyen		Bien triés	X	Traces de racines Bioturbation	Oncolithes rare	Décantation suspension	Pluri-métrique
F22	Argile à grès moyen et gravier	X	Silt à sable moyen		Mal triés présence rare de gravier	X	Traces de racines	gastéropodes rare	Décantation suspension	Pluri-métrique

Tableau de faciès (2/2)


F1


F2

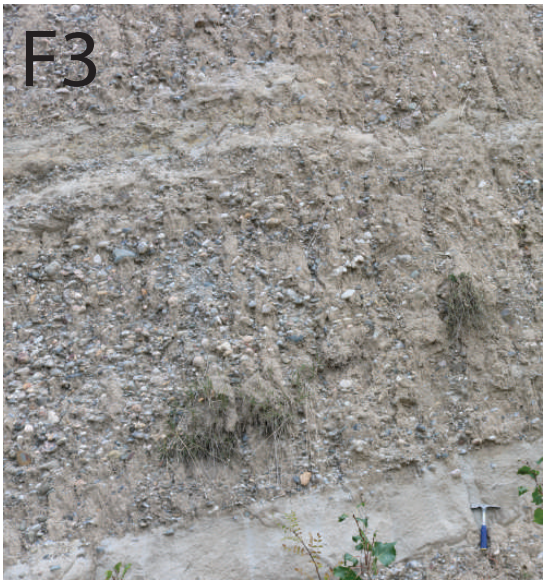
F3


F4


F5


F6


F7


F8


F9


F10


F11


F12


F13

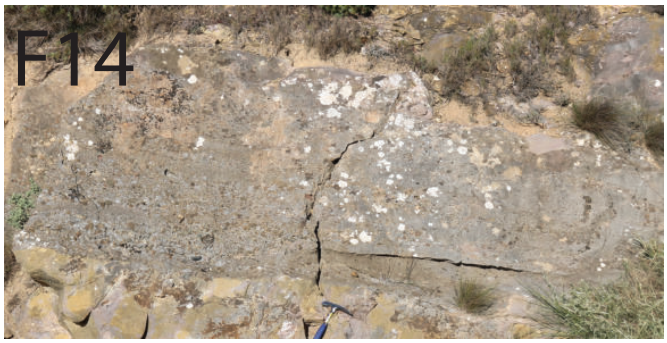
F14


F16


F17


F18

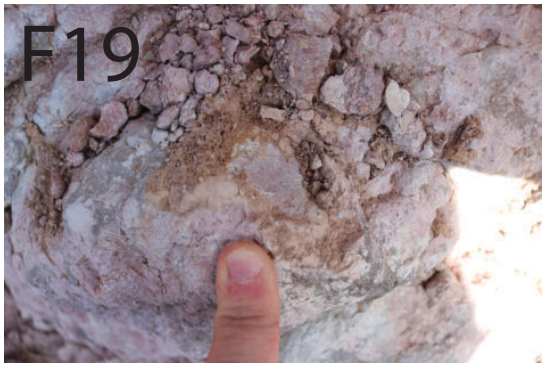
F19

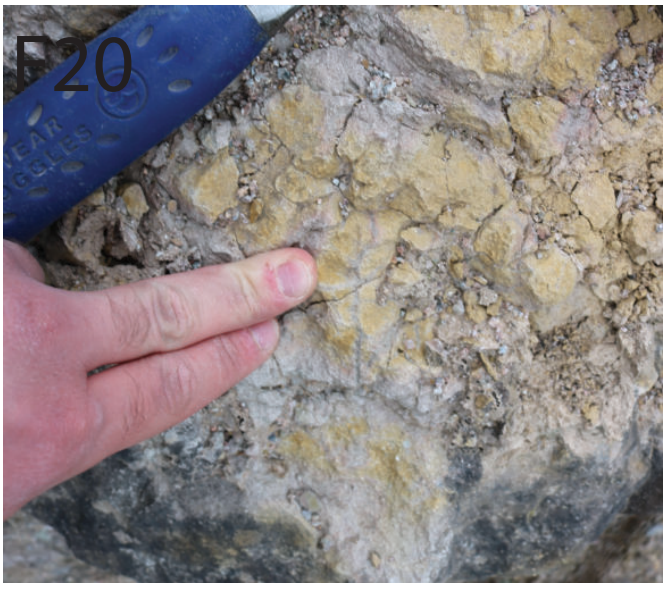
F20


F21

Habillage en facies des logs

Habillage en faciès des logs Villerouge/Talairan, la vallée de l'Orbieu, Labastide-en-Val/Clermont-sur-Lauquet et Caunette-en-Val/Pomas

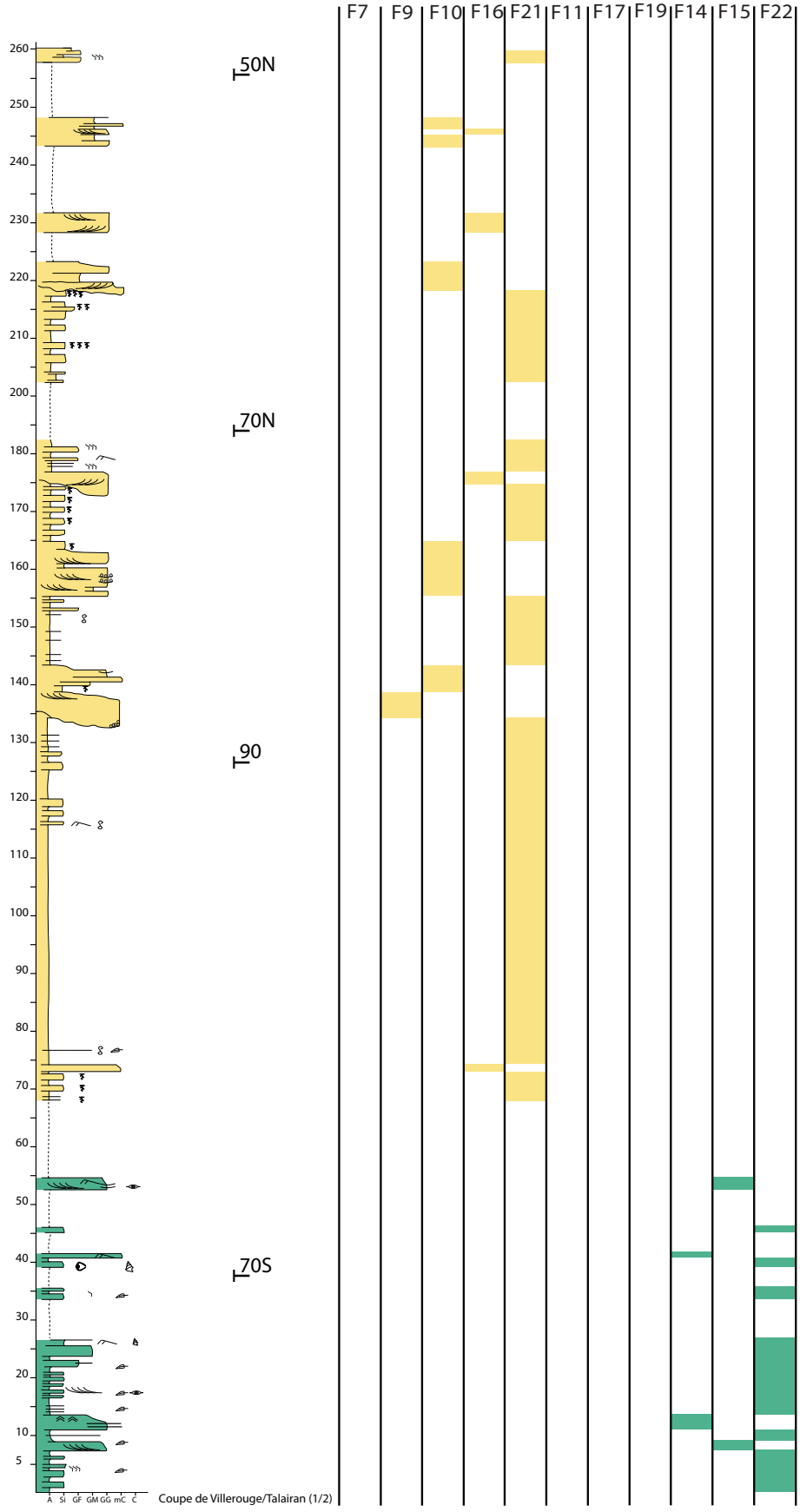

Coupe de Villerouge/Talairan (1/2)

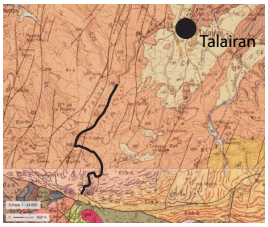
Talairan

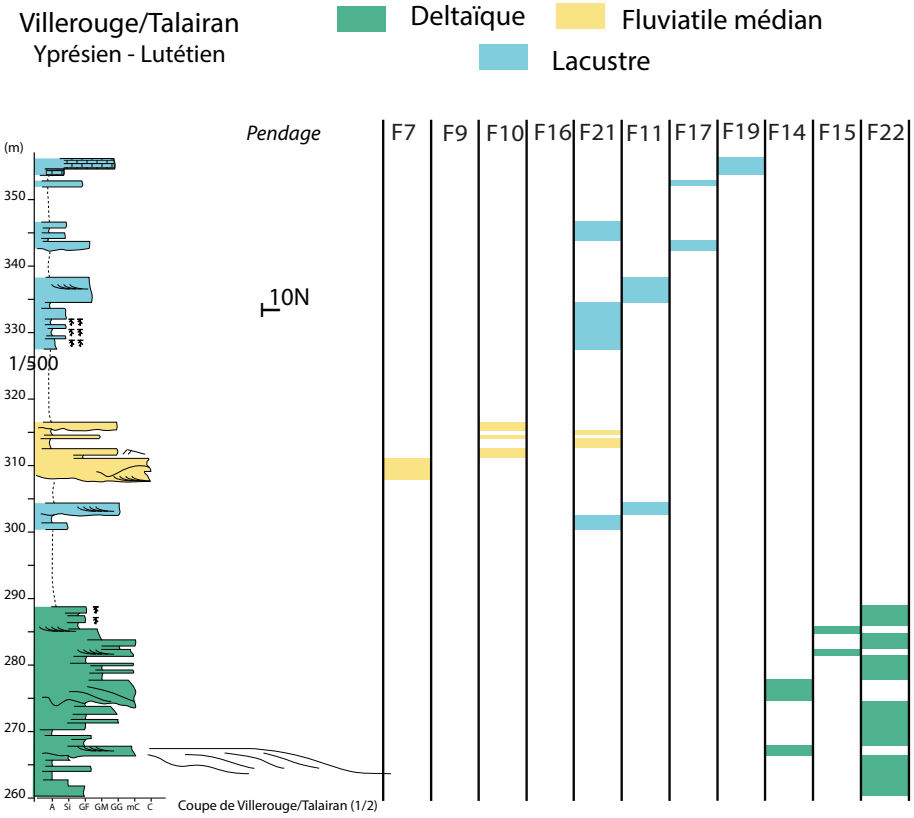
Villerouge/Talairan
Yprésien - Lutétien
Deltaïque
Fluviatile médian
Lacustre
Pendage
10N
1/500
(m)
350
340
330
320
310
300
290
280
270
260
A SI GF GM GG mC C
F7
F9
F10
F16
F21
F11
F17
F19
F14
F15
F22
Coupe de Villerouge/Talairan (1/2)

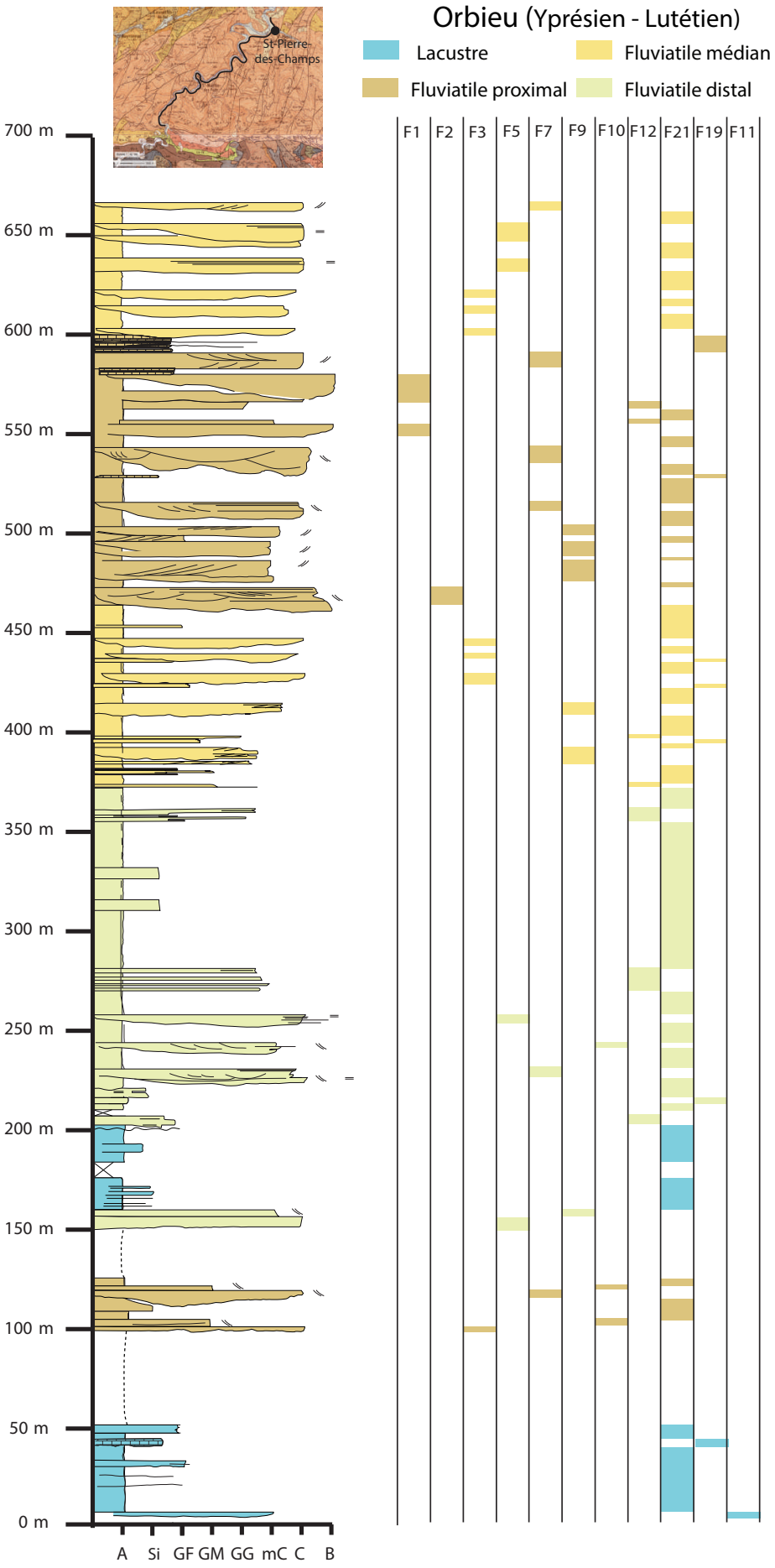
Orbieu (Yprésien - Lutétien)
Lacustre
Fluviatile médian
Fluviatile proximal
Fluviatile distal
St-Pierre-des-Champs
700 m
650 m
600 m
550 m
500 m
450 m
400 m
350 m
300 m
250 m
200 m
150 m
100 m
50 m
0 m
A Si GF GM GG mC C B
F1 F2 F3 F5 F7 F9 F10 F12 F21 F19 F11

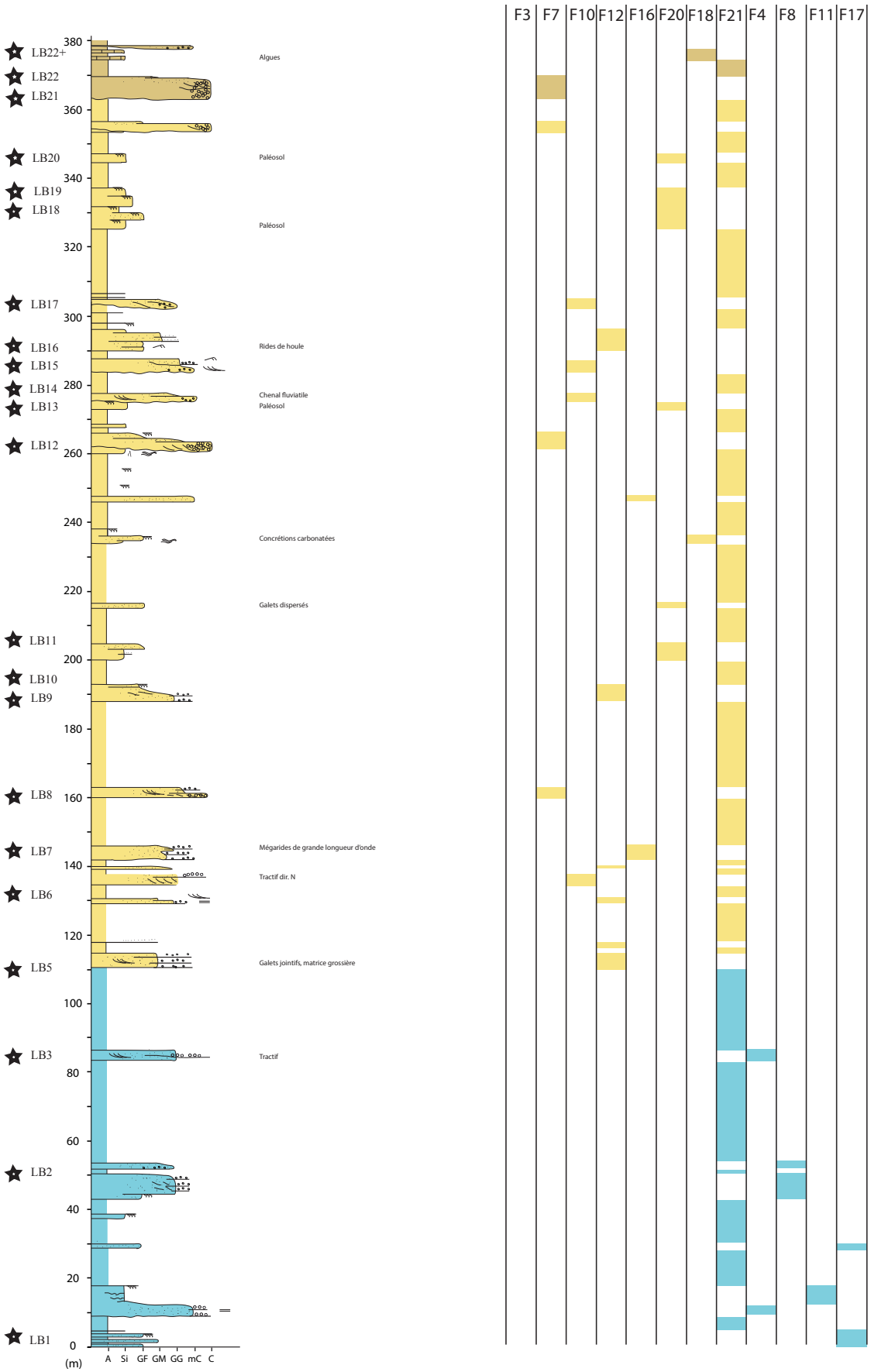

Labastide-en-Val (1/2)

1/1000

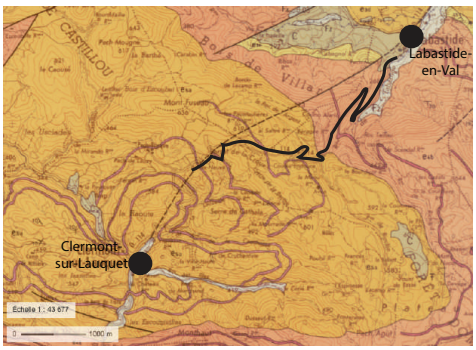

Fluviatile proximal

Fluviatile médian

Lacustre

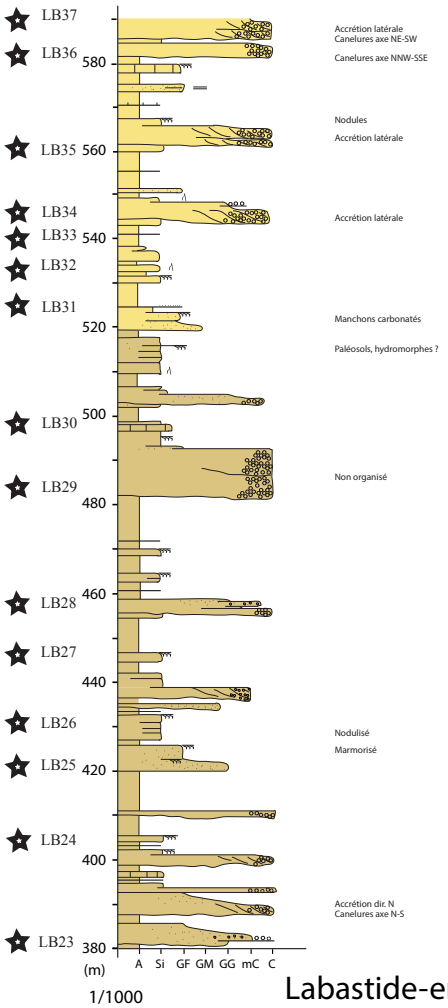

1/1000

Labastide-en-Val (2/2)

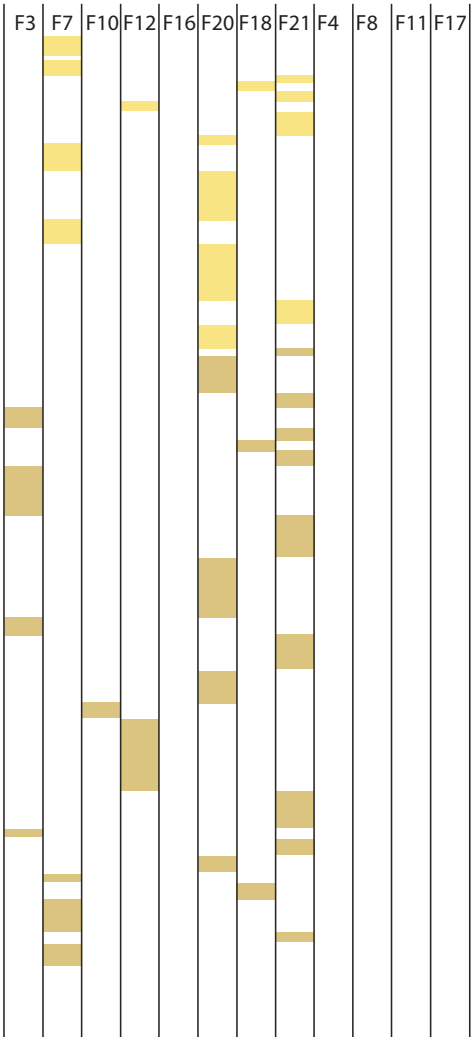

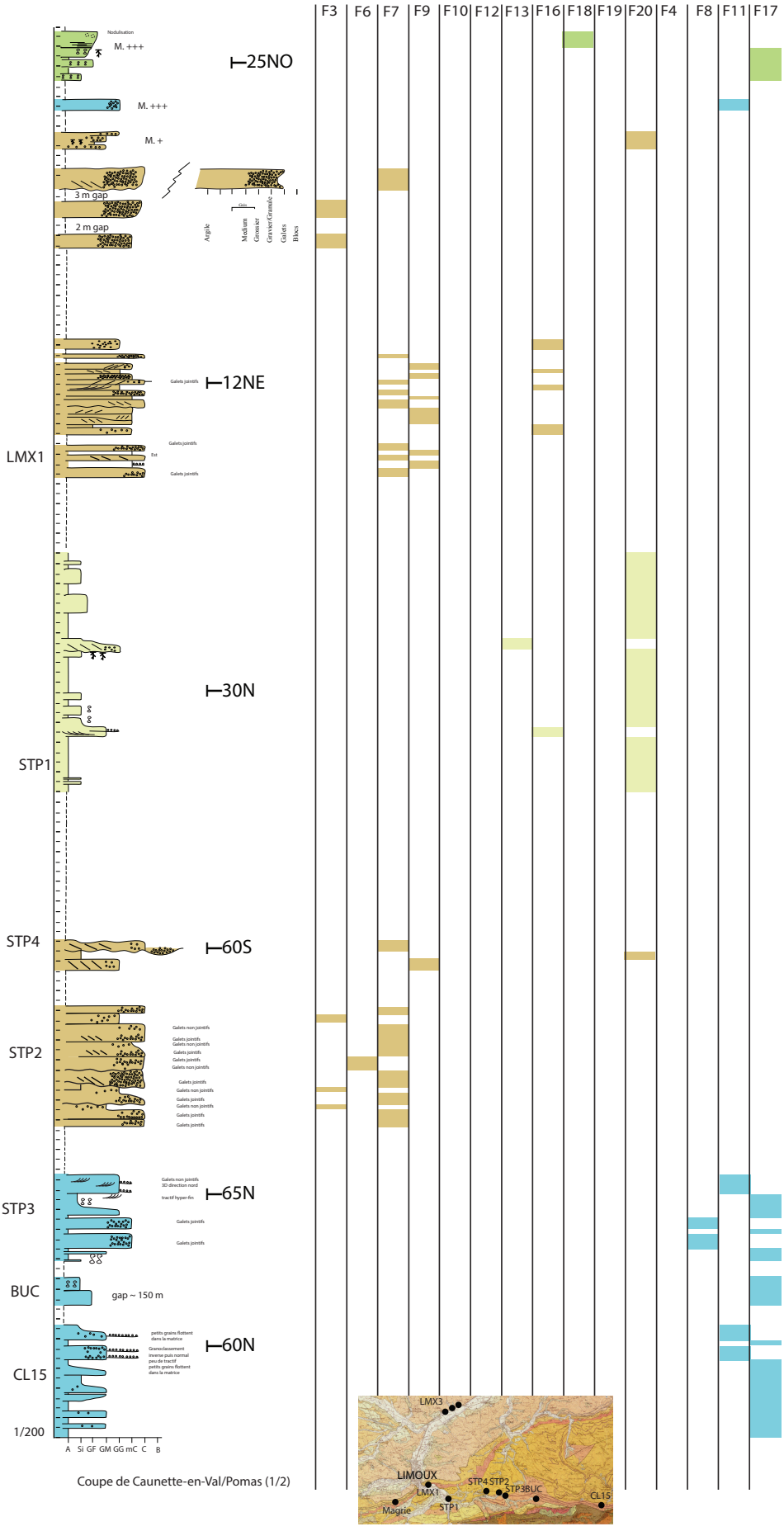

Coupe de Caunette-en-Val/Pomas (1/2)

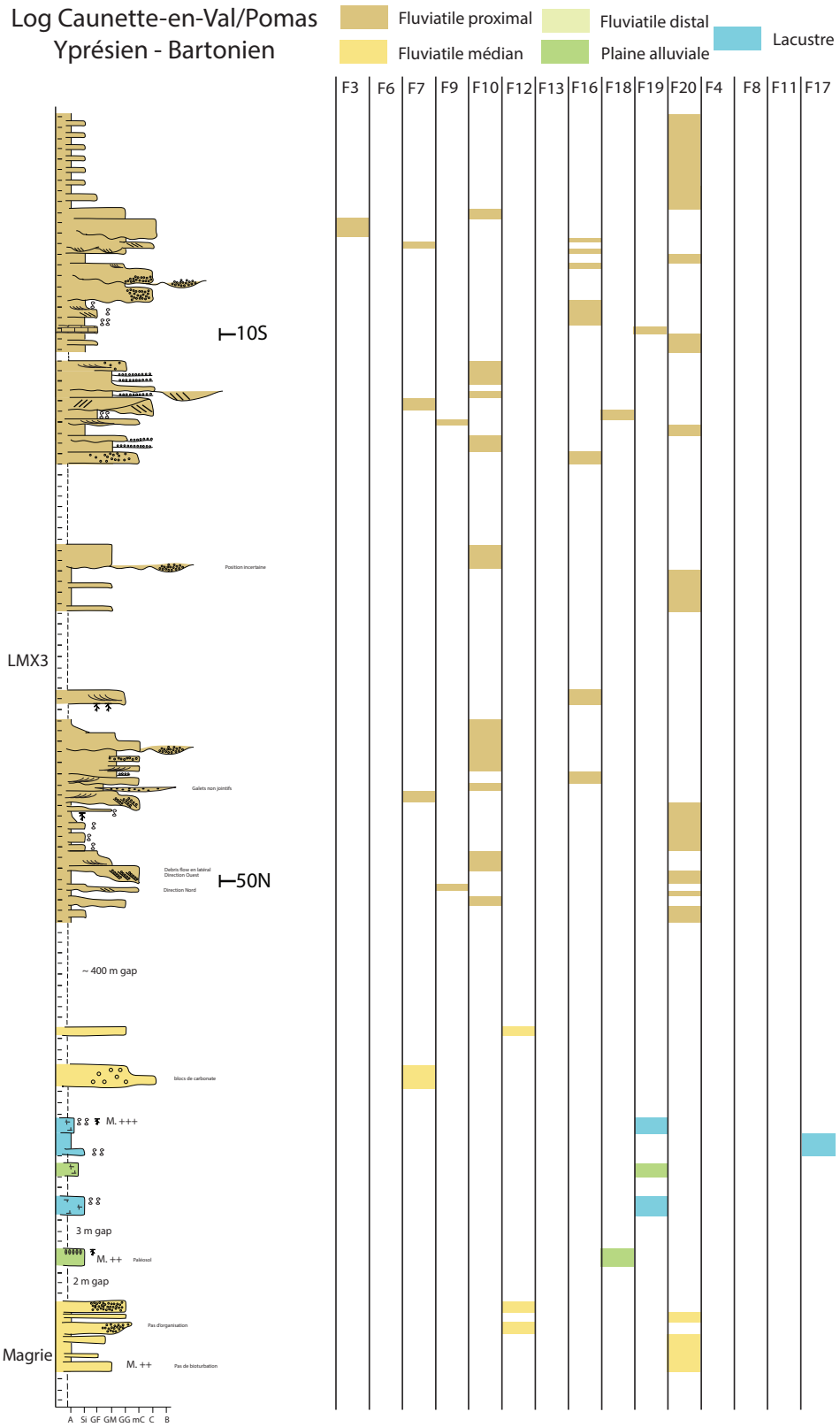

Coupe de Caunette-en-Val/Pomas (2/2)

Tableaux d'association de facies des logs

Association de faciès pour les logs Villerouge/Talairan, la vallée de l'Orbieu, Labastide-en-Val/Clermont-sur-Lauquet et Caunette-en-Val/Pomas

VILLEROUGE/TALAIRAN

SYMBOLE	LITHOLOGIE	GEOMETRIE	INTERPRETATION
A1	F7, F9, F10, F16 & F21	Plurimétrique	Fluviatile médian
A2	F17, F19& F21	Métrique à plurimétrique	Lacustre
A3	F11, F14, F15& F22	Métrique à plurimétrique	Deltaïque

LA VALLEE DE L'ORBIEU

SYMBOLE	LITHOLOGIE	GEOMETRIE	INTERPRETATION
A1	F1, F2, F7, F9, F10, F12, F19 & F21	Plurimetrique	Fluviatile proximal
A2	F3, F5, F7, F9, F12 & F21	Plurimetrique	Fluviatile médian
A3	F5, F7, F10, F12, F19 & F21	Plurimetrique	Fluviatile distal
A4	F11, F19& F21	Metrique à plurimetrique	Lacustre

LABASTIDE-EN-VAL/CLERMONT-SUR-LAUQUET

SYMBOLE	LITHOLOGIE	GEOMETRIE	INTERPRETATION
A1	F3, F7, F10, F12, F16, F18, F20 & F21	Plurimetrique	Fluviatile proximal
A2	F7, F10, F12, F16, F18, F20 & F21	Plurimetrique	Fluviatile médian
A3	F4, F8, F11, F17, & F21	Metrique à plurimetrique	Lacustre

CAUNETTE-SUR-LAUQUET/POMAS

SYMBOLE	LITHOLOGIE	GEOMETRIE	INTERPRETATION
A1	F3, F6, F7, F9, F10, F16, F18, F19 & F20	Plurimetrique	Fluviatile proximal
A2	F7, F12 & F20	Metrique à plurimetrique	Fluviatile médian
A3	F13, F16 & F20	Metrique à plurimetrique	Fluviatile distal
A4	F17, F18 & F19	Metrique à plurimetrique	Plaine alluviale
A5	F4, F8, F11, F17, F18& F19	Metrique à plurimetrique	Lacustre

Chapter 4: Thermal record in the Corbières region

Les sédiments de l'unité 2 de la série de Palassou (Bartonien) ont fait l'objet d'une étude en thermochronologie basse température dans ce chapitre. Des datations de traces de fission (AFT) et (U-Th-Sm)/He sur apatites (AHe) ont été réalisées sur des clastes de granite dans le but de mieux comprendre le développement de la chaîne et caractériser les phases d'érosion enregistrées dans le bassin. Les données de thermochronologie basse température sur la chaîne pyrénéenne ont montré que la phase majeure du développement des Pyrénées (Éocène) est accompagnée par des taux d'érosion très importants et un transfert de sédiments vers les bassins d'avant-pays (Yelland, 1991; Fitzgerald et al., 1999; Sinclair et al., 2005; Gibson et al., 2007; Metcalf et al., 2009; Vacherat et al., 2016). De plus, l'étude de la morphologie de la chaîne par Babault et al. (2005) et Bosch et al. (2016) indique la présence de surfaces de très faible relief localisées en altitude. Le mode de formation de ces surfaces est lié à l'aggradation des sédiments au niveau des piémonts au cours de la phase finale de l'orogenèse. Cette aggradation a été caractérisée au sud et est suivie par une phase d'érosion Miocène supérieur – Pliocéne selon Fillon et al. (2013). Elle n'a jamais été étudiée au nord d'où l'intérêt de cette étude. Les résultats de modélisation thermique présentés dans ce chapitre constituent une première preuve d'une aggradation des sédiments au nord, comparable à celle au sud, et suivie aussi d'une phase d'érosion avec un « timing » différent. Ces résultats ont permis de discuter l'hypothèse de formation des surfaces de faible relief à haute altitude et de comparer l'évolution des deux bassins d'avant-pays sud et nord au cours de l'Éocène.

Des détails sur la lithologie des échantillons datés, ainsi que les données d'AFT et AHe obtenus, sont présents dans la partie « supplementary information » de ce chapitre.

Thermal record of the building of an orogen in the retro-foreland basin: insight from detrital thermochronology in the north Pyrenean basin (France)

Al Reda Stéphane[1*], Barbarand Jocelyn[1], Gautheron Cécile[1], Lasseur Eric[2], Loget Nicolas[3], Pinna-Jamme Rosella[1], Briais Justine[2]

[1] Université Paris-Saclay, CNRS, GEOPS, 91405, Orsay, France
[2] Bureau de Recherches Géologiques et Minières – BRGM – Orléans
[3] Sorbonne Université, CNRS-INSU, Institut des Sciences de la Terre de Paris, ISTeP UMR 7193, F-75005 Paris, France

**Corresponding author : stephane.alreda@gmail.com*

Acknowledgement

This work is funded by Total and Brgm (French geological survey) within the framework of the Source to Sink project.

Abstract

An understanding of the evolution of foreland basins improves our knowledge of how mountain belts have grown and helps us to decipher events which are not usually preserved in the orogen. The infilling of the north Pyrenean retro-foreland basin (the Aquitaine basin, France) during the main exhumation of the Pyrenees and its corresponding thermal history have not been fully investigated. We applied apatite fission track (AFT) and (U-Th-Sm)/He (AHe) methods coupled with thermal inversions on both the detrital Eocene syn-orogenic Palassou conglomerates of the eastern part of the Aquitaine basin (47 to 33 Ma) and in-situ massifs of the North Pyrenean Zone and Axial Zone of the Pyrenees. AFT ages range from 27±2 to 43±4 Ma, and AHe ages from 13±1 Ma to 76±5 Ma. AFT ages are similar to deposition ages, whereas AHe ages are older and younger than deposition ages and reflect a thermal event. A detailed analysis of the obtained ages and thermal histories shows that ages reflect (1) slow exhumation from 70 to 55 Ma revealed by a long stay in the Partial Retention Zone, (2) a Paleocene-Eocene cooling in the belt, (3) a post-depositional episode of moderate heating of the sediments in the basin represented by young AHe ages compared to deposition ages, and (4) a final exhumation of the basin deposits. These results show a common history with the south Pyrenean foreland basin characterized by high piedmont aggradation during the syn to late orogenic phase possibly connected with well-known high elevation low relief surfaces in the core of the Pyrenees and followed by a Miocene exhumation event that is already proposed on the southern flank. However, the timing of the aggradation and exhumation events is different between the north and the south. Erosion occurred during the early to mid-Miocene on the northern piedmont and during the late Miocene- early Pliocene on the southern piedmont.

Keywords: Corbières region, low temperature thermochronology, syn-orogenic deposits, Pyrenees, retro-foreland.

Introduction

Alluvial piedmonts are a major component of the source to sink system in compressive settings along which various amounts of trapping of the coarsest fraction take place. They represent an important archive of the dynamics of mountain belt erosion and bypass in the source to sink system (Romans et al., 2016). Piedmont sedimentation and preservation result from a balance between mountain belt exhumation, horizontal shortening, tectonic style, catchment evolution and a complex interplay between tectonics, climate and geomorphological evolution in the orogen and its foreland (Sinclair and Allen, 1992; Sinclair and Naylor, 2012; Allen et al., 2013).

Analysis of the piedmont sediments by means of sources tracing and sedimentology is currently performed in order to understand the catchment evolution, the source characterization (Gehrels et al. 2011; Thomas 2011; Saylor et al. 2013; Roigé et al. 2016; Roigé et al. 2017; Roigé et al. 2019) and the dynamics of exhumation in the belt. However, preservation of these dynamic deposits in the fossil record, is by its very nature highly relictual. In the analysis of these relict deposits, detrital thermochronology is a first order method to question the interplay between exhumation dynamics and sedimentation through the analysis of lag times (Whitchurch et al., 2011; Odlum et al., 2019). It is also used to characterize the thermal history of potentially overburdened (or overthrusted) levels and secondary eroded levels in the foreland (Fillon et al., 2013; Schwartz et al., 2017). Low temperature thermochronology (LTT) methods, such as apatite fission tracks (AFT) and (U-Th-Sm)/He (AHe), provide important elements of proof when interpreting complex geological histories and when identifying the main phases of development of mountain belts throughout the erosion phase of the first 1-4 km of depth (Ault et al., 2019). Detrital LTT applications, in particular, on syn-orogenic sediments in foreland basins give us insight into how erosion occurs from the source to the basin (Willingshofer et al., 2001; Whitchurch et al., 2011; Filleaudeau et al., 2012; Thomson et al., 2017; Odlum et al., 2019).

Several stages describe the building of the Pyrenees (Mouthereau et al., 2014; Grool et al., 2018) starting with (a) the early orogenic stage that occurred during the Late Cretaceous (including collisional suturing and onset of tectonic inversion), (b) the southward propagation of exhumation and early crustal stacking during the Paleocene, (c) the main orogenic phase in the Eocene-early Oligocene time characterized by a large nappe stacks, (d) the late orogenic stage in the late Oligocene-Aquitanian, and (e) the post-orogenic stage starting from ~20 Ma. The Pyrenees are characterized by high erosion rates during the main orogenic phase with the transfer of large amounts of sediment to the southern and northern foreland basins as shown by low temperature thermochronology data acquired primarily in the core of the belt (Yelland, 1991; Fitzgerald et al., 1999; Sinclair et al., 2005; Gibson et al., 2007; Metcalf et al., 2009; Bosch et al. 2016; Labaume et al. 2016a; Labaume et al.

2016b; Vacherat et al., 2016). The morphology of the chain is also characterized by the occurrence of high elevation low relief surfaces (HELRS) on both flanks of the inner belt. In the southern flank, these HELRS were connected to the local base level induced by the piedmont aggradation (Babault et al., 2005; Bosch et al., 2016). The delivering of high amount of sediments to the basins during the main orogenic phase and the aggradation of sediments on the southern piedmont are two contradictory elements and constitute a source of debate about the late to post-orogenic evolution of the Pyrenees. Information may be obtained for the nearby sedimentary basins and most of the work has been carried out in the south Pyrenean foreland basin. The results show the deposition of a large thickness of syn-orogenic sediments (Eocene – Oligocene) in the basin at the same time as the main phase of exhumation of the belt (Coney et al., 1996; Beamud et al., 2003, 2011; Michael et al., 2014; Labaume et al., 2016b) and this lead to the piedmont aggradation during the late orogenic phase. In addition, it has been suggested that such aggradation of sediments in the piedmont is mainly due to endorheism of the south Pyrenean foreland basin (Coney et al., 1996; Costa et al., 2012; Filleaudeau et al., 2012). This was followed by a late-Miocene – early Pliocene erosion phase activated principally by the excavation of new valleys and the connection of the south Pyrenean foreland basin drainage system to the Mediterranean sea (Garcia-Castellanos et al., 2003; Fillon et al., 2013). The origin of the high elevation low relief surfaces has not been properly investigated and demonstrated in the north Pyrenean foreland basin.

This study focuses on the Pyrenean retro-foreland basin, in particular, the Eocene syn-orogenic sediments preserved in its eastern part. As retro-foreland basins record the majority of the orogenic history of the belt (Naylor & Sinclair, 2008; Sinclair & Naylor, 2012), the north Pyrenean foreland basin recorded the full geological history associated to the Pyrenean orogeny (Angrand et al., 2018; Grool et al., 2018). Sediments deposited in the basin are key to better understand the development of the Pyrenean orogenic prism, determine the timing of basin infilling and assessing the extent of the orogenic phase of the Pyrenees. The northern flank of the Pyrenees accumulated a thick syn-orogenic conglomeratic series (middle Ypresian – Oligocene) known as “Série de Palassou” in its eastern part. However, the sedimentary infilling of the basin, its exhumation history and the burial of the foreland basin have only rarely been studied (Christophoul et al., 2003; Mouthereau et al., 2014; Ford et al., 2016; Rougier et al., 2016; Grool et al., 2018). In this paper we present new AFT and AHe data on granite boulders from the late Lutetian-Bartonian continental series cropping out in the Corbières region (eastern part of the northern foreland basin) and from Saint-Arnac, Millas and Foix massifs in the North Pyrenean Zone (NPZ) and Axial Zone to complete the data set already acquired in the NPZ and Axial Zone massifs (Yelland, 1991; Gunnell et al., 2009; Vacherat et al., 2016 and Ternois et al., 2019). The AFT and AHe thermochronometers cover temperature ranges of 60-110±10°C and 40-120°C respectively (Ault et al., 2019). Modelling of AHe and AFT data using QTQt (Gallagher et al.,

2009; Gallagher, 2012) provides a suitable method for demonstrating the thermal history of the Corbières region and gives us information about the phases of cooling in the orogen during the early and main convergence phases. Understanding the thermal history of the northern foreland is important to question the formation of HELRS in the Pyrenees. In the southern foreland, current interpretations link their genesis to piedmont aggradation due to the interplay of high sediment flux and endoreic conditions of the Ebro basin. While HELRS are documented in northern Pyrenees (Bosch et al., 2016b), no aggradation is evidenced until now there and no endorheic conditions are proposed in the paleogeographic reconstructions of the Aquitaine basin.

Geological setting

The Pyrenees constitute an asymmetrical double-wedged range resulting from the convergence between the Iberian and European plates from the Late Cretaceous to the early Miocene (Roure et al., 1989; Munoz, 1992; Vergés et al., 1995; Mouthereau et al., 2014; Macchiavelli et al., 2017; Teixell et al., 2018). The orogen is flanked by two foreland basins, a southern pro-foreland basin (the Ebro basin) and a northern retro-foreland basin (the Aquitaine basin). The Pyrenean domain is divided into five areas from south to north (Figure 4.1): the Ebro Basin (EB), the South Pyrenean Zone (SPZ), the Axial Zone (AZ), the North Pyrenean Zone (NPZ) and the Aquitaine retro-foreland Basin (AB). In the Aquitaine basin a thrusted part, the Sub-Pyrenean Zone, located north of the North Pyrenean Frontal Thrust (NPFT) is individualized (Figure 4.1). The NPZ, located between the North Pyrenean Fault (NPF) and the NPFT, represents a severely shortened part of the crust which was stretched during Lower Cretaceous rifting (e.g., Lagabrielle et al., 2010). This rifting event was associated with a HT-LP metamorphism which affected the Mesozoic cover of the NPZ and is estimated to have occurred between the Albian (110 Ma) and Santonian (85 Ma) periods (Albarède & Michard-Vitrac, 1978; Montigny et al., 1986; Schärer et al., 1999; Clerc & Lagabrielle, 2014; Clerc et al. 2015). The Axial Zone consists of Precambrian to Carboniferous rocks affected by metamorphism during the Variscan orogeny and intruded by crustally-derived granitic bodies (Zwart, 1962; Zwart & De Sitter, 1979; Gleizes et al., 1998; Denèle et al., 2014; Olivier et al., 2016). The North Pyrenean Thrust system corresponds to an imbricate system of north-directed thrust faults including Hercynian basement and Mesozoic-early Cenozoic cover rocks (Souquet, 1986; Deramond et al., 1990; Ford et al., 2016). North Pyrenean massif basement rocks are involved in this thrust system as inversion or short-cuts of Mesozoic extensional faults (Baby et al., 1988; Espurt et al., 2019).

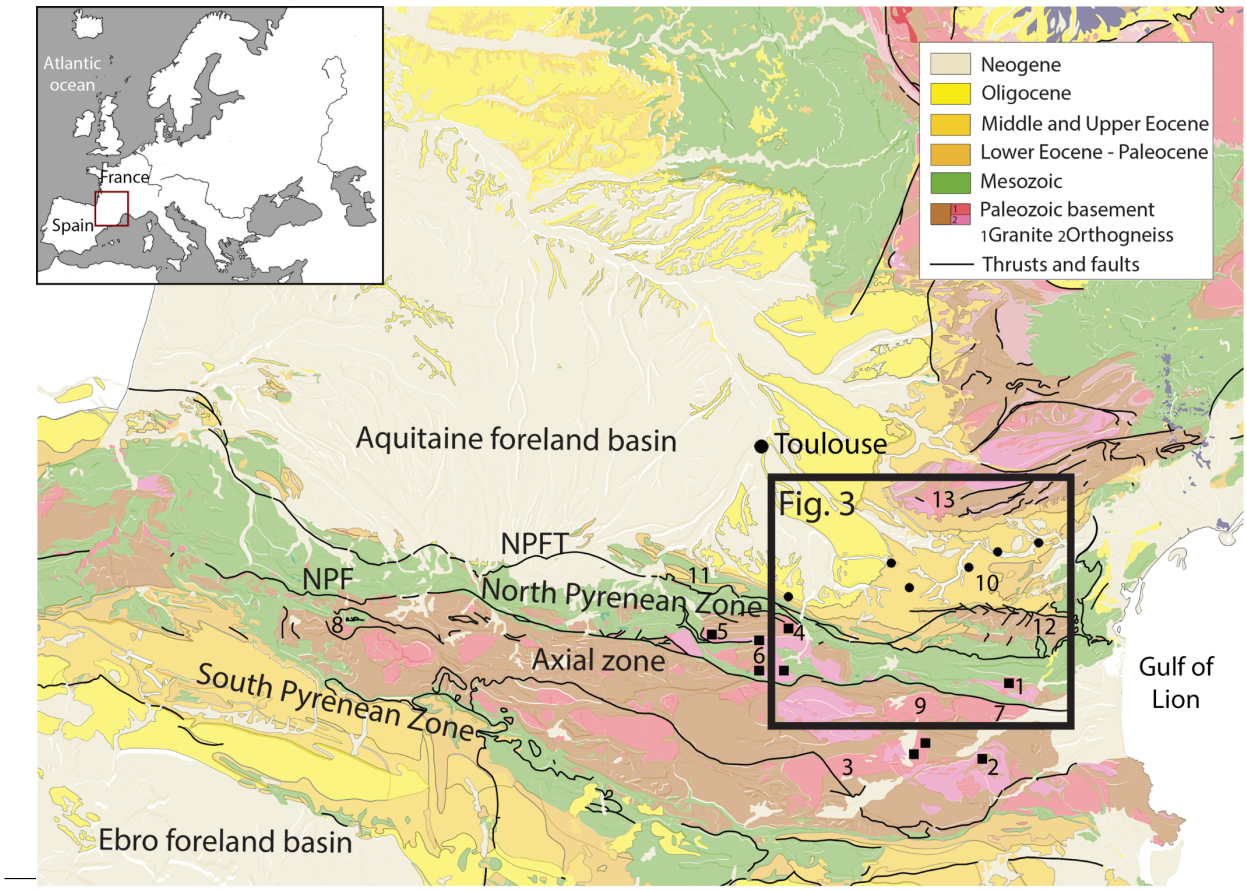

Figure 4.1: Geological map of the Pyrenees showing five structural domains from the south to the North: the Ebro foreland basin, the South Pyrenean Zone, the Axial Zone, the North Pyrenean Zone and the Aquitaine basin. Numbers refer to massifs and valleys mentioned in this study: 1. Agly massif, 2. Canigou massif, 3. Andorra Mont Louis massif, 4. Foix massif, 5. Lacourt massif, 6. Trois Seigneurs massif, 7. Millas massif, 8. Eaux Chaudes massif, 9. Quérigut massif, 10. Corbières region, 11. Sub-Pyrenean Zone, 12. Mouthoumet massif, 13. Montagne Noire. Black dots represent the location of the studied samples and squares represent the location of samples used for Temperature-time paths in figure 4.2. (modified from the 1/1 000 000 geologic map of France, Bonnefoy et al. 1996)

Convergence between the Iberian and European plates started during the Santonian period (~83 Ma) (Roest & Srivastava, 1991; Olivet, 1996) and is first expressed by the closure of the hyper-extended rifted domain (Mouthereau et al., 2014). An early collision stage started in the late Campanian period (~71 Ma) characterized by thick-skin tectonics, inversion of Early Cretaceous basins, and the onset of subsidence in foreland basins (Mouthereau et al., 2014; Ford et al., 2016; Rougier et al., 2016; Grool et al., 2018). The first crustal stacks and exhumation in the Axial Zone occurred during the middle Eocene-early Oligocene interval (47-34 Ma) (Munoz, 1992; Fitzgerald et al., 1999) and corresponds to a strong subsidence stage in foreland basins (Christophoul et al., 2003; Mouthereau et al., 2014; Rougier et al., 2016).

The Axial Zone and the North Pyrenean Zone contain numerous igneous and high-grade metamorphic crystalline basement rocks that yield minerals suitable for thermochronological analysis. Time-temperature paths produced by low temperature thermochronology demonstrate that

the north-eastern part of the NPZ exhumed first (Agly and Trois Seigneurs massifs ~ 60 Ma) followed by the exhumation of the Foix massif (~ 50 Ma) and the north-eastern part of the Axial Zone (Quérigut, Ax-les-Thermes, Riberot ~ 45 Ma) (Figure 4.2) (Yelland, 1991; Fitzgerald et al., 1999; Maurel et al., 2008; Gunnell et al., 2009; Vacherat et al., 2016; Ternois et al., 2019). Subsequently, the southern part of the Pyrenean Axial Zone, stretching from the Canigou and Mont Louis massifs in the east to the west, is exhumed starting around 40 Ma (Figures 4.1 and 4.2) (Maurel et al., 2008).

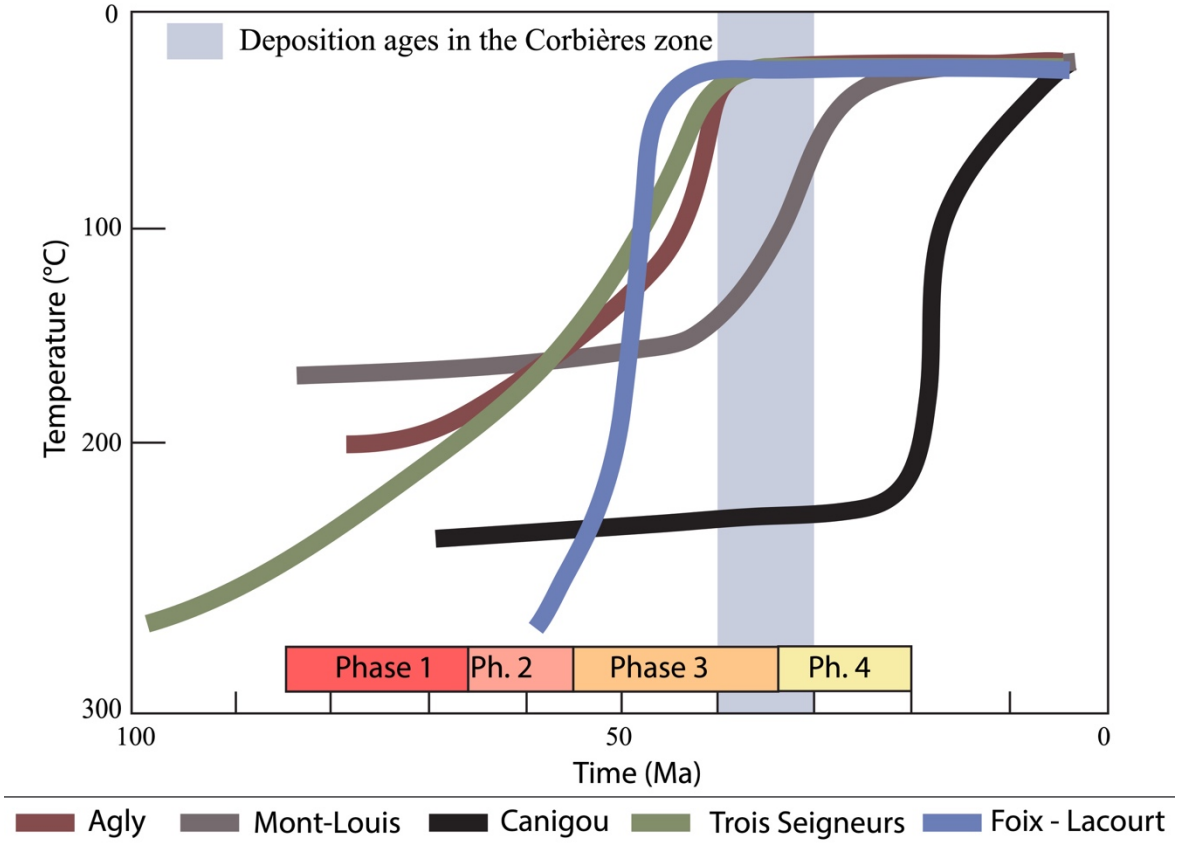

Figure 4.2: Temperature-time paths of the eastern and central parts of the NPZ and the Axial Zone massifs as recorded by low temperature thermochronology modelling exercices. Phases 1 to 4 refer to the timing of Pyrenean mountain building (Mouthereau et al., 2014). Phase 1 : early orogenic phase; phase 2: quiescence phase; phase 3: main orogenic phase and phase 4 late orogenic phase. References: Canigou & Mont-Louis massifs (Maurel et al., 2007), Trois Seigneurs massif (Vacherat et al., 2016) and Agly massif (Ternois et al., 2019).

During the Eocene period, a strong subsidence rate is recorded in the northern foreland basin (Christophoul et al., 2003; Ford et al., 2016; Rougier et al., 2016; Grool et al., 2018) due mainly to thrusting in the Pyrenees that propagates rapidly northward in response to the acceleration of shortening in the Aquitaine basin, particularly in its eastern part (Ford et al., 2016). The early Oligocene-Miocene interval is associated with a brief period of rapid exhumation in the Axial Zone and thrust activation in the front of the belt (Macchiavelli et al., 2017). Rifting in the Ligurian-Provençal basin started in the late Oligocene period and lead to the opening up of the Gulf of Lion and the thinning of the crust (Séranne et al., 1995; Séranne, 1999; Mauffret et al., 2001; Jolivet et al.,

2015; Jolivet et al., 2020).

Eastern Aquitaine basin stratigraphy

The first stage of compression is described as early Campanian-Maastrichtian. From the onset of convergence estimated around 83 Ma (Roest & Srivastava, 1991; Olivet, 1996; Rosenbaum et al., 2002; Bilotte et al., 2005; Bilotte, 2007; Mouthereau et al., 2014), mainly Campanian platform/deltaic to calcareous turbidites (BRGM, 1974; Rougier et al., 2016) infilled the Sub-Pyrenean Zone from the east to the west (Bilotte et al., 2005). They are overlain by Maastrichtian-Paleocene sediments composed of fluvial, lacustrine, and shallow marine platform sediments.

The "Paleocene quiet phase" is actually Danian-Selandian in age and subsidence only increased during the Thanetian (Grool et al., 2018). Early Eocene deposits (Ypresian) correspond to marine platform, marls and deltaic deposits (Coustouge group of Rougier et al., 2016) imputed to the onset of a second stage of foreland subsidence (Plaziat, 1984; Christophoul et al., 2003). This marine sedimentation ended within Middle Ypresian, SBZ 9 benthic foraminifera biozone of Serra-kiel et al. (1998) (Tambareau et al., 1995; Christophoul et al., 2003) and are overlain with middle Eocene to Oligocene continental deposits that represent an overfilled stage of the eastern Aquitaine basin (Crochet, 1989).

The Palassou series, around 2000 m in thickness, are principally alluvial fan, fluvial and lacustrine in nature. The deposition ages of these series have been estimated as going from the Ypresian to the Priabonian period. They were probably fed from eastward and southward sources and are composed of three depositional sequences described as three tectono-sedimentary units separated by unconformities (Baby et al., 1988; Crochet, 1989). Each unit is characterized by conglomeratic deposits coarsening upward and finer intervals containing lacustrine limestone. The first unit – middle Ypresian to Lutetian - is defined by well-consolidated conglomerates with boulders sourced mostly in the Meso-Cenozoic sedimentary cover (Figure 4.3). The second unit, of late Lutetian-Bartonian age, is characterized by a high number of clasts derived from plutonic rocks. The third unit deposited during the Priabonian period, is similar to the first unit with carbonate and sandstone clasts derived mainly from the Mezo-Cenozoic cover, in addition to few granite clasts (Crochet, 1989) (Figure 4.3).

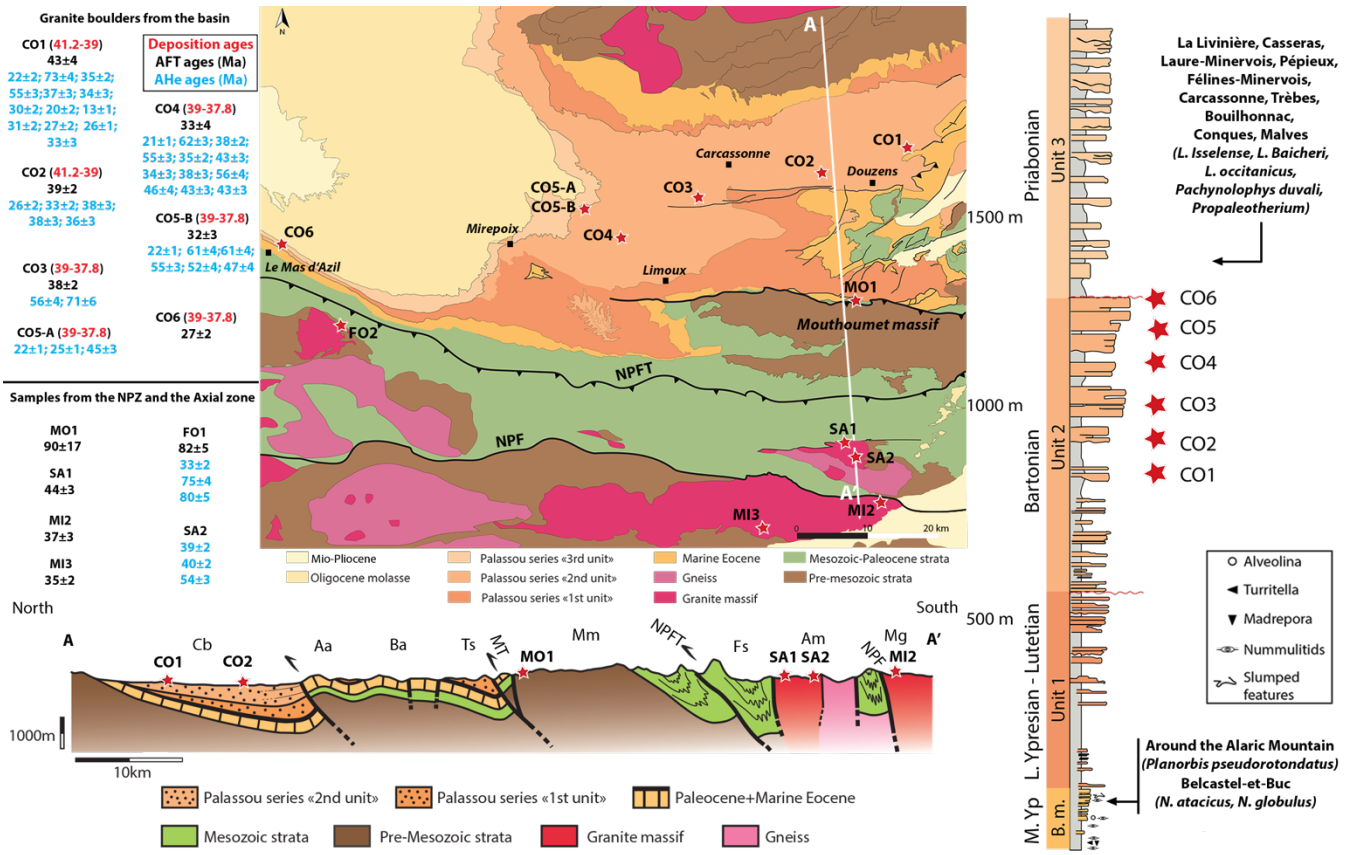

Figure 4.3: Location of the studied samples (stars) on the geological map of the Corbières region and the adjacent NPZ and Axial Zone. On the right, the stratigraphic log of the Middle Ypresian Blue marls (B. m.) overlaid with the Palassou conglomerates. Fossils studied using biostratigraphy are presented on the stratigraphic log (in italic) with the corresponding localities. On the left, the list of samples with their corresponding deposition ages and AFT and AHe ages obtained in this study. The eastern part sediments have deposition age between 41.2 and 39 Ma and the western part sediments are deposited between 39 and 37.8 Ma. Yielded AFT and AHe ages, in addition to the deposition ages are presented in this figure. Geological cross section AA' going from the Carcassonne basin (Cb) in the north to the Axial Zone of the Pyrenees in the south is represented in the bottom with the location of some samples. Cb: Carcassonne basin, Aa: Alaric anticline, Ba: Boucher anticline, Ts: Talairan syncline, Mm : Mouthoumet massif, MT : Mouthoumet Thrust, Fs : St-Paul-de-Fenouillet syncline, Am: Agly massif, Mg: Millas massif. The geologic map is obtained by correlating 1/50 000 geologic maps of the region edited by the BRGM.

Deposition ages in the eastern Aquitaine region

The stratigraphy of the formations observed in the Corbières region has been studied using biostratigraphy and has been correlated laterally with the surrounding basins. The evolution from marine to continental sedimentation in the eastern part of the Aquitaine basin occurred during the middle Ypresian period, as shown by biostratigraphy on nummulitids (*Nummulites atacicus, N. globulus*) (Doncieux, 1912; Hottinger, 1962; Plaziat, 1970; Plaziat, 1984) and molluscs (Calcaires de Ventenac (*Planorbis pseudorotondatus*) (Ovtracht & Lenguin, 1977)). Micro-mammals fossils in Mirepoix (Crochet, 1989) and north of Douzens (MP12-13) (Ellenberger et al., 1988; Sudre et al., 1992), in addition to palynology data from Bilotte et al. (1988) have allowed the acquisition of a middle Lutetian to lower Bartonian age to the transition from the unit 1 to the unit 2. The molasse de

Castelnaudary deposits start at the lower Bartonian according to the ages attributed by Sudre et al. (1992) based on the study of the deposits of La Livinière 2, Siran, Pépieux and Casseras, and are the distal equivalent of the unit 2. The base of the molasse de Castelnaudary is equivalent to the base of the unit 2 deposits as defined by Crochet (1989). These continental deposits are known as «Molasse de Carcassonne», mainly used for the distal equivalent of the Poudingue de Palassou. The upper part of the "Molasse de Carcassonne", equivalent to the unit 3, is attributed to the Priabonian based on biostratigraphy on mammals (*Lophiodon Issilense, Lophiodon lautricense*) (Depéret, 1910; Hartenberger et al., 1968; Plaziat, 1984; Berger, 1990) and on vertebrate fossils (*Lophiaspis baicheri, Lophiaspis occitanicus, Pachynolophys duvali, Propaleotherium*) (Hartenberger et al., 1968; Plaziat, 1984; Berger, 1990; Berger et al., 1993). A Priabonian-Oligocene age is commonly attributed to a calcareous series named "calcaire d'Hounoux", located in the eastern Corbières region and marks the stratigraphic limit between Eocene and Oligocene deposits (Cavaillé, 1975). The Oligocene deposits from the Rupelian stage have been dated by comparison with nearby limestone series known as the 'Calcaires de Briatexte' (Cavaillé, 1975). The location of the fossils dated using biostratigraphy and cited above are shown on the stratigraphic log of the Figure 4.3. Samples collected in this study for LTT are from different locations than the dated fossils, their deposition ages were determined in Crochet (1989) by extrapolating discontinuities in the Corbières region and by analysing clast contents, facies and geometry of the Palassou deposits.

Sampling and methods

The second unit of the Palassou conglomerates has been sampled throughout the region, and seven samples of granitic boulders distributed in the basin were collected. Samples CO1 and CO2 are located in the eastern part of the outcropping unit 2 and samples CO3 to CO6 are located in its western part (Figure 4.3). In order to complete the orogen exhumation history, granitic massifs located in the north of the Axial Zone and in the North Pyrenean Zone have also been sampled for LTT. We collected five samples from the Saint Arnac, Millas and Foix massifs (SA1, SA2, MI2, MI3 and FO1 respectively) (Figure 4.3). The Saint Arnac and Foix massifs are located north of the NPF and the Millas massif is south of the NPF. LTT data are partly available for these massifs (Yelland, 1991; Gunnell et al., 2009; Vacherat et al., 2016; Ternois et al., 2019) and will be considered together with the newly produced data. The Paleozoic basement was also sampled in the Mouthoumet massif which represents the nearest basement close to the Corbières sub-basin. Lithologies are not effective in obtaining apatite crystals but a lamprophyre sample (MO1) has been collected and produced a few crystals. Petrography, location and analysis performed on the collected samples are available in Table 4.1.

Samples	Location	Petrography	Deposition ages	Coordinates		Altitude
			(Ma)	Latitude (°N)	Longitude(°E)	(m)
Eocene granite boulders						
CO1	Tourouzelle	M-grained Mono-Leucogranite	41.2-39	43°15’14’	2°43’25’’	74
CO2	Douzens	Medium-grained Two-Leucogranite	41.2-39	43°10’54’’	2°37’45’’	83
CO3	Pomas	Medium-grained Two-Leucogranite	39-37.8	43°6’49’’	2°16’26’’	196
CO4	Monthaut	Medium-grained Mono-Leucogranite	39-37.8	43°2’52’’	2°3’41’’	428
CO5-A	Hounoux	Fine-grained Two-Leucogranite	39-37.8	43°7’42’’	2°0’6’’	384
CO5-B	Hounoux	Medium-grained Mono-Leucogranite	39-37.8	43°7’42’’	2°0’6’’	384
CO6	Maison-neuve	Medium-grained Mono-Leucogranite	39-37.8	43°5’41’’	1°26’19’’	321
Granitic massifs						
SA1	Lesquerdes	Medium-grained Two-Leucogranite		42°47’48’’	2°30’48’’	310
SA2	Saint-Arnac	Medium-grained Two-Leucogranite		42°46’50’’	2°32’21’’	392
MI2	Île-sur-Têt	Medium-grained Two-Leucogranite		42°40’55’’	2°36’45’’	204
Mi3	Rodès	Medium-grained Two-Leucogranite		42°39’19’’	2°31’44’’	344
FO2	St-Martin de Caralp	Medium-grained Mono-Leucogranite		42°58’54’’	1°32’35’’	560

Table 4.1: Petrography and location of Eocene granite boulders from the basin and granitic massifs from the North Pyrenean Zone and the Axial Zone.

Sample preparation

Collected samples have been crushed and sieved with a 400 μm mesh. Apatite grains were separated from low density grains using heavy-liquid and magnetic separation techniques. Apatite fission track and (U-Th-Sm)/He analyses were performed at the GEOPS laboratory (Université Paris Saclay, Orsay – France).

Apatite fission track

Crystals were mounted in epoxy, polished to expose the surface crystal and etched at 5 M HNO_3 for 20 s at 20 ± 1 °C. Low U-muscovite sheets and three glass CN-5 dosimeters as well as two apatite standards (Durango and Fish Canyon Tuff; Hurford, 1990) covered the apatite crystals. Samples were irradiated at the Garching facility (München, Germany) with a nominal fluence of $5x10^{15}$ neutrons/cm^2. After irradiation, mica detectors were etched for 20 min in 40% HF at 20 ± 1 °C. Tracks were counted and measured with a x1250 magnification using a digitized tablet coupled with an optical microscope (Laslett et al., 1984). Fission track ages were calculated using the zeta-calibration method described in Hurford & Green (1982) and have central ages with two-sigma errors. The Chi2 test and age dispersion suggest the presence of only one age population in the samples (Galbraith, 1981; Galbraith & Laslett, 1993). No track length has been measured due to the relatively young age of the samples and the low U content. AFT data are reported in Table 4.2.

Apatite (U-Th-Sm)/He method

Inclusion free, euhedral apatite grains having a width and thickness >70 μm with no visible fractures were hand-picked for analysis. The dimensions of apatite crystals were measured under a binocular microscope and equivalent sphere radii (Rs) were calculated to represent the He diffusion domain (Gautheron & Tassan-Got, 2010). Four to thirteen single aliquot replicates were analysed per sample following the procedure described by Gautheron et al. (2013). Each aliquot was heated twice using a diode laser at 1030 ± 50 °C for 5 minutes, leading to total He degassing during the first heating and allowing for checking for the presence of He trapped in small inclusions during the second heating. AHe ages were corrected morphometrically for alpha-ejection (F_T) using the Monte Carlo simulation (Ketcham et al., 2011; Gautheron et al., 2012). Apatite grains were dissolved in a HNO_3 solution containing a known concentration of ^{42}Ca, ^{235}U, ^{230}Th and ^{149}Sm and analyses were performed using an HR-ICPMS, ThermoScientific Element XR. Durango apatite was also analysed at the same time and provided a mean age of 31.2 ± 1.9 Ma in agreement with previously documented data 31.02 ± 0.22 Ma (McDowell et al., 2005). 14 Durango apatite fragments were analyzed, 1 every

5 grains. The one-sigma error on each AHe age to be considered is 9%, reflecting errors in the F_T and analytical error. (U-Th-Sm)/He data are reported in Table 4.3. The sample CO6 have not been analyzed using this method due to the lack of suitable apatite crystals.

Major, minor and trace element analysis for granite boulders

The composition of ~160 apatite crystals dated by fission tracks was determined using Electron Probe Micro-Analysis (EPMA). Analyses were carried out in the Institut des Sciences de la Terre de Paris (Sorbonne Université) with a Cameca SX Five microprobe. The mean composition (in equivalent oxide weight percent) and standard deviation for each sample are reported in Table 4.4. Measurements include anions (F, Cl), major (Ca, P) and minor cations (Na, Mg, Al, Si, Fe) and rare earth elements (La, Nd, Sm, Ce). Errors in major elements are between 0.3 and 0.58% for F, P and Ca respectively and range from 0.02 and 0.06% for minor elements.

Data inversion and Temperature-time paths

Data have been inverted for modelling purposes using the QTQt software (Gallagher et al., 2009; Gallagher, 2012). The inversion procedure consists of fitting as best as possible the AFT and AHe ages in order to determine the most robust time-temperature history and kinetic parameters of low temperature thermochronology systems. It uses a Bayesian trans-dimensional Markov Chain Monte Carlo (MCMC) algorithm that enables us to specify a wide range of thermal history models. For AFT modelling, the Ketcham et al. (2007) multi-kinetic annealing model was used, with the Dpar parameter as kinematic constraint. (U-Th-Sm)/He ages were modelled using a spherical diffusion domain (based on crystal's equivalent spherical radius) and following the model of Gautheron et al. (2009). T-t paths have been produced for the 6 samples of granite clasts (three paths are presented in this paper and the others are in the supplementary information (SI)). Given that low temperature thermochronology does not have the same resolution as stratigraphy, we have simplified the stratigraphic age. An interval of 40-35 Ma has been chosen for modelling of the deposition age for samples in the eastern part of the Corbières (CO1 & CO2), and an interval of 35-30 Ma has been chosen for samples in the western part (CO3, CO4, CO5-A, CO5-B and CO6). Pre and post-burn in the MCMC chain were set at 100,000 using the following constraints: 75 ± 5 Ma and 70 ± 40 °C as the starting point (the early orogenic phase), 37 ± 3 Ma for samples in the eastern Corbières region (CO1 and CO2) and 33 ± 3 Ma for samples in the western Corbières region (CO4, CO5 and CO6) at a temperature of 10 ± 10 °C.

Low temperature thermochronology results

Sample location, deposition ages and acquired AFT and AHe ages are reported in Figure 4.3 and Table 4.1. AFT and AHe results are reported in Tables 4.2 and 4.3 (AFT radial plots are available in the SI). Results from the eastern and western Corbières are presented separately.

Eastern part of the Corbières region

AFT ages range from 39 ± 2 (CO2) and 43 ± 4 Ma (CO1) and are more recent towards the west side. The CO1 sample yields 13 AHe ages ranging from 13 ± 1 to 73 ± 4 Ma with an effective uranium content (eU=U+0.234×Th+0.0046×Sm; Ault et al., 2019) from 23 to 61 ppm and a Th/U ratio mainly between 0.3 and 3.4. The CO2 sample yields 5 AHe ages ranging from 26 ± 2 to 38 ± 3 Ma, an eU concentration ranging from 19 to 34 ppm and a Th/U ratio between 0.5 and 1.7. Most of the AHe ages range from 20 to 40 Ma. (Figures 4.3 and 4.4; Tables 4.2 and 4.3). AFT ages are close to deposition ages (early Bartonian) and most AHe ages are less than 40 Ma.

Western part of the Corbières region

Five samples CO3, CO4, CO5-A, CO5-B and CO6 yield AFT ages more recent going from east to west and ranging from 38 ± 2 to 27 ± 2 Ma. The CO3 sample yields 2 AHe ages of 56 ± 4 and 71 ± 6 Ma and an eU concentration of 28 and 91 ppm with a Th/U ratio of 1.1 to 1.9 respectively. The CO4 sample yields 12 AHe ages ranging between 21 ± 1 and 62 ± 3 Ma, an eU content between 18 and 48 ppm and a Th/U ratio between 1.8 and 3.3. Most of the ages are between 30 and 50 Ma. The CO5-A sample yields 3 AHe ages ranging from 22 ± 1 to 45 ± 3 Ma with an eU concentration between 14 and 18 ppm and a Th/U ratio between 4.2 and 6.4. The CO5-B sample yields 6 AHe ages ranging from 22 ± 1 to 55 ± 3 Ma and an eU concentration between 27 and 58 ppm and a Th/U ratio between 2.1 and 2.7. Most of the ages are between 50 and 70 Ma (Figures 4.3 and 4.4; Tables 4.2 and 4.3), older than the deposition ages (middle to late Bartonian).

Variscan massifs of the northern Pyrenean domains

Foix massif AFT age is 82 ± 5 Ma and AHe ages are 75 ± 4, 80 ± 5 Ma and 33 ± 2 Ma. The Saint Arnac massif has an AFT age of 44 ± 3 Ma (SA1) and three AHe ages of 39 ± 2 Ma, 40 ± 2 and 54 ± 3 Ma (SA2). For the Millas massif, the AFT ages are 37 ± 3 and 35 ± 2 Ma for the MI2 and MI3 samples respectively (Figure 4.3). An additional AFT age of 90 ± 17 Ma was obtained for a Lamprophyre sample from the Mouthoumet massif.

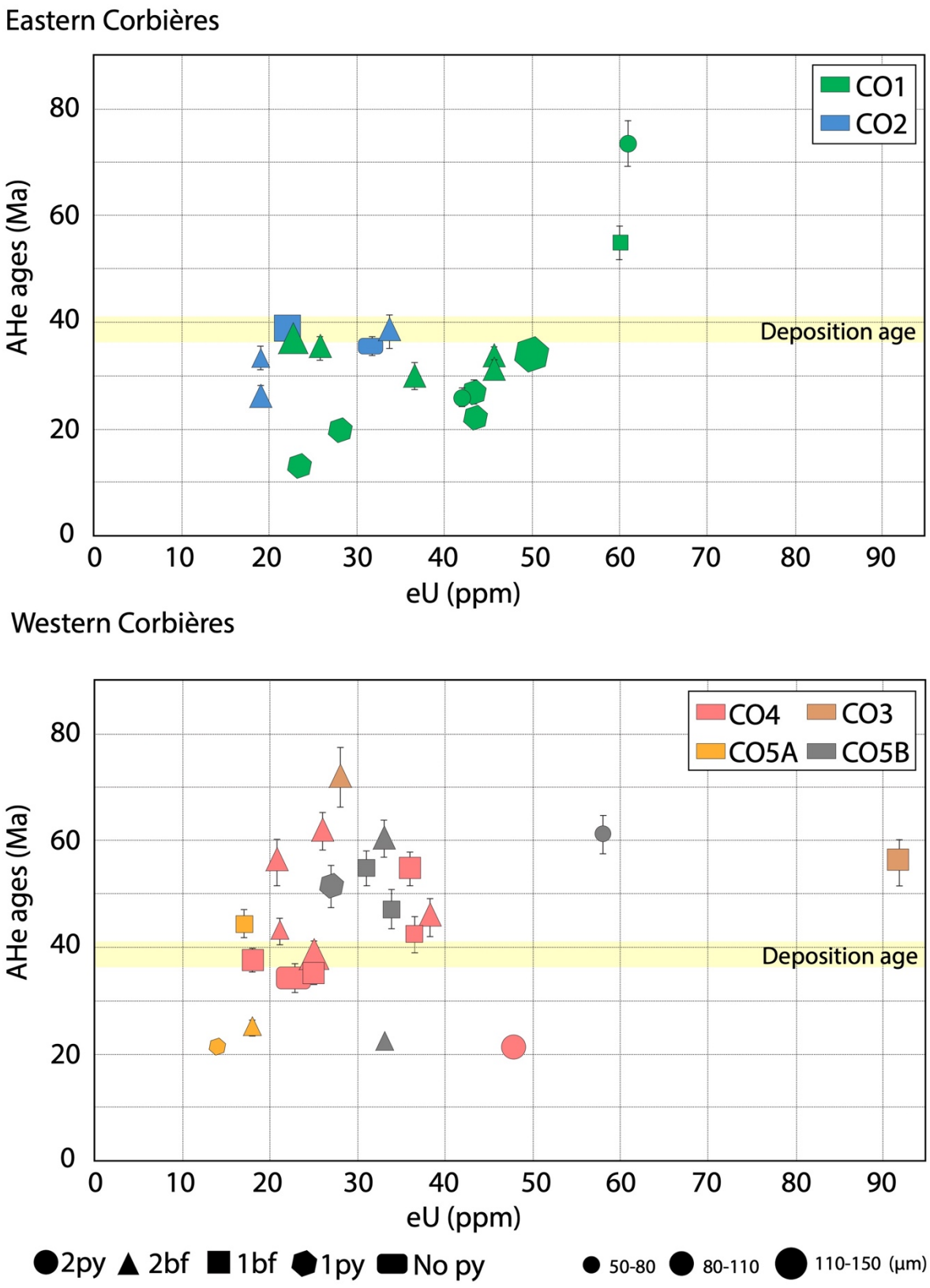

Figure 4.4: AHe ages vs. eU for analyzed granite boulders from the basin with their corresponding geometries and crystal size. 2py: 2 pyramids, 2bf: 2 broken faces, 1bf: 1 broken face, 1py: 1 pyramid and No py: no pyramids.

Table 4.2: Samples names and apatite fission track data

Label	n	ρs x10^5 t/cm^2	Ns	ρi x10^5 t/cm^2	Ni	ρd x10^5 t/cm^2	Nd	P(X2) %	RE %	U ppm	FT age Ma ± 1σ	Dpar µm
Eocene granite boulders												
CO1	19	0.583	180	1.563	483	6.786	6710	80.85	0.4	28.0	**44 ±4**	1.5 ±0.2
CO2	30	0.503	441	1.481	1299	6.735	6710	87.74	0.2	26.8	**39 ±2**	1.4 ±0.1
CO3	22	1.086	657	2.757	1668	5.726	5177	11.4	13.7	58.6	**38 ±2**	1.5 ±0.2
CO4	20	0.225	137	0.802	489	6.634	6710	9.2	27.6	14.7	**33 ±4**	1.4 ±0.1
CO5-B	22	0.29	165	1.076	611	6.886	6710	42.05	5.6	19.0	**32 ±3**	1.4 ±0.1
CO6	20	0.637	325	2.255	1150	5.564	5177	12.04	17	49.3	**27 ±2**	1.5 ±0.2
Granitic massifs and lamprophyre												
SA1	20	0.804	458	1.768	1008	5.523	5177	17.05	13.4	39.0	**44 ±3**	1.5 ±0.2
MI2	13	1.074	218	2.847	578	5.645	5177	73.95	0.0	61.4	**37 ±3**	1.5 ±0.2
MI3	20	1.246	724	3.503	2035	5.605	5177	56.59	2.2	76.1	**35 ±2**	1.5 ±0.2
FO2	18	1.612	606	1.851	696	5.442	5177	32.1	4.8	41.4	**82 ±5**	1.5 ±0.2
MO1	8	0.495	52	0.648	68	6.836	6710	68.32	0.0	11.5	**90 ±17**	1.7 ±0.2

Name	Shape	L	H	W	R_Sphere	FT	weight	4He ±s	238U	232Th	147Sm	eU	Th/U	Age	Age corrigé ±s
		(µm)	(µm)	(µm)	(µm)		(g)	(nccSTP/g)	(ppm)	(ppm)	(ppm)	(ppm)		(Ma)	
Granite boulders															
CO1															
CO1-1	2py	78	238	81	47	0.70	2.7	96380 ±963	31	47	40	42	1.5	**18**	**26** ±1.5
CO1-2	2py	64	147	70	38	0.63	1.1	364206 ±3642	50	45	67	61	0.9	**46**	**73** ±4.4
CO1-3	2bf	57	170	63	36	0.66	1.4	78354 ±783	18	32	43	26	1.8	**23**	**35** ±2.1
CO1-4	1bf	69	145	71	39	0.67	1.6	275067 ±2750	48	51	38	60	1.1	**37**	**55** ±3.3
CO1-5	2bf	112	141	131	61	0.83	4.6	83482 ±834	17	20	60	22	1.1	**31**	**37** ±2.9
CO1-6	1py	122	194	144	69	0.82	7.26	168981 ±1689	27	93	58	49	3.4	**28**	**34** ±2.7
CO1-7	2bf	99	116	100	49	0.78	2.3	104770 ±1047	28	37	67	37	1.3	**23**	**30** ±2.4
CO1-8	2bf	107	165	107	56	0.80	3.5	149195±1491	37	35	49	46	0.9	**27**	**33** ±2.7
CO1-9	1py	93	100	103	43	0.74	1.9	49665 ±496	15	53	39	28	3.4	**15**	**20** ±1.6
CO1-10	1py	86	109	150	48	0.77	2.8	90603 ±906	35	36	60	44	1,0	**17**	**22** ±1.8
CO1-11	1py	89	110	104	45	0.74	1.5	27399 ±273	15	34	25	23	2.2	**10**	**13** ±1.1
CO1-12	2bf	103	168	124	60	0.82	4.5	141510 ±1415	37	33	48	45	0.9	**26**	**31.5** ±2.5
CO1-13	1py	87	126	105	48	0.75	2.9	107448 ±1074	40	13	49	44	0.3	**20**	**27** ±2.2
CO2															
CO2-1*	No Py	95	103	108	48	0.71	2.5	87598 ±875	14	7	20	15	0.5	**44**	**62** ±3.7
CO2-2*	No Py	79	112	85	42	0.67	1.7	142038 ±1420	15	29	24	22	2,0	**51**	**75** ±4.5
CO2-3	2bf	84	99	95	44	0.77	1.9	50904 ±509	14	23	36	19	1.7	**20**	**26** ±1.6
CO2-4	2bf	60	112	70	36	0.68	1.1	55809 ±558	13	21	40	19	1.6	**22.5**	**33** ±2.0
CO2-5	2bf	149	88	146	57	0.85	3.9	129217 ±1292	30	17	51	34	0.5	**31**	**38** ±3.1
CO2-6	1bf	126	173	186	77	0.84	1.9	84559 ±845	17	20	24	22	1.1	**32**	**38** ±3.0
CO2-7*	2bf	90	179	135	61	0.81	4.7	135811 ±1358	50	47	59	62	0.9	**18**	**22** ±1.8
CO2-8	No Py	92	154	112	54	0.74	4.2	105351 ±1053	25	30	48	32	1.2	**27**	**36** ±2.9
CO3															
CO3-1*	No Py	64	55	129	34	0.60	0.62	220412 ±2204	43	43	73	53	1.0	**34**	**57** ±4.5
CO3-2*	No Py	61	57	121	33	0.59	0.82	476409 ±7464	50	48	58	61	1.0	**64**	**108** ±8.6
CO3-3*	No Py	77	60	112	37	0.63	0.76	675760 ±6758	156	74	105	174	0.5	**32**	**50** ±4.0

CO3-4	1bf	87	116	96	47	0.74	2.0	457927 ±4579	71	82	55	91	1.1	**41**	**56** ±4.5
CO3-5	2bf	86	117	100	47	0.78	2.6	186868 ±1868	19	36	65	28	1.9	**55**	**71** ±5.7
CO4															
CO4-1	1bf	88	156	99	51	0.75	3.3	65324 ±653	12	25	27	18	2.2	**28**	**38** ±2.3
CO4-2	1bf	85	163	94	49	0.74	3.1	183927 ±1839	24	48	32	36	2.0	**41**	**55** ±3.3
CO4-3	1bf	75	194	115	54	0.76	4.3	85092 ±850	16	36	29	25	2.2	**27**	**35** ±2.1
CO4-4	2bf	77	88	82	39	0.74	1.3	153711 ±1537	16	39	43	26	2.4	**46**	**62** ±3.3
CO4-5	2bf	61	173	67	38	0.68	1.7	80557 ±805	13	33	34	21	2.5	**29**	**43** ±2.6
CO4-6	2p	89	196	100	53	0.73	2.9	94120 ±941	34	61	42	48	1.8	**15**	**21** ±1.3
CO4-7	No Py	125	137	133	62	0.77	3.3	74050 ±740	13	40	49	23	3.1	**26**	**34** ±2.7
CO4-8	2bf	126	132	138	62	0.84	4.4	98359 ±983	14	44	55	25	3.0	**32**	**38** ±3.1
CO4-9	2bf	104	119	157	61	0.84	4.1	120644 ±1206	14	30	51	21	2.1	**47**	**56** ±4.5
CO4-10	2bf	94	94	112	48	0.80	1.9	170027 ±1700	23	64	68	38	2.8	**36**	**46** ±3.7
CO4-11	1bf	63	97	86	39	0.69	0.9	130144 ±1301	20	68	71	37	3.3	**29**	**43** ±3.4
CO4-12*	1bf	59	134	76	39	0.67	1.5	226446 ±2264	17	41	40	27	2.4	**64**	**95** ±5.7
CO4-13*	No Py	98	135	150	61	0.77	4.3	145300 ±1453	12	24	45	18	2.0	**66**	**86** ±6.9
CO4-14*	2bf	71	115	89	42	0.74	1.9	528928 ±5289	24	55	62	37	2.3	**118**	**159** ±12.8
CO4-15	2bf	95	117	111	51	0.80	2.5	77691 ±776	11	32	51	19	2.9	**34**	**43** ±3.4
CO5-A															
CO5-A-1	1bf	54	118	66	34	0.63	1.0	63983 ±639	8	38	41	17	4.9	**28**	**45** ±2.7
CO5-A-2	1p	59	150	68	37	0.62	1.2	26671 ±266	6	36	39	14	6.4	**13**	**22** ±1.3
CO5-A-3	2bf	47	97	60	30	0.62	0.7	37188 ±371	9	37	41	18	4.2	**16**	**25** ±1.5
CO5-A-4*	bf	44	109	61	30	0.62	0.7	147792 ±1478	7	37	43	16	5.4	68	111 ±6.6
CO5-B															
CO5-B-1	2p	67	138	84	41	0.66	1.2	300423 ±3004	38	81	76	58	2.1	**40**	**61** ±3.7
CO5-B-2	2bf	73	129	82	42	0.73	1.8	188895 ±1888	21	51	48	33	2.4	**44**	**61** ±3.6
CO5-B-3	2bf	58	74	63	30	0.66	0.6	62455 ±624	21	49	54	33	2.4	**15**	**22** ±1.3
CO5-B-4	1bf	65	83	91	38	0.69	1.2	153595 ±1535	20	45	50	31	2.2	**38**	**55** ±3.3
CO5-B-5	1p	75	119	96	44	0.68	1.4	115634 ±1156	16	44	58	27	2.7	**35**	**52** ±4.1
CO5-B-6*	1bf	66	160	77	41	0.69	2.0	88500 ±885	13	26	30	19	2.1	**36**	**52** ±3.1

CO5-B-7*	No Py	70	93	91	40	0.66	0.8	103679 ±1037	12	41	59	22	3.5	**39**	**59** ±4.7
CO5-B-8*	1bf	171	177	187	84	0.86	11.4	114484 ±1145	13	30	45	20	2.4	**47**	**55** ±4.4
CO5-B-9*	2bf	69	95	74	37	0.71	1.2	385910 ±3859	11	37	34	20	3.3	**157**	**221** ±17.7
CO5-B-10*	2bf	65	70	82	35	0.72	1.1	88551 ±889	10	24	40	16	2.3	**46**	**63** ±5.1
CO5-B-11	1bf	61	103	62	33	0.62	0.8	122833 ±1228	21	56	73	34	2.7	**30**	**47** ±3.8
Granitic massifs															
SA2															
SA2-1	2bf	106	86	114	48	0.81	2.0	114278 ±1142	23	24	34	29	1.0	**32**	**40** ±2.4
SA2-2	2bf	106	108	126	54	0.82	3.0	127841 ±1278	20	14	28	24	0.6	**44**	**54** ±3.2
SA2-3	No Py	80	128	90	45	0.69	8.8	58705 ±587	16	7	41	18	0.4	**27**	**39** ±2.3
FO2															
FO2-1	1p	71	95	75	36	0.62	1.1	444675 ±4446	51	98	73	74	1.9	**49**	**80** ±4.8
FO2-2	1p	73	102	72	36	0.62	1.1	185401 ±1854	51	98	73	74	1.9	**21**	**33** ±1.9
FO2-3	2bf	65	83	79	36	0.72	0.8	364079 ±3640	43	53	78	56	1.2	**54**	**75** ±4.5

Table 4.3: AHe data for granite boulders and massifs. Samples with asterisk (*) are not considered in the interpretation (low amount of U compared to the very old age of the sample). Shape abbreviations: 2 pyramids (2py), 1 pyramid (1p), No pyramids (No Py), 1 broken face (1bf) and 2 broken faces (2bf).

Major, minor and trace element results

Major element content is similar for the six analysed samples: CaO ranges between 55.3 and 55.8 wt%, P_2O_5 between 41.5 to 42.4 wt% and F composition ranges between 2.5 and 3.1 wt%. The CO4 and CO5-B chlorine content is slightly higher (0.12±0.07 wt% compared to 0.03-0.06 wt% in the other samples) and the Fe composition for the CO3 sample is also higher than the other samples (0.6±0.2 wt% compared to 0.1±0.1 wt% in the other samples) (Table 4.4). In general, there is no direct correlation between the chemical composition of apatite crystals and AFT ages (Table 4.2). As apatite composition is quite complex, it can be expressed following the formula $X_{10}YO_4Z_2$, where X is mostly Ca substituted by Fe^{2+}, Mn^{2+}, Na^{+}, REE^{3+}, Sr^{2+}, U^{4+}; Y is primarily P with Si substitution and Z is F, Cl or OH (Barbarand et al., 2003). The triangular diagram in Figure 4.5 illustrates the similarity of the amounts (%wt) of X, Y and F for the analysed samples. It has been demonstrated that, in general, apatite crystals chemistry could have an impact on the damage annealing temperature (Gautheron et al., 2013; Fox & Shuster, 2014).

Thermal modelling

All thermal modelling have been carried out with a starting point at 75±10 Ma (early orogenic phase). This 75 Ma starting point corresponds to the beginning of the exhumation of the eastern Pyrenean massifs according to ZHe ages obtained by Ternois et al. (2019). The temperature is also higher than the He diffusion range in apatite crystals.

Time-temperature paths of the samples CO1, CO4 and CO6 are presented in Figure 4.6. For sample CO1 located in the eastern Corbières, the modelled thermal history shows a cooling period (55-40 Ma) in the source massif followed by a heating episode occurring after deposition (35 Ma) and a second cooling phase (6 Ma – Figure 4.6A). A comparable path is observed for the sample CO2 with a fast first cooling period (Figure 4.4 in the SI). Most of the AFT and AHe ages for those samples are reproduced in the model (Figure 4.6A for CO1 and Figure 4.4 in the SI for CO2). Modelling results for samples CO3, CO4 and CO5 (A&B) show very fast pre-deposition cooling at 45 Ma (Figure 4.6B for sample CO4, Figure 4.4 in the SI for samples CO3, 5A and 5B), without the post-deposition heating episode observed for samples CO1 and CO2. AFT ages and a few AHe ages for samples CO3 to CO5 are reproduced in the modelling (observed vs. predicted age – Figure 4.6B for CO4, Figure 4.4 in the SI for CO3, Figure 4.5A and 5B). The majority of AHe ages are older than the deposition ages obtained for these samples. The time-temperature path of the westernmost sample CO6 (Figure 4.6C) shows a pre-deposition cooling (55-40 Ma), a significant post-deposition heating episode (~30 Ma) and a second cooling from ~15 Ma to present.

Table 4.4: Apatite mean composition for samples of granite boulders from the basin (

Sample name	Number of grains	CaO	P_2O_5	Y_2O_3	Na_2O	SiO_2	FeO	La_2O_3	Nd_2O_3	Sm_2O_3	Ce_2O_3	F	Cl	Total
CO1	18	55.3 ±0.3	41.5 ±1.4	0.3 ±0.1	0.1 ±0.0	0.1 ±0.1	0.1 ±0.1	0.0 ±0.0	0.1 ±0.0	0.04 ±0.02	0.1 ±0.0	2.9 ±0.2	0.04 ±0.02	100.6
CO2	33	55.4 ±0.4	41.8 ±0.5	0.2 ±0.1	0.1 ±0.0	0.1 ±0.1	0.1 ±0.1	0.0 ±0.0	0.1 ±0.0	0.04 ±0.02	0.1 ±0.0	2.8 ±0.2	0.03 ±0.03	100.8
CO3	21	54.5 ±0.6	41.5 ±0.7	0.3 ±0.1	0.1 ±0.1	0.03 ±0.1	0.6 ±0.2	0.0 ±0.0	0.1 ±0.0	0.04 ±0.03	0.1 ±0.0	3.1 ±0.2	0.03 ±0.02	100.5
CO4	41	55.4 ±0.3	42.3 ±0.6	0.2 ±0.1	0.1 ±0.0	0.2 ±0.1	0.1 ±0.0	0.1 ±0.0	0.2 ±0.1	0.04 ±0.02	0.2 ±0.1	2.5 ±0.2	0.12 ±0.03	101.5
CO5-B	22	55.8 ±0.5	42.0 ±0.8	0.2 ±0.1	0.1 ±0.0	0.2 ±0.1	0.1 ±0.1	0.1±0.0	0.2 ±0.1	0.04 ±0.03	0.2 ±0.1	2.7 ±0.5	0.12 ±0.07	101.7
CO6	21	55.8 ±0.5	42.4 ±0.8	0.1 ±0.1	0.1 ±0.0	0.01 ±0.1	0.1 ±0.1	0.0 ±0.0	0.1 ±0.1	0.02 ±0.03	0.03 ±0.1	2.8 ±0.2	0.06 ±0.07	101.5

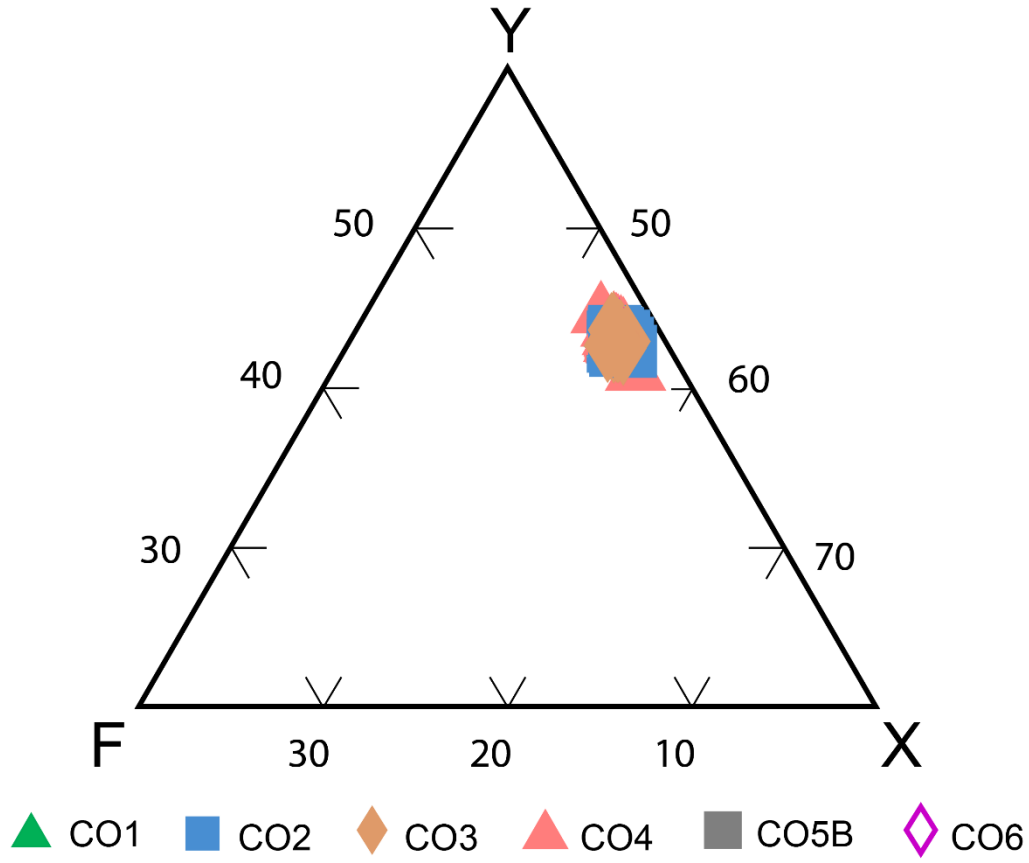

Figure 4.5: X, Y and F percentages (wt%) in apatite crystals from the granite boulders. X: mostly Ca with substituting cations (Fe, Mg, Na, Sr and Al), Y: mostly P possibly substituted by Si, and F is Fluorine.

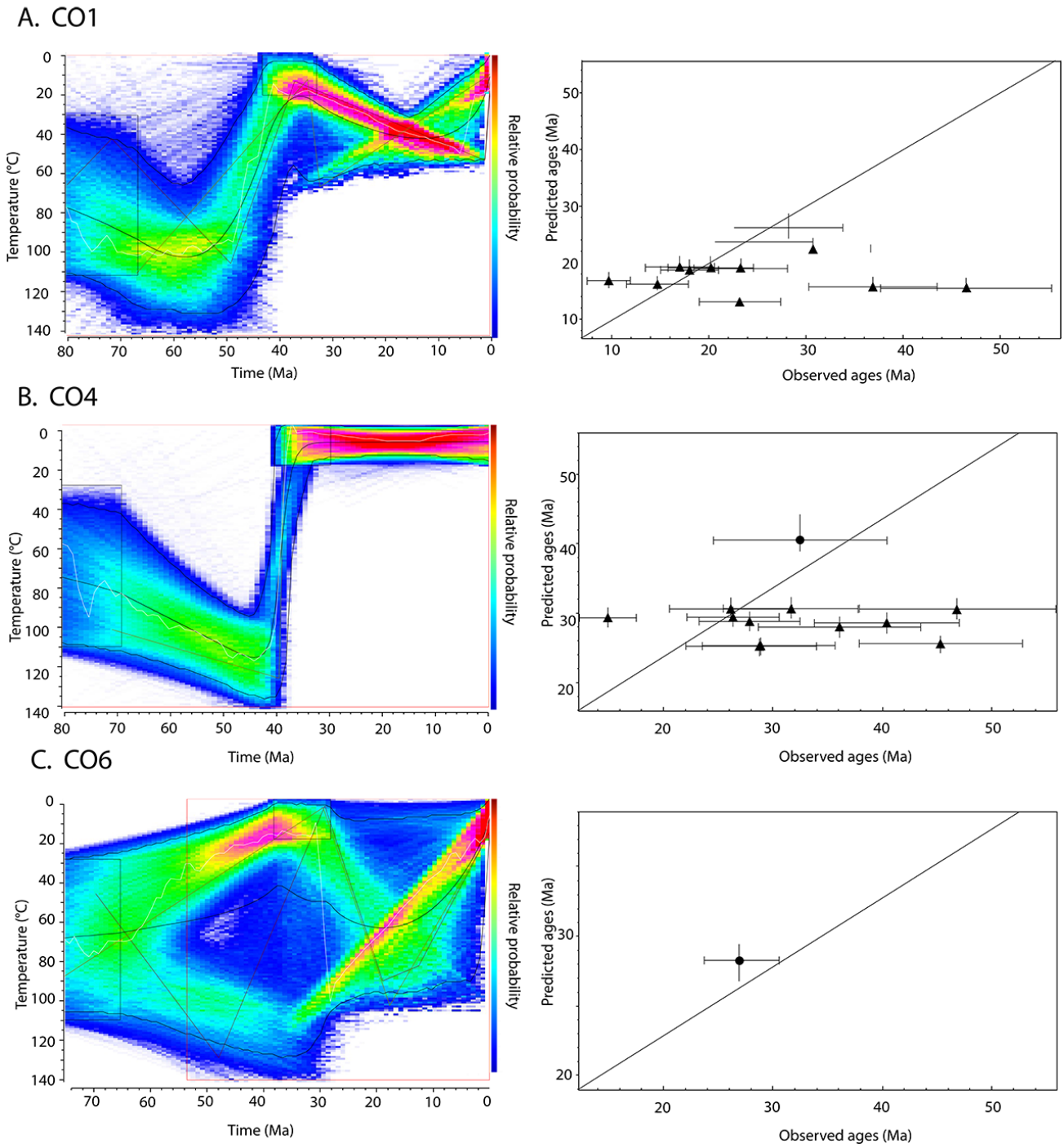

Figure 4.6: Temperature-time paths of the samples CO1 (eastern Corbières region), CO4 and CO6 (western Corbières region) and their corresponding predicted vs. observed ages graphs. Paths and graphs are obtained by data inversion using QTQt software (Gallagher et al., 2009; Gallagher 2012). Triangles represent AHe ages and dots represent AFT ages.

Discussion

AFT and AHe age distribution

All AFT ages are very close to the deposition ages, the younger AFT ages mirror the younger stratigraphic ages, rock outcroppings being older from west to east. As these ages are similar to the ages in the potential source domains, in particular the eastern and central NPZ and Axial Zone (Yelland, 1991; Morris et al., 1998; Fitzgerald et al., 1999; Maurel et al., 2008; Gunnell et al., 2009; Vacherat et al., 2016), it could show very short lag time between exhumation and sedimentation (i.e. fast exhumation and highly effective transport). However, as AHe ages are younger than stratigraphic ages for several replicates (18-35 Ma), we consider that the relatively young ages show that samples have undergone a partial resetting event due to a heating phase after deposition. In addition, AHe ages have a wide dispersion from 73±4 Ma to 13±1 Ma, that indicates the impact of a heating event, affecting the He budget by diffusion (Ault et al., 2019). The strongly dispersed AHe ages indicate a partial reset at temperature below 120°C and a long stay in the Partial Retention Zone (PRZ) (Flowers, 2009; Gautheron et al., 2009; Fox et al., 2019). AHe ages older and younger than AFT ages (73-43 Ma) show that AFT and AHe ages have been partially reset.

Since the last decade, several authors have investigated the different parameters influencing He diffusion in apatite for different geological contexts. The maximum of AHe ages dispersion have been found in craton, margin and sedimentary basins where the samples have stayed long time in the PRZ. The main mechanisms impacting AHe age dispersion is the amount of alpha recoil damage and the impact of microvoids that strongly trap He within the apatite structure (Shuster et al., 2006; Flowers, 2009; Gautheron et al., 2009; Gerin et al., 2017; McDannell et al., 2018). The amount of recoil damage will depend on the concentration of effective uranium, time since alpha recoil damage creation and annealing. In addition, grain chemistry has been proposed to impact the annealing rate (Gautheron et al., 2013; Fox & Shuster, 2014; Djimbi et al., 2015). Secondary parameters such as grain size, morphology (Reiners & Farley, 2001; Beucher et al., 2013; Brown et al., 2013) and alpha implantation (Spiegel et al., 2009; Murray et al., 2014; Janowski et al., 2017) have also an impact on AHe ages. See the review of Ault et al. (2019) for more details. All these parameters will strongly influence the AHe age distribution, and the correlation between age and alpha recoil damage content caused by the effective uranium content is not always expected and depends on the impact of other parameters (Fox et al., 2019). AHe ages obtained for granite boulders from the

basin are plotted against the effective amount of uranium (eU) (Figure 4.4). The positive correlation between AHe ages and eU content indicates that the alpha recoil damage is the primary parameter influencing the He diffusion in this study. However, other parameters also influence the ages and explain why the ages are scattered. In order to identify the combined impact of other parameters such as grain size and morphology on AHe age dispersion, we detail the hexagonal termination and grain size in Figure 4.4 as identified by Brown et al. (2013). In addition, no obvious relationship is shown when the radius sphere of apatite crystals is plotted against the grain size (plots available in the SI), hence the grain size and geometry appear to have a secondary effect on the diffusion domain size. He implantation could also have an effect on AHe ages, and could be shown by a negative AHe-eU correlation (Spiegel et al., 2009; Murray et al., 2014). The new data presented in this study reveal a mostly positive correlation between AHe ages and eU concentration (Figure 4.4), indicating a negligible impact of He implantation on the obtained ages.

Apatite chemistry appears to play an important role in damage annealing, but no effective substitute for the AHe method has been found at present (Recanati et al., 2017). Here we observe that the Th/U ratios are variable from sample to sample with a mean low ratio (0.5 – 3.4) for samples recovered in the eastern part of the study area and higher ratio (1.1-6.4) for the western samples (Table 2, Th/U plots are available in the Figure 4.2 of the SI). These differing ratios point to different sources and potentially different chemistries. The variations of AHe ages may then be related to grains with various chemistries, eastern samples having younger AHe ages than western samples. Major elemental chemistry may explain part of these variations since chlorine content in the western samples is insignificantly higher (0.12%wt for samples CO4 and CO5). Grain compositions are in general very similar and no significant variation in the amount of oxides is mentioned (Table 4.4). This means that the major element chemistry of apatite seems to have no major impact on the dispersion of AHe ages, as already demonstrated by Recanati et al. (2017). However, trace element content or annealing models for apatite should be investigated further (e.g. Willett et al., 2017; Fox et al., 2019). Some authors have also shown that alpha recoil damage seems to be annealed at a higher temperature than AFT (Gautheron et al., 2013; Fox & Shuster, 2014; Willett et al., 2017). This implies that during heating associated with burial, AFT ages will be impacted more significantly than AHe ages (e.g. Flowers, 2009; Recanati et al., 2017; Wildman et al., 2016).

Exhumation and burial history

Inverse modelling of AFT and AHe ages reveal four events. The first event corresponds to the early exhumation of the mountain belt, demonstrated by AHe ages older than 55 Ma. These ages, older than the depositional age, preserve some parts of the source signal. The second event (55-40 Ma) corresponds to the cooling of the belt at the Eocene time and the third event (post 37 Ma) corresponds to a post-deposition burial observed as some AHe ages are younger than the deposition age (Figure 4.4). This is characteristic of higher temperatures than surface temperatures which were at the origin of the partial loss of He atoms or annealing of fission tracks. The fourth event identified in these new detrital thermochronological data occurred during the Miocene and is related to a final exhumation of the basin deposits.

Early orogenic exhumation and preservation of the source signals

Pre-deposition AHe ages of granite boulders sampled in the Palassou unit indicate a Late Cretaceous cooling in the source massifs. Some of these ages may be affected by the partial reset during basin burial and are younger than their true source region cooling ages. However, low temperature thermochronology results obtained in the NPZ and the north-eastern part of the Axial Zone also show Upper Cretaceous ages (Yelland, 1991; Maurel et al., 2008; Vacherat et al., 2016; Ternois et al., 2019) interpreted as an early orogenic phase in the Pyrenees (Ternois et al., 2019). The AHe ages ranging from 75 to 55 Ma probably reflect a long stay in the PRZ at this time (40-120°C; Ault et al., 2019), which is congruent with the occurrence of a quiescent period during the Paleocene.

The CO1 sample is located in the north of the Corbières region, north of the Alaric anticline that was probably uplifted during the Bartonian (Christophoul et al., 2003). According to the results of CO1 sample and considering LTT results in the NPZ (Ternois et al., 2019), the sediment sourcing of the northern Corbières could originate from an earlier emerged NPZ south-eastward, that was slowly exhumed from the Campanian to the Paleocene and that fed this area with sediments. This hypothesis seems to be compatible with paleogeographic maps proposed by Plaziat (1981) and Vacherat et al. (2017). CO3 to CO6 are located west of the small fold and thrust belt that take place in the eastern Corbières, this area was thus more directly fed by the orogen to the south.

Content and source analysis of the Palassou series is proposed by Ovtracht & Lenguin (1977) and Crochet (1989). The first unit (middle Ypresian-Lutetian) contains mainly calcareous clasts sourced from Jurassic to middle Albian deposits of the NPZ, followed by the

second unit deposits (late Lutetian- Bartonian) that consists of calcareous clasts sourced from early Paleozoic units more to the south and granite clasts that are probably fed from the Pyrenees.

Late Eocene and early Oligocene burial episode

Late Eocene and early Oligocene sediments are deposited in most of the Aquitaine basin (Rougier et al., 2016; Ortiz et al., 2020) but are typically absent in the eastern Corbières. In the western Corbières late Eocene (Priabonian)-early Oligocene deposits can reach more than 600 m in Mirepoix (Crochet, 1989) and 700 m in Mas d'Azil areas (Crochet, 1989).

According to Ortiz et al. (2020), during the late Oligocene (Chattian) occurred a strong preservation pattern change in the Aquitaine foreland, from important accumulation on the piedmont to by pass. This Chattian transition is registered in the piedmont by pronounced erosional truncation and is tentatively interpreted as recording the transition to post-orogenic phase. Based on these results, we interpret the post-deposition thermal event in our study as being due to the deposition of a thick layer of sediments, during the Priabonian and the Early Oligocene. We cannot fully exclude a late Eocene thermal event that could have affected the thermal history but it is not reported in the literature. Moreover, detrital thermochronological data published westward in the Sub-Pyrenean Zone indicate a similar pattern with burial then exhumation during the late Paleogene and Neogene periods (Mouthereau et al., 2014). We suggest thus that a maximum burial took place during the Late Eocene- early Oligocene time in the eastern part of the retro-foreland basin.

The estimation of the thickness of eroded sediments requires knowledge of the local geothermal gradient in the Pyrenean domain. A geothermal gradient of 30°C/km was used by Beamud et al. (2011) and Fillon et al. (2013) in the interpretation of AFT data acquired on the southern flank of the Pyrenees, as demonstrated by numerical modelling (Zeyen & Fernàndez, 1994). A present-day geothermal gradient of about 22°C/km is estimated by Fernàndez et al. (1998) in the southern Pyrenees. As there is no geothermal gradient estimated in the northern foreland basin, and because of the absence of general agreement about the thermal gradient in the Pyrenees, a 30 °C/km geothermal gradient could be chosen. However, we cannot exclude an increase of the geothermal gradient during the early Oligocene period associated with the Gulf of Lion opening (Mauffret et al., 2001; Séranne et al., 1995). Ter Voorde & Cloetingh, (1996) propose that the geothermal gradient can reach 40°C/km in the onshore domain of the Valencia Through, normal faulting is reported in the eastern Corbières during the Oligo- Miocene, crustal stretching in the studied area is much more limited compared to the Gulf of Lion thus 40°C/km

must be regarded as a maximum. Using a surface temperature of 20°C during the Oligocene (Bosellini & Perrin, 2008), and a maximum of 30 to 40°C/km geothermal gradient, burial is estimated at 1150 ± 150 m for sample CO1 in the eastern Corbières and 1300 ± 150 m for sample CO6 more to the west.

Late cooling/exhumation during Oligo-Miocene times

AFT and AHe ages younger than the deposition ages (< ~37 Ma) are interpreted as recording cooling induced during the final erosion phase in the basin. To estimate the timing of this erosion event, we have done several forward modelling exercises to test different time and temperature end-members in order to obtain a higher level of reproducibility of the data. Three time-temperature paths with different post-Bartonian exhumation times and a fixed burial temperature of 60°C are produced for sample CO1 (Figure 4.7): (1) a T-t path with an early exhumation starting at 20 Ma (model B); (2) a T-t path produced by our inverse modelling with exhumation starting at around 6±2 Ma (black line); (3) a T-t path with an exhumation at 12 Ma (model A). Uncorrected, observed and predicted AHe ages for sample CO1 and predicted ages produced using models A and B are plotted with measured eU in Figure 4.7B.

The choice of 20 and 12 Ma final exhumation ages is based on two possible geological events: (1) The marine Langhian deposits resting uncomfortably over lower Ypresian sediments in the eastern Corbières region (Aguilar & Magné, 1978), that could traduce erosion prior to the Langhian.

(2) A difference of preservation in the Aquitaine piedmont around 12 My demonstrated by Ortiz et al. (2020) on the downstream part of the same routing system. The Aquitaine basin evolved following three stages: a first foreland stage (up to 25.2 My) with sediments mainly trapped on the piedmont/platform section followed by two different configurations during the post-foreland stage (a first one from 25.2 to 12 My with low accumulation in the Aquitaine basin and a second with by-pass to erosion patterns on the same section).

Models A and B reproduced quite well AHe ages for eU concentrations ranging between 20 and 50 ppm, but poorly for a high eU concentration (> 50 ppm). In all, old AHe ages obtained in this study reflect a long stay in the PRZ (between 40 and 120°C) before exhuming toward the surface. As the ensuing burial did not reset ages, it must have not exceeded 70°C, and the timing of burial ranges from 20 to 10 Ma (Figure 4.7).

We thus interpret the Miocene exhumation being as due to the conjugated effects of two phenomena:

(1) the progressive connection of the proximal foreland to the westward deep basin

starting from the late Oligocene, and interpreted by Ortiz et al. (2020) as the transition to post orogenic conditions, and

(2) the Oligo-Miocene rifting event in the nearby Gulf of Lion (Séranne et al., 1995) inducing a base-level fall and possible uplift for the eastern Corbières system.

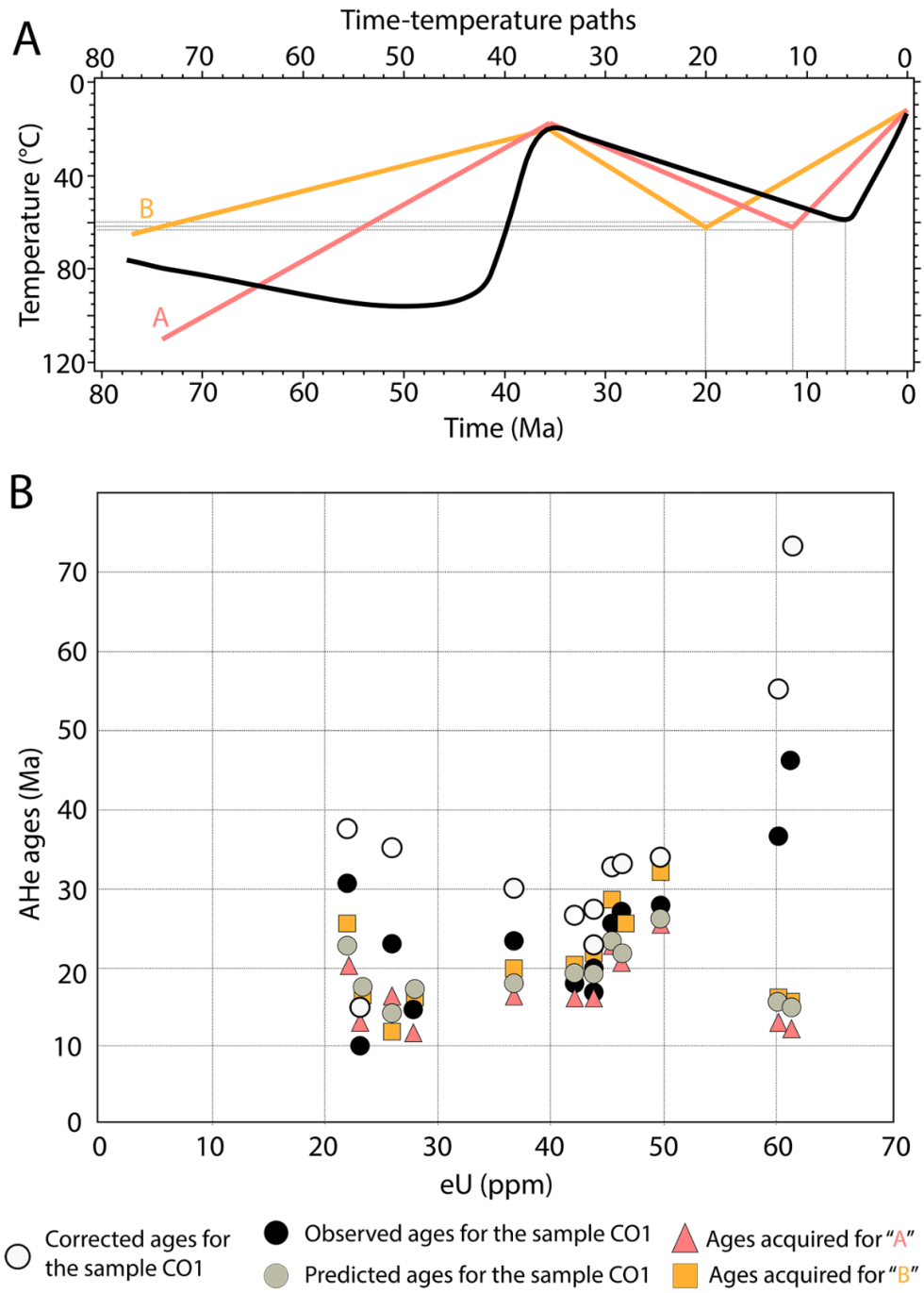

Figure 4.7: A: Temperature-time paths by forward modelling of the sample CO1 using QTQt and 2 tests (A&B) having different timing of final exhumation. Black line: time-temperature path produced by our inverse modelling for the sample CO1, path A: 12 Ma exhumation at a temperature of 60°C and path B: 20 Ma exhumation at the same temperature. B: ages vs. eU graph showing the corrected, predicted and observed ages of the sample CO1. Both tests, A and B, have predicted ages closer to the observed and predicted ages of the sample CO1.

Sedimentary routing and topographic evolution on both flank of the Pyrenees during Oligo-Miocene times

Our results show that ~1.3 km of late Eocene-Oligocene sediments were locally deposited in the northern Pyrenean retro-foreland basin from the Bartonian, before being eroded starting from the early-middle Miocene. This implies an important aggradation of the piedmont deposits. This aggradation is similar to the one observed in the southern Pyrenean piedmont and due to both the preservation of Oligo-Miocene post-orogenic deposits reaching up to 1000-1500 m and remnants of concomitant low-relief erosional surfaces at high elevations (up to more than 2000 m) (Babault et al., 2005). Fillon & van der Beek (2012) have shown that the late orogenic filling in the southern Pyrenean piedmont could have reached a maximum elevation of 2.6 km. They proposed that the thickness of the post-orogenic deposits could have reached 1.6 km implying some burial heating detected by LTT in the underlying sediments before a Late Neogene exhumation (Fillon et al., 2013). According to Babault et al. (2005), this aggradation is implied by the increase of the local base-level along the piedmont in the Late Eocene to Miocene, and it triggered the development of high-elevation, low relief-surfaces (HELRS). Both the aggradation of sediments and the development of HELRS in the south Pyrenean foreland are linked to endorheism as mentioned in Babault et al. (2005), Costa et al. (2012) and Filleaudeau et al. (2012).

Our results show an aggradation in the northern Pyrenean piedmont, comparable to the one occurring in the south, but not linked to endorheism; the Aquitaine basin was open to the Atlantic Ocean. The aggradation of sediments and their preservation is currently related to base level rise. In the Aquitaine basin, during the Ypresian and lower Lutetian time, the infilling of sediments is shown by the prograding deltas and associated fluvial deposits (Gely and Sztrakos, 2000; Serrano et al., 2001; Vacherat et al., 2017). The paleogeography has durably changed later (Ortiz et al., 2020) from the Bartonian to the Early Oligocene where the coastline remained relatively stable in the western part of the Aquitaine basin (Gely and Sztrakos, 2000; BRGM-AGSO, 2018). At the same time, the central and eastern Aquitaine basin (studied area) were filled by thick continental deposits (including the Palassou series) revealing overfilled conditions and consisting mainly of alluvial fans deposits preserved in the Sub-Pyrenean Zone and (from our results) in the Corbières region. Although the sediment routing is not precisely known, the length of the transfer zone (i.e. the distance between the piedmont of the study area

and the coastline) as raised during the Bartonian, have reached more than 200 km. Moreover, the downstream part of the alluvial fans located in the piedmont, the Molasse d'Aquitaine continental deposits, consist of abundant occurrence of lacustrine and palustrine deposits (Capdeville et al., 1996; Sztrakos et al., 1998; AGSO BRGM 2018; Ortiz et al., 2020), alternating with fluvial deposits, all revealing domains with a very low slope (Ortiz et al., 2020). Large coastal plains, evaporitic or more humid, are also reported (Sztrakos et al., 1998, Ortiz et al., 2020). During the Late Eocene, marine sediments mostly consist of carbonate platform deposits (Sztrakos et al., 1998; Gély and Sztrakos, 2000; AGSO-BRGM, 2018; Ortiz et al., 2020), and volumes exported to the final sink (deep sea Bay of Biscay) are very low (Ortiz et al., 2020). This reveals a low transit of eroded material toward the marine areas, and the trapping of most of the sediments coming from the mountain range in the piedmont. All these elements argue for the occurrence of a large transfer zone with low slope, poor transport capacities and sediment accumulation on the piedmont. Part of this accumulation is probably due to the increase of subsidence in the foreland (Ford et al., 2016), mainly induced by topographic load that reached its maximum during the Late Eocene (Angrand et al., 2018, Curry et al., 2019). Restoration of the geometry of the piedmont (figure 4.8) with a thickness of deposits (1.3 km) higher than the actual elevation of HELRS remnants argues that the transfer zone might be wider and extending on the mountain range. Late tectonic deformation might perturb this geometry but the deformation in front of the North Pyrenean Zone after the Oligocene is probably very low.

We conclude that despite no endorheism such as in the Ebro basin occurred in the studied area, high sedimentary flux and low drainage in a very large transfer zone enabled a base level rise and piedmont aggradation in the eastern part of the retro-foreland.

Maximum burial and piedmont aggradation occurred earlier in the northern than in the southern foreland. Overfilled conditions and following piedmont aggradation in the southern foreland occurs from the Priabonian to the Miocene after the closure of the Ebro basin that induced the endorheic conditions. In the retro-foreland, overfilled conditions started during the Bartonian. This offset may be related to both the structural pattern of the retro-foreland and the asymmetric growth of the Axial Zone from north to south. Indeed, in eastern and central Pyrenees, most of the exhumation is located in the NPZ and northern part of the Axial Zone during lower (for the NPZ) and middle Eocene (for the northern part of the AZ) (Mouthereau et al., 2014), probably leading to increase the sedimentary flux toward the retro-foreland. During the Priabonian and the Oligocene, the orogen was mainly growing toward the south and probably feeding the southern foreland.

Bernard et al., 2020 recently modelled the evolution of the Pyrenean topography to explain sediment drapes and HELRS development in northern Pyrenees. They propose that sediment draping, considered as post-orogenic, occurred through the combination of sustained high sediment flux from the range into the basin, relative to the efflux out of the basin, and combined the cessation of the generation of accommodation space through basin subsidence. While we agree with the main driving parameters (aggrading piedmonts related to high sedimentary flux in excess relative to subsidence), following Babault et al. (2005), Carretier and Lucazeau (2005) and Babault et al. (2007), we think that piedmont aggradation and HELRS do not necessarily develop only during post-orogenic conditions but may start during syn-orogenic period. In the eastern Corbières, HELRS on the Mouthoumet massif are well below the summit of recomposed Eocene-Oligocene piedmont sediments and were probably onlapped by aggrading piedmont deposits after their genesis. Moreover, as suggested by Ortiz et al. (2020) the transition to post-orogenic conditions occurred early (Chattian 27 My) and is associated with the transition to a low accumulation of sediments in the piedmont, such conditions are not prone to develop piedmont aggradation.

The timing of exhumation and rejuvenation of both forelands is different. The southern flank started to excavate in the late Miocene (around 10 Ma, Garcia-Castellanos et al., 2003; Fillon et al., 2013) to early Pliocene periods (Babault et al., 2006), however the northern flank excavated earlier in the early-middle Miocene period as shown by this study. Numerous studies report also mid-Miocene to recent, localized exhumation in the eastern to western Pyrenees (Suc & Fauquette, 2012; Bosch et al., 2016; Sartegou et al., 2018; Uzel et al., 2019). The driving mechanisms of this uplift are still debated. Driving forces of this erosion may be associated with opening of the Gulf of Lion that creates base level drop but also potential uplift (Huyghe et al., 2020). Huyghe et al., (2020) recently proposed that the last stage of topographic growth in the eastern Pyrenees (late Miocene) is related to the regional uplift that initiated in the late Burdigalian in response to the back-arc rifting event (opening of the Gulf of Lion and rotation of the Corsica-Sardinia block) (Huyghe et al., 2020). In addition, the combination of geological and geophysical data show a density changes in the sublithospheric mantle that is associated to crustal thinning and resulted of the high topography of the region (Huyghe et al., 2020). This hypothesis would explain the excavation in the eastern region but is less convincing for the exhumation of the Sub Pyrenean Zone (CO6 sample). Another hypothesis is that excavation of the piedmont results from post orogenic isostatic rebound. Ortiz et al. (2020) demonstrates strong changes in accumulation pattern in the Aquitaine basin, the first one during the Chattian from high accumulation in the foredeep during the Eocene-early Oligocene to low accumulation

during the lower Miocene and the second one during the Late Miocene from low accumulation to by-pass. Ortiz et al. (2020) interpret the Chattian evolution as the transition from orogenic to post-orogenic conditions. Bernard et al. (2020) propose a similar pattern of evolution although with some discrepancy in the ages of turnaround where a rebound of the basin is registered several Ma after the end of the syn-orogenic conditions.

The dynamic of excavation of the southern Pyrenees could be explained by the particular evolution of the Ebro basin (Priabonian closure and reconnection through the deep incision associated with the Messinian salinity crisis). Our results from the retro-foreland show different timing but similar evolution patterns. This suggests that piedmont aggradation and subsequent excavation reported from a long time in southern Pyrenees is not exceptional but could be a much more representative behavior of mountain ranges and routing system evolution.

Conclusion

Results acquired by inverse modelling of low-temperature thermochronology data (AFT and AHe) obtained from granite boulders of the syn-orogenic Palassou deposits show (1) a late-Campanian-Maastrichtian cooling, (2) a Paleocene-Eocene cooling in the Pyrenees, (3) a post deposition burial caused by a thick sedimentary layer ranging between 1150±150 and 1300±150 m, and (4) an early to middle Miocene erosion in the basin. The Miocene erosion phase could be linked to the change from sediment accumulation to sediment transportation during the late Oligocene. It could also be due to the opening up of the Gulf of Lion during the Oligo-Miocene time.

Our results show a comparable history with the south Pyrenean foreland basin characterized by an aggradation of sediments on the piedmont followed by erosion. However, the timing of aggradation and excavation between the north and the south are different. The north Pyrenean basin started the accumulation of sediments during the Bartonian due to the increase of subsidence in the basin, the poor connection between the piedmont and the westward deep basin, and the high sedimentary flux to the basin. In the southern part, the aggradation started during the Priabonian and was mainly linked to endorheism. The earlier accumulation of sediments in the north is probably due to the structural pattern of the retro-foreland and the asymmetrical exhumation of the Axial Zone.

The excavation phase occurred earlier in the north (early to middle Miocene) and may be linked to the conjugated effect of the regional uplift that initiated in the late Burdigalian in response to the opening of Gulf of Lion and the post-orogenic isostatic rebound. In the southern

piedmont, excavation is activated by the end of the endorheic conditions.

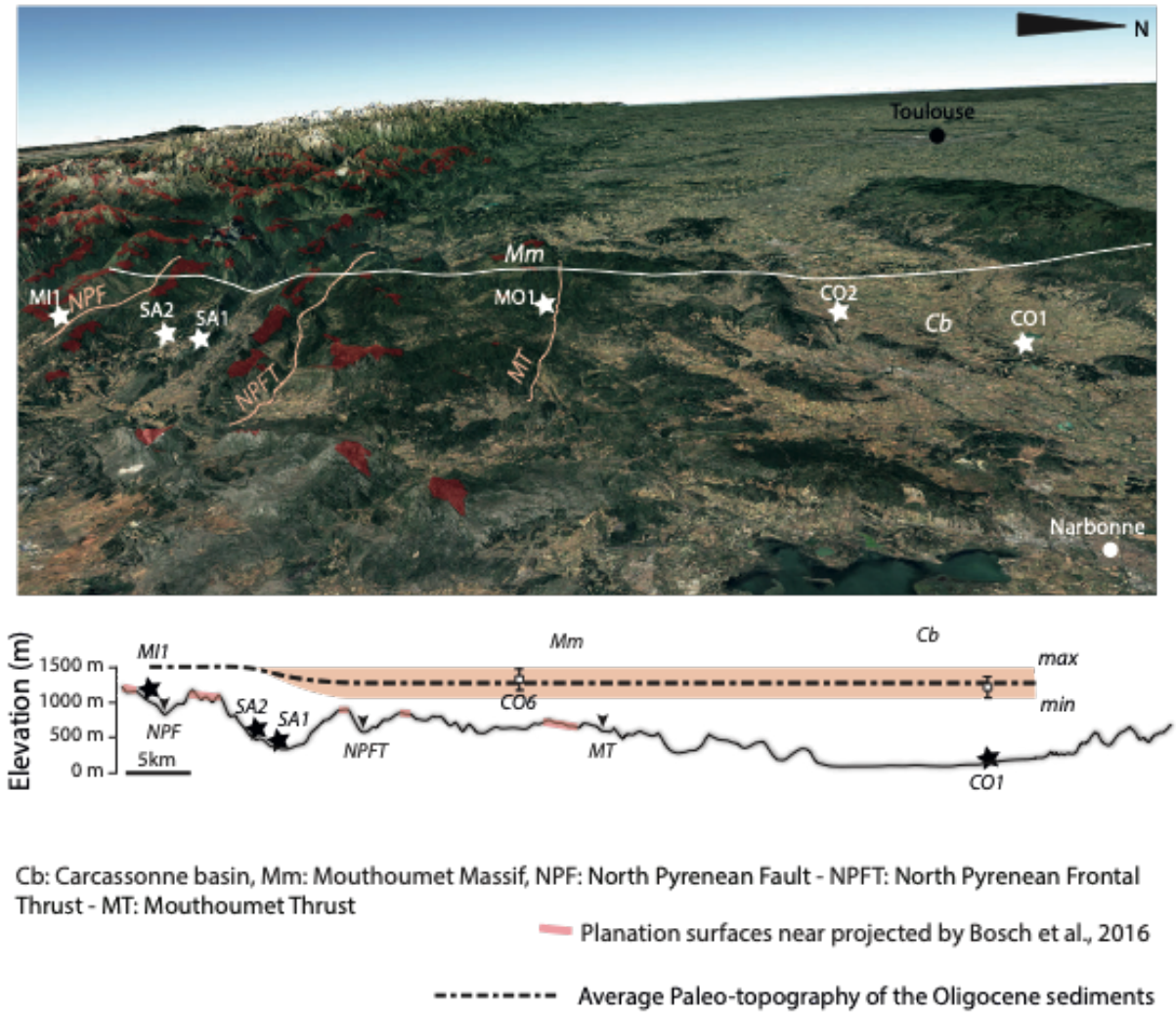

Figure 4.8: Planation surfaces in the Pyrenees from by Bosch et al. (2016) (top) and paleo-topography of the Oligocene sediments according to low temperature thermochronology results (bottom).

Supplementary information

Lithology of the collected samples

Four sampling missions have been done in the Palassou deposits during this PhD (Figure 1). Eight samples have been collected from the unit 1, three of them are conglomerate matrix samples (CO7, MX-1 and MX-2), one is a limestone (CO8) and four clasts of black flysch pieces (Figure 1). From the unit 2, five samples of granite boulders (CO1 to CO5) and three samples of conglomerate matrix (MX-3, MX-4and MX-5) have been collected (Figure 1). One sample of granite boulders (CO6) and one conglomerate matrix sample have been collected from the unit 3 in the western part of the Corbières zone. Boulders of the same sample have a common lithology. Seven granite samples are collected from the North Pyrenean Zone and the Axial Zone of the Pyrenees, in particular from the St-Arnac, Millas and Foix massifs (SA1, SA2, MI1, MI2, MI3, FO1 and FO2). Only two of the collected samples (FO1 and MI1), apatite crystals were not recovered (Figure 1). The Mouthoumet massif has been also investigated using low temperature thermochronology, with one sample (MO1) over three (MO1, MO2 and MO3) dated in apatite fission-track method (Figure 1). Samples CO7 and CO8 from the unit 1 do not contain suitable minerals for dating, only MX-1 and MX-2 have been analysed by zircon U/Pb geochronology (Figure 1). Black flysch samples have been analysed using Raman Spectroscopy of Carbonaceous Material (RSCM). Two granite boulder samples (CO1 to CO5) from the unit 2 have been analysed by fission track and (U-Th)/He on apatite, and U/Pb on zircon grains. Sandstone samples MX-3, MX-4 and MX-5 (unit 2) have been analysed using U/Pb zircon method. Sample CO6 from the unit 3 has been dated by apatite fission track and sample MX-6 by zircon U/Pb methods. Collected samples are presented in Table 1 with their corresponding lithology and location.

Figure 2 shows granite boulders collected from the “Hounoux” site (samples CO5-A and CO5-B). As boulders collected from this location are not similar from a macroscopic point of view, and display also apatite crystals with different sizes, we preferred to study them separately.

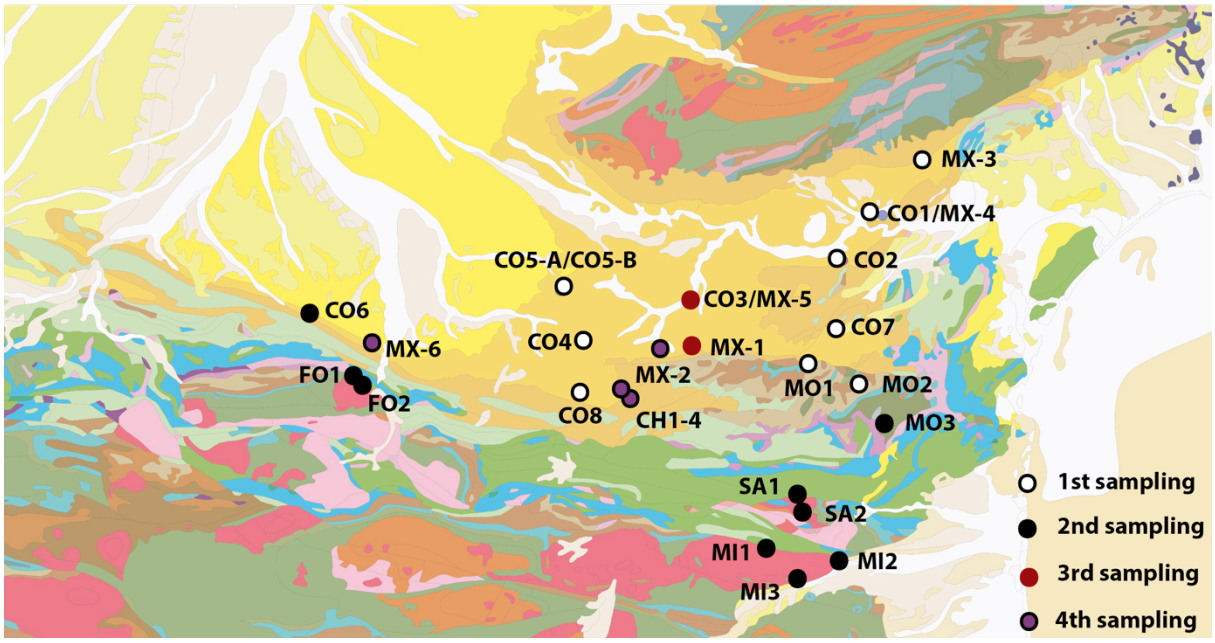

Figure 1: Location of collected samples during fieldtrips.

Figure 2: Granite boulders from Hounoux – (Corbières)

Table 1: Names, locations, rock types and deposition ages of samples collected during field trips in the Corbières region.

Sample name	Provenance	Rock type	Deposition age
CO8	Villefort	Sandstone	
CO4	Monthaut	Granite boulders	Bartonian
CO7	St-Pierre-Des-Champs	Sandstone	Cuisian
CO2	Entre Douzens et Moux	Granite boulders	Bartonian
CO1	Tourouzelle	Granite boulders	Bartonian
MO1	Mouthoumet	Lamprophyre	
MO2	Mouthoumet	Volcanic rocks	
CO5-A	Hounoux	Granite boulders	Ludian
CO5-B			
MX-3	Aigne	Sandstone	Bartonian
MO3	Tuchan	Microdiorite	-
SA1	Saint-Arnac	Granite sample	-
SA2	Saint-Arnac	Granite sample	-
MI1	Trevillach	Granite sample	-
MI2	Ile-sur-Têt	Granite sample	-
MI3	Vinça	Granite sample	-
FO1	St-Pierre-de-Rivière	Granite sample	-
FO2	St-Pierre-de-Rivière	Granite sample	-
CO6	Sabarat	Granite boulders	Priabonian
MX-1	Saint-Polycarpe	Conglomerate matrix	Lutétien
MX-4	Tourouzelle	Conglomerate matrix	Bartonian
MX-5	Pomas	Conglomerate matrix	Bartonian
MX-2	Magrie	Conglomerate matrix	Bartonian
MX-6	Dalou	Conglomerate matrix	Bartonian
CH1	Courtalpha	Black flysch clast	Ypresian
CH2	Montjardin	Black flysch clast	Lutetian
CH3	Courtalpha	Black flysch clast	Lutetian
CH4	St-Benoît	Black flysch clast	Late Lutetian

Apatite fission track data

Echantillon :	**CO1**	
Irradiation :	**OR19**	
Analyste :	**JB**	
Date :	20/06/2017	
Facteur zéta ± erreur :	346,7	± 5,70
ρ_d :	6,786	10^5 traces/cm^2
N_d :	6710	
Unité de surface :	1,00	10^{-6} cm^2
U verre (ppm) :	12,17	(CN5)

Grain	N_s	N_i	N_g	ρ_s	ρ_i	ρ_s / ρ_i	U (ppm)	Age	erreur	Dpar
1	9	17	8	1,125	2,125	0,5294	38,1	**61,98**	**25,58**	**1,2**
2	9	15	16	0,563	0,938	0,6000	16,8	**70,20**	**29,63**	**1,4**
3	7	21	18	0,389	1,167	0,3333	20,9	**39,09**	**17,08**	**1,3**
4	5	14	16	0,313	0,875	0,3571	15,7	**41,88**	**21,83**	**1,4**
5	6	18	8	0,750	2,250	0,3333	40,4	**39,09**	**18,45**	**1,4**
7	16	25	12	1,333	2,083	0,6400	37,4	**74,85**	**24,01**	**1,5**
8	9	34	24	0,375	1,417	0,2647	25,4	**31,06**	**11,66**	**1,5**
9	32	82	16	2,000	5,125	0,3902	91,9	**45,74**	**9,58**	**1,4**
10	5	15	12	0,417	1,250	0,3333	22,4	**39,09**	**20,20**	**1,2**
11	16	41	16	1,000	2,563	0,3902	46,0	**45,74**	**13,52**	**1,3**
12	14	37	36	0,389	1,028	0,3784	18,4	**44,36**	**13,95**	**1,4**
13	5	23	18	0,278	1,278	0,2174	22,9	**25,52**	**12,60**	**1,6**
14	10	33	24	0,417	1,375	0,3030	24,7	**35,55**	**12,85**	**1,4**
15	3	8	12	0,250	0,667	0,3750	12,0	**43,96**	**29,78**	**1,8**
16	3	9	16	0,188	0,563	0,3333	10,1	**39,09**	**26,07**	**1,5**
17	18	34	12	1,500	2,833	0,5294	50,8	**61,98**	**18,11**	**1,4**
18	3	10	15	0,200	0,667	0,3000	12,0	**35,19**	**23,18**	**1,9**
19	10	47	30	0,333	1,567	0,2128	28,1	**24,98**	**8,71**	**1,7**
∑	180	483	309	0,583	1,563	0,3727	28,0			**1,5**
										0,2

Pooled Age	**43,69**	**3,92**	
Mean Crystal Age	**44,42**	**14,16**	
Central Age	**43,7**	**3,9**	**0,4 %**

Chi-squared	**11,86**	avec	17	degrés de liberté
P (Chi-Sq)	**80,85**	**%**		

Echantillon :	**CO2**	
Irradiation :	**OR19**	
Analyste :	**JB**	
Date :	19/06/2017	
Facteur zéta ± erreur :	346,7	± 5,70
ρ_d :	6,735	10^5 traces/cm^2
N_d :	6710	
Unité de surface :	1,00	10^{-6} cm^2
U verre (ppm) :	12,17	(CN5)

Grain	N_s	N_i	N_g	ρ_s	ρ_i	ρ_s / ρ_i	U (ppm)	Age	erreur	Dpar
1	9	19	36	0,250	0,528	0,4737	9,5	**55,07**	**22,31**	**1,3**
2	8	14	25	0,320	0,560	0,5714	10,1	**66,37**	**29,45**	**1,3**
3	20	62	30	0,667	2,067	0,3226	37,3	**37,55**	**9,69**	**1,4**
4	10	33	36	0,278	0,917	0,3030	16,6	**35,28**	**12,76**	**1,4**
6	19	63	36	0,528	1,750	0,3016	31,6	**35,11**	**9,22**	**1,6**
8	9	48	30	0,300	1,600	0,1875	28,9	**21,85**	**7,95**	**1,5**
9	10	35	30	0,333	1,167	0,2857	21,1	**33,27**	**11,95**	**1,4**
10	6	28	40	0,150	0,700	0,2143	12,6	**24,97**	**11,24**	**1,5**
11	25	60	35	0,714	1,714	0,4167	31,0	**48,46**	**11,58**	**1,4**
12	19	65	49	0,388	1,327	0,2923	24,0	**34,04**	**8,90**	**1,4**
13	16	44	24	0,667	1,833	0,3636	33,1	**42,32**	**12,38**	**1,3**
14	17	45	35	0,486	1,286	0,3778	23,2	**43,96**	**12,55**	**1,3**
15	20	60	28	0,714	2,143	0,3333	38,7	**38,80**	**10,05**	**1,4**
16	15	68	40	0,375	1,700	0,2206	30,7	**25,70**	**7,35**	**1,4**
17	10	20	12	0,833	1,667	0,5000	30,1	**58,11**	**22,54**	**1,3**
18	10	26	18	0,556	1,444	0,3846	26,1	**44,75**	**16,68**	**1,3**
19	35	75	25	1,400	3,000	0,4667	54,2	**54,25**	**11,16**	**1,5**
20	13	50	35	0,371	1,429	0,2600	25,8	**30,28**	**9,45**	**1,5**
21	12	50	36	0,333	1,389	0,2400	25,1	**27,96**	**9,01**	**1,5**
22	22	48	40	0,550	1,200	0,4583	21,7	**53,29**	**13,76**	**1,6**
23	14	41	25	0,560	1,640	0,3415	29,6	**39,74**	**12,33**	**1,4**
24	18	54	36	0,500	1,500	0,3333	27,1	**38,80**	**10,59**	**1,5**
25	48	127	42	1,143	3,024	0,3780	54,6	**43,98**	**7,51**	**1,7**
26	10	24	25	0,400	0,960	0,4167	17,3	**48,46**	**18,27**	**1,3**
27	11	40	25	0,440	1,600	0,2750	28,9	**32,03**	**10,92**	**1,4**
28	10	28	25	0,400	1,120	0,3571	20,2	**41,56**	**15,34**	**1,4**
29	15	36	24	0,625	1,500	0,4167	27,1	**48,46**	**14,93**	**1,3**
30	10	36	35	0,286	1,029	0,2778	18,6	**32,35**	**11,58**	**1,6**
∑	441	1299	877	0,503	1,481	0,3395	26,8			**1,4**
										0,1

Pooled Age	**39,51**	**2,32**
Mean Crystal Age	**40,61**	**10,81**

Central Age	**39,5**	**2,3**	**0,2 %**

Chi-squared	**18,79**	avec	27	degrés de liberté
P (Chi-Sq)	**87,74**	**%**		

Echantillon :	**CO3**	
Irradiation :	**OR20**	
Analyste :	**JB**	
Date :	21/03/2018	
Facteur zéta ± erreur :	346,7	± 5,70
ρ_d :	5,726	10^5 traces/cm^2
N_d :	5177	
Unité de surface :	1,00	10^{-6} cm^2
U verre (ppm) :	12,17	(CN5)

Grain	N_s	N_i	N_g	ρ_s	ρ_i	ρ_s / ρ_i	U (ppm)	Age	erreur	Dpar
1	10	30	8	1,250	3,750	0,3333	79,7	**33,00**	**12,07**	**1,5**
2	13	27	16	0,813	1,688	0,4815	35,9	**47,62**	**16,11**	**1,5**
3	15	28	24	0,625	1,167	0,5357	24,8	**52,96**	**16,98**	**1,5**
4	22	57	40	0,550	1,425	0,3860	30,3	**38,20**	**9,62**	**1,5**
5	16	42	18	0,889	2,333	0,3810	49,6	**37,70**	**11,11**	**1,5**
6	42	114	20	2,100	5,700	0,3684	121,1	**36,47**	**6,63**	**1,5**
7	45	94	20	2,250	4,700	0,4787	99,9	**47,35**	**8,64**	**1,5**
8	7	27	20	0,350	1,350	0,2593	28,7	**25,68**	**10,91**	**1,5**
9	59	130	28	2,107	4,643	0,4538	98,7	**44,89**	**7,11**	**1,5**
10	36	110	25	1,440	4,400	0,3273	93,5	**32,40**	**6,26**	**1,5**
11	13	47	35	0,371	1,343	0,2766	28,5	**27,40**	**8,61**	**1,5**
12	14	53	25	0,560	2,120	0,2642	45,1	**26,17**	**7,88**	**1,5**
13	16	37	60	0,267	0,617	0,4324	13,1	**42,78**	**12,83**	**1,5**
14	39	140	100	0,390	1,400	0,2786	29,8	**27,59**	**5,03**	**1,5**
15	32	85	18	1,778	4,722	0,3765	100,4	**37,26**	**7,77**	**1,5**
16	55	138	25	2,200	5,520	0,3986	117,3	**39,44**	**6,35**	**1,5**
18	73	169	35	2,086	4,829	0,4320	102,6	**42,74**	**6,06**	**1,5**
19	17	67	28	0,607	2,393	0,2537	50,9	**25,14**	**6,85**	**1,5**
21	17	67	18	0,944	3,722	0,2537	79,1	**25,14**	**6,85**	**1,5**
22	58	103	21	2,762	4,905	0,5631	104,2	**55,66**	**9,21**	**1,5**
22	58	103	21	2,762	4,905	0,5631	104,2	**55,66**	**9,21**	**1,5**
∑	657	1668	605	1,086	2,757	0,3939	58,6			**1,5**
										0,0

Pooled Age	**38,98**	**1,98**	
Mean Crystal Age	**38,16**	**10,06**	
Central Age	**38,5**	**2,3**	**13,7 %**

Chi-squared	**27,82**	avec	20	degrés de liberté
P (Chi-Sq)	**11,37**	**%**		

Echantillon :	**CO4 (1)**	
Irradiation :	**OR19**	
Analyste :	**JB**	
Date :	15/06/2017	
Facteur zéta ± erreur :	346,7	± 5,70
ρ_d :	6,634	10^5 traces/cm^2
N_d :	6710	
Unité de surface :	1,00	10^{-6} cm^2
U verre (ppm) :	12,17	(CN5)

Grain	N_s	N_i	N_g	ρ_s	ρ_i	ρ_s / ρ_i	U (ppm)	Age	erreur	Dpar
1	9	40	49	0,184	0,816	0,2250	15,0	**25,82**	**9,54**	**1,3**
4	7	65	100	0,070	0,650	0,1077	11,9	**12,37**	**4,93**	**1,4**
5	3	38	28	0,107	1,357	0,0789	24,9	**9,07**	**5,44**	**1,5**
6	20	49	40	0,500	1,225	0,4082	22,5	**46,77**	**12,45**	**1,7**
7	8	21	40	0,200	0,525	0,3810	9,6	**43,66**	**18,16**	**1,4**
8	8	38	30	0,267	1,267	0,2105	23,2	**24,17**	**9,41**	**1,5**
9	3	9	21	0,143	0,429	0,3333	7,9	**38,22**	**25,49**	**1,4**
10	5	16	9	0,556	1,778	0,3125	32,6	**35,84**	**18,38**	**1,4**
11	8	12	32	0,250	0,375	0,6667	6,9	**76,21**	**34,82**	**1,2**
12	6	28	70	0,086	0,400	0,2143	7,3	**24,60**	**11,08**	**1,1**
14	11	38	48	0,229	0,792	0,2895	14,5	**33,20**	**11,39**	**1,5**
15	12	28	25	0,480	1,120	0,4286	20,5	**49,10**	**16,97**	**1,4**
16	12	43	32	0,375	1,344	0,2791	24,7	**32,01**	**10,47**	**1,5**
17	5	14	30	0,167	0,467	0,3571	8,6	**40,94**	**21,35**	**1,6**
18	7	19	16	0,438	1,188	0,3684	21,8	**42,23**	**18,69**	**1,3**
19	2	9	15	0,133	0,600	0,2222	11,0	**25,51**	**19,95**	**1,5**
20	11	22	25	0,440	0,880	0,5000	16,1	**57,25**	**21,17**	**1,5**
∑	137	489	610	0,225	0,802	0,2802	14,7			**1,4**
										0,1

Pooled Age	**32,14**	**3,18**
Mean Crystal Age	**36,31**	**16,34**

Central Age	**33,0**	**4,0**	**27,6 %**

Chi-squared	**23,89**	avec	16	degrés de liberté
P (Chi-Sq)	**9,20**	**%**		

Echantillon :	**CO4 (2)**	
Irradiation :	**OR19**	
Analyste :	**JB**	
Date :	16/06/2017	
Facteur zéta ± erreur :	346,7	± 5,70
ρ_d :	6,685	10^5 traces/cm^2
N_d :	6710	
Unité de surface :	1,00	10^{-6} cm^2
U verre (ppm) :	12,17	(CN5)

Grain	N_s	N_i	N_g	ρ_s	ρ_i	ρ_s / ρ_i	U (ppm)	Age	erreur	Dpar
1	6	21	12	0,500	1,750	0,2857	31,9	**33,03**	**15,30**	**1,5**
2	7	27	30	0,233	0,900	0,2593	16,4	**29,97**	**12,73**	**1,6**
3	6	29	36	0,167	0,806	0,2069	14,7	**23,93**	**10,74**	**1,5**
4	6	34	40	0,150	0,850	0,1765	15,5	**20,42**	**9,05**	**1,5**
5	13	34	30	0,433	1,133	0,3824	20,6	**44,16**	**14,43**	**1,6**
6	7	16	35	0,200	0,457	0,4375	8,3	**50,50**	**22,91**	**1,6**
7	2	11	16	0,125	0,688	0,1818	12,5	**21,04**	**16,18**	**1,6**
8	5	16	32	0,156	0,500	0,3125	9,1	**36,11**	**18,52**	**1,6**
9	13	44	35	0,371	1,257	0,2955	22,9	**34,15**	**10,80**	**1,6**
10	12	37	70	0,171	0,529	0,3243	9,6	**37,48**	**12,47**	**1,7**
11	13	35	24	0,542	1,458	0,3714	26,5	**42,90**	**13,96**	**1,4**
12	5	26	25	0,200	1,040	0,1923	18,9	**22,25**	**10,87**	**1,5**
13	12	41	35	0,343	1,171	0,2927	21,3	**33,83**	**11,12**	**1,6**
14	6	15	15	0,400	1,000	0,4000	18,2	**46,19**	**22,33**	**1,7**
15	5	38	35	0,143	1,086	0,1316	19,8	**15,23**	**7,25**	**1,5**
16	8	12	18	0,444	0,667	0,6667	12,1	**76,80**	**35,09**	**1,4**
17	5	28	30	0,167	0,933	0,1786	17,0	**20,66**	**10,04**	**1,5**
18	6	17	16	0,375	1,063	0,3529	19,3	**40,77**	**19,38**	**1,6**
19	5	18	30	0,167	0,600	0,2778	10,9	**32,11**	**16,25**	**1,4**
20	2	16	24	0,083	0,667	0,1250	12,1	**14,47**	**10,86**	**1,6**
21	5	16	30	0,167	0,533	0,3125	9,7	**36,11**	**18,52**	**1,4**
22	11	35	24	0,458	1,458	0,3143	26,5	**36,32**	**12,58**	**1,5**
23	6	14	25	0,240	0,560	0,4286	10,2	**49,47**	**24,16**	**1,4**
24	4	9	24	0,167	0,375	0,4444	6,8	**51,30**	**30,85**	**1,4**
25	8	16	18	0,444	0,889	0,5000	16,2	**57,68**	**25,01**	**1,6**
26	8	17	60	0,133	0,283	0,4706	5,2	**54,30**	**23,31**	**1,6**
27	6	22	24	0,250	0,917	0,2727	16,7	**31,53**	**14,53**	**1,3**
28	8	24	21	0,381	1,143	0,3333	20,8	**38,51**	**15,74**	**1,6**
29	12	24	20	0,600	1,200	0,5000	21,8	**57,68**	**20,43**	**1,5**
30	9	50	30	0,300	1,667	0,1800	30,3	**20,83**	**7,55**	**1,5**
∑	221	742	864	0,256	0,859	0,2978	15,6			**1,5** 0,1

Pooled Age	**34,42**	**2,73**
Mean Crystal Age	**37,01**	**14,43**

Central Age	**34,4**	**2,7**	**0,6 %**

Chi-squared	**22,75**	avec	29	degrés de liberté
P (Chi-Sq)	**78,79**	**%**		

Echantillon :	**CO5-B**	
Irradiation :	**OR19**	
Analyste :	**JB**	
Date :	21/06/2017	
Facteur zéta ± erreur :	346,7	± 5,70
ρ_d :	6,886	10^5 traces/cm^2
N_d :	6710	
Unité de surface :	1,00	10^{-6} cm^2
U verre (ppm) :	12,17	(CN5)

Grain	N_s	N_i	N_g	ρ_s	ρ_i	ρ_s / ρ_i	U (ppm)	Age	erreur	Dpar
1	2	27	25	0,080	1,080	0,0741	19,1	**8,84**	**6,48**	**1,8**
2	10	22	21	0,476	1,048	0,4545	18,5	**54,03**	**20,64**	**1,5**
3	10	34	30	0,333	1,133	0,2941	20,0	**35,01**	**12,62**	**1,5**
4	11	42	24	0,458	1,750	0,2619	30,9	**31,19**	**10,58**	**1,4**
5	5	20	24	0,208	0,833	0,2500	14,7	**29,77**	**14,90**	**1,4**
6	29	100	100	0,290	1,000	0,2900	17,7	**34,52**	**7,32**	**1,4**
7	4	15	24	0,167	0,625	0,2667	11,0	**31,75**	**17,88**	**1,4**
8	9	31	35	0,257	0,886	0,2903	15,7	**34,56**	**13,11**	**1,5**
9	4	8	18	0,222	0,444	0,5000	7,9	**59,41**	**36,40**	**1,3**
10	5	10	9	0,556	1,111	0,5000	19,6	**59,41**	**32,56**	**1,3**
11	20	53	49	0,408	1,082	0,3774	19,1	**44,89**	**11,82**	**1,6**
12	4	15	16	0,250	0,938	0,2667	16,6	**31,75**	**17,88**	**1,4**
13	3	38	15	0,200	2,533	0,0789	44,8	**9,42**	**5,65**	**1,5**
14	8	30	24	0,333	1,250	0,2667	22,1	**31,75**	**12,65**	**1,4**
15	5	29	25	0,200	1,160	0,1724	20,5	**20,55**	**9,96**	**1,3**
16	7	41	32	0,219	1,281	0,1707	22,6	**20,35**	**8,33**	**1,3**
17	6	11	16	0,375	0,688	0,5455	12,2	**64,78**	**32,91**	**1,4**
18	7	20	24	0,292	0,833	0,3500	14,7	**41,64**	**18,31**	**1,4**
19	4	9	15	0,267	0,600	0,4444	10,6	**52,84**	**31,77**	**1,3**
20	5	17	18	0,278	0,944	0,2941	16,7	**35,01**	**17,83**	**1,4**
21	3	9	9	0,333	1,000	0,3333	17,7	**39,67**	**26,46**	**1,3**
22	4	30	15	0,267	2,000	0,1333	35,3	**15,90**	**8,47**	**1,4**
∑	165	611	568	0,290	1,076	0,2700	19,0			**1,4**
										0,1

Pooled Age	**32,16**	**2,90**
Mean Crystal Age	**35,79**	**15,60**

Central Age	**32,1**	**2,9**	**5,6 %**	
Chi-squared	**21,64**	avec	21	degrés de liberté
P (Chi-Sq)	**42,05**	**%**		

Echantillon : **CO6**
Irradiation : **OR20**
Analyste : **JB**
Date :

Facteur zéta ± erreur : 346,7 ± 5,70
ρ_d : 5,564 10^5 traces/cm^2
N_d : 5177
Unité de surface : 1,00 10^{-6} cm^2
U verre (ppm) : 12,17 (CN5)

Grain	N_s	N_i	N_g	ρ_s	ρ_i	ρ_s / ρ_i	U (ppm)	Age	erreur	Dpar
1	27	97	25	1,080	3,880	0,2784	84,9	**26,79**	**5,86**	**1,5**
2	14	50	30	0,467	1,667	0,2800	36,5	**26,95**	**8,17**	**1,5**
3	14	41	30	0,467	1,367	0,3415	29,9	**32,85**	**10,19**	**1,5**
4	27	62	25	1,080	2,480	0,4355	54,2	**41,87**	**9,70**	**1,5**
6	6	20	20	0,300	1,000	0,3000	21,9	**28,87**	**13,45**	**1,5**
7	6	43	18	0,333	2,389	0,1395	52,3	**13,44**	**5,87**	**1,5**
8	19	57	12	1,583	4,750	0,3333	103,9	**32,07**	**8,52**	**1,5**
9	16	39	15	1,067	2,600	0,4103	56,9	**39,45**	**11,74**	**1,5**
11	26	108	25	1,040	4,320	0,2407	94,5	**23,18**	**5,09**	**1,5**
12	21	100	24	0,875	4,167	0,2100	91,1	**20,22**	**4,87**	**1,5**
13	15	52	12	1,250	4,333	0,2885	94,8	**27,76**	**8,16**	**1,5**
14	9	67	49	0,184	1,367	0,1343	29,9	**12,94**	**4,60**	**1,5**
15	34	126	20	1,700	6,300	0,2698	137,8	**25,97**	**5,05**	**1,5**
16	67	176	28	2,393	6,286	0,3807	137,5	**36,61**	**5,31**	**1,5**
17	9	53	42	0,214	1,262	0,1698	27,6	**16,36**	**5,91**	**1,5**
18	2	13	25	0,080	0,520	0,1538	11,4	**14,82**	**11,26**	**1,5**
19	4	23	100	0,040	0,230	0,1739	5,0	**16,75**	**9,08**	**1,5**
20	9	23	10	0,900	2,300	0,3913	50,3	**37,63**	**14,82**	**1,5**
∑	325	1150	510	0,637	2,255	0,2826	49,3			**1,5**
										0,0

Pooled Age	**27,20**	**1,81**
Mean Crystal Age	**26,37**	**9,23**

Central Age	**26,7**	**2,2**	**17,0 %**

Chi-squared	**23,97**	avec	17	degrés de liberté
P (Chi-Sq)	**12,01**	**%**		

Echantillon :	**MO1**	
Irradiation :	**OR19**	
Analyste :	**JB**	
Date :	20/06/2017	
Facteur zéta ± erreur :	346,7	± 5,70
ρ_d :	6,836	10^5 traces/cm^2
N_d :	6710	
Unité de surface :	1,00	10^{-6} cm^2
U verre (ppm) :	12,17	(CN5)

Grain	N_s	N_i	N_g	ρ_s	ρ_i	ρ_s / ρ_i	U (ppm)	Age	erreur	Dpar
1	15	18	14	1,071	1,286	0,8333	22,9	**98,00**	**34,32**	**1,7**
2	13	15	18	0,722	0,833	0,8667	14,8	**101,89**	**38,67**	**1,6**
5	10	12	8	1,250	1,500	0,8333	26,7	**98,00**	**42,01**	**1,8**
6	9	9	12	0,750	0,750	1,0000	13,4	**117,43**	**55,41**	**2,0**
7	4	9	35	0,114	0,257	0,4444	4,6	**52,45**	**31,54**	**1,3**
8	1	5	18	0,056	0,278	0,2000	4,9	**23,66**	**25,92**	**1,5**
∑	52	68	105	0,495	0,648	0,7647	11,5			**1,7**
										0,2

Pooled Age	**89,99**	**16,68**
Mean Crystal Age	**81,99**	**35,89**

Central Age	**90,0**	**16,7**	**0,0 %**	
Chi-squared	**3,11**	avec	5	degrés de liberté
P (Chi-Sq)	**68,32**	**%**		

Echantillon :	**FO2**	
Irradiation :	**OR20**	
Analyste :	**JB**	
Date :	14/03/2018	
Facteur zéta ± erreur :	346,7	± 5,70
ρ_d :	5,442	10^5 traces/cm^2
N_d :	5177	
Unité de surface :	1,00	10^{-6} cm^2
U verre (ppm) :	12,17	(CN5)

Grain	N_s	N_i	N_g	ρ_s	ρ_i	ρ_s / ρ_i	U (ppm)	Age	erreur	Dpar
1	28	31	16	1,750	1,938	0,9032	43,3	**84,65**	**22,14**	**1,5**
2	32	41	20	1,600	2,050	0,7805	45,8	**73,21**	**17,34**	**1,5**
3	12	27	20	0,600	1,350	0,4444	30,2	**41,79**	**14,53**	**1,5**
4	32	27	9	3,556	3,000	1,1852	67,1	**110,85**	**29,07**	**1,5**
5	28	33	48	0,583	0,688	0,8485	15,4	**79,55**	**20,51**	**1,5**
6	36	29	12	3,000	2,417	1,2414	54,0	**116,06**	**29,07**	**1,5**
7	35	49	30	1,167	1,633	0,7143	36,5	**67,04**	**14,91**	**1,5**
8	37	64	30	1,233	2,133	0,5781	47,7	**54,31**	**11,28**	**1,5**
9	42	44	24	1,750	1,833	0,9545	41,0	**89,43**	**19,39**	**1,5**
10	23	34	21	1,095	1,619	0,6765	36,2	**63,50**	**17,20**	**1,5**
11	53	46	16	3,313	2,875	1,1522	64,3	**107,79**	**21,84**	**1,5**
12	52	56	21	2,476	2,667	0,9286	59,6	**87,01**	**16,86**	**1,5**
13	29	35	16	1,813	2,188	0,8286	48,9	**77,70**	**19,58**	**1,5**
14	35	32	25	1,400	1,280	1,0938	28,6	**102,37**	**25,13**	**1,5**
15	27	38	16	1,688	2,375	0,7105	53,1	**66,68**	**16,85**	**1,5**
16	26	20	12	2,167	1,667	1,3000	37,3	**121,49**	**36,23**	**1,5**
17	20	20	12	1,667	1,667	1,0000	37,3	**93,66**	**29,68**	**1,5**
18	59	70	28	2,107	2,500	0,8429	55,9	**79,03**	**14,07**	**1,5**
∑	606	696	376	1,612	1,851	0,8707	41,4			**1,5**
										0,0

Pooled Age	**81,62**	**4,86**
Mean Crystal Age	**84,26**	**21,77**

Central Age	**81,6**	**5,0**	**4,8 %**

Chi-squared	**19,13**	avec	17	degrés de liberté
P (Chi-Sq)	**32,10**	**%**		

Echantillon :	**SA1**	
Irradiation :	**OR20**	
Analyste :	**JB**	
Date :	12/04/2018	
Facteur zéta ± erreur :	346,7	± 5,70
ρ_d :	5,523	10^5 traces/cm^2
N_d :	5177	
Unité de surface :	1,00	10^{-6} cm^2
U verre (ppm) :	12,17	(CN5)

Grain	N_s	N_i	N_g	ρ_s	ρ_i	ρ_s / ρ_i	U (ppm)	Age	erreur	Dpar
1	15	24	24	0,625	1,000	0,6250	22,0	**59,57**	**19,65**	
2	16	25	16	1,000	1,563	0,6400	34,4	**60,99**	**19,57**	**1,5**
3	28	65	20	1,400	3,250	0,4308	71,6	**41,11**	**9,34**	**1,5**
4	21	28	28	0,750	1,000	0,7500	22,0	**71,41**	**20,67**	**1,5**
5	19	60	35	0,543	1,714	0,3167	37,8	**30,25**	**7,99**	**1,5**
6	53	78	50	1,060	1,560	0,6795	34,4	**64,73**	**11,61**	**1,5**
7	32	47	50	0,640	0,940	0,6809	20,7	**64,86**	**14,93**	**1,5**
8	35	89	30	1,167	2,967	0,3933	65,4	**37,54**	**7,53**	**1,5**
9	21	47	50	0,420	0,940	0,4468	20,7	**42,64**	**11,23**	**1,5**
10	40	108	36	1,111	3,000	0,3704	66,1	**35,36**	**6,59**	**1,5**
11	16	45	20	0,800	2,250	0,3556	49,6	**33,95**	**9,91**	**1,5**
12	29	61	35	0,829	1,743	0,4754	38,4	**45,36**	**10,28**	**1,5**
13	24	53	42	0,571	1,262	0,4528	27,8	**43,21**	**10,67**	**1,5**
14	18	62	40	0,450	1,550	0,2903	34,2	**27,74**	**7,45**	**1,5**
15	10	33	16	0,625	2,063	0,3030	45,4	**28,95**	**10,47**	**1,5**
16	20	43	10	2,000	4,300	0,4651	94,7	**44,38**	**12,05**	**1,5**
17	17	28	9	1,889	3,111	0,6071	68,6	**57,87**	**17,84**	**1,5**
18	16	46	14	1,143	3,286	0,3478	72,4	**33,22**	**9,67**	**1,5**
19	12	22	15	0,800	1,467	0,5455	32,3	**52,01**	**18,70**	**1,5**
20	16	44	30	0,533	1,467	0,3636	32,3	**34,72**	**10,16**	**1,5**
∑	458	1008	570	0,804	1,768	0,4544	39,0			**1,5**
										0,0

Pooled Age	**43,36**	**2,62**
Mean Crystal Age	**45,51**	**13,52**

Central Age	**43,5**	**3,0**	**13,4 %**	

Chi-squared	**24,70**	avec	19	degrés de liberté
P (Chi-Sq)	**17,05**	**%**		

Echantillon :	**MI2**	
Irradiation :	**OR20**	
Analyste :	**JB**	
Date :	27/03/2018	
Facteur zéta ± erreur :	346,7	± 5,70
ρ_d :	5,645	10^5 traces/cm^2
N_d :	5177	
Unité de surface :	1,00	10^{-6} cm^2
U verre (ppm) :	12,17	(CN5)

Grain	N_s	N_i	N_g	ρ_s	ρ_i	ρ_s / ρ_i	U (ppm)	Age	erreur	Dpar
1	15	25	9	1,667	2,778	0,6000	59,9	**58,45**	**19,13**	**MIL2**
2	13	33	8	1,625	4,125	0,3939	88,9	**38,44**	**12,61**	**1,5**
3	44	118	48	0,917	2,458	0,3729	53,0	**36,39**	**6,47**	**1,5**
4	13	38	25	0,520	1,520	0,3421	32,8	**33,39**	**10,75**	**1,5**
6	20	45	15	1,333	3,000	0,4444	64,7	**43,35**	**11,69**	**1,5**
9	22	58	30	0,733	1,933	0,3793	41,7	**37,01**	**9,30**	**1,5**
10	17	63	16	1,063	3,938	0,2698	84,9	**26,35**	**7,22**	**1,5**
11	13	46	12	1,083	3,833	0,2826	82,6	**27,60**	**8,69**	**1,5**
12	20	40	12	1,667	3,333	0,5000	71,9	**48,74**	**13,39**	**1,5**
13	41	112	28	1,464	4,000	0,3661	86,2	**35,72**	**6,57**	**1,5**
∑	218	578	203	1,074	2,847	0,3772	61,4			**1,5**
										0,0

Pooled Age	**36,80**	**3,03**
Mean Crystal Age	**38,55**	**9,62**

Central Age	**36,8**	**3,0**	**0,0 %**	
Chi-squared	**6,00**	avec	9	degrés de liberté
P (Chi-Sq)	**73,95**	**%**		

Echantillon :	**MI3**	
Irradiation :	**OR20**	
Analyste :	**JB**	
Date :	26/03/2018	
Facteur zéta ± erreur :	346,7	± 5,70
ρ_d :	5,605	10^5 traces/cm^2
N_d :	5177	
Unité de surface :	1,00	10^{-6} cm^2
U verre (ppm) :	12,17	(CN5)

Grain	N_s	N_i	N_g	ρ_s	ρ_i	ρ_s / ρ_i	U (ppm)	Age	erreur	Dpar
1	58	132	30	1,933	4,400	0,4394	95,5	**42,55**	**6,77**	**1,5**
2	52	133	36	1,444	3,694	0,3910	80,2	**37,87**	**6,25**	**1,5**
3	28	101	24	1,167	4,208	0,2772	91,4	**26,88**	**5,77**	**1,5**
4	57	186	36	1,583	5,167	0,3065	112,2	**29,70**	**4,54**	**1,5**
5	30	90	25	1,200	3,600	0,3333	78,2	**32,30**	**6,85**	**1,5**
6	42	82	32	1,313	2,563	0,5122	55,6	**49,57**	**9,47**	**1,5**
7	31	75	24	1,292	3,125	0,4133	67,9	**40,03**	**8,59**	**1,5**
8	26	95	24	1,083	3,958	0,2737	86,0	**26,53**	**5,90**	**1,5**
9	28	94	28	1,000	3,357	0,2979	72,9	**28,87**	**6,25**	**1,5**
10	33	120	36	0,917	3,333	0,2750	72,4	**26,66**	**5,27**	**1,5**
11	44	130	30	1,467	4,333	0,3385	94,1	**32,80**	**5,76**	**1,5**
12	27	75	30	0,900	2,500	0,3600	54,3	**34,88**	**7,86**	**1,5**
13	19	44	16	1,188	2,750	0,4318	59,7	**41,82**	**11,51**	**1,5**
14	27	85	32	0,844	2,656	0,3176	57,7	**30,79**	**6,83**	**1,5**
15	25	63	20	1,250	3,150	0,3968	68,4	**38,44**	**9,12**	**1,5**
16	41	150	32	1,281	4,688	0,2733	101,8	**26,50**	**4,70**	**1,5**
17	21	48	12	1,750	4,000	0,4375	86,9	**42,37**	**11,12**	**1,5**
18	23	58	25	0,920	2,320	0,3966	50,4	**38,41**	**9,50**	**1,5**
19	28	66	25	1,120	2,640	0,4242	57,3	**41,09**	**9,31**	**1,5**
20	42	104	32	1,313	3,250	0,4038	70,6	**39,12**	**7,20**	**1,5**
20	42	104	32	1,313	3,250	0,4038	70,6	**39,12**	**7,20**	**1,5**
∑	724	2035	581	1,246	3,503	0,3558	76,1			**1,5**
										0,0

Pooled Age	**34,47**	**1,67**
Mean Crystal Age	**35,54**	**6,58**

Central Age	**34,5**	**1,7**	**2,2 %**	
Chi-squared	**18,33**	avec	20	degrés de liberté
P (Chi-Sq)	**56,59**	**%**		

Apatite fission track radial plots of the analysed samples

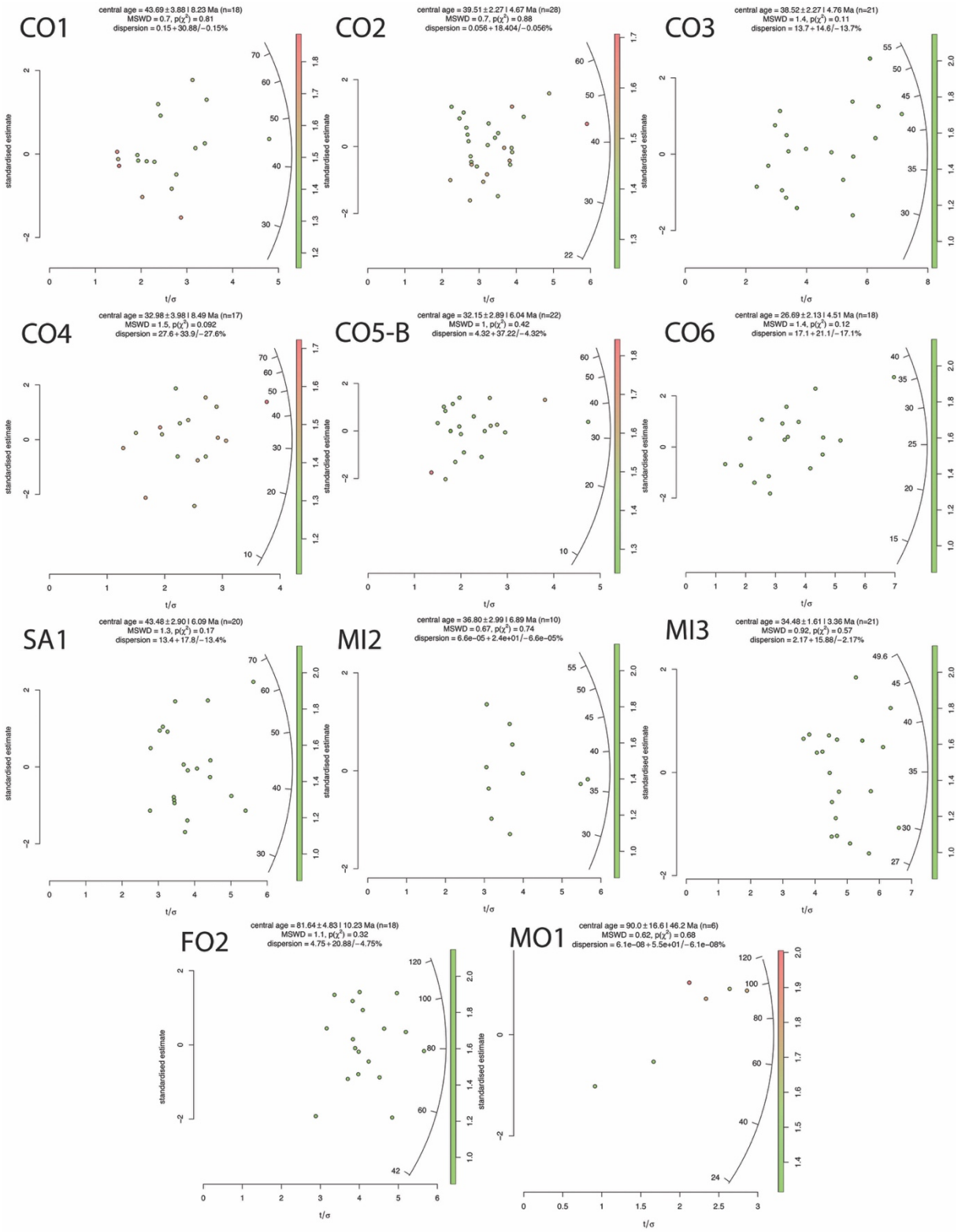

Figure 3: Radial plots of AFT ages acquired in this study

(U-Th-Sm)/He ages vs. Th/U content for samples collected in the eastern and western part of the Corbières zone

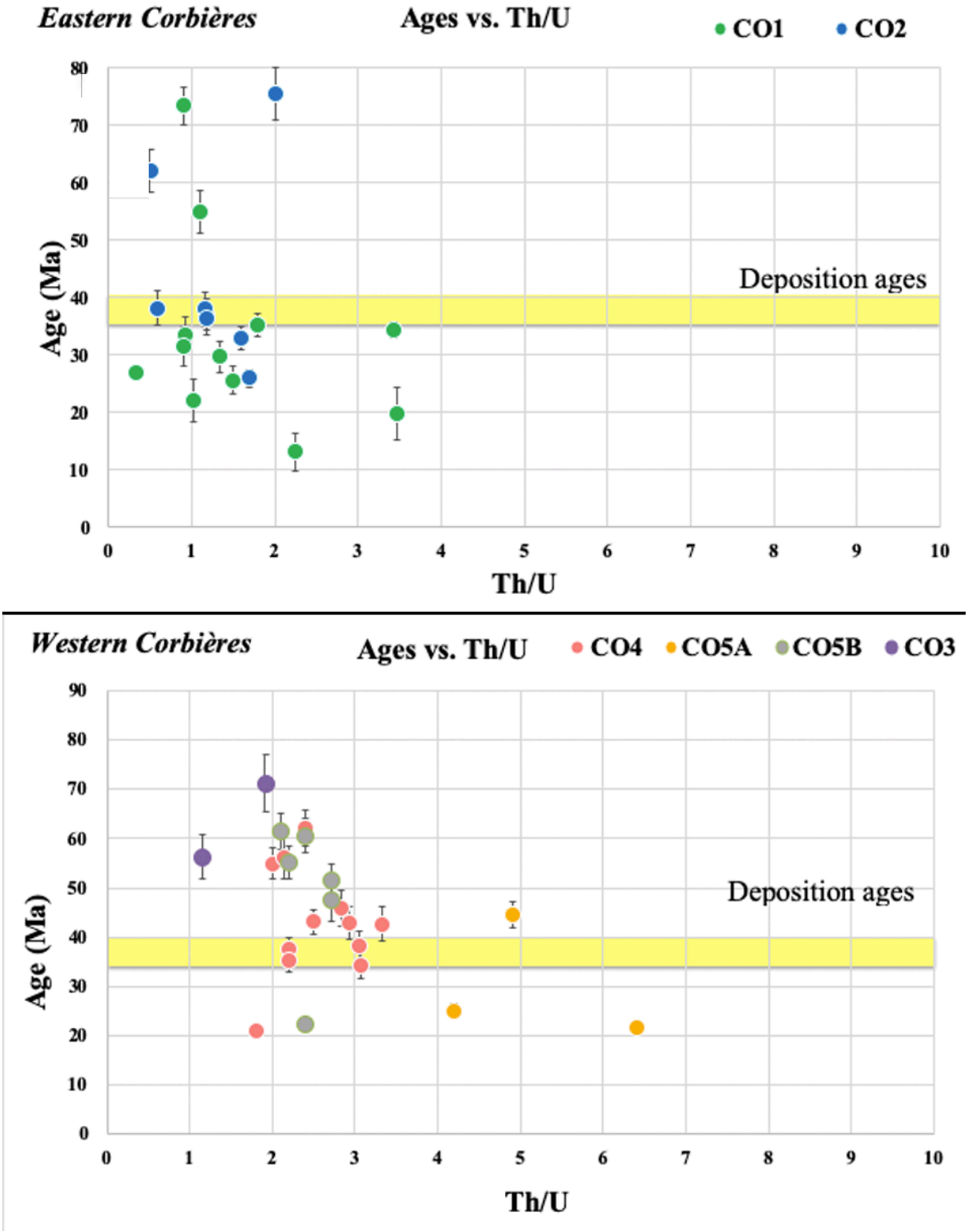

Figure 4: Th/U ratio for samples from the eastern and western part of the Corbières region

Time temperature paths for the samples CO2 and CO3 from the eastern part of the Corbières and sample CO5 from its western part

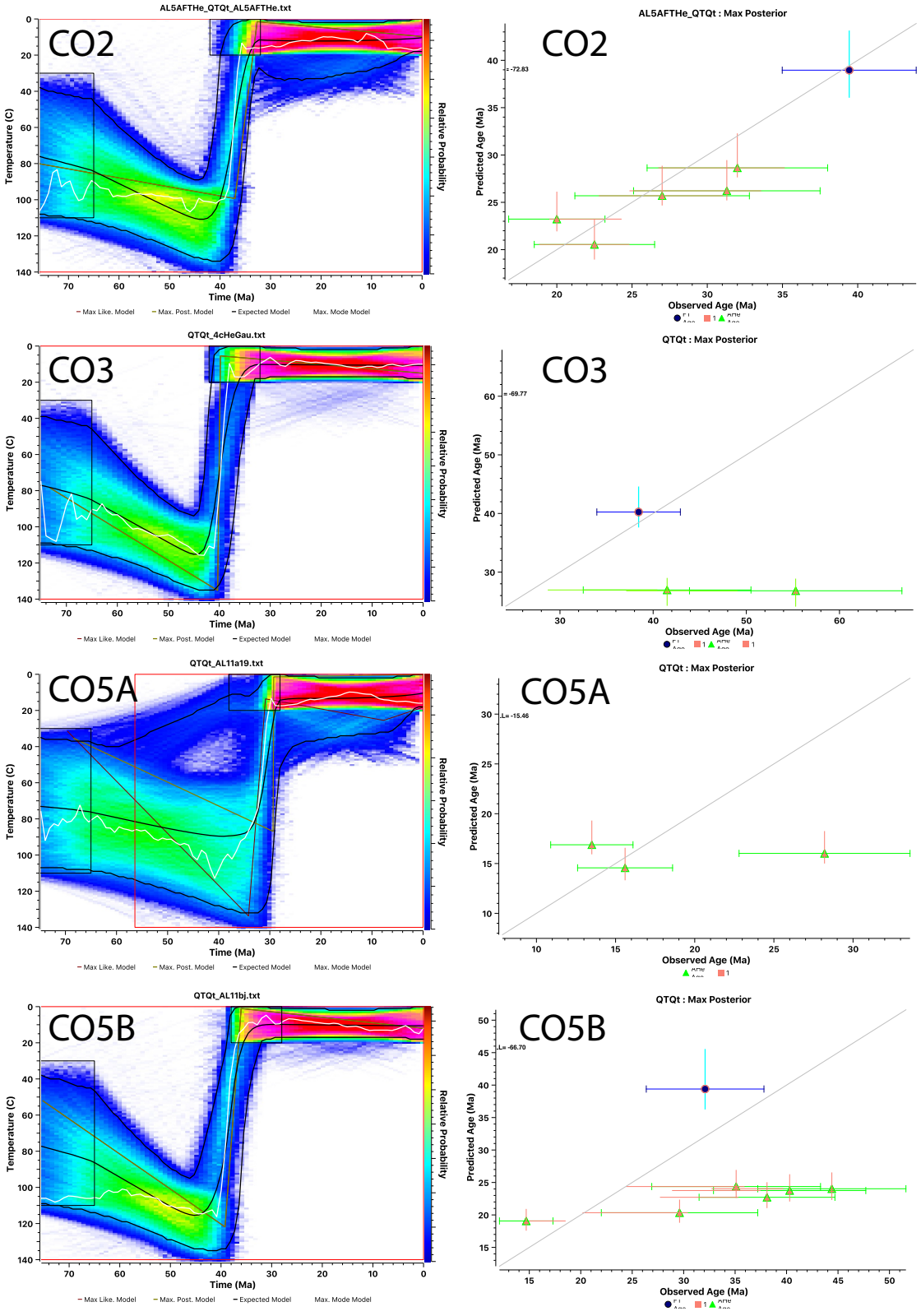

Figure 5: T-t paths for the samples CO2, CO3 and CO5 with their corresponding Predicted vs. observed graphs.

Chapter 5: Origin and dynamics of syn-orogenic deposits in the north Pyrenean foreland basin (France)

Ce chapitre présente les résultats de traçage des sources de la série de Palassou. L'objectif de cette étude est d'identifier les zones sources des sédiments et de reconstruire le remplissage du bassin au cours de l'Éocène. Pour cela, plusieurs approches ont été utilisées, dont le choix est principalement basé sur les données disponibles pour les reliefs autour de notre zone d'étude. La première approche est la datation U/Pb sur zircon, effectuée sur des clastes de granite issues des unités 1 et 2 et sur la matrice de conglomérats des trois unités. Ces résultats, ont été discutés en prenant en compte des données U/Pb dans les Pyrénées, le bloc Corso-Sarde et la Montagne Noire, avant d'être couplés à l'étude sédimentologique présentées dans le chapitre 3 et aux directions de paléocourant mesurées sur le terrain. Dans la partie ouest des Corbières, des analyses de spectroscopie Raman sur des échantillons de flysch noirs ont permis de déterminer des pics de température. Ces températures ont été comparés avec ceux obtenus dans la Zone Nord Pyrénéenne par Clerc et al. (2015). L'interprétation de l'ensemble de ces données a permis de présenter une première étude sur le routage des sédiments syn-orogéniques du Bassin d'Aquitaine.

Une étude pétrographique sur les clastes de granites datés par U/Pb sur zircon est présentée dans les informations supplémentaires de ce chapitre, ainsi qu'une étude bibliographique sur la typologie des granites dans la chaîne pyrénéenne. Les diagrammes concordia pour les datations U/Pb sur zircon obtenus sur les géo-standards « 91500 » et « Plesovice » sont présents dans les informations supplémentaires avec des données détaillées de spectroscopie Raman.

Origin and dynamics of syn-orogenic deposits in the north Pyrenean foreland basin (France)

Al Reda S. M. [1], Barbarand J.[1], Lasseur E.[2], Delpech G. [1], Briais J.[2], Gautheron C.[1], Loget N.[3]*

[1] GEOPS, Université Paris Saclay, CNRS, 91405 Orsay Cedex, France
[2] Bureau de Recherches Géologiques et Minières – BRGM – Orléans
[3] Institut de Sciences de la Terre de Paris – ISTEP UMR 7193 – UPMC

**Corresponding author : mustafa.al-reda@u-psud.fr / mustafa.alreda@gmail.com*

Abstract

Understanding the sediment routing system in a basin allows us to identify the sources of the deposited material and better constrain the exhumation of the belt. The origin and dynamics of the syn-orogenic series of the north Pyrenean foreland basin, known as the Palassou series, have not been fully investigated. The Palassou series (late Ypresian – Priabonian) has been classified into three units based essentially on their content of clasts. The first unit – late Ypresian/Lutetian – is defined by well consolidated conglomerates with boulders sourced mostly in the Meso-Cenozoic sedimentary cover. The second unit – Bartonian – is characterized by a high number of clasts derived from plutonic rocks and the third unit – Priabonian – contains clasts similar to the first unit derived from the Meso-Cenozoic cover. We present here new detrital zircon U/Pb results obtained for granite clasts and conglomerate matrix from the Palassou series. The obtained data have been coupled to new Raman Spectroscopy of Carbonaceous Materials results for black flysch samples, sedimentary analysis and paleocurrent directions. For unit 1, U/Pb results show a Variscan signal and RSCM peak temperatures ranging between 495 and 587°C, reflecting a source from the sedimentary cover in the North Pyrenean Zone. The unit 2 U/Pb results for granite clasts show mostly a 330 Ma age and a more extended Variscan signal compared to the unit 1. Sedimentary analysis shows a larger drainage area during the Bartonian. The changing in the clasts content could be explained by the change in the drainage network caused by the end of inversion in the NPZ and the transition to the Axial Zone crustal stacking. The unit 3 U/Pb results show a wider and varied signal for granite clasts and matrix samples. The U/Pb signal and the location of the unit 3 samples near the central Pyrenees reflect the increase of the drainage area covering the central and eastern parts of the Pyrenees as they were exhumed during the Priabonian.

Introduction

Tracking of the origin of sediments deposited in a basin allows us to understand their dynamics from their source to sink and the link between exhumed domain and sedimentation areas and the corresponding routing systems (Whitchurch et al., 2011; Yang et al., 2013; Roigé et al., 2016). The analysis of sediment provenances using zircon U/Pb geochronology has been shown as a powerful tool for reconstructing ancient drainage network and relate it to the development of the belt (Gehrels et al. 2011; Thomas 2011; Saylor et al. 2013). Detrital zircon U/Pb method has been widely used in various geologic contexts because of the widespread occurrence of zircon grains in detrital sediments, the fast analysis time and the accuracy of the results (Fernández-Suárez et al. 2014; Gehrels 2014; Linnemann et al. 2014; Hart et al. 2016). The application of this method to track sources of detrital sediments in the basin requires a knowledge about the ages of the possible source areas in the surrounding reliefs (Gehrels 2014).

The Pyrenean mountain belt (France, Spain) resulted from the collision between the Iberian and European plates started during the Late Cretaceous (Mouthereau et al., 2014). Two flexural foreland basins are developed on both sides of the belt, a pro-foreland basin in the south and a retro-foreland basin in the north (Willett, et al. 1993). The timing of exhumation of the Pyrenean massif as provided by low temperature thermochronology is a key data to recompose the sediment routing system. As extensive structural, kinematical, thermochronometric and geochronometric studies have been conducted on the Pyrenees, they constitute a great opportunity to explore the basin content and provide the source to sink system evolution over time.

Our study focuses on the north Pyrenean foreland basin, in particular its eastern side, where syn-orogenic sediments crop out. The transition from underfilled to overfilled basin started during the Ypresian (Plaziat, 1984) contemporaneous to the major phase of exhumation of the Pyrenees. It is illustrated by depositional environments changing from marine to continental with the sedimentation of the Palassou conglomerate continental unit. The Palassou series is a key point to better constrain the sources of the deposited material in the eastern part of the Aquitaine Basin, known as the Corbières region (France), and to reconstruct the infilling of the basin according to the drainage areas that delivered sediments.

The Palassou series in the north Pyrenean foreland basin have been poorly studied in terms of sediment routing system and sedimentary infilling (Ovtracht and Lenguin, 1977; Crochet, 1989). This series is classified into three tectono-sedimentary units of which the first

one - late Ypresian/Lutetian - contains clasts essentially divided from the Meso-Cenozoic cover, the unit 2 – Bartonian - contains a high number of clasts derived from a basement source, and the unit 3 contains the same source of clasts as the unit 1, derived from the Meso-Cenozoic cover. We present in this study new detrital zircon U/Pb ages obtained for the sandstone matrix in the units 1, 2 and 3, and for granite clasts from the units 2 and 3. Raman Spectroscopy of Carbonaceous Materials (RSCM) results obtained for 4 clasts of black flysch from the basin are presented in this paper. Results have been coupled to sedimentary analysis and paleocurrent direction determinations in order to constrain the source of the deposited material.

Geological context

The development of the Pyrenees is preceded by a pre-collision history characterized by an Albian - Coniacian (110 – 86 Ma) rifting phase that led to hyperextension and localized mantle exhumation (Clerc and Lagabrielle 2014). A HT-LP metamorphism (Albian – Santonian (Albarède and Michard-Vitrac, 1978; Montigny et al., 1986)) accompanied the rifting phase and affected the Mesozoic cover of the NPZ. Metamorphism temperatures were estimated using Raman spectroscopy of the carbonaceous material (RSCM). They are around 300 to 400°C in the western part of the North Pyrenean Zone (NPZ) and >450°C in the central and eastern part of the NPZ (Clerc and Lagabrielle 2014).

The Pyrenees constitutes a doubly vergent orogenic belt subdivided into five distinct structural domains: the Aquitaine Basin, the North Pyrenean Zone, the Axial Zone, the South Pyrenean Zone and the Ebro Basin, from the north to the south respectively (Figure 5.1). The Aquitaine Basin represents the retro-foreland basin of the belt and contains essentially syn- to post-orogenic deposits. It is separated from the North Pyrenean Zone (NPZ) by the North Pyrenean Frontal Thrust (NPFT). The NPZ is characterized by north-vergent reverse faults, exhuming Paleozoic basement rocks including granitic bodies (Agly, Ansignan, Trois Seigneurs, Lacourt, Foix and Ercé), highly deformed Mesozoic deposits, Paleocene and lower Eocene cover rocks (Figure 5.1) (Souquet 1986; Roure et al. 1989; Deramond et al. 1990). The North Pyrenean Zone is separated from the Axial Zone by the North Pyrenean Fault (NPF) (Muñoz, 1992). The Axial Zone (AZ) consists of Paleozoic rocks affected by LP-HT metamorphism during the Variscan orogeny and deformed by compressional events during the Late Carboniferous. Basement rocks are represented by the Early Cambrian and the Ordovician gneiss bodies (orthogneiss: Aston-Hospitalet, Roc-de-France, Cap-de-Creus, Albera and Canigou massifs; Deloule et al. 2002; Cocherie et al. 2005; Castiñeiras et al. 2008; Denele et

al. 2009; Casas et al. 2010; Liesa et al. 2011; Martínez et al. 2011; Casas et al. 2015; Padel et al. 2018) and Variscan plutonic rocks (Agly, Quérigut-Millas, Foix, Hospitalet, Trois Seigneurs, Maladeta, Bassiès (Zwart, 1962; Zwart and De Sitter, 1979; Respaut and Lancelot, 1983; Gleizes et al., 1998; Olivier et al., 2008; Aguilar et al., 2014; Denèle et al., 2014; Olivier et al., 2016; Vacherat et al., 2017). The AZ is bounded to the south by the South Pyrenean Zone (SPZ) characterized by south-vergent faults translating the Mesozoic and the Cenozoic deposits above the Triassic evaporites (Puigdefàbregas et al., 1992; Thomson et al. 2017) (Figure 5.1). The SPZ terminates by the South Pyrenean Frontal Thrust (SPFT) where the Ebro Basin starts.

The earliest stages of convergence in the Pyrenees occurred from 83 to 71 Ma and are characterized by a slow cooling according to low temperature thermochronology results (Vergés et al., 1995a; Mouthereau et al., 2014). By the middle Campanian, the European and Iberian crusts are in contact and this results in the development of an early orogenic edifice with low relief (Ternois et al., 2019). The main exhumation phase was occurring in the early Eocene due to the continent-continent collision. The NPFT accommodated shortening resulting in the uplift of the NPZ, before shortening being progressively transferred southward to the Axial Zone during the Bartonian and to the South Pyrenean foreland basin (Yelland, 1991; Fitzgerald et al., 1999; Sinclair et al., 2005; Maurel et al., 2008; Mouthereau et al., 2014; Ford et al., 2016; Vacherat et al., 2016; Ternois et al., 2019).

The last stage of development of the Pyrenees during the late Oligocene is associated with the rifting phase of the Ligurian-Provençal basin that spaced the Corsica-Sardinia block from the Pyrenees and leaded to the opening up of the Gulf of Lion (Malusà et al 2016).

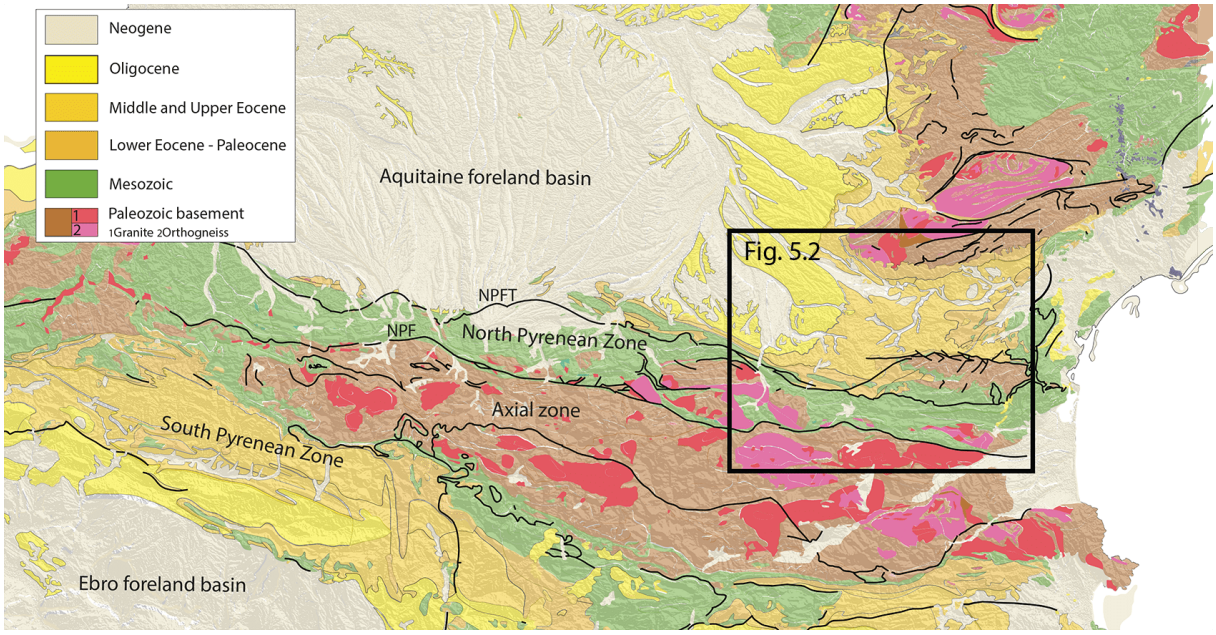

Figure 5.1: Geologic map of the Pyrenean mountain belt and the north retro-foreland basin (Aquitaine

Basin) and the location of the Corbières region (black frame). NPTF: North Pyrenean Frontal Thrust, NPF: North Pyrenean Fault.

The stratigraphy of the Aquitaine Basin

The Aquitaine Basin evolved as a passive margin until the opening of the bay of Biscaye during the lower Cretaceous (Biteau et al., 2006). From the second half of the Late Cretaceous, early orogenesis resulted in the infilling of the Early Cretaceous rifted basin to the east of the Pyrenees with turbidites to continental deposits and followed by Palaeocene red beds and Thanetian to Ypresian shelf platform carbonates (Plaziat, 1981; Martín-Martín et al., 2001; Christophoul et al. 2003) (Figure 5.1). The main exhumation phase of the Pyrenees is recorded in the basin by the deposition of alluvial and fluvial deposits starting at the late Ypresian known as the Palassou conglomeratic series (Buis and Rey, 1975; Ford et al., 2016). Outcrops of these series are well preserved on the eastern part of the Aquitaine Basin, the Corbières region; westward, these deposits are buried below the Oligocene to Pliocene post-orogenic units. The Palassou series is composed of three depositional units of late Ypresian to Priabonian ages (Crochet, 1989) with thicknesses around 600 to 700 m each (Figure 5.2). The three tectono-sedimentary units have been classified following the nature of the clasts observed in the conglomerates (Crochet, 1989) (Figure 5.2). Stratigraphic attributions have been defined by Plaziat (1984) and Crochet (1989). The first unit – late Ypresian to Middle Lutetian - is defined by well-consolidated conglomerates with boulders sourced mostly in the Meso-Cenozoic carbonate sedimentary cover (Figure 5.2). The second unit, of Bartonian age is characterized by a high proportion of clasts derived from plutonic rocks, essentially granitic clasts. The third unit deposited during Priabonian time, is similar to the first unit with carbonate and sandstone clasts derived mainly from the Meso-Cenozoic cover (Figure 5.2). Due to post-deposition evolution of the area, these three units are presently outcropping from east to west in the Corbières region (Figure 5.2).

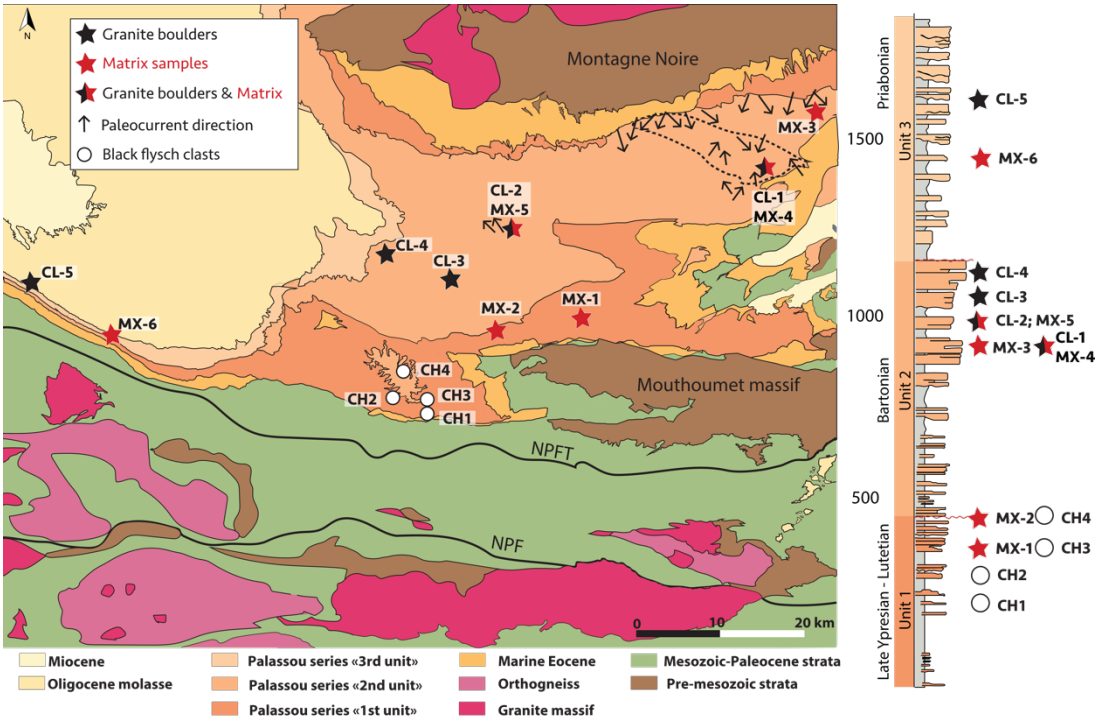

Figure 5.2: Geological map of the eastern part of the Aquitaine Basin including the Corbières region and the location of the collected samples, as well as paleocurrent directions measured in the field and from Chaigne (1964).

Low temperature thermochronology records in the Pyrenees

Low temperature thermochronology studies of the NPZ and the AZ rocks reveal the phases of orogenic development of the Pyrenean domain. Zircon (U-Th)/He ages in the eastern part of the NPZ, in particular in the Agly massif, recorded a cooling phase around 75 Ma interpreted as an early orogenic phase (Yelland, 1991; Ternois et al., 2019). This event is followed by the main exhumation of the orogen occurring from the late Ypresian to the Oligocene and characterized by basement cooling and a rapid thrust propagation (Yelland, 1991; Morris et al., 1998; Fitzgerald et al., 1999; Sinclair et al., 2005; Rushlow et al., 2013). Apatite and zircon fission track and (U-Th)/He results show more recent cooling ages from north to south (Yelland, 1991; Sinclair et al., 2005; Maurel et al., 2008; Gunnell et al., 2009; Mouthereau et al., 2014; Vacherat et al., 2016) and from east to west (Fitzgerald et al., 1999).

Sampling and methodology

Sampling of granite clasts, conglomerate matrix and black flysch clasts

Two groups of samples have been collected assuming present-day location: three samples are located close to the Montagne Noire (CL-1, MX-3 and MX-4) and the others in the southern part of the basin.

Five samples of granite clasts have been collected in the second and the third unit of the Palassou series. Samples CL-1, CL-2, CL-4 and CL-5 represent two to four granite pebbles (7-10 cm) of medium grain size, and sample CL-3 is a single boulder (20 cm in length). The location of the samples is shown on the geologic map of the Corbières region and in the stratigraphic log of the three syn-orogenic units (Figure 5.2).

Six sandstone samples, of 5 to 8 kg each, have been recovered from the matrix of the conglomerates. Sample MX-1 is collected from unit 1; sample MX-2 is collected at the transition from unit 1 to unit 2; samples MX-3, MX-4 and MX-5 are collected from unit 2 (Figure 5.2) and sample MX-6 is collected from unit 3. For two sites, boulders and matrix are available (CL-1 & MX-4 and CL-2 and MX-5) (Figure 5.2).

Four clasts of black flysch, of 1 to 2 kg each, have been collected from the transition between units 1 and 2 to the west of the Mouthoumet massif (Figure 5.2).

Methodology

Paleocurrent directions have been measured in channel beds of fluvial fan and fluvial deposits depositional environments for the first and second units of the Palassou series (Prieur et al., in prep). These paleocurrent directions are compiled with other directions measured in the north-eastern Corbières region by Chaigne (1964).

Samples have been crushed and sieved with a 400 μm mesh before being separated using heavy liquids (bromoform). Zircon crystals ranging between 80 and 350 μm in size have been recovered after separation using a Frantz magnetic separator, handpicked, mounted in epoxy and polished to expose their surface for laser ablation. Sample preparation was carried out at the GEOPS laboratory (Université Paris Saclay, Orsay, France). Scanning Electron Microscope (SEM) coupled to a Variable Pressure Secondary Electron (VPSE) images are performed using a Zeiss SUPRA 55VC at the Institut de Sciences de la Terre de Paris (Sorbonne Université). SEM analysis have been made before and after laser ablation in order to better visualize the ablated zone.

Uranium, thorium and lead isotopes were analysed using a ThermoScientific Element

XR HR-ICPMS spectrometer coupled with a Photon Machines Teledyne Laser Excimer ArF 193 nm. The laser was operated at a repetition rate of 10 Hz, with an ablation time of 30s, spot of 40 μm and a fluence of 2.5 J.cm^{-2}. Calibration for zircon analyses was carried out using the geostandard 91500 zircon (Wiedenbeck et al., 1995), which was probed every 12 analyses, and quality control was achieved for most samples using the Plesovice standard (337±1 Ma) (Sláma et al., 2008). The obtained U/Pb age of the 91500 zircon is 1065±3 Ma, with a total of 138 analyses, and 337±1 Ma for Plesovice zircon with a total of 77 analyses (see the supplementary information for more details). As there is no general agreement about the minimum number of grains that should be analysed, and because in most of the zircon U/Pb analysis on plutonic rocks, a minimum number of 20 grains were ablated, we have targeted 20 to 40 grains for U/Pb analysis for granite clast samples. For matrix samples, a minimum of 70 grains are analysed in order to identify a peak signal, depending on the abundance of suitable size of zircon crystals (>100 μm length). Low amount of ^{204}Pb obtained during the analysis demonstrates that very little common lead has been recorded (averaged ^{204}Pb ~ 700 counts/second). Data reduction was done with GLITTER software package (Van Actherbergh, 2001) by filtering time resolved signal to remove disturbed ratios. The resulted plots are generated using IsoplotR (Vermeesch, 2018) following the concordant age treatment of Ludwig (1998).

Raman spectroscopy has been used to characterize the structural evolution of carbonaceous material. The Raman spectrum reflects the transformation from disordered to well-ordered material during metamorphism (Wopenka and Pasteris, 1993), and this allows the determination of peak temperatures attained by metamorphic rocks (Beyssac et al., 2002). In this study, Raman analysis were performed using a Renishaw InVia Reflex spectrometer coupled to 3 output laser power of 514.5, 632.8 and 785 nm at the BRGM-Orléans (France). The output laser power reached the surface of the sample through a Leica DM2500 microscope with a x50LW objective. Edge filters eliminated the Rayleigh diffusion and the Raman light was dispersed before being analysed by a Peltier-cooled CCD NIR/UV deep depletion 1024x256 pixels detector. Measurements were done on polished thin sections.

Results

Petrography of the boulders

All granite clast samples are white and display similar macroscopic mineralogy. The mineral composition of granite clasts samples has been determined using optical petrography.

Samples CL-1, CL-2, CL-3, CL-4 and CL-5 are built by quartz, potassium feldspar, plagioclase, muscovite and biotite minerals and are leucogranites (Figure 5.3). Two types of leucogranite are determined from thin section analysis, a one-mica leucogranite containing biotite (samples CL-1, CL-3 and CL-4) and a two-mica leucogranite containing biotite and muscovite (CL-2 and CL-5).

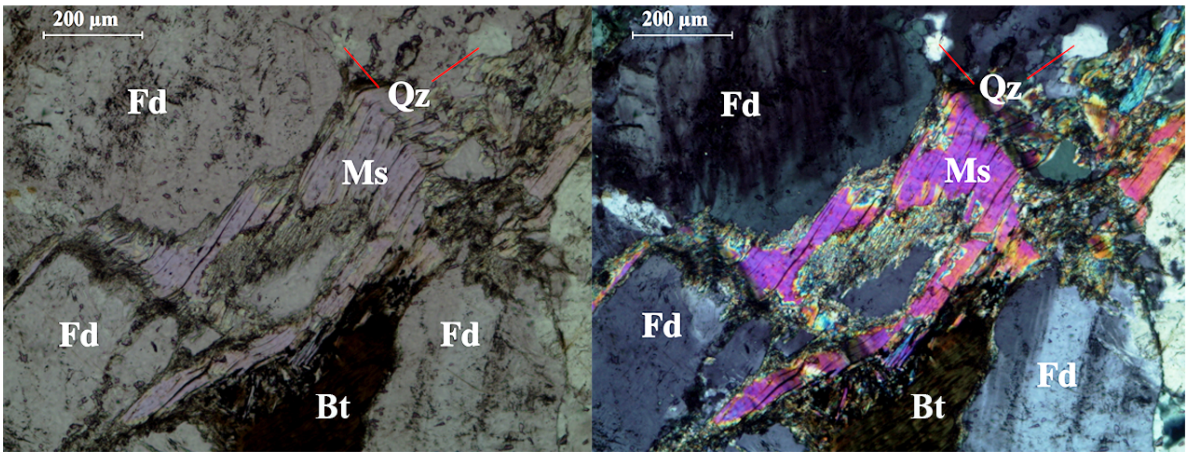

Figure 5.3: Mineralogical main contents of the thin section of the sample CL-5 observed using plane polarized (on the left) and cross-polarized (on the right) lights of optical microscope. Qz: Quartz, Fd: Potassium feldspar, Pg: Plagioclase, Ms: Muscovite and Bt: Biotite.

SEM analysis

Zircon grains are transparent or yellowish and have lengths ranging between 80 and 300 µm for the five analysed samples of granite clasts (CL-1, CL-2, CL-3, CL-4 and CL-5). Crystals have mostly prismatic shape and well-preserved pyramidal termination except for the sample CL-5 where a large number of grains are slightly rounded. More than 600 zircon grains from granite clasts and conglomerate matrix samples have been analysed using SEM. SEM coupled to a Variable Pressure Secondary Electron (VPSE) images show euhedral zircon grains with double-ended prismatic shape when unbroken, a bright core with a magmatic zoning surrounded by darker oscillatory zoning (Fig. 5.4a, b and c). Some zircon grains show micro-inclusions. Recrystallisation of the core of zircon crystals is rarely observed and only for sample CL-3 (Fig. 5.4d). Such zircon crystals have not been analysed.

Zircon U/Pb ages of granite clasts

39 grains have been analysed for the sample CL-1 of which 24 are concordant. 6 of

concordant ages have been rejected due to the laser spot location close to micro-inclusions and fractures in the crystals. The Wetherill plot for sample CL-1 show a Concordia age of 330±2 Ma (n=18; MSWD=0.28) (Figure 5.5). Only 10 concordant ages over 42 are obtained for the sample CL-2 with a Concordia age of 324±2 Ma (n=10; MSWD=3.7) (Figure 5.5). Sample CL-3 show 18 concordant ages over 39 and an age of 304±2 Ma (n=14; MSWD=2.9) (Figure 5.5). Sample CL-4 show 38 concordant ages over 54 and a Concordia age of 335±1 Ma (n=38; MSWD=1.8) (Figure 5.5). Sample CL-5 show 29 concordant ages over 47. Results for this sample show three groups of ages, the first one ranging from 300 to 380 Ma, the second one from 430 to 500 Ma and the third one from 540 to 600 Ma (MSWD= 0.091) (Figure 5.5). Such MSWD indicated that the observed scatter in the ages is less than that *expected* by the analytical uncertainties. In this case, the data are considered to be "under-dispersed", indicating that the analytical uncertainties were overestimated. This dispersion might be related to different sources for the 7 boulders analysed for this sample although macroscopic and microscopic characterizations do not evidence any variation between boulders from the same sample.

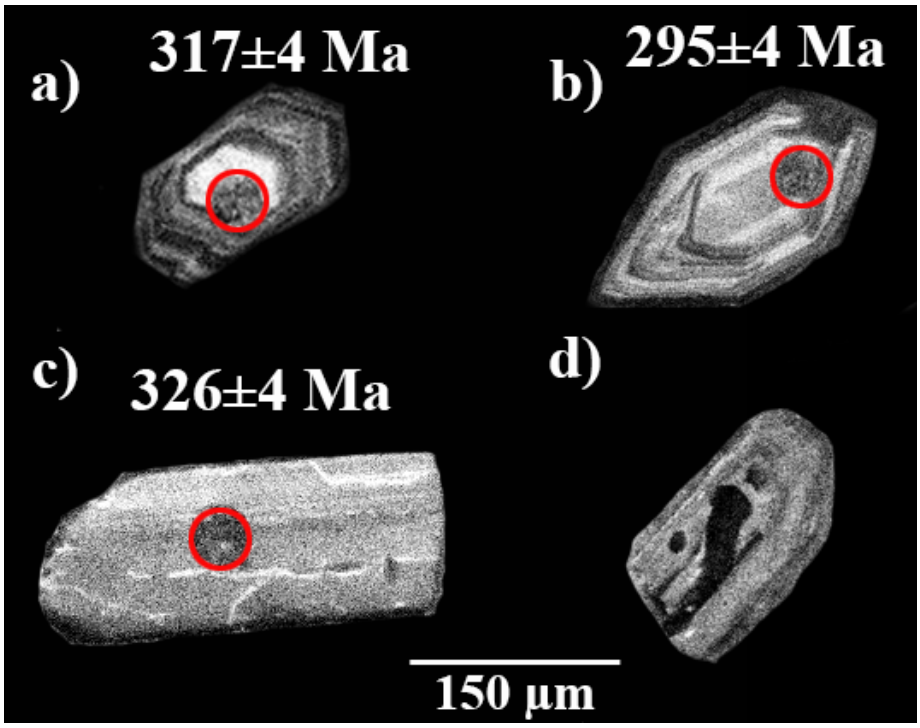

Figure 5.4: SEM-CL image of representative zircon grains analysed in this study. a) and b) are oscillated zircon grains from the samples MX-1 and MX-2 respectively. Zircon crystal in c) is a non-oscillated grain abundant in this study and d) is a recrystallized zircon core. Both grains in c) and d) are from the sample CL-3

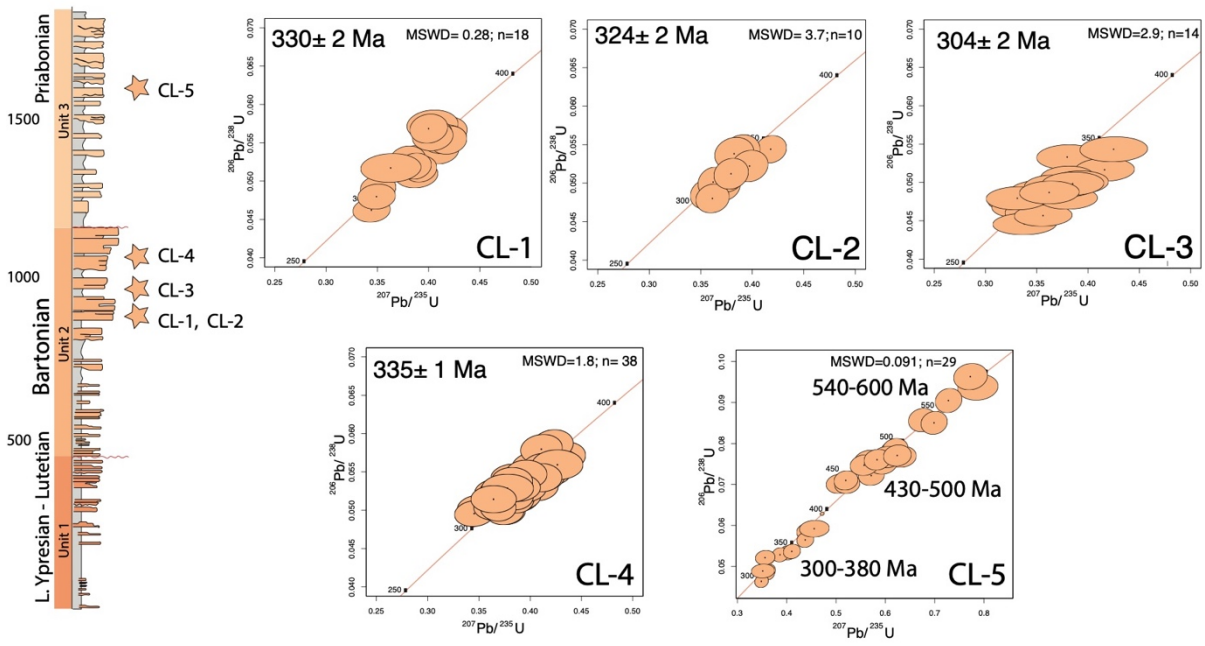

Figure 5.5: U/Pb zircon ages for granite clasts from the Palassou deposits in the Corbières region with their corresponding location on the stratigraphic log. Errors on ages are 1 sigma.

Zircon ages of conglomerate matrix

Detrital zircon U/Pb results are summarized as Kernel Density Estimates (KDE) and histograms in Figure 5.6 (Vermeesch, 2018). Analysed samples have been binned into groups reflecting the most significant components of the distribution divided as follows: Permian-Triassic (200-290 Ma), Late Variscan (290-310 Ma), Early Variscan (310-340 Ma) (Hoÿm de Marien et al., 2019), Pre-Variscan (340-420 Ma), Caledonian (420-520 Ma) (McKerrow et al., 2000), Cadomian-Pan African (520-700 Ma) (Linnemann et al., 2014), Neoproterozoic (700-900 Ma), Kibaran (900-1200 Ma), Mesoproterozoic (1200-1500 Ma), Paleoproterozoic (1500-2400 Ma) and Archean (2400-4000 Ma) (Thomson et al., 2017). 171, 132, 74, 120, 125 and 69 zircon crystals have been analysed for the samples MX-1, MX-2, MX-3, MX-4, MX-5 and MX-6 respectively. Obtained ages for detrital zircon grains are reported as percentages in the Table 5.1. The highest percentage of zircon ages for the samples MX-1 and MX-2 is 33% and 40% respectively and corresponds to ages from 310 to 340 Ma. A percentage of 51% is the highest one observed for sample MX-3 and refers to ages from 520 to 700 Ma. For sample MX-4, results show a dominant percentage of 41% corresponding to the same range of ages. Sample MX-5 has 28% as highest percentage of zircon ages from 340 to 420 Ma and the last sample MX-6 has 33% as highest percentage of zircon ages between 520 and 700 Ma.

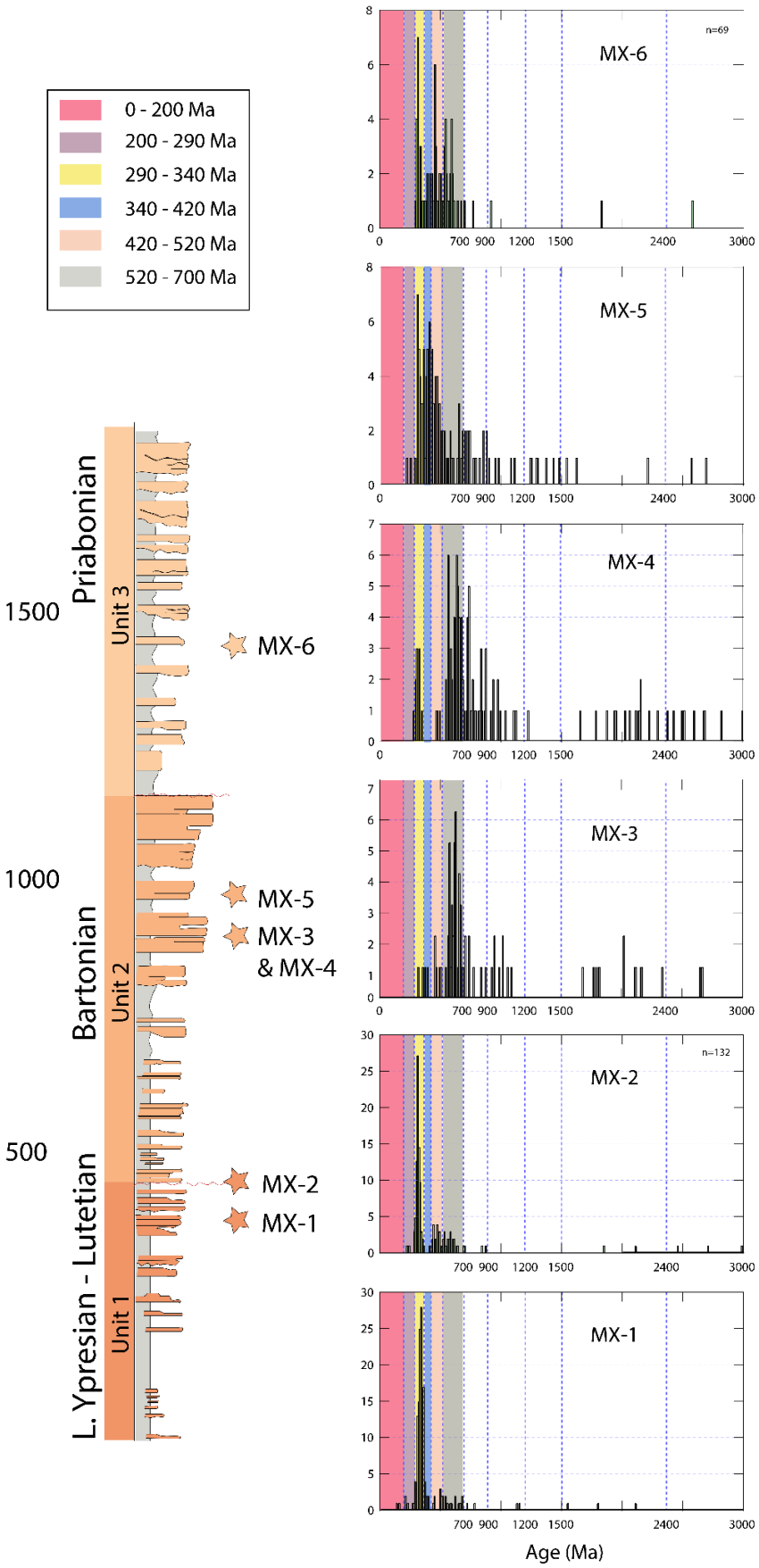

Figure 5.6: zircon U/Pb ages for sandstone matrix samples from the first and second unit of the Palassou series.

Paleocurrent directions and geometry of alluvial systems

Paleocurrent directions have been measured in the north-eastern part of the Corbières region, in a fluviatile proximal depositional environment near to the location where the samples CL-1 and MX-4 are collected. These paleocurrent directions have been combined with others from Chaigne (1964) in the same area and show that most of them are going towards the north and the north-west as shown in Figure 5.2. More to the north, near to the location of the sample MX-3, paleocurrent directions from Chaigne (1964) show a southward directed sediments and a mixing zone of opposite paleocurrent directions (Figure 5.2). Given the paleocurrent directions, sediments seem to have different sources, from the north for sample MX-3 and from the south for the samples MX-4 and CL-1. In the zone between these samples, southward and northward paleocurrent directions are measured indicating a mixed paleocurrent directions area. The paleogeographic position of sample MX-3 to the south of the Montagne Noire is consistent with a different source compared to the rest of the samples located closer to the Pyrenees.

The source area of samples CL-1, MX-3 and MX-4 must be the Montagne Noire, as it is the only relief located to the north of the Corbières region. A compilation of U/Pb ages in the Montagne Noire is represented in Figure 5.7. Most of the ages are in the Axial Zone and show a Variscan age. The southern flank of the Montagne Noire is characterized by sedimentary rocks ranging between the Early Cambrian and the Visean periods, and the northern flank is characterized by sedimentary rocks ranging between the Early Cambrian and the Silurian (Figure 5.7). Paleozoic sediments in the southern part of the Montagne Noire host Neoproterozoic – Early Cambrian (Cadomian) U/Pb ages that are sourced from the Gondwana, to the South of the French Massif Central and transported northward by a river drainage network as demonstrated in Lin et al. (2016). Such ages fit well with the Cadomian signals obtained for the samples located in the north-eastern part of the Corbières region (MX-3 and MX-4). In addition, the signals obtained for these samples is larger than those obtained for the samples MX-1, MX-2, MX-5 and MX-6 (Figure 5.6).

Outcrop analysis for the unit 1 deposits show four sedimentary systems with an increasing size and geometry from east to west demonstrating a growing amount of sediments transported to the basin (Prieur et al., submitted). The unit 2 deposits are characterized by coarser sediments and a progradation toward a fluvial depositional environment interpreted as the distal part of an alluvial fan (the alluvial fan location is where samples CL-2 and MX-5 were collected). Paleocurrent directions measured in the alluvial fan deposits are going toward the north-west.

RSCM results

Raman spectroscopy results obtained for four clasts of black flysch are presented in Table 5.2. Peak temperatures and their corresponding uncertainties are estimated using the RSCM method described in Beyssac et al. (2002). The analysis shows a well-ordered carbonaceous material with mean peak temperatures ranging from 495 to 587°C.

Petrography of the granite clast samples

The petrography of the granite clasts samples consists essentially of quartz, potassium-feldspar, microcline, plagioclase, biotite and muscovite. All samples reveal low abundance of mica crystals and have a similar composition. As the petrography of the clasts evidences the dominant presence of leucogranites, we have compiled leucogranite massifs in the eastern and central Pyrenees. Leucogranites types similar to the those collected in the Palassou conglomerates are widely distributed throughout the Pyrenees. Olivier et al. (2004) mentioned, in the Agly massif, the presence of two-mica granite in various places. The Saint-Arnac granite in the eastern part of the Pyrenees contains also various spots of two-mica granite (Olivier et al. 2008), in addition to the Ax-les-thermes massif (Mezger 2010; Denèle et al. 2014) and the Maladeta massif in the central Pyrenees (Michard-Vitrac et al. 1980) (Figure 5.7). In all, leucogranite are widespread in the Pyrenean massif but are not the only type of granite existing in this area. Granodioritic-tonalitic granite, monzogranite, porphyritic monzogranite, and biotite calc-alkaline granite are also widespread in the Pyrenean massifs near to the Corbières region (Fourcade and Allegre, 1981; Leterrier, 1972). However, none of the clasts in the basin shows a similar petrography. The compilation of U/Pb ages in the Pyrenean massifs (Figure 5.7) show that most of the ages are late Variscan, ranging from 298 to 313 Ma.

Discussion

Zircon U/Pb ages for the Palassou deposits are ranging from ~290 to ~600 Ma for granite clasts, with only one late Variscan age obtained for sample CL-3 (304±15 Ma) while the ages obtained for samples CL-1, CL-2 and CL-4 are ranging between 320 and 330 Ma. This result was not expected as most of the Variscan Pyrenean massifs have late Variscan ages (Figure 5.7). This peculiar 320-330 Ma range might track specific lithologies and sources areas discussed below. For zircon grains collected in the sand matrix, and for the granite clast sample CL-5, ages are much more scattered ranging from 290 Ma to 3 Ga containing three main modes:

Variscan (290-340 Ma), Caledonian (420-520 Ma) and Cadomian-Panafrican (520-700 Ma). Provenance, origin of the lateral and vertical variations observed in the data and the regional variations of the source across the whole Palassou unit will be discussed in the light of the geology of the surrounding areas. Finally, a reconstruction of the source to sink system in the eastern Pyrenees is proposed.

Potential sources of the 320-330 Ma ages

The potential origins of the 320-330 Ma ages are reviewed by searching for Variscan ages in the Pyrenees and the Corsica-Sardinia block. Paleocurrent directions measured in the Palassou sediments from the southern domain of the studied area indicate a south to south-east origin. The Pyrenean belt is considered as a potential source area for the granitic boulders, as the range was emerging during the deposition of the Palassou series. Basement rocks outcropping in the central and eastern Pyrenees host mainly Variscan magmatic rocks having ages ranging from 298 to 335 Ma, most of them between 298±2 and 313±13 Ma (late Variscan) (Figure 5.7) (Respaut and Lancelot, 1983; Olivier et al., 2008; Aguilar et al., 2014; Denèle et al., 2014; Vacherat et al., 2017). Abundance in the chain of late Variscan ages of granitic massifs, and large presence of boulders with 320-330 Ma ages in the basin, question the lithological selection of the source to sink system (Figure 5.7) and require the analysis of possible other sources.

Corsica-Sardinia block located eastward of the studied area might represent a potential candidate for the sources of sediments in the basin. A compilation of zircon U/Pb ages obtained for this block is investigated in order to check this hypothesis. Sardinia and Corsica represent a segment of the Southern European Variscan belt extended from the Axial Zone in Corsica and northern Sardinia (Figure 5.8) to the External Zone in south-western Sardinia (Carmignani et al., 1994) (Figure 5.8). The crystalline basement of the Sardinia-Corsica block is formed in the Early Carboniferous as a result of the collision between northern Gondwana and southern Armorica continents. Petrography of the basement of Corsica includes biotite-monzogranites and leuco-monzogranites (Gaggero et al. 2017) and is similar to some rocks sampled in the Corbières basin. Zircon U/Pb ages are ranging from 295 to 360 Ma (Ferrara et al. 1991; Di Vincenzo et al., 2004; Giacomini et al., 2005; Giacomini et al. 2006; Giacomini et al. 2008; Cortesogno et al. 2004; Palmeri et al. 2004; Helbing and Tiepolo 2005; Oggiano et al. 2010; Carosi et al. 2012; Casini et al. 2012; Pavanetto et al. 2012; Padovano et al. 2014; Cuccuru et al. 2016; Malusà et al., 2016; Gaggero et al. 2017). In Sardinia, two ages (between 320 and 330 Ma) are available as shown in the compilation in Figure 5.8.

Four ages ranging from 329 to 337 Ma in north Corsica and two ages of 321±8 and 330±14 Ma in north Sardinia fit well the ages obtained in this study (Figure 5.8). However, the structural and kinematic evolution of the Corsica-Sardinia block during the Pyrenean orogeny indicates that the location of the block is far from the Corbières region (Lacombe and Jolivet, 2005, Malusà et al., 2016). Frasca et al., (submitted) suggest that the Corsica-Sardinia block during the Bartonian was disconnected from the retro-foreland basin due to the emergence of the easternmost part of the Pyrenees, actually buried below the sediments of the Gulf of Lion. Furthermore, no major tectonic event that could deliver such an amount of sediment occured in the Corsica-Sardinia block at the Bartonian, and the opening of the Gulf of Lion started later during the Oligocene time (Lacombe and Jolivet, 2005). All these reasons have led to the exclusion of this block as a possible source of sediments.

The paleocurrent directions measured in the alluvial fan depositional environment of the unit 2 are directed to the north-west. The Pyrenean range appears thus as the ideal main potential source of the boulders collected in the Palassou deposits. Compilation of U/Pb ages in the Pyrenean belt (Figure 5.7) lists only few massifs having 320-330 Ma ages: this includes the Bossòst and Aston-Hospitalet massifs (324±2 and 334±6 Ma, Mezger and Gerdes (2016)) and Ax-les-thermes (321±7 Ma, Denele (2007)) in the central part of the Pyrenean Axial Zone. But also, the Mesozoic strata should be considered to know whether it is a potential source of the deposits or no. The existence of an Upper Mississipian igneous activity in the Axial Zone is however debated. Mezger and Gerdes (2016) and Mezger and Régnier (2016) interpret these ages as a first phase of a LP-HT event and propose the existence of two separate magmatic events or a single event diachronic across the Pyrenean domain. On the contrary many other studies interpret the 290 to 310 Ma range of ages as the single Variscan LP-HT event in the Pyrenees (Aguilar et al., 2014; Denèle et al., 2014; Druguet et al., 2014; Esteban et al., 2015), and argue for an inherited component for the 330 Ma ages (Denèle et al. 2014; Lopez-Sanchez et al., 2018). In general, on the European scale, the Early Variscan phase is illustrated as a part of the Variscan orogeny as demonstrated in Central Europe by Franke (2006). The obtained U/Pb ages in this study, seem to be sourced from the Pyrenees, in particular from the Axial Zone (325 and 335 Ma U/Pb ages, Figure 5.7).

Sources are much more widespread for boulders with a ~300 Ma age as for sample CL-3 (304±15 Ma). Similar ages have been measured in the Céret massif in the eastern part of the Axial Zone (307±4 Ma; Figure 5.7 (Aguilar et al., 2014)), Andorra- Mont Louis (Maurel et al. 2004; Denèle et al. 2014), Carança (Denèle et al., 2014) and Ercé (Vacherat et al., 2017) massifs in the central part of the Axial Zone having U/Pb ages of 305±5 (Maurel et al. 2004), 305±1

(Denèle et al., 2014) and 306±2 Ma (Vacherat et al., 2017) respectively (Figure 5.7); in addition, Quérigut-Millas and St Arnac-Agly massifs in the eastern part of the NPZ have ages of 307±2 (Roberts et al. 2000) and 308±1 Ma (Olivier et al., 2008) respectively (Figure 5.7).

Potential sources of the Caledonian and Cadomian ages

The Cadomian-Panafrican signature represents the second population recorded by the samples in the matrix (MX-3, MX-4 and MX-6) and in the boulders (CL-5). A Cadomian-Panafrican signature can be related to Cadomian rocks observed regionally but also to Paleozoic sedimentary rocks that have been sourced partly or totally from these primary rocks. The Pyrenean and Montagne Noire potential source areas are discussed below.

For samples MX-3 and MX-4 located in the north-east of the Corbières region, the closest relief holding Cadomian ages is the Montagne Noire. Cadomian (Neoproterozoic – Early Cambrian) ages have been obtained for Paleozoic sandstones in the southern flank of this belt (Lin et al., 2016).

Basement rocks outcropping in the central Pyrenees host Caledonian (420-520 Ma) and Cadomian (~600 Ma) orthogneiss, paragneiss, rhyodacitic tuffs and metabasites (Figure 5.7) (Cocherie et al. 2005; Castiñeiras et al. 2008; Denele et al. 2009; Casas et al. 2010; Vacherat et al. 2017). Furthermore, Ordovician-Devonian metasediments host detrital zircon ages showing a large dominance of Cadomian component (520 to 700 Ma) and a minor Caledonian component (450 to 475 Ma) (Hart et al., 2016; Margalef et al. 2016).

For samples MX-6 and CL-5, the Cadomian signal indicate a central Pyrenean source, that could be a basement rock or recycled Paleozoic sedimentary and metasedimentary units as mentioned before by Thomson et al. (2017). They are sourced from the Gondwana, located to the south of the French Massif Central and the Pyrenees, and transported northward by a river drainage network (Lin et al., 2016). For the Caledonian ages obtained on sample CL-5, the eastern part of the Axial Zone contains several orthogneiss massifs that have U/Pb zircon ages ranging from 457 to 477 Ma (Roc-de-France (Castiñeiras et al., 2008b), Nuria (Martínez et al., 2011), Canigou (Delaperrière and Respaut 1995; Guitard et al. 1996) and Albera (Liesa et al. 2011)) and that can be the source of these clasts.

Evolution of the sediment routing system in the eastern part of the Aquitaine Basin

The evolution of the source signal defined by the late Ypresian to Priabonian clasts and sand matrix crystals in the basin shows mostly a single source per site of sampling. A single Variscan signal is obtained for samples MX-1, MX-2, CL-1, CL-2, MX-5, CL-3 and CL-4, and a single Cadomian signal is obtained for samples MX-3, MX-4 and MX-6.

The evolution of clast content in unit 1 shows mostly boulders sourced from the Meso-Cenozoic cover (Crochet, 1989), followed by granite clasts in its upper part as mentioned by Ovtracht and Lenguin (1977). The signal of U/Pb ages for the matrix sample MX-5 in unit 2 is more extended compared to the signal for the matrix samples MX-1 and MX-2 in unit 1 (Figure 5.6). This demonstrates the increase of the source area during time. Facies analysis and associated depositional environments characterization in unit 1 show a progradation from deltaic to fluvial depositional environments (alluvial fan and meandering rivers) in the southern part of the Corbières region from the late Ypresian to the Lutetian period (Prieur, 2019). Laterally, to the west of the Mouthoumet massif, RSCM analysis for black flysch clasts from the unit 1 and the transition unit1-unit2 shows mean peak temperatures ranging from 495 to 587°C. Comparable RSCM temperatures are obtained in Clerc et al. (2015) for samples collected in the NPZ. U/Pb analysis for unit 1 show a Variscan signal for the samples MX-1 and MX-2 reflecting the exposition of the basement massifs to erosion from the Lutetian and not the Bartonian period as shown before by clasts analysis in Crochet (1989) and Christophoul et al. (2003). These results demonstrate that the Ypresian-Lutetian sediment routing system is mainly fed from the NPZ (Figure 5.9). The lower deposits of unit 1 are fed from the sedimentary cover in the NPZ. They are overlaid by the Albo-Cenomanian black flysch and laterally by a Variscan source.

The unit 2 clasts include a large portion of granitic rocks most of them having a 330 Ma U/Pb age. The signal of U/Pb ages for sample MX-5 from unit 2 is more-extended compared to the one for the samples of unit 1. Facies analysis shows a pluri-metric alluvial fan depositional environment in unit 2 reflecting a larger drainage area. The change in the clasts content and the source of sediment could be explained by the change in the drainage network activated due to the end of inversion in the NPZ and the transition to the Axial Zone crustal stacking. The potential source area of the deposits of unit 2 is the Axial Zone, in particular the massifs having zircon U/Pb ages in the 320-330 Ma range, like Aston-Hospitalet (324±2 and 334±6 Ma, Mezger and Gerdes,2016) and Ax-les-thermes (321±7 Ma, Denele,2007) (Figure 5.9).

Sample CL-5, collected from unit 3, contains concordant ages dispersed into three groups, Variscan, Caledonian and Cadomian. Sample MX-6, also collected in unit 3 shows the same distribution of U/Pb ages. Considering the location of more western samples CL-5 and MX-6 to the north of the NPZ and their deposition age (Priabonian), the source of the zircons must be Pyrenean, from a close location to the central part of the Pyrenees. Concordant ages distributed into three groups are observed only in these samples. As the Pyrenean orogeny exhumation is diachronous from east to west and from north to south, the exposition of the exhumed surface of the Pyrenees to erosion increases with time. Such an increase is observed in the evolution of the U/Pb signals with time, as the surface exposed to erosion is wider and varied in terms of sources in the samples from unit 3 CL-5 and MX-6. The results of these samples reflect, therefore, the increase of the drainage area covering the whole central and eastern part of the Pyrenees as they were totally exhumed at that time.

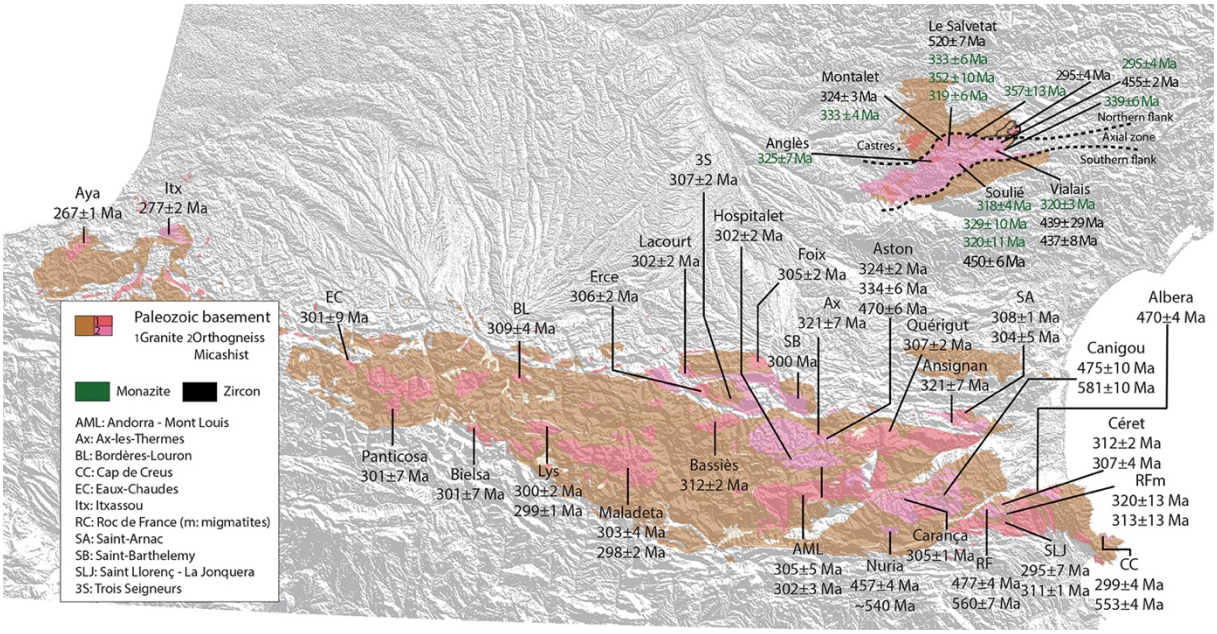

Figure 5.7: Compilation of zircon and monazite U/Pb ages for the Montagne Noire and the Pyrenees. References: Guitard 1970; Postaire et al. 1983; Respaut and Lancelot 1983; Liesa and Carreras 1989; Evans 1993; Paquette et al. 1997; Roberts et al. 2000; Deloule et al. 2002; Maurel 2003; Maurel et al. 2004; Cocherie et al. 2005; Gleizes et al. 2006; Denele 2007; Castiñeiras et al. 2008; Olivier et al. 2008; Denele et al. 2009; Casas et al. 2010; Liesa et al. 2011; Martínez et al. 2011; Denèle et al. 2012; Aguilar et al. 2014; Denèle et al. 2014; Druguet et al. 2014; Pereira et al. 2014; Esteban et al. 2015; Lemirre et al. 2016; Van Lichtervelde et al. 2017.

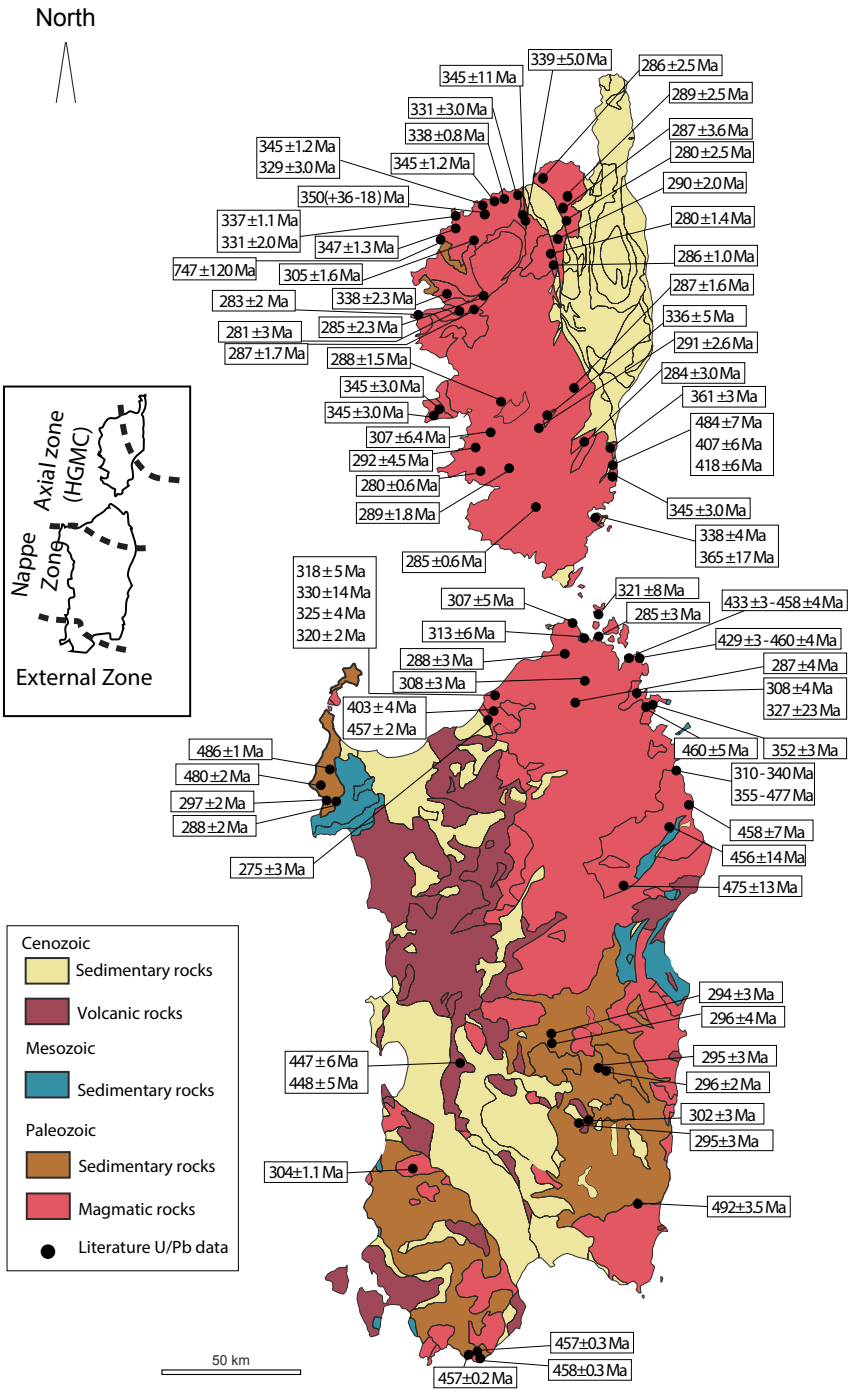

Figure 5.8: Compilation of zircon U/Pb ages obtained for the Corsica-Sardinia bloc. References: Rossi et al., 1988 ; Cocherie et al., 1992 ; Rossi et al., 1995 ; Paquette et al., 2003 ; Cortesogno et al., 2004 ; Palmeri et al., 2004 ; Cocherie et al., 2005 ; Helbing et al., 2005 ; Giacomini et al., 2005 ; Oggiano et al., 2007 ; Renna et al., 2007 ; Giacomini et al.2008 ; Rossi et al., 2009 ; Oggiano et al., 2010 ; Carosi et al., 2012 ; Casini et al., 2012 ; Pavanetto et al., 2012 ; Edel et al., 2014 ; Faure et al., 2014 ; Li et al., 2014 ; Padovano et al., 2014 ; Cuccuru et al., 2015 ; Malusa et al., 2015 ; Gaggero et al., 2017.

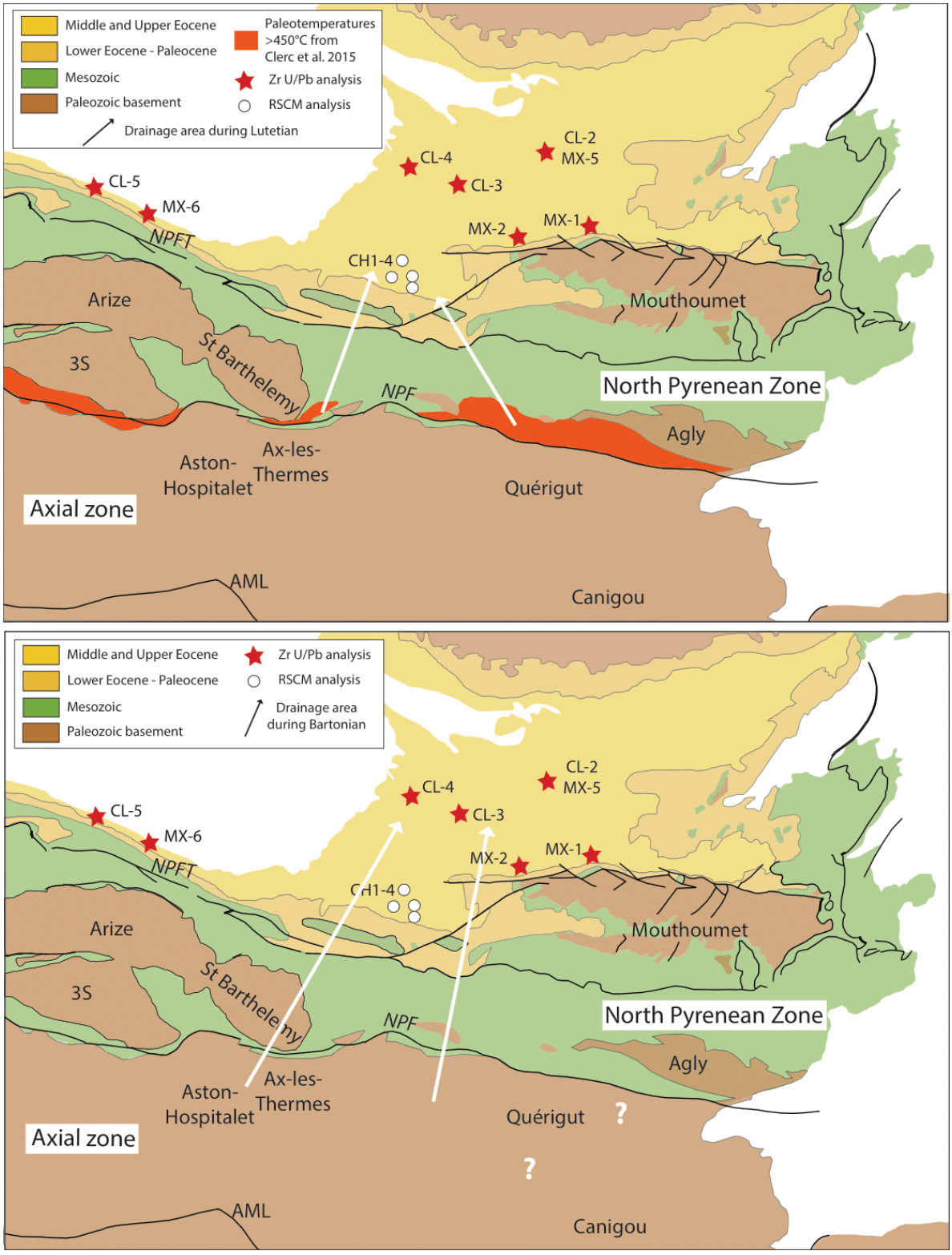

Figure 5.9: Drainage areas during Lutetian and Bartonian as constrained by U/Pb geochronology, RSCM results, paleocurrent directions.

Conclusion

The combination of detrital U/Pb analysis for sandstone matrix and granite clasts with paleocurrent directions, RSCM results and sedimentary analysis allowed the characterization of the sediment routing system in the Corbières region. It also allowed the identification of the sources of the deposited material and the characterization of the infilling mode of sediments in the basin. Results show that the majority of the deposits in the basin are sourced from the Pyrenees. U/Pb results for matrix samples from unit 1 of the Palassou formation show a Variscan signal, and RSCM analysis for black flysch clasts show temperatures comparable to those obtained for the NPZ. This reflect that the main source of unit 1 deposits is the NPZ. For the unit 2, U/Pb results for granite clasts and conglomerate matrix show Variscan ages. They have been coupled to the measured paleocurrent directions and sedimentary analysis. The interpretation of these results demonstrated an Axial Zone and probably Mesozoic strata source of unit 2 deposits. In addition, the change in clast content between units 1 and 2 can be explained by a change in the drainage network due to the end of the NPZ inversion and the transition to the Axial Zone crustal stacking. U/Pb zircon signals obtained for granite clasts and matrix samples from unit 3 show varied and extended signal with three groups of ages: Variscan, Caledonian and Cadomian. The location of the samples and their deposition at that time reflect a central and east Pyrenean source.

Sample	Grains number	Ceno-Mesozoic	Permo-Triassic	Late Variscan	Early Variscan	Pre-Variscan	Caledonian	Caledonian/ pan-African	Neoproterozoic	Kibaran	Meso-proterozoic	Paleo-proterozoic	Archean-Paleoproterozoic
		0-180 Ma	180-280 Ma	280-310 Ma	310-340 Ma	340-420 Ma	420-520 Ma	520-700 Ma	700-900 Ma	900-1200 Ma	1200-1500 Ma	1500-2200 Ma	2200-4600 Ma
MX-1	171	1.7	7.0	19.3	**33.3**	19.9	5.3	8.2	2.3	1.2	0	0.6	1.2
MX-2	132	0	3.8	15.9	**40.1**	5.3	15.2	15.9	2.3	0	0	0.8	2.3
MX-3	74	0	0	0	1.4	4.0	6.8	**51.4**	6.8	10.8	0	8.1	10.8
MX-4	120	0	2.5	4.1	1.7	0	2.5	**40.8**	20.0	5.8	0	10.8	11.7
MX-5	125	0	1.6	9.6	7.2	**28.0**	19.2	12	9.6	3.2	0	3.2	6.4
MX-6	69	0	1.5	15.9	5.8	10.1	27.5	**33.3**	1.5	1.5	0	1.4	1.4

Table 5.1 : Detrital U/Pb results summarized in percentage.

Sample	Position	Deposition age	Nb spectra	Raman parameter		RSCM temperature (°C)		
				Mean	SD	Mean	SD	SE
CH1	42°56'43.96"N 2°4'49.79"E	late Ypresian	10	0.34	0.05	495	19	6
CH2	42°59'1.01"N 2°1'42.76"E	Lutetian	10	0.22	0.06	551	21	6
CH3	42°57'17.09"N 2°5'36.76"E	Lutetian	10	0.19	0.04	555	17	5
CH4	43°0'14.16"N 2°3'40.32"E	Late Lutetian	10	0.13	0.08	587	31	10

Table 5.2: RSCM peak temperature from black flysch clasts of the unit 1 and the transition unit1-unit2. The parameters from Beyssac et al. (2002) have been used to estimate temperatures. SD: Standard deviation, SE: Standard Error

Supplementary information

Petrography of the granite boulders

Petrography of granite boulders constitutes a first methodology to characterize the possible sources of the materials forming the Palassou conglomerates. 12 granitic samples have been analysed using optical microscope in order to determine the cardinal minerals and their distribution of which only 9 are presented here. Figures 1 to 9 represent thin section photos of the nine samples, analysed using plane polarized light (PPL, on the left) and cross-polarized light (CPL, on the right). These samples consist essentially of quartz, potassium-feldspar, microcline, plagioclase, biotite and muscovite. Crystal abundance and granite type for each sample are shown in Table 1. All samples reveal a low abundance of mica crystals.

Sample CO1 consists of large quartz crystals and two generations of K-feldspar and plagioclase (one consists of megacrysts and the other corresponds to small crystals) (Figure 1). Sample CO2 has two quartz types referring to their size (big crystals and very small ones) with megacrysts of plagioclase and K-feldspar. It contains biotite and muscovite minerals (**Error! Reference source not found.**). Sample CO3 sample has the same mineralogical composition as sample CO2 with an average size of crystals (Figure 3). The mineralogical composition of samples CO4 and CO5-B is similar to the one of sample CO1 (Figures 4 and 6 respectively). For sample CO5-A, all quartz, K-feldspar and mica crystals have a medium to small size (Figure 5). The samples CO6, SA1 and MI2 have the same mineralogical composition as sample CO5-A with smaller crystals in CO6 compared to SA1 and MI2 (Figures 7, 8 and 9). The studied samples are leucogranites and have a comparable content of minerals with mainly 2 types: one-mica and two-mica leucogranites (Table 1).

Table 1: Crystal abundance, composition and type of granite boulders from field trips.

S.name	Qz	K-Fd	Pg	Bt	Ms	Granite type
CO4	XX	XX		X		One-mica
CO2	XX	X	X	X	X	Two-mica
CO1	XXX	X	X	X		One-mica
CO5-A	XXX	XX		X	X	Two-mica
CO5-B	XXX	XX	X	X		One-mica
CO3	XXX	XX	X	X	X	Two-mica
CO6	XX	XX	X	X	X	Two-mica
SA1	XX	XX		XX	X	Two-mica
FO2	XX	X	X	XX		One-mica
MI2	XXX	X		XX	X	Two-mica
MI3	XXX	XX		X	X	Two-mica
SA3	XX	X	X	XX	X	Two-mica

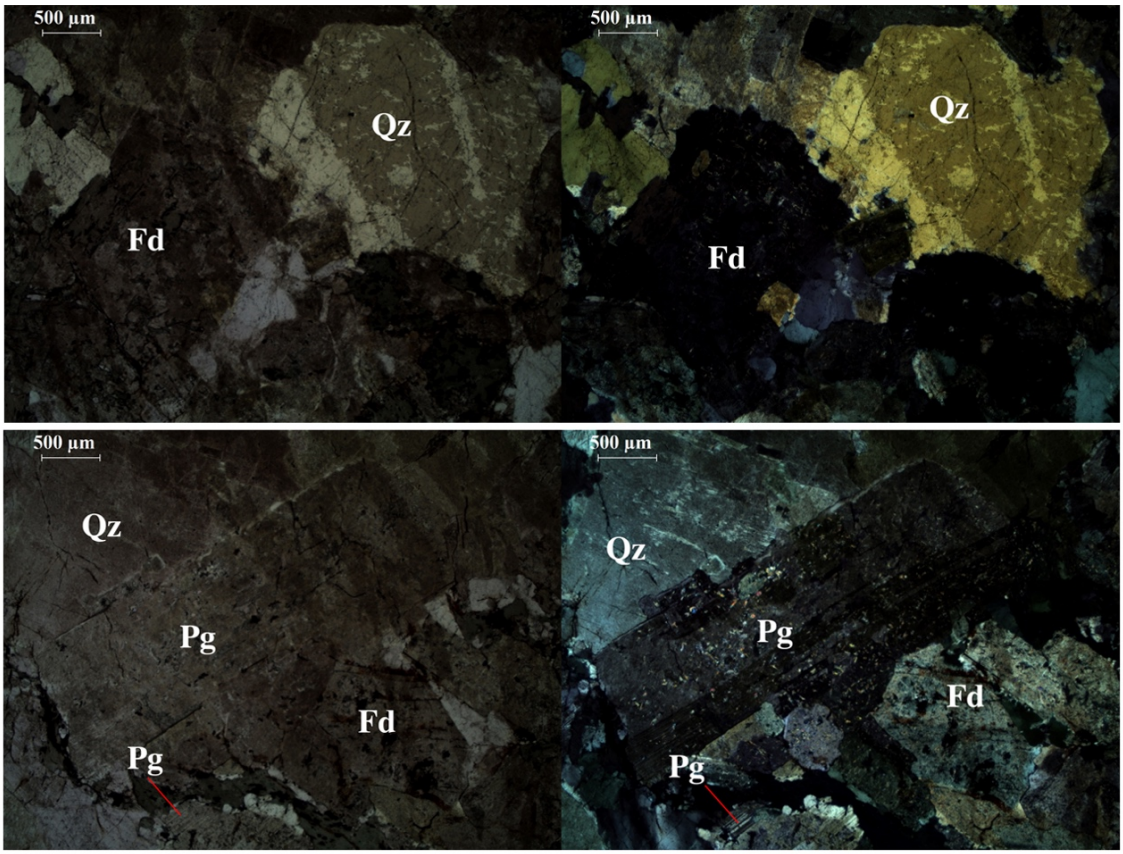

Figure 1: CO1 thin section shown under PPL(on the left) and CPL (on the right). Qz: quartz, Fd: K-felspar, Bt: biotite, Ms: muscovite.

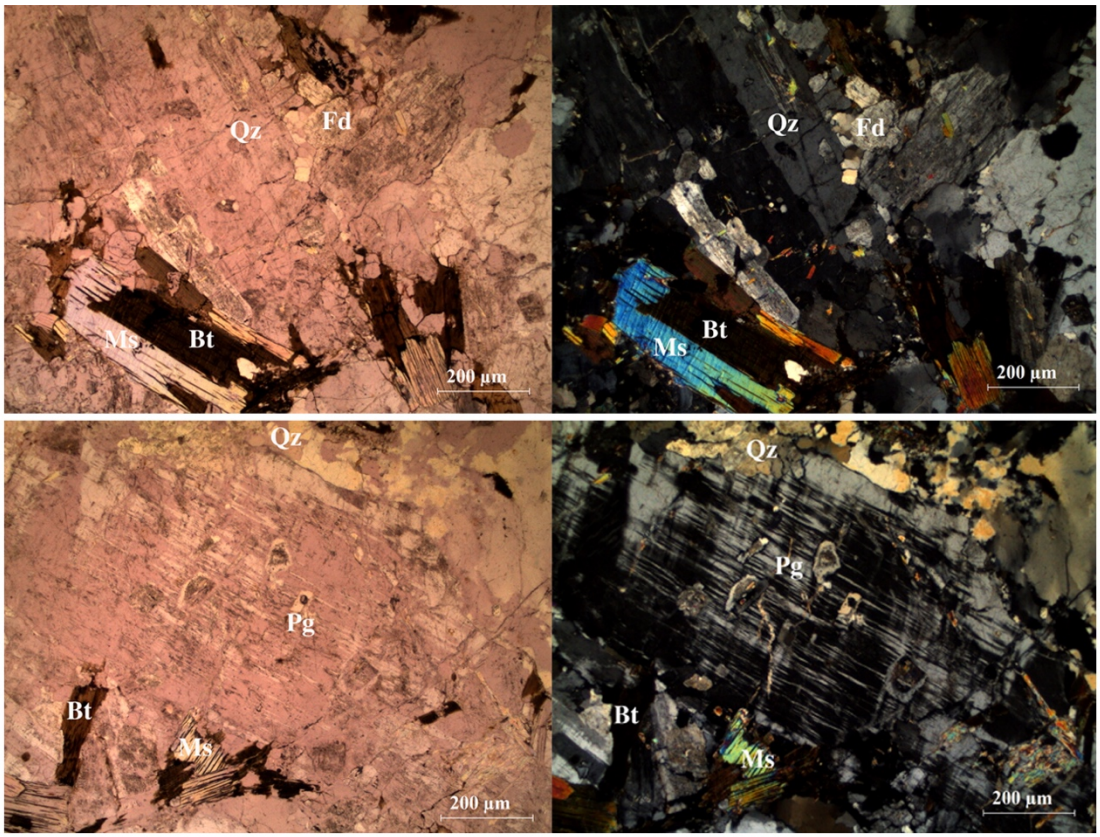

Figure 2: CO2 thin section shown under PPL (on the left) and CPL (on the right). Qz: quartz, Fd: K-felspar, Bt: biotite, Ms: muscovite and Mc: microcline.

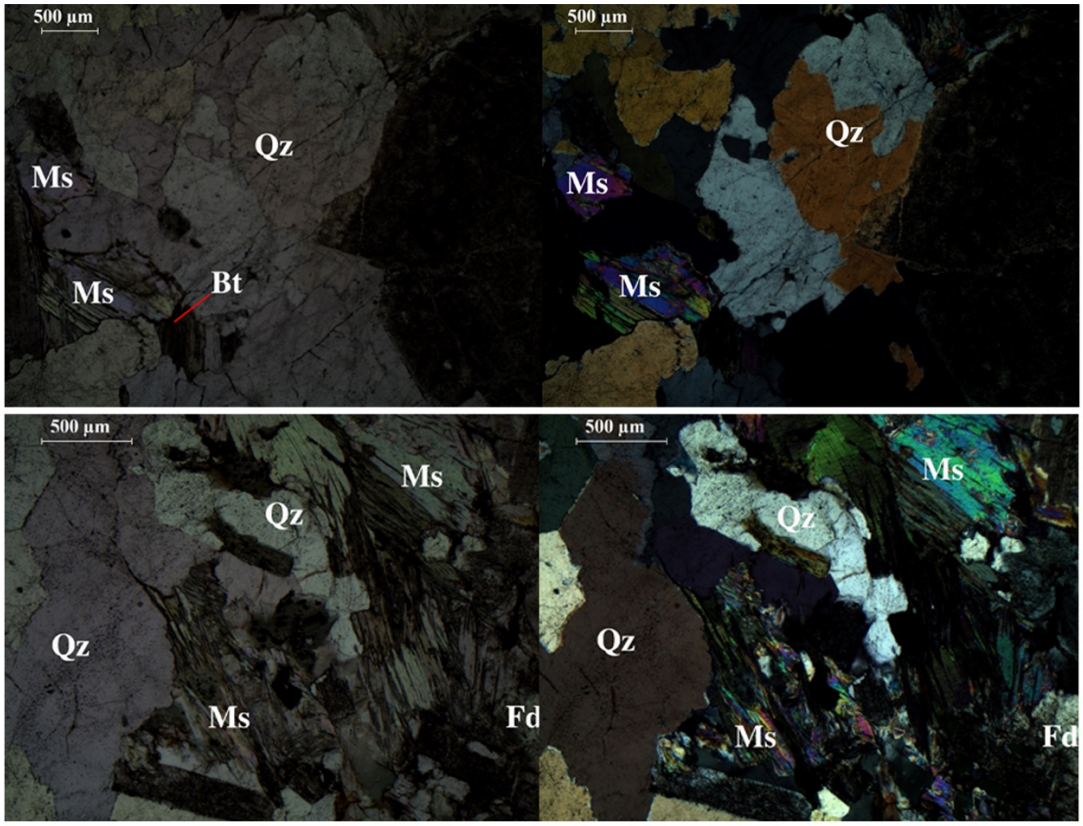

Figure 3: CO3 thin section shown under PPL (on the left) and CPL (on the right). Qz: quartz, Ms: muscovite.

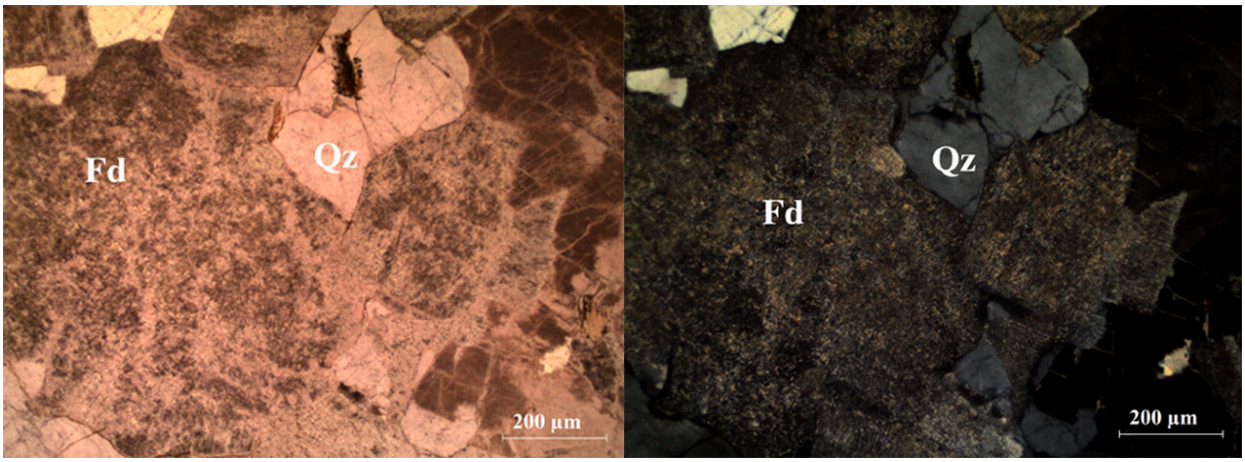

Figure 4: CO4 thin section shown under PPL (on the left) and CPL (on the right). Qz: quartz, Fd: K-felspar.

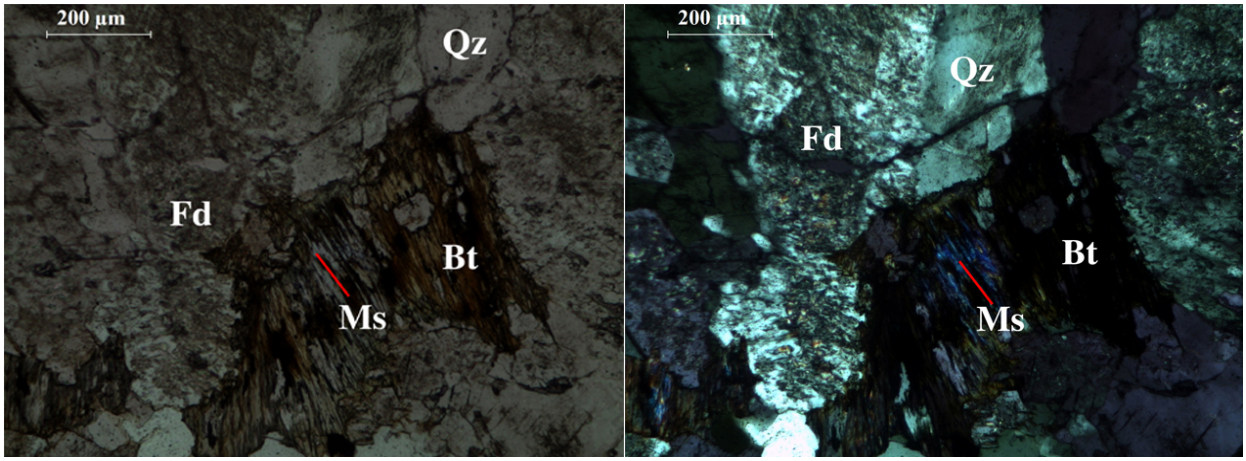

Figure 5: CO5-A thin section shown under PPL (on the left) and CPL (on the right). Qz: quartz, Fd: K-felspar, Bt: biotite, Ms: muscovite.

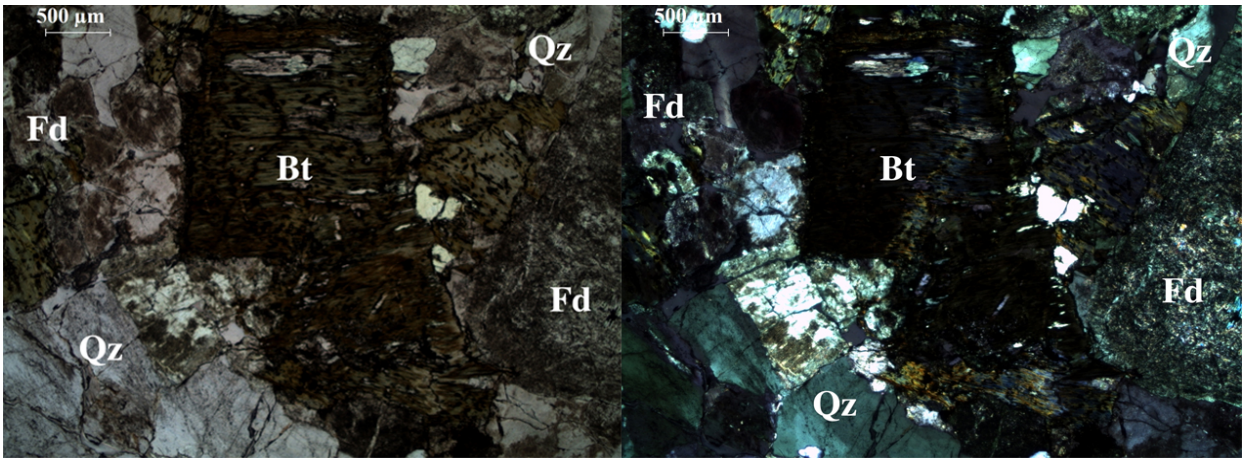

Figure 6: CO5-B thin section shown under PPL (on the left) and CPL (on the right). Qz: quartz, Fd: K-felspar, Bt: biotite.

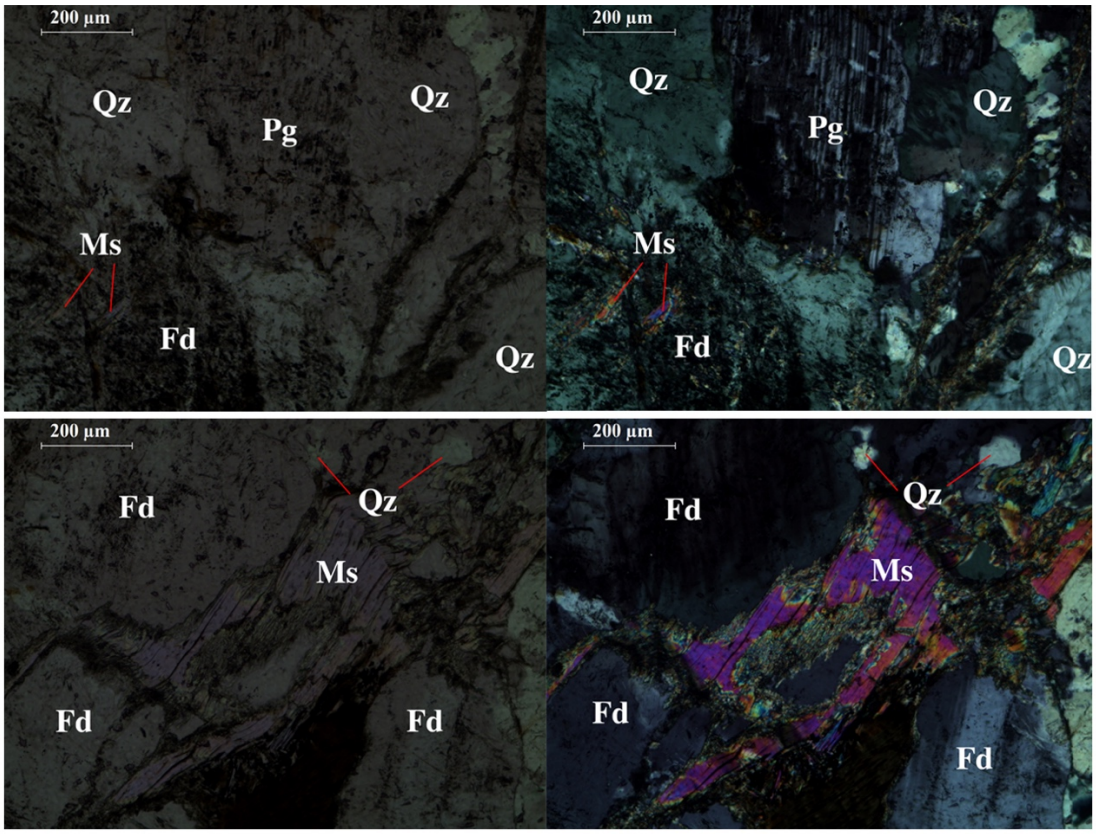

Figure 7: CO6 thin section shown under PPL (on the left) and CPL (on the right). Qz: quartz, Fd: K-felspar, Pg: plagioclases, Ms: muscovite.

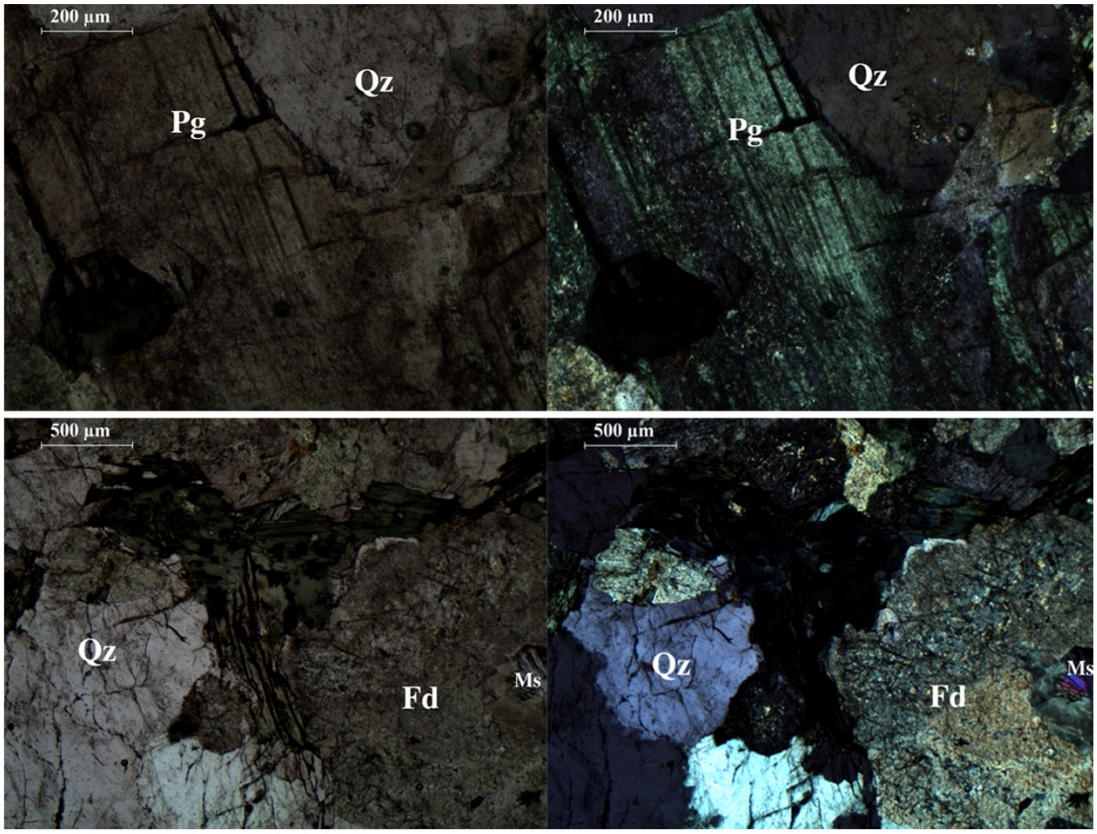

Figure 8: SA1 thin section shown under PPL (on the left) and CPL (on the right). Qz: quartz, Fd: K-felspar, Pg: plagioclases.

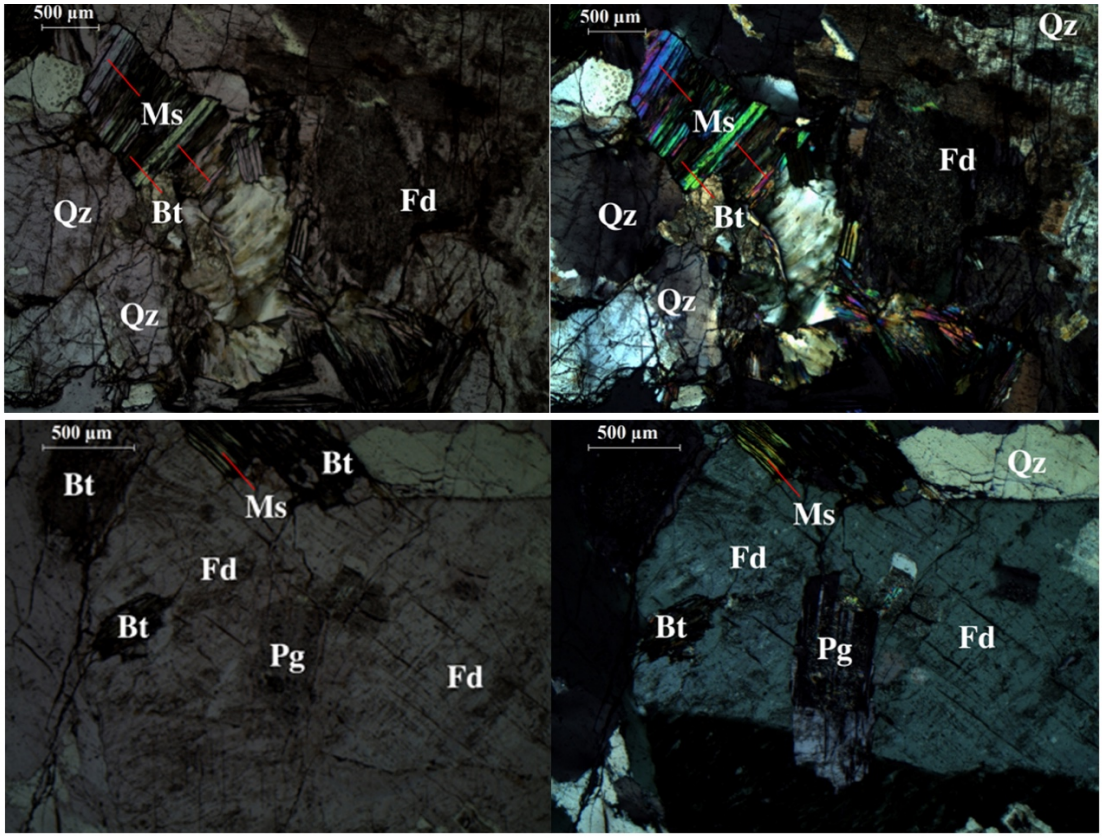

Figure 9: MI2 thin section shown under PPL (on the left) and CPL (on the right). Qz: quartz, Fd: K-felspar,Pg: plagioclases, Bt: biotite, Ms: muscovite.

Bibliographic research about granite typology

The major part of the Variscan plutonic magmatism, setting aside the post-tectonic alkaline granites of minor extent, is represented by two dominant groups (Didier and Lameyre, 1969): the first group is two-mica granitoids subdivided into leucogranites and aluminous two-mica calc-alkaline granitoids; the second group is calc-alkaline granitoids (mainly granodiorites) which are the dominant magmatism. Most of the two-mica granitic bodies are affected by major tectonic events of the orogeny and are generally emplaced in a high-grade metamorphic environment (Fourcade and Allegre, 1981). Here we show the petrographic composition of the Quérigut massif. The choice of this massif relies on its location close to the Corbières region (in the north-eastern part of the Axial Zone). The massif is composed of an association of mafic and acidic rocks. Four acidic units from edge to centre are described by Fourcade and Allegre, (1981) and Leterrier (1972): a granodioritic-tonalitic unit, a monzogranite, a porphyritic monzogranite and a biotite calc-alkaline granite. Some small veins of 2-mica granite are found in various parts of this massif. Mafic rocks outcrop in three different settings and are essentially dioritic rocks, granitoids and granodioritic to tonalitic rocks.

Leucogranites and two-mica granites are the two types of magmatic rocks collected in the Corbières region and they are widely distributed along the Pyrenees. For example, Olivier et al. (2004) mentioned, in the Agly massif, the presence of two-mica granite in various places. In the Saint-Arnac granite, Olivier et al. (2008), identified three zones by referring to their magnetic susceptibilities, of which the northern one contains two-mica granite in various places. Denèle et al., (2014) described a two-mica granite in the Ax-les-Thermes massif in the central Pyrénées when studying the timing of granite emplacement in the Variscan segment of the Pyrenees. Mezger (2010) studied the same granite while deciphering events preserved in the Axial Zone the Pyrenees. Two-mica granite is also described in the Maladeta massif by Michard-Vitrac et al. (1980) and in the Montagne Noire by Faure et al. (2010). In the Corsica-Sardinia batholith, granitoid rocks are also observed. They are grouped into three main suites (Li et al., 2014), of which the second one forms the main part of the Corsica batholith, which consists mainly of biotite-monzogranite and leucomonzogranite (Gaggero et al. 2017). In Sardinian, Cuccuru et al., (2016) revealed the presence of leucogranite in the Arbus pluton in South West Sardinia when recomposing the structural map of the late Variscan Arbus pluton. In conclusion, the petrography of the granite clasts collected in the basin is widespread over the surrounding reliefs.

RSCM data, parameters and associated temperatures

Table 2: RSCM data and associated temperatures for the samples CH1, CH2, CH3 and CH4. For more details about the R2 Raman parameters see Beyssac et al. (2002).

	R2 : paramètre Raman	valeur moyenne	Déviation standard	RSCM T°C	valeur moyenne	Déviation standard	1 sigma
Echantillon CH2							
spectre 01	0,26			526			
spectre 02	0,20			553			
spectre 03	0,19			556			
spectre 04	0,15			575			
spectre 05	0,27			519			
spectre 06	0,17			566			
spectre 07	0,13			584			
spectre 08	0,22			543			
spectre 09	0,20			551			
spectre 10	0,23	0,22	0,06	539	551	21	6
Echantillon CH4							
spectre 01	0,03			626			
spectre 02	0,17			565			
spectre 03	0,06			612			
spectre 04	0,22			541			
spectre 05	0,06			613			
spectre 06	0,07			608			
spectre 07	0,21			549			
spectre 08	0,06			616			
spectre 09	0,16			572			
spectre 10	0,15	0,13	0,08	572	587	31	10
Echantillon CH1							
spectre 01	0,33			494			
spectre 02	0,41			457			
spectre 03	0,30			508			
spectre 04	0,29			512			
spectre 05	0,36			479			
spectre 06	0,33			493			
spectre 07	0,32			499			
spectre 08	0,34			490			
spectre 09	0,26			525			
spectre 10	0,33	0,34	0,05	495	495	19	6
Echantillon CH3							
spectre 01	0,16			571			
spectre 02	0,24			533			

spectre 03	0,20			553			
spectre 04	0,19			558			
spectre 05	0,22			543			
spectre 06	0,18			559			
spectre 07	0,11			593			
spectre 08	0,21			548			
spectre 09	0,23			540			
spectre 10	0,21	0,19	0,04	549	555	17	5

Zircon U/Pb ages obtained for the geostandards 91500 and Plesovice

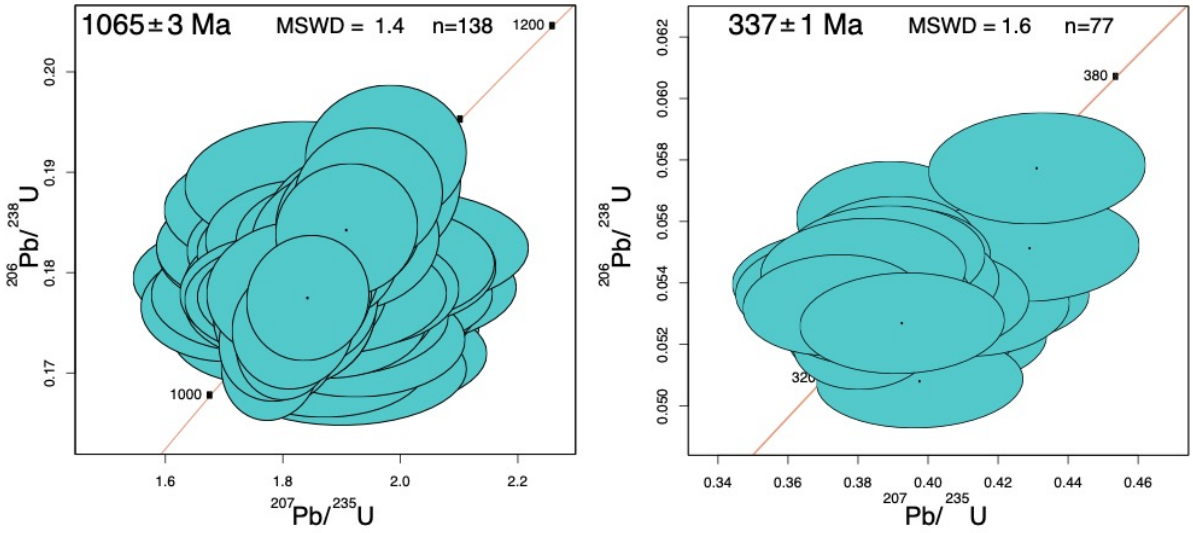

Figure 10: 91500 (on the left) and Plesovice (on the right) zircon standard ages acquired in this study

SEM coupled to a Variable Pressure Secondary Electron (VPSE) images for zircons from all granite clasts samples and four matrix samples

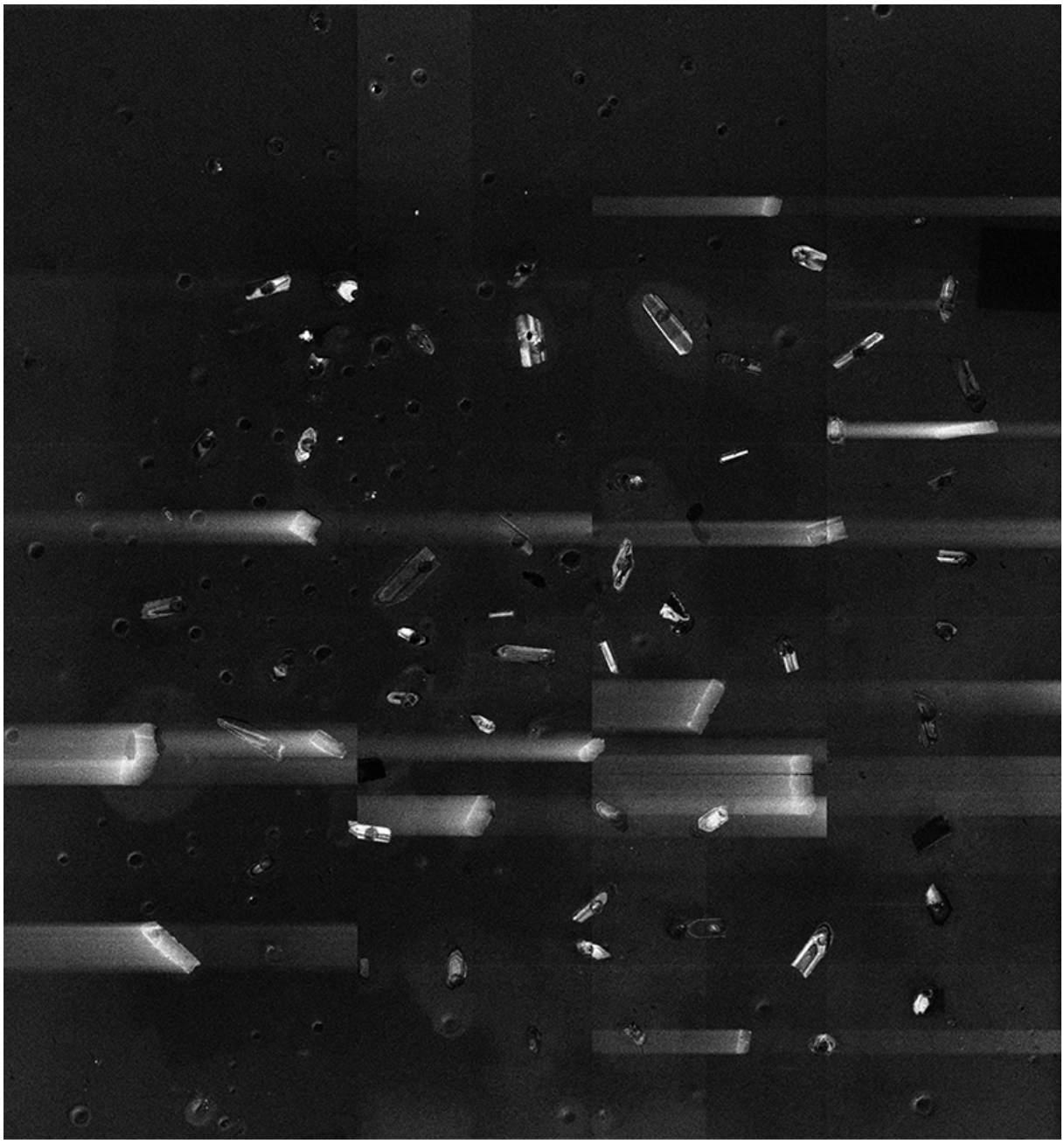

Figure 11 : CL-1 sample observed using Scanning Electron Microscope (SEM) coupled to Variable Pressure Secondary Electron (VPSE).

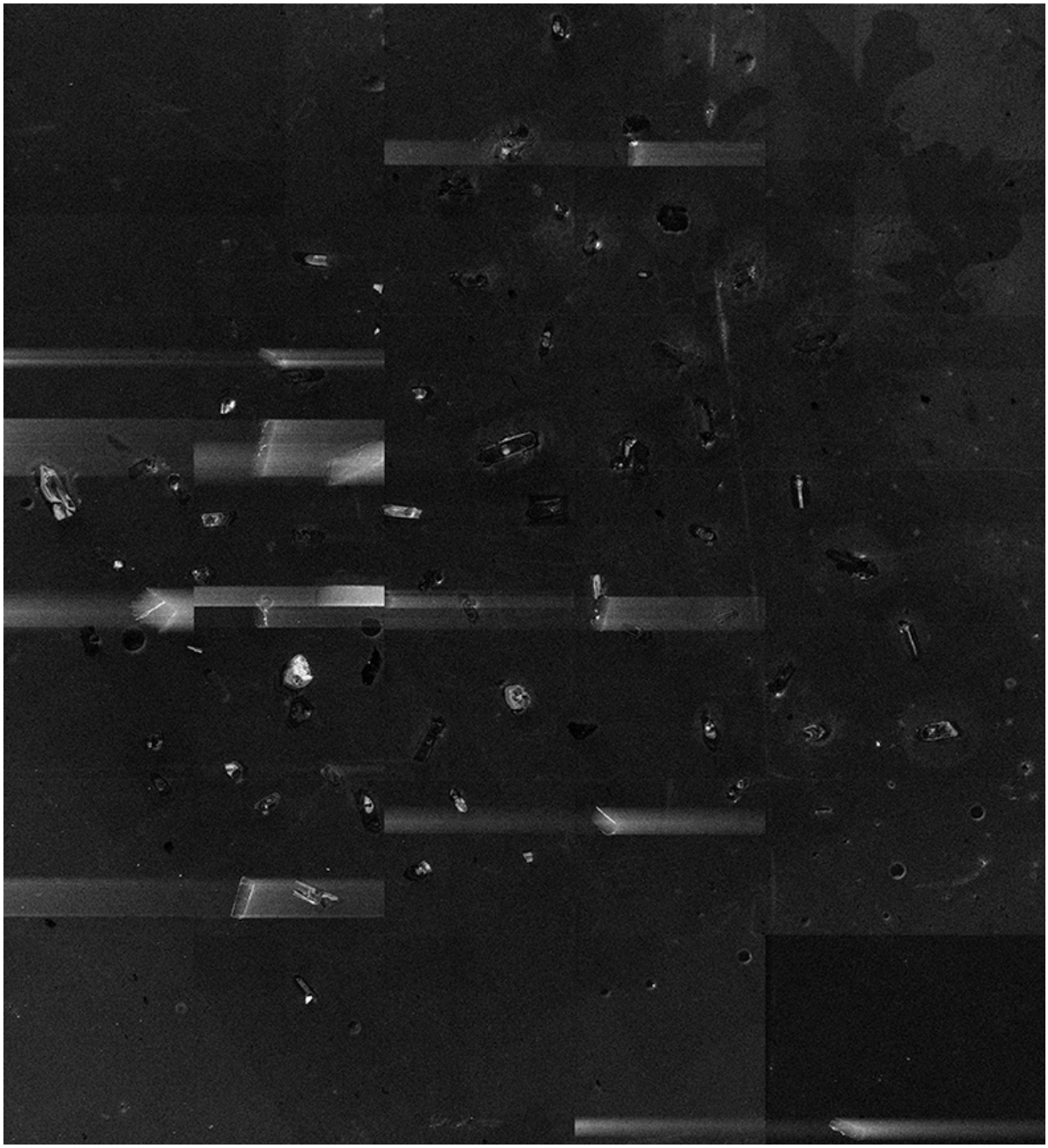

Figure 12: CL-2 sample observed using SEM coupled to a VPSE.

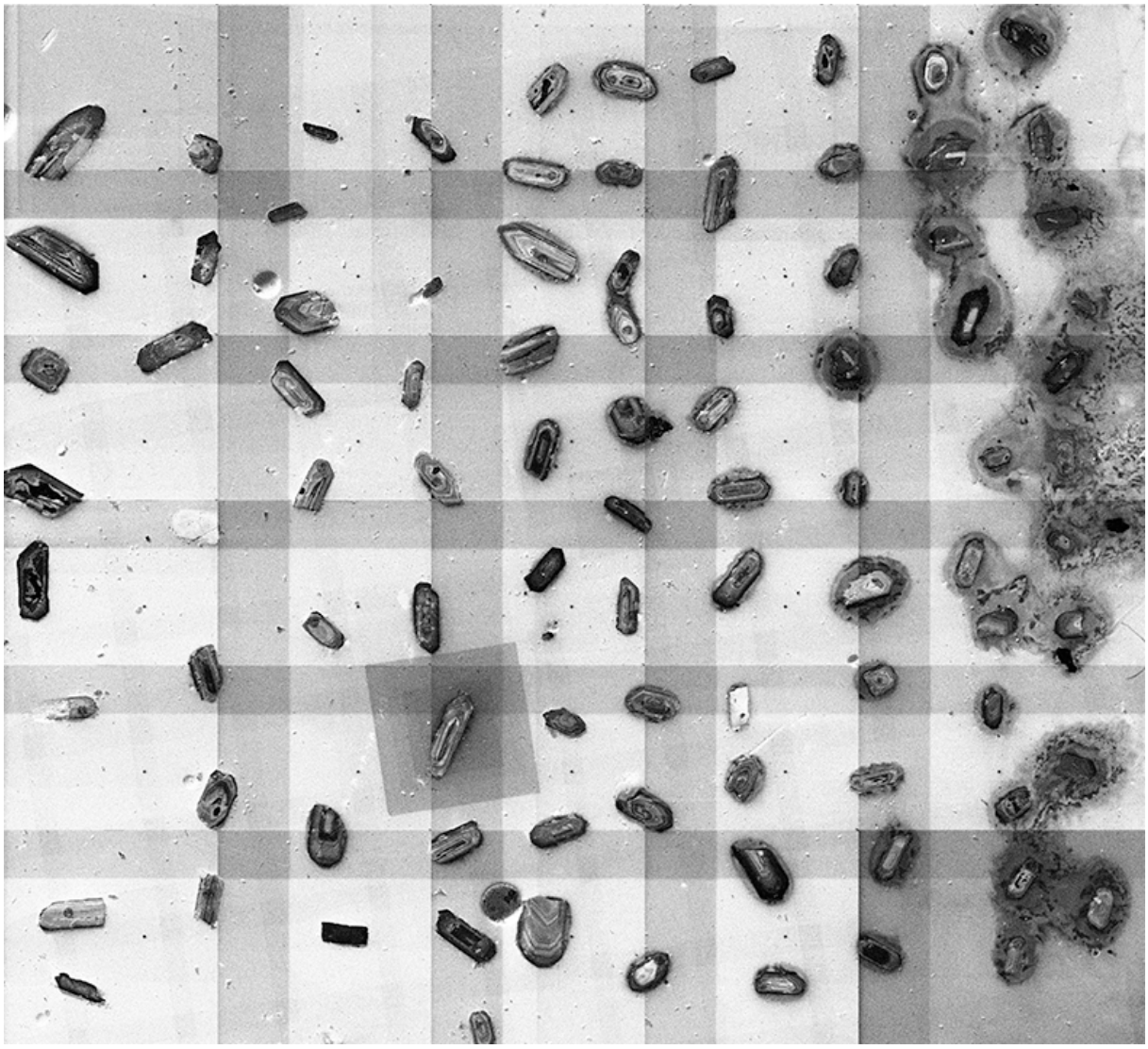

Figure 13: CL-3 sample observed using SEM coupled to a VPSE.

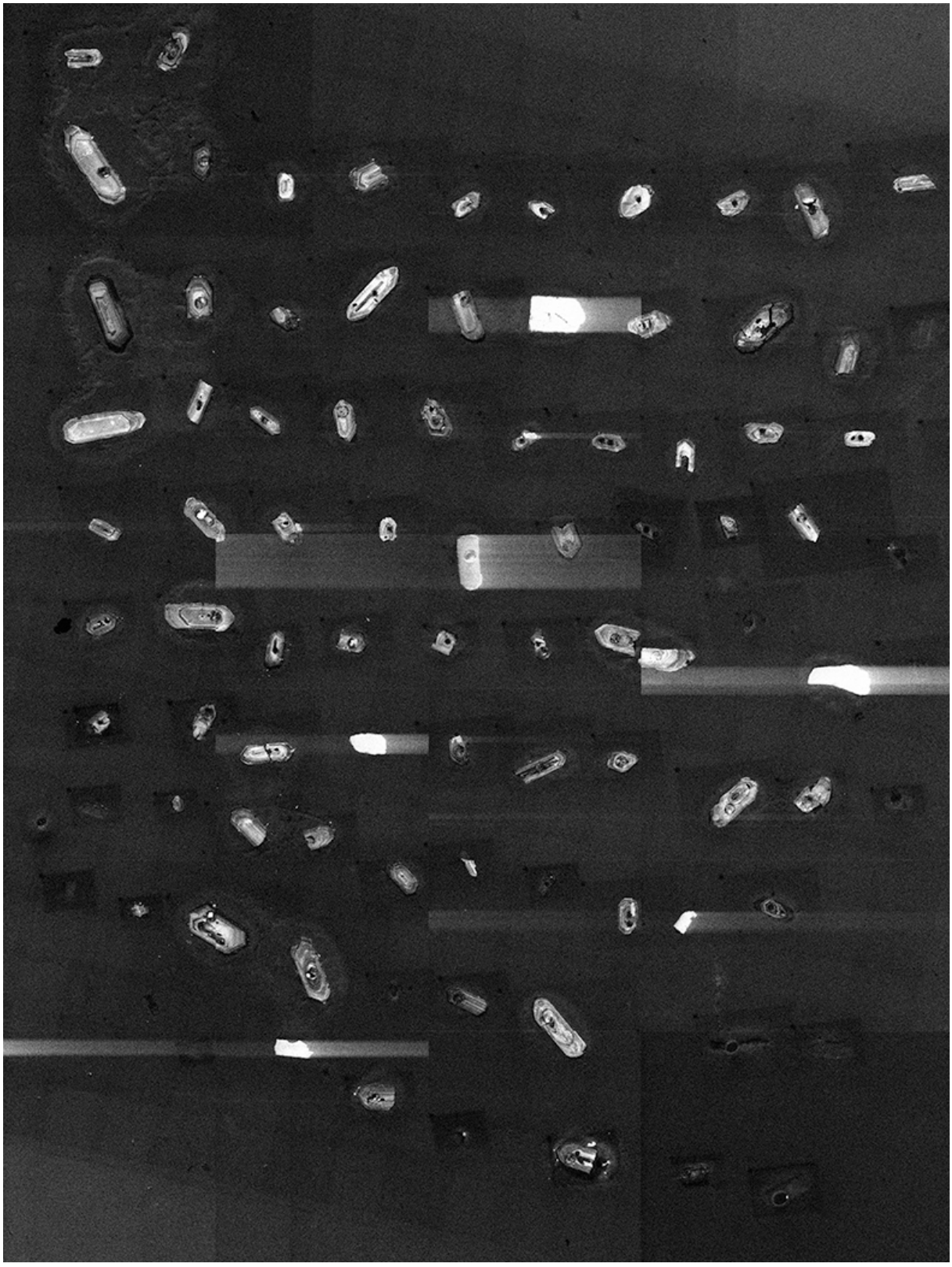

Figure 14: CL-4 1st sample observed using SEM coupled to a VPSE.

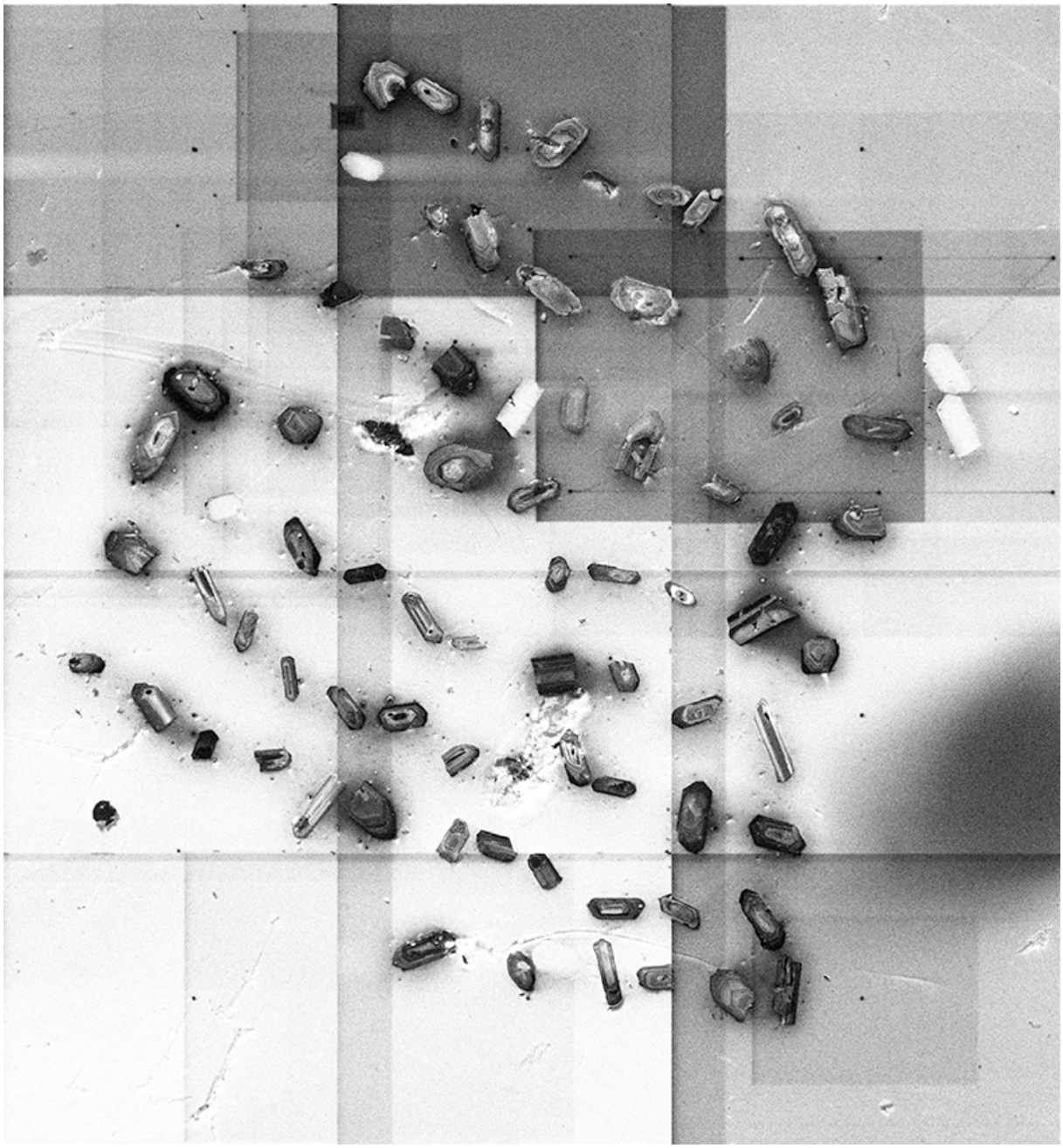

Figure 15: CL-4 2nd sample observed using SEM coupled to a VPSE.

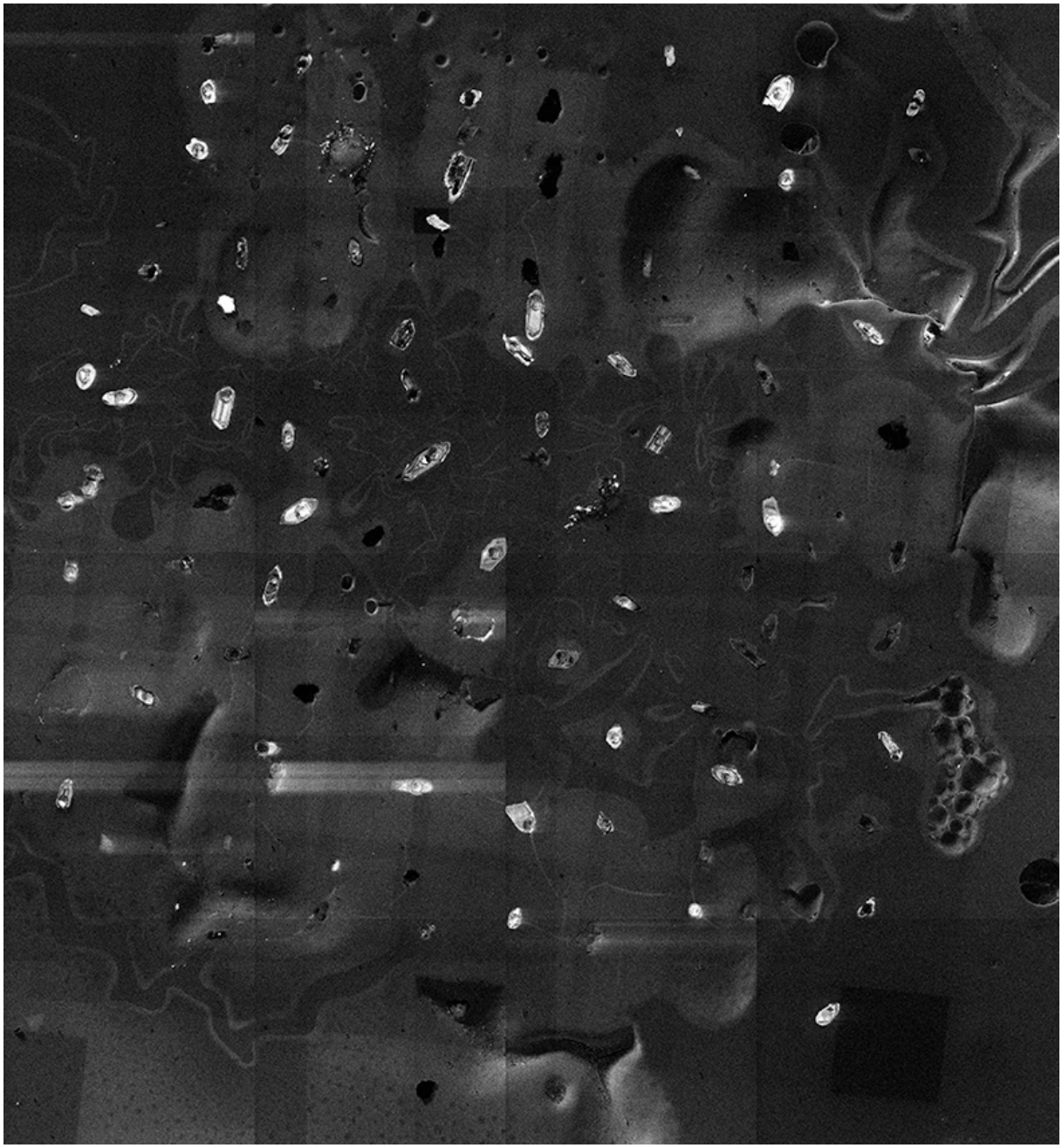

Figure 16: CL-5 sample observed using SEM coupled to a VPSE.

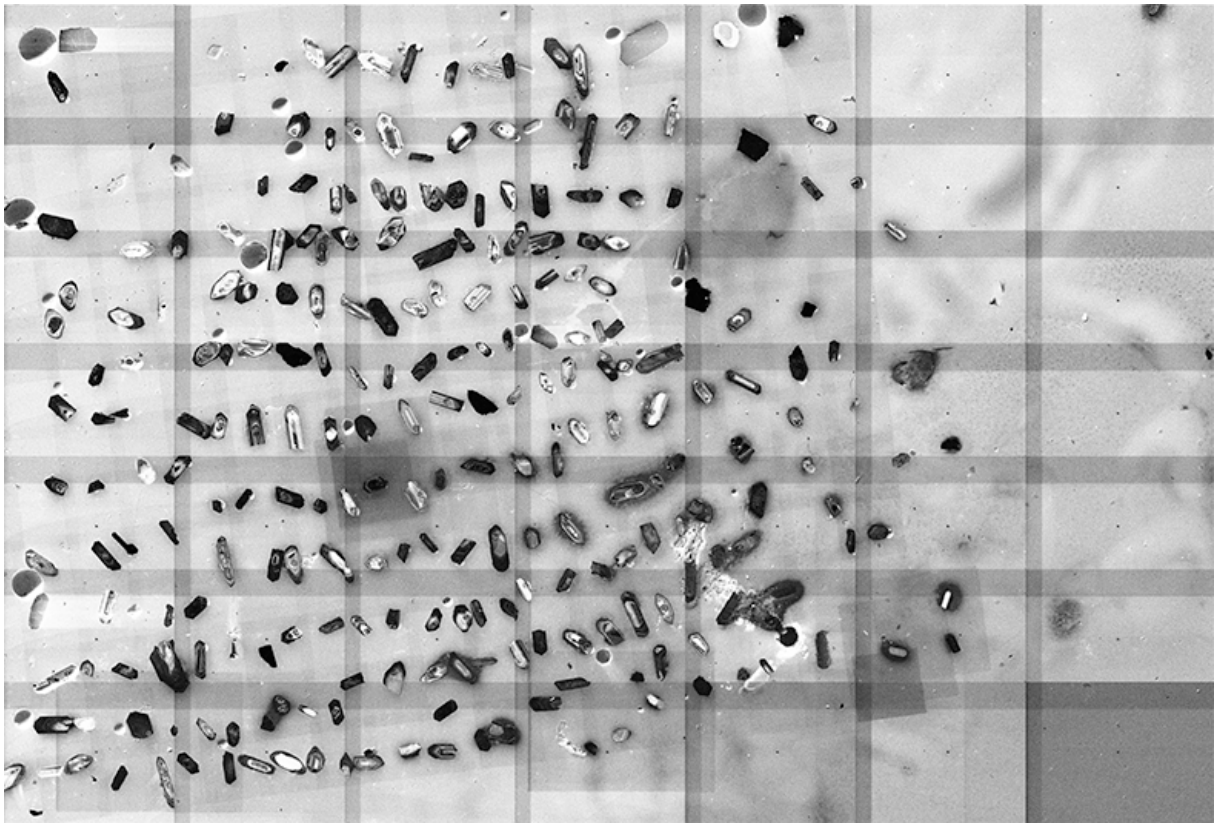

Figure 17: MX-1 sample observed using SEM coupled to a VPSE.

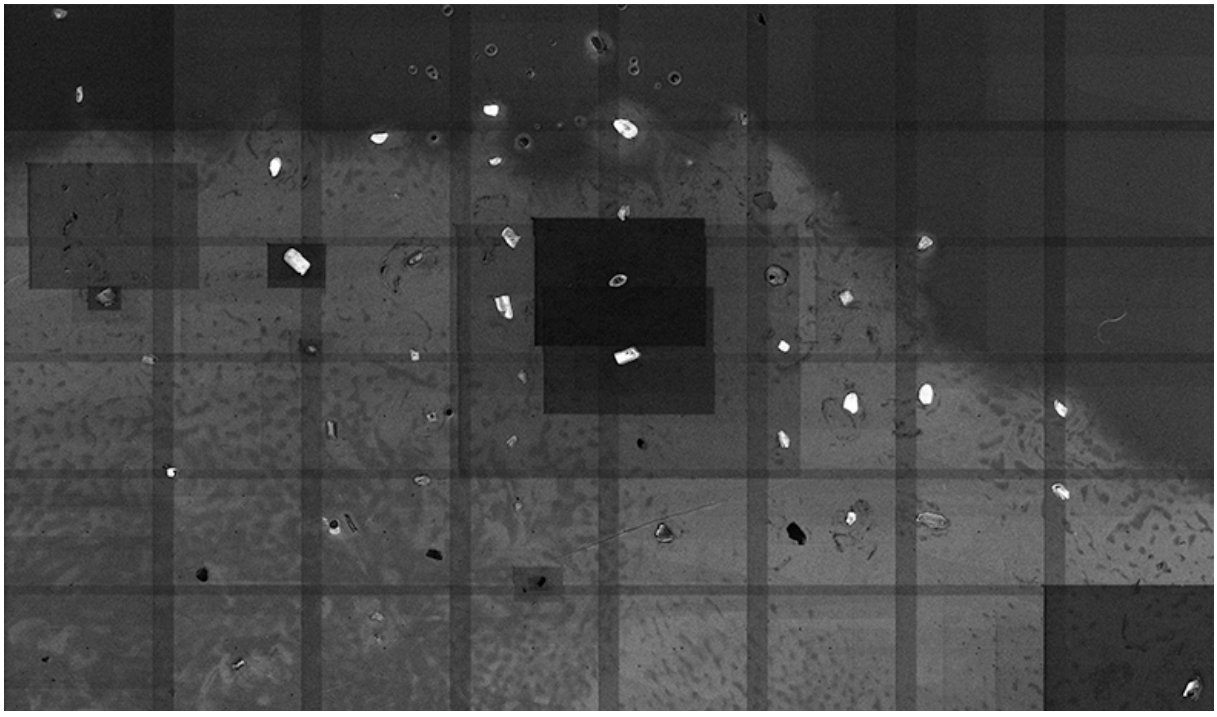

Figure 18: MX-2 sample observed using SEM coupled to a VPSE.

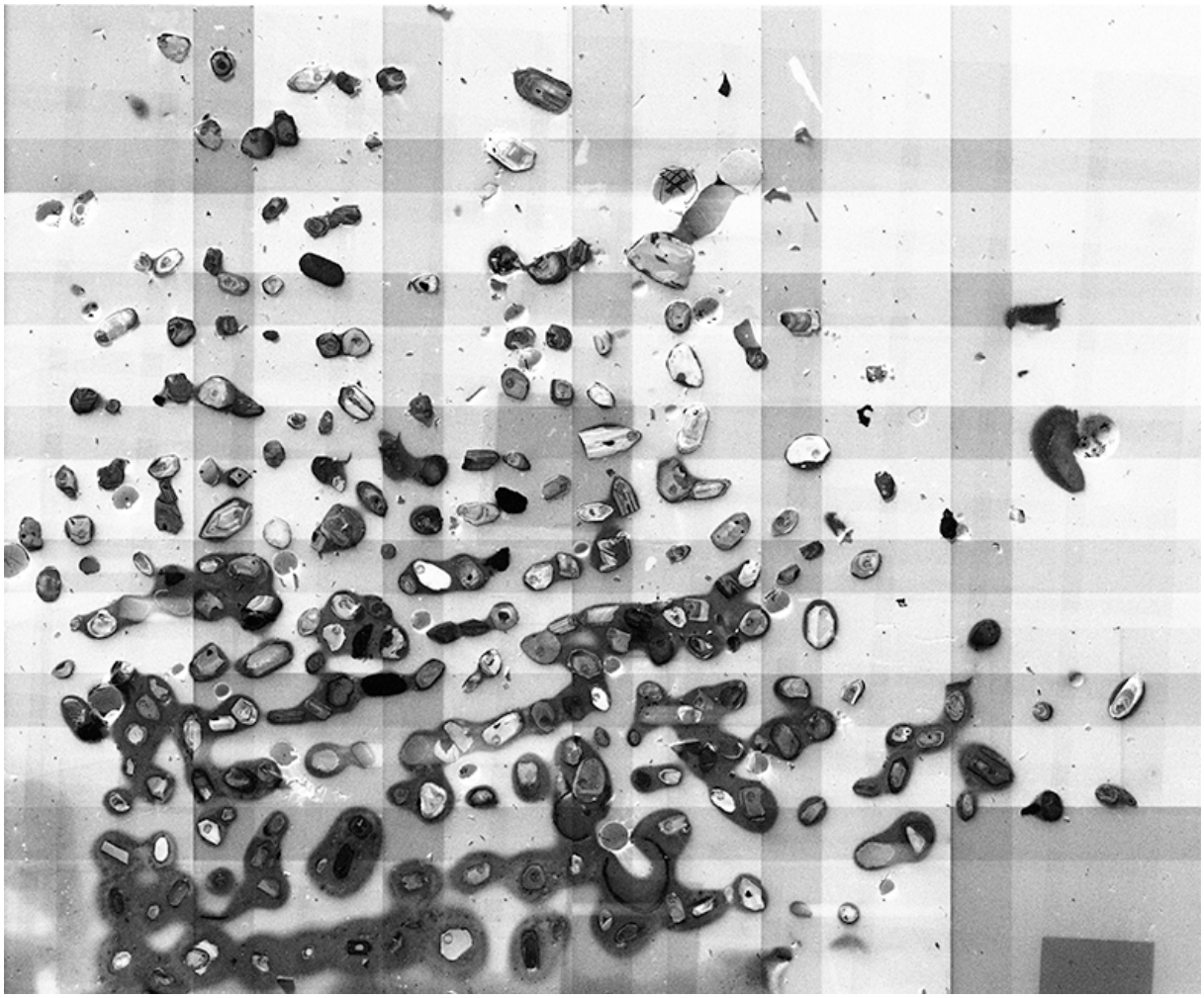

Figure 19: MX-3 sample observed using SEM coupled to a VPSE.

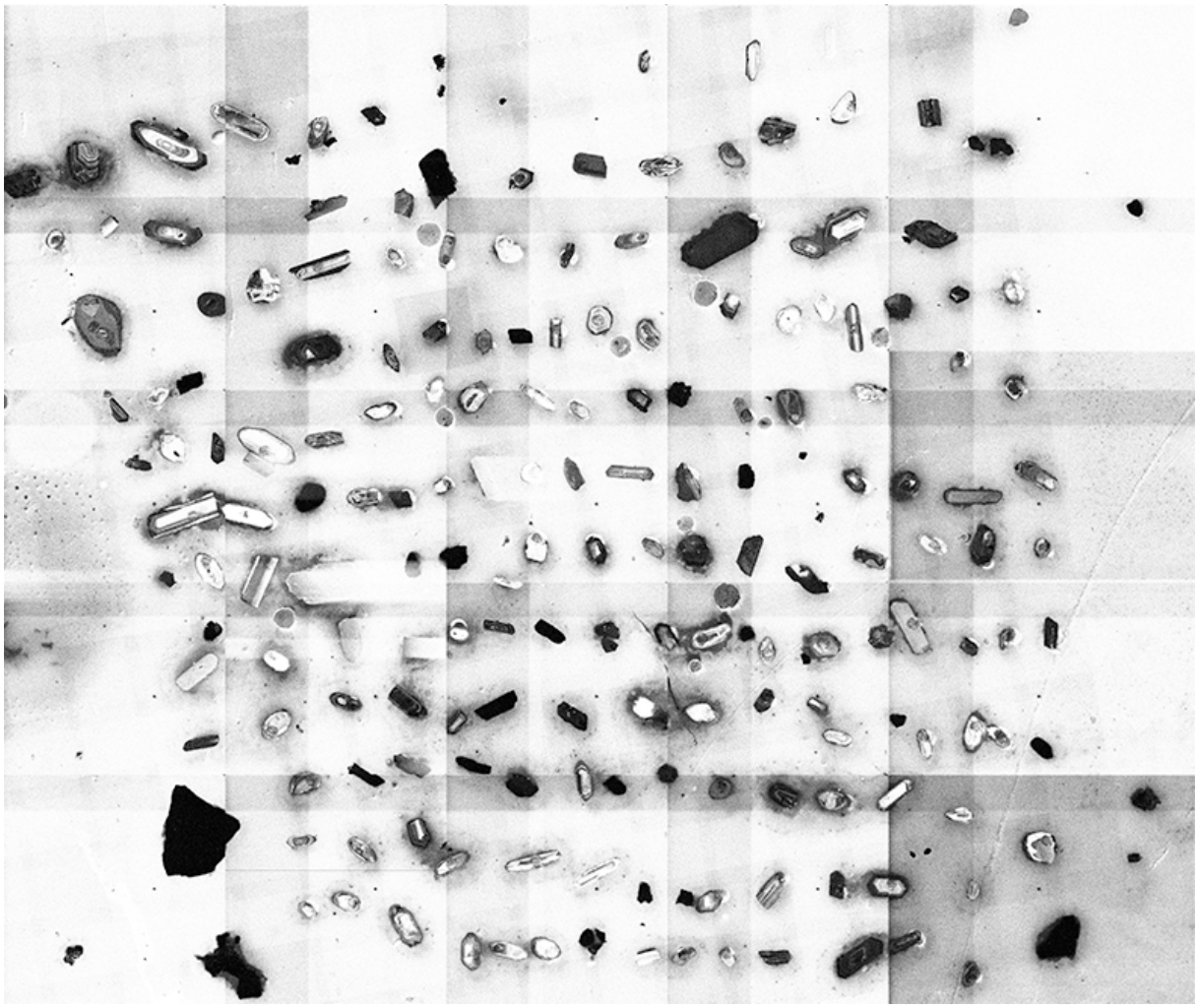

Figure 20: MX-4 sample observed using SEM coupled to a VPSE.

Chapter 6: Sediment routing system evolution in the Corbières region

Paleogeographic reconstruction of the Corbières region from the Eocene to the Miocene; overview of the Pyrenean domain from the Santonian to the Oligocene time

In this chapter, we propose a paleogeographic reconstruction of the eastern part of the Aquitaine Basin, the Corbières region, from the Eocene to the Miocene time, based on the combination of low temperature thermochronology, U/Pb geochronology and sedimentology results obtained during this PhD. The main results of this thesis are summarized in Table 6. Obtained data, in addition to sediment routing system data on the south Pyrenean foreland basin (Whitchurch et al. 2011; Michael et al. 2014; Roigé et al. 2016; Roigé et al. 2017; Odlum et al. 2019) are integrated into a new paleogeographic reconstruction of the Pyrenean domain from the Maastrichtian to the Oligocene. A particular attention is given to the evolution of the drainage divide during time.

Evolution of the eastern part of the Aquitaine Basin – the Corbières region – from the Eocene to the Miocene

During the Ypresian, the eastern part of the north Pyrenean foreland basin became rapidly filled. The infilling is evidenced in the basin by a progressive progradation from delta to fluviatile depositional environment (unit 1 of the Palassou series) (Figure 6.1). As provided in chapter 3, the geometry of the unit 1 of the Palassou deposits is larger from east to west, showing four sedimentary systems (Villerouge/Talairan, vallée de l'Orbieu and Labastide-en-Val/Clermont-sur-Lauquet and Caunette-sur-Lauquet/Pomas) that are illustrated in the stratigraphic logs and reflects the evolution of unit 1 (Prieur, 2019). The fourth sedimentary system started in unit 1 during the Lutetian and show the overfilling of the Talairan syncline and the exportation of sediments northward. This unit contains boulders from the Mezo-Cenozoic cover and few Paleozoic clasts in its upper part. U/Pb zircon ages obtained for conglomerate matrix from this unit show a Variscan peak age (~310-330 Ma). In addition, RSCM analysis obtained for black flysch clasts collected from the western Corbières show temperatures between 495 and 587°C comparable to those obtained for the NPZ in Clerc et al. (2015). Based on these results, we suggest a NPZ source for the sediments of unit 1. The infilling of the basin in the late Ypresian/Lutetian time is mainly sourced from the Meso-Cenozoic cover in the NPZ then from the Albo-Cenomanian black flysch and the Variscan basement. According to Christophoul et al. (2003), the Palassou conglomerates depositional patterns at the contact of the Mouthoumet massif and the Alaric anticline, as well as the presence of lacustrine sediments in the Talairan and Carcassonne synclines indicate that the deposition of such series is controlled by the propagation of

the Mouthoumet and Alaric frontal thrusts.

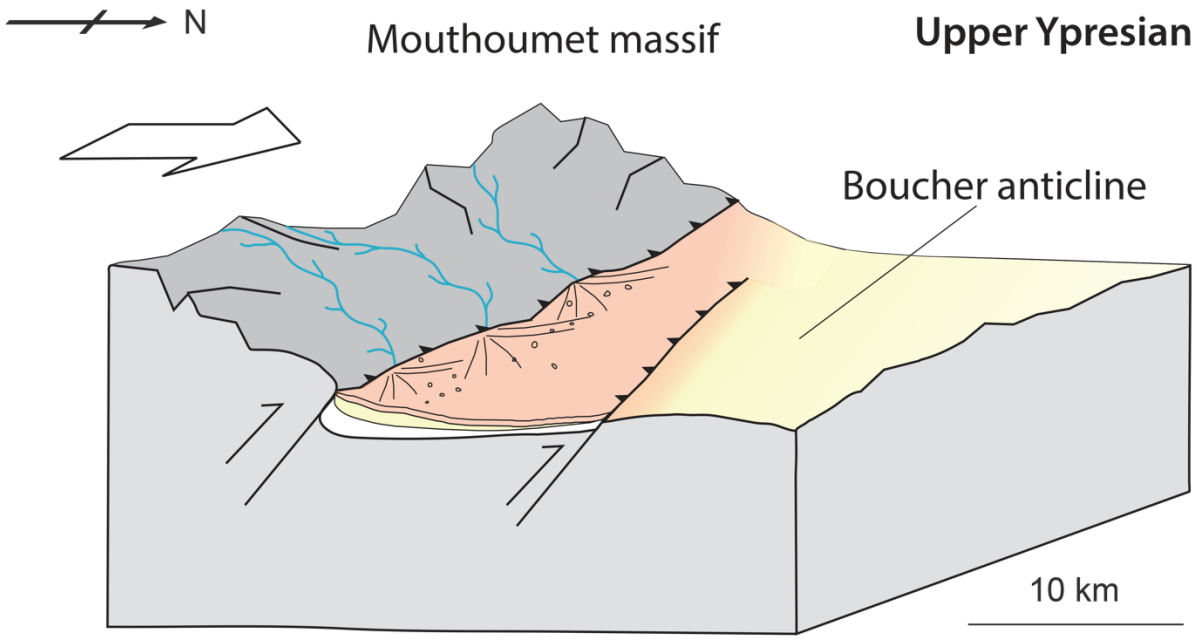

Figure 6.1: Schematic evolution of the Corbières region during the late Ypresian based on the results acquired in this thesis. Three sedimentary systems delivering the Palassou series to the basin from the NPZ.

The unit 2 of the Palassou conglomerates is deposited during the middle/late Lutetian – early Bartonian and contains granite clasts associated to a paleocurrent direction toward the north and the northwest (Figure 6.2). The deposited material, in addition to the megafan characterized in this unit (cf. the top of the stratigraphic log of Caunette-sur-Lauquet/Pomas) reflects the acceleration of the exhumation and the exposition of granite basement to erosion in the Pyrenees. This acceleration is accompanied by a change in clasts content with mostly plutonic clasts for unit 2. The evolution of the Corbières region during the Bartonian has been characterized by combining apatite low temperature thermochronology, zircon U/Pb geochronology and sedimentology studies. Low temperature thermochronology (LTT) results for the Eocene granite boulders from the Corbières region reveal an early orogenic exhumation in the Pyrenees represented by AHe ages older than deposition ages and consistent with Upper Cretaceous LTT ages obtained in the NPZ and the Axial Zone (Yelland 1991; Maurel et al. 2008; Vacherat et al. 2016; Ternois et al. 2019). In the unit 2 of the Palassou series, paleocurrent directions are northward and north-west and most of granite clasts and matrix samples show Variscan ages. We have suggested that the changing in clast content is explained by a change in the drainage network. This change occurred due to the end of inversion in the NPZ and the transition to the Azial Zone crustal stacking. The source area of the unit 2 deposits are thus the Axial Zone of the Pyrenees, in particular the massifs having zircon U/Pb ages around 330 Ma (Aston-Hospitalet (324±2 and 334±6 Ma, Mezger and Gerdes (2016)) and Ax-les-thermes (321±7 Ma, Denele (2007)) as granite clast samples from the basin have comparable ages.

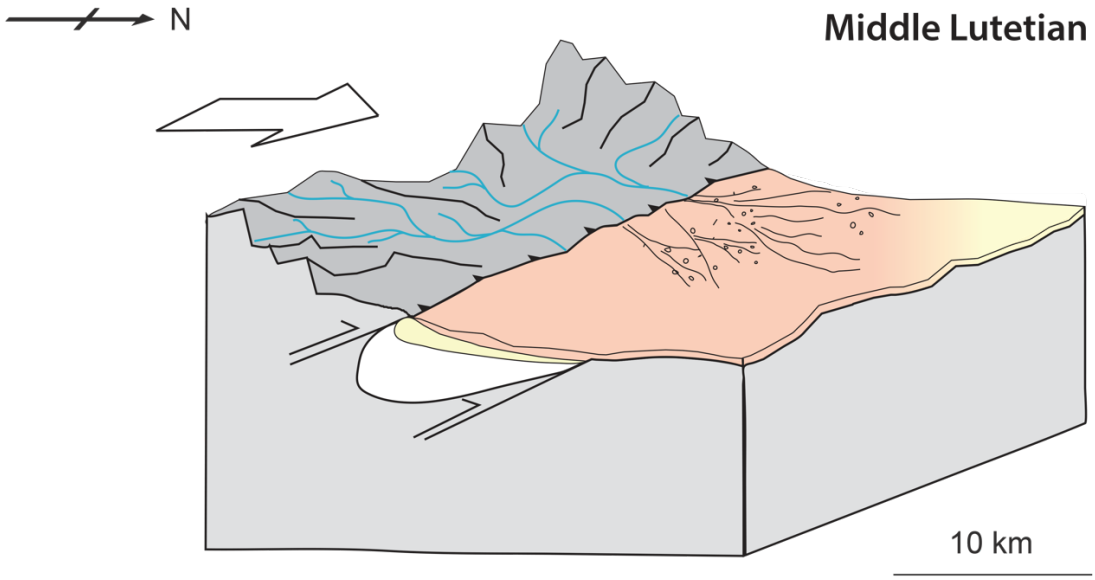

Figure 6.2: Schematic evolution of the Corbières region during the middle Lutetian as constrained by the PhD results. Sediment amount to the basin increased significantly due to the accelerated exhumation of the Pyrenean belt.

The late Priabonian granite clasts deposits in the western part of the Corbières region show three groups of zircon U/Pb ages: ages ranging between 300 and 380 Ma, ages ranging between 430 and 500 Ma and finally ages ranging from 540 to 600 Ma. Comparable U/Pb results are obtained for matrix samples of Early Oligocene deposition age reflecting the emergence of the whole Pyrenean belt and its exposition to erosion during this period. Low temperature thermochronology results obtained for the unit 2 granite clasts allowed to constrain a thermal event interpreted as a post-Bartonian/Priabonian burial caused by the deposition of a thick layer of sediments ranging around 1150±150 m in the Carcassonne basin and 1300±150 m in the Mas d'Azil. The age of the erosion phase following burial has been estimated according to thermal modelling tests and sedimentology approaches. In fact, as the Miocene deposits of Langhian age (~16 Ma) in the eastern part of the Aquitaine Basin are discordant on the marine Ypresian sediments (Aguilar and Magné 1978; Ellenberger et al. 1985), the erosion phase timing is estimated as pre-Langhian time and could be linked to the connection of the proximal foreland to the deep basin and the rifting event near the Gulf of Lion occurring during the Oligo-Miocene time. Such erosion is also characterized from the cross-section construction of Rougier et al. (2016) as they determined a post-Oligocene erosion phase in the Mirande basin. Results suggest a comparable aggradation of sediments between the north Pyrenean foreland basin and the South Pyrenean basin followed by an erosion. However, the timing of the erosion phase is different as it occurs during the late Miocene – early Pliocene in the pro-foreland basin and during the early to middle Miocene in the retro-foreland basin.

	Low temperature thermochronology	U/Pb geochronology and RSCM analysis	Sedimentology
Late Ypresian – Lutetian (unit 1)		*U/Pb zircon ages for matrix samples show Variscan peak signal (310-330 Ma) *The unit 1 deposits are mainly fed from the NPZ *RSCM analysis for black flysch clasts show temperature comparable to the one obtained in the NPZ.	*Four sedimentary systems characterized by an increasing size from east to west
Middle/late Lutetian - Bartonian (unit 2)	*AHe ages older than the deposition age indicate a Late Cretaceous cooling in the source massifs. Comparable LTT ages obtained in the NPZ and the Axial Zone are interpreted as an early orogenic phase in the Pyrenees.	*Zircon U/Pb ages for granite clasts and matrix samples from the unit 2 show a Variscan signal. Most of the granite clast samples have age around 330 Ma. *Comparable U/Pb ages are obtained for the Aston-Hospitalet and Ax-les-Thermes massifs in the Axial Zone of the Pyrenees. *The unit 2 deposits are mostly fed from the Axial Zone of the Pyrenees. This is confirmed by the obtained results and the change in clast content compared to the unit 1. This change is linked to the end of inversion in the NPZ and the transition to the Axial Zone crustal stacking. *Samples located in the northern Corbières (MX-3, MX-4 and CL-1) are fed from the Montagne Noire	*A megafan characterized at the base of the unit 2 (log Caunette-sur-Lauquet/Pomas) reflects the acceleration of exhumation in the mountain belt. * Paleocurrent direction in the unit 2 deposits are mainly toward the north and the north-west
Priabonian –Oligocene (unit 3)	*Post-Bartonian/Priabonian burial event due to the deposition of 1150±150 m thickness of	*Three populations of U/Pb ages are obtained for granite clasts and matrix samples: (1) 300-380 Ma, (2) 430-500 Ma and (3) 540-600 Ma. The multimodal distribution of U/Pb ages suggest a central and eastern Pyrenean	

	sediments in the Carcassonne basin and 1300±150 m of sediments in the Mas d'Azil area.	source.	
Early – Middle Miocene	*Pre-Langhian erosion phase that may be linked to the connection of the proximal foreland to the deep basin and the rifting event near the Gulf de Lion.		

Table 6.1: Summary of the main results obtained during this PhD in the Corbières region from the Ypresian to the Miocene.

Evolution of the Pyrenees and its foreland basins from the Santonian to the Miocene.

Santonian – Maastrichtian paleogeographic evolution of the Pyrenean domain

The onset of convergence, estimated at 83 Ma (Mouthereau et al., 2014), is followed by the emergence of the Agly-Salvezines block in the eastern NPZ as demonstrated by Ternois et al. (2019) (Figure 6.4). In addition, the uplift of the Boixols-Sant Cornelli high occurred during the Campanian as a result of the inversion of the Organya basin in the central part of the SPZ (Berastegui et al., 1990; Bond and McClay, 1995) (Figure 6.4). Low temperature thermochronology results obtained for granite boulders in this thesis (AHe ages older than deposition ages) indicate a Late Cretaceous cooling episode interpreted as an early orogenic exhumation in the Pyrenees. This result is consistent with other low temperature thermochronology data reflecting a synchronous exhumation of the Axial Zone at this time as mentioned by Whitchurch et al. (2011) and Filleaudeau et al. (2012).

In the NPZ, the Santonian sandstone "Grès de Celles" deposited in the eastern and central NPZ are topped in the eastern part by the continental deposits of "Grès de Labastide" and "Grès d'Alet" formations of Campanian age (Vacherat et al., 2017). Paleocurrent directions measured in the Campanian to Maastrichtian sandstones to the north of the NPFT near the Arize massif show a south-southeast source that could probably be the Agly-Salvezine block emerged at this time (Cavaillé and Paris 1976; Vacherat et al. 2017) (Figure 6.4). Such result suggests that the drainage divide location is to the south of the Agly-Salvezine block.

In the eastern part of the SPZ, detrital geochronology results from Odlum et al. (2019) show that the Late Cretaceous deposits in the Ripoll basin are sourced from a south-eastern to eastern location probably in the Coastal Catalan Range and Corsica-Sardinia block (Figure 6.4). The Tremp basin located in the central part of the SPZ is filled by westward prograding Santonian to Campanian deltaic shales with slope carbonate and siliclastic turbidites (Ardèvol et al. 2000) topped by shoreface to deltaic sandstone of late Campanian to Maastrichtian age. Deposits in the basin became fluvial and lacustrine from the early Maastrichtian to the Paleocene (Plaziat 1975; Nijman 1990; Nijman 1998; Ardèvol et al. 2000; Clevis et al. 2004; Pujalte et al. 2009). As these sediments are sourced from the east until the late Maastrichtian as demonstrated by Arbués et al. (1996) and Ardèvol et al. (2000), sources located in the Coastal Catalan Range and the Corsica-Sardinia block are proposed by Odlum et al. (2019) for the Late Cretaceous sediments in the Ripoll basin.

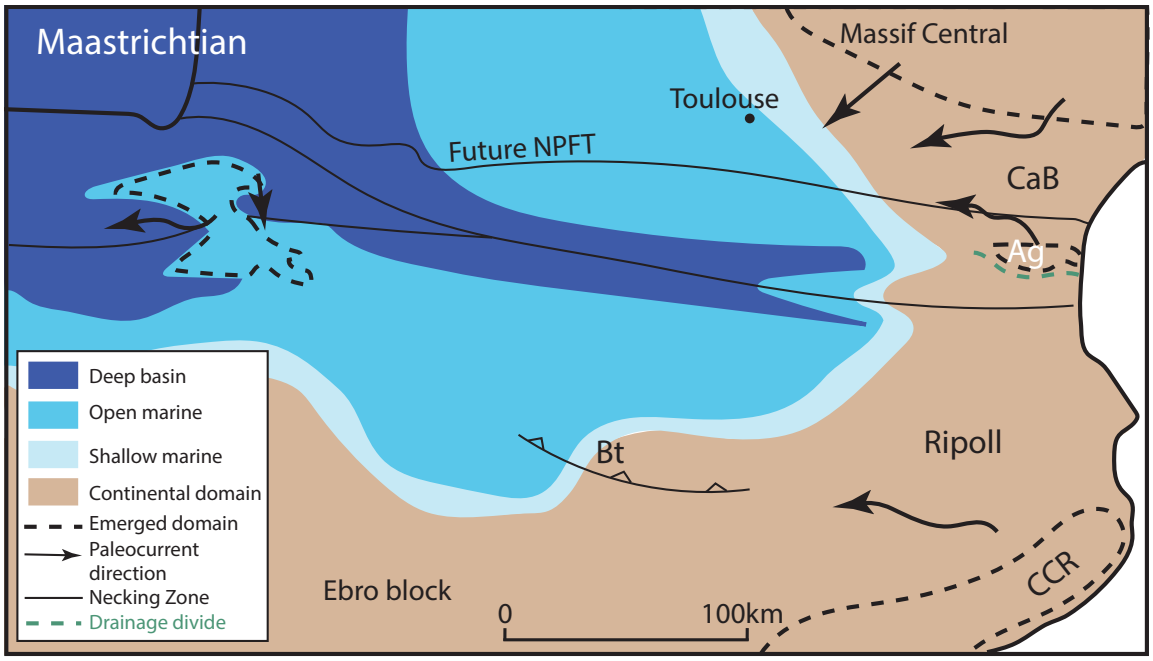

Figure 6.4: Updated paleogeographic reconstruction of the Pyrenean domain during the Maastrichtian. Bt: Boixols thrust, CaB: Carcassonne Basin, CCR: Catalan Coastal Range, NPFT: North Pyrenean Frontal Thrust.

Ypresian to Bartonian paleogeographic evolution of the Pyrenean domain

After a quiescence phase during the Paleocene, the main exhumation phase of the Pyrenees started during the early Eocene. Around 30 km of shortening is suggested by Mouthereau et al. (2014) from the early Paleocene to the Middle Eocene, accommodated in the north-eastern part of the Pyrenees. This led to a major cooling in the Pyrenean massifs demonstrated by low temperature thermochronology on the North Pyrenean Zone like for the Agly-Salvezines block, Trois Seigneurs, Lacourt and Foix massifs, and on the eastern part of the Axial Zone like for the Quérigut, Aston, Andorra-Mont Louis and Riberot massifs (Yelland, 1991; Fitzgerald et al., 1999; Maurel et al., 2008;

Gunnell et al., 2009; Mouthereau et al., 2014; Vacherat et al., 2016; Vacherat et al., 2017; Ternois et al., 2019). Later, the exhumation is accelerated during the Bartonian (Yelland 1991; Maurel et al. 2008; Gunnell et al. 2009; Mouthereau et al. 2014; Vacherat et al. 2017) leading to the emergence of the whole mountain belt according to kinematic and low temperature thermochronology studies (Fitzgerald et al., 1999; Sinclair et al., 2005; Metcalf et al., 2009; Fillon and van der Beek, 2012; Mouthereau et al., 2014; Bosch et al., 2016).

During the early Eocene time, a transition from marine (Ilerdian formations) to continental sedimentation (the Palassou fluviatile series, also called Carcassonne group) occurred in the Corbières region (Figure 6.5). The Ilerdian formations contain essentially Ypresian blue marls, oysters and nummulitids sandstones that recorded a marine transgression having penetrated across the foreland basin to its eastern part (Rougier et al., 2016). The deposition of the early Ypresian marine sediments is controlled by the development of the Mouthoumet frontal thrust propagation fold during thrust wedge advance (Christophoul et al. 2003) (Figure 6.5). The Talairan syncline is likely to represent the foredeep during this period according to DeCelles and Giles (1996) and Christophoul et al. (2003) (Figure 6.5). The transition from marine to continental sedimentation occurred during the late Ypresian according to Plaziat (1984) and Crochet (1989). Sedimentological analysis made during this PhD provide four sedimentary systems, deposited from the late Ypresian to the late Lutetian time (unit 1), having a geometry increasing from east to west. They are sourced mainly from the NPZ as demonstrated by U/Pb geochronology results, RSCM analysis and paleocurrent directions. For the unit 2 deposits, the log of Caunette-sur-Lauquet/Pomas shows a megafan at the base of unit 2 associated to paleocurrent directions indicating a south/south-eastern Pyrenean source. Results reflect a large amount of sediments transported to the basin, linked to the rapid emergence of the belt during this time. A change in the drainage system is evidenced by the deposition of granite clasts in the basin during the Bartonian. Zircon U/Pb geochronology indicates Variscan signals for granite clasts and matrix samples. On the basis of these results we suggested an Axial Zone source for the Bartonian deposits in the Corbières region.

In the southern domain of the Pyrenees, the Ripoll basin deposits show a north/north-east source during the Ypresian demonstrated from a multi-modal signal (Figure 6.5) dated by detrital zircon U/Pb data (Whitchurch et al., 2011; Odlum et al., 2019). Such signal is contemporaneous with an increased subsidence and accommodation space marked by a shift from shallow carbonate to deep-marine turbidites (Puigdefabregas et al., 1986; Burbank et al., 1992; Grool et al., 2018; Odlum et al., 2019). According to zircon (U-Th)/He (ZHe) results, the first appearance of a Pyrenean source deposits during the Ypresian is accompanied by a near to zero lag time, which means that the major exhumation of the Pyrenees is accompanied by an erosion phase and rapid transportation to the basin. The eastern part of the Axial Zone may be the source of sediments during this time. Only one U/Pb age of ~100 Ma for a rutile grain is obtained by Odlum et al. (2019) and interpreted as having its

source from the NPZ. Based on this, they placed the drainage divide to the north of the north Pyrenean fault. Our zircon U/Pb results for two matrix samples from the Palassou unit 1 show a Variscan peak age between 320 and 330 Ma accompanied by a paleocurrent direction from the south (Figure 6.5). In addition, RSCM analysis and sedimentary studies suggest a NPZ source of the unit 1 sediments. We thus suggest that the location of the drainage divide should be somewhere in the NPZ or more to the south in the Axial Zone (Figures 6.5 and 6.6). Detrital zircon U/Pb ages acquired by Odlum et al. (2019) for the southern Lutetian samples show a relative proportions of Variscan ages, that may reflect the erosion of the Pyrenean Axial Zone basement. Such ages are associated to paleocurrent directions from the east and north-east. A detrital zircon U/Pb age for a late Lutetian sample from the Ripoll basin dated by Odlum et al. (2019) represents a shift in age distribution compared to other samples and an increased lag time in ZHe associated with multimodal age spectra. The deposition age of the sample is coincident with the Mid-Eocene Climatic Optimum (MECO) and is interpreted as a possible result of a climate driven catchment expansion and enhanced erosion leading to increased exhumation in the Pyrenean belt (Odlum et al., 2019). The timing of the MECO (~40 Ma, Bohaty et al. 2009) is also coincident with the changing in clast sources in the eastern part of the north Pyrenean foreland basin from Meso-Cenozoic clasts sources during the late Ypresian-Lutetian time to a plutonic source, essentially granite during the Bartonian time, and the increasing amount of sediments delivered to the basin. Further data are needed to constrain whether or not climate is really involved in the source changes.

To the west, the Ebro Basin developed as underfilled with marine sedimentation during the early and middle Eocene (Puigdefàbregas and Souquet 1986; Puigdefabregas et al. 1986; Puigdefàbregas et al. 1992; Vergés et al. 1995; 1998) with western paleoflow direction towards the central and western Pyrenees and southward prograding deltaic sediments (Figures 6.5 and 6.6). The contribution of these deposits is from the north (Whitchurch et al., 2011). The Tremp and Jaca basins encountered a shallowing-up sedimentation from marine, during the early to middle Eocene, to fluviatile, during the late Eocene. Detrital zircon U/Pb ages obtained for the early Eocene sediments from the Tremp basin show a strong Variscan source signal that is supposed to come from the emerged eastern and central part of the Pyrenees (Whitchurch et al., 2011) (Figures 6.5 and 6.6). Several source changes have been recorded in the early-middle Eocene marine deposits in the Jaca basin according to petrological analysis from Roigé et al. (2016). Results show that the middle and upper Lutetian deposits, known as the Banastón, and the lower Jaca turbidite system, are mainly fed from an eastward source. However, the upper Jaca turbidite system having a deposition age at the Lutetian-Bartonian transition shows a different component and are fed from the north (Figure 6.6). Such source change is interpreted as a consequence of the uplift of the Eaux-Chaudes/Lakora thrust sheet in the Axial Zone (Roigé et al. 2016). The location of the drainage divide should thus be set to the north of the Eaux-Chaudes massif (Figures 6.6). Lutetian-Bartonian turbidites deposits in the Jaca

basin are topped by a sandstone formation, known as Sabiñánigo sandstone of middle Bartonian age, revealing an eastern-northeastern source. This formation reflects a change in the source of the delivered sediments (Roigé et al. 2016). Petrological analysis of the late Bartonian- early Priabonian deposits in the same basin, known as the Atarès delta records, are fed from the east according to Roigé et al. (2016).

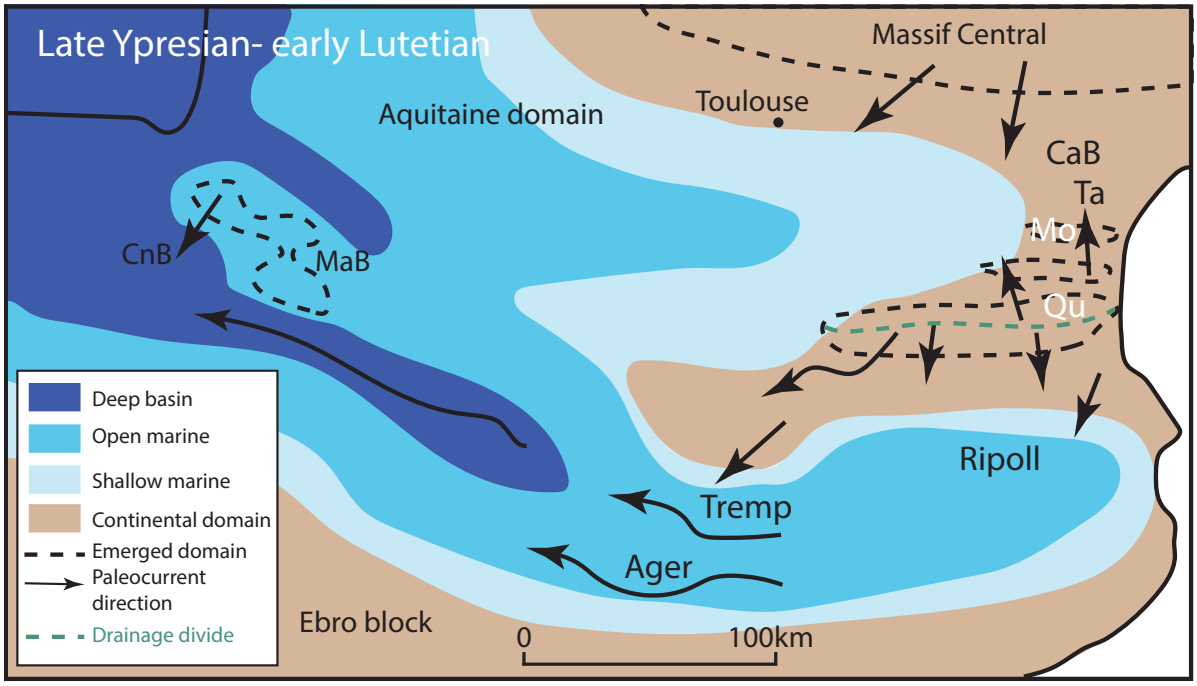

Figure 6.5: Updated paleogeographic reconstruction of the Pyrenean domain during the late Ypresian - Lutetian. CaB: Carcassonne Basin, CnB : Cantabrian Basin, MaB: Mauléon Basin, Mo: Mouthoumet massif, Qu: Quérigut-Millas massif, Ta : Talairan syncline.

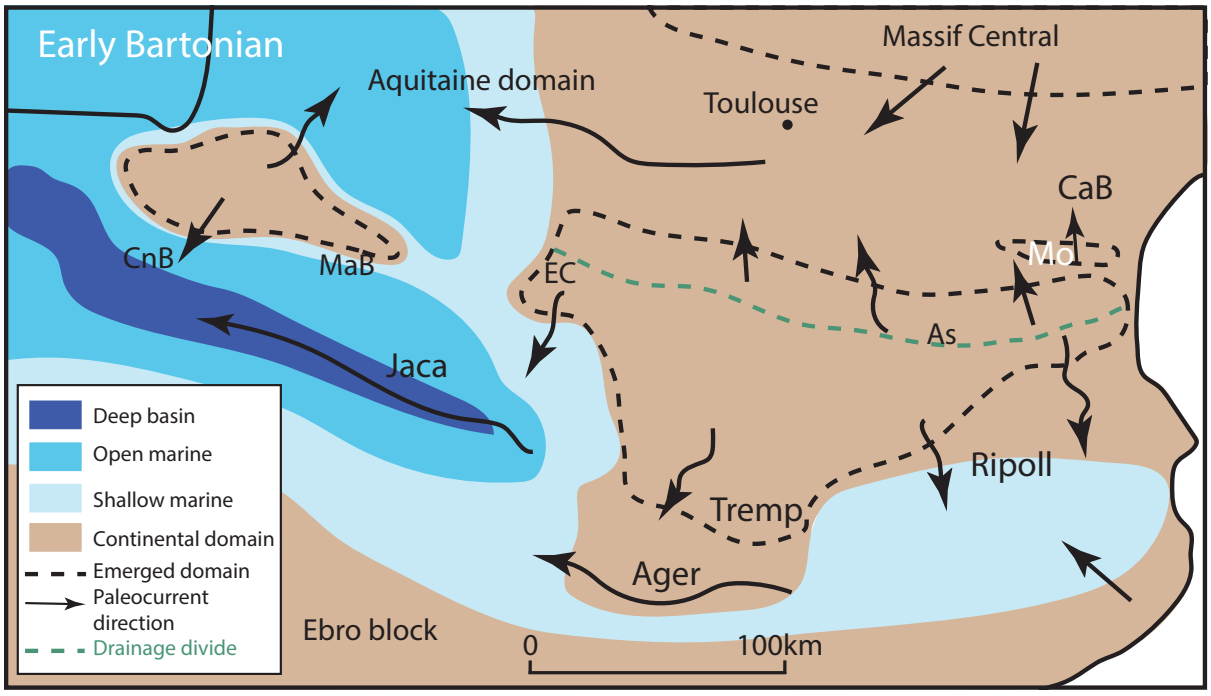

Figure 6.6: Updated paleogeographic reconstruction of the Pyrenean domain during the Bartonian. As : Aston massif, CaB: Carcassonne Basin, CnB : Cantabrian Basin, EC: Eaux-Chaudes massif, MaB: Mauléon Basin, Mo : Mouthoumet massif.

Late Eocene to Miocene paleogeographic evolution of the Pyrenean domain

LTT studies in the NPZ and the Axial Zone show that most of the Pyrenean Paleozoic basement was involved in the orogenic prism during the middle – late Eocene (Yelland, 1991; Morris et al., 1998; Fitzgerald et al., 1999; Sinclair et al., 2005; Jolivet et al., 2007; Gibson et al., 2007; Maurel et al., 2008; Gunnell et al., 2009; Metcalf et al., 2009; Whitchurch et al., 2011; Rushlow et al., 2013; Mouthereau et al., 2014; Bosch et al., 2016; Labaume et al., 2016; Vacherat et al., 2016). During the late Eocene to Oligocene time, the pattern of exhumation became asymmetric as evidenced by LTT results (Whitchurch et al., 2011), and denudation focused on the southern flank of the Pyrenees with the exhumation of the Riberot, Marimaña, Arties and Maladeta massifs (Fitzgerald et al., 1999; Sinclair et al., 2005; Gibson et al., 2007).

AFT and AHe results obtained for granite clasts from the unit 2 deposits, allowed to constrain the thermal history of the basin. They enable the recognition of a Late Cretaceous exhumation phase in the belt, followed by a post-Bartonian burial episode that traduces a thicker sedimentary layer deposited in the basin, and an early to middle Miocene exhumation that has been interpreted as an erosion phase. The latter erosion phase could be linked to the connection of the proximal foreland to the deep basin and the rifting event near the Gulf of Lion occurring during the Oligo-Miocene time. A comparable post-Oligocene erosion phase is characterized by Rougier et al. (2016) in the Mirande basin. Three populations of zircon U/Pb ages are obtained for granite clasts and conglomerate matrix from unit 3 that range between 300 and 380 Ma, 430 and 500 Ma and 540 to 600 Ma and reflect a source from the eastern and central Pyrenees.

In the central part of the north Pyrenean foreland basin, subsidence increased from the middle to late Eocene leading to the northward migration of the depocenter of the Mirande basin contemporaneous with an increase in sediment amount deposited in the basin as suggested by Rougier et al. (2016) (Figure 6.7). Shortening in the central part of the north Pyrenean foreland basin lasted until the early Miocene as recorded by the development of Mas d'Azil and Lavelanet anticlines (Mouthereau et al., 2014; Vacherat et al., 2017). These last deformations are sealed by the middle Miocene-Pliocene Lannemezan alluvial system located further to the west (Azambre et al., 1989; Mouchené et al., 2017).

During the late Eocene time in the pro-foreland basin, the sediment routing system is transverse with respect to the belt as the paleocurrent direction measured in the Ripoll basin deposits are toward the west (Figure 6.7). Detrital zircon U/Pb ages acquired by Odlum et al. (2019) for the middle to late Eocene sediments in the Ripoll basin show a strong signal of Variscan age (280-420 Ma). In addition, ZHe results in the Ripoll basin show Pyrenean ages ranging between 40 and 70 Ma interpreted as sourced from the Carboniferous-late Permian plutons in the Axial Zone of the Pyrenees. However, detrital rutile U/Pb results record ages older than 520 Ma interpreted as sourced from the

Paleozoic metasediments in the Pyrenees (Odlum et al., 2019). Similar U/Pb ages (Variscan and older than 520 Ma) on zircon grains are obtained for granite clasts and conglomerate matrix from middle to late Eocene sediments from the northern Pyrenean foreland basin. As the Variscan signal is observed on both flanks of the Pyrenees during the late Eocene, and because the zircon U/Pb ages obtained for granite boulders in the north Pyrenean basin are mostly around 330 Ma and correspond to few plutonic massifs in the belt, we propose that the location of the drainage divide should be to the south of the Aston massif (Figure 6.7) during this time.

U/Pb results obtained for the late Eocene fluvial and alluvial deposits in the Tremp Basin show a multimodal mixed signal with a strong Variscan source combined with a Cadomian source. During this period, the basin recorded a transition between orogen-parallel to orogen-transverse sediment dispersal at this time (Whitchurch et al., 2011). Compared to the period where Variscan records are shown in the Tremp basin, significantly strong during the early and late Eocene (Whitchurch et al. 2011), this signal is recorded later for the first time in the Ripoll basin (Filleaudeau, 2011; Whitchurch et al., 2011; Thomson et al., 2017) showing an important contribution of the Axial Zone of the Pyrenees in delivering material to the basin (Figure 6.7) (Burbank et al. 1992; Puigdefàbregas et al.1992; Whitchurch et al. 2011). This period is characterized in the central part by increasing tectonic activity in the Sierras Exteriores, as evidenced by the formation of several N-S anticlines (Millán et al. 1994; Huyghe et al. 2009; Vacherat et al. 2017) and by the dismantling of the carbonate platform into turbidites filling the Jaca Basin (Mutti, 1977; Labaume et al., 1987; Caja et al., 2010; Pohl and McCann, 2014). In the Jaca Basin, the late Eocene- Oligocene terrestrial sedimentation is represented by four alluvial fan systems: the Santa Orosia, Canciás, Peña Oroel and San Juan de la Peña alluvial systems appearing diachronously from east to west (Roigé et al. 2017). The Santa Orosia alluvial system shows a dominance of sandstone clasts supposed to be derived from the lower Jaca turbidite system located toward the north, associated with the activation of the Gavarnie thrust in the Axial Zone (Roigé et al. 2016). Sandstone clasts in this basin reveal a source from the North Pyrenean Zone according to Roigé et al. (2017) providing Cretaceous carbonate flysch, Jurassic dolostones and Triassic dolerites. The location of the drainage divide should be thus set to the north of the NPZ in the central part of the Pyrenean domain (Figure 6.7). A significant increase in sediment flux to the Jaca basin is recognized in the late Bartonian- late Priabonian time according to Michael et al. (2014) and resulted from the increase of the amount of terrestrial material delivered to the basin and the export of sediment to the deep-marine depocenter causing the progressive continentalization of the basin. U/Pb results for late Oligocene deposits in the Ebro Basin show a multimodal mixed source (Whitchurch et al., 2011). Thrusting in the Sierra Exteriores during the late Oligocene signs the last stage of thrusting (Muñoz et al. 1986).

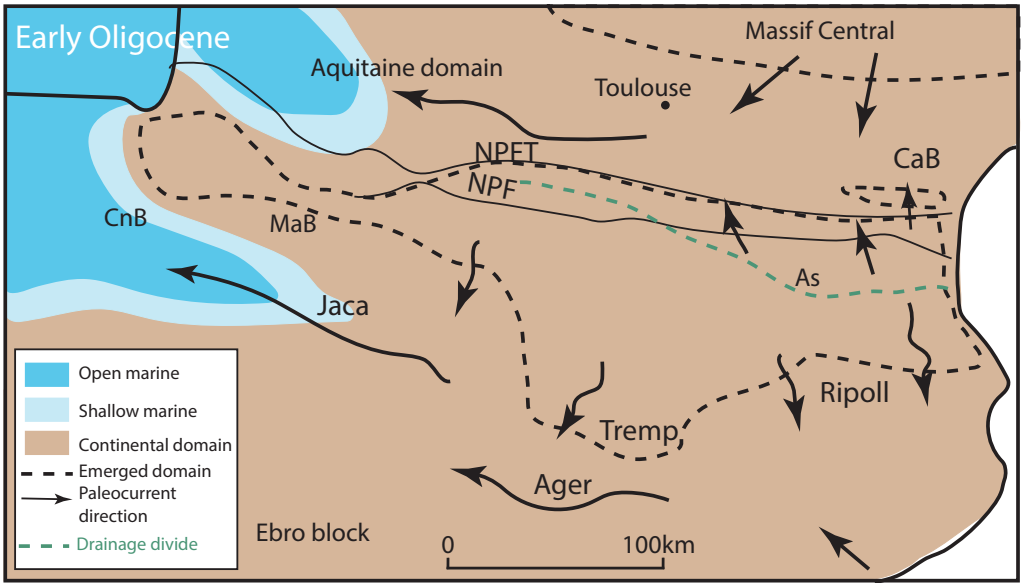

Figure 6.7: Paleogeographic reconstruction of the Pyrenean domain during the early Oligocene. As: Aston massif, CaB: Carcassonne Basin, CnB: Cantabrian Basin, MaB: Mauléon Basin. NPF: North Pyrenean Fault, NPFT: North Pyrenean Frontal Thrust.

Conclusions

This thesis aimed at characterizing the sediment routing system in the north Pyrenean foreland basin. The syn-orogenic deposits in the Corbières region represent the transfer zone of the exhumed Pyrenees during the Eocene. This zone recorded the complete exhumation of the eastern and central Pyrenees. Three approaches have been combined together: (i) sediments analysis that allowed the characterization of deposition environments and provided information about the geometry of the deposits. It allows understanding the implication of deformations on the sediment routing system (ii) AFT and AHe analysis for granite boulders from the unit 2 of the Palassou series allowed understanding the thermal history of the basin and its infilling mode, (iii) U/Pb zircon analysis have been useful to identify the source of the deposited material for each unit and to reconstruct the source to sink system. The sediment routing system in the northern flank of the Pyrenees is compared to the one in the southern flank to give a global overview of the evolution of both basins during the Pyrenean orogenesis.

Sedimentological studies have led to the characterization of four sequences of sediment infilling along unit 1. The first sequence is observed in the stratigraphic log of Villerouge/Talairan, the second one is observed in the Orbieu valley, the third sequence in the log of Labastide-en-Val/Clermont-sur-Lauquet and the fourth one in the log of Caunette-sur-Lauquet/Pomas. The results show that the Talairan syncline has acted as a piggy-back basin during the deposition of the unit 1 sediments, limited to the north by “les chaînons de Lagrasse”. The unit 1 sediments are interpreted as syn-tectonic deposits marked by the propagation of thrusts and folds. The maximum progradation of the fourth sequence is located out of the Talairan syncline and show the overfilling of the piggy-back basin and the exportation of sediment more to the west.

Low temperature thermochronology results and their corresponding thermal histories acquired for granite boulders from unit 2, confirmed the existence of an early orogenic phase represented by AHe ages ranging from 50 to 75 Ma, and reflecting a cooling event in the belt with a long stay in the Partial Retention Zone. Moreover, Time-temperature paths show a post-Bartonian thermal event that corresponds to the deposition of a kilometric layer of sediment revealing that the Palassou series were ~1 km thick. The burial event is followed by a final exhumation interpreted as an erosion phase occurring during the late Burdigalian – early Langhian time. We interpret the final exhumation as linked to the Oligo-Miocene event in the near Gulf de Lion. Furthermore, the aggradation of a kilometric Palassou deposit in the northern foreland basin has an observed counterpart in the southern piedmont in the preservation of the Oligo-Miocene post-orogenic deposits reaching up to 1000-1500 m. The erosion of these deposits in the southern piedmont is accompanied by remnants of low-relief erosional surfaces at high elevations. If we considered that the low-relief high elevation surfaces mapped in the northern flank of the Pyrenees by Bosch et al. (2016) are interpreted as late-post orogenic erosional surfaces, it means that the two foreland basins of the Pyrenees have a comparable

aggradation to erosion history but different timing. To sum up, the south Pyrenean flank data show excavation in the late Miocene to the early Pliocene, while the northern flank was excavated before.

Matrix and granite clasts samples from units 1, 2 and 3 have been studied using zircon U/Pb geochronology. They have been coupled to RSCM (Raman Spectroscopy of the Carbonaceous Material) results obtained for black flysch clasts from unit 1 and paleocurrent directions measured in the Corbières region. The obtained U/Pb results show a single source per site of sampling with two population of ages, Variscan and Cadomian ages, mostly fed from the Pyrenees. The RSCM results show peak temperature ranging from 495 and 587°C comparable to the temperatures obtained for the NPZ in Clerc et al. (2015). The interpretation of these results, combined with sedimentology analysis, has led to the identification of the source areas for each unit. The lower deposits of unit 1 are fed from the sedimentary cover in the NPZ. They are followed by the Albo-Cenomanian black flysch clasts and the Variscan zircons (including granite clasts observed in the upper part of unit 1). The change in the clasts content for unit 2 is explained by the change in the drainage network activated by the end of inversion in the NPZ and the transition to the Axial Zone crustal stacking. The potential source area of the deposits of unit 2 is the Axial Zone, in particular the massifs having zircon U/Pb ages around 330 Ma, Aston-Hospitalet (Mezger and Gerdes 2016) and Ax-les-thermes (Denele 2007) massifs. Granite clasts and matrix samples from unit 3 show a multimodal signal containing three groups of ages (Variscan, Caledonian and Cadomian) reflecting the increase of the drainage area covering the whole central and eastern part of the Pyrenees.

This thesis provided a reconstruction of the source to sink system in the Corbières zone, and defined the evolution of basin infilling during Eocene in the northen flank of the Pyrenees. The combination of kinematic, LTT, geochronology and stratigraphy data on the Pyrenean belt and the two foreland basins, that are obtained in this thesis, has led to the proposition of a complete reconstruction of the Pyrenean domain during Eocene. Such a study is key to the comprehension of foreland basin infilling and can be used in other orogens having a comparable geological context.

Perspectives:

Mineralogical content analyses using X-Ray Diffractometer have been made among 3 stratigraphic logs in the unit 1 during this thesis: Villerouge/Talairan, Labastide-en-Val/Clermont-sur-Lauquet and Mouthoumet/Pomas. Given the significance of the results in having information about climate, we propose the same analysis for samples from the units 2 and 3 in order to have a better idea about climate during Eocene.

The sediment routing system of the Pyrenean domain proposed in this thesis could be used as a basis to refine the location of the drainage divide in the Pyrenees during Eocene. As demonstrated by Odlum et al. (2019) the deposited sediments in the southern foreland basin during the Eocene are mainly sourced from Mesozoic sediments, Paleozoic metasediments and Carbonifereous – early Permian plutonic rocks (late Variscan ages 320-290 Ma). Such ages, in particular late Variscan, are also acquired on the Eocene deposits in the northern foreland basin (this thesis).We propose further analysis that permits to fix the location of the drainage divide in the eastern part of the Pyrenees.

The reconstruction of the paleogeography and the sediment routing system proposed in Vacherat et al. (2017) is a first approach that deserves to be improved. The application of the same methods used in this thesis (sedimentology, low temperature thermochronology and geochronology) for the Eocene deposits on the central part of the north Pyrenean foreland could be very useful to refine to reconstructed paleogeography. Only one sample has been dated using ZHe and U/Pb methods in the Palassou series from the central part of the basin in Mouthereau et al. (2014) and more data are needed to better constrain the evolution of this zone. Such work is important to be done and compared with the results of Whitchurch et al. (2011) on the southern part of the basin.

References

Aguilar, C., Liesa, M., Castiñeiras, P., & Navidad, M. (2014). Late Variscan metamorphic and magmatic evolution in the eastern Pyrenees revealed by U–Pb age zircon dating. Journal of the Geological Society, 171(2), 181–192.

Aguilar, C., Liesa, M., Štípská, P., Schulmann, K., Muñoz, J. A., & Casas, J. M. (2015). P–T–t–d evolution of orogenic middle crust of the Roc de Frausa Massif (Eastern Pyrenees): A result of horizontal crustal flow and Carboniferous doming? Journal of Metamorphic Geology, 33(3), 273–294. https://doi.org/10.1111/jmg.12120

Aguilar, J. P., & Magné, J. (1978). Nouveaux gisements a Rongeurs dans des formations marines miocenes du Languedoc mediterraneen. Bulletin de La Société Géologique de France, 7(6), 803–805.

Albarede, F., & Michard-Vitrac, A. (1978). Datation du metamorphisme des terrains secondaires des Pyrenees par les methodes 39 Ar-40 Ar et 87 Rb-87 Sr; ses relations avec les peridotites associees. Bulletin de La Société Géologique de France, 7(5), 681–687.

Allen, G., Barnes, J., Pavelsky, T., & Kirby, E. (2013). Lithologic and tectonic controls on bedrock channel form at the northwest Himalayan front. Journal of Geophysical Research-Earth Surface, 118(3), 1806–1825. https://doi.org/10.1002/jgrf.20113

Angrand, P., Ford, M., & Watts, A. B. (2018). Lateral Variations in Foreland Flexure of a Rifted Continental Margin: The Aquitaine Basin (SW France). Tectonics, 37(2), 430–449. https://doi.org/10.1002/2017TC004670

Arbués, P., Pi, E., & Berástegui, X. (1996). Relaciones entre la evolución sedimentaria del Grupo de Arén y el Cabalgamiento de Boixols (Campaniense terminalMaastrichtiense del Pirineo Meridional-Central).

Ardèvol, L., Klimowitz, J., Malagón, J., & Nagtegaal, P. (2000). Depositional sequence response to foreland deformation in the Upper Cretaceous of the Southern Pyrenees, Spain. AAPG Bulletin, 84(4), 566–587.

Arenas, C., Millán, H., Pardo, G., & Pocoví, A. (2001). Ebro Basin continental sedimentation associated with late compressional Pyrenean tectonics (north-eastern Iberia): Controls on basin margin fans and fluvial systems. Basin Research, 13(1), 65–89.

Arthaud, F., & Matte, P. (1977). Late Paleozoic strike-slip faulting in southern Europe and northern Africa: Result of a right-lateral shear zone between the Appalachians and the Urals. Geological Society of America Bulletin, 88(9), 1305–1320.

Astre, G. (1959). Terrains stampiens du Lauragais et du Tolosan. Bull. Soc. Hist. Nat. Toulouse, 9, 8–168.

AGSO-BRGM, les cartes de la synthèse géologique des Pyrénées, cycle Alpin, 2018, Association des Géologues du Sud-Ouest, 2, n/a

Ault, A., Gautheron, C., & King, G. (2019). Innovations in (U-Th)/He, fission-track, and trapped-charge thermochronometry with applications to earthquakes, weathering, surface-mantle connections, and the growth and decay of mountains. Tectonics.

Autran, A., Fonteill, M., & Guitard, G. (1966). Discordance du Paléozoïque inférieur métamorphique sur un socle gneissique antéhercynien dans le massif des Albères (Pyrénées orientales). Comptes Rendus Hebdomadaires Des Séances de l'académie Des Sciences Série D, 263(4), 317.

Autran, A., & Guitard, G. (1969). Mise en évidence de nappes hercyniennes de style penninique dans la série métamorphique du massif du Roc de France (Pyrénées orientales): Liaison avec la nappe du Canigou. Comptes Rendus de l'Académie Des Sciences, 269, 2479–2499.

Azambre, B., Crouzel, F., Debroas, E. J., Soulé, J. C., & Ternet, Y. (1989). Notice explicative, carte géol. France (1/50000), Feuille Bagnères-de-Bigorre (1053). BRGM, Orléans (80pp).

Babault, J., Loget, N., Van Den Driessche, J., Castelltort, S., Bonnet, S., Davy, P., 2006. Did the Ebro basin connect to the Mediterranean before the Messinian salinity crisis? Geomorphology 81, 155–165.

Babault, J., Van Den Driessche, J., Bonnet, S., 2007. High elevation of low-relief surfaces in mountain belts: does it equate to post-orogenic surface uplift? Terra Nova, 19 (4), 272-277.

Babault, J., Van Den Driessche, J., Bonnet, S., Castelltort, S., Crave, A., 2005. Origin of the highly elevated Pyrenean peneplain: Origin of the highly elevated Pyrenean peneplain. Tectonics 24, n/a-n/a. https://doi.org/10.1029/2004TC001697

Baby, P., Crouzet, G., Specht, M., & Deramond, J. (1988). Role des paléostructures albo- cénomaniennes dans la géométrie des chevauchements frontaux nord-pyrénéens.

Barbarand, J., Carter, A., Wood, I., & Hurford, T. (2003). Compositional and structural control of fission-track annealing in apatite. Chemical Geology, 198(1–2), 107–137.

Barbarand, J., & Pagel, M. (2001). Importance of the chemistry to characterise apatite fission-track annealing. Comptes Rendus de l'Academie Des Sciences. Serie 2a, Sciences de La Terre et Des Planetes, 259–265.

Barrier, L., Proust, J., Nalpas, T., Robin, C., & Guillocheau, F. (2010). Control of alluvial sedimentation at foreland-basin active margins: A case of study from the northeastern Ebro basin (southeastern Pyrenees, Spain). Journal of Sedimentary Research, 80(7–8), 728–749. https://doi.org/10.2110/jsr.2010.069

Barrouquère, G., Castaing, C., & Pélissonier, H. (1976). Carte géol., France (1/50000). In: Feuille Saint-Girons (1074). BRGM Orléans.

Barrouquère, G., Roux, L., Souquet, P., Peybernès, B., Ray, J., Debroas, E. J., Lagasquie, J., Ternet, Y., Bois, J. P., & Bambier, A. (1976). Notice explicative, carte géol. In: France (1/50000), feuille Saint-Girons (1074). BRGM Orléans.

Beamud, E., Garcés, M., Cabrera, L., Muñoz, J.A., Almar, Y., 2003. A new middle to late Eocene continental chronostratigraphy from NE Spain. Earth Planet. Sci. Lett. 216, 501–514.

Beamud, E., Muñoz, J. A., Fitzgerald, P., Baldwin, S., Garcés, M., Cabrera, L., & Metcalf, J. (2011). Magnetostratigraphy and detrital apatite fission track thermochronology in syntectonic conglomerates: Constraints on the exhumation of the South-Central Pyrenees. Basin Research, 23(3), 309–331.

Beaumont, C., Munoz, J., Hamilton, J., & Fullsack, P. (2000). Factors controlling Alpine evolution of the Central Pyrenees inferred from a comparison of observations and geodynamical models. Journal of Geophysical Research, 105, NO. B4, 8121–8145.

Bellot, J.-P. (2001). La structure de la croûte varisque du Sud-Limousin (Massif-Central français) et ses relations avec les minéralisations aurifères tardi-orogéniques: Apport des données géologiques, gitologiques, géophysiques et de la modélisation 3D [PhD Thesis]. Montpellier 2.

Berastegui, X., García-Senz, J. M., & Losantos, M. (1990). Tecto-sedimentary evolution of the Organyà extensional basin (central south Pyrenean unit, Spain) during the Lower Cretaceous. Bulletin de La Société Géologique de France, 6(2), 251–264.

Berger, G. M. (1990). Carte géologique de la France à 1/50 000. Feuille de Lézignan-Corbières, no 1038. Bureau de Recherches Géologiques et Minières, Orléans, France.

Bernard, T., Sinclair, D. H., Naylor, M., Christophoul, F., Ford, M., 2020. Post-orogenic sediment drape in the Northern Pyrenees explained using a box model. Basin Research, n/a, https://doi.org/10.1111/bre.12457

Beucher, R., Brown, R., Roper, S., Stuart, F., & Persano, C. (2013). Natural age dispersion arising from the analysis of broken crystals: Part II. Practical application to apatite (U–Th)/He thermochronometry. Geochimica et Cosmochimica Acta, 120, 395–416.

Beyssac, O., Goffé, B., Chopin, C., & Rouzaud, J. N. (2002). Journal of Metamorphic Geology.

Bhandari, N., Bhat, S. G., Lal, D., Rajagopalan, G., Tamhane, A. S., & Venkatavaradan, V. S. (1971). Fission fragment tracks in apatite: Recordable track lengths. Earth and Planetary Science Letters, 13(1), 191–199.

Bickford, M. E., Chase, R. B., Nelson, B. K., Shuster, R. D., & Arruda, E. C. (1981). U-Pb Studies of Zircon Cores and Overgrowths, and Monazite: Implications for Age and Petrogenesis of the Northeastern Idaho Batholith. The Journal of Geology, 89(4), 433–457. https://doi.org/10.1086/628607

Bilotte, M., Crochet, B., Peybernès, B., Roche, J., Taillefer, F., Ternet, Y., & Tambareau, Y. (1988). Notice de la carte géologique de Lavelanet à l'échelle 1/50 000.

Bilotte, M., Koess, L., & Debroas, E. J. (2005). Relations tectonique–sedimentation sur la marge nord-orientale du sillon sous-pyreneen au cours du Santonien superieur (11 fig.). Bulletin de La Société Géologique de France, 176(5), 443–456.

Bilotte, M. (2007). Permanence, au Crétacé supérieur, de la position de la limite plateforme/ basin dans la zone sous-pyrénéenne orientale (Aude, France). Géologie de La France, 1, 33‑53.

Biteau, J.-J., Le Marrec, A., Le Vot, M., & Masset, J.-M. (2006). The aquitaine basin. Petroleum Geoscience, 12(3), 247–273.

Bjørlykke, K., & Aagaard, P. (1992). Clay minerals in North Sea sandstones.

Bohaty, S. M., Zachos, J. C., Florindo, F., & Delaney, M. L. (2009). Coupled greenhouse warming and deep-sea acidification in the middle Eocene. Paleoceanography, 24(2). https://doi.org/10.1029/2008PA001676

Bonnefoy, D., Chantraine, J., Lebret, P., Rabu, D., (1996) Carte géologique de la France à 1:1000000 numérique. Rapport BRGM.

Boissonnas, J., Le Pochat, G., Thibault, C., & Bernatzky, M. (1974). Notice explicative, carte géol. In: France (1/50000), feuille Iholdy (1027). BRGM Orléans. https://scholar.google.com/scholar_lookup?title=Notice%20explicative%2C%20carte%20g%C3%A9ol&author=J.%20Boissonnas&publication_year=1974

Boltenhagen, C., Le Pochat, G., & Thibault, C. (1976). Carte géol. In: France (1/50000), feuille Mauléon-Licharre (1028). BRGM Orléans.

Bond, R. M. G., & McClay, K. R. (1995). Inversion of a Lower Cretaceous extensional basin, south central Pyrenees, Spain. Geological Society, London, Special Publications, 88(1), 415–431.

Bosch, G., Teixell, A., Jolivet, M., Labaume, P., Stockli, D., Domenech, M., & Monié, P. (2016). Timing of Eocene–Miocene thrust activity in the Western Axial Zone and Chaînons Béarnais (west-central Pyrenees) revealed by multi-method thermochronology. Comptes Rendus Géoscience, 348(3), 246–256.

Bosch, G., Van Den Driessche, J., Babault, J., Robert, A., Carballo, A., Le Carlier, C., Loget, N., Prognon, C., Wyns, R., & Baudin, T. (2016). Peneplanation and lithosphere dynamics in the Pyrenees. Comptes Rendus Geoscience, 348(3), 194–202. https://doi.org/10.1016/j.crte.2015.08.005

Bosellini, F., & Perrin, C. (2008). Estimating Mediterranean Oligocene‐Miocene sea-surface temperatures: An approach based on coral taxonomic richness. Palaeogeography, Palaeoclimatology, Palaeoecology, 258(1‐2), 71‐88. https://doi.org/10.1016/j.palaeo.2007.10.028

Braun, J., Simon-Labric, T., Murray, K., & Reiners, P. (2014). Topographic relief driven by variations in surface rock density. Nature Geoscience, 7(7), 534.

BRGM, & IGME. (1998). Synthèse géologique et géophysique des Pyrénées. Tectonique Hercynienne. Carte Struturale, vol. 1, Géologie Régionale. BRGM IGME.

BRGM, 1974. Geologie du bassin d'Aquitaine. Atlas.

Brown, R., Beucher, R., Roper, S., Persano, C., Stuart, F., & Fitzgerald, P. (2013). Natural age dispersion arising from the analysis of broken crystals. Part I: Theoretical basis and implications for the apatite (U–Th)/He thermochronometer. Geochimica et Cosmochimica Acta, 122, 478–497.

Bruguier, O., Becq-Giraudon, J. F., Champenois, M., Deloule, E., Ludden, J., & Mangin, D. (2003). Application of in situ zircon geochronology and accessory phase chemistry to constraining basin

development during post-collisional extension: A case study from the French Massif Central. Chemical Geology, 201(3–4), 319–336.

Buis, MG., & Rey, J. (1975). Une évolution sédimentaire de type déltaique: Le passage du Tertiaire marin au Tertiaire continental entre l'Ariège et le Douctouyre (Pyrénées Ariègoise). Bulletin Naturel de La Societé d'histoire de Toulouse.

Burbank, D., PuigdefàBregas, C., & Muoz, J. A. (1992). The chronology of the Eocene tectonic and stratigraphic development of the eastern Pyrenean foreland basin, northeast Spain. Geological Society of America Bulletin, 104(9), 1101–1120. https://doi.org/10.1130/0016-7606(1992)104<1101:TCOTET>2.3.CO;2

Caja, M. A., Marfil, R., Garcia, D., Remacha, E., Morad, S., Mansurbeg, H., Amorosi, A., Martínez-Calvo, C., & Lahoz-Beltrá, R. (2010). Provenance of siliciclastic and hybrid turbiditic arenites of the Eocene Hecho Group, Spanish Pyrenees: Implications for the tectonic evolution of a foreland basin. Basin Research, 22(2), 157–180.

Carayon, B. (2010). Evolution tectono sédimentaire du bassin corbières Minervois à l'éocène inférieur. Mémoire de stage M2, Ensegid.

Capdeville, J., F._Charnet,_and A._Turq_(1996)._Notice explicative de_la_feuille cancon_à 1/50000.

Carretier, S. and Lucazeau, F., 2005. How does alluvial sedimentation at range fronts modify the erosional dynamics of mountain catchments? Basin Research, 17, 361–381.

Carlson, W., Donelick, R., & Ketcham, R. (1999). Variability of apatite fission-track annealing kinetics; I, Experimental results. American Mineralogist, 84(9), 1213–1223. https://doi.org/10.2138/am-1999-0901

Carmignani, L., Carosi, R., Di Pisa, A., Gattiglio, M., Musumeci, G., Oggiano, G., & Carlo Pertusati, P. (1994). The hercynian chain in Sardinia (Italy). Geodinamica Acta, 7(1), 31–47.

Carosi, R., Montomoli, C., Tiepolo, M., & Frassi, C. (2012). Geochronological constraints on post-collisional shear zones in the Variscides of Sardinia (Italy). Terra Nova, 24(1), 42–51.

Cartannaz, C., Rolin, P., Cocherie, A., Marquer, D., Legendre, O., Fanning, C. M., & Rossi, P. (2007). Characterization of wrench tectonics from dating of syn-to post-magmatism in the northwestern French Massif Central. International Journal of Earth Sciences, 96(2), 271–287.

Casas, J., Castiñeiras, P., Navidad, M., Liesa, M., & Carreras, J. (2010). New insights into the Late Ordovician magmatism in the Eastern Pyrenees: U–Pb SHRIMP zircon data from the Canigó massif. Gondwana Research, 17(2–3), 317–324.

Casas, J. M., Navidad, M., Castiñeiras, P., Liesa, M., Aguilar, C., Carreras, J., Hofmann, M., Gärtner, A., & Linnemann, U. (2015). The Late Neoproterozoic magmatism in the Ediacaran series of the Eastern Pyrenees: New ages and isotope geochemistry. International Journal of Earth Sciences, 104(4), 909–925.

Casini, L., Cuccuru, S., Maino, M., Oggiano, G., & Tiepolo, M. (2012). Emplacement of the Arzachena Pluton (Corsica–Sardinia Batholith) and the geodynamics of incoming Pangaea. Tectonophysics, 544–545, 31–49. https://doi.org/10.1016/j.tecto.2012.03.028

Cassinis, G., Cap, Di Stefano, P., Massari, F., Neri, C., & Venturini, C. (2000). Permian of south Europe and its interregional correlation. Elsevier Science B. V. All Rights Reserved, pp. 37-70. http://www.academia.edu/download/42994161/Permian_of_South_Europe_and_its_interreg20160223-24258-1v3qoda.pdf

Castelltort, S., & Van Den Driessche, J. (2003). How plausible are high-frequency sediment supply-driven cycles in the stratigraphic record? Sedimentary Geology, 157(1), 3–13. https://doi.org/10.1016/S0037-0738(03)00066-6

Castiñeiras, P., Navidad, M., Liesa, M., Carreras, J., & Casas, J. (2008a). U–Pb zircon ages (SHRIMP) for Cadomian and Early Ordovician magmatism in the Eastern Pyrenees: New insights into the pre-Variscan evolution of the northern Gondwana margin. Tectonophysics, 461(1–4), 228–239.

Castiñeiras, P., Navidad, M., Liesa, M., Carreras, J., & Casas, J. (2008b). U–Pb zircon ages (SHRIMP) for Cadomian and Early Ordovician magmatism in the Eastern Pyrenees: New insights into the pre-Variscan evolution of the northern Gondwana margin. Tectonophysics, 461(1–4), 228–239.

Cavaillé, A. (1975). Carte géologique de Mirepoix à l'échelle 1/50 000.

Cavaillé, A., & Paris, J. P. (1976). Carte géol. France (1/50000), Feuille Pamiers (1057). BRGM, Orléans.

Chaigne, M. (1964). Contribution à l'étude stratigraphique et sédimentologique du secteur Aigne-Tourouzelle, Bassin tertiaire de Carcassonne, Aude [PhD Thesis].

Chamley, H., Proust, J.-N., Mansy, J.-L., & Boulvain, F. (1997). Diagenetic and palaeogeographic significance of clay, carbonate and other sedimentary components in the middle Devonian limestones of western Ardenne, France. Palaeogeography, Palaeoclimatology, Palaeoecology, 129(3–4), 369–385.

Chelalou, R., Nalpas, T., Bousquet, R., Prevost, M., Lahfid, A., Poujol, M., Ringenbach, J.-C., & Ballard, J.-F. (2016). New sedimentological, structural and paleo-thermicity data in the Boucheville Basin (eastern North Pyrenean Zone, France). Comptes Rendus Géoscience, 348(3–4), 312–321.

Chenin, P., Manatschal, G., Picazo, S., Müntener, O., Karner, G., Johnson, C., & Ulrich, M. (2017). Influence of the architecture of magma-poor hyperextended rifted margins on orogens produced by the closure of narrow versus wide oceans. Geosphere, 13(2), 559–576.

Cherniak, D.J., Watson, E.B., 2001. Pb diffusion in zircon. Chem. Geol. 172, 5–24. http://dx.doi.org/10.1016/S0009-2541(00)00233-3.

Chevrot, S., Sylvander, M., Diaz, J., Martin, R., Mouthereau, F., Manatschal, G., Masini, E., Calassou, S., Grimaud, F., & Pauchet, H. (2018). The non-cylindrical crustal architecture of the Pyrenees. Scientific Reports, 8(1), 9591.

Choukroune, P. (1989). The ECORS Pyrenean deep seismic profile reflection data and the overall structure of an orogenic belt. Tectonics, 8(1), 23–39.

Choukroune, P., & Mattauer, M. (1978). Tectonique des plaques et Pyrenées: Sur le fonctionnement de la faille transformante Nord_Pyrenéenne; Comparaison avec des modèles actuels. Bulletin de La Societé Géologique de France, 7, t. XX, NO. 5, 689–700.

Choukroune, P., & Séguret, M. (1973). Carte structurale des Pyrénées. ELF-ERAP.

Christophoul, F., Soula, J.-C., Brusset, S., Elibana, B., Roddaz, M., Bessiere, G., & Deramond, J. (2003). Time, place and mode of propagation of foreland basin systems as recorded by the sedimentary fill: Examples of the Late Cretaceous and Eocene retro-foreland basins of the north-eastern Pyrenees. Geological Society, London, Special Publications, 208(1), 229–252. https://doi.org/10.1144/GSL.SP.2003.208.01.11

Clerc, C. (2012). Evolution du domaine nord-pyrénéen au Crétacé: Amincissement crustal extrême et thermicite élevée: un analogue pour les marges passives [PhD Thesis]. Paris 6.

Clerc, C., & Lagabrielle, Y. (2014). Thermal control on the modes of crustal thinning leading to mantle exhumation: Insights from the Cretaceous Pyrenean hot paleomargins. Tectonics, 33(7), 1340–1359.

Clerc, C., Lagabrielle, Y., Labaume, P., Ringenbach, J.-C., Vauchez, A., Nalpas, T., Bousquet, R., Ballard, J.-F., Lahfid, A., & Fourcade, S. (2016). Basement – Cover decoupling and progressive exhumation of metamorphic sediments at hot rifted margin. Insights from the Northeastern Pyrenean analog. Tectonophysics, 686, 82–97. https://doi.org/10.1016/j.tecto.2016.07.022

Clerc, C., Lahfid, A., Monié, P., Lagabrielle, Y., Chopin, C., Poujol, M., Boulvais, P., Ringenbach, J.-C., Masini, E., & de St Blanquat, M. (2015). High-temperature metamorphism during extreme thinning of the continental crust: A reappraisal of the North Pyrenean passive paleomargin. Solid Earth, 6(2), 643–668. https://doi.org/10.5194/se-6-643-2015

Clevis, Q., De Jager, G., Nijman, W., & De Boer, P. (2004). Stratigraphic signatures of translation of thrust-sheet top basins over low-angle detachment faults. Basin Research, 16(2), 145–163.

Cochelin, B., Chardon, D., Denèle, Y., Gumiaux, C., & Le Bayon, B. (2017). Vertical strain partitioning in hot Variscan crust: Syn-convergence escape of the Pyrenees in the Iberian-Armorican syntax. Bulletin de La Société Géologique de France, 188(6), 39.

Cocherie, A., Baudin, T., Autran, A., Guerrot, C., Fanning, M., & Laumonier, B. (2005). U-Pb zircon (ID-TIMS and SHRIMP) evidence for the early ordovician intrusion of metagranites in the late Proterozoic Canaveilles Group of the Pyrenees and the Montagne Noire (France). Bulletin de La Société Géologique de France, 176(3), 269–282.

Cocherie, A., Guerrot, C., & Rossi, P. H. (1992). Single-zircon dating by step-wise Pb evaporation: Comparison with other geochronological techniques applied to the Hercynian granites of Corsica, France. Chemical Geology: Isotope Geoscience Section, 101(1–2), 131–141.

Colombo, F., & Cuevas, J. (1993). Características estratigráficas y sedimentológicas del" Garumniense" en el sector de Ager (Pre-Pirineo, Lleida). Acta Geologica Hispanica, 28(4), 15–32.

Coney, P.J., Muñoz, J.A., McClay, K.R., Evenchick, C.A., 1996. Syntectonic burial and post-tectonic exhumation of the southern Pyrenees foreland fold–thrust belt. J. Geol. Soc. 153, 9–16.

Corfu, F., & Ayres, L. D. (1984). U-Pb age and genetic significance of heterogeneous zircon populations in rocks from the Favourable Lake area, Northwestern Ontario. Contributions to Mineralogy and Petrology, 88(1), 86–101. https://doi.org/10.1007/BF00371414

Cortesogno, L., Gaggero, L., Oggiano, G., & Paquette, J.-L. (2004). Different tectono-thermal evolutionary paths in eclogitic rocks from the axial zone of the Variscan chain in Sardinia (Italy) compared with the Ligurian Alps. Ofioliti, 29(2), 125–144.

Costa, E., Garcés, M., López-Blanco, M., Beamud, E., Gómez-Paccard, M., Larrasoaña, J.C., 2012. Closing and continentalization of the South Pyrenean Foreland Basin (NE Spain) and its impact on basin fill trends and thrust-belt evolution, in: EGU General Assembly Conference Abstracts. p. 10345.

Crochet, B., Tambareau, Y., Villatte, 1976. Modalités de la régression ilerdienne entre l'Ariège et \'Aude. Les plages à Eoscutum doncieuxi (Lambert).

Crochet, B. (1989). Molasses syntectoniques du versant nord des Pyrénées: La série de Palassou. Toulouse 3.

Cuccuru, S., Naitza, S., Secchi, F., Puccini, A., Casini, L., Pavanetto, P., Linnemann, U., Hofmann, M., & Oggiano, G. (2016). Structural and metallogenic map of late Variscan Arbus Pluton (SW Sardinia, Italy). Journal of Maps, 12(5), 860–865. https://doi.org/10.1080/17445647.2015.1091750

Curry, M., van der Beek, P., Huismans, R., Wolf, S., & Muñoz, J. A. (2019). Evolving paleotopography and lithospheric flexure of the Pyrenean Orogen from 3D flexural modeling and basin analysis. Earth and Planetary Science Letters, 515, 26‑37.

Dahlen, F., Suppe, J., & Davis, D. (1984). Mechanics of fold-and-thrust belts and accretionary wedges—Cohesive coulom theory. Journal of Geophysical Research, 89(NB12), 87–101. https://doi.org/10.1029/JB089iB12p10087

Dauteuil, O., & Ricou, L.-E. (1989). Une circulation de fluides de haute-température à l'origine du métamorphisme crétacé nord-pyrénéen. Geodinamica Acta, 3(3), 237–249.

Davis, S., Suppe, J., & Dahlen, F. (1983). Mechanics of fold-and-thrust belts and accretionary wedges. Journal of Geophysical Research, 88(NB2), 1153–1172. https://doi.org/10.1029/JB088iB02p01153

Debroas, E. J. (1978). Evolution de la fosse du flysch ardoisier de l'Albien superieur au Senonien inferieur (zone interne metamorphique des Pyrenees navarro-languedociennes). Bulletin de La Societé Géologique de France, 7(5), 639–648.

Debroas, E. J. (1987). Le flysch à fucoïdes d'Uchentein témoin d'un escarpement turono-sénonien inférieur de la paléofaille nord pyrénéenne. Pyrénées Centrales, France, Strata, 3, 77–93.

Debroas, E. J., & Souquet, P. (1976). Sédimentogenèse et position structurale des flyschs crétacés du versant nord des Pyrénées centrales. Bull. Bur. Rech. Géol. Min., I, 305–320.

Debroas, E.-J. (1990). Le flysch noir albo-cénomanien témoin de la structuration albienne à sénonienne de la Zone nord-pyrénéenne en Bigorre (Hautes-Pyrénées, France). Bulletin de La Société Géologique de France, 6(2), 273–285.

DeCelles, P., & Giles, K. (1996). Foreland basin systems. Basin Research, 8(2), 105–123.

Del Moro, A., Di Pisa, A., Oggiano, G., Villa, I. M., Cappelli, B., & Liotta, D. (1991). Isotopic ages of two contrasting tectonometamorphic episodes in the Variscan chain in northern Sardinia. Geol. Basem. It., 33–35.

Del Río, P., Barbero, L., & Stuart, F. M. (2009). Exhumation of the Sierra de Cameros (Iberian Range, Spain): Constraints from low-temperature thermochronology. Geological Society, London, Special Publications, 324(1), 153–166.

Delaperrière, E., & Respaut, J.-P. (1995). Un âge ordovicien de l'orthogneiss de La Preste par la méthode d'évaporation directe du plomb sur monozircon remet en question l'existence d'un socle précambrien dans le Massif du Canigou (Pyrénées Orientales, France). Comptes Rendus de l'Académie Des Sciences. Série 2. Sciences de La Terre et Des Planètes, 320(12), 1179–1185.

Deloule, E., Alexandrov, P., Cheilletz, A., Laumonier, B., & Barbey, P. (2002). In-situ U–Pb zircon ages for Early Ordovician magmatism in the eastern Pyrenees, France: The Canigou orthogneisses. International Journal of Earth Sciences, 91(3), 398–405.

Denèle, Y. (2007). Formation des dômes gneissiques hercyniens dans les Pyrénées: Exemple du massif de l'Aston-Hospitalet [PhD Thesis]. Toulouse 3.

Denele, Y. (2007). Formation des dômes gneissiques hercyniens dans les Pyrénées: Exemple du massif de l'Aston-Hospitalet [Phd, Université de Toulouse, Université Toulouse III - Paul Sabatier]. http://thesesups.ups-tlse.fr/184/

Denele, Y., Barbey, P., Deloule, E., Pelleter, E., Olivier, P., & Gleizes, G. (2009). Middle Ordovician U-Pb age of the Aston and Hospitalet orthogneissic laccoliths: Their role in the Variscan evolution of the Pyrenees. Bulletin de La Société Géologique de France, 180(3), 209–216.

Denèle, Y., Laumonier, B., Paquette, J.-L., Olivier, P., Gleizes, G., & Barbey, P. (2014). Timing of granite emplacement, crustal flow and gneiss dome formation in the Variscan segment of the Pyrenees. Geological Society, London, Special Publications, 405(1), 265–287. https://doi.org/10.1144/SP405.5

Denèle, Y., Paquette, J.-L., Olivier, P., & Barbey, P. (2012). Permian granites in the Pyrenees: The Aya pluton (Basque Country). Terra Nova, 24(2), 105–113.

Depéret, C. (1910). Le gisement de mammifères d'Euzet-les-Bains: Iudien inférieur. Soc. géolog.

Deramond, J., Baby, P., Specht, M., & Crouzet, G. (1990). Thrust geometry in the Ariègoise north Pyrenean Zone reconstruct unsing ECORS data. Bulletin de la Societé géologique de France, 6(2), 287–294.

Derer, C., Kosinowski, M., Luterbacher, H. P., Schäfer, A., & Süss, M. P. (2003). Sedimentary response to tectonics in extensional basins: The Pechelbronn Beds (Late Eocene to early Oligocene)

in the northern Upper Rhine Graben, Germany. Geological Society, London, Special Publications, 208(1), 55–69.

Djimbi, D.M., Gautheron, C., Roques, J., Tassan-Got, L., Gerin, C., Simoni, E., 2015. Impact of apatite chemical composition on (U-Th)/He thermochronometry: An atomistic point of view. Geochim. Cosmochim. Acta 167, 162–176.

Di Vincenzo, G., Carosi, R., & Palmeri, R. (2004). The relationship between tectono-metamorphic evolution and argon isotope records in white mica: Constraints from in situ 40Ar–39Ar laser analysis of the Variscan basement of Sardinia. Journal of Petrology, 45(5), 1013–1043.

Diaz, J., Vergés, J., Chevrot, S., Antonio-Vigil, A., Ruiz, M., Sylvander, M., & Gallart, J. (2018). Mapping the crustal structure beneath the Eastern Pyrenees. Tectonophysics, 744, 296–309.

Didier, J., & Lameyre, J. (1969). Les granites du Massif Central Français: Étude comparée des leucogranites et granodiorites. Contributions to Mineralogy and Petrology, 24(3), 219–238. https://doi.org/10.1007/BF00376049

Doncieux, L. (1912). Révision de la faune lacustre de l'Eocène moyen des Corbières Septentrionales. Victor Bonnafous-Thomas, imprimeur de la société.

Donelick, R. (1991). Crystallographic orientation dependence of mean etchable fission track length in apatite: An empirical model and experimental observations. American Mineralogist, 76(1–2), 83–91.

Donelick, R. (1993). Method of fission track analysis utilizing bulk chemical etching of apatite.

Donelick, R., & Miller, D. (1991). Enhanced TINT fission track densities in low spontaneous track density apatites using 252Cf-derived fission fragment tracks: A model and experimental observations. International Journal of Radiation Applications and Instrumentation. Part D. Nuclear Tracks and Radiation Measurements, 18(3), 301–307.

Donelick, R., O'Sullivan, P., & Ketcham, R. (2005). 3. Apatite Fission-Track Analysis. In Low-Temperature Thermochronology:Techniques, Interpretations, and Applications (Vol. 58). De Gruyter. https://doi.org/10.1515/9781501509575-005

Druguet, E., Castro, A., Chichorro, M., Pereira, F., & Fernández, C. (2014). Zircon geochronology of intrusive rocks from Cap de Creus, Eastern Pyrenees. Geological Magazine, 151(6), 1095–1114. https://doi.org/10.1017/S0016756814000041

Druguet, E., & Hutton, D. H. W. (1998). Syntectonic anatexis and magmatism in a mid-crustal transpressional shear zone: An example from the Hercynian rocks of the eastern Pyrenees. Journal of Structural Geology, 20(7), 905–916.

Ducassou, C., Poujol, M., Ruffet, G., Bruguier, O., & Ballevre, M. (2014). Relief variation and erosion of the Variscan belt: Detrital geochronology of the Palaeozoic sediments from the Mauges Unit (Armorican Massif, France). Geological Society, London, Special Publications, 405(1), 137–167.

Duguet, M., Le Breton, N., & Faure, M. (2007). P–T paths reconstruction of a collisional event: The example of the Thiviers-Payzac Unit in the Variscan French Massif Central. Lithos, 98(1–4), 210–232.

Duller, R. A., Whittaker, A. C., Fedele, J. J., Whitchurch, A. L., Springett, J., Smithells, R., Fordyce, S., & Allen, P. A. (2010). From grain size to tectonics. Journal of Geophysical Research, 115(3).

Edel, J.-B., Schulmann, K., Lexa, O., Diraison, M., & Géraud, Y. (2015). Permian clockwise rotations of the Ebro and Corso-Sardinian blocks during Iberian–Armorican oroclinal bending: Preliminary paleomagnetic data from the Catalan Coastal Range (NE Spain). Tectonophysics, 657, 172–186.

Einsele, G. (1992). Sedimentary Basins." Evolution, Facies and Sediments Budget, (Springer-Verlag).

Ellenberger, F., Plaziat, J. C., Bessiere, G., Viallard, P., Berger, G. M., & Marchal, J. P. (1988). Feuille de Capendu, Carte géologique de la France à 1/50000, n°1090. BRGM Orléans.

Ellenberger, F., Plaziat, J. C., Freytet, P., Jaffrézo, M., Charriere, A., L'Homer, A., Legrand-Lespinasse, N., Huguet, J., Bessiere, G., & Berger, G. (1985). Carte géologique de la France à 1/50 000–Feuille Capendu (1060)–BRGM. Orléans, France.

Elter, F. M., Corsi, B., Cricca, P., & Muzio, G. (2004). The south-western Alpine foreland: Correlation between two sectors of the Variscan chain belonging to "stable Europe": Sardinia (-) Corsica and the Maures Massif (south-eastern France). Geodinamica Acta, 17(1), 31–40.

Elter, F. M., Musumeci, G., & Pertusati, P. C. (1990). Late Hercynian shear zones in Sardinia. Tectonophysics, 176(3–4), 387–404.

Elter, F. M., & Pandeli, E. (2005). Structural-metamorphic correlations between three variscan segments in Southern Europe: Maures Massif (France), Corsica (France)–Sardinia (Italy), and Northern Appennines (Italy). Journal of the Virtual Explorer, 9.

Esteban, J. J., Aranguren, A., Cuevas, J., Hilario, A., Tubía, J. M., Larionov, A., & Sergeev, S. (2015). Is there a time lag between the metamorphism and emplacement of plutons in the Axial Zone of the Pyrenees? Geological Magazine, 152(5), 935–941.

Espurt, N., Angrand, P., Teixell, A., Labaume, P., Ford, M., de Saint Blanquat, M., & Chevrot, S. (2019). Crustal-scale balanced cross-section and restorations of the Central Pyrenean belt (Nestes-Cinca transect): Highlighting the structural control of Variscan belt and Permian-Mesozoic rift systems on mountain building. Tectonophysics, 764, 25‑45.

Evans, N. (1993). Deformation during the emplacement of the Maladeta granodiorite, Spanish Pyrenees [PhD Thesis]. University of Leeds.

Fallourd, S., Poujol, M., Boulvais, P., Paquette, J.-L., de Saint Blanquat, M., & Rémy, P. (2014). In situ LA-ICP-MS U–Pb titanite dating of Na–Ca metasomatism in orogenic belts: The North Pyrenean example. International Journal of Earth Sciences, 103(3), 667–682.

Farley, K. A. (2000). Helium diffusion from apatite: General behavior as illustrated by Durango fluorapatite. Journal of Geophysical Research: Solid Earth, 105(B2), 2903–2914.

Farley, K. A., Wolf, R. A., & Silver, L. T. (1996). The effects of long alpha-stopping distances on (U□ Th)/He ages. Geochimica et Cosmochimica Acta, 60(21), 4223–4229.

Farley, K., & Stockli, D. (2002). 15. (U-Th)/He Dating of Phosphates: Apatite, Monazite, and Xenotime. In PhosphatesGeochemical, Geobiological and Materials Importance (Vol. 48). De Gruyter. https://doi.org/10.1515/9781501509636-018

Farley, Kenneth A. (2002). (U-Th)/He dating: Techniques, calibrations, and applications. Reviews in Mineralogy and Geochemistry, 47(1), 819–844.

Farrell, S. G., Williams, G. D., & Atkinson, C. D. (1987). Constraints on the age of movement of the Montsech and Cotiella Thrusts, south central Pyrenees, Spain. Journal of the Geological Society, 144(6), 907–914.

Faure, M., Bé Mézème, E., Cocherie, A., Rossi, P., Chemenda, A., & Boutelier, D. (2008). Devonian geodynamic evolution of the Variscan Belt, insights from the French Massif Central and Massif Armoricain. Tectonics, 27(2).

Faure, M., Cocherie, A., Gaché, J., Esnault, C., Guerrot, C., Rossi, P., Wei, L., & Qiuli, L. (2014). Middle Carboniferous intracontinental subduction in the Outer zone of the Variscan belt (Montagne Noire axial zone, French Massif Central): Multimethod geochronological approach of polyphase metamorphism. Geological Society, London, Special Publications, 405(1), 289–311.

Faure, M., Cocherie, A., Mezeme, E., Charles, N., & Rossi, P. (2010). Middle carboniferous crustal melting in the Variscan belt: New insights from U–Th–Pb tot. monazite and U–Pb zircon ages of the Montagne Noire Axial Zone (southern French Massif Central). Gondwana Research, 18(4), 653–673.

Faure, M., Lardeaux, J.-M., & Ledru, P. (2009). A review of the pre-Permian geology of the Variscan French Massif Central. Comptes Rendus Geoscience, 341(2–3), 202–213.

Faure, M., Leloix, C., & Roig, J.-Y. (1997). L'évolution polycyclique de la chaîne hercynienne. Bulletin de La Société Géologique de France, 168(6), 695–705.

Faure, M., Mezeme, E. B., Cocherie, A., Melleton, J., & Rossi, P. (2009). The South Millevaches Middle Carboniferous crustal melting and its place in the French Variscan belt. Bulletin de La Société Géologique de France, 180(6), 473–481.

Faure, M., Mézème, E. B., Duguet, M., Cartier, C., & Talbot, J.-Y. (2005). Paleozoic tectonic evolution of medio-Europa from the example of the French Massif Central and Massif Armoricain. Journal of the Virtual Explorer, 19(5), 1–25.

Faure, M., Monié, P., Pin, C., Maluski, H., & Leloix, C. (2002). Late Viséan thermal event in the northern part of the French Massif Central: New 40 Ar/39 Ar and Rb–Sr isotopic constraints on the Hercynian syn-orogenic extension. International Journal of Earth Sciences, 91(1), 53–75.

Faure, M., Rossi, P., Gaché, J., Melleton, J., Frei, D., Li, X., & Lin, W. (2014). Variscan orogeny in Corsica: New structural and geochronological insights, and its place in the Variscan geodynamic framework. International Journal of Earth Sciences, 103(6), 1533–1551.

Fernàndez, M., Marzán, I., Correia, A., Ramalho, E., 1998. Heat flow, heat production, and lithospheric thermal regime in the Iberian Peninsula. Tectonophysics 291, 29–53.

Fernández-Suárez, J., Gutiérrez-Alonso, G., Pastor-Galán, D., Hofmann, M., Murphy, J. B., & Linnemann, U. (2014). The Ediacaran–Early Cambrian detrital zircon record of NW Iberia: Possible sources and paleogeographic constraints. International Journal of Earth Sciences, 103(5), 1335–1357.

Ferrara, G., Ricci, C.-A., & Rita, F. (1978). Isotopic ages and tectono-metamorphic history of the metamorphic basement of north-eastern Sardinia. Contributions to Mineralogy and Petrology, 68(1), 99–106.

Ferre, E., & Leake, B. (2001). Geodynamic significance of early orogenic high-K crustal and mantle melts: Example of the Corsica Batholith. Lithos, 59(1–2), 47–67.

Feuillee, P., Villanova, M., & Winnock, E. (1973). La dynamique des fosses a" turbidites" et de leur contenu sedimentaire dans le systeme pyreneen. Bulletin de La Société Géologique de France, 7(1), 61–76.

Filleaudeau, P.-Y. (2011). Croissance et dénudation des Pyrénées du Crétacé supérieur au Paléogène: Apports de l'analyse de bassin et thermochronométrie détritique [PhD Thesis]. Université Pierre et Marie Curie-Paris VI.

Filleaudeau, P.-Y., Mouthereau, F., & Pik, R. (2012). Thermo-tectonic evolution of the south-central Pyrenees from rifting to orogeny: Insights from detrital zircon U/Pb and (U-Th)/He thermochronometry. Basin Research, 24(4), 401–417. https://doi.org/10.1111/j.1365-2117.2011.00535.x

Fillon, C., Gautheron, C., & van der Beek, P. (2013). Oligocene–Miocene burial and exhumation of the Southern Pyrenean foreland quantified by low-temperature thermochronology. Journal of the Geological Society, 170(1), 67–77.

Fillon, C., & van der Beek, P. (2012). Post-orogenic evolution of the southern P yrenees: Constraints from inverse thermo-kinematic modelling of low-temperature thermochronology data. Basin Research, 24(4), 418–436.

Fitzgerald, P. G., Baldwin, S. L., Webb, L. E., & O'Sullivan, P. B. (2006). Interpretation of (U–Th)/He single grain ages from slowly cooled crustal terranes: A case study from the Transantarctic Mountains of southern Victoria Land. Chemical Geology, 225(1), 91–120. https://doi.org/10.1016/j.chemgeo.2005.09.001

Fitzgerald, P. G., Muñoz, J. A., Coney, P. J., & Baldwin, S. L. (1999). Asymmetric exhumation across the Pyrenean orogen: Implications for the tectonic evolution of a collisional orogen. Earth and Planetary Science Letters, 173(3), 157–170.

Fleischer, R. L., Price, P. B., Walker, R., & Walker, R. M. (1975). Nuclear tracks in solids: Principles and applications. Univ of California Press.

Flowers, R. (2009). Exploiting radiation damage control on apatite (U–Th)/He dates in cratonic regions. Earth and Planetary Science Letters, 277(1–2), 148–155.

Flowers, R., & Kelley, S. (2011). Interpreting data dispersion and "inverted" dates in apatite (U–Th)/He and fission-track datasets: An example from the US midcontinent. Geochimica et Cosmochimica Acta, 75(18), 5169–5186.

Flowers, R., Ketcham, R., Shuster, D., & Farley, K. (2009). Apatite (U–Th)/He thermochronometry using a radiation damage accumulation and annealing model. Geochimica et Cosmochimica Acta, 73(8), 2347–2365.

Flowers, R. M., Ault, A. K., Wolin, E., Kelley, S., & Bowring, S. A. (2009). From Texas to the Northwest Territories: Low temperature history of the North American craton using a radiation damage model for apatite He diffusion. AGU Fall Meeting Abstracts, 41, V41D-2199.

Flowers, R. M., Shuster, D. L., Wernicke, B. P., & Farley, K. A. (2007). Radiation damage control on apatite (U-Th)/He dates from the Grand Canyon region, Colorado Plateau. Geology, 35(5), 447–450.

Ford, M., Hemmer, L., Vacherat, A., Gallagher, K., & Christophoul, F. (2016). Retro-wedge foreland basin evolution along the ECORS line, eastern Pyrenees, France. Journal of the Geological Society, 173(3), 419–437.

Fourcade, S., & Allegre, C. (1981). Trace elements behavior in granite genesis: A case study The calc-alkaline plutonic association from the Querigut complex (Pyrénées, France). Contributions to Mineralogy and Petrology, 76(2), 177–195. https://doi.org/10.1007/BF00371958

Fox, M., Dai, J.-G., & Carter, A. (2019). Badly Behaved Detrital (U-Th)/He Ages: Problems With He Diffusion Models or Geological Models? Geochemistry, Geophysics, Geosystems.

Fox, M., Shuster, D.L., 2014. The influence of burial heating on the (U–Th)/He system in apatite: Grand Canyon case study. Earth Planet. Sci. Lett. 397, 174–183. https://doi.org/10.1016/j.epsl.2014.04.041

Franke, W. (2006). The Variscan orogen in Central Europe: Construction and collapse. Geological Society, London, Memoirs, 32(1), 333–343. https://doi.org/10.1144/GSL.MEM.2006.032.01.20

Franke, W., Cocks, R., & Torsvik, T. (2017). The Palaeozoic Variscan oceans revisited. Gondwana Research, 48, 257–284. https://doi.org/10.1016/j.gr.2017.03.005

Gaggero, L., Gretter, N., Langone, A., & Ronchi, A. (2017). U–Pb geochronology and geochemistry of late Palaeozoic volcanism in Sardinia (southern Variscides). Geoscience Frontiers.

Galbraith, R. F. (1981). On statistical models for fission track counts. Journal of the International Association for Mathematical Geology, 13(6), 471–478.

Galbraith, R. F., & Laslett, G. M. (1993). Statistical models for mixed fission track ages. Nuclear Tracks and Radiation Measurements, 21(4), 459–470.

Gallagher, K. (2012). Transdimensional inverse thermal history modeling for quantitative thermochronology. Journal of Geophysical Research: Solid Earth, 117(B2).

Gallagher, K., Brown, R., & Johnson, C. (1998). Fission track analysis and its application to geological problems | Annual Review of Earth and Planetary Sciences. https://www.annualreviews.org/doi/abs/10.1146/annurev.earth.26.1.519

Gallagher, K., Charvin, K., Nielsen, S., Sambridge, M., & Stephenson, J. (2009). Markov chain Monte Carlo (MCMC) sampling methods to determine optimal models, model resolution and model choice for Earth Science problems. Marine and Petroleum Geology, 26(4), 525–535.

Garcia-Castellanos, D., Vergés, J., Gaspar-Escribano, J., Cloetingh, S., 2003. Interplay between tectonics, climate, and fluvial transport during the Cenozoic evolution of the Ebro Basin (NE Iberia). J. Geophys. Res. Solid Earth 108.

Gautheron, C., Barbarand, J., Ketcham, R., Tassan-Got, L., van der Beek, P., Pagel, M., Pinna-Jamme, R., Couffignal, F., & Fialin, M. (2013). Chemical influence on α-recoil damage annealing in apatite: Implications for (U–Th)/He dating. Chemical Geology, 351, 257–267.

Gautheron, C., & Tassan-Got, L. (2010). A Monte Carlo approach to diffusion applied to noble gas/helium thermochronology. Chemical Geology, 273(3–4), 212–224.

Gautheron, C., Tassan-Got, L., Barbarand, J., & Pagel, M. (2009). Effect of alpha-damage annealing on apatite (U–Th)/He thermochronology. Chemical Geology, 266(3–4), 157–170.

Gautheron, C., Tassan-Got, L., Ketcham, R., & Dobson, K. (2012). Accounting for long alpha-particle stopping distances in (U–Th–Sm)/He geochronology: 3D modeling of diffusion, zoning, implantation, and abrasion. Geochimica et Cosmochimica Acta, 96, 44–56.

Gebauer, D., & Grünenfelder, M. (1976). U-Pb zircon and Rb-Sr whole-rock dating of low-grade metasediments example: Montagne Noire (Southern France). Contributions to Mineralogy and Petrology, 59(1), 13–32.

Gehrels, G. (2014). Detrital zircon U-Pb geochronology applied to tectonics. Annual Review of Earth and Planetary Sciences, 42, 127–149.

Gehrels, G., Blakey, R., Karlstrom, K., Timmons, J. M., Dickinson, B., & Pecha, M. (2011). Detrital zircon U-Pb geochronology of Paleozoic strata in the Grand Canyon, Arizona. Lithosphere, 3(3), 183–200.

Geisler, T., Pidgeon, R., Kurtz, R., Bronswijk, W., & Schleicher, H. (2003). Experimental hydrothermal alteration of partially metamict zircon. American Mineralogist, 88(10), 1496–1513. https://doi.org/10.2138/am-2003-1013

Geisler, T., Pidgeon, R. T., van Bronswijk, W., & Kurtz, R. (2002). Transport of uranium, thorium, and lead in metamict zircon under low-temperature hydrothermal conditions. Chemical Geology, 191(1), 141–154. https://doi.org/10.1016/S0009-2541(02)00153-5

Gely, J.-P., Sztrákos, K., 2000. L'évolution paléogéographique et géodynamique du Bassin aquitain au Paléogène : enregistrement et datation de la tectonique pyrénéenne. Géologie de la France, Num 2, 31-57.

Gerin, C., Gautheron, C., Oliviero, E., Bachelet, C., Djimbi, D. M., Seydoux-Guillaume, A.-M., Tassan-Got, L., Sarda, P., Roques, J., & Garrido, F. (2017). Influence of vacancy damage on He diffusion in apatite, investigated at atomic to mineralogical scales. Geochimica et Cosmochimica Acta, 197, 87–103.

Giacomini, F., Bomparola, R. M., & Ghezzo, C. (2005). Petrology and geochronology of metabasites with eclogite facies relics from NE Sardinia: Constraints for the Palaeozoic evolution of Southern Europe. Lithos, 82(1–2), 221–248.

Giacomini, F., Bomparola, R. M., Ghezzo, C., & Guldbransen, H. (2006). The geodynamic evolution of the Southern European Variscides: Constraints from the U/Pb geochronology and geochemistry of the lower Palaeozoic magmatic-sedimentary sequences of Sardinia (Italy). Contributions to Mineralogy and Petrology, 152(1), 19. https://doi.org/10.1007/s00410-006-0092-5

Giacomini, F., Dallai, L., Carminati, E., Tiepolo, M., & Ghezzo, C. (2008). Exhumation of a Variscan orogenic complex: Insights into the composite granulitic–amphibolitic metamorphic basement of south-east Corsica (France). Journal of Metamorphic Geology, 26(4), 403–436.

Gibson, M., Sinclair, H. D., Lynn, G. J., & Stuart, F. M. (2007). Late- to post-orogenic exhumation of the Central Pyrenees revealed through combined thermochronological data and modelling. Basin Research, 19(3), 323–334. https://doi.org/10.1111/j.1365-2117.2007.00333.x

Gleadow, A. J. W. (1981). Fission-track dating methods: What are the real alternatives? Nuclear Tracks, 5(1–2), 3–14.

Gleadow, A. J. W., & Duddy, I. R. (1981). A natural long-term track annealing experiment for apatite. Nuclear Tracks, 5(1–2), 169–174.

Gleadow, A. J. W., & Lovering, J. F. (1977). Geometry factor for external detectors in fission track dating. Nuclear Track Detection, 1(2), 99–106.

Gleizes, G., Crevon, G., Asrat, A., & Barbey, P. (2006). Structure, age and mode of emplacement of the Hercynian Bordères-Louron pluton (Central Pyrenees, France). International Journal of Earth Sciences, 95(6), 1039–1052.

Gleizes, G., Leblanc, D., Santana, V., Olivier, P., & Bouchez, J. L. (1998). Sigmoidal structures featuring dextral shear during emplacement of the Hercynian granite complex of Cauterets–Panticosa (Pyrenees). Journal of Structural Geology, 20(9), 1229–1245. https://doi.org/10.1016/S0191-8141(98)00060-1

Golberg, J. M., & Leyreloup, A. F. (1990). High temperature-low pressure Cretaceous metamorphism related to crustal thinning (Eastern North Pyrenean Zone, France). Contributions to Mineralogy and Petrology, 104(2), 194–207.

Golberg, J.-M. (1987). Le métamorphisme mésozoïque dans la partie orientale des Pyrénées: Relations avec l'évolution de la chaîne au Crétacé [PhD Thesis]. Montpellier 2.

Gómez, J. J., Sandoval, J., Aguado, R., O'Dogherty, L., & Osete, M. L. (2019). The Alpine Cycle in Eastern Iberia: Microplate Units and Geodynamic Stages. In C. Quesada & J. T. Oliveira (Eds.), The Geology of Iberia: A Geodynamic Approach: Volume 3: The Alpine Cycle (pp. 15–27). Springer International Publishing. https://doi.org/10.1007/978-3-030-11295-0_2

Gómez-Gras, D., Roigé, M., Fondevilla, V., Oms, O., Boya, S., & Remacha, E. (2016). Provenance constraints on the Tremp Formation paleogeography (southern Pyrenees): Ebro Massif vs Pyrenees sources. Cretaceous Research, 57, 414–427.

Goujou, J.-C., Golberg, J.-M., & Leyreloup, A. (1988). Réactions de décarbonatation dans les roches calcaréopélitiques de la Ballongue (Zone Nord Pyrénéenne). I: Formation de biotite et de plagioclase. Comptes Rendus de l'Académie Des Sciences. Série 2, Mécanique, Physique, Chimie, Sciences de l'univers, Sciences de La Terre, 307(1), 39–44.

Gradstein, F., Ogg, J. G., Schmitz, M., & Ogg, G. (2012). The geologic time scale 2012. elsevier.

Green, P. F. (1988). The relationship between track shortening and fission track age reduction in apatite: Combined influences of inherent instability, annealing anisotropy, length bias and system calibration. Earth and Planetary Science Letters, 89(3–4), 335–352.

Green, P. F., & Duddy, I. R. (2006). Interpretation of apatite (U–Th)/He ages and fission track ages from cratons. Earth and Planetary Science Letters, 244(3–4), 541–547.

Green, P. F., Duddy, I. R., Gleadow, A. J. W., Tingate, P. R., & Laslett, G. M. (1986). Thermal annealing of fission tracks in apatite: 1. A qualitative description. Chemical Geology: Isotope Geoscience Section, 59, 237–253.

Green, P. F., & Durrani, S. A. (1978). A quantitative assessment of geometry factors for use in fission track studies. Nuclear Track Detection, 2(4), 207–213.

Grool, A., Ford, M., Vergés, J., Huismans, R., Christophoul, F., & Dielforder, A. (2018). Insights Into the Crustal-Scale Dynamics of a Doubly Vergent Orogen From a Quantitative Analysis of Its Forelands: A Case Study of the Eastern Pyrenees. Tectonics, 37(2), 450–476.

Guenthner, W. R., Reiners, P. W., Ketcham, R. A., Nasdala, L., & Giester, G. (2013). Helium diffusion in natural zircon: Radiation damage, anisotropy, and the interpretation of zircon (U-Th)/He thermochronology. American Journal of Science, 313(3), 145–198. https://doi.org/10.2475/03.2013.01

Guille, T., Olivier, P., Paquette, J.-L., Bosse, V., & Guillaume, D. (2019). Evolution of the middle crust of the Pyrenees during the Paleozoic: New data on the plutonic rocks from the North Pyrenean Agly Massif. International Journal of Earth Sciences, 108(1), 245–265. https://doi.org/10.1007/s00531-018-1652-4

Guitard, G. (1970). Le métamorphisme hercynien mésozonal et les gneiss oeillés du massif du Canigou:(Pyrénées-Orientales) [PhD Thesis]. Éditions BRGM [Bureau de recherches géologiques et minières].

Guitard, G., Autran, A., & Fonteilles, M. (1996). Le substratum précambrien du Paléozoïque. Synthèse Géologique et Géophysique Des Pyrénées, 1, 137–155.

Gunnell, Y., Calvet, M., Brichau, S., Carter, A., Aguilar, J.-P., & Zeyen, H. (2009). Low long-term erosion rates in high-energy mountain belts: Insights from thermo-and biochronology in the Eastern Pyrenees. Earth and Planetary Science Letters, 278(3), 208–218.

Hanchar, J. M., & Miller, C. F. (1993). Zircon zonation patterns as revealed by cathodoluminescence and backscattered electron images: Implications for interpretation of complex crustal histories. Chemical Geology, 110(1), 1–13. https://doi.org/10.1016/0009-2541(93)90244-D

Hanchar, J. M., & Rudnick, R. L. (1995). Revealing hidden structures: The application of cathodoluminescence and back-scattered electron imaging to dating zircons from lower crustal xenoliths. Lithos, 36(3), 289–303. https://doi.org/10.1016/0024-4937(95)00022-4

Hart, N., Stockli, D., & Hayman, N. (2016). Provenance evolution during progressive rifting and hyperextension using bedrock and detrital zircon U-Pb geochronology, Mauléon Basin, western Pyrenees. Geosphere, 12(4), 1166–1186.

Hartenberger, J. L., Sigé, B., & Sudre, J. (1968). Nouveaux gisements de vertébrés dans l'Éocène continental du Minervois. CR Somm. Soc. Geol. France, 1, 22–23.

Helbing, H., & Tiepolo, M. (2005). Age determination of Ordovician magmatism in NE Sardinia and its bearing on Variscan basement evolution. Journal of the Geological Society, 162(4), 689–700. https://doi.org/10.1144/0016-764904-103

Herman, F., Seward, D., Valla, P. G., Carter, A., Kohn, B., Willett, S. D., & Ehlers, T. (2013). Worldwide acceleration of mountain erosion under a cooling climate. Nature, 504(7480), 423–426.

Hottinger, L. (1962). Recherches sur les Alvéolines du Paléocène et de l'Eocène.

Hourigan, J., Reiners, P., & Brandon, M. (2005). U-Th zonation-dependent alpha-ejection in (U-Th)/He chronometry. Geochimica et Cosmochimica Acta, 69(13), 3349–3365.

House, M. A., Wernicke, B. P., Farley, K. A., & Dumitru, T. A. (1997). Cenozoic thermal evolution of the central Sierra Nevada, California, from (UTh)/He thermochronometry. Earth and Planetary Science Letters, 151(3), 167–179. https://doi.org/10.1016/S0012-821X(97)81846-8

Hovius, N., & Stark, C. P. (2006). Landslide-driven erosion and topographic evolution of active mountain belts. In Landslides from massive rock slope failure (pp. 573–590). Springer.

Hoÿm de Marien, L., Le Bayon, B., Pitra, P., Van Den Driessche, J., Poujol, M., & Cagnard, F. (2019). Two-stage Variscan metamorphism in the Canigou massif: Evidence for crustal thickening in the Pyrenees. Journal of Metamorphic Geology, jmg.12487. https://doi.org/10.1111/jmg.12487

Hurford, A. (1990). Standardization of fission track dating calibration: Recommendation by the Fission Track Working Group of the IUGS Subcommission on Geochronology. Chemical Geology: Isotope Geoscience Section, 80(2), 171–178.

Hurford, A., & Green, P. (1982). A users' guide to fission track dating calibration. Earth and Planetary Science Letters, 59(2), 343–354.

Hurford, A., & Green, P. (1983). The zeta age calibration of fission-track dating. Chemical Geology, 41, 285–317.

Huyghe, D., Castelltort, S., Mouthereau, F., Serra-Kiel, J., Filleaudeau, P.-Y., Emmanuel, L., Berthier, B., & Renard, M. (2012). Large scale facies change in the middle Eocene South-Pyrenean foreland basin: The role of tectonics and prelude to Cenozoic ice-ages. Sedimentary Geology, 253, 25–46.

Huyghe, D., Mouthereau, F., Castelltort, S., Filleaudeau, P.-Y., & Emmanuel, L. (2009). Paleogene propagation of the southern Pyrenean thrust wedge revealed by finite strain analysis in frontal thrust sheets: Implications for mountain building. Earth and Planetary Science Letters, 288(3–4), 421–433.

Huyghe, D., Mouthereau, F., Ségalen, L., & Furió, M. (2020). Long-term dynamic topographic support during post-orogenic crustal thinning revealed by stable isotope (δ 18 O) paleo-altimetry in eastern Pyrenees. Scientific Reports, 10(1), 1‑8.

Jammes, S., Manatschal, G., Lavier, L., & Masini, E. (2009). Tectonosedimentary evolution related to extreme crustal thinning ahead of a propagating ocean: Example of the western Pyrenees: extreme crustal thinning in the Pyrenees. Tectonics, 28(4), n/a-n/a. https://doi.org/10.1029/2008TC002406

Jammes, S., Tiberi, C., & Manatschal, G. (2010). 3D architecture of a complex transcurrent rift system: The example of the Bay of Biscay–Western Pyrenees. Tectonophysics, 489(1), 210–226. https://doi.org/10.1016/j.tecto.2010.04.023

Janowski, M., Loget, N., Gautheron, C., Barbarand, J., Bellahsen, N., Van den Driessche, J., Babault, J., Meyer, B., 2017. Neogene exhumation and relief evolution in the eastern Betics (SE Spain): insights from the Sierra de Gador. Terra Nova 29, 91–97.

Jolivet, L., Gorini, C., Smit, J., & Leroy, S. (2015). Continental breakup and the dynamics of rifting in back-arc basins: The Gulf of Lion margin. Tectonics, 34(4), 662–679.

Jolivet, M., Ritz, J.-F., Vassallo, R., Larroque, C., Braucher, R., Todbileg, M., Chauvet, A., Sue, C., Arnaud, N., De Vicente, R., & others. (2007). Mongolian summits: An uplifted, flat, old but still preserved erosion surface. Geology, 35(10), 871–874.

Juez-Larré, J., & Andriessen, P. A. M. (2006). Tectonothermal evolution of the northeastern margin of Iberia since the break-up of Pangea to present, revealed by low-temperature fission-track and (U–Th)/He thermochronology: A case history of the Catalan Coastal Ranges. Earth and Planetary Science Letters, 243(1–2), 159–180.

Juncal, M., Lloret, J., Diez, J., López-Gómez, J., Ronchi, A., De la Horra, R., Barrenechea, J., & Arche, A. (2019). New Upper Carboniferous palynofloras from Southern Pyrenees (NE Spain): Implications for palynological zonation of Western Europe. Palaeogeography, Palaeoclimatology, Palaeoecology, 516, 307–321. https://doi.org/10.1016/j.palaeo.2018.12.010

Ketcham, R. (2005). Forward and inverse modeling of low-temperature thermochronometry data. Reviews in Mineralogy and Geochemistry, 58(1), 275–314.

Ketcham, R., Carter, A., Donelick, R., Barbarand, J., & Hurford, A. (2007). Improved modeling of fission-track annealing in apatite. American Mineralogist, 92(5–6), 799–810.

Ketcham, R., Gautheron, C., & Tassan-Got, L. (2011). Accounting for long alpha-particle stopping distances in (U–Th–Sm)/He geochronology: Refinement of the baseline case. Geochimica et Cosmochimica Acta, 75(24), 7779–7791.

Ketcham, R., Van Der Beek, P., Barbarand, J., Bernet, M., & Gautheron, C. (2018). Reproducibility of Thermal History Reconstruction From Apatite Fission-Track and (U-Th)/He Data. Geochemistry, Geophysics, Geosystems, 19(8), 2411–2436.

Kisch, H. (1979). Mineralogy and petrology of burial diagenesis (burial metamorphism) and incipient metamorphism in clastic rocks. In Developments in Sedimentology (Vol. 25, pp. 289–493). Elsevier.

Labaume, P., Meresse, F., Jolivet, M., & Teixell, A. (2016). Exhumation sequence of the basement thrust units in the west-central Pyrenees. Constraints from apatite fission track analysis. Geogaceta, 60, 11–14.

Labaume, P., Mutti, E., & Seguret, M. (1987). Megaturbidites: A depositional model from the Eocene of the SW-Pyrenean foreland basin, Spain. Geo-Marine Letters, 7(2), 91–101.

Lacombe, O., Jolivet, L. (2005). Structural and kinematic relationships between Corsica and the Pyrenees-Provence domain at the time of the Pyrenean orogeny. Tectonics 24. doi:10.1029/2004TC001673, 2005

Lagabrielle, Y., Clerc, C., Vauchez, A., Lahfid, A., Labaume, P., Azambre, B., Fourcade, S., & Dautria, J.-M. (2016). Very high geothermal gradient during mantle exhumation recorded in mylonitic marbles and carbonate breccias from a Mesozoic Pyrenean palaeomargin (Lherz area, North Pyrenean Zone, France). Comptes Rendus Geoscience, 348(3–4), 290–300. https://doi.org/10.1016/j.crte.2015.11.004

Lagabrielle, Y., Labaume, P., de Saint Blanquat, M., 2010. Mantle exhumation, crustal denudation, and gravity tectonics during Cretaceous rifting in the Pyrenean realm (SW Europe): Insights from the geological setting of the lherzolite bodies. Tectonics 29.

Lardeaux, J. M., Ledru, P., Daniel, I., & Duchene, S. (2001). The Variscan French Massif Central—a new addition to the ultra-high pressure metamorphic 'club': Exhumation processes and geodynamic consequences. Tectonophysics, 332(1–2), 143–167.

Laslett, G. M., Gleadow, A. J. W., & Duddy, I. R. (1984). The relationship between fission track length and track density in apatite. Nuclear Tracks and Radiation Measurements (1982), 9(1), 29–38.

Laumonier, B., Autran, A., Barbey, P., Cheilletz, A., Baudin, T., Cocherie, A., & Guerrot, C. (2004). Conséquences de l'absence de socle cadomien sur l'âge et la signification des séries prévarisques (anté-Ordovicien supérieur) du sud de la France (Pyrénées, Montagne Noire). Bull. Soc. Géol. Fr, 175(6), 643–655.

Laumonier, B., Calvet, M., Wiazemsky, M., Barbey, P., Marignac, C., Lambert, J., Lenoble, J., Autran, A., Cocherie, A., & Baudin, T. (2015). Notice explicative de la feuille de Céret à 1/50 000.

Laumonier, B., Canérot, J., Colin, J.-P., Platel, J.-P., & Bilotte, M. (2008). Les Pyrénées pré-hercyniennes et hercyniennes. Pyrénées d'hier et d'aujourd'hui, Pau, 20–21.

Le Pochat, G., Boissonnas, J., & Destombes, J. P. (1974). Carte géol. In: France (1/50000), feuille Iholdy (1027). BRGM Orléans.

Le Pochat, G., Lenguin, M., & Thibault, C. (1976). Notice explicative, carte géol. In: France (1/50000), feuille Mauléon-Licharre (1028). BRGM Orléans.

Ledru, P., Lardeaux, J. M., Santallier, D., Autran, A., Quenardel, J. M., Floc'h, J. P., Lerouge, G., Maillet, N., Marchand, J., & Ploquin, A. (1989). Ou sont les nappes dans le massif central francais? Bulletin de La Société Géologique de France, V(3), 605–618. https://doi.org/10.2113/gssgfbull.V.3.605

Lemirre, B., Duchêne, S., De Saint Blanquat, M., & Poujol, M. (2016). État thermique de la croûte varisque dans le massif nord-pyrénéen du Saint Barthélémy. 25 Ème Réunion Des Sciences de La Terre (RST 2016), 198.

Leterrier, J. (1972). Etude pétrographique et géochimique du massif granitique de Quérigut (Ariège). Fondation scientifique de la géologie et de ses applications.

Li, X., Faure, M., & Lin, W. (2014). From crustal anatexis to mantle melting in the Variscan orogen of Corsica (France): SIMS U–Pb zircon age constraints. Tectonophysics, 634, 19–30.

Liesa, M., & Carreras, J. (1989). On the structure and metamorphism of the Roc de Frausa Massif (Eastern Pyrenees). Geodinamica Acta, 3(2), 149–161.

Liesa, M., Carreras, J., Castiñeiras, P., Casas, J. M., Navidad, M., & Vilá, M. (2011). U–Pb zircon age of Ordovician magmatism in the Albera Massif (Eastern Pyrenees). Geol. Acta 9, 93–101.

Lin, W., Faure, M., Li, X., Chu, Y., Ji, W., & Xue, Z. (2016). Detrital zircon age distribution from Devonian and Carboniferous sandstone in the Southern Variscan Fold-and-Thrust belt (Montagne Noire, French Massif Central), and their bearings on the Variscan belt evolution. Tectonophysics, 677, 1–33.

Linnemann, U., Gerdes, A., Hofmann, M., & Marko, L. (2014). The Cadomian Orogen: Neoproterozoic to Early Cambrian crustal growth and orogenic zoning along the periphery of the West African Craton—Constraints from U–Pb zircon ages and Hf isotopes (Schwarzburg Antiform, Germany). Precambrian Research, 244, 236–278. https://doi.org/10.1016/j.precamres.2013.08.007

Lippolt, H. J., Leitz, M., Wernicke, R. S., & Hagedorn, B. (1994). (Uranium+ thorium)/helium dating of apatite: Experience with samples from different geochemical environments. Chemical Geology, 112(1–2), 179–191.

Lopez-Sanchez, M., García-Sansegundo, J., & Martínez, F. (2018). The significance of early Permian and early Carboniferous U-Pb zircon ages in the Bossòst and Lys-Caillaouas granitoids (Pyrenean Axial Zone). Geological Journal. https://doi.org/10.1002/gj.3283

Ludwig, K. (1998). On the treatment of concordant uranium-lead ages. Geochimica et Cosmochimica Acta, 62(4), 665–676.

Ludwig, K. (2003). User's manual for isoplot 3.00, a geochronlogical toolkit for microsoft excel. Berkeley Geochronl. Cent. Spec. Publ., 4, 25–32.

Ludwig, K. (2008). Isoplot version 4.15: A geochronological toolkit for microsoft Excel. Berkeley Geochronology Center, Special Publication, 4, 247–270.

Ludwig, K. R. (2003). ISOPLOT 3.00: A geochronological toolkit for Microsoft Excel. Berkeley Geochronology Center Special Publication, 1–70.

Macchiavelli, C., Vergés, J., Schettino, A., Fernàndez, M., Turco, E., Casciello, E., Torne, M., Pierantoni, P., & Tunini, L. (2017). A new southern North Atlantic isochron map: Insights into the drift of the Iberian plate since the Late Cretaceous. Journal of Geophysical Research: Solid Earth, 122(12), 9603–9626.

Malusà, M., Anfinson, O., Dafov, L., & Stockli, D. (2016). Tracking Adria indentation beneath the Alps by detrital zircon U-Pb geochronology: Implications for the Oligocene–Miocene dynamics of the Adriatic microplate. Geology, 44(2), 155–158. https://doi.org/10.1130/G37407.1

Malusà, M., Danišík, M., & Kuhlemann, J. (2016). Tracking the Adriatic-slab travel beneath the Tethyan margin of Corsica–Sardinia by low-temperature thermochronometry. Gondwana Research, 31, 135–149.

Margalef, A., Castiñeiras, P., Casas, J. M., Navidad, M., Liesa, M., Linnemann, U., Hofmann, M., & Gärtner, A. (2016). Detrital zircons from the Ordovician rocks of the Pyrenees: Geochronological constraints and provenance. Tectonophysics, 681, 124–134.

Marignac, C., Laumonier, B., & Kister, P. (2010). Polymétamorphisme et évolution crustale dans les Pyrénées orientales pendant l'orogenèse varisque au Carbonifère supérieur. Bulletin de La Societé Géologique de France, t. 181, N 5, 411–428.

Martínez, F. J., Iriondo, A., Dietsch, C., Aleinikoff, J. N., Peucat, J.-J., Cirès, J., Reche, J., & Capdevila, R. (2011). U-Pb SHRIMP-RG zircon ages and Nd signature of lower Paleozoic rifting-related magmatism in the Variscan basement of the Eastern Pyrenees. Lithos, 127(1–2), 10–23.

Martin-Martin, M., Rey, J., Alcala-Garcia, F. J., Tosquella, J., Deramond, J., Lara-Corona, E., Duranthon, F., & Antoine, P.-O. (2001). Tectonic controls on the deposits of a foreland basin: An example from the Eocene Corbières–Minervois basin, France. Basin Research, 13(4), 419–433. https://doi.org/10.1046/j.0950-091x.2001.00158.x

Massieux, M. (1973). Micropaléontologie stratigraphique de l'Eocéne des Corbières Orientales (Aude). Cahiers de Paléontologie, 146.

Massieux, Michèle. (1973). Micropaléontologie stratigraphique de l'éocène des Corbières septentrionales, Aude (Vol. 14). Editions du CNRS.

Matenco, L., & Andriessen, P. (2013). Quantifying the mass transfer from mountain ranges to deposition in sedimentary basins: Source to sink studies in the Danube Basin–Black Sea system. Global and Planetary Change, 103, 1–18.

Mathey, B. (1986). Les flyschs crétacé supérieur des Pyrénées basques: Âge, anatomie, origine du matériel, milieu de dépôt et relations avec l'ouverture du Golfe de Gascogne [PhD Thesis]. Dijon.

Mathey, B., Floquet, M., & Martînez-Torres, L. M. (1999). The Leiza palaeo-fault: Role and importance in the Upper Cretaceous sedimentation and palaeogeography of the Basque Pyrenees (Spain). Comptes Rendus de l'Académie Des Sciences-Series IIA-Earth and Planetary Science, 328(6), 393–399.

Matte, P. (1991). Accretionary history and crustal evolution of the Variscan belt in Western Europe. Tectonophysics, 196(3–4), 309–337.

Matte, P. (2001). The Variscan collage and orogeny (480–290 Ma) and the tectonic definition of the Armorica microplate: A review. Terra Nova, 13(2), 122–128.

Maufrangeas, A., Leleu, S., Loisy, C., Roperch, P., Jolley, D., Vinciguerra, C., & Nguyen-Thuyet, O. (2020). Stratigraphy in Palaeocene continental sedimentary succession of the Northern Pyrenean Basin (Corbières, southern France) using δ13Corg isotopes. Journal of the Geological Society. https://doi.org/10.1144/jgs2019-084

Mauffret, A., de Grossouvre, B.D., Dos Reis, A.T., Gorini, C., Nercessian, A., 2001. Structural geometry in the eastern Pyrenees and western Gulf of Lion (Western Mediterranean). J. Struct. Geol. 23, 1701–1726.

Maurel, O. (2003). L'exhumation de la Zone Axiale des Pyrénées orientales: Une approche thermochronologique multi-méthodes du rôle des failles. [PhD Thesis].

Maurel, O., Monie, P., Pik, R., Arnaud, N., Brunel, M., & Jolivet, M. (2008). The Meso-Cenozoic thermo-tectonic evolution of the Eastern Pyrenees: An 40Ar/39Ar fission track and (U–Th)/He thermochronological study of the Canigou and Mont-Louis massifs. International Journal of Earth Sciences, 97(3), 565–584.

Maurel, O., Respaut, J.-P., Monié, P., Arnaud, N., & Brunel, M. (2004). U/Pb emplacement and 40Ar/39Ar cooling ages of the eastern Mont-Louis granite massif (Eastern Pyrenees, France). Comptes Rendus Geoscience, 336(12), 1091–1098.

Mazur, S., Aleksandrowski, P., Turniak, K., Krzemiński, L., Mastalerz, K., Górecka-Nowak, A., Kurowski, L., Krzywiec, P., Żelaźniewicz, A., & Fanning, M. C. (2010). Uplift and late orogenic deformation of the Central European Variscan belt as revealed by sediment provenance and structural record in the Carboniferous foreland basin of western Poland. International Journal of Earth Sciences, 99(1), 47–64.

McDannell, K.T., Zeitler, P.K., Janes, D.G., Idleman, B.D., Fayon, A.K., 2018. Screening apatites for (U-Th)/He thermochronometry via continuous ramped heating: He age components and implications for age dispersion. Geochim. Cosmochim. Acta 223, 90–106. https://doi.org/10.1016/j.gca.2017.11.031

McDowell, F., McIntosh, W., & Farley, K. (2005). A precise 40Ar–39Ar reference age for the Durango apatite (U–Th)/He and fission-track dating standard. Chemical Geology, 214(3–4), 249–263.

McKerrow, W. S., Mac Niocaill, C., & Dewey, J. F. (2000). The Caledonian Orogeny redefined. Journal of the Geological Society, 157(6), 1149–1154. https://doi.org/10.1144/jgs.157.6.1149

McKinley, J. M., Worden, R. H., & Ruffell, A. H. (1999). Smectite in sandstones: A review of the controls on occurrence and behaviour during diagenesis. Clay Mineral Cements in Sandstones, 109–128.

Meesters, A., & Dunai, T. J. (2002). Solving the production–diffusion equation for finite diffusion domains of various shapes: Part II. Application to cases with α-ejection and nonhomogeneous distribution of the source. Chemical Geology, 186(1–2), 57–73.

Meigs, A., Vergés, J., & Burbank, D. (1996). Ten-million-year history of a thrust sheet. Geological Society of America Bulletin, 108(12), 1608–1625.

Melleton, J., Cocherie, A., Faure, M., & Rossi, P. (2010). Precambrian protoliths and Early Paleozoic magmatism in the French Massif Central: U–Pb data and the North Gondwana connection in the west European Variscan belt. Gondwana Research, 17(1), 13–25.

Ménot, R.-P., & Orsini, J.-B. (1990). Evolution du socle anté-stéphanien de Corse: Événements magmatiques et métamorphiques. Schweizerische Mineralogische Und Petrographische Mitteilungen, 70(1), 35–53.

Metcalf, J. R., Fitzgerald, P. G., Baldwin, S., Muñoz, J., Perry, S. E., & Feinberg, E. B. (2009). Thermochronological Constraints on the Exhumation of the Lys Caillaouas Massif, West-Central Pyrenees. AGU Fall Meeting Abstracts.

Mezger, J. (2010). Cadomian, Ordovician and Variscan igneous events preserved in gneiss domes of the Central Pyrenean Axial Zone. 13. Symposium “Tektonik, Struktur-Und Kristallingeologie”(TSK 13), Frankfurt, 6–12.

Mezger, J. E., & Régnier, J.-L. (2016). Stable staurolite–cordierite assemblages in K-poor metapelitic schists in Aston and Hospitalet gneiss domes of the central Pyrenees (France, Andorra). Journal of Metamorphic Geology, 34(2), 167–190.

Mezger, J., & Gerdes, A. (2016). Early Variscan (Visean) granites in the core of central Pyrenean gneiss domes: Implications from laser ablation U-Pb and Th-Pb studies. Gondwana Research, 29(1), 181–198.

Miall, A.D. (1996) The Geology of Fluvial Deposits, Sedimentary Facies, Basin Analysis and Petroleum Geology. Springer-Verlag.

Michael, N., Carter, A., Whittaker, A., & Allen, P. (2014). Erosion rates in the source region of an ancient sediment routing system: Comparison of depositional volumes with thermochronometric estimates. Journal of the Geological Society, 171(3), 401–412.

Michael, N., Whittaker, A., & Allen, P. (2013). The functioning of sediment routing systems using a mass balance approach: Example from the Eocene of the southern Pyrenees. The Journal of Geology, 121(6), 581–606.

Michael, N., Whittaker, A., Carter, A., & Allen, P. (2014). Volumetric budget and grain-size fractionation of a geological sediment routing system: Eocene Escanilla Formation, south-central Pyrenees. Bulletin, 126(3–4), 585–599.

Michard-Vitrac, A., Albarede, F., Dupuis, C., & Taylor, H. (1980). The genesis of Variscan (Hercynian) plutonic rocks: Inferences from Sr, Pb, and O studies on the Maladeta igneous complex, central Pyrenees (Spain). Contributions to Mineralogy and Petrology, 72(1), 57–72.

Miguet, J. (2015). Etude sédimentologique des molasses du bassin nord-Oyrénéen: Le Poudingue de Palassou.

Millán, H., Aurell, M., & Meléndez, A. (1994). Synchronous detachment folds and coeval sedimentation in the Prepyrenean External Sierras (Spain): A case study for a tectonic origin of sequences and systems tracts. Sedimentology, 41(5), 1001–1024.

Monod, B., Bourroullec, I., Chévremont, P., LeBayon, B., Nehlig, P., Aretz, M., Bilotte, M., Christophoul, F., Debroas, Denèle, Y., Faure, M., Laumonier, Lézin, C., Nardin, E., Olivier, Ph., Regard, V., & de St Blanquat, M. (2014). Carte géologique numérique à 1/250 000 de la région Midi-Pyrénées, Notice. BRGM Orléans.

Montgomery, D., & Brandon, M. (2002). Topographic controls on erosion rates in tectonically active mountain ranges. Earth and Planetary Science Letters, 201(3–4), 481–489.

Montigny, R., Azambre, B., Rossy, M., & Thuizat, R. (1986). K-Ar study of cretaceous magmatism and metamorphism in the pyrenees: Age and length of rotation of the Iiberian Peninsula. Tectonophysics, 129(1–4), 257–273.

Morris, R. G., Sinclair, H. D., & Yelland, A. J. (1998). Exhumation of the Pyrenean orogen: Implications for sediment discharge. Basin Research, 10(1), 69–85.

Mouchené, M., van der Beek, P., Carretier, S., & Mouthereau, F. (2017). Autogenic versus allogenic controls on the evolution of a coupled fluvial megafan–mountainous catchment system: Numerical modelling and comparison with the Lannemezan megafan system (northern Pyrenees, France). Earth Surface Dynamics, 5(1), 125–143.

Mouthereau, F., Filleaudeau, P.-Y., Vacherat, A., Pik, R., Lacombe, O., Fellin, M. G., Castelltort, S., Christophoul, F., & Masini, E. (2014). Placing limits to shortening evolution in the Pyrenees: Role of margin architecture and implications for the Iberia/Europe convergence: Plate convergence in the Pyrenees. Tectonics, 33(12), 2283–2314. https://doi.org/10.1002/2014TC003663

Munoz, J. A. (1992). Evolution of a continental collision belt: ECORS-Pyrenees crustal balanced cross-section. 235–245.

Munoz, J. A., Martinez, A., & Verges, J. (1986). Thrust sequences in the eastern Spanish Pyrenees. Journal of Structural Geology, 8(3–4), 399–405. https://doi.org/10.1016/0191-8141(86)90058-1

Murray, K. E., Orme, D. A., & Reiners, P. W. (2011). Apatite (U-Th)/He date dispersion due to secondary grain boundary phases: An example from the Henry Mountains, Utah. AGU Fall Meeting Abstracts.

Murray, K. E., Reiners, P. W., & Thomson, S. N. (2016). Rapid Pliocene–Pleistocene erosion of the central Colorado Plateau documented by apatite thermochronology from the Henry Mountains. Geology, 44(6), 483–486.

Murray, K., Orme, D., & Reiners, P. (2014). Effects of U–Th-rich grain boundary phases on apatite helium ages. Chemical Geology, 390, 135–151.

Mutti, E. (1977). Distinctive thin-bedded turbidite facies and related depositional environments in the Eocene Hecho Group (South-central Pyrenees, Spain). Sedimentology, 24(1), 107–131.

Mutti, E., Rosell, J., Allen, G. P., Fonnesu, F., & Sgavetti, M. (1985). The Eocene Baronia tide dominated delta-shelf system in the Ager Basin. Excursion Guidebook: 6th International Association of Sedimentologists European Regional Meeting, 577–600.

Neubauer, F. (2002). Evolution of late Neoproterozoic to early Paleozoic tectonic elements in Central and Southeast European Alpine mountain belts: Review and synthesis. Tectonophysics, 352(1–2), 87–103.

Nichols, G., & Hirst, J.-P. (1998). Alluvial fans and fluvial distributary systems, Oligo-Miocene, northern Spain; contrasting processes and products. Journal of Sedimentary Research, 68(5), 879–889.

Nijman, W. (1990). Thrust sheet rotation?—The South Pyrenean Tertiary basin configuration reconsidered. Geodinamica Acta, 4(1), 17–42.

Nijman, W. (1998). Cyclicity and basin axis shift in a piggyback basin: Towards modelling of the Eocene Tremp-Ager Basin, South Pyrenees, Spain. Geological Society, London, Special Publications, 134(1), 135–162. https://doi.org/10.1144/GSL.SP.1998.134.01.07

Odlum, M. L., Stockli, D. F., Capaldi, T. N., Thomson, K. D., Clark, J., Puigdefàbregas, C., & Fildani, A. (2019). Tectonic and sediment provenance evolution of the South Eastern Pyrenean foreland basins during rift margin inversion and orogenic uplift. Tectonophysics.

Oggiano, G., Casini, L., Rossi, P., & Mameli, P. (2007). Long-lived strike–slip tectonics in the southern Variscan Belt: Evidences from two synkinematic intrusions of North Sardinia (Italy). Mechanics of Variscan Orogeny: A Modern View in Orogenic Research, 141.

Oggiano, G., Gaggero, L., Funedda, A., Buzzi, L., & Tiepolo, M. (2010). Multiple early Paleozoic volcanic events at the northern Gondwana margin: U–Pb age evidence from the Southern Variscan branch (Sardinia, Italy). Gondwana Research, 17(1), 44–58. https://doi.org/10.1016/j.gr.2009.06.001

Olariu, C., Steel, R., Dalrymple, R., & Gingras, M. (2012). Tidal dunes versus tidal bars: The sedimentological and architectural characteristics of compound dunes in a tidal seaway, the lower Baronia Sandstone (Lower Eocene), Ager Basin, Spain. Sedimentary Geology, 279, 134–155.

Olivet, J. L. (1996). La cinématique de la plaque ibérique. Bull. Cent. Rech. Explor. Prod. Elf Aquitaine, 20(1), 131–195.

Olivier, P., Druguet, E., Castaño, L. M., & Gleizes, G. (2016). Granitoid emplacement by multiple sheeting during Variscan dextral transpression: The Saint-Laurent – La Jonquera pluton (Eastern Pyrenees). Journal of Structural Geology, 82, 80–92. https://doi.org/10.1016/j.jsg.2015.10.006

Olivier, P., Gleizes, G., & Paquette, J. L. (2004). Gneiss domes and granite emplacement in an obliquely convergent regime: New interpretation of the Variscan Agly Massif (Eastern Pyrenees, France). In Special Paper 380: Gneiss Domes in Orogeny (Vol. 380, pp. 229–242). Geological Society of America. https://doi.org/10.1130/0-8137-2380-9.229

Olivier, P., Gleizes, G., Paquette, J.-L., & Sáez, C. M. (2008). Structure and U–Pb dating of the Saint-Arnac pluton and the Ansignan charnockite (Agly Massif): A cross-section from the upper to the middle crust of the Variscan Eastern Pyrenees. Journal of the Geological Society, 165(1), 141–152. https://doi.org/10.1144/0016-76492006-185

O'Sullivan, P., & Parrish, R. (1995). The importance of apatite composition and single-grain ages when interpreting fission track data from plutonic rocks: A case study from the Coast Ranges, British Columbia. Earth and Planetary Science Letters, 132(1–4), 213–224.

Ovtracht, A., & Lenguin, M. (1977). Carte géol. France (1/50000), feuille Limoux (1059).

Owen, A., Nichols, G., Hartley, A., Weissmann, G., & Scuderi, L. (2015). Quantification of a Distributive Fluvial System: The Salt Wash DFS of the Morrison Formation, SW U.S.A. quantification of the Salt Wash DFS. Journal of Sedimentary Research, 85(5), 544–561. https://doi.org/10.2110/jsr.2015.35

Padel, M. (2016). Influence cadomienne dans les séries pré-sardes des Pyrénées Orientales: Approche géochimique, stratigraphique et géochronologique. PhD, Univ. Lille I.

Padel, M., Clausen, S., Álvaro, J. J., & Casas, J. M. (2018). Review of the Ediacaran-Lower Ordovician (pre-Sardic) stratigraphic framework of the Eastern Pyrenees, southwestern Europe. Geologica Acta, 16(4), 339–355.

Padovano, M., Dörr, W., Elter, F. M., & Gerdes, A. (2014). The East Variscan Shear Zone: Geochronological constraints from the Capo Ferro area (NE Sardinia, Italy). Lithos, 196–197, 27–41. https://doi.org/10.1016/j.lithos.2014.01.015

Palmeri, R., Fanning, M., Franceschelli, M., Memmi, I., & Ricci, C. A. (2004). SHRIMP dating of zircons in eclogite from the Variscan basement in north-eastern Sardinia (Italy). Neues Jahrbuch Für Mineralogie-Monatshefte, 2004(6), 275–288.

Paquette, J.-L., Gleizes, G., Leblanc, D., & Bouchez, J.-L. (1997). Le granite de Bassiès (Pyrénées): Un pluton syntectonique d'âge Westphalien. Géochronologie U-Pb sur zircons. Comptes rendus de l'Académie des sciences. Série 2. Sciences de la terre et des planètes, 324(5), 387–392.

Paquette, J-L, Ménot, R.-P., Pin, C., & Orsini, J.-B. (2003). Episodic and short-lived granitic pulses in a post-collisional setting: Evidence from precise U–Pb zircon dating through a crustal cross-section in Corsica. Chemical Geology, 198(1–2), 1–20.

Parseval, D. (1999). Formation of the Trimouns talc-chlorite deposit (Pyrenees) from persistent hydrothermal activity between 112 and 97 Ma. Terra Nova, 11(1), 30–37.

Paul, T., & Fitzgerald, P. (1992). Transmission electron microscopic investigation of fission tracks in fluorapatite. American Mineralogist, 77(3–4), 336–344.

Pautal, Lydie. (1985). Populations fossiles, associations micropaleontologiques et paleoenvironnements de series deltaiques ilerdiennes des Corbieres (Aude, France) (Vol. 3). Laboratoire de géologie sédimentaire et paléontologie, Université Paul Sabatier.

Pavanetto, P., Funedda, A., Northrup, C. J., Schmitz, M., Crowley, J., & Loi, A. (2012). Structure and U-Pb zircon geochronology in the Variscan foreland of SW Sardinia, Italy. Geological Journal, 47(4), 426–445. https://doi.org/10.1002/gj.1350

Pereira, M. F., Castro, A., Chichorro, M., Fernandez, C., Diaz-Alvarado, J., Marti, J., & Rodriguez, C. (2014). Chronological link between deep-seated processes in magma chambers and eruptions: Permo-Carboniferous magmatism in the core of Pangaea (Southern Pyrenees). Gondwana Research, 25(1), 290–308.

Pin, C., & Marini, F. (1993). Early Ordovician continental break-up in Variscan Europe: Nd/Sr isotope and trace element evidence from bimodal igneous associations of the Southern Massif Central, France. Lithos, 29(3–4), 177–196.

Pin, C., & Peucat, J.-J. (1986). Ages des épisodes de métamorphisme paléozoïques dans le Massif central et le Massif armoricain. Bulletin de La Société Géologique de France, 2(3), 461–469.

Pinter, N., & Brandon, M. (1997). How Erosion Builds Mountains. Scientific American, 74–79.

Pitra, P., Poujol, M., Van Den Driessche, J., Poilvet, J.-C., & Paquette, J.-L. (2012). Early Permian extensional shearing of an ordovician granite: The saint-eutrope “c/s-like” orthogneiss (montagne noire, French massif central). Comptes Rendus Géoscience, 344(8), 377–384.

Plaziat, J-C. (1964). Pistes d’oiseaux et remaniements synsedimentaires dans le Lutetien du detroit de Carcassonne (Aude). Bulletin de La Société Géologique de France, S7-VI(2), 289–293. https://doi.org/10.2113/gssgfbull.S7-VI.2.289

Plaziat, J-C. (1970). Contribution à l’étude de la faune et de la flore du Sparnacien des Corbières septentrionales.

Plaziat, J.-C. (1975). L’Ilerdien a l’interieur du Paleogene languedocien; ses relations avec le Sparnacien, l’Ilerdien sud-pyreneen, l’Ypresien et le Paleocene. Bulletin de La Société Géologique de France, 7(2), 168–182.

Plaziat, J-C. (1981). Late Cretaceous to Late Eocene palaeogeographic evolution of southwest Europe. Palaeogeography, Palaeoclimatology, Palaeoecology, 36(3–4), 263–320.

Plaziat, J-C. (1984a). Le domaine pyrénéen de la fin du Crétacé à la fin de l’Eocène: Stratigraphie, paléoenvironnements et évolution paléogéographique. Université de Paris-Sud.

Plaziat, J-C. (1984b). Mollusk distribution in the mangal. Hydrobiology of the Mangal: The Ecosystem of the Mangrove Forests. Junk, Boston, 111–143.

Poblet, J., Muñoz, J., Travé, A., & Serra-Kiel, J. (1998). Quantifying the kinematics of detachment folds using three-dimensional geometry: Application to the Mediano anticline (Pyrenees, Spain). Geological Society of America Bulletin, 110(1), 111–125.

Pohl, F., & McCann, T. (2014). Architecture and depositional development of the Eocene deep-marine Morillo and Coscojuela Formations, Aínsa Basin, Spain. Geological Journal, 49(3), 221–238.

Poilvet, J.-C., Poujol, M., Pitra, P., Van den Driessche, J., & Paquette, J.-L. (2011). The Montalet granite, Montagne Noire, France: An Early Permian syn-extensional pluton as evidenced by new U-Th-Pb data on zircon and monazite. Comptes Rendus Géoscience, 343(7), 454–461.

Postaire, B. (1983). sur zircons. Applications aux roches de haut grade m&amorphique impliqures dans la chalne herc) haienne (Europe de l'Ouest) et aux granulites de Laponie (Finlande). Bull. Soc. Geol. Min&al. Bretagne, 15, 29–72.

Poujol, M., Boulvais, P., & Kosler, J. (2010). Regional-scale Cretaceous albitization in the Pyrenees: Evidence from in situ U–Th–Pb dating of monazite, titanite and zircon. Journal of the Geological Society, 167(4), 751–767.

Prieur, M. (2019). Etude sédimentaire de la série de Palassou. Ensegid Bordeaux.

Puigdefàbregas, C., Muñoz, J. A., & Vergés, J. (1992). Thrusting and foreland basin evolution in the southern Pyrenees. In Thrust tectonics (pp. 247–254). Springer. http://link.springer.com/chapter/10.1007/978-94-011-3066-0_22

Puigdefàbregas, C., & Souquet, P. (1986). Tecto-sedimentary cycles and depositional sequences of the Mesozoic and Tertiary from the Pyrenees. Tectonophysics, 129, 173–203.

Puigdefabregas et al. (1986). Foreland Basins. The International Association of Sedimentologists.

Pujalte et al. (2009). Redefinition of the Ilerdian Stage (early Eocene). Geologica Acta, 7.1. https://doi.org/10.1344/105.000000268

Rahl, J., Haines, S., & Van der Pluijm, B. (2011). Links between orogenic wedge deformation and erosional exhumation: Evidence from illite age analysis of fault rock and detrital thermochronology of syn-tectonic conglomerates in the Spanish Pyrenees. Earth and Planetary Science Letters, 307(1–2), 180–190.

Ramos, E., Busquets, P., & Vergés, J. (2002). Interplay between longitudinal fluvial and transverse alluvial fan systems and growing thrusts in a piggyback basin (SE Pyrenees). Sedimentary Geology, 146(1–2), 105–131.

Rasser, M., Scheibner, C., & Mutti, M. (2005). A paleoenvironmental standard section for Early Ilerdian tropical carbonate factories (Corbieres, France; Pyrenees, Spain). Facies, 51(1–4), 218–232.

Rat, J., Mouthereau, F., Brichau, S., Crémades, A., Bernet, M., Balvay, M., Ganne, J., Lahfid, A., & Gautheron, C. (2019). Tectonothermal Evolution of the Cameros Basin: Implications for Tectonics of North Iberia. Tectonics, 38(2), 440–469. https://doi.org/10.1029/2018TC005294

Rat, P. (1988). The Basque-Cantabrian basin between the Iberian and European plates: Some facts but still many problems. Revista de La Sociedad Geológica de España, 1(3–4), 327–348.

Recanati, A., Gautheron, C., Barbarand, J., Missenard, Y., Pinna-Jamme, R., Tassan-Got, L., Carter, A., Douville, E., Bordier, L., & Pagel, M. (2017). Helium trapping in apatite damage: Insights from (U-Th-Sm)/He dating of different granitoid lithologies. Chemical Geology, 470, 116–131.

Reddy, R., & Manikyamba, P. (2006). Linear free energy relationship in reactions between diphenyl amine and benzyl bromides. Journal of Chemical Sciences, 118(3), 257–260. https://doi.org/10.1007/BF02708285

Reimer, G. M., Storzer, D., & Wagner, G. A. (1970). Geometry factor in fission track counting. Earth and Planetary Science Letters, 9(5), 401–404.

Reiners, P.W., Farley, K.A., 2001. Influence of crystal size on apatite (U–Th)/He thermochronology: an example from the Bighorn Mountains, Wyoming. Earth Planet. Sci. Lett. 188, 413–420.

Renna, M. R., Tribuzio, R., & Tiepolo, M. (2007). Origin and timing of the post-Variscan gabbro–granite complex of Porto (Western Corsica). Contributions to Mineralogy and Petrology, 154(5), 493–517.

Respaut, J. P., & Lancelot, J. R. (1983). Datation de la mise en place synmétamorphe de la charnockite d'Ansignan (massif de l'Agly) par la méthode U/Pb sur zircons et monazites. Neues Jahrbuch Für Mineralogie, Abhandlungen, 147, 21–34.

Reston, T. J. (2009). The structure, evolution and symmetry of the magma-poor rifted margins of the North and Central Atlantic: A synthesis. Tectonophysics, 468(1–4), 6–27.

Rey, J., & Bousquet, J.-P. (1981). Observations Préliminaires Sur Les Pali# x000E9; oenvironnements De L'ilerdien De Coustouge (Corbières, France). Geobios, 14(5), 655–659.

Ribes, C., Manatschal, G., Ghienne, J.-F., Karner, G. D., Johnson, C. A., Figueredo, P. H., Incerpi, N., & Epin, M.-E. (2019). The syn-rift stratigraphic record across a fossil hyper-extended rifted margin: The example of the northwestern Adriatic margin exposed in the Central Alps. International Journal of Earth Sciences, 108(6), 2071–2095. https://doi.org/10.1007/s00531-019-01750-6

Richard, M. (1946). Les gisements de mammifères tertiaires: Contribution a l'étude du bassin d'Aquitaine. Societé Géologique de France.

Roberts, J. H., Gold, R., & Armani, R. (1968). Spontaneous-Fission Decay Constant of U 238. Physical Review, 174(4), 1482.

Roberts, M., Pin, C., Clemens, J., & Paquette, J.-L. (2000). Petrogenesis of mafic to felsic plutonic rock associations: The calc-alkaline Quérigut complex, French Pyrenees. Journal of Petrology, 41(6), 809–844.

Roest, W.R., Srivastava, S.P., 1991. Kinematics of the plate boundaries between Eurasia, Iberia, and Africa in the North Atlantic from the Late Cretaceous to the present. Geology 19, 613–616.

Roger, F., Respaut, J.-P., Brunel, M., Matte, P., & Paquette, J.-L. (2004). Première datation U□ Pb des orthogneiss ø eillés de la zone axiale de la Montagne noire (Sud du Massif central): Nouveaux témoins du magmatisme ordovicien dans la chaîne Varisque. Comptes Rendus Geoscience, 336(1), 19–28.

Roger, F., Teyssier, C., Respaut, J.-P., Rey, P., Jolivet, M., Whitney, D., Paquette, J.-L., & Brunel, M. (2015). Timing of formation and exhumation of the Montagne Noire double dome, French Massif Central. Tectonophysics, 640, 53–69.

Roig, J.-Y., & Faure, M. (2000). La tectonique cisaillante polyphasee du Sud Limousin (Massif central francais) et son interpretation dans un modele d'evolution polycyclique de la chaine hercynienne. Bulletin de La Société Géologique de France, 171(3), 295–307.

Roigé, M., Gómez-Gras, D., Remacha, E., Boya, S., Viaplana-Muzas, M., & Teixell, A. (2017). Recycling an uplifted early foreland basin fill: An example from the Jaca basin (Southern Pyrenees, Spain). Sedimentary Geology, 360, 1–21.

Roigé, M., Gómez-Gras, D., Stockli, D.F., Teixell, A., Boya, S., Remacha, E. (2019). Detrital zircon U-Pb insights into the timing and provenance of the South Pyrenean Jaca basin. Journal of the Geological Society, 176, 1182-1190. https://doi.org/10.1144/jgs2018-228

Roigé, Marta, Gómez-Gras, D., Remacha, E., Daza, R., & Boya, S. (2016). Tectonic control on sediment sources in the Jaca basin (Middle and Upper Eocene of the South-Central Pyrenees). Comptes Rendus Geoscience, 348(3–4), 236–245.

Romans, B., Castelltort, S., Covault, J., Fildani, A., & Walsh, J. P. (2016). Environmental signal propagation in sedimentary systems across timescales. Earth-Science Reviews, 153, 7–29. https://doi.org/10.1016/j.earscirev.2015.07.012

Rosell, J., Linares, R., & Llompart, C. (2001). El "garumniense" prepirenaico. Revista de La Sociedad Geológica de España, 14(1–2), 47–56.

Rosenbaum, G., Lister, G., & Duboz, C. (2002). Relative motions of Africa, Iberia and Europe during Alpine orogeny. Tectonophysics, 359(1), 117–129.

Rossi, P., Calvez, J.-Y., & Cocherie, A. (1988). Age varisque précoce du plutonisme magnésio-potassique en Corse occidentale: Conséquences géodynamiques. Comptes Rendus de l'Académie Des Sciences. Série 2, Mécanique, Physique, Chimie, Sciences de l'univers, Sciences de La Terre, 307(13), 1541–1547.

Rossi, P., Cocherie, A., & Durand-Delga, M. (1995). Arguments géochronologiques en faveur de la présence d'un socle panafricain (cadomien) en Corse, conséquences sur la paléogéographie de l'orogène varisque sud-européen. Comptes Rendus de l'Académie Des Sciences. Série 2. Sciences de La Terre et Des Planètes, 321(11), 983–992.

Rossi, P., Durand-Delga, M., & Cocherie, A. (1991). Distinction de deux séries sédimentaires d'âge carbonifère supérieur en Corse. Comptes Rendus de l'Académie Des Sciences. Série 2, Mécanique, Physique, Chimie, Sciences de l'univers, Sciences de La Terre, 313(4), 443–450.

Rossi, P., Oggiano, G., & Cocherie, A. (2009). A restored section of the "southern Variscan realm" across the Corsica–Sardinia microcontinent. Comptes Rendus Geoscience, 341(2–3), 224–238.

Rougier, G., Ford, M., Christophoul, F., & Bader, A.-G. (2016). Stratigraphic and tectonic studies in the central Aquitaine Basin, northern Pyrenees: Constraints on the subsidence and deformation history of a retro-foreland basin. Comptes Rendus Geoscience, 348(3–4), 224–235. https://doi.org/10.1016/j.crte.2015.12.005

Roure, F., Choukroune, P., Berastegui, X., Munoz, J., Villien, A., Matheron, P., Bareyt, M., Seguret, M., Camara, P., & Deramond, J. (1989). ECORS deep seismic data and balanced cross sections: Geometric sontraints on the evolution of the Pyrenees. Tectonics, 8, NO. 1, 41–50.

Rushlow, C., Barnes, J., Ehlers, T., & Vergés, J. (2013). Exhumation of the southern Pyrenean fold-thrust belt (Spain) from orogenic growth to decay. Tectonics, 32(4), 843–860.

Sadler, P., & Jerolmack, D. (2015). Scaling laws for aggradation, denudation and progradation rates: The case for time-scale invariance at sediment sources and sinks. Geological Society, London, Special Publications, 404(1), 69–88. https://doi.org/10.1144/SP404.7

Sartégou, A., Bourlès, D., Blard, P.-H., Braucher, R., Tibari, B., Zimmermann, L., Leanni, L., Aumaitre, G., & Keddadouche, K. (2018). Deciphering landscape evolution with karstic networks: A Pyrenean case study. Quaternary Geochronology, 43, 12–29.

Savostin, L., Sibuet, J.-C., Zonenshain, L., Le Pichon, X., & Roulet, M.-J. (1986). Kinematic evolution of the Tethys belt from the Atlantic Ocean to the Pamirs since the Triassic. Tectonophysics, 123(1–4), 1–35.

Saylor, J., Knowles, J., Horton, B., Nie, J., & Mora, A. (2013). Mixing of source populations recorded in detrital zircon U-Pb age spectra of modern river sands. The Journal of Geology, 121(1), 17–33.

Schenk, V. (1980). U-Pb and Rb-Sr radiometric dates and their correlation with metamorphic events in the granulite-facies basement of the serre, Southern Calabria (Italy). Contributions to Mineralogy and Petrology, 73(1), 23–38. https://doi.org/10.1007/BF00376258

Schettino, A., & Turco, E. (2011). Tectonic history of the western Tethys since the Late Triassic. Bulletin, 123(1–2), 89–105.

Schoene, B. (2014). U–Th–Pb Geochronology. In Treatise on Geochemistry (pp. 341–378). Elsevier. https://doi.org/10.1016/B978-0-08-095975-7.00310-7

Schumm, S. A. (1977). The fluvial system. http://agris.fao.org/agris-search/search.do?recordID=XF2016024872

Schwartz, S., Gautheron, C., Dumont, T., Nomade, J., Audin, L., Pinna-Jamme, R., Barbarand, J., 2015. Late exhumation of the Alpine foreland (Digne nappe, France) constrained by low temperature thermochronology. Presented at the EGU General Assembly Conference Abstracts, p. 13482.

Séranne, M. (1999). The Gulf of Lion continental margin (NW Mediterranean) revisited by IBS: An overview. Geological Society, London, Special Publications, 156(1), 15–36.

Séranne, M., Benedicto, A., Labaum, P., Truffert, C., Pascal, G., 1995. Structural style and evolution of the Gulf of Lion Oligo-Miocene rifting: role of the Pyrenean orogeny. Mar. Pet. Geol., Integrated Basin Studies 12, 809–820. https://doi.org/10.1016/0264-8172(95)98849-Z

Serra-Kiel, J., Mató, E., Saula, E., Travé i Herrero, A., Ferràndez i Cañadell, C., Tosquella i Angrill, J., Barnolas, A., Álvarez Pérez, G., Franquès i Faixa, J., & Romero, J. (2003). An inventory of the marine and transitional Middle/Upper Eocene deposits of the Southeastern Pyrenean Foreland Basin (NE Spain). Geologica Acta, 2003, Vol. 1, Núm. 2, p. 201-229.

Serra-Kiel, Josep, Hottinger, L., Caus, E., Drobne, K., Ferrandez, C., Jauhri, A. K., Less, G., Pavlovec, R., Pignatti, J., & Samso, J. M. (1998). Larger foraminiferal biostratigraphy of the Tethyan Paleocene and Eocene. Bulletin de La Société Géologique de France, 169(2), 281–299.

Shuster, D., & Farley, K. (2009). The influence of artificial radiation damage and thermal annealing on helium diffusion kinetics in apatite. Geochimica et Cosmochimica Acta, 73(1), 183–196.

Shuster, D., Flowers, R., & Farley, K. (2006). The influence of natural radiation damage on helium diffusion kinetics in apatite. Earth and Planetary Science Letters, 249(3–4), 148–161. https://doi.org/10.1016/j.epsl.2006.07.028

Sibuet, J.-C., Srivastava, S., & Spakman, W. (2004). Pyrenean orogeny and plate kinematics. Journal of Geophysical Research: Solid Earth, 109(B8). https://doi.org/10.1029/2003JB002514

Sinclair, H. D., Gibson, M., Naylor, M., & Morris, R. G. (2005). Asymmetric growth of the Pyrenees revealed through measurement and modeling of orogenic fluxes. American Journal of Science, 305(5), 369–406.

Sinclair, H. D., & Naylor, M. (2012). Foreland basin subsidence driven by topographic growth versus plate subduction. GSA Bulletin, 124(3–4), 368–379. https://doi.org/10.1130/B30383.1

Sláma, J., Košler, J., Condon, D., Crowley, J., Gerdes, A., Hanchar, J., Horstwood, M., Morris, G., Nasdala, L., & Norberg, N. (2008). Plešovice zircon—A new natural reference material for U–Pb and Hf isotopic microanalysis. Chemical Geology, 249(1–2), 1–35.

Souquet, P. (1985). Le Groupe du Flysch Noir (Albo-Cenomanien) dans les Pyrenees: Bulletin des Centres de Recherches Exploration-Production Elf-Aquitaine, v. 9.

Souquet, P. (1986). Facies sequence and downcurrent changes in large-volume debris and turbidity flow deposits. AAPG Bulletin-American Association of Petroleum Geologists, 70(5), 651.

Souquet, P., Bilotte, M., Canerot, J., Debroas, E.-J., Peybernès, B., & Rey, J. (1975). Carte géologique de la France à 1/50 000–Feuille Le Mas d'Azil (1056)–BRGM. BRGM Orléans.

Spiegel, C., Kohn, B., Belton, D., Berner, Z., & Gleadow, A. (2009). Apatite (U–Th–Sm)/He thermochronology of rapidly cooled samples: The effect of He implantation. Earth and Planetary Science Letters, 285(1–2), 105–114.

Spiegel, C., Kohn, B., Raza, A., Rainer, T., & Gleadow, A. (2007). The effect of long-term low-temperature exposure on apatite fission track stability: A natural annealing experiment in the deep ocean. Geochimica et Cosmochimica Acta, 71(18), 4512–4537.

Srivastava, S. P., Schouten, H., Roest, W. R., Klitgord, K. D., Kovacs, L. C., Verhoef, J., & Macnab, R. (1990). Iberian plate kinematics: A jumping plate boundary between Eurasia and Africa. Nature, 344, 756–759.

Stampfli, G. M. (1996). The intra-Alpine terrain: A Paleotethyan remnant in the Alpine Variscides. Eclogae Geologicae Helvetiae, 89, 13–42.

Stampfli, G. M., & Borel, G. D. (2002). A plate tectonic model for the Paleozoic and Mesozoic constrained by dynamic plate boundaries and restored synthetic oceanic isochrons. Earth and Planetary Science Letters, 196(1–2), 17–33.

Stampfli, G. M., Borel, G., Marchant, R., & Mosar, J. (2002). Western Alps geological constraints on western Tethyan reconstructions. Journal of the Virtual Explorer, 8, 77.

Suc, J-. P. & Fauquette, S. (2012) The use of pollen floras as a tool to estimate palaeoaltitude of mountains: The eastern Pyrenees in the Late Neogene, a case study Paleogeography, Paleoclimatology, Paleoecology, 321-322, 41-54. https://doi.org/10.1016/j.palaeo.2012.01.014

Sudre, J., Brunet, M., De Bonis, L., Crochet, J. Y., Duranthon, F., Godinot, M., Hartenberger, J. L., Jehenne, Y., Legendre, S., Marandat, B., Remy, J. A., Ringeade, M., Sigé, B., & Vianey, M. (1992). a biochronologie mammalienne du Paléogène au Nord et au Sud des Pyrénées; état de la question [Mammalian biochronology from the Paleogene North and South of the Pyrenees: An updated survey.

Sudre, J., Brunet, M., De Bonis, L., Crochet, J. Y., Duranthon, F., Godinot, M., Hartenberger, J. L., Jehenne, Y., Legendre, S., Marandat, B., Remy, J. A., Ringeade, M., Sig., B., & Vianey, M. (1992). a biochronologie mammalienne du Pal.og.ne au Nord et au Sud des Pyr.n.es; .tat de la question [Mammalian biochronology from the Paleogene North and South of the Pyrenees: An updated survey.

Sutra, E., Manatschal, G., Mohn, G., & Unternehr, P. (2013). Quantification and restoration of extensional deformation along the Western Iberia and Newfoundland rifted margins. Geochemistry, Geophysics, Geosystems, 14(8), 2575–2597.

Sztrákos, K., Gély, J.P., Blondeau, A., Müller, C., 1998. L'Eocéne du Bassin sud-aquitain: lithostratigraphie, biostratigraphie et analyse séquentielle. Géol. France 57–105.

Tambareau, Y. (1972). Thanétien supérieur et Ilerdien Inférieur des Petites Pyrénées, du Plantarnel et des Chaînons andois. Laboratoire de Géologie-Petrologie, Université Paul Sabatier.

Tambareau, Y. (1976). Sur l'âge des dernières assises marines de l'Eocène sous-pyrénéen au mur du Poudingue de Palassou. CR Somm. Soc. Géol. Fr, 18, 210–212.

Tambareau, Y., Crochet, B., Villatte, J., & Deramond, J. (1995). Evolution tectono-sedimentaire du versant nord des Pyrenees centre-orientales au Paleocene et a l'Eocene inferieur. Bulletin de La Societé Géologique de France, 166(4), 375–387.

Ter Voorde, M., Cloetingh, S., 1996. Numerical modelling of extension in faulted crust: effects of localized and regional deformation on basin stratigraphy. Geol. Soc. Lond. Spec. Publ. 99, 283–296.

Ternois, S., Odlum, M., Ford, M., Pik, R., Stockli, D., Tibari, B., Vacherat, A., & Bernard, V. (2019). Thermochronological evidence of early orogenesis, eastern Pyrenees, France. Tectonics.

Thomas, W. (2011). Detrital-zircon geochronology and sedimentary provenance. Lithosphere, 3(4), 304–308.

Thomson, K., Stockli, D., Clark, J., Puigdefàbregas, C., & Fildani, A. (2017). Detrital zircon (U-Th)/(He-Pb) double-dating constraints on provenance and foreland basin evolution of the Ainsa Basin, south-central Pyrenees, Spain. Tectonics, 36(7), 1352–1375.

Torsvik, T., & Cocks, R. (2016). Earth History and Palaeogeography. Cambridge University Press.

Tugend, J., Manatschal, G., & Kusznir, N. J. (2015). Spatial and temporal evolution of hyperextended rift systems: Implication for the nature, kinematics, and timing of the Iberian-European plate boundary. Geology, 43(1), 15–18.

Tugend, J., Manatschal, G., Kusznir, N. J., Masini, E., Mohn, G., & Thinon, I. (2014). Formation and deformation of hyperextended rift systems: Insights from rift domain mapping in the Bay of Biscay-Pyrenees. Tectonics, 33(7), 1239–1276.

Uzel, J., Nivière, B. and Lagabrielle, Y. (2020) 'Fluvial Incisions in the North-Western Pyrenees (Aspe Valley): Dissection of a Former Planation Surface and Some Tectonic Implications'. Terra Nova, 32(1), pp. 11–22.

Uzel, J., Nivière, B. and Lagabrielle, Y. (2019) 'Fluvial Incisions in the Western Pyrenees (Aspe Valley): Insights on the Modes of Dissection of a Former Planation Surface.' In Geophysical Research Abstracts.

Vacherat, A. (2014). Inversion d'une marge hyper-amincie: Contexte thermo-cinématique et interactions tectonique-érosion au Nord des Pyrénées [Université Pierre et Marie Curie-Paris VI]. https://tel.archives-ouvertes.fr/tel-01127615/

Vacherat, A., Mouthereau, F., Pik, R., Bellahsen, N., Gautheron, C., Bernet, M., Daudet, M., Balansa, J., Tibari, B., & Pinna Jamme, R. (2016). Rift-to-collision transition recorded by tectonothermal evolution of the northern Pyrenees. Tectonics, 35(4), 907–933.

Vacherat, A., Mouthereau, F., Pik, R., Huyghe, D., Paquette, J.-L., Christophoul, F., Loget, N., & Tibari, B. (2017). Rift-to-collision sediment routing in the Pyrenees: A synthesis from sedimentological, geochronological and kinematic constraints. Earth-Science Reviews, 172, 43–74.

Van Actherbergh, E. (2001). Data reduction software for LA-ICP-MS. Laser Ablation-ICP-Mass Spectrometry in the Earth Sciences: Principles and Applications, 239–243.

Van Lichtervelde, M., Grand'Homme, A., de Saint-Blanquat, M., Olivier, P., Gerdes, A., Paquette, J.-L., Melgarejo, J. C., Druguet, E., & Alfonso, P. (2017). U-Pb geochronology on zircon and columbite-group minerals of the Cap de Creus pegmatites, NE Spain. Mineralogy and Petrology, 111(1), 1–21.

Vauchez, A., Clerc, C., Bestani, L., Lagabrielle, Y., Chauvet, A., Lahfid, A., & Mainprice, D. (2013). Preorogenic exhumation of the North Pyrenean Agly massif (Eastern Pyrenees-France). Tectonics, 32(2), 95–106.

Verges and Garcia-Senz. (2001). Mesozoic evolution and Cainozoic inversion of the Pyrenean Rift (Editions du Muséum, Vol. 186, pp. 187–212).

Vergés, J., Fernàndez, M., & Martìnez, A. (2002). The Pyrenean orogen: Pre-, syn-, and post-collisional evolution. Journal of the Virtual Explorer, 08. https://doi.org/10.3809/jvirtex.2002.00058

Vergés, J., Marzo, M., Santaeulària, T., Serra-Kiel, J., Burbank, D. W., Muñoz, J. A., & Giménez-Montsant, J. (1998). Quantified vertical motions and tectonic evolution of the SE Pyrenean foreland basin. Geological Society, London, Special Publications, 134(1), 107–134.

Vergés, J., Millán, H., Roca, E., Muñoz, J. A., Marzo, M., Cirés, J., Den Bezemer, T., Zoetemeijer, R., & Cloetingh, S. (1995). Eastern Pyrenees and related foreland basins: Pre-, syn-and post-collisional crustal-scale cross-sections. Marine and Petroleum Geology, 12(8), 903–915.

Vermeesch, P. (2018). IsoplotR: A free and open toolbox for geochronology. Geoscience Frontiers, 9(5), 1479–1493.

Vermeesch, P., Seward, D., Latkoczy, C., Wipf, M., Günther, D., & Baur, H. (2007). α-Emitting mineral inclusions in apatite, their effect on (U–Th)/He ages, and how to reduce it. Geochimica et Cosmochimica Acta, 71(7), 1737–1746. https://doi.org/10.1016/j.gca.2006.09.020

Visser, R. L. M. (1992). Variscan extension in the Pyrenees. Tectonics, 11, NO. 6, 1369–1384.

Vissers, R. L. M., & Meijer, P. T. (2012a). Iberian plate kinematics and Alpine collision in the Pyrenees. Earth-Science Reviews, 114(1–2), 61–83.

Vissers, R. L. M., & Meijer, P. T. (2012b). Mesozoic rotation of Iberia: Subduction in the Pyrenees? Earth-Science Reviews, 110(1–4), 93–110.

Vitrac-Michard, A., & Allègre, C. (1975). 238 U-206 Pb, 235 U-207 Pb, systematics on Pyrenean basement. Contributions to Mineralogy and Petrology, 51(3), 205–212.

Von Blanckenburg, F. (2006). The control mechanisms of erosion and weathering at basin scale from cosmogenic nuclides in river sediment. Earth and Planetary Science Letters, 242(3–4), 224–239.

von Raumer, J., Stampfli, G., & Bussy, F. (2003). Gondwana-derived microcontinents—The constituents of the Variscan and Alpine collisional orogens. Tectonophysics, 365(1–4), 7–22.

Wagner, G. A. (1968). Fission track dating of apatites. Earth and Planetary Science Letters, v. 4, no. 5, 411–415,. https://doi.org/10.1016/0012- 821X(68)90072-1.

Wagner, G. A. (1992). Fission Track Dating–Kluwer. Dordrecht.

Watson, B., Wanser, K., & Farley, K. (2010). Anisotropic diffusion in a finite cylinder, with geochemical applications. Geochimica et Cosmochimica Acta, 74(2), 614–633. https://doi.org/10.1016/j.gca.2009.10.013

Wayne, D., Sinha, A. K., & Hewitt, D. (1992). Differential response of zircon U−Pb isotopic systematics to metamorphism across a lithologic boundary: An example from the Hope Valley Shear Zone, southeastern Massachusetts, USA. Contributions to Mineralogy and Petrology, 109(3), 408–420. https://doi.org/10.1007/BF00283328

Wayne, D., & Sinha, K. (1988). Physical and chemical response of zircons to deformation. Contributions to Mineralogy and Petrology, 98(1), 109–121. https://doi.org/10.1007/BF00371915

Weber, W. J., Wald, J. W., & Matzke, H. (1986). Effects of self-radiation damage in Cm-doped Gd2Ti2O7 and CaZrTi2O7. Journal of Nuclear Materials, 138(2–3), 196–209.

Weisberg, W., Metcalf, J., & Flowers, R. (2018). Distinguishing slow cooling versus multiphase cooling and heating in zircon and apatite (U-Th)/He datasets: The case of the McClure Mountain syenite standard. Chemical Geology, 485, 90–99.

Weissmann, G. S., Hartley, A. J., Nichols, G. J., Scuderi, L. A., Olson, M., Buehler, H., & Banteah, R. (2010). Fluvial form in modern continental sedimentary basins: Distributive fluvial systems. Geology, 38(1), 39–42. https://doi.org/10.1130/G30242.1

Wendt, I., & Carl, C. (1991). The statistical distribution of the mean squared weighted deviation. Chemical Geology: Isotope Geoscience Section, 86(4), 275–285.

Wetherill, G. (1956). Discordant uranium-lead ages, I. Eos, Transactions American Geophysical Union, 37(3), 320–326. https://doi.org/10.1029/TR037i003p00320

Whipple, K. (2009). The influence of climate on the tectonic evolution of mountain belts. Nature Geoscience, 2(2), 97.

Whitchurch, A. L., Carter, A., Sinclair, H. D., Duller, R. A., Whittaker, A. C., & Allen, P. A. (2011). Sediment routing system evolution within a diachronously uplifting orogen: Insights from detrital zircon thermochronological analyses from the South-Central Pyrenees. American Journal of Science, 311(5), 442–482.

Wiedenbeck, M., Hanchar, J., Peck, W., Sylvester, P., Valley, J., Whitehouse, M., Kronz, A., Morishita, Y., Nasdala, L., & Fiebig, J. (2004). Further characterisation of the 91500 zircon crystal. Geostandards and Geoanalytical Research, 28(1), 9–39.

Wildman, M., Brown, R., Beucher, R., Persano, C., Stuart, F., Gallagher, K., Schwanethal, J., Carter, A., 2016. The chronology and tectonic style of landscape evolution along the elevated Atlantic continental margin of South Africa resolved by joint apatite fission track and (U-Th-Sm)/He thermochronology. Tectonics 35, 511–545.

Willett, C., Fox, M., & Shuster, D. (2017). A helium-based model for the effects of radiation damage annealing on helium diffusion kinetics in apatite. Earth and Planetary Science Letters, 477, 195–204.

Willett, S., Beaumont, C., & Fullsack, P. (1993). Mechanical model for the tectonics of doubly vergent compressional orogens. Geology, 21(4), 371–374.

Winn, C., Karlstrom, K., Shuster, D., Kelley, S., & Fox, M. (2017). 6 Ma age of carving Westernmost Grand Canyon: Reconciling geologic data with combined AFT,(U–Th)/He, and 4He/3He thermochronologic data. Earth and Planetary Science Letters, 474, 257–271.

Wolf, R. A., Farley, K. A., & Kass, D. M. (1998). Modeling of the temperature sensitivity of the apatite (U–Th)/He thermochronometer. Chemical Geology, 148(1), 105–114. https://doi.org/10.1016/S0009-2541(98)00024-2

Wolf, R. A., Farley, K. A., & Silver, L. T. (1996). Helium diffusion and low-temperature thermochronometry of apatite. Geochimica et Cosmochimica Acta, 60(21), 4231–4240.

Wopenka, B., & Pasteris, J. D. (1993). Structural characterization of kerogens to granulite-facies graphite: Applicability of Raman microprobe spectroscopy. American Mineralogist, 78(5–6), 533–557.

Worden, R., & Morad, S. (2009). Clay mineral cements in sandstones (Vol. 19). John Wiley & Sons.

Yang, W., Jolivet, M., Dupont-Nivet, G., Guo, Z., Zhang, Z., & Wu, C. (2013). Source to sink relations between the Tian Shan and Junggar Basin (northwest China) from Late Palaeozoic to Quaternary: Evidence from detrital U-Pb zircon geochronology. Basin Research, 25(2), 219–240.

Yelland, A. J. (1991). Thermo-tectonics of the Pyrenees and Provence from fission track studies. Unpublished PhD, Thesis, Birkbeck College, University of London.

Zeitler, P. K., Herczeg, A. L., McDougall, I., & Honda, M. (1987). U-Th-He dating of apatite: A potential thermochronometer. Geochimica et Cosmochimica Acta, 51(10), 2865–2868.

Zeyen, H., Fernàndez, M., 1994. Integrated lithosphericmodelingcombiningthermal, gravity, and local isostasyanalysis' Application to the NE SpanishGeotransec. J. Geophys. Res. 99, NO. B9, 18,089-18,102.

Zwart, H. (1962). On the determination of polymetamorphic mineral associations, and its application to the Bosost area (Central Pyrenees). Geologische Randschau, 38–65.

Zwart, H. J., & De Sitter, L. U. (1979). The geology of the Central Pyrenees. http://dare.uva.nl/cgi/arno/show.cgi?fid=549278

université PARIS-SACLAY
ÉCOLE DOCTORALE
Sciences mécaniques et énergétiques, matériaux et géosciences (SMEMAG)

Titre : Traçage des sédiments dans les séries syn-orogéniques du Bassin d'Aquitaine

Mots clés : Corbières, thermochronologie basse température, géochronologie, routage des sédiments

Résumé: La dynamique de formation d'une chaîne de montagne peut être reconstruite à partir de l'étude des bassins réceptacles des produits d'érosion. Les travaux présentés ont été réalisés dans la partie orientale du Bassin d'Aquitaine (Corbières), à partir de l'étude de la série de Palassou. Ces sédiments traduisent une phase d'érosion majeure des reliefs, accompagnant la continentalisation des bassins au cours de l'Yprésien et la période de raccourcissement principal de l'orogenèse pyrénéenne. Trois unités tectono-stratigraphiques ont été défini dans cette série : l'unité 1 - Yprésien supérieur-Lutétien – caractérisée par la présence de galets Méso-Cénozoïques, l'unité 2 – Bartonien – caractérisée par la présence des galets de socle et l'unité 3 – Priabonien- caractérisée par la présence à nouveau de galets Méso-Cénozoïques. L'objectif de cette thèse est de comprendre le mode de remplissage du bassin d'avant-pays nord pyrénéen et son évolution au cours de l'Éocène. Ceci permettra d'appréhender la formation des reliefs à l'intérieur de la chaîne et de caractériser les différentes sources d'apport. Trois approches ont été utilisées pour reconstruire le routage des sédiments dont la première est l'étude sédimentaire et la caractérisation des environnements de dépôts des deux premières unités. Les résultats obtenus montrent l'identification de quatre séquences de remplissage sédimentaire dans l'unité 1, dont l'essentiel s'est déposé dans le synclinal de Talairan jusqu'à son débordement au cours du dépôt de la troisième séquence. Ceci amène à interpréter le synclinal de Talairan comme un bassin en piggy back. La deuxième approche est la thermochronologie basse température appliquée sur des clastes de granites issus de l'unité 2. Les résultats de traces de fission sur apatite montrent des âges équivalents à l'âge de dépôts et plus jeunes d'est en ouest alors que les résultats de (U-Th-Sm)/He sur apatite varient de plus vieux à plus jeune que les âges traces de fission sur apatite. La modélisation thermique de ces données indique un réchauffement post-Bartonien, traduisant une série sédimentaire plus épaisse au moment du dépôt puis partiellement érodée. La phase d'érosion est estimée comme pré-Langhienne suite aux résultats de modélisation thermique et des contraintes stratigraphiques. La troisième approche utilisée au cours de cette thèse est la datation U/Pb sur zircon. Des échantillons de matrice de conglomérat ainsi que des galets de granite issus des trois unités ont fait l'objet d'étude par cette approche. Les résultats obtenus montrent un signal Varisque majeur. Ils ont été couplés avec des analyses de spectroscopie Raman afin de mesurer des pics de températures, et des directions de paléo-courant pour caractériser les sources des sédiments pour chaque unité. Les dépôts de l'unité 1 sont issues de la Zone Nord Pyrénéenne. Les dépôts de l'unité 2 ont comme source la Zone Axiale des Pyrénées alors que les dépôts de l'unité 3 présentent un spectre d'âges assez large dont la source est la partie orientale et centrale des Pyrénées. Ces résultats ont permis de reconstruire le cheminement des sédiments dans les Corbières.

Université Paris-Saclay
Espace Technologique / Immeuble Discovery
Route de l'Orme aux Merisiers RD 128 / 91190 Saint-Aubin, France

ÉCOLE DOCTORALE
Sciences mécaniques et énergétiques, matériaux et géosciences (SMEMAG)

Title : Sediment routing in the syn-orogenic series of the Aquitaine Basin

Keywords : Corbières region, low temperature thermochronology, geochronology, sediment routing.

Abstract : Characterizing the evolution of the syn-orogenic sediment routing system improves our understanding of the development of mountain belts. The North Pyrenean foreland basin evolved from underfilled to overfilled during the Eocene time. The deposited syn-orogenic conglomerate, known as Palassou series, recorded the exhumation and the denudation of the mountain belt. Three tectono-sedimentary units with different facies characteristics, lateral extension and petrographic content have been identified in the Corbières region (east of the Aquitaine Basin): The first unit - late Ypresian-Lutetian - contains clasts from the Meso-Cenozoic sedimentary cover; the second unit -Bartonian – contents are of magmatic and metamorphic origin clasts and the third unit - Priabonian – contents are similar to the first unit. Clasts origins and sediment routing from source to sink are poorly constrained. This thesis is focused on the understanding of the infilling of the Corbières region during the Eocene. Multiple approaches have been combined together to reconstruct the sediment routing system during this time. The characterization of the depositional environments for the unit 1 has led to the definition of four sequences of sediment infilling that overfilled the Talairan syncline (southern Corbières) and contribute to the exportation of sediments westward. Analysis showed that the Talairan syncline was acting as a piggy-back basin during the deposition of the unit 1 sediments. Low temperature thermochronology data obtained for granite clasts from the unit 2 showed apatite fission track ages more recent from east to west and dispersed AHe ages. Inverse thermal history modelling indicates that the Corbières region experienced a post-deposition (post-Bartonian) kilometric burial and a subsequent Miocene exhumation characterized by erosion of detrital sediments. Zircon U/Pb geochronology applied for conglomerate matrix and granite clasts from the units 1, 2 and 3 allowed the identification of the source areas of the deposited sediments. Most of the obtained ages are Variscan. Results are coupled to Raman spectroscopy analysis and paleocurrent measurements in order to determine the drainage area for each unit. The unit 1 sediments are fed from the North Pyrenean Zone. The unit 2 sediments are sourced from the Axial Zone and the unit 3 sediments show multiple sources from the eastern and central Pyrenees. Obtained results allowed the reconstruction of the sediment routing system in the Corbières basin during the Eocene.

Université Paris-Saclay
Espace Technologique / Immeuble Discovery
Route de l'Orme aux Merisiers RD 128 / 91190 Saint-Aubin, France